Imperial College London

cep Centre for Environmental Policy

A framework for recognising the value proposition of CO_2 capture and storage technologies

Renato Manuel Pereira Cabral
Centre for Environmental Policy
Faculty of Natural Sciences
Imperial College London

March 5, 2021

Submitted in part fulfilment of the requirements for the degree of Doctor of Philosophy from the Faculty of Natural Sciences of Imperial College London

Supervisor: Dr. Niall Mac Dowell
Funding body: Natural Environment Research Council, Science and Solutions for a Changing Planet Doctoral Training Program
Examiners: Prof. Paul Fennell, Dr. Solomon Brown

Declaration of Originality

I hereby certify that all the material in this work is my own and all information contained within that is not my own is properly acknowledged.

Copyright Declaration

The copyright of this thesis rests with the author. Unless otherwise indicated, its contents are licensed under a Creative Commons Attribution-Non Commercial-No Derivatives 4.0 International Licence (CC BY-NC-ND). Under this licence, you may copy and redistribute the material in any medium or format on the condition that; you credit the author, do not use it for commercial purposes and do not distribute modified versions of the work. When reusing or sharing this work, ensure you make the licence terms clear to others by naming the licence and linking to the licence text. Please seek permission from the copyright holder for uses of this work that are not included in this licence or permitted under UK Copyright Law.

Abstract

Carbon capture and storage (CCS) technologies are considered the most cost-effective means of curbing anthropogenic carbon dioxide (CO_2) emissions from both the power and industrial sectors at a system level. Indeed, several studies consider CCS essential to limit global warming below 1.5 °C by 2050 and curb the impacts of climate change. However, this technology is prohibitively expensive without government subsidies relative to unabated plants.

In this thesis, oxy-fuel combustion was used as a model CCS technology to develop cost-reduction frameworks. Process inefficiencies were analysed using the first and second laws of thermodynamics and the process was improved via a heat integration strategy. This strategy improved the efficiency of an oxy-combustion process whilst reducing its capital cost.

A solvent-based capture unit was proposed to substitute the gas processing unit (GPU) and its key performance indicators were compared with the traditional GPU. However, cryogenic methods to process the flue gas from oxy-combustion are still superior, providing comparable capture rates and CO_2 purity at lower costs.

A framework to value negative emissions from bioenergy with CCS (BECCS) was proposed to simultaneously decarbonise the power and industrial sectors. However, the high CO_2 price required to generate profits from auctioning negative emission credits makes this framework unlikely to be implemented.

Lastly, the flexible operation of a CCS plant to take advantage of the daily electricity price variation was evaluated. The flexible operation of a plant with liquid oxygen storage depends upon the region it operates as electricity price fluctuation plays a critical role in its profitability.

There is potential to significantly reduce CCS costs by the concurrent application of several approaches. The general nature of most of the framework developed in this thesis means that they can be applied in other CCS processes, such as post- or pre-combustion capture.

Acknowledgements

I want to thank Dr Niall Mac Dowell for taking me as his PhD student and allowing me to pursue this thesis. I want to mention his enormous patience in dealing with my perpetual delay in delivering results. These delays occurred because I was stuck with small details that obscured my understanding of the larger picture. I am also thankful for your guidance towards the right path, giving me insights into CCS and always challenging me towards more remarkable achievements. It was a great honour working alongside you trying to contribute to solving one of the world's greatest crises. I am eternally grateful for that.

I want to thank the group that I belonged to during my PhD, particularly to Dr Mai Bui for always helping me with new ideas and revising our manuscripts; Patrick Brandl for dragging me for lunch, even when it only comprised of instant noodles, and wake me from my general state of aloofness; Habiba Daggash for having all those great conversation topics; and Mayte Mota for helping me out during my first years.

I want to thank the Grantham Institute for all the support they gave and the seemingly endless DTP training (I actually enjoyed quite a few). The three-day residential training was exciting because I had the opportunity to hang out with the people from my cohort and pick up a few soft skills.

I am infinitely indebted to my dear girlfriend, Márcia Boura, for taking up with my ill-temper since we first met. Without you, doing this PhD would have never been possible, as you served both as a source of inspiration and as an anchor, preventing me from drifting during turbulent times.

I want to acknowledge my family for always being there for me, even when I was nowhere to be found. Lastly, a big thank you to my parents for their unconditional love and support throughout my life.

Contents

Abstract **4**

Acknowledgements **6**

List of Figures **12**

List of Tables **17**

Nomenclature **21**

1 Introduction **24**
1.1 Background on climate change 24
1.2 Carbon capture and storage 26
1.2.1 Pre-combustion CO_2 capture 26
1.2.2 Post-combustion CO_2 capture 27
1.2.3 Oxy-fuel combustion CO_2 capture 27
1.2.4 Bioenergy with CCS 28
1.2.5 CO_2Storage 28
1.3 Research Goal and Structure 28

2 Literature Review **31**
2.1 Oxy-combustion overview 31
2.2 Air Separation Unit 32
2.2.1 Cryogenic air separation units 35
2.2.2 Adsorptive Air Separation 40
2.2.3 Membrane technology 41
2.2.4 Chemical production of oxygen 43
2.3 Power plants 44
2.3.1 Unabated coal power plants 44
2.3.2 Oxy-fuel combustion 51
2.3.3 Opportunities for improvement 61
2.4 Gas Processing Unit 61
2.5 Negative emission technologies 64

2.5.1 Oxy-combustion of biomass 65
2.6 Exergy 66
2.7 Summary 67

3 Methodology **68**
3.1 Air Separation Unit 68
3.1.1 Compressors and pumps 68
3.1.2 Heat Exchangers 69
3.1.3 Multiple-Stream Heat Exchangers 70
3.1.4 Distillation 70
3.1.5 Double Column Design 71
3.2 Power plant 74
3.2.1 Coal combustion 76
3.2.2 Air Pre Heater 81
3.2.3 Boiler 81
3.3 Gas processing unit 83
3.4 Determining power plant efficiency 85
3.5 Techno-economic analysis 86

4 Exergy analysis **88**
4.1 Introduction 88
4.2 Methods 89
4.2.1 General model 89
4.2.2 Power plant 89
4.2.3 Oxy-combustion 89
4.2.4 Heat integration 91
4.2.5 Thermodynamics analysis 92
4.2.6 Exergy analysis 93
4.3 Results and Discussion 94
4.3.1 Oxy-combustion 94
4.3.2 Simulation and model validation 94
4.3.3 Thermodynamic analysis 95
4.3.4 Process improvement and heat integration 96
4.3.5 Techno-economic analysis 104
4.4 Conclusions 105

5 Solvent-based GPU **107**
5.1 Introduction 107
5.2 Model description 109
5.2.1 Oxy-combustion model 109

5.2.2 EDEA . . . 110
5.2.3 Economic model . . . 111
5.3 Results . . . 111
5.3.1 Model output . . . 111
5.3.2 Heat requirement leads to heat integration . . . 112
5.3.3 Dropping below the power consumption baseline . . . 112
5.3.4 Efficiency and CAPEX . . . 114
5.3.5 Reformulating the analysis: efficiency and LCOE . . . 114
5.3.6 Potential of oxy-solvent hybrid CCS . . . 117
5.4 Conclusion . . . 119

6 Oxy-BECCS auctioning NEC 122
6.1 Introduction . . . 122
6.1.1 Industrial CO_2 emissions . . . 123
6.2 Framework . . . 123
6.2.1 Oxy-BECCS model description . . . 123
6.2.2 Achieving negative emissions . . . 125
6.2.3 Fuel . . . 127
6.2.4 Economic model . . . 127
6.2.5 The cost of electricity . . . 127
6.2.6 CO_2 avoided costs . . . 128
6.3 Results and discussion . . . 128
6.3.1 Model validation . . . 128
6.3.2 Economic impact of BECCS-generated electricity . . . 130
6.3.3 Potential of NECs to offset global industrial emissions . . . 132
6.3.4 How supply chain emissions impact the costs of BECCS . . . 133
6.3.5 Negative emission credits . . . 134
6.3.6 BECCS and industry . . . 136
6.4 Conclusions . . . 136

7 Flexible oxy-combustion 138
7.1 Introduction . . . 138
7.2 Model development . . . 140
7.2.1 Load changing rate . . . 140
7.2.2 Daily electricity price . . . 140
7.2.3 Storage tank design . . . 142
7.2.4 Economic evaluation . . . 145
7.3 Results and Discussion . . . 146
7.3.1 Scheduling liquid oxygen storage . . . 146

7.3.2 Sensitivity analysis . . . 149
7.3.3 To store, or not to store? . . . 158
7.4 Conclusions . . . 158

8 Conclusions and future work **160**

Bibliography **165**

A Materials for components **205**

B Simulations **208**
B.1 Single-column design . . . 208
B.2 Double-column design . . . 210
B.3 Air-fired power plant . . . 213
B.4 GPU . . . 218
B.5 Oxy-combustion power plant . . . 220
B.5.1 Without heat integration . . . 220
B.5.2 With heat integration . . . 264
B.5.3 With heat integration and smaller ASU . . . 302
B.6 EDEA for oxy-combustion . . . 332
B.6.1 Scenarios 1 and 2 . . . 332
B.6.2 Scenarios 3, 4, 5, and 6 . . . 344
B.6.3 Scenarios 7 and 8 . . . 366

C Validation exercises **380**

D Sensitivity analysis **382**

E Techno-economic analysis **388**
E.1 CEPCI . . . 388
E.2 ASU . . . 388
E.3 GPU . . . 388

F Flexibility **390**
F.0.1 Coal-fired . . . 390
F.0.2 Biomass-fired . . . 401

List of Figures

2.1 Process Flow Diagram (PFD) of oxy-coal combustion 33
2.2 Specific power consumption of oxygen production via pressure swing adsorption (PSA) and cryogenic distillation 34
2.3 PFD of a double column cryogenic ASU for gaseous oxygen production . 35
2.4 Variation of liquid and vapour compositions for the O_2/N_2 and O_2/Ar at 1.01 and 5 bar. 38
2.5 PFD of cryogenic oxygen storage 39
2.6 Schematic representation of an ITM 42
2.7 Thermodynamic principles of a Rankine cycle 47
2.8 Evolution of ferritic steels for boilers 50
2.9 Performance of improved combustion technologies 51
2.10 Simplified PFD of a pulverised coal oxy-combustion power plant 59
2.11 Simplified PFD of a double-flash GPU 63
2.12 Simplified PFD of a cryogenic distillation GPU 64

4.1 Methodology for first and second law analysis 90
4.2 Process Flow Diagram (PFD) of the oxy-combustion power plant with heat integration 91
4.3 Grand composite curve of the oxy-combustion process without heat integration. 95
4.4 Effect of thermodynamic efficiency on ASU, GPU, and boiler 96
4.5 Potential process efficiency 97
4.6 Grand composite curve of the oxy-combustion process with heat integration. 98
4.7 Grand composite curve of the oxy-combustion process with heat integration and smaller ASU. 99
4.8 Exergy destruction of the boiler in oxy-combustion process before and after heat integration 100
4.9 Exergy destruction of feedwater heating train in oxy-combustion process before and after heat integration 101

4.10 Exergy destruction of the ASU in the oxy-combustion process before and after heat integration . . . 103
4.11 Exergy destruction of the GPU in the oxy-combustion process before and after heat integration . . . 104
4.12 Exergy destruction of the oxy-combustion process before and after heat integration . . . 105
4.13 Efficiency vs CAPEX . . . 106

5.1 Simplified process flow diagram (PFD) of the oxy-combustion process with a solvent-based GPU . . . 108
5.2 Reaction of EDEA with CO_2. Applying pressure favours the direct reaction to form the zwitterion EDEA-CO_2. Adding heat and reducing pressure favours the reverse reaction, releasing CO_2 and regenerating EDEA. 109
5.3 Specific electricity consumption of the GPU as a function of flash inlet temperature and pressure drop . . . 113
5.4 PFD of the solvent-based GPU with and without heat integration . . . 114
5.5 Specific power consumption broken down into its components . . . 116
5.6 Net efficiency plotted against CAPEX for several process configurations . 117
5.7 OPEX for different case scenarios . . . 118
5.8 EDEA make-up is plotted against flash inlet temperature and pressure drop 119
5.9 Net efficiency is plotted against LCOE for several configurations . . . 120
5.10 LCOE vs EDEA cost . . . 121

6.1 Global distribution of anthropogenic CO_2 emissions . . . 124
6.2 Amount of CO_2 emitted annually in the UK from the industrial sector . . 125
6.3 Process flow diagram of the proposed approach to offset industrial CO_2 emission . . . 126
6.4 Validation of the oxy-combustion model . . . 129
6.5 Normal probability density function (PDF) of LCOE . . . 130
6.6 Effect of biomass co-fired . . . 131
6.7 Effect of biomass co-firing (%) and supply chain emissions . . . 133
6.8 Effect of NEC and wood chips co-fired . . . 134

7.1 PFD of oxy-combustion with LOX storage for both schedules studied herein. 141
7.2 Daily electricity price variation of a representative winter month, extracted from Nord Pool group. The bars represent the average price for that time period with the corresponding standard deviation. . . . 143
7.3 Daily electricity price variation of a representative summer month, extracted from Nord Pool group. The bars represent the average price for that time period with the corresponding standard deviation. . . . 144

7.4 LOX storage schedules simulated 146
7.5 Amount of oxygen produced in the ASU and specific power consumption as function of the amount of LOX extracted from the LP column 147
7.6 Cumulative profit levelised to the daily power output 148
7.7 Biomass price and day electricity price variation effect on NPV for double discharge 149
7.8 Biomass price and day electricity price variation effect on NPV for single discharge 149
7.9 Biomass price and day electricity price variation effect on NPV difference for double discharge 150
7.10 Biomass price and day electricity price variation effect on NPV difference for single discharge 150
7.11 Biomass price and night electricity price variation effect on NPV for double discharge 151
7.12 Biomass price and night electricity price variation effect on NPV for single discharge 152
7.13 Biomass price and night electricity price variation effect on NPV difference for double discharge 152
7.14 Biomass price and night electricity price variation effect on NPV difference for single discharge 153
7.15 Day and night electricity price variation effect on NPV for double discharge153
7.16 Day and night electricity price variation effect on NPV for single discharge154
7.17 Day and night electricity price variation effect on NPV difference for double discharge 155
7.18 Day and night electricity price variation effect on NPV difference for single discharge 155
7.19 Off-peak capacity factor and peak electricity price variation effect on NPV for double discharge 156
7.20 Off-peak capacity factor and peak electricity price variation effect on NPV for single discharge 156
7.21 Off-peak capacity factor and peak electricity price variation effect on NPV difference for double discharge 157
7.22 Off-peak capacity factor and peak electricity price variation effect on NPV difference for single discharge 157

B.1 Process Flow Diagram of a Single Column Cryogenic Air Separation Unit 209
B.2 Process Flow Diagram of a Double Column Cryogenic Air Separation Unit 210
B.3 Process Flow Diagram of a Coal Power Plant 215

B.4 CO_2 compression and purification unit with a 6-stage distillation colum PFD as described by Kolster. 218
B.5 Oxy-fuel combustion process developed according to the works of Spero and Stanger. 220
B.6 Oxy-fuel combustion process after heat integration. 264
B.7 PFD of the EDEA-based GPU for scenarios 1 and 2. 332
B.8 PFD of the EDEA-based GPU for scenarios 3, 4, 5, and 6. 344
B.9 PFD of the EDEA-based GPU for scenarios 7, and 8. 366

D.1 Effect of booster outlet pressure on power consumption and O_2 flow reduction. 382
D.2 Actual work from initial simulation and optimised simulation against minimum thermodynamic work required for air separation 383
D.3 Fuel savings potential based on air inlet temperature. 383
D.4 Adiabatic flame temperature and fraction of O_2 in flue gas based on air to fuel ratio. 384
D.5 Minimum thermodynamic separation work of CO_2 from a gas mixture for different CO_2 concentrations in the flue gas (FG). 384
D.6 Sensitivity analysis on flue gas amount sent to the GPU. 385
D.7 Effect of cooling water sent to DCC on flue gas temperature leaving the DCC and power plant net efficiency. 386
D.8 Effect of O_2 purity on oxidizer and GPU process on LCOE. 387

F.1 Coal price and day electricity price variation effect on profit for single discharge 390
F.2 Coal price and day electricity price variation effect on profit difference for single discharge 391
F.3 Coal price and day electricity price variation effect on NPV for single discharge 392
F.4 Coal price and day electricity price variation effect on NPV difference for single discharge 393
F.5 Coal price and night electricity price variation effect on profit for single discharge 394
F.6 Coal price and night electricity price variation effect on profit difference for single discharge 395
F.7 Coal price and night electricity price variation effect on NPV for single discharge 396
F.8 Coal price and night electricity price variation effect on NPV difference for single discharge 397

F.9 Day and night electricity price variation effect on profit for single discharge 398
F.10 Day and night electricity price variation effect on profit difference for single discharge 399
F.11 Day and night electricity price variation effect on NPV for single discharge 400
F.12 Day and night electricity price variation effect on NPV difference for single discharge 401
F.13 Biomass price and day electricity price variation effect on profit difference for double discharge 401
F.14 Biomass price and day electricity price variation effect on profit difference for single discharge 402
F.15 Biomass price and night electricity price variation effect on profit difference for double discharge 402
F.16 Biomass price and night electricity price variation effect on profit difference for single discharge 402
F.17 Day and night electricity price variation effect on profit difference for double discharge 403
F.18 Day and night electricity price variation effect on profit difference for single discharge 403

List of Tables

2.1 Boiling temperature (T_b) of air components at 1.01 bar and 5 bar. 37
2.2 Effect of fuel properties on plant's performance. 46
2.3 Kinetic parameters of gasification of short rotation coppice. 55
2.4 Amount of global primary energy from sustainable biomass 66

3.1 Feed composition and operating parameters of the ASU. 72
3.2 ASU validation exercise 73
3.3 Parameters to simulate the grinder 77
3.4 Typical compositions of coal ash. 79
3.5 Turbine bleed amount 82
3.6 Fuel parameters 83
3.7 Boiler and flue gas pre-treatment operating conditions. 83
3.8 Operating conditions of the boiler simulated in this thesis. 84
3.9 Operating conditions of the GPU simulated in this thesis. 85
3.10 Assumptions used for the techno-economic analysis of the proposed framework. 87

4.1 Turbine bleed fractions after heat integration 92
4.2 Results comparison 94
4.3 Parasitic energy losses from ASU, GPU, and power plant 96

5.1 Operating conditions of the solvent-based GPU 110
5.2 Chemical and physical properties of EDEA 110
5.3 Breakdown of the specific power consumption (kWh/t_{CO_2}) of scenario 1. 111
5.4 Pressure drop in the flash unit and rich stream outlet temperature in the heat exchangers. 115

6.1 CAPEX, OPEX, fuel consumption cost, LCOE, and LCOC for oxy-combustion using coal and wood-chips. 132

7.1 Daily electricity price variation 142
7.2 Assumptions required for the storage tank design. 142

A.1 Possible materials used in the construction of boiler tubes, headers, and pipings. 206
A.2 Possible materials used in the construction of steam turbine components. 207

B.1 Stream tables of the oxy-combustion process without heat integration. . 233
B.2 Heat tables of the oxy-combustion process without heat integration. . . . 260
B.3 Power table of the oxy-combustion process without heat integration. . . 261
B.4 Overall carbon balance of the oxy-combustion process without heat integration. 262
B.5 Energy balance of the oxy-combustion process without heat integration. Energy in. 262
B.6 Energy balance of the oxy-combustion process without heat integration. Energy out. 263
B.7 Stream tables of the oxy-combustion process with heat integration. . . . 274
B.8 Heat tables of the oxy-combustion process with heat integration. 299
B.9 Power tables of the oxy-combustion process with heat integration. 300
B.10 Overall carbon balance of the oxy-combustion process with heat integration. 301
B.11 Energy balance of the oxy-combustion process with heat integration. Energy in. 301
B.12 Energy balance of the oxy-combustion process with heat integration. Energy out. 302
B.13 Stream tables of the oxy-combustion process with heat integration and smaller ASU. 303
B.14 Heat tables of the oxy-combustion process with heat integration and smaller ASU. 328
B.15 Power tables of the oxy-combustion process with heat integration and smaller ASU. 329
B.16 Overall carbon balance of the oxy-combustion process with heat integration and smaller ASU. 330
B.17 Energy balance of the oxy-combustion process with heat integration and small ASU. Energy in. 330
B.18 Energy balance of the oxy-combustion process with heat integration and small ASU. Energy out. 331
B.19 Stream tables of the capture plant using EDEA for a flue gas obtained from oxy-combustion of coal. Scenario 1. 334
B.20 Heat tables of the capture plant using EDEA for a flue gas obtained from oxy-combustion of coal. Scenario 1. 338

B.21 Work tables of the capture plant using EDEA for a flue gas obtained from oxy-combustion of coal. Scenario 1. 338
B.22 Stream tables of the capture plant using EDEA for a flue gas obtained from oxy-combustion of coal. Scenario 2. 339
B.23 Heat tables of the capture plant using EDEA for a flue gas obtained from oxy-combustion of coal. Scenario 2. 343
B.24 Work tables of the capture plant using EDEA for a flue gas obtained from oxy-combustion of coal. Scenario 2. 343
B.25 Stream tables of the capture plant using EDEA for a flue gas obtained from oxy-combustion of coal. Scenario 3. 346
B.26 Heat tables of the capture plant using EDEA for a flue gas obtained from oxy-combustion of coal. Scenario 3. 350
B.27 Work tables of the capture plant using EDEA for a flue gas obtained from oxy-combustion of coal. Scenario 3. 350
B.28 Stream tables of the capture plant using EDEA for a flue gas obtained from oxy-combustion of coal. Scenario 4. 351
B.29 Heat tables of the capture plant using EDEA for a flue gas obtained from oxy-combustion of coal. Scenario 4. 355
B.30 Work tables of the capture plant using EDEA for a flue gas obtained from oxy-combustion of coal. Scenario 4. 355
B.31 Stream tables of the capture plant using EDEA for a flue gas obtained from oxy-combustion of coal. Scenario 5. 356
B.32 Heat tables of the capture plant using EDEA for a flue gas obtained from oxy-combustion of coal. Scenario 5. 360
B.33 Work tables of the capture plant using EDEA for a flue gas obtained from oxy-combustion of coal. Scenario 5. 360
B.34 Stream tables of the capture plant using EDEA for a flue gas obtained from oxy-combustion of coal. Scenario 6. 361
B.35 Heat tables of the capture plant using EDEA for a flue gas obtained from oxy-combustion of coal. Scenario 6. 365
B.36 Work tables of the capture plant using EDEA for a flue gas obtained from oxy-combustion of coal. Scenario 6. 365
B.37 Stream tables of the capture plant using EDEA for a flue gas obtained from oxy-combustion of coal. Scenario 7. 368
B.38 Heat tables of the capture plant using EDEA for a flue gas obtained from oxy-combustion of coal. Scenario 7. 373
B.39 Work tables of the capture plant using EDEA for a flue gas obtained from oxy-combustion of coal. Scenario 7. 373

B.40 Stream tables of the capture plant using EDEA for a flue gas obtained from oxy-combustion of coal. Scenario 8. 374
B.41 Heat tables of the capture plant using EDEA for a flue gas obtained from oxy-combustion of coal. Scenario 8. 379
B.42 Work tables of the capture plant using EDEA for a flue gas obtained from oxy-combustion of coal. Scenario 8. 379

C.1 Composition of bituminous coal 380
C.2 Power plant validation exercise 381

E.1 CEPCI values 388

Nomenclature

Symbol	Explanation
APH	Air pre heater
AR	Afforestation/ reforestation
Ar	Argon
ASU	Air separation unit
BECCS	Bioenergy with carbon capture and storage
BWI	Bond work index
CAPEX	Capital expenditure
CCC	Committee on Climate Change
CCS	Carbon capture and storage
CES	Cryogenic energy storage
CF	Cash flow
CHP	Combined heat and power
CI	Carbon intensity
CO	Carbon monoxide
CO_2	Carbon dioxide
COP21	21st Conference of Parties
CPU	Compression and purification unit
CV	Calorific value
DAC	Direct air capture
DCC	Direct contact cooler
DECC	Department of Energy & Climate Change
ED	Exergy destruction
EDEA	N-Ethyldiethanolamine
ESP	Electrostatic particulate collectors
EOR	Enhanced oil recovery
F_{80}	Mean particle size of coal feed to grinder
FGD	Flue gas desulphurisation
FWH	Feedwater heater

G	Grindability
GHG	Greenhouse gas
GPU	Gas processing unit
h	Specific enthalpy
H_2O	Water
HHV	Higher heating value
HP	High pressure
HX	Heat Exchanger
IAM	Integrated assessment model
IEA	International Energy Agency
IECM	Integrated Environmental Control Model
IGCC	Integrated gasification combined cycle
IP	Intermediate pressure
IPCC	Intergovernmental Panel on Climate Change
IRR	Internal rate of return
ITM	Ion transport membrane
KPI	Key performance indicators
LCA	Life-cycle assessment
LCOE	Levelised cost of electricity
LHV	Lower heating value
LOX	Liquid oxygen
LP	Low pressure
MAC	Main air compressor
MEA	Monoethanolamine
MHX	Multiple-stream heat exchanger
MSW	Municipal solid waste
n	Molar flow
N_2	Nitrogen
NEC	Negative emission credits
NET	Negative emission technology
NGCC	Natural gas combined cycle
NO_x	Nitrogen oxides
NPV	Net present value
O_2	Oxygen
OPEX	Operating expenditure
P_1	Target particle size of grinding process
P_{80}	Mean particle size at grinder outlet
PCC	Pulverised coal combustion

PDF	Probability density function
PFD	Process flow diagram
ppb	Parts per billion
ppm	Parts per million
PSA	Pressure-swing adsorption
Q	Heat
R	Perfect gas constant
RFG	Recycled flue gas
RH	Reheater
RHX	Regenerative heat exchanger
RS	Radiant superheater
s	Specific enthropy
SD	Spray dryer
SH	Superheater
SO_x	Sulfur oxides
T	Temperature
T_{ad}	Adiabatic flame temperature
tpd	Tons per day
TSA	Temperature swing adsoprtion
UNFCCC	United Nations Framework Convention on Climate Change
UA	Overall heat transfer coefficient
VPSA	Vacuum pressure swing adsoprtion
W	Work
W_i	Bond work index
W_{min}	Minimum separation work
y	Molar fraction
η	Efficiency
η_{gross}	Gross efficiency of the plant
η_{net}	Net efficiency of the plant
λ	Air-fuel ratio

Chapter 1

Introduction

1.1 Background on climate change

Anthropogenic carbon dioxide (CO_2) emissions from fossil fuel use have consistently increased since the industrial revolution, currently standing at 36 Gt_{CO_2}/year[1–5]. Despite being but a small fraction of the natural carbon cycle, this extra amount is sufficiently higher than the possible uptake from natural CO_2 sinks, leading to its atmospheric accumulation over the last centuries[6]. Currently, atmospheric CO_2 concentrations surpassed 400 parts per million (ppm), 40 % higher than the maximum recorded during the natural swings between ice ages[1] [7, 8].

Fossils corresponding to fauna and flora typically found in warm climates were excavated at high altitudes, suggesting warmer, more homogenous global temperatures during the Eocene epoch, which occurred between 33 and 55 million years ago[9]. Furthermore, some studies suggest that there was over 1000 ppm of CO_2 in the atmosphere during this period[7, 8], showing a possible link between global average temperature and atmospheric CO_2.

A cooling event that spanned 40 million years started to occur during this epoch, accompanied by a reduction of atmospheric CO_2 concentration[7]. Glaciers began to appear in the poles during this period, culminating with the earth in a similar state as today[7]. Afterwards, temperatures stabilised into the natural swing accompanied with similar patterns of atmospheric CO_2 concentrations[7].

Whilst we must be aware of the statisticians' maxim that correlation does not necessarily mean causation, we should also not ignore the overwhelming evidence linking atmospheric CO_2 concentrations with global average temperature[10–12]. Indeed, the scientific community reached a consensus on the causal effect of anthropogenic CO_2 emissions to climate change through models developed in the 19^{th} century, which have

[1] Atmospheric composition from these pre-record ages were obtained by analysing gas bubbles trapped in ice cores from the accumulation of new snow layers. The natural atmospheric CO_2 was analysed from these bubbles, and a natural swing between 180 and 280 ppm was observed.

since been improved, based on the physical properties of CO_2[10–13]. On a particular study, Stips et al. [14] used information flow to conclude that anthropogenic CO_2 emissions have a one-way causal effect in increasing global average surface temperatures, corroborating the consensus.

Human activity had such an immense impact on the climate, ecosystem, and earth's geology since the industrial age that some authors name the current epoch as the "Anthropocene"[15]. The global average temperature has been increasing at such high rates that fears of drastic climate change led to 154 nations sign the Kyoto protocol in 1997, pledging an 80 % greenhouse gas (GHG) reduction by 2050[16]. However, Aylett et al. [17] suggested that the Kyoto protocol may be insufficient to maintain the global average temperature rise below the 1.5 °C target agreed during the 21st Conference of Parties (COP21)[18].

The extreme heat experienced in the UK during March 2017 and July 2018, with maximum temperatures of 3 °C higher than the 1961 – 1990 period highlighted climate change into the news broadcasts[19]. A similar situation was observed in Norway during the winter of 2000 – 2001, where the media attributed several flooding events and a two-month delay in snowfall to climate change[20]. Whether these occurrences are indeed due to climate change is challenging to prove; however, these phenomena fall well within scientific predictions, making them "feel" real both by media outlets and by the population[20]. Such events are indeed alarming, especially considering that the consequences of climate change are already manifesting at an average temperature increase of only 1 °C above pre-industrial levels[8].

The Intergovernmental Panel on Climate Change (IPCC) special report on global warming of 1.5 °C stresses that we are not reducing GHG emissions fast enough to prevent the adverse effects of climate change[21]. Meeting this temperature target will require deep reductions in GHG across all sectors[22]. The launch of this report coincided with worldwide protests to make climate change part of governments' agenda, culminating with 18 European countries[2] pledging a complete decarbonisation by 2050[23, 24].

Increasing the share of variable renewable energy sources has been a significant contributor to decarbonise the power sector whilst phasing out fossil fuels[25, 26]. Indeed, renewable energy has been displacing fossil fuel energy from the grid at a rate of 0.2 %/year[25]. At these penetration rates, the International Energy Agency (IEA) predicts a 30 % share of renewable energy sources in the electricity grid by 2023 divided between hydropower, wind, solar PV, and bioenergy[27].

Achieving the 1.5 °C target will require a further expansion of the renewable fleet, with China planning to reach 61 % of total renewable share by 2040, where 60 %

[2]The countries that intend on backing the 2050 net-zero GHG emissions are France, Spain, the Netherlands, Belgium, Sweden, Portugal, Denmark, Luxembourg, Latvia, UK, Germany, Italy, Finland, Slovenia, Austria, Greece, Malta and Cyprus.

of this fleet accounts for solar PV and wind[22]. The Committee on Climate Change (CCC) suggests that a 50 – 60 % share of renewable power generation technologies in the United Kingdom is achievable by 2030[28–30]. Indeed, the UK's prime minister pledged a legally binding target in June 2019 to entirely cut its GHG emissions by 2050 and lead the world towards clean growth[31–34]. The CCC suggested that the UK must remove 45 – 50 Mt of atmospheric CO_2 to achieve its proposed target[29].
However, expanding the renewable fleet alone will unlikely be enough to decarbonise the power sector. Fossil fuels will still be essential to satisfy the global energy demand[2] and maintain a firm power supply because coal-fired plants generate 38 % of global electricity[35–40]. Indeed, the premature decommission of thermal power plants is likely to be a costly endeavour[41] and might raise questions about job security[42] and electricity prices[43]. It is then paramount to evaluate the deployment of multiple low carbon technologies and have a diverse portfolio of power-generating technologies instead of looking at each technology separately[35, 37, 38]. Therefore, fossil fuels are expected to maintain a considerable share in future electricity markets[2, 44–46]. Hence, carbon capture and storage (CCS) technologies are essential[47–49] to achieve the "rapid and unprecedented decarbonisation" pledged by some governments[21, 50].

1.2 Carbon capture and storage

Carbon capture and storage can be used in the power and industrial sectors to significantly reduce their CO_2 emissions[47–49, 51–54], offering the opportunity for a just transition to a low carbon economy[55]. Most integrated assessment models (IAMs) feature CCS deployment in their pathways to limit global warming below 1.5 °C[21, 54]. Furthermore, this group of technologies may also provide a low-carbon, flexible operation required from the increasing share of variable renewable energy technologies in the grid[44–46]. Consequently, timely deployment of CCS seems sensible, reducing our dependency on a unicorn technology[3] to solve all issues in the electricity grid[21, 50].
There are three categories of CCS technologies, which depend upon the capture process: Pre-combustion, post-combustion, and oxy-combustion[48, 53]. These categories will be explained for the context of capturing CO_2 from a flue gas originated from a thermal power plant.

1.2.1 Pre-combustion CO_2 capture

This category is based on the gasification of a solid fuel into syngas, consisting mainly of carbon monoxide (CO), hydrogen (H_2) and CO_2. The integrated gasification combined cycle (IGCC) is the most studied pre-combustion capture technology for power

[3] A unicorn technology is a currently non-existing technology that is renewable, carbon-free, and able to operate flexibly.

generation[53, 56–58]. Here, fuel reacts with controlled amounts of oxygen (O_2) at 1300 – 1600 °C and 30 – 40 bar to maximize CO and H_2 production[53, 56–58].
This mixture then reacts with steam in a water-gas shift reaction, converting CO and H_2O into a mixture of CO_2 and H_2 that requires further separation[51, 53, 56–58]. Physical solvents at high pressure are used to capture CO_2 from this stream, whilst H_2 is either stored for later use or burned to satisfy the energy demand of the process[51, 59].

1.2.2 Post-combustion CO_2 capture

Post-combustion capture separates CO_2 from flue gas using an aqueous alkanolamine, typically monoethanolamine (MEA), at atmospheric pressure and 30 – 60 °C[48, 49, 51, 53, 60, 61]. Here, the lean-solvent stream[4] is introduced at the absorber's top and flows down through a packing material whilst absorbing CO_2 from the flue gas[48, 49, 51, 53, 60, 61]. The rich-solvent stream exiting the absorber regenerates in a stripper column by removing the absorbed CO_2, which is dispatched to a storage site via pipeline[48, 49, 51, 53, 60, 61].
Solvent regeneration is an energy-intensive process, often requiring steam from the power plant[48], reducing the plant's gross power generation. Afterwards, the regenerated solvent is recycled to the absorber to absorb more CO_2[48, 49, 51, 53, 60, 61]. A CO_2-clean gas, mainly consisting of nitrogen (N_2) and water (H_2O) is vented to the atmosphere[48, 49, 53], significantly reducing the emissions of thermal power generation using fossil fuels.
Post-combustion is considered an "end-of-pipe" technology and suitable to retrofit existing power plants because it marginally affects the plant's operation[48]. Furthermore, this technology can be readily accepted by the power sector due to its similarities to technologies already implemented to mitigate sulphur oxides (SO_x) emissions[48].

1.2.3 Oxy-fuel combustion CO_2 capture

Burning fuel with medium-purity oxygen (O_2)[5] produces a flue gas with high CO_2 concentration, increasing combustion efficiency and flame temperatures[48, 49, 51, 62]. Recycling flue gas (RFG) to the furnace reduces these high combustion temperatures to manageable levels, thus preventing equipment damage[1, 48, 49, 51, 62–65]. The high CO_2 concentration in the flue gas simplifies CO_2 purification via condensation on a gas processing unit (GPU)[1, 48, 49, 51, 62, 64, 66].
It is also possible to retrofit this technology into existing power plants by managing the amount of RFG to obtain temperatures similar to air-firing; however, concerns about air ingress might discourage this practice[48, 67–69]. Although test units were operated

[4] A lean-solvent stream refers to a stream with a small amount of CO_2 absorbed by the solvent. Contrastingly, a rich-solvent stream has high amounts of CO_2 absorbed.

[5] Medium-purity oxygen is 85 – 95 % pure, high-purity oxygen is above 95 % pure, whilst low-purity oxygen is below 85 % pure.

by retrofitting existing plants, such as the Callide Oxyfuel project[70], this CCS category may have a higher acceptance if the power plant is designed for oxy-combustion.

1.2.4 Bioenergy with CCS

Capturing atmospheric CO_2 emissions is essential to achieve the 1.5 °C target by 2050 in what is termed negative emissions[71–73]. Negative emission technologies (NET) encompass a group of technologies that can perform this task through photosynthesis or chemical processes. Examples of photosynthetic processes are bioenergy with carbon capture and storage (BECCS) and afforestation/ reforestation (AR); whilst direct air capture (DAC) is an example of chemical processes[71, 73–75].

1.2.5 CO_2Storage

Regardless of the chosen capture technology, CO_2 must be compressed to pipeline pressure[6] before being safely stored in a deep saline aquifer or some other suitable reservoir[76–79]. Enhanced oil recovery (EOR), the current primary use for CO_2[1], provided experience in transport and storage of small CO_2 quantities; however, there is lack of experience regarding the permanent storage of sizeable CO_2 quantities in these reservoirs[80]. Furthermore, the general public is reluctant of CCS[81–83], despite being considered essential by experts to combat climate change[21]. This discrepancy between the public and the experts indicate the requirement to conduct awareness campaigns and instruct the general public of the benefits of CCS.

1.3 Research Goal and Structure

This thesis aims to determine the value of CCS for the power generating sector by analysing its economic attractiveness and environmental benefits. More specifically, oxy-combustion will serve as a model CCS technology to develop frameworks that make it cost-competitive with other power generation sources.

A thorough description of the oxy-combustion process is presented in Chapter 2, identifying the main advantages and disadvantages of this CCS category. The current means of producing O_2 using cryogenic separation and membrane technologies under development are summarily discussed in this chapter. Cryogenic GPU technologies are also reviewed in this chapter, noting the differences in CO_2 capture rates and purity between each of them. Both the air separation unit (ASU) and the gas processing unit (GPU) are critical to the successful operation of oxy-combustion because of these units' large power consumption[49]. Hence, these units should be designed carefully to satisfy both O_2 and CO_2 demand at the requested conditions whilst minimising their power consumption. Following this, the design equations and operating parameters used to simulate the unit operations of an oxy-combustion process are described in Chapter 3.

[6] Commonly 110 – 120 bar, however, this is dependant upon the CO_2 transport infrastructure design.

A second-law efficiency analysis is used in Chapter 4 to identify opportunities to improve the net efficiency of an oxy-combustion process. This analysis was conducted by calculating the exergy destruction of each unit operation in the process. Afterwards, a heat integration exercise between several units of the process was proposed to reduce these losses, and its thermodynamic benefit was assessed by re-examining the exergy destruction of the new process. This method culminated into a simple procedure to aid project selection via a graphical analysis that charts the proposed projects regarding two key performance indicators (KPI).

The second-law analysis identified the GPU as being the least thermodynamically efficient unit of the simulated oxy-combustion process. Ergo, a novel solvent-based GPU design is evaluated in Chapter 5. The thermodynamic improvement of the capture unit was analysed using the methodology proposed in Chapter 4, enabling a simple comparison with an oxy-combustion process with a cryogenic GPU.

Biomass can be used as fuel to generate negative emissions because it is carbon-neutral and renewable[84]. After all, atmospheric CO_2 is consumed during a plant's growth process[84]. Theoretically, the same amount of CO_2 is released to the atmosphere by burning this type of fuel to generate heat or power, thus closing the carbon cycle. In practice, this carbon neutrality is unlikely to be achieved without any sort of CO_2 capture technology due to CO_2 leakages across the supply chain[73, 85–89]. Therefore, atmospheric CO_2 can be reduced if sufficient biogenic CO_2 is captured via CCS, generating the so-called negative emissions. However, bioenergy with carbon capture and storage (BECCS) is more expensive than using fossil fuels, since it suffers from the same disadvantages of CCS whilst consuming a fuel with lower heat capacity[84]. Nonetheless, this venture has the opportunity to value negative emissions.

The potential benefits of generating negative emissions from an oxy-BECCS process is analysed in Chapter 6. Auctioning these emissions in the form of credits can enable the simultaneous decarbonisation of the power and industrial sectors whilst providing sufficient revenues to reduce the penalties associated with BECCS.

A deep penetration of variable renewable energy sources changes the supply pattern of the power grid[29, 30, 37, 38], which can be manifested through sharp increases in electricity prices during periods that cannot be satisfied using renewable sources. This price fluctuation may come from several causes, the most commons being an increased demand that cannot be met by the current renewable fleet, or that no renewable resource is available during that particular period. Consequently, flexible sources must be readily available to satisfy the electricity demand during these periods[30, 37, 38].

Currently, only thermal power generation can operate in a sufficiently flexible way to satisfy the electricity demand reliably; however, this practice emits CO_2 and other GHG to the atmosphere[30, 38, 90–93]. Photovoltaic (PV), wind, or hybrid systems[94–

96] coupled with pumped hydro or batteries to store electricity[29] provide another means of flexible power generation, particularly beneficial for remote areas[95, 97]. Indeed, specific authors identified the combination of renewable energy with storage as offering the lowest cost solution for a flexible and carbon-free electricity[95, 97–99]. Energy storage options already exist for rapid- and long-term storage[100]. However, this depends on the local climate wherein some cases it may still be more economical to use fossil fuels, such as diesel generators, in combination with renewable energy sources[95, 96]. Furthermore, climate change may impact the operational performance of renewable energy sources, increasing the uncertainty of these technologies[101], leading to increased political motivation to rely on fossil fuels for power generation. Hence, CCS applied to thermal power plants can significantly reduce these processes' emissions whilst allowing a flexible operation to satisfy the electricity demand. However, opponents state that CCS is a costly technology with significant economic, environmental, and social risks, questioning its ability to reduce CO_2 and the need of continuous management for generations to prevent leakages[98, 99].
The challenges of operating a flexible oxy-combustion process with and without liquid oxygen (LOX) storage is addressed in Chapter 7. Here, the plant reduces its capacity during low electricity prices, stores LOX if there is a storage tank, and operates at full capacity, discharging stored oxygen during high electricity prices. The net present value of a flexible oxy-combustion plant is calculated, and the attractiveness of this option discussed for a range of regions that follow different daily electricity price profiles.

Chapter 2

Literature Review

2.1 Oxy-combustion overview

Oxy-combustion follows the idea of burning a fuel with medium-purity oxygen (O_2), increasing combustion efficiency and flame temperature compared to air-firing[47–49, 62–64, 102–104]. Obtaining high flame temperatures by burning a fuel with pure O_2 was first introduced in 1903 by French engineers Edmond Fouché and Charles Picard to weld and cut metals[105].[1] It was not until 1982 that Abraham *et al.* proposed oxy-combustion to produce carbon dioxide (CO_2) for enhanced oil recovery (EOR)[105–107]. However, this EOR strategy was considered uneconomical owing to the relatively low oil prices during the 1980s and 1990s[49, 64, 102]. Recently, oxy-combustion has been the target of increased interest to curb anthropogenic CO_2 emissions as one of many climate change mitigation options[49, 64, 102].

The high flame temperature originated from burning a fuel with O_2 is controlled by recycling part of the flue gas to the furnace[102, 108]. Removing nitrogen (N_2) from the combustion media results in a flue gas with a high CO_2 concentration and the remainder being mostly water[47–49, 62, 64, 102–104]. Hence, a high-purity CO_2 stream can be obtained by condensing water, simplifying the CO_2 capture process. However, recycling flue gas will increase the number of sulphur species and chlorine which, combined with the high CO_2 concentrations, enhances the corrosion rates in materials typically used for ultra-supercritical (USC) plants[64, 108]. Applying this strategy to take advantage of the higher efficiencies of USC plants requires materials that can withstand higher temperatures and are more resistant to corrosion[64, 108].

Medium- to high-purity O_2 with composition between 95 and 98 mol% is obtained by separating the air constituents using an air separation unit (ASU). This O_2 stream is subsequently mixed with recycled flue gas (RFG) and used as the oxidant during combustion[47–49, 62–64, 102–104]. The flame temperature and CO_2 concentration

[1] This technology can be referred to as oxy-fuel, oxyacetylene, oxy, or gas welding/cutting.

in the flue gas are regulated by varying the amount of RFG; however, CO_2 must still be upgraded to pipeline specifications using a gas processing unit (GPU)[49, 63, 65, 66, 77–79, 103, 109, 110]. A process flow diagram (PFD) representing the main components of oxy-combustion can be observed in Figure 2.1.
The ASU and GPU require considerable amounts of energy and resources, which increase the cost of electricity[49, 103, 111–115].[2] Thus, reducing this parasitic energy consumption has been the target of several research projects.[103, 111–116].
Several demonstration projects have been performed due to the increased interest in this technology, such as the Callide Oxyfuel Project[70, 117, 118] in Australia, Lacq pilot plant[119] in France, Compostilla OXYCFB[120] in Spain, and Vattenfall[121, 122] in Germany. These projects gathered much needed physical data along with both technical and operational experience.
This chapter offers an overview of the oxy-combustion process. It starts by analysing the ASU, discussing cryogenic units and the developments of membrane technology to produce oxygen. A brief introduction to the operation of thermal power plants is subsequently presented, followed by the changes and opportunities provided by oxy-combustion. Lastly, two different GPU are discussed to demonstrate that CO_2 purity depends on the chosen process.

2.2 Air Separation Unit

Air separation began around 1870 with Carl von Linde's experiments to develop a cooling unit to crystallise paraffin[123]. Liquid air was first produced in 1885 from an air liquefaction apparatus at a rate of three L/h after three days of operation[123, 124]. Further developments led to the rectification of air to produce pure N_2 at reduced costs, catching the fertiliser industry's attention[123, 124]. The process was patented in 1902[125], and the first cryogenic ASU sold in 1905[123, 124, 126].
A rapid technological development gave rise to a two-column design in 1910, reducing production costs by simultaneously producing O_2 and N_2[123, 126]. Pure N_2 experienced high demand to produce explosives and fertilisers during the first world war[123, 126]. The ASU's roles shifted to produce synthetic rubber and fuel from coal during the second world war[123, 126]. Afterwards, the petrochemical industry became the primary consumer of cryogenic ASU, promoting large-scale plants[123].
Nowadays, O_2 can be produced on-site or delivered by a specialist company and stored on-site in cryogenic tanks. Delivery and storage of cryogenic O_2 have the lowest capital requirements; however, this O_2 is more expensive, and the amount is limited by storage capacity[127]. On-site production is obtained via vacuum swing adsorption or cryogenic air separation. Vacuum swing adsorption processes are more competitive

[2] For a power plant. The idea is similar for any other process, where the cost of product increases.

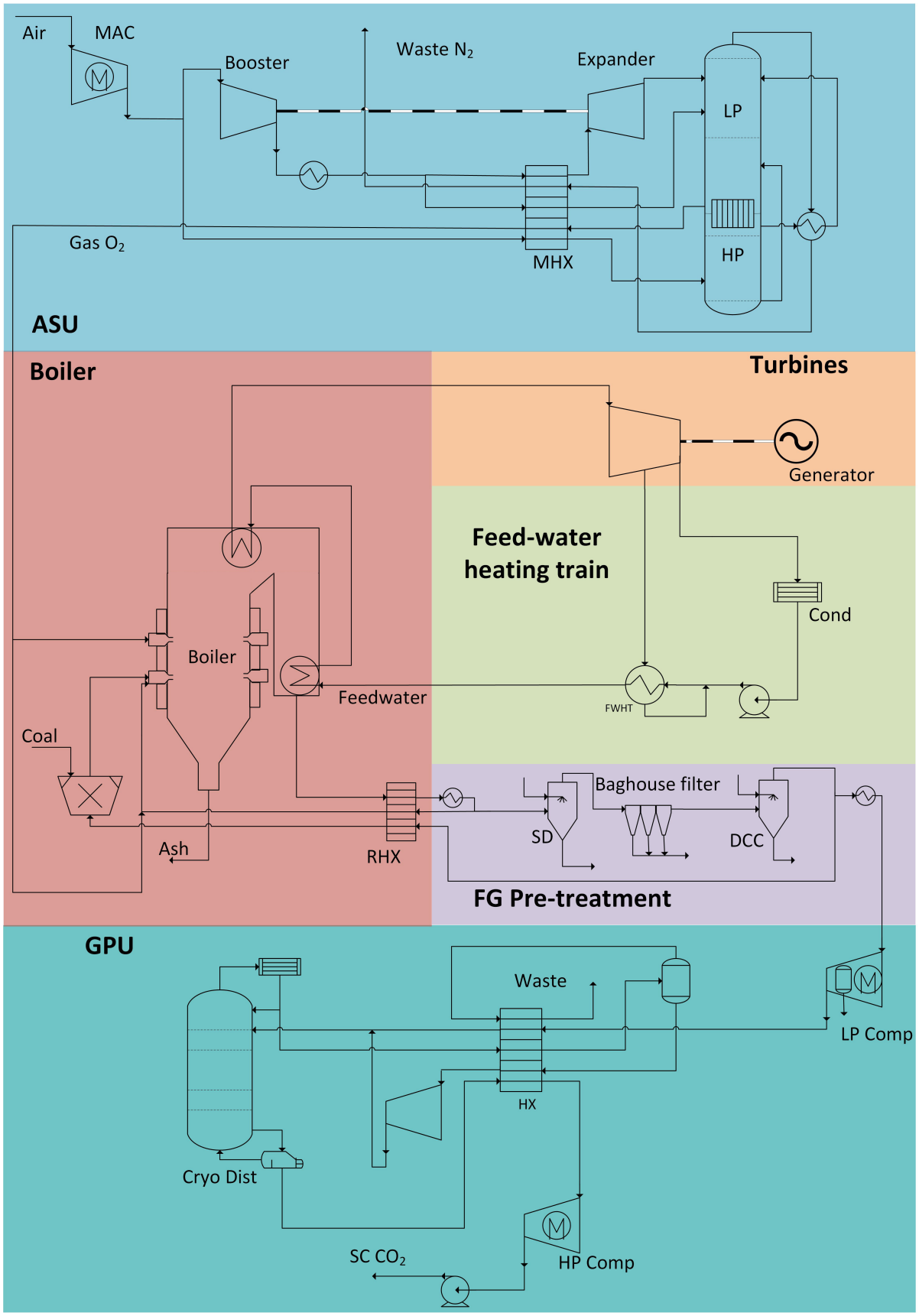


Figure 2.1: Process Flow Diagram (PFD) of oxy-coal combustion consisting of a double column cryogenic ASU for O_2 production, a pulverised coal boiler with flue gas treatment plant, and a cryogenic GPU, as published by Cabral and Mac Dowell [103].

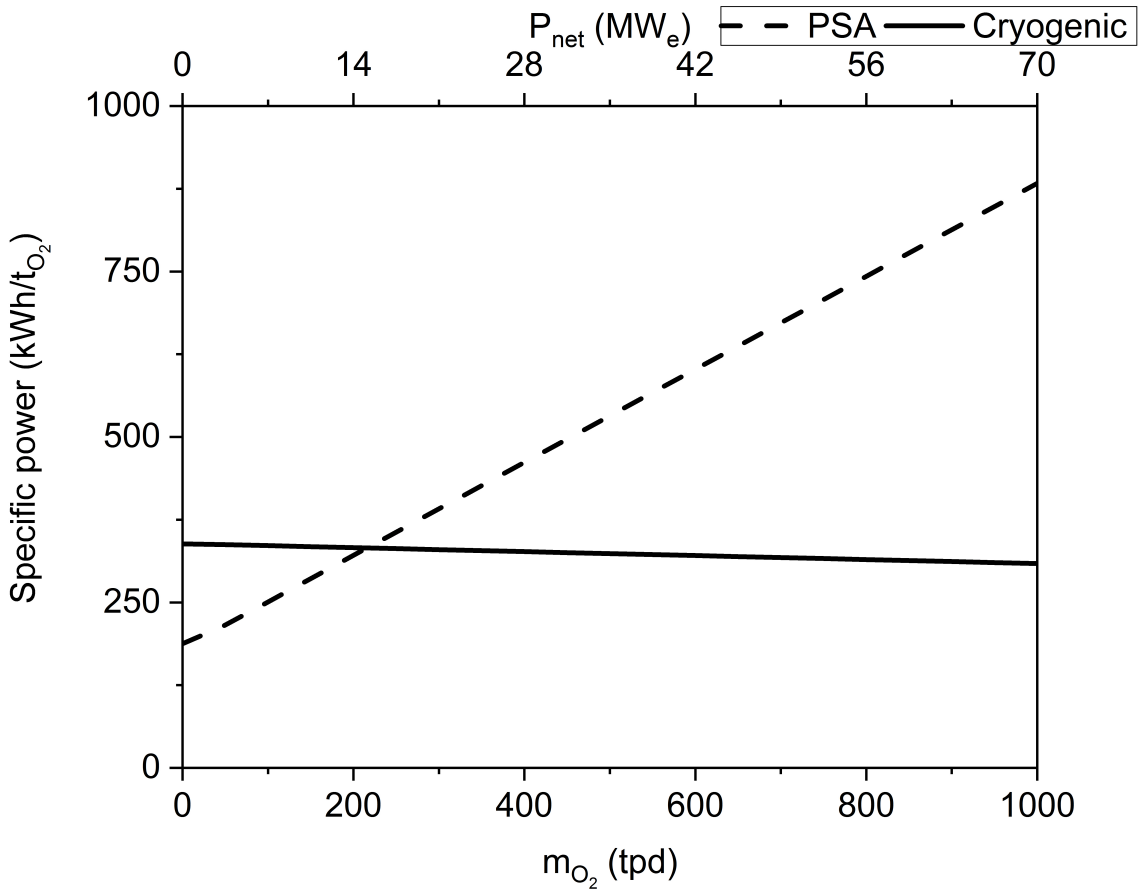


Figure 2.2: Specific power consumption of oxygen production via pressure swing adsorption (PSA) and cryogenic distillation. PSA consumes less power than cryogenic distillation up to 200 tpd of O_2, equating to a 14 MW net electrical output from an oxy-combustion process. Power plants with higher capacity demand more O_2, making cryogenic distillation more cost-effective.

than cryogenic ASU for O_2 production rates between 10 and 100 tonnes per day (tpd); however, the maximum allowable vessel size limits this technology[127–129]. Cryogenic air separation units have a more comprehensive range of product flowrate, with state-of-the-art single train sizes operating up to 5000 tpd achieving O_2 purity from 90 to 99.9 vol%[68, 114, 123, 124, 126, 127, 130–135].

Cryogenic units can produce streams with lower O_2 purity; however, the cost reduction does not justify this practice[127]. Instead, it is more cost-effective to achieve the required purity by mixing air with a medium- to high-purity O_2 stream[127].

Oxy-combustion for electricity production requires[3] 600 kg_{O_2}/MWh, making cryogenic distillation the most cost-effective technology to satisfy this demand, as can be seen in Figure 2.2[68, 135–140]. However, it is challenging to obtain detailed costs and performance data for cryogenic distillation units due to this industry's high competitiveness and confidentiality[114].

[3] A 500 MW_{net} power plant requires 7200 tpd of oxygen.

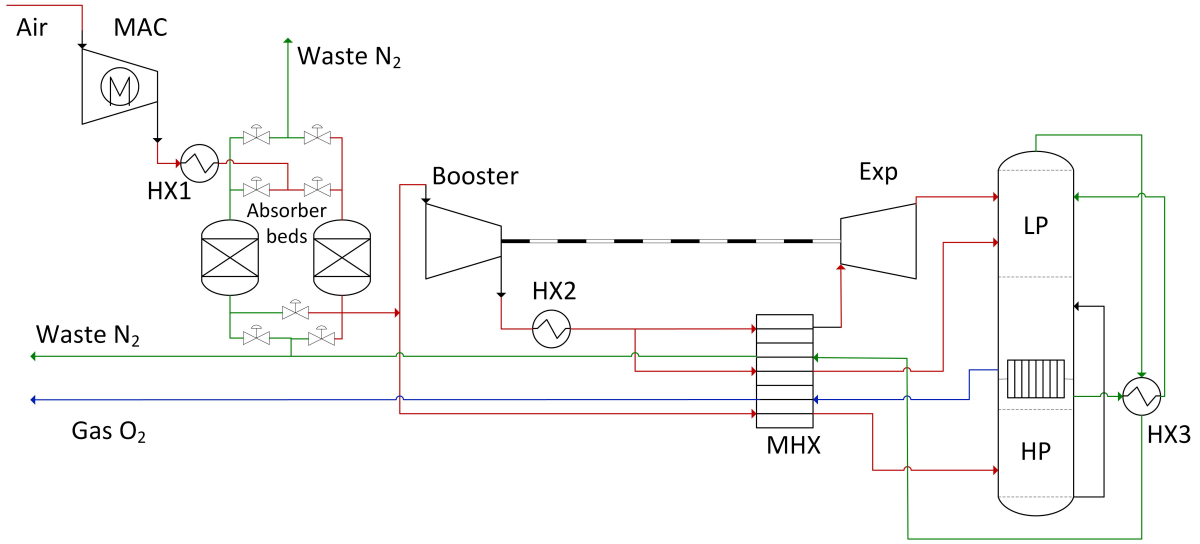


Figure 2.3: PFD of a double column cryogenic ASU for gaseous oxygen production. The flow path of air is represented in red; Black represents the flow path of oxygen-enriched air; Green represents the flow path of nitrogen-rich streams; Blue represents the flow path of oxygen-rich stream. MAC – Main air compressor; Booster - Booster compressor; Exp - Expander; HX1 and HX2 - Coolers; MHX - Main heat exchanger; HX3 - Subcooler; HP - High pressure column; LP - Low pressure column.

2.2.1 Cryogenic air separation units

Cryogenic air separation starts with air compression from atmospheric pressure to 3.5 – 6.9 bar, depending on the desired product specifications[103, 114, 124, 126, 127]. Axial flow compressors with inter- and after-coolers are required to satisfy the large air demand from cryogenic ASU[114, 124]. These coolers are introduced to condense some humidity whilst reducing air temperature to operating levels[127]. A PFD of a typical double column cryogenic ASU is presented in Figure 2.3.

Trace impurities with high freezing temperatures were initially removed with reversing heat exchangers by regularly switching the hot and cold streams inlet side[114, 127]. This strategy was designed to prevent damage to the cryogenic equipment but generated a significant strain on the heat exchanger, reducing its lifetime[114, 127]. Nowadays, most plants with high O_2 production capacity, termed in the field as tonnage plants, use temperature swing adsorption (TSA) units with 13X molecular sieves to remove these trace impurities[141–146]. This molecular sieve is a sodium zeolite with high water and adequate CO_2 adsorption capacity[141–146]. There are usually several adsorption vessels (known as beds) simultaneously operating between adsorption and regeneration modes[141–146]. Impurities from the air are removed in vessels operating in adsorption mode, whilst hot waste gas with a mass flow between 10 and 20 % of air regenerates the remaining vessels[127, 141–146].

TSA vessels can be built either horizontally or vertically with a maximum diameter of 4.2 m, allowing them to be shop fabricated and shipped to the site[127]. This

thesis will not focus on the specifics of this technology, but a typical operating sequence is[127, 146]:

1. Parallel flow, where both beds are online for a short period of time.
2. Depressurisation, where the spent bed is depressurised to waste gas pressure.
3. Heating, where waste gas flows through a heater and increases bed temperature.
4. Cooling with cold waste gas, starting after sufficient heat has been added.
5. Pressurisation, where the regenerated bed is pressurised and brought online.

If both O_2 and large quantities of N_2 are required, the air is pre-cooled against boiling Freon in a heat exchanger using an inline mechanical refrigeration unit[127]. Alternatively, air can be pre-cooled in a direct contact cooler (DCC) using chilled water, obtained using cold waste gas in a humidification tower, when O_2 and small or no amounts of N_2 are required[127]. This practice has the advantage of removing water-soluble acid gases[127].
Compressed air (cooling stream) is cooled to cryogenic temperatures against the cold distillation products (warming stream) inside aluminium brazed plate-fin heat exchangers, allowing heat exchange between more than two fluids[114, 126, 127, 131, 134]. Stainless steel must be used instead of aluminium if O_2 is vaporised at high pressure to prevent explosive reactions between aluminium and O_2[114]. These heat exchangers are composed of corrugated fins sandwiched between plates, allowing heat transfer areas as high as 1500 m^2/m^3, held together using sidebars[114, 126]. The fins create 5 – 9.5 mm height channels at a density of 7 fins/cm, where cooling and warming streams alternate between each layer allowing average temperature differences of 2 to 3 °C at the warm end[114, 126, 127]. Due to these plants' large size, it is common to use an assembly of plate-fin heat exchangers located inside a cold box. These assemblies are typically 1.4 m wide by 1.4 m stack height by 8 m long manifolded together[126, 127].[4]
A cold box encases the equipment operating at cryogenic temperatures and provides structural support and insulation using perlite or rock wool[126, 127]. This material avoids heat leaks to ambient air by eliminating heat convection through the material's small voids[126, 127]. Perlite can be blown in from the top of the cold box and offers a more even insulation, but it must be removed entirely to access the site in case of a leakage[127]. Rock wool is more labour intensive as it must be manually packed, but it allows easy access by tunnelling through the frozen material if a leak occurs[127]. It is essential to dry this insulation material with N_2 before the operation starts to avoid ice formation inside the cold box[126, 127].

[4]Actual dimensions of these heat exchangers are a function of process and operating conditions.

Table 2.1: Boiling temperature (T_b) of air components at 1.01 bar and 5 bar.

Component	T_b (°C) at 1.01 bar	T_b (°C) at 5 bar
O_2	-184	-164
N_2	-196	-179
Ar	-186	-167

A sub-cooler unit made of brazed aluminium is commonly used to cool down N_2 from the high pressure (HP) column using the waste gas from the low pressure (LP) column, minimizing flash losses[127, 147]. This unit can also sub-cool liquid products before storage and avoid gas formations during transport[127, 147].
Maintaining cryogenic temperatures inside the cold box is essential for the successful operation of the ASU[126, 127, 131]. These temperatures are obtained by expanding a fraction of incoming air, determined by performing an enthalpy balance to the cold box (typically assuming a heat leak of 47 kJ/kmol), using a turboexpander[127]. This gas expansion generates the required refrigeration due to the Joule-Thomson effect[127]. The refrigeration required inside the cold box increases if liquid oxygen (LOX) is produced, creating an enthalpy change that requires a higher fraction of air dispatched to the turboexpander[127].
Advances in expander technology improved the isentropic efficiency of turboexpanders above 90 %[127, 148, 149]. The power generated from these units can be either recovered by geared generators or directly connecting the shaft to a compressor, known as a compander when high-pressure O_2 is required[127, 148, 149]. Choosing the most suitable power recovery method must consider the trade-off between higher reliability and flow range for generators, and fewer parasitic losses for companders[127]. Another benefit of companders is the possibility of having an adjustable speed to maintain high plant efficiencies due to flowrate variations[127].
The difference between each component's boiling point allows their separation via distillation, albeit at cryogenic temperatures. As shown in Table 2.1 and Figure 2.4, it is easier to separate O_2 from N_2 than O_2 from argon (Ar) due to the difference in boiling points between each component[126, 127, 131].
Cryogenic distillation columns generally use an aluminium-based structured packing. This packing is composed of corrugated metal sheets that are arranged to optimize fluid flow, inducing three kPa pressure drop across the LP column[114, 127]. Surface areas ranging from 250 m^2/m^3 to 1000 m^2/m^3 of packing volume are obtained by perforating and folding the packing into a V-shaped geometry[114, 127]. Sieve trays can also be used but they inflict a substantial pressure drop across the column[114, 127].
The LP column is stacked on top of the HP column, reaching up to 45 m and 6 m diameter[114, 126, 131, 134, 147]. These columns are thermally linked by a condenser/ reboiler. Here, N_2 condensing at the top of the HP column vaporizes O_2

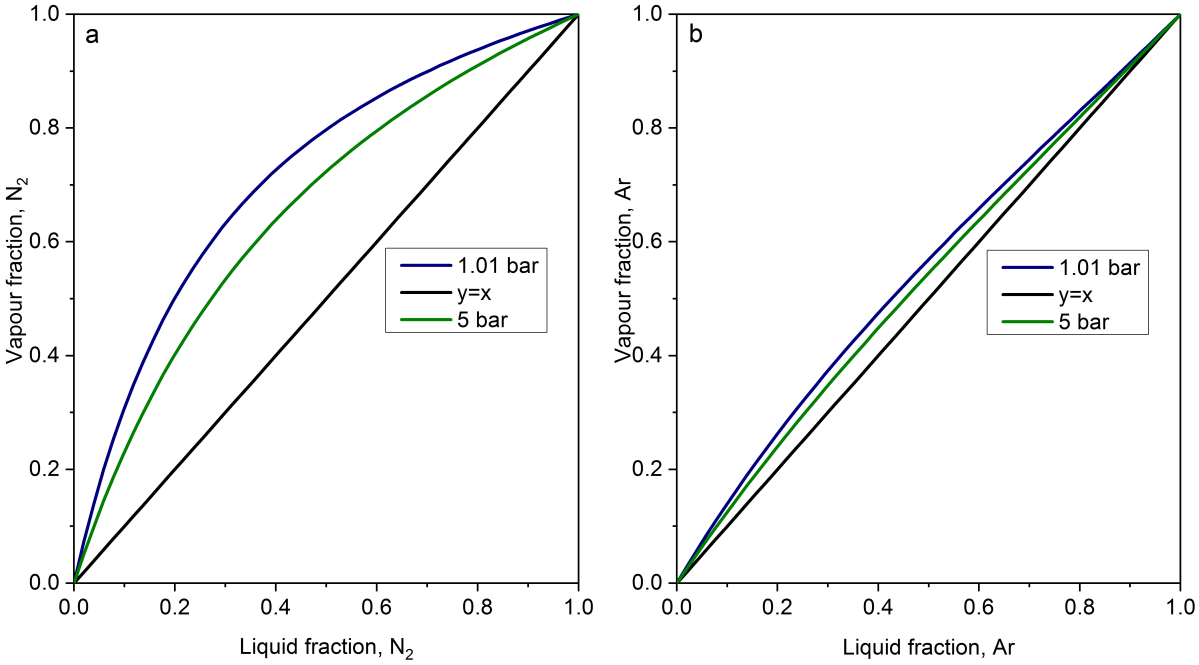


Figure 2.4: Variation of liquid and vapour compositions for the O_2/N_2 and O_2/Ar at 1.01 and 5 bar.

from the bottom of the LP column[114, 126, 131, 134, 147]. Typical operating pressures for the HP and LP columns for oxy-combustion are 5 and 1.1 bar, respectively. This unit achieves O_2 purities between 95 and 97 wt% whilst consuming 190 -– 240 kWh/t_{O_2}[48, 49, 51, 62, 103, 111, 114, 115, 136, 137, 150, 151]. However, higher pressures must be used if the O_2 is supplied to a natural gas combined cycle (NGCC), which operates at 40 bar[114].

This operation mode takes advantage of the fact that a component's boiling point increases with pressure (Table 2.1)[114, 126, 131, 134, 147]. Hence, the HP column's pressure must produce N_2 with a higher boiling point than the boiling point of O_2 in the LP column[114, 126, 131, 134, 147].

There are two types of condenser/ reboilers used in cryogenic distillation:

- Thermosiphon reboiler – where the equipment is submerged in a pool of LOX at the bottom of the LP column. Here, N_2 condenses inside closed passages whilst the O_2 passages are open at the top and bottom of the equipment so that it freely flows. LOX is boiled outside of the core and this liquid's height determines the required recirculation rate.

- Downflow reboiler – where LOX enters the top of the equipment and both liquid and vapour exit at the base.

A constant purge is required in both condenser/ reboiler types to prevent a build-up of hydrocarbons with a high boiling point in the LP's sump. Failing to purge hydrocarbons

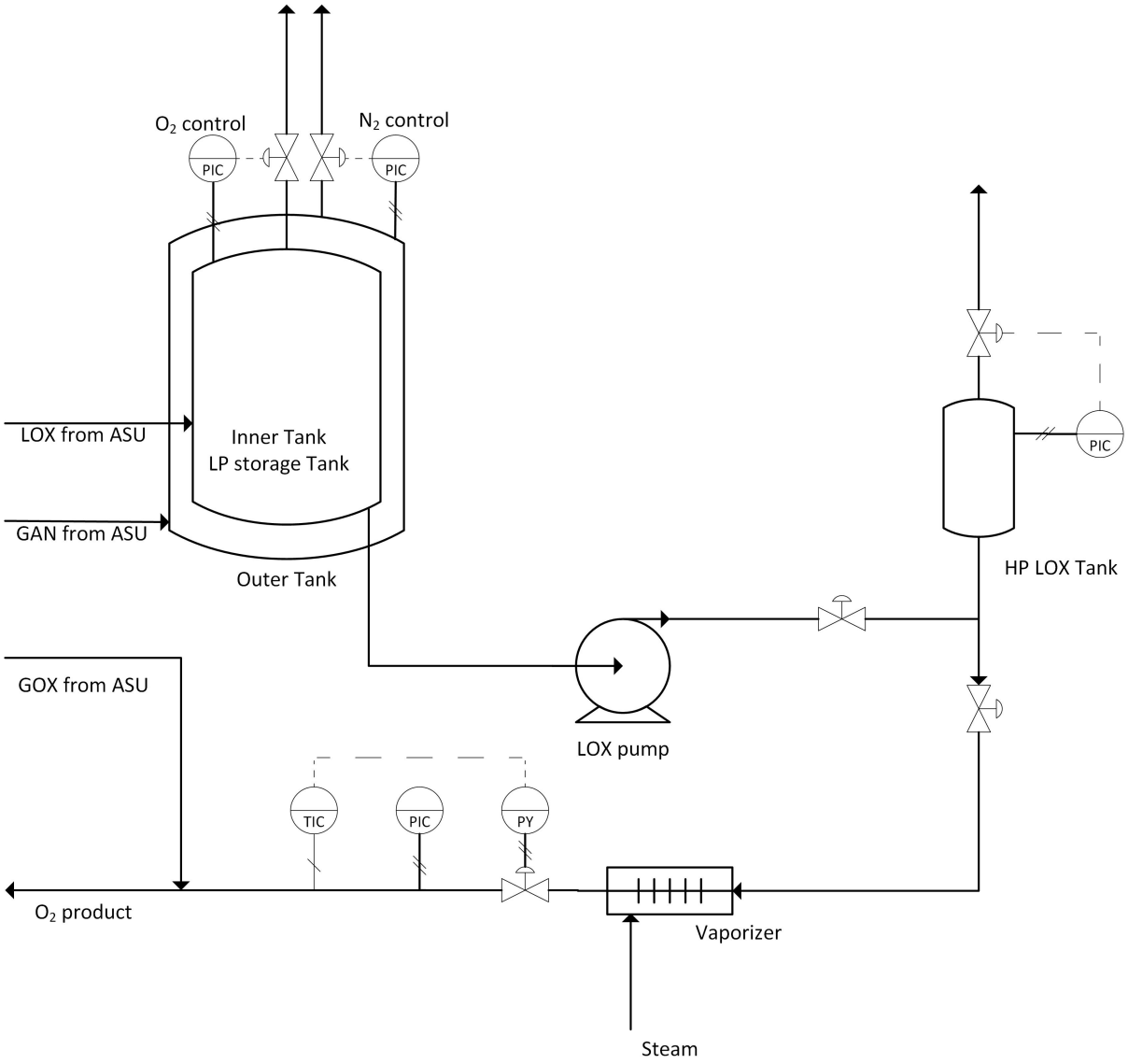


Figure 2.5: PFD of cryogenic oxygen storage, adapted from McGuinness and Kleinberg [127], and Hu et al. [152] The LP storage tank has an inner tank where liquid oxygen (LOX) is stored and kept at low temperatures by the gaseous nitrogen (GAN) injected in the outer tank.

from the LP's sump can lead to combustion[127].

ASUs have an excellent service record, with the vast majority of historical plant outages being from scheduled compressor maintenance and defrosting, occurring every four years[114, 127, 152]. It is then possible to coincide the ASU's shutdown with the power plant's routine annual maintenance[114, 127, 152]. However, it is possible to implement backup O_2 storage using the equipment outlined in Figure 2.5 to cover any planned or unplanned outage[114, 127, 152].

The backup unit's pump and vaporiser start when production stops. This process takes up to 20 minutes to be operational, but an instantaneous backup system can be installed if process continuity is an issue[127]. The LP storage tank is made of steel with an outer layer of carbon steel to hold perlite as an insulating material between those layers[127].

These tanks are generally designed to provide 24 hours of product backup. These backup units can alleviate the burden associated with planned and unplanned plant outages; however, the ASU suffers from a refrigeration penalty during LOX storage, increasing its specific power consumption[127].
When required, LOX is discharged from the storage tank and vaporised. If small amounts of LOX are required, it passes through an ambient vaporiser; otherwise, large amounts of LOX are vaporised in steam, electric, or natural gas vaporisers[127].
Material selection must consider the auto-ignition temperature at the operating conditions when using high O_2 concentrations[131]. Whenever cryogenic fluids are involved, materials that lose their ductility at these operating conditions should also be avoided[131]. The equipment must be cleaned before introducing O_2 to remove any combustible source such as organic materials, inorganic materials, rust, and dirt[131].
Improvements to cryogenic ASU technology are mainly obtained by adding more thermally integrated columns, such as a triple column process, improved process integration, and increasing the single plant train size, thus reducing the energy to produce O_2[112, 114, 153]. These changes are expected to reduce the ASU's specific energy consumption by 17 %[137].
Despite their technical maturity, the high power consumption of cryogenic ASU promoted alternative technologies for air separation, such as adsorption[143, 144, 154], ion transport membranes (ITM)[155–159], and chemical looping[160–162]. However, the lack of technical maturity or high costs of these alternative technologies make cryogenic ASU the only current viable technology to satisfy the O_2 demand of an oxy-combustion process[68, 133].

2.2.2 Adsorptive Air Separation

Adsorptive air separation is typically achieved by preferentially adsorbing N_2 in a pressurised zeolite bed whilst the O_2-rich stream escapes the bed[68, 131, 132]. This is a semi-continuous operation termed pressure-swing adsorption (PSA)[68, 131, 132]. Afterwards, the bed is regenerated by reducing the pressure, desorbing N_2 from the zeolites and preparing the bed for a new adsorption cycle[68, 131, 132]. A vacuum pump can be used to enhance N_2 desorption from the zeolite bed in a process known as vacuum pressure swing adsorption (VPSA). However, more power is required to produce this vacuum, increasing O_2 production costs[68, 131, 132].
The most straightforward PSA unit comprises two zeolite beds with a system controlling a set of valves that define the adsorption-desorption sequence[68, 131]. One of the beds is adsorbing N_2, creating an O_2-rich air stream, whilst the other is being regenerated by depressurisation[68, 131]. The valves switch once the first bed is full and the second bed is regenerated, reversing their operating modes[68, 131].
More beds can be introduced to approximate this technology to a continuous process

and reduce the pressure pulses obtained from opening and closing the valves[131]. However, this increases the valve switching sequence's complexity[131]. Buffer tanks are typically used to dampen the pressure pulses from the bed switching and maintain a constant product supply[131]. Introducing more beds is also the only method to increase these units' production capacity past the maximum vessel sizes[131].
PSA can achieve O_2 concentrations up to 93 – 95 vol%, making this an ideal technology when low quantities of medium-purity O_2 is required[68, 131, 163]. However, capital costs significantly increase with product quantity[68], making this technology unsuitable for the high O_2 demand from oxy-combustion (Figure 2.2).

2.2.3 Membrane technology

Developing membranes for oxygen production has been researched to reduce the energy consumption of air separation[155–159, 164–167]. Polymeric membranes operate based on the different diffusion rates of O_2 and N_2 across the membrane, driven by a pressure difference between the feed and the permeate (stream with the components that penetrated the membrane)[68, 131]. Flux through the membrane depends on this pressure difference and its thickness, establishing the required surface area to separate the components[68, 131]. However, these membranes are limited to O_2-enriched air production with concentrations between 25 wt% and 50 wt%[68].
Polymeric membranes only require an additional blower to provide adequate pressure through the membrane, making this technology exceptionally simple with swift start-up times[68]. However, the low O_2 purity and production rates make them most suitable for applications where H_2O and CO_2 in the product are not a problem[68].
A promising use for polymeric membranes is to produce oxygen-enriched air before a cryogenic ASU[112, 131] to reduce equipment size and energy consumption. Skorek-Osikowska et al. [112] simulated this hybrid process for an oxy-combustion process. The author observed that the new ASU consumed 13 % less power than the base case, reducing the electricity's break-even price by 4 %[112]. Further improvement of these two key performance indicators is expected as the process is optimised[112].
Ion transport membranes (ITM) have been developed to address polymeric membranes' limitations by producing high-purity O_2[68, 114, 155–159, 164–167]. These ITMs are made of solid oxide ceramic materials and require high temperatures to allow the passage of oxygen ions through the ceramic crystal lattice[68, 114, 155–159, 164–167]. This operation's driving force can be obtained by applying an electric voltage to the membrane material (for small O_2 amounts) or by O_2 partial pressure difference (for large O_2 amounts)[68, 114, 131, 155–159, 164–167]. This last method is known as mixed conducting membranes because both oxygen ions and electrons are conducted through a pressurised membrane, as seen in Figure 2.6[68, 131, 157].
Oxygen ions have very high flow rates across the ITM, and either high-purity O_2 is

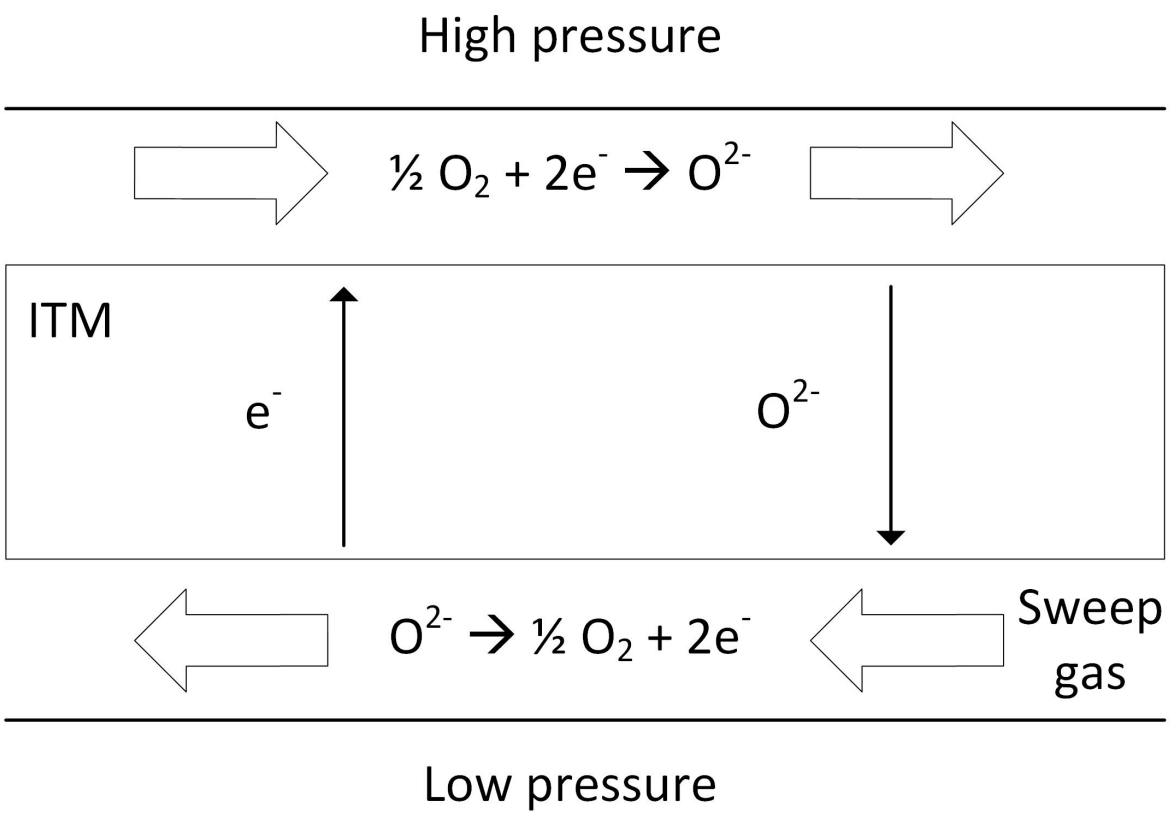


Figure 2.6: Schematic representation of an ITM, adapted from Hashim et al. [157]. Oxygen present in air at the high pressure side of the membrane is ionised by electrons at the surface and transported through the membrane to the sweep gas with low O_2 concentration.

produced on the membrane's permeate side or directly mixed with a sweep gas that creates the pressure difference to drive the process[68, 131, 155–159, 164–167]. Oxy-combustion benefits from this last method, as recycled flue gas sweeps O_2 from the membrane. This method creates the required mixture composition whilst improving operational safety by avoiding the circulation of high-purity O_2. However, current membrane materials are not compatible with flue gas, requiring alternatives to operate this membrane. Therefore, the only option to create the driving force required to separate O_2 from the air is to apply vacuum, increasing production costs and reducing the net efficiency of the oxy-combustion process[68].

An ITM for oxy-combustion starts by compressing air to 10 bar and heating the membrane and incoming air above 730 °C through a combination of air compression, heat from the boiler, and flue gas recycle[68, 131, 155–159, 164–167]. The high flux rates and selectivity of these membranes can reduce costs by 50 % relative to cryogenic distillation, making this technology particularly suitable for oxy-combustion[114].

2.2.4 Chemical production of oxygen

Chemical oxygen production was patented in 1867 by du Motay and Maréchal [168], where oxides or silicates of certain metals react with atmospheric oxygen in the presence of sulphurous acid to produce sulphuric acid. The reaction is reverted by adding heat, re-forming sulphurous acid and releasing O_2, thus regenerating the mixture[168] according to reaction 2.1.

$$M + H_2SO_3 + \frac{1}{2}O_2 \underset{\text{Heat}}{\overset{\text{Air}}{\rightleftharpoons}} M + H_2SO_4 \tag{2.1}$$

Where M is the metal oxide/ silicate; H_2SO_3 is sulphurous acid; O_2 is oxygen; and H_2SO_4 is sulphuric acid. Reaction 2.1 is a simplification of the actual reaction pathway. In reality, the metal reacts with sulphuric acid to generate a metal sulphite and release O_2[168]. This sulphite is then decomposed under heat, regenerating sulphurous acid, and the cycle is ready to begin again[168].

Another method of producing oxygen is by alternating air and steam in a closed retort over a metallic acid or oxide[168]. The incoming air oxidises this compound and subsequently releases the chemically bound oxygen by contacting with steam[168–170]. The initial idea developed by du Motay and Maréchal [168] resulted in low oxygen production rate whilst also requiring large amounts of steam[169, 170]. Furthermore, the mixture deteriorated rather quickly, rendering the process uncompetitive with other oxygen production technologies[169, 170]. Hence, Brimm [169] proposed to capture atmospheric oxygen using hot alkali manganate in the form of a double manganate-meta aluminate salt[169], a double manganate-metasilicate salt[170], or a similar compound, following reaction 2.2.

$$Na_2MnO_4 + H_2O \underset{\text{Air}}{\overset{\text{Steam}}{\rightleftharpoons}} 2\,NaOH + MnO_2 + \frac{1}{2}O_2 \tag{2.2}$$

Where Na_2MnO_4 is sodium manganate; H_2O is water; NaOH is sodium hydroxide; and MnO_2 is manganese dioxide.

Simulations using Aspen HYSYS suggested that chemical looping consumes 0.041 – 0.053 kWh/$m^3{}_{O_2}$[171]. The simplicity of this process, which only requires two reactors, coupled with its low power consumption, makes it a promising alternative to traditional oxygen producing methods[160, 171]. Flue gas can be recycled to reduce the metal without using an external energy source for steam generation, traditionally used for this purpose[160]. This recycle is favourable for oxy-combustion by also controlling the flame temperature[160]. Using flue gas from the power plant to decouple oxygen can reduce the air separation's energy footprint compared to a traditional chemical looping process[160]. Furthermore, this integrated process can also reduce capital

costs by simplifying the hardware and integrating both units more effectively[160].
However, the presence of impurities such as sulphur oxides (SO_x), nitrogen oxides (NO_x), halides, mercury, and excess O_2 can deteriorate the air separation performance of the chemical looping process[160]. Indeed, these components can deactivate the oxygen carrier particles[160]. Therefore, impurities present in the flue gas must be reduced to allowable levels, which increases costs and forces operating at lower flue gas temperatures[160]. This lower temperature reduces the amount of heat available to decouple oxygen from the carrier, thus reducing this unit's efficiency[160].
Chemical looping for O_2 production is currently not a mature technology, with only a few pilot-scale studies performed[171]. Hence, the uncertainty surrounding this technology makes it less likely for deployment in the near-future despite showing a better performance than cryogenic air separation units[171].

2.3 Power plants

This thesis only covers the combustion aspects of coal and biomass with an oxygen stream (oxy-firing), providing only a brief introduction on unabated pulverised-coal power plants. More detailed information on power plant fundamentals and air-firing operation can be found in the work of Kunzemann [172].

2.3.1 Unabated coal power plants

Coal is an organic sedimentary rock formed from different types of fossilised vegetation over 400 million years by different temperatures and pressures[1, 69]. It is extracted either in deep mines or close to the surface and is primarily used to provide energy[1, 69]. This material is a complex amorphous mixture of carbon (C), hydrogen (H), oxygen (O), nitrogen (N), sulphur (S), moisture, ash, and trace metals, divided into several ranks depending on carbon content[1, 69]. The most significant coal ranks are lignite, subbituminous, bituminous, and anthracite ordered from youngest to older and with increasing carbon content[1, 69]. Blending different coal ranks is common practice to manage the fuel's heat capacity based on availability and cost[1, 69].
Coal power plants generate electricity by converting the enthalpy of steam into rotary motion in a turbine connected to an alternator[173]. These plants are defined as thermal power plants, or steam power plants because steam is generated from water[173]. In a pulverised-fired (PF) power plant, coal is pulverised to 50 – 100 μm diameter, ensuring rapid and efficient combustion in the furnace[173–175]. The mills used to pulverise coal are a very mature, off-the-shelf technology[173].
Coal is transported to the furnace using primary air, or a mixture of flue gas and O_2 for oxy-combustion, preheated to 300 – 400 °C[173, 174]. Here, combustion occurs in burners mounted on either the corners or the walls of the furnace, depending on configuration, producing hot flue gas, which is a mixture of N_2, CO_2, water vapour,

fly and bottom ash, amongst others[173, 176]. Bottom ash (10 – 30 % of total ash) is collected at the bottom of the furnace whilst fly ash (70 – 90 % of total ash) flows with the flue gas and is collected on electrostatic precipitators (ESP) or fabric filters (FF)[173, 175]. Ash with less than 2 % carbon content can be used as an abrasive for sandblasting, a cement aggregate, or filler material in construction projects[173, 175]. However, changes in ash composition can affect its potential to be used[177].

The burners have high heat flux and operate substoichiometrically[178]. Here, hydrogen sulfide (H_2S) is formed, creating a highly corrosive environment[178]. Solid particles containing iron sulfates (FeS/FeS_2), alkali sulfates, and alkali chlorides in conjunction with hydrogen sulfide can corrode the tubes at a rate of up to 2 mm/year[178]. Hence, it is common practice to apply a coating with more than 20 % chrome for moderately corroding conditions, and coatings with more than 40 % chrome for severely corrosive conditions to protect the tubes[178].

The combustion temperature depends on the fuel's composition but generally peaks around 1200 – 1500 °C[173]. At this temperature range, heat is transferred to the furnace walls covered with water tubes via radiation[173]. Hot flue gases rise to the superheater and reheater where more heat is transferred through convection, generating superheated steam[173].

Furnace exit temperature is a crucial design choice as this determines the ratio between radiative and convective heat transfer in this unit[173]. This ratio influences ash slagging in the furnace, ash fouling on the convective heat transfer sections, and boiler size[173]. For example, if the furnace exit temperature is too high, molten ash flows to the convective sections, increasing severe ash deposition in the superheater and reheater sections[173]. On the other hand, if the furnace exit temperature is too low, the size of both the furnace and the convective heat transfer sections would have to increase, consequentially increasing capital costs[173].

Coal quality defines the plant's design, and it affects its performance during operation, such as combustion efficiency, boiler efficiency, ash deposition, corrosion issues, and emissions[177]. Generally, lower rank coals require larger boilers to optimise the plant's efficiency[177]. However, coals with higher quality are more expensive, so a trade-off between cost and performance must be obtained[177]. Blending coals is routinely done to manage this trade-off, sometimes with biomass or waste[177].

Performance issues can be expected when biomass is used as a fuel due to its high moisture content, low heating value, and low bulk density[177]. Furthermore, the biomass mineral content, particularly potassium and chlorine, exacerbates deposition and corrosion. This issue reduces the heat transfer coefficient, leads to additional maintenance, and reduces heat exchange surfaces' lifetime[177, 179]. However, using biomass as a fuel reduces SO_x and NO_x emissions due to its lower sulphur and

Table 2.2: Effect of fuel properties on plant's performance, adapted from Miller [177].

Property	Performance impact
Heating value	Determines fuel mass flow. Affects plant capacity, pulverisers, burners, feeding systems, fans, pollution control equipment, and coal and ash handling.
Moisture content	Affects coal and ash handling and storage. Influences excess air required, thermal efficiency, and pollution control equipment.
Volatile matter content	Affects storage, pulveriser outlet temperature, fuel particle diameter, and combustion.
Ash	Affects coal and ash handling, pulverisers, furnace, heat exchange sections, unburnt carbon in ash, slagging, fouling, erosion, corrosion, and pollution control equipment.
Sulphur	Affects slagging, corrosion, and pollution control equipment. Higher content increases SO_x, which increases acid dew point temperature.
Nitrogen	Affects pollution control equipment. Nitrogen from the fuel generates 75 – 95 % of total NO.

nitrogen content[177, 179]. Biomass is also considered a carbon-neutral fuel because it emits the same amount of CO_2 during combustion as it captured from the atmosphere during growth[179].

Changing fuel quality from the design coal impacts the plant's performance[177]. This fuel quality issue is expected to happen during the plant's lifetime due to several factors such as mine closures, price fluctuations, and environmental regulations[177]. The effect of fuel properties on plant performance is detailed in Table 2.2.

The amount of heat released from combustion depends on the fuel's heating value[177]. There are generally two heating values: the lower heating value (LHV), which is commonly used in Europe, and the higher heating value (HHV), which is commonly used in the United States and Canada[180]. The HHV is greater than the LHV and the water's heat of vaporisation provides the difference between these values[180], following the relationship

$$LHV = HHV - h_g \left(\frac{9H}{100} + \frac{M}{100} \right) \tag{2.3}$$

where h_g is the latent heat of steam (2260 kJ/kg); H is the fuel's hydrogen content (%); and M is the fuel's moisture content (%). Hence, higher efficiencies are calculated when using the fuel's LHV.

Pulverised-coal power plants follow the Rankine cycle, a thermodynamic cycle where heat is converted into work[173]. Water is the fluid of choice in the loop because of its thermodynamic properties, availability, and cost; however, organic compounds can also be used in what is called the organic Rankine cycle (ORC)[173, 181].

A Rankine cycle differs from a Carnot cycle by pressurising a liquid, obtained by con-

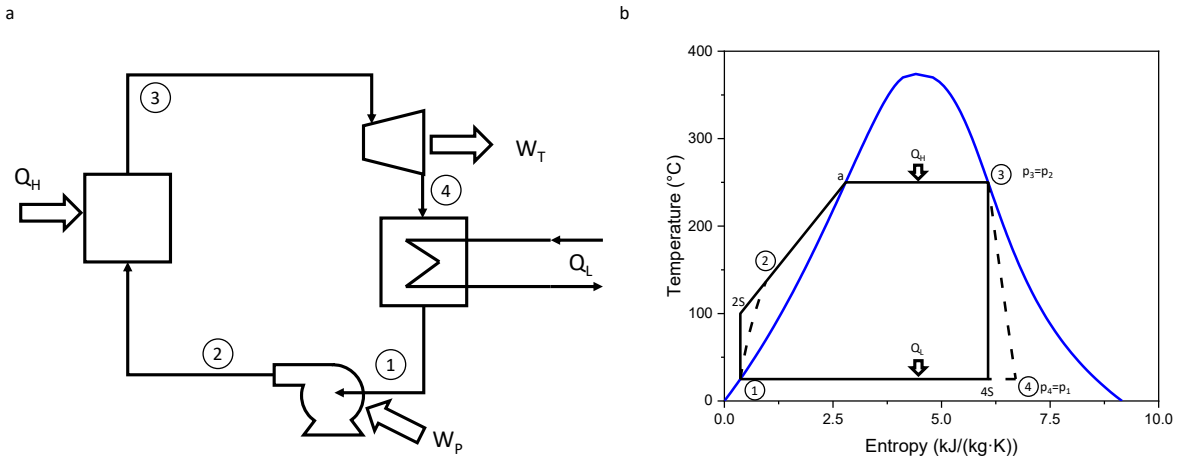


Figure 2.7: A simple Rankine cycle exemplified as a schematic of the cycle (a) and a temperature entropy diagram (b), adapted from Zhang [173].

densing steam, instead of pressurising steam using a compressor, resulting in 1 – 3 % of the power consumption of a Carnot cycle[173]. Pressurising liquid water is what makes the Rankine cycle a practical Carnot cycle[173]. On the downside, this cycle requires that heat is spent vaporising water, thus reducing the amount of heat available to increase the steam's temperature[173].

A schematic diagram of a simple Rankine cycle is presented in Figure 2.7 (a) where water is pumped to high pressure ($1 \rightarrow 2$) using power W_P, then heat Q_H is absorbed in the furnace at constant pressure ($2 \rightarrow 3$) to generate a dry saturated steam[173]. In practice, steam is superheated before entering the turbines[173]. This steam is then expanded in a series of turbines ($3 \rightarrow 4$) generating power W_T[176], decreasing temperature and pressure with some condensation[173]. In practice, steam is bled at several stages in the turbines to increase the feedwater temperature before entering the furnace[173]. Then, steam is condensed to saturated water ($4 \rightarrow 1$) releasing heat Q_L to the environment and pumped again, thus closing the cycle[173].

The feedwater heating train is composed of shell-and-tube heat exchangers designed to increase feedwater's temperature to near boiling before entering the furnace[173, 174]. Nowadays, up to nine feedwater pre-heaters are used in coal power plants[174]. The feedwater's temperature is increased this way against hot steam bled from the turbines, which will be mixed with the feedwater after transferring its heat in the heat exchangers and pumped to the operating pressure[173, 174]. Higher temperatures will enable higher live steam pressures, improving the heat rate inside the boiler, ultimately improving the steam cycle's efficiency[173, 174].

It is possible to improve the Rankine cycle efficiency by increasing the superheater temperature and pressure[173]. Changing the operating conditions from subcritical to supercritical operation improves the plant's efficiency. This improvement is accom-

plished by using steam above 221 bar and 374 °C[182, 183]. No boiling occurs when operating above this point, and as such, there is no distinction between liquid water and steam[182, 183]. This lack of boiling lead to the replacement of drum-type boilers (where liquid water is separated from steam) to once-through units in supercritical plants[183]. Hence, these plants should technically be termed steam generators, but are still commonly referred to as boilers[182].
Increasing the operating temperature and pressure requires the use of more advanced and expensive equipment, which delayed the widespread implementation of ultra-supercritical technology for power generation[173]. An evolution of ferritic steels used in boilers is exemplified in Figure 2.8. In general, tungsten (W), molybdenum (Mo), and cobalt (Co) are primary solid-solution strengtheners; vanadium (V) and niobium (Nb) are precipitation strengtheners; nickel (Ni) increases toughness and reduces creep strength, and carbon (C) forms carbide precipitates which must be optimised to achieve adequate weldability[173].
The distinction of four types of pulverised coal combustion (PCC) power plants are based on their thermodynamic cycles and operating parameters[173]:

- **Sub-critical power plant**
  The first generation of PCC power plants are built with creep-resistant ferritic steels, low-alloy CMn and Mo ferritic steels to enable safe operation at high temperature during long periods[178, 182, 184]. They are usually operated with subcritical steam at 14 – 17 MPa and up to 566 °C[183, 185]. These plants generally achieve 25 – 37 % lower heating value (LHV) efficiency[183, 184], although higher efficiencies can be achieved[185].

- **Supercritical power plant**
  Steam pressure and temperature are increased to the supercritical region, above 22.1 MPa and 374 –593 °C, increasing the plant's efficiency to 35 – 40 % LHV[182–185]. However, this requires the use of higher quality materials, generally low alloy CrMo steels and 9 – 12 % chromium martensitic steels[178, 182, 184].

- **Ultra-supercritical power plant**
  This type of power plants operate with steam conditions between 580 and 620 °C at 22 – 25 MPa increasing the power plant's efficiency to 40 – 45 % LHV[182–184, 186]. This led to the development of new alloys, with improved 9 – 25% chromium martensitic steels and austenitic steels[178, 182, 184, 186]. State-of-the-art ultra-supercritical plants can achieve net efficiencies of 47 % LHV[184].

- **Advanced ultra-supercritical power plant**
  This type of power plants operate between 700 and 760 °C at 30 – 35 MPa. They

are able to achieve 50 % LHV efficiency, reducing CO_2 emissions per MWh[173, 182–184, 186, 187]. The extreme operating conditions of these plants demand the use of high technical construction materials based on nickel alloys for the steam generator, critical steam piping and turbines[178, 182, 184, 186, 187]. Reducing equipment costs should consider new plant arrangements whilst enabling adequate operability and maintainability[184, 186, 187]. Plant Barry Unit 4 in Bucks, Alabama successfully operated a prototype of this type over 17 thousand hours in 2014, proving its feasibility[184, 186, 187].

A comparison between these power plants can be seen in Figure 2.9, demonstrating a significant efficiency improvement of the newer technologies. Increasing the power plant's net efficiency by 20 % will decrease the CO_2 emissions per MWh by more than 30 %[175]. Hence, adopting ultra- and advanced ultra-supercritical power plants, even without carbon capture, can reduce the electricity's carbon intensity. Furthermore, the lower amount of flue gas per MWh will likely decrease the relative capital costs of the flue gas processing equipment[188].
Boilers can be designed to operate under constant- or sliding-pressure[183]. However, once-through ultra-supercritical plants are usually operated at sliding-pressure as this configuration requires lower start-up times and minimum load[183].
All new plants must come equipped with a flue gas desulphurisation (FGD) system, post-combustion NO_x treatment and in-furnace NO_x control before the flue gas is sent to the stack[172, 184]. Ultra-supercritical plants show improved environmental performance compared with their sub-critical counterparts, showing reduced CO_2, NO_x, and SO_x emissions per unit of electric power generated[173]. Water must be cooled before being discharged to the environment to reduce thermal pollution, which affects the ecosystem by decreasing dissolved O_2 in water[172, 184].
The most common FGD used in coal power plants is wet-scrubbing[175]. Wet-scrubbing is generally done by adsorption in a spray tower using a slurry of lime (CaO) or limestone removing up to 99 % of sulphur from the flue gas[175]. This system operates below 100 °C and also removes other acid gases such as hydrogen chloride (HCl)[175]. Wet gypsum formed in this unit can be sold for plasterboard manufacture[175].
Nitrogen oxides are formed in three different pathways[175]. The first is thermal NO, occurring when N_2 and O_2 dissociate at higher temperatures and re-associate at lower temperatures[175]. The second, considered less significant for pulverised coal plants, is prompt NO, where N_2 dissociates at higher temperatures and reacts with hydrocarbon radicals until NO is formed[175]. The third and most significant NO_x source comes from the fuel and is commonly referred to as fuel NO_x[175]. However, only part of fuel-N converts to NO_x, with the remainder being converted to elemental nitrogen (N_2) since both oxidation and reduction reactions occur in the flame[175]. Nitrogen oxide

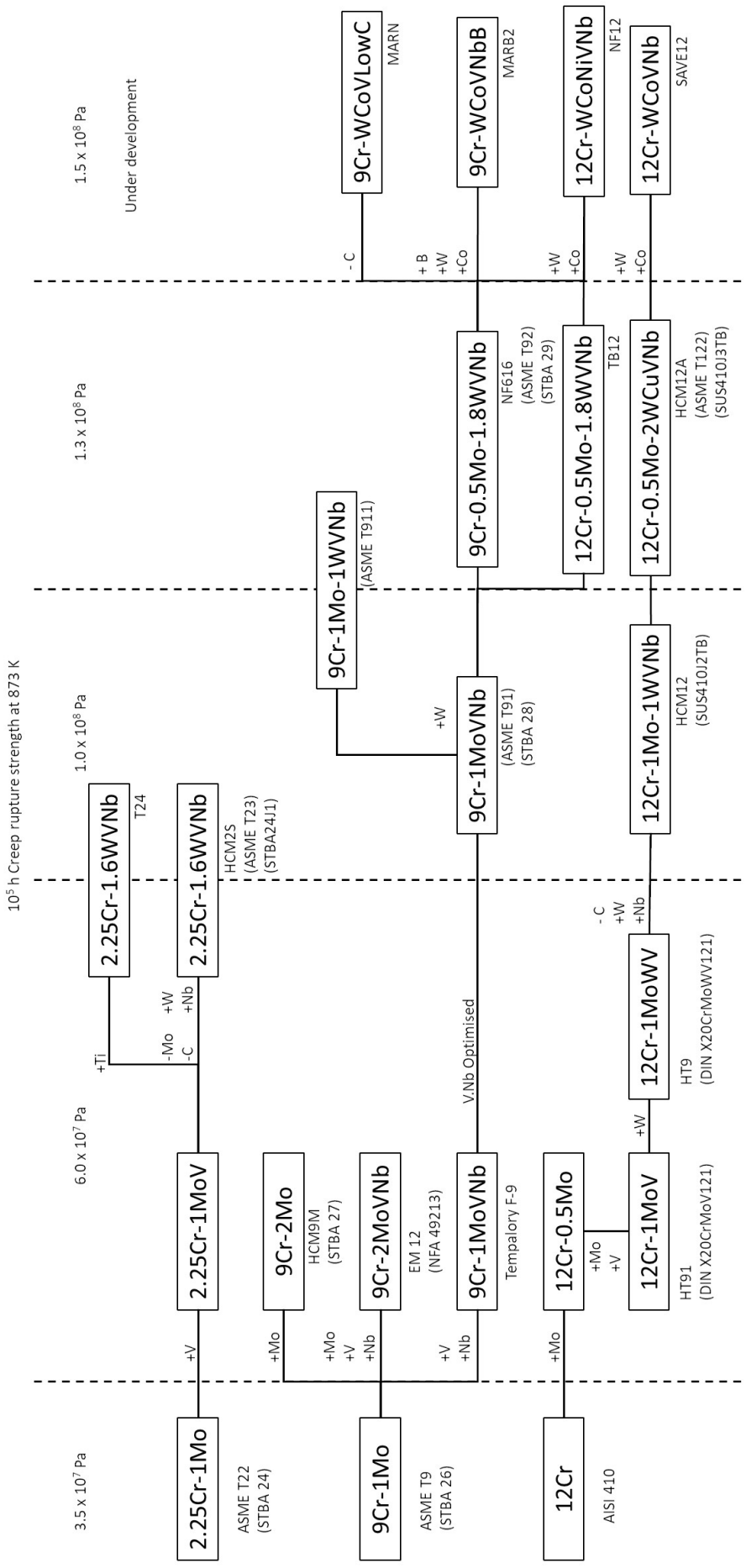


Figure 2.8: Evolution of ferritic steels for boilers, adapted from Zhang [173].

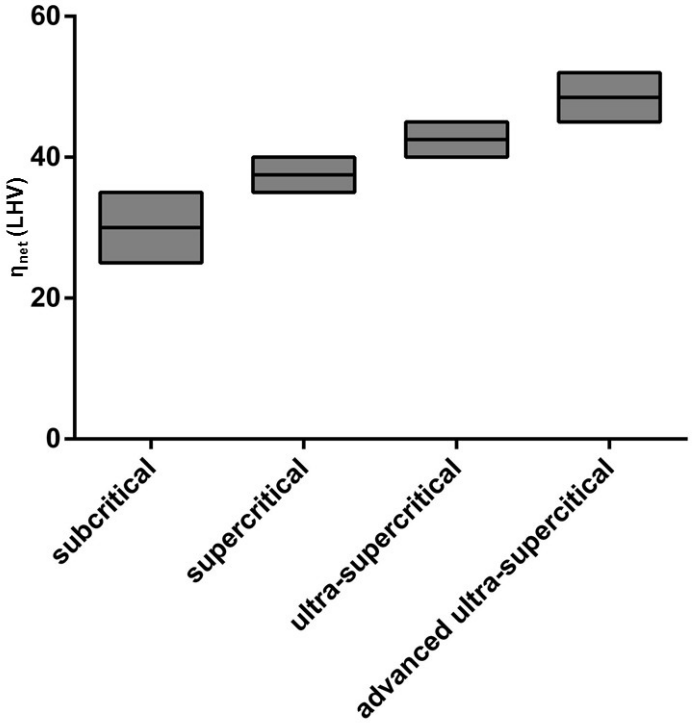


Figure 2.9: Net efficiency for each pulverised-coal power plant technologies. The plot was constructed using data from Nicol [184], Weitzel et al. [186].

emissions can be reduced by controlling fuel combustion, through air staging or low NO_x burners, or using a post-combustion treatment such as selective catalytic reduction (SCR), usually using vanadium supported on a titanium base[175].

2.3.2 Oxy-fuel combustion

The number of binary collisions per combustion volume increase at higher oxygen concentrations[47, 69, 131, 172, 189] according to Equation 2.4.

$$Z_{O_2-Fuel} = \sqrt{\frac{8\pi k_B T}{\mu_{O_2-fuel}}} d^2_{O_2-fuel} \frac{n_{O_2}}{V} \frac{n_{fuel}}{V} \tag{2.4}$$

Where Z_{O_2-Fuel} is the total rate of collisions of oxygen and fuel per unit volume (m^3/s); k_B is Boltzmann's constant, equal to 1.38×10^{-23} (J/K); T is the absolute temperature (K); μ is the reduced mass of oxygen and fuel, equal to $\frac{m_{O_2} m_{fuel}}{m_{O_2}+m_{fuel}}$; d_{O_2-fuel} is the collision diameter between O_2 and the fuel molecules (m); n_{O_2} and n_{fuel} are the number of moles of oxygen and fuel, respectively; and V is the combustion volume (m^3). Equation 2.4 assumes that the gas behaves ideally and that molecules are solid spheres, and serves as an approximation of the physical interactions between oxygen and fuel. Hence, we can use the ideal gas law from Equation 2.5

$$pV = nRT \Leftrightarrow \frac{n}{V} = \frac{p}{RT} \Leftrightarrow \frac{n}{V} = \frac{p}{k_B N_A T} \tag{2.5}$$

where p is pressure (Pa); R is the ideal gas constant, equal to 8.314 (J/(K.mol)); and N_A is the Avogadro constant, equal to 6.022×10^{23} molecules per mole. Substituting Equation 2.5 into Equation 2.4 demonstrates that the number of binary collisions between oxygen and fuel molecules is proportional to their partial pressure.

$$Z_{O_2-Fuel} = \sqrt{\frac{8\pi k_B T}{\mu_{O_2-fuel}}} d^2_{O_2-fuel} \frac{p_{O_2}}{k_B N_A T} \frac{p_{fuel}}{k_B N_A T} \tag{2.6}$$

Assuming that the total pressure remains constant, reducing the partial pressure of nitrogen in the oxidant will increase the partial pressure of oxygen and fuel in the combustion volume. Hence, the number of collisions between oxygen and fuel will increase according to Equation 2.6, increasing the amount of heat released per combustion volume, which increases flame velocity and temperature[131]. These characteristics led to the use of oxy-combustion in steel-making processes, welding, and metal cutting, as mentioned earlier[105, 131].

Coal combustion

During pulverised-fuel combustion, the first step is the release of volatile matter trapped in the particle, called devolatilisation. Afterwards, the combustion of solid matter, or char, takes place. The combustion of solid matter is the limiting step because the kinetic rates of heterogeneous combustion are much lower than the gas-phase reactions[190]. The combustion of solid carbons involves a series of reactions where oxygen forms complex surface oxides before the loss of carbon[191]. Thermal decomposition of these carbon-oxygen complexes is characterised by their activation energy, usually in the range of 160 and 420 kJ/mol[192, 193]. The structure of the solid carbon, which varies according to its type, affects the kinetic rate of the combustion reactions[191, 193, 194]. This structure impacts thermal annealing, which relates the structural modification of carbon during combustion, or gasification, at high temperature with the rate of heterogeneous reactions[194].

The mechanism of complex formation was first evaluated using coal and pure-carbon sources at low temperatures (below 500 °C)[191, 194]. The chemical nature of the surface complexes has been identified using wet chemical methods, electron spectroscopy (XPS), infrared spectroscopy, and temperature-programmed desorption[192]. Oxygen carbon moieties identified through these methods include acid anhydride, alcohol, carboxylic acid, ether, ketene, lactone, phenol, and quinone[195]. First, a metastable oxide complex is obtained following Equation 2.7[191, 194].

$$-C^*_s + O_2 \longrightarrow -C(O_2)^\#_s \tag{2.7}$$

Continuous exposure to oxygen further stabilises the complex with the release of gaseous

carbon oxides following Equation 2.8[191, 194].

$$-C(O_2)_s^{\#} + O_2 \longrightarrow -C(O)_s + CO_2,\ CO \tag{2.8}$$

Thermal decomposition of the metastable oxide occurs following Equation 2.9[191, 194].

$$-C(O_2)_s^{\#} \longrightarrow -C(O)_s + CO_2,\ CO \tag{2.9}$$

The stable complexes are desorbed at higher temperatures following Equation 2.10[191, 194].

$$-C(O)_s \longrightarrow -C_s^* + CO_2,\ CO \tag{2.10}$$

The presence of steam or CO_2 was found to reduce the formation of carbon-oxygen complexes, demonstrating that substitution of N_2 for CO_2 or steam, such as in oxy-combustion, was not trivial[192, 194]. This CO_2 presence also affects the heat capacity of the gas, radiant transport, and other gas transport properties[190, 193, 194, 196].
The reactivity between CO_2 and char was found to be one order of magnitude lower than N_2-char[194]. Also, the different evolution of microstructure and porosity under oxy-combustion changes the thermal annealing process[194]. This microstructure and porosity change implies that char combustion rates are different in oxy-combustion than in air-fired[194]. Thus, using kinetic parameters obtained for air-fired conditions to simulate oxy-combustion will predict results that deviate from the actual values.
The gasification rates of carbonaceous materials under CO_2 and steam were investigated using thermogravimetric analysers[193, 197]. Insights gained from these new investigations motivated researchers to propose two new gasification mechanisms, Equations 2.11 and 2.12, to account for the high concentrations of CO_2 and steam under oxy-combustion conditions.

$$-C_s^* + CO_2 \longrightarrow 2CO \tag{2.11}$$

$$-C_s^* + H_2O \longrightarrow -C(O)_s + H_2 \tag{2.12}$$

The water gas-shift reaction can also occur under these conditions following Equation 2.13[197].

$$CO + H_2O \rightleftharpoons CO_2 + H_2 \tag{2.13}$$

The rates of reaction are obtained using a Langmuir-Hinshelwood kinetic expression with a first-order concentration dependence[193, 197]. Karlström et al. [197] used the

global reactions shown in Equations 2.14 to 2.18 to model the char-C reactions by O_2, CO_2, or H_2O.

$$2C(s) + O_2 \longrightarrow 2CO(g) \tag{2.14}$$

$$C(s) + CO_2(g) \longrightarrow 2CO(g) \tag{2.15}$$

$$C(s) + H_2O(g) \longrightarrow CO(g) + H_2(g) \tag{2.16}$$

$$2CO(g) + O_2(g) \longrightarrow 2CO_2(g) \tag{2.17}$$

$$CO(g) + H_2O(g) \rightleftharpoons CO_2(g) + H_2(g) \tag{2.18}$$

Then, the reaction rate constants (mol/(m^3.s)) for heterogeneous reactions (Equations 2.14 to 2.16) can be calculated according to Equations 2.19 to 2.21[197].

$$K_{O_2} = \frac{C_{O_2} k_{ads,O_2}}{1 + \frac{k_{ads,O_2}}{k_{des,O_2}} C_{O_2}} \tag{2.19}$$

$$K_{CO_2} = \frac{C_{CO_2} k_{ads,CO_2}}{1 + \frac{k_{ads,CO_2}}{k_{des,CO_2}} C_{CO_2}} \tag{2.20}$$

$$K_{H_2O} = \frac{C_{H_2O} k_{ads,H_2O}}{1 + \frac{k_{ads,H_2O}}{k_{des,H_2O}} C_{H_2O}} \tag{2.21}$$

Where C_i is the concentration of component i in mol/m^3, and k_i is an Arrhenius rate calculated using Equation 2.22.

$$k = Ae^{\frac{-Ea}{RT}} \tag{2.22}$$

Where A is the pre-exponential factor in s^{-1} for adsorption and mol/(m^3.s) for desorption; Ea is the activation energy in kJ/mol; R is the gas constant in kJ/(mol.K); and T is the temperature in K.

The homogeneous reaction rates (mol/(m^3.s)) of CO oxidation (Equation 2.17) and water gas shift (Equation 2.18) can be calculated according to Equations 2.23 and 2.24, respectively[197].

$$K_{CO} = k_{CO} C_{CO} \sqrt{C_{O_2} C_{H_2O}} \tag{2.23}$$

Table 2.3: Kinetic parameters of gasification of short rotation coppice, extracted from Karlström et al. [197].

Parameter	Value
A_{ads,CO_2}	7.33×10^{11}
Ea_{ads,CO_2}	226
A_{des,CO_2}	3.38×10^{12}
Ea_{des,CO_2}	234
A_{ads,H_2O}	4.26×10^{12}
Ea_{ads,H_2O}	223
A_{des,H_2O}	1.31×10^{11}
Ea_{des,H_2O}	192
A_{ads,O_2}	$+\infty$
Ea_{ads,O_2}	1
A_{des,O_2}	$+\infty$
Ea_{des,O_2}	1

$$K_{CO+H_2O} = k_{CO+H_2O}\left(C_{CO}C_{H_2O} - \frac{C_{CO_2}C_{H_2}}{K_{eq}(T)}\right) \tag{2.24}$$

Where $K_{eq}(T)$ is the equilibrium constant of the reaction shown in Equation 2.18 at a given temperature T.

Karlström et al. [197] determined the kinetic parameters listed in Table 2.3 for a short rotation coppice, a type of biomass, by minimising the least-squares difference of the residuals between the computed and experimental char conversions. The experiments were performed using an electrically-heated single-particle reactor of quartz glass at 800, 900, and 1050 °C and 34 mol% CO_2 or 34 mol% H_2O with N_2 balance[197]. However, the variability of adsorption between each fuel type makes the kinetic parameters listed in Table 2.3 limited to this type of fuel.

The experiments used to determine the kinetic parameters were performed at lower temperatures than commonly encountered during pulverised-fuel conditions. Indeed, Haynes [192] reported that using these parameters at temperatures above 1000 °C leads to a significant deviation of the simulated gasification rates due to the higher oxygen chemisorption predicted by the model at higher temperatures. This deviation makes the kinetic parameters obtained from these experiments of limited value for the simulation of pulverised-fuel conditions.

Another consequence of reducing the amount of nitrogen in the oxidant lies in increasing the concentration of combustion products in the flue gas, mostly carbon dioxide and water[47, 64, 102]. Separating CO_2 from the flue gas would then be done by condensing water, providing a cheaper separation than post-combustion capture for dilute systems (*i.e.* air-fired combustion)[47].

This simple, low cost of separating CO_2 from the flue gas made it an attractive option

to retrofit coal-fired utility boilers and use the captured CO_2 for enhanced oil recovery (EOR)[105–107, 198]. However, the heat transfer characteristics of the flue gas from oxy-combustion are distinct from air combustion, impacting the steam cycle[64]. This impact can be minimised by recycling a fraction of flue gas back to the furnace to achieve similar heat transfer characteristics to that of an air fired plant[64, 102, 198]. Payne et al. [198] also observed changes in the heat flux distribution inside the boilers. These changes occur because the high concentration of steam in the flue gas increases the convective heat transfer in the low-temperature heat exchangers[198]. This issue is controlled by varying burner tilt, load distributions, or excess O_2 amount[198].
Burning a fuel with a medium- to high-purity O_2 stream instead of air improves combustion efficiency and emits less NO_x to the atmosphere[47, 62, 63, 69, 131]. These benefits are attained because N_2 present in air, which acts as a ballast gas and uses the heat of combustion to increase its temperature and produce small amounts of thermal NO_x in air-fired plants, is removed from the combustion media[63, 131, 174]. Nitrogen oxides evolve during combustion of fossil fuels following three different mechanisms[174]:

- Thermal NO_x, which accounts for approximately 20 % of total NO_x in coal-fired combustion using air as oxidant.
- Prompt NO_x.
- Fuel NO_x, if the fuel contains nitrogen.

Thermal NO_x forms above 1300 °C from the reaction between N_2 from air and atomic oxygen[174]. This atomic oxygen results from breaking the molecular O_2 bonds at high-temperature[174]. Most of the NO_x formed in the furnace (90 %) are in the form of NO, so the reaction mechanisms will follow only NO formation. The reaction follows the Zeldovich mechanism[174], shown in Equations 2.25 – 2.27.

$$N_2 + O \rightleftharpoons NO + N \tag{2.25}$$

This reaction is proportional to the concentration of atomic oxygen, and its conversion rate increases exponentially with temperature[174]. The nitrogen atom then reacts with an oxygen molecule according to Equation 2.26.

$$N + O_2 \rightleftharpoons NO + O \tag{2.26}$$

If combustion occurs during fuel-rich conditions, then NO_x formation primarily occurs via reaction with existing hydroxide ions following Equation 2.27.

$$N + OH \rightleftharpoons NO + H \tag{2.27}$$

Prompt NO_x is of minor importance during pulverised coal combustion[174]. Here, nitrogen from air reacts with hydrocarbon radicals in an early phase in the flame front following Equation 2.28.

$$CH + N_2 \rightleftharpoons HCN + N \tag{2.28}$$

The intermediate product (HCN) later oxidises to form NO_x[174].
The conversion of nitrogen present in coal to NO is approximately 30 %[174]. The actual amount depends on the properties of coal, the nitrogen content, air ratio, and combustion temperature[174]. It is possible to reduce the conversion to as low as 5 % by using efficient air- and fuel-staging during combustion[174].
Nitrogen from a fuel can be released during devolatilisation in the form of amines and cyanogens[174]. The rest of the nitrogen remains in the char, where only a small fraction converts to NO_x[174].
The removal of N_2 reduces the oxidant's volumetric flow by ca. 80 %, thus reducing the size of the furnace required to obtain the same amount of thermal energy when using pure O_2 instead of air[63, 131].
Oxy-combustion only requires 3 – 5 % excess oxidant to obtain similar O_2 fractions in the flue gas to air-fired, typically operating with 20 % excess air[47, 69, 131, 172]. The high costs associated with O_2 production is another reason to reduce excess O_2 compared with air-fired, where the oxidant is essentially free[47, 69, 131, 172]. Reducing excess oxidant also reduces the boiler's size and, consequently, reduces the capital costs to erect the plant, opening opportunities to use advanced steam technologies at reduced costs per MWh[47, 69, 131, 172].
High flame temperatures (over 2400 °C) can be reduced to air-firing levels by recycling 60 – 70 % of the flue gas to the furnace, creating an oxidant with 30 vol% of O_2, avoiding the use of expensive materials for pure O_2[47–49, 51, 62, 63, 65, 69, 77, 103, 110, 131, 150, 199]. These higher O_2 concentrations in the oxidant, relative to air, are required to obtain a similar flame temperature due to the higher gas emissivities of CO_2 and H_2O relative to N_2[47, 69, 199]. Corrosive species such as sulphur oxides (SO_x) must be removed to prevent build-up in the system from recycling flue gas when coal is used as fuel[47, 69, 199–201].
Indeed, SO_x in the flue gas from oxy-combustion (724 to 866 ppm) can be up to five times higher than during air-combustion (176 to 218 ppm) because of the recycled flue gas and lack of N_2 dilution[200, 202]. Higher SO_x concentrations in the flue gas from oxy-combustion increase the acid dew point from 116 °C to 141.6 °C[200, 201]. This issue can be avoided using a suitable method to remove SO_x from the flue gas before recycling. Limestone appears to be particularly useful in oxy-combustion[202]. Stanger and Wall [202] suggest that this enhanced effect may be due to the inhibition of the

$CaCO_3 \longrightarrow CaO$ reaction from the high partial pressure of CO_2.
Sulphur exists in coal mostly as organic sulphur and pyrite (a sulphide), although some amounts of sulphates and elemental sulphur can also be present[174]. Most of this sulphur converts to SO_2, with reported conversions as high as 90 %[174].
Sulphur oxides can be captured in ash if it contains alkaline earth components, which is more common in brown coals[174]. Higher levels of sulphur were found in fly ash particles below 0.1 μm during oxy-combustion compared to air-firing[202]. Otherwise, there appears to be no significant difference in sulphur deposition between oxy- and air-fired conditions[202].
A mass balance on pilot plant studies indicated a sulphur build-up in the recirculation pipework[202]. Hence, this section should be constructed using suitable corrosion-resistant materials.
Ash is also an issue when using coal as a fuel because it can damage the recirculating fans, so removing at least part of it is recommended by using either electrostatic precipitators (ESP) or baghouse filters[201, 203]. A careful selection of the materials that can operate under these conditions must be performed to avoid reducing this equipment's lifetime because it is necessary to operate at higher temperatures than air-firing to avoid acid dew point.

Oxy-combustion power plant

The first oxy-combustion pilot plant was built in the 1980s to test the process's viability and operated at 537 °C and 106 bar with a 50 MW_e capacity[198]. Payne et al. [198] observed adequate combustion characteristics at the recycle ratios of $CO_2/O_2 = 2.7$ and $(CO_2 + H_2O)/O_2 = 3.2$ when using dry or wet recycle, respectively. These recycle ratios result in an overall flue gas recycle between 65 and 75 %[102].
There are usually two flue gas recycles in an oxy-coal combustion process, termed primary and secondary recycle and taken at different locations[64, 70, 77, 102, 114, 198]. These locations vary according to coal type, rank, impurities, warm or cold recycle, and whether a dry or wet recycle is chosen[102]. A warm recycle, for low S coals, and a cold recycle process, for high S coals, are illustrated in Figure 2.10 a) and b) respectively.
Coal combustion takes place in the burners using a mixture of the secondary RFG with the O_2 supplied by the ASU, creating a hot flue gas rich in CO_2 (60 – 70 vol%) and H_2O (20 – 25 vol%) with some amount of O_2 (3 – 4 vol%) and N_2 (0 – 10 vol%) depending on coal rank and process design[63]. This flue gas enters the boiler and heats the working fluid, typically water, creating high-pressure steam that generates power via expansion inside the turbines[63]. Flue gas is cooled against the primary and secondary RFG at the boiler's exit using a regenerative heat exchanger[63]. Afterwards, approximately 50 wt% is recycled as the secondary RFG and fly ash removed in a suitable equipment, avoiding build-up inside the boiler and damage to other equipment[63].

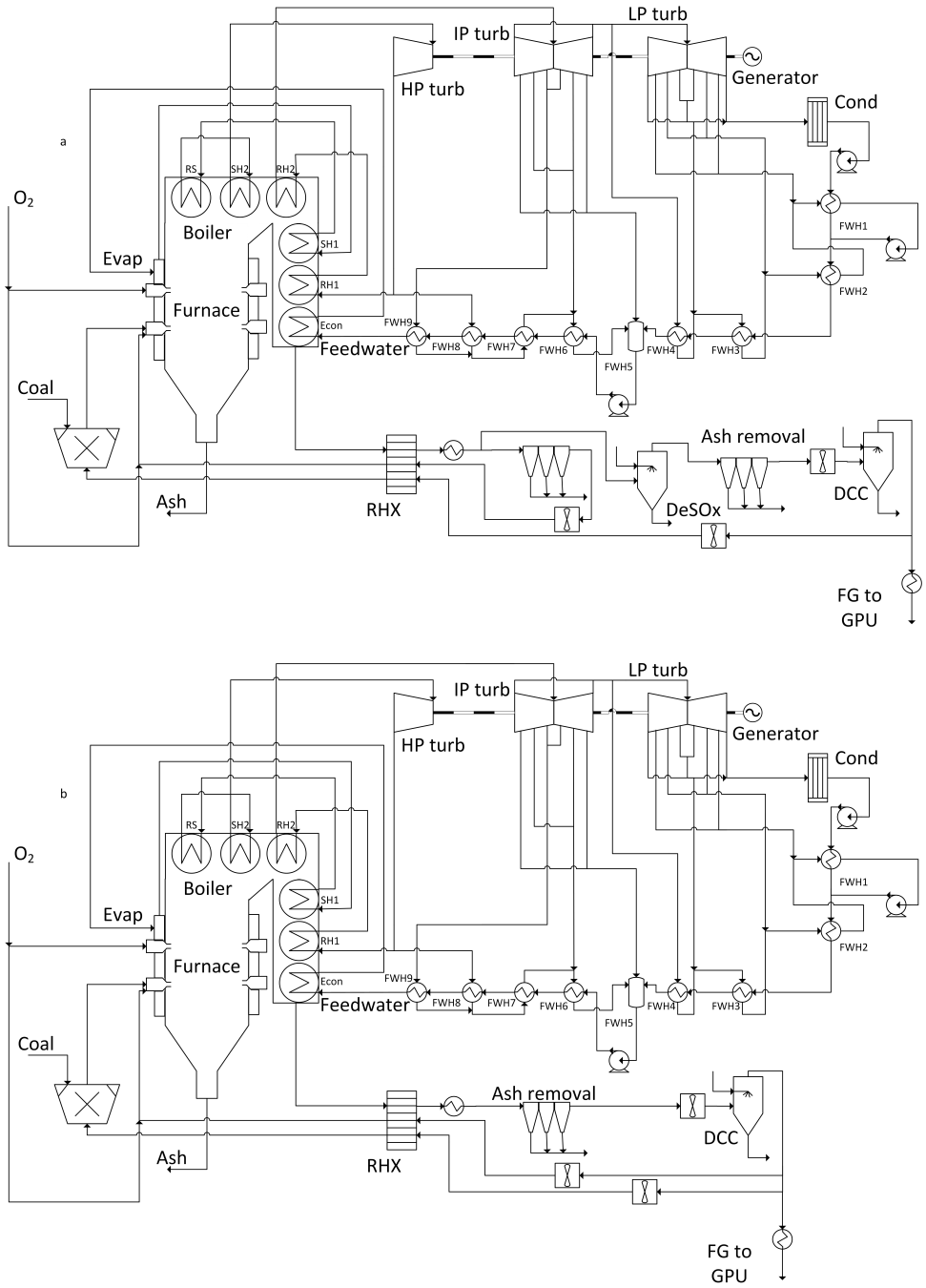


Figure 2.10: Simplified PFD of a pulverised coal oxy-combustion power plant for a) low S coals, and b) high S coals[102] complete with coal mill, boiler, turbine, feedwater heating train, ash collection and flue gas desulphurisation. The boiler is divided into two sections: the furnace, where combustion takes place, and the boiler, where heat increases the temperature of feedwater and generate supercritical steam. HP turb - High pressure turbine; IP turb - Intermediate pressure turbine; LP turb - Low pressure turbine; Cond - Condenser; Econ - Economiser; Evap - Evaporator; SH1 and SH2 - Superheater 1 and 2; RS - Radiant superheater; RH1 and RH2 - Reheater 1 and 2, FWH1 to FWH9 - Feedwater heater 1 to 9; RHX - Regenerative heat exchanger; SD - Spray dryer for desulphurization.

Ash-free secondary RFG is then mixed with O_2 and dispatched to the furnace[63]. The remainder of the flue gas may need to be treated using a desulphurisation unit to avoid corroding the downstream equipment due to acid condensation when firing high-sulphur content coal[63]. Fly ash is also removed from this stream using another ash removal equipment, and flue gas is subsequently cooled using a direct contact cooler (DCC) if dry RFG is required before recycling 37 wt% as primary RFG[1, 49, 64, 70]. On a wet recycle, only the fraction dispatched to the GPU passes through a DCC[70, 102]. This stream is not mixed with O_2, regardless of using dry or wet recycle, but it is used to pulverise ground coal from the mill to the furnace[70, 102].

One of the challenges of this technology is to design a plant that can supply low cost electricity that is robust and able to ramp up or down in production according to demand[47, 69, 199]. Smaller units have been identified as more economical to operate flexibly than larger units due to their lower capital investment[204]. The increasing importance of flexible operation of fossil-fired power plants comes from the increasing penetration of variable renewable energy into the grid[90, 205, 206]. As more renewable sources are introduced to the grid, the more fossil-fired power plants will require to operate in a flexible, load-following manner, with increasingly larger periods of part-load operation[90, 205, 206]. Indeed, this shift is causing the electricity prices to fluctuate so that zero or even negative prices become a regular occurrence[206]. Power plant operators will be faced with no other option than to run the plant at a loss[206]. This price variation poses additional challenges for CCS because these plants will likely be required to operate flexibly at faster start-up and load changing rates[205, 206].

Assuming that CCS is implemented, simulations using the Merit Order Stack with Step Investments (MOSSI) and Unit Commitment Capacity Optimisation (UCCO) models showed that the first coal-CCS plants would operate at baseload capacity alongside nuclear plants due to their low variable costs[206]. However, these units must ramp and shut down if there is a spike in renewable energy output during low demand periods[206]. The authors then evaluated the hourly operational pattern from three coal CCS units at different positions in the merit order[206]. The flexible operation of a supercritical coal-fired power plant with an amine-based post-combustion CO_2 capture process was simulated in gPROMS to obtain the maximum profits from such operation[206]. A 2 % efficiency penalty was observed when the plant operated at minimum stable capacity due to lower temperatures of the flue gas in the steam-generating sections, which reduced the driving force for heat transfer in these sections[206]. The authors noted that as more renewable energy sources penetrate the grid, these spikes will become more frequent and lengthier, forcing some baseload units to become mid-merit and follow the electricity demand[206]. This switch to mid-merit will change unit availability from 93 % down to 46 %, thus increasing the levelised cost of elec-

tricity (LCOE) from $141/MWh to $219/MWh, making these units less economically attractive[206]. However, the authors note the relatively low marginal costs of these units, ranging from $60/MWh to $73/MWh and point out that these units could still be exploited for additional electricity generation, heat generation, or contribute to energy storage systems[206].
This work explores the oxy-combustion of coal-fired power plants for carbon capture and sequestration. This work differs from the analysis performed by Mac Dowell and Staffell [206] by changing the oxidant from air to 95 vol% O_2 mixed with recycled flue gas. Using this mixture results in a higher CO_2 purity during combustion, reducing the energy demand to separate the resulting CO_2 from the flue gas stream compared to a typical post-combustion capture process[47, 69, 199].

2.3.3 Opportunities for improvement

Integrating the ASU, power plant, and the GPU can lead to cost benefits by using low-grade heat of compression from the ASU and GPU to pre-heat the feedwater, thus reducing the number of feedwater heaters and turbine bleeds[111, 114]. New power plants designed for oxy-combustion do not require an alternative air-firing capability because the ASU can be started using power from the grid[114]. Then, the power plant can be started once the ASU produces adequate amounts of O_2 at the required purity[114].
Currently, an oxy-combustion process can ramp up at rates of 2 %/min, but this technology's successful operation requires it to ramp up at rates of 5 %/min[114, 135]. Achieving these rates is a challenge that can be supported by storing 0.5 % of the total oxygen produced as liquid oxygen with only a 0.75 % increase in power consumption and by creating more reliable dynamic simulations and control systems[114, 135].

2.4 Gas Processing Unit

Oxy-combustion increases CO_2 concentration in the flue gas; however, this stream is not at the purity required for pipeline transport, usually set as 95 wt% for enhanced oil recovery activities[49, 63, 66, 77–79, 110, 114, 207, 208]. Flue gas from an oxy-combustion process must still be compressed and upgraded in what is commonly known as a gas processing unit (GPU)[5] to remove impurities, mainly water and excess oxygen to obtain the requirements for pipeline transport[49, 49, 63, 66, 77–79, 110, 114, 207, 208]. Because this GPU does not rely on a solvent-based system, the upstream emissions of oxy-CCS are greatly reduced by eliminating the CO_2 emissions associated with solvent production and supply chain[209]. A schematic representation of a GPU can be observed in Figure 2.11, where flue gas departing from the power plant is cooled after compression to extract water and remove traces of ash

[5] Also referred to as CO_2 compression and purification unit (CO_2 CPU).

and soluble gases. This technology is known as sour gas compression and consists of a two-stage compressor with inter- and after-cooler operating at 25 °C using water as a coolant[49, 49, 63, 66, 77–79, 110, 114, 202, 207, 208]. This technology enables the removal of SO_x and NO_x present in the flue gas by taking advantage of the faster reaction rates to form acid condensates (H_2SO_4 and HNO_3, respectively) at higher pressures with a pH of 0.8[202, 210]. Removing SO_x and NO_x this way has the potential benefit of removing, or at least reducing the size, of traditional flue gas desulphurisation and NO_x control systems, but this will come at the expense of using suitable materials to withstand the highly acidic conditions[202, 210]. Indeed, high NO_x concentrations in the flue gas may be beneficial in this technology to act as a catalyst for SO_x removal[202, 210].

Flue gas is directed to a dehydration unit to remove water vapour and avoid ice formation inside the first multiple stream heat exchanger operating at -27 °C[66, 208, 210]. Compressed flue gas is then sent to a flash unit where a CO_2 rich liquid stream is obtained and subsequently expanded to be used as a cooling agent in the first multiple stream heat exchanger[66, 208, 210]. A gaseous product with lower CO_2 concentration is extracted at the flash unit's top and cooled in a second multiple stream heat exchanger to -54 °C before further separation in another flash unit[211].

A CO_2-rich liquid stream is extracted from the flash unit and used as a cooling agent in the second multiple stream heat exchanger[211]. This stream is subsequently expanded to 8 bar, recycled back to the second multiple stream heat exchanger, and used as a cooling agent in the first multiple stream heat exchanger[211]. The gas with low CO_2 concentration obtained from the second flash unit is used as a cooling agent in the first multiple stream heat exchanger and then vented[211]. The CO_2 rich streams are mixed, obtaining a 97.5 wt% CO_2 product, compressed to 80 bar using a two-stage compressor with inter-cooling at 25 °C, and then pumped to pipeline design pressure[211].

Different GPU types can be designed depending on the required CO_2 purity with a power consumption of 100 – 180 kWh/t_{CO_2}[51, 66, 103, 115, 136, 150, 151]. A comprehensive analysis of the effects that each GPU type has in the power requirement, cooling duty, separation efficiency, and CO_2 purity was performed by Posch and Haider [208]. Kolster et al. [66] evaluated the capital and operating costs of each GPU type.

This thesis will only review two GPU types: the double flash gas processing unit, already discussed during the process description and represented in Figure 2.11; and the GPU with distillation, represented in Figure 2.12, where the second multiple-stream heat exchanger is replaced with a distillation column to obtain high purity CO_2.

A high-purity CO_2 (> 99.9 wt%) is discharged from the bottom of the distillation column and is subsequently compressed to pipeline pressure and cooled to 30 °C[66, 211]. A low-purity CO_2 stream is obtained from the top of the distillation column and cooled

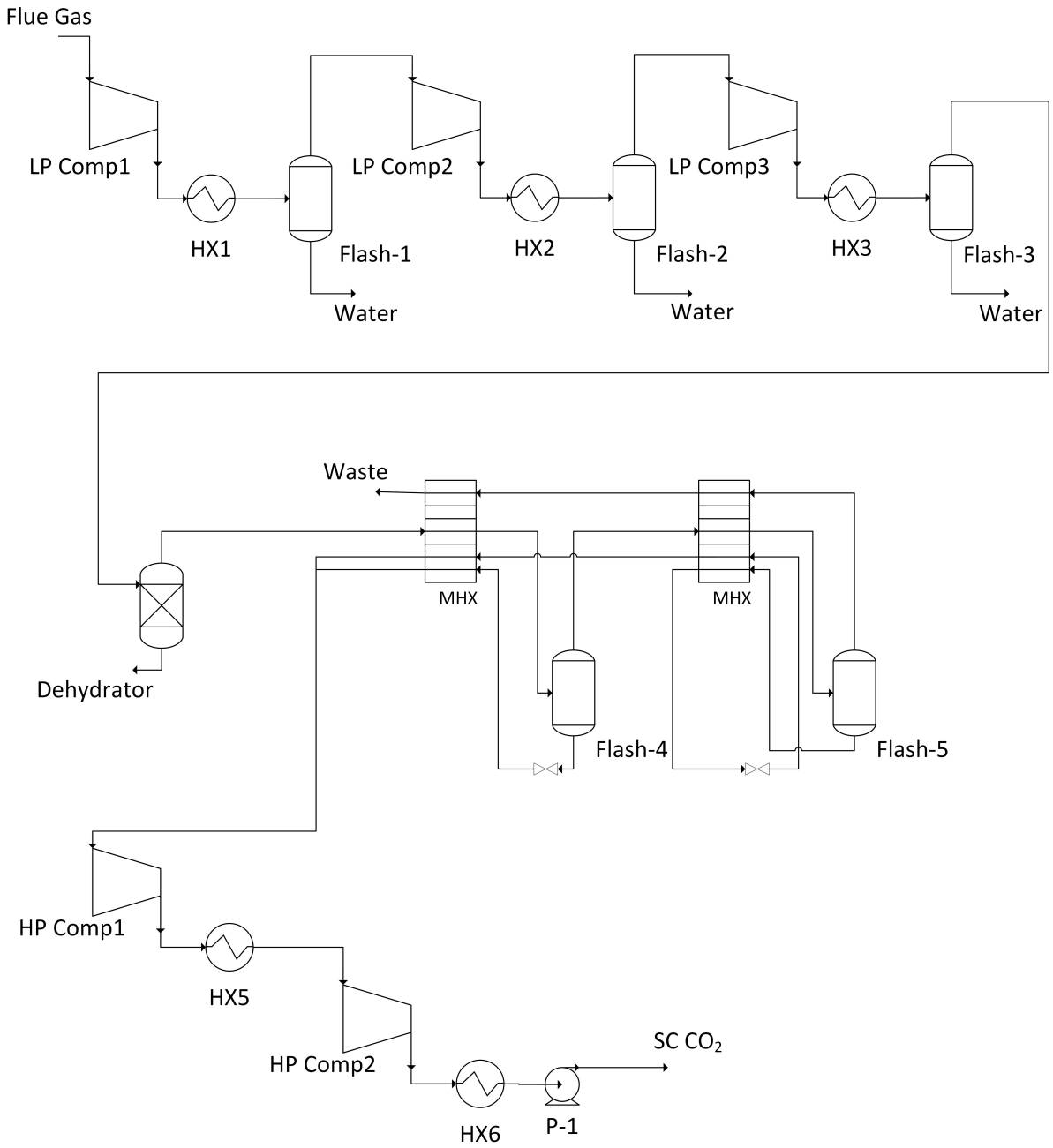


Figure 2.11: Simplified PFD of a double-flash GPU adapted from Posch and Haider [208] and Kolster et al. [66]. LP Comp1 to LP Comp3 - Low pressure compressors 1 to 3; HX1 to HX6 - Coolers; MHX - Multiple heat exchanger; Flash-1 to Flash-5 - Flash separator 1 to 5; P-1 - Pump.

in the multiple stream heat exchanger until partly liquefied[66, 211]. The CO_2-lean vapour phase is expanded and used as a cooling agent in the multiple stream heat exchanger and either vented or used somewhere where cryogenic cooling is required[66, 211]. The CO_2-rich liquid phase is expanded and used as a cooling agent in the multiple stream heat exchanger and subsequently compressed and recycled to the distillation column to improve the separation efficiency[66, 211].

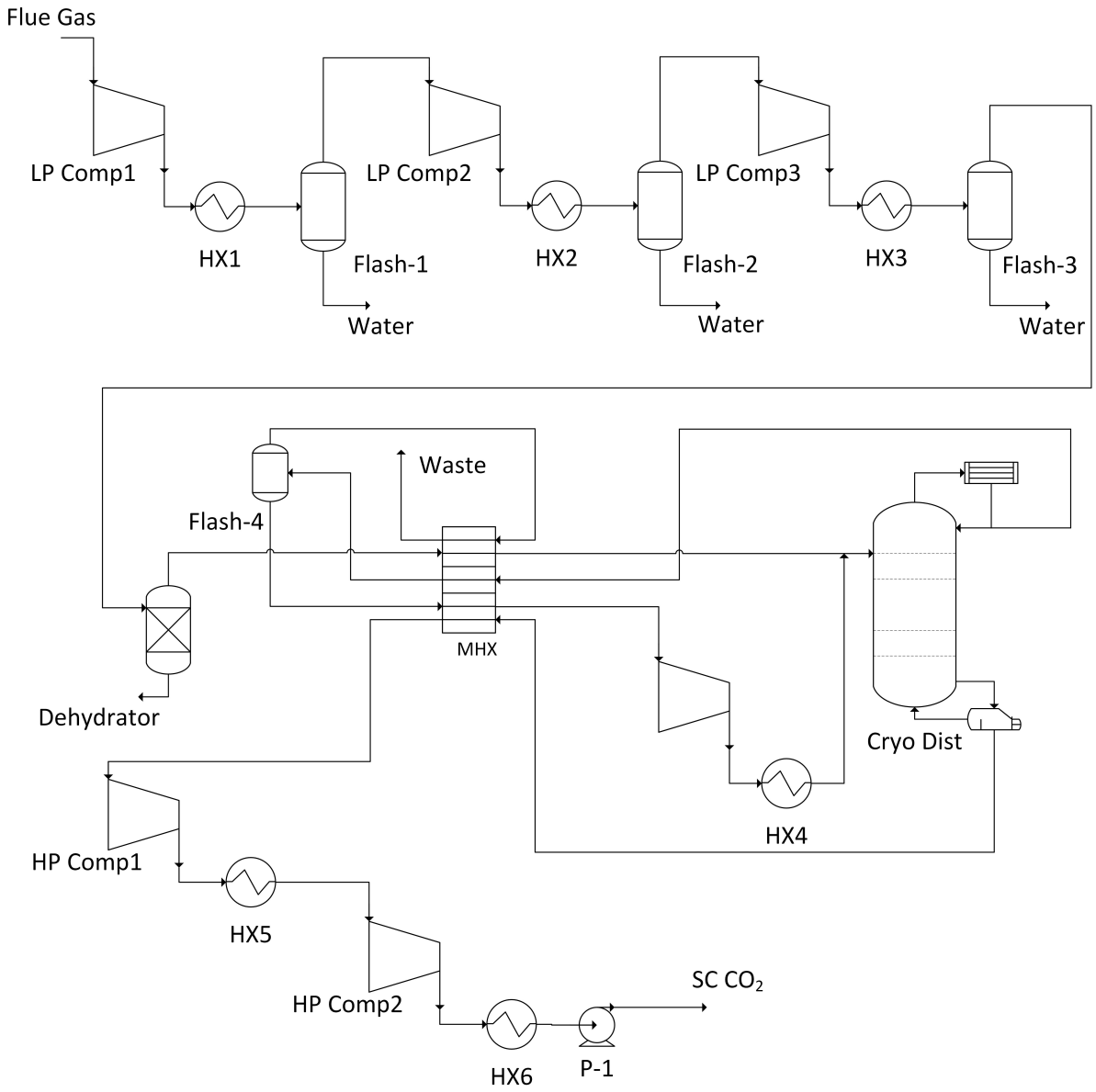


Figure 2.12: Simplified PFD of a cryogenic distillation GPU adapted from Posch and Haider [208] and Kolster et al. [66]. LP Comp1 to LP Comp3 - Low pressure compressors 1 to 3; HX1 to HX6 - Coolers; MHX - Multiple heat exchanger; Flash-1 to Flash-4 - Flash separator 1 to 4; Cryo Dist - Distillation column; P-1 - Pump, as published by Cabral and Mac Dowell [103].

2.5 Negative emission technologies

Negative emission technologies (NET) can complement the residual emissions from hard-to-decarbonise sectors by capturing and storing atmospheric CO_2 underground[71, 73, 74]. Bioenergy with CCS (BECCS), afforestation/reforestation, soil carbon sequestration, biochar, and ocean fertilisation are negative emission technologies that require photosynthesis to capture atmospheric CO_2[71, 73–75, 85]. Negative emissions can also be obtained by capturing atmospheric CO_2 through chemical processes via direct air capture (DAC) and enhanced weathering/ocean alkalinisation[71, 73, 74].

Aforestation/reforestation (AR) has the same potential as BECCS to remove 0.5 – 7 Gt_{CO_2}/yr in 2050; however, BECCS can provide other services, such as generating dispatchable electricity or heat[73, 74]. BECCS also offers the potential to retain existing jobs in thermal power generation units whilst bolstering employment in operations, manufacturing, forestry and transport/logistics, promoting a just transition of the power sector[55, 212].

Atmospheric CO_2 removal through BECCS requires a careful evaluation of the biomass supply chain by applying a full cradle-to-grave life-cycle assessment (LCA)[75, 85, 87, 213, 214]. Carbon leakages on the order of 10 – 30 % across the biomass supply chain have been known to occur[73, 85–89]. Thus, continuous monitoring and recertification of biomass supply chains would be required to guarantee biomass sustainability throughout the project's lifetime.

BECCS is currently a controversial technology from fears of competing with food production and promoting deforestation[74]. It is a renewable energy source that could use waste biomass from agricultural residues or municipal solid waste (MSW) to reduce demand from virgin biomass, avoiding the competition mentioned above[215, 216]. Waste biomass is already being incinerated in some power plants, such as the Drax plant in North Yorkshire, UK using wood pellets,[217] and in Shenzhen, China, using MSW[218], implying that BECCS has potential to be socially accepted[216]. Indeed, Drax considers BECCS a critical technology and is currently pursuing this mitigation option in collaboration with C-Capture[219].

The choice of biomass requires careful investigation regarding its heating value[84] whilst maintaining high environmental and economic sustainability. Indeed, high CO_2 capture cost of \$45/t_{CO_2} – \$250/t_{CO_2}[73, 74] have been documented, mostly from a combination of its heating value with wide fuel costs of \$100/t_{pellet} – \$210/t_{pellet}[220]. Other important factors affecting pellet cost are the pelletisation method, drying, transport, land use, and water consumption[85, 87, 216, 220].

The amount of global sustainable biomass has been reported between 60 and 300 EJ/yr[73, 221, 222] (Table 2.4), similar to the existing global coal fleet capacity[40]. This fact shows the potential to retrofit existing coal-fired power plants to biomass instead of building entirely new infrastructure, incurring only the costs of adapting the plant to this new fuel[223]. Retrofitting existing plants would drastically reduce their carbon intensity because biomass is a carbon-neutral fuel[224]. After all, it uses atmospheric CO_2 for growth during photosynthesis[224]. These units could even become carbon-negative if the resulting CO_2 from combustion is captured and stored[224].

2.5.1 Oxy-combustion of biomass

Oxy-combustion of cereal co-product[225, 226], wood pellets[226], olive waste[227], miscanthus pellets[226], sugarcane bagasse[228], pine sawdust[228–230], and munic-

Table 2.4: Amount of global primary energy from sustainable biomass, extracted from Fuss et al. [73]. A 30 % efficient BECCS plant was used to convert between primary energy and electricity generated.

Parameter	Pessimistic	Median	Optimistic
Primary energy (EJ/yr)	60	130 – 160	350
Electricity (10^3 TWh/yr)	5	11 – 13	29
Contribution (%)	20	42 – 52	120

ipal solid waste (MSW)[218] were successfully performed at test conditions. Therefore, commercial-scale oxy-biomass combustion processes are expected to behave like oxy-coal combustion processes, albeit at higher maintenance costs from increased slagging, agglomeration, and corrosion[231].

2.6 Exergy

Exergy is defined as the amount of work obtained by a system when brought to equilibrium with the environment via reversible processes[232]. Therefore, exergy considers the state of the system and the environment[232].
The concept of exergy combines the first and second law of thermodynamics to determine the quality and degradation of energy in real processes[233]. Exergy can be calculated using Equation 2.29 [232, 233].

$$Ex = (H - H_0) - T_0 (S - S_0) \tag{2.29}$$

Where Ex is the exergy, in J; H and H_0 are a stream's enthalpy at the operating conditions and at ambient conditions, respectively, in J; S and S_0 are the stream's entropy at the operating conditions and at ambient conditions, respectively, in J/K; and T_0 is the ambient temperature. The above Equation resembles the Gibbs free energy or Helmholtz free energy[234], described by Equations 2.30 and 2.31.

$$\Delta G = \Delta H - T\Delta S \tag{2.30}$$

$$F = U - T\ S \tag{2.31}$$

Where ΔG is the Gibbs free energy, in J; F is the Helmholtz free energy, in J; T is the operating temperature, in K; and U is the internal energy, in J. Equations 2.29 – 2.31 represent the amount of available energy that is free from entropy restrictions[234].
When applied to a unit operation, exergy calculations can determine the minimum, or maximum, amount of energy required, or generated, by the unit operation. Identifying this ideal energy allows the calculation of energy losses by comparing with the actual energy consumption or generation of the unit operation. These inefficiencies can then

be compared to evaluate the least efficient units and focus the researchers' attention on either improving those units or finding alternatives to improve the overall efficiency of a process.

2.7 Summary

The lack of air-nitrogen allows the purification of carbon dioxide in the flue gas through condensation, thus avoiding solvent use which could spill to the environment. This lack of solvent makes oxy-fuel combustion a more environmentally friendly CCS technology than post-combustion capture. This technology's main drawback is the high-energy requirement to separate oxygen from the air. Currently, cryogenic ASU is the only possible technology that can satisfy both the purity and amounts required by oxy-combustion technologies for power production. The parasitical energy consumption is exacerbated by the necessity to purify CO_2 using a cryogenic GPU[149]. Exergy analysis will be used in this work to evaluate process inefficiencies. Afterwards, reducing these inefficiencies via process integration and intensification will be proposed, and the new inefficiencies will be evaluated and compared with the initial process.
This work will also evaluate the use of a solvent to capture CO_2 from the flue gas of the oxy-combustion process as an alternative to cryogenic processes. Several process configurations and operating conditions will be evaluated and compared with a cryogenic gas processing unit.
BECCS is currently being pursued as a mitigation option with high potential to decarbonise the power and heating sectors whilst capturing atmospheric CO_2. More specifically, oxy-BECCS is expected to be viable from several test studies but still requires a large demonstration project to assess its potential. This work will evaluate the opportunities and obstacles of using biomass in an oxy-combustion process.
Lastly, this work will evaluate the flexible operation of oxy-combustion. Opportunities and obstacles from using liquid oxygen storage to improve flexibility and using biomass as a fuel will also be evaluated.

Chapter 3

Methodology

The previous chapter reviewed current knowledge on carbon capture and storage (CCS) technologies, specifically oxy-combustion for power generation using coal and biomass. This chapter will analyse the methods used to simulate the unit operations encountered in an oxy-combustion process. The model was developed based on the Callide Oxyfuel project's configuration[70], and it was simulated using Aspen HYSYS and gPROMS.

3.1 Air Separation Unit

This work only evaluated oxygen (O_2) production from cryogenic air separation units. The following subsections will provide an overview as to how the unit operations were simulated. Unit operations common in all processes will be detailed in this section.

3.1.1 Compressors and pumps

Compressors are essential components in air separation units (ASU) and gas processing units (GPU) to increase gas pressure, which has a low compression ratio[235]. Similarly, pumps increase the pressure of a liquid, which has high compression ratios[235]. Expanders are the opposite of a compressor and are used to reduce the pressure of a gas by converting its internal energy to shaft work that can be used elsewhere[235].
Aspen HYSYS solves the unknown variables of these unit operations as a function of flow, pressure change, applied energy, and efficiency[235]. The solution depends on the given specifications and whether the compressor's characteristic curves are used[235]. The isentropic line from inlet to outlet pressure is first determined, followed by using the specified efficiency to calculate the fluid's actual outlet enthalpy, providing its temperature[235]. The work of a process can be determined using Equation 3.1.

$$W = \int V dp \tag{3.1}$$

Where W is the work required to drive the compressor; V is the volume of the fluid; and p is its pressure.

3.1.2 Heat Exchangers

Heat exchangers allow heat transfer between two or more streams where a hot fluid increases the temperature of a cold fluid[126, 130, 134]. Temperature differences between 1 and 10 °C at one end of the heat exchanger are allowed depending on its type, with smaller differences requiring more expensive equipment[126, 130, 134].
High-efficiency heat exchangers with low-temperature differences are essential components in cryogenic processes[126, 130, 134]. Heat exchangers made from aluminium alloys are chosen for these processes because they are ductile and have an excellent thermal conductivity at the equipment's operating conditions[126, 130, 134].
Two material balances (Equation 3.2) and one energy balance (Equation 3.3) can be written for heat exchangers[236]

$$\left.\begin{aligned} F_{hot\ out} &= F_{hot\ in} \\ F_{cold\ out} &= F_{cold\ in} \end{aligned}\right\} \tag{3.2}$$

$$H_{hot\ in}F_{hot\ in} + H_{cold\ in}F_{cold\ in} = H_{hot\ out}F_{hot\ out} + H_{cold\ out}F_{cold\ out} \tag{3.3}$$

where F_i is the mass flow of stream i and H_i is the mass enthalpy of stream i. Internal temperature crosses are avoided by analysing the heat exchanger across several points[126, 134]. A typical calculation to determine the required area of heat exchangers is given by Equation 3.4[126, 134]

$$dQ = U\ A dT \tag{3.4}$$

where Q is the heat rate transferred (J/s); A is the heat exchanger's surface area (m^2); and dT is the temperature difference (K). The heat transfer coefficient U ($Jm^{-2}.K^{-1}.s^{-1}$) can be collected from the literature[126, 134]. This heat transfer coefficient can also be calculated by first determining the amount of heat transfer using Equation 3.5.

$$Q = F_i \Delta H_i \tag{3.5}$$

Where F_i is the flowrate of stream i, and ΔH_i is the enthalpy variation of stream i. Then, a logarithmic mean temperature difference (LMTD) is determined by Equation 3.6 and is calculated, along with UA in Equation 3.7, for each interval of the heat exchanger[126, 134, 235]

$$\Delta T_{LM} = \frac{\Delta T_1 - \Delta T_2}{\ln(\frac{\Delta T_1}{\Delta T_2})} \tag{3.6}$$

where:

$\Delta T_1 = T_{hot\ out} - T_{cold\ in}$
$\Delta T_2 = T_{hot\ in} - T_{cold\ out}$

$$UA = \frac{Overall\ Duty}{\Delta T_{LM}} \tag{3.7}$$

3.1.3 Multiple-Stream Heat Exchangers

Multiple-stream heat exchangers (MHX) allow heat transfer between more than two streams, reducing the number of a plant's heat exchangers[126, 130, 134]. Plate-fin heat exchangers are used in cryogenic plants and designed either as cross flow or counter flow with small temperature differences and pressure drops[126, 130, 134]. Materials with high thermal expansion should be chosen for cryogenic equipment to prevent damage from the high-temperature difference between the cryogenic fluid and the environment[126, 130, 134].
The energy balance on the hot and cold fluids is performed using Equation 3.8[235]

$$F\left(H_{in} - H_{out}\right) + Q_{internal} + Q_{external} = \rho \frac{d\left(V \times H_{out}\right)}{dt} \tag{3.8}$$

where F is fluid flow rate on the specified layer; H is the fluid's enthalpy; ρ is the fluid's density; $Q_{internal}$ is the heat gained from the surrounding layers; $Q_{external}$ is the heat gained from the external surroundings; and V is shell volume or tube holdup.

3.1.4 Distillation

Distillation is a widely used method to separate a mixture based on the different boiling points of its components[126, 134, 237, 238]. This process is simulated in most commercial packages by simultaneously solving mass and energy conservation balances for each phase present in each stage, generally assuming thermodynamic equilibrium at the interface[126, 134, 237, 238]. Rate equations and transfer coefficients are used at the interface to simulate the mass and energy transfer[126, 134, 237, 238].
The mass balance for component i on stage j (m_{ij}) is given by Equation 3.9 for the vapour phase (V), liquid phase (L), heat flow (Q), and enthalpy (H) going into and out of the stage.

$$m_{ij} \equiv \left(1 + r_j^V\right) v_{ij} + \left(1 + r_j^L\right) l_{ij} - v_{i,j+1} - l_{i,j-1} - f_{ij} = 0 \tag{3.9}$$

Where v_{ij}, l_{ij}, and f_{ij} are the mass flow rates of the vapour, liquid, and feed of component i in stage j; and

$$r_j^V = \frac{S_j^V}{V_j};\ r_j^L = \frac{S_j^L}{L_j} \tag{3.10}$$

where

$$S_j^V = \sum_{i=1}^{C} y_{ij}^I - 1 = 0;\ S_j^L = \sum_{i=1}^{C} x_{ij}^I - 1 = 0 \tag{3.11}$$

where y_{ij}^I is the vapour composition at the interface; x_{ij}^I is the liquid composition at the interface; and C is the number of components. The energy balance for each stage is determined through Equation 3.12.

$$E_j \equiv \left(1 + r_j^V\right) V_j H_j^V - V_{j+1} H_{j+1}^V + \left(1 + r_j^L\right) L_j H_j^L - L_{j-1} H_{j-1}^L + Q_j - F_j H_j^F = 0 \tag{3.12}$$

These equations are the basis for distillation column modelling, and a more complete description of the equations used is given by Krishnamurthy and Taylor [237].

3.1.5 Double Column Design

The double column design was modelled in Aspen HYSYS (Figure 2.3 and Figure B.2) according to the work developed by Raibhole and Sapali [147] and Sapali and Raibhole [239] with 40 stages in the HP column and 56 stages in the LP column.

Air is compressed to 4.2 bar using a five-staged isothermal compressor known as the main air compressor (MAC) with inter-coolers to keep air temperature at 28 °C[126, 130, 131, 134, 239]. Compressed air is cooled to 45 °C using a heat exchanger (HX1), and 25 % of this stream is compressed to 50 bar using a booster compressor partly powered by an expansion turbine, and then cooled down to 45 °C in HX2[126, 130, 131, 134, 239]. Nine per cent of this stream is cooled to 10 °C in the main heat exchanger (MHX) and expanded to 1.25 bar and −171.4 °C in the expander (Exp) before being fed to the LP column[126, 130, 131, 134, 239]. The remaining 91 % of this stream is cooled to −179 °C in the MHX[126, 130, 131, 134, 239]. Afterwards, it is expanded using a Joule-Thomson valve to 1.25 bar and −192 °C before entering the LP column[126, 130, 131, 134, 239]. The stream bypassing the Booster is cooled to −178 °C and partially condensed in the MHX before being fed to the high pressure (HP) column for the pre-separation of oxygen (O_2) and nitrogen(N_2) [126, 130, 131, 134, 239]. Table 3.1 presents the operating parameters of the ASU.

An O_2 enriched air stream exiting the HP column's bottom (with 38.8 wt% of O_2) at 4.1 bar is expanded to 1.25 bar and sent to the LP column for further separation[126, 130, 131, 134, 239]. High purity N_2 is condensed at the top of the HP column using a condenser/ reboiler against boiling O_2 from the LP column's sump with a temperature difference as low as 0.4 °C[132]. The condenser/ reboiler was simulated by connecting the HP column's condenser with the LP column's reboiler[126, 130, 131, 134, 239]. Liquid N_2 from the HP column is subcooled (HX3) using waste N_2 from the LP column

Table 3.1: Feed composition and operating parameters of the ASU.

Parameter	Unit	Value
Inlet air temperature	°C	10
Inlet air pressure	bar	1.01
Air composition		
N_2	mol%	79
O_2	mol%	20
Ar	mol%	1
MAC compression ratio		2.04
MAC adiabatic efficiency	%	90
Intercoolers outlet temperature	°C	28
Air sent to booster compressor	%	25
Air sent to expander	%	9
Expander outlet pressure	bar	1.06
HP column pressure	bar	4.1
CO_2 in bottom of HP column	mol%	39
LP column pressure	bar	1.1

and subsequently expanded to 1.25 bar and introduced to the LP column as reflux[126, 130, 131, 134, 239]. Waste N_2 from the LP column is used as a cooling agent in the MHX and subsequently vented[126, 130, 131, 134, 239]. High-purity O_2 (97 wt%) is produced from the bottom of the LP column and heated to 38 °C in the MHX against incoming air before being dispatched to the power plant[126, 130, 131, 134, 239].
The properties of gases and vapours were simulated using the Peng-Robinson equation of state, a cubic equation of state, with empirical mixing rules that relate the mixture's parameters with the pure components[240, 241]. This is a simple and accurate equation to estimate the properties of gases whilst providing good predictions of liquid phase densities[240, 241]. The simulation of the air separation unit had an average absolute deviation of 10 % from Sapali and Raibhole [239] (Table 3.2). The power consumption of this unit was 449 kWh/t_{O_2}[239], typical for high-pressure oxygen applications[242]. Thus, it was necessary to adapt the ASU described by Sapali and Raibhole [239] to a configuration more suitable to oxy-combustion.
The effects of air inlet, LM1 stream's temperature, HP and LP pressure, the number of stages in both columns, the air fraction sent to both the booster and the turbine, and MAC and Booster outlet pressure were evaluated. This analysis demonstrated that the booster compressor's outlet pressure significantly affected the power consumption of the ASU. Indeed, a 50 % power reduction can be achieved by optimising this unit with minimal product losses (Figure D.1).

Table 3.2: Validation exercise between this work and the simulation performed by Sapali and Raibhole [239].

	Sapali				**This work**			
Parameters	**FEED**	**GASN2**	**GASO2**	**LM1**	**FEED**	**GASN2**	**GASO2**	**LM1**
Temperature (K)	95.5	300.1	302.8	283.1	95.4	307.8	302.8	283.2
Pressure (bar)	4.1	1.1	1.15	50	4.1	1.1	1.15	50
Vapor Fraction	0.9	1	1	1	0.9	1	1	1
Mole Flow (kmol/h)								
N_2	29.6	34.8	0.0	5.1	25.1	34.8	0.0002	1.7
O_2	8.0	0.001	9.4	1.4	6.7	0.01	9.4	0.4
Ar	0.4	0.049	0.4	0.1	0.3	0.1	0.3	0.0
Mole Fraction								
N_2	0.78	1.0	0.0	0.78	0.78	1.0	0.0	0.78
O_2	0.21	0.0	0.96	0.21	0.21	0.0	0.96	0.21
Ar	0.009	0.001	0.04	0.009	0.009	0.001	0.04	0.009
MainCompressor	47.22	kW			51.57	kW		
Booster	12.22	kW			29.15	kW		
Expander	9.32	kW			1.34	kW		

Another way of reducing the power consumption is by diverting more air to the expander. Power consumption decreases with an increased amount of air sent to this unit; however, this reduces the separation efficiency (Figure B.2).
The number of stages of a distillation column can have a significant impact on product purity. O_2 purity is not sensitive to the number of stages of the HP column; however, the number of stages of the LP column significantly affect O_2 purity. These results indicate that the HP column should be operated with 15 stages and the LP column operated between 40 and 45 stages.
The ASU's specific power consumption was reduced to 204 kWh/t_{O_2} at 98 wt% purity after this optimisation, similar to Tranier et al. [137] and Higginbotham et al. [138]. This optimisation exercise improved the ASU's thermodynamic efficiency from 19 % to 25 % (Figure D.2).

3.2 Power plant

The theory of steam power plants and the cycles they can operate was detailed in Chapter 2. We start by evaluating the amount of useful work extracted from the Carnot cycle, where two isentropic changes and two isothermal changes occur to form a closed reversible cycle, as given by Equation 3.13[174].

$$|W| = q_{in} - |q_{out}| \tag{3.13}$$

The ratio of useful work to the amount of heat input into the cycle is defined as the thermal efficiency and can be calculated using Equation 3.14[174].

$$\eta_{th,Carnot} = \frac{Net\ work\ output}{Heat\ input} = \frac{|W|}{q_{in}} = \frac{q_{in} - |q_{out}|}{q_{in}} = 1 - \frac{|q_{in}|}{q_{out}} \tag{3.14}$$

Or, substituting to evaluate temperature (T) and entropy (S), Equation 3.14 becomes Equation 3.15[174].

$$\eta_{th,Carnot} = \frac{T_{hot}\,(S_{boiler\ out} - S_{boiler\ in}) - T_{cold}\,(S_{boiler\ out} - S_{boiler\ in})}{T_{hot}\,(S_{boiler\ out} - S_{boiler\ in})} = \frac{T_{hot} - T_{cold}}{T_{hot}} = 1 - \frac{T_{cold}}{T_{hot}} \tag{3.15}$$

Where $S_{boiler\ in}$ and $S_{boiler\ out}$ are the fluid entropy before and after receiving heat, respectively. This equation shows that the efficiency of the reversible Carnot cycle depends only on the hot and cold temperatures. From Equation 3.15, the cycle is more efficient when the fluid is expanded at higher temperatures and condensed at lower temperatures[174].
However, most supercritical power plants, including the one simulated in this work, adopt the more practical Rankine cycle, where the working fluid is condensed after

expansion[174]. This fluid is then compressed to high-pressure using a pump and pre-heated before entering the steam generating section[174]. Hence, the net work output of a Rankine cycle can be defined by Equation 3.16[174].

$$|W| = |W_{turbines}| - W_{pre-heating} = |\Delta H_{turbines}| - \Delta H_{pre-heating} \tag{3.16}$$

The thermal efficiency of the Rankine cycle is calculated using Equation 3.17[174].

$$\eta_{th,Rankine} = \frac{|W|}{q_{in}} = \frac{|\Delta H_{turbines}| - \Delta H_{pre-heating}}{\Delta H_{steam\ generator}} \tag{3.17}$$

To compare the Rankine cycle with the Carnot cycle, we define the hot side temperature exiting the superheater using Equation 3.18[174].

$$T_{hot} = T_{Superheater} = \frac{q_{in}}{\Delta S_{steam\ generator}} = \frac{\Delta H_{steam\ generator}}{\Delta S_{steam\ generator}} \tag{3.18}$$

The cold temperature exiting the condenser is defined by Equation 3.19[174].

$$T_{cold} = T_{condenser} = \frac{|q_{out}|}{\Delta S_{Turbine\ inlet \rightarrow condenser\ outlet}} = \frac{\Delta H_{Turbine\ inlet \rightarrow condenser\ outlet}}{\Delta S_{Turbine\ inlet \rightarrow condenser\ outlet}} \tag{3.19}$$

The efficiency of a reversible Rankine cycle given by Equation 3.20 is obtained by using these temperatures[173, 174].

$$\eta_{th,Rankine} = \frac{Net\ work\ output}{Heat\ input} = \frac{T_{superheater} - T_{condenser}}{T_{superheater}} = 1 - \frac{T_{condenser}}{T_{superheater}} \tag{3.20}$$

This efficiency is limited by the steam temperature leaving the superheater (hot source) and the condenser temperature (cold sink), as noted in Equation 3.20. The maximum temperature is limited by the superheater's creep temperature whilst the cooling water reservoir's temperature limits the condenser temperature[173]. The Carnot cycle's efficiency is higher than the Rankine cycle because of the inefficiencies of feedwater pre-heating, evaporation, and superheating observed during the Rankine cycle[174].
The gross capacity (P_{gross}) is the power generated by the turbines and measured at the generator[174]. The net capacity (P_{net}) is the power exported to the grid after all auxiliary load (P_{aux}) is subtracted from the gross capacity (Equation 3.21)[174].

$$P_{net} = P_{gross} - P_{aux} \tag{3.21}$$

The net efficiency of a power plant generating only electricity can be obtained by the ratio between the amount of net power and the heat input to the system[174]. Assuming a lower heating value (LHV) and the mass flow of fuel into the process, the gross and

net efficiency on an LHV basis can be calculated using Equations 3.22 and 3.23[174].

$$\eta_{gross} = \frac{P_{gross}}{\dot{m}_{fuel} LHV} \tag{3.22}$$

$$\eta_{net} = \frac{P_{gross} - P_{aux}}{\dot{m}_{fuel} LHV} \tag{3.23}$$

Where P_{gross} is the power generated by the high-pressure (HP), intermediate pressure (IP), and low pressure (LP) turbines; P_{aux} is the power required from the auxiliary equipment; LHV is the fuel's lower heating value; and $\dot{m}_{fuel}$ is the fuel's mass flow.

3.2.1 Coal combustion

Coal is primarily composed of carbon, hydrogen, and oxygen, and it is usually written as CH_mO_n, where m $<$ 1 and m $<$ n[1, 69]. However, as stated previously, coal also contains nitrogen and sulphur, leading to the formation of NO_x and SO_x, along with volatile trace metals present in flue gases at ppb levels[1, 69].
Coal must be ground or pulverised before combustion takes place. The power consumed for grinding the coal can be calculated according to Equation 3.24[243].

$$W = 10 W_i \left(\frac{1}{P_{80}} - \frac{1}{F_{80}} \right) \tag{3.24}$$

Where W is the work input in kWh/t; W_i is the Bond work index in kWh/t; F_{80} and P_{80} are the 80 % size of feed and product, respectively, in μm. The Bond work index represents the material's resistance to crushing and grinding, given by Equation 3.25.

$$W_i = \frac{44.5}{P_1^{0.23}} G^{0.82} \left(\frac{10}{P_{80}} - \frac{10}{F_{80}} \right) \tag{3.25}$$

Where P_1 is the closing sieve size in μm and G is the grindability in net g/rev. The number of mills required for this operation was determined by assuming a maximum flow of 110 t/h per mill[244]. The values provided by Williams et al. [243] for La Loma bituminous coal were used as a representative value for coal to estimate the power consumption of the mill throughout this thesis (Table 3.3).
Coal combustion is a complex, heterogeneous process where pulverised porous particles with sizes ranging from 75 to 300 μm react with O_2 after moisture and volatiles are expelled and subsequently burned[1]. Combustion is caused by an ignition source accompanied by flame propagation on a self-supporting exothermic reaction[1, 69, 243]. This initial reaction is followed by the pyrolysis of the remaining solid, or char, leading to devolatilisation[1, 69, 243]. Devolatilisation can take place simultaneously, sequentially, or with some overlapping with the ignition, depending on the furnace

Table 3.3: Values for feed size (F_{80}), target coal size (P_{80}), coal grindability (G), and closing sieve size (P_1) for La Loma bituminous coal[243].

Parameter	Value
$\mathbf{F_{80}}$	2709
$\mathbf{P_{80}}$	77
G	0.664
$\mathbf{P_1}$	90

conditions[1, 69, 243]. Coal pyrolysis is a complex mechanism where several chemical and transport phenomena occur in the flame, influenced by coal rank and physical properties[1, 69, 243]. A simplified set of coal combustion reactions can be represented by Equation 3.26[1, 69, 243].

$$\left.\begin{aligned} &C_{coal} + O_2 \longrightarrow CO_2 \\ &4\,H_{coal} + O_2 \longrightarrow 2\,H_2O \\ &C_{coal} + H_2O \longrightarrow CO + H_2 \\ &N_{coal} + \tfrac{x}{2}O_2 \longrightarrow NO_x \\ &S_{coal} + \tfrac{x}{2}O_2 \longrightarrow SO_x \end{aligned}\right\} \tag{3.26}$$

The Boudouard reaction (Equation 3.27) and oxidation of sulphur and nitrogen (Equations 3.28) should also be considered when developing detailed combustion models.

$$CO_2 + C \longrightarrow 2\,CO \tag{3.27}$$

$$\left.\begin{aligned} &S_{coal} + O_2 \longrightarrow SO_2 \\ &2\,SO_2 + O_2 \longrightarrow 2\,SO_3 \\ &N_{coal} + O_2 \longrightarrow 2\,NO \\ &2\,NO + O_2 \longrightarrow 2\,NO_2 \\ &N_{coal} + O_2 \longrightarrow NO_2 \end{aligned}\right\} \tag{3.28}$$

This work does not consider the Boudouard reaction to simplify the combustion model. Here, complete combustion was assumed as a simplification, resulting in a flue gas composed of CO_2, H_2O, SO_2, and N_2. This approximation will provide more heat to generate steam than during an actual plant's operation. However, this should be a reasonable approximation, as only less than 0.5 % of carbon is unburnt during actual operations[245]. However, the operators must be aware that the amount of carbon in the ash cannot exceed 2 % when selling it as filler for concrete[245]. This concern is not addressed in this work, and it is assumed that the costs of removing fly ash are covered by selling it as a cement filler.

The stoichiometric amount of oxygen required for the complete combustion of coal was determined via

$$\begin{aligned} CH_xN_yS_zO_w + \alpha\left(O_2 + \frac{y^{ox}_{N_2}}{y^{ox}_{O_2}}N_2 + \frac{y^{ox}_{Ar}}{y^{ox}_{O_2}}Ar\right) \longrightarrow CO_2 + \\ \frac{x}{2}H_2O + zSO_2 + \left(\frac{y^{ox}_{N_2}}{y^{ox}_{O_2}}\alpha + \frac{y}{2}\right)N_2 + \left(\frac{y^{ox}_{Ar}}{y^{ox}_{O_2}}\alpha\right)Ar \end{aligned} \tag{3.29}$$

where α is the molar stoichiometric amount of oxygen provided by Equation 3.30.

$$\alpha = 1 + \frac{x}{4} + z - \frac{w}{2} \tag{3.30}$$

Then, the stoichiometric oxidant/fuel mass ratio is calculated using Equation 3.31

$$\left(\frac{m_{ox}}{m_f}\right)_s = \frac{\alpha\left(MW_{\mathrm{O_2}} + \frac{y^{ox}_{N_2}}{y^{ox}_{O_2}}MW_{\mathrm{N_2}} + \frac{y^{ox}_{Ar}}{y^{ox}_{O_2}}MW_{\mathrm{Ar}}\right)}{m_f} \tag{3.31}$$

where m_{ox} is the oxidant mass flow (kg/s); m_f is the fuel mass flow (kg/s); and MW_i is the molecular weight of component i (kg/kmol).
The real/stoichiometric ratio (λ) allows the actual composition of flue gas to be obtained according to Equation 3.32

$$\lambda = \frac{m_{ox}/m_f}{\left(m_{ox}/m_f\right)_s} \tag{3.32}$$

This changes the combustion reaction to

$$\begin{aligned} CH_xN_yS_zO_w + \alpha\lambda\left(O_2 + \frac{y^{ox}_{N_2}}{y^{ox}_{O_2}}N_2 + \frac{y^{ox}_{Ar}}{y^{ox}_{O_2}}Ar\right) \longrightarrow \\ CO_2 + \frac{x}{2}H_2O + \alpha(\lambda-1)O_2 + zSO_2 + \\ \left(\frac{y^{ox}_{N_2}}{y^{ox}_{O_2}}\alpha\lambda + \frac{y}{2}\right)N_2 + \left(\frac{y^{ox}_{Ar}}{y^{ox}_{O_2}}\alpha\lambda\right)Ar \end{aligned} \tag{3.33}$$

The presence of S and N in the fuel leads to SO_x and NO_x formation during combustion. These components react with atmospheric moisture and create sulphuric and nitric acids, responsible for acid rains[69]. NO_2 and NO formation was then included in the simulation using Nakata *et al.*'s equation[246]

Table 3.4: Typical compositions of coal ash.

Ash Component	Amount (wt%)
Silica (SiO_2)	40 - 90 %
Aluminium oxide (Al_2O_3)	20 - 60 %
Iron (ferric) oxide (Fe_2O_3)	5 - 25 %
Calcium oxide (CaO)	1 - 15 %
Magnesium oxide (MgO)	0.5 - 4 %
Sodium oxide (Na_2O) + potassium oxide (K_2O)	1 - 4 %

$$V_{NO_x} = N_{fuel} \frac{V_0}{MW_N} \frac{10^4}{V_{FG}^{dry}} \left(4.89 \frac{FR}{N_{fuel}} + 4.57 \right) \tag{3.34}$$

where V_{NO_x} is the amount of NOx in the flue gas (ppm); N_{fuel} is the fuel's nitrogen content ($wt\%_{ar}$); MW_N is the molecular weight of atomic nitrogen (kg/kmol); V_0 is the ideal gas volume (22.4 m^3/kmol at STP); and V_{FG}^{dry} is the flue gas volume per kg of raw fuel (m^3/kg at STP). This equation only considers fuel NO_x[246], providing a good approximation for oxy-combustion since it is virtually free of atmospheric N_2.
Ash formation can be detrimental to the plant's operation by fouling and corroding the material of the tubes responsible for heat exchange, decreasing boiler efficiency[247]. Coal ash typically has a composition range shown in Table 3.4.
The adiabatic flame temperature (T_{ad}) can be determined from the first law of thermodynamics by solving Equation 3.35.

$$\begin{aligned} &LHV_{fuel}^m + \left(\sum_n x_{i,\ fuel}\ n_{i,\ fuel} \right)_{fuel} \left[h_{i,\ fuel}^m \left(T_{fuel} \right) - h_{i,\ fuel}^0 \right]_{fuel} + \\ &(\lambda C)_{O_2} \left[h_{O_2}^m \left(T_{oxidant} \right) - h_{O_2}^0 \right] + \left(\frac{x_{N_2}}{x_{O_2}} \lambda C \right)_{N_2} \left[h_{N_2}^m \left(T_{oxidant} \right) - h_{N_2}^0 \right]_{N_2} = \\ &\left(\sum_n x_{i,\ flue\ gas}\ n_{i,\ flue\ gas} \right)_{flue\ gas} \left[h_{i,\ flue\ gas}^m \left(T_{ad} \right) - h_{i,\ flue\ gas}^0 \right]_{fluegas} + \\ &\left[(\lambda - 1) C \right]_{O_2} \left[h_{O_2}^m \left(T_{ad} \right) - h_{O_2}^0 \right] + \left(\frac{x_{N_2}}{x_{O_2}} \lambda C \right)_{N_2} \left[h_{N_2}^m \left(T_{ad} \right) - h_{N_2}^0 \right]_{N_2} \end{aligned} \tag{3.35}$$

Where LHV_{fuel}^m is the fuel's molar lower heating value (LHV); $x_{i,\ fuel}$ and $x_{i,\ flue\ gas}$ are the molar fractions of component i in the fuel and the flue gas; x_{N_2}, and x_{O_2} are the molar fractions of nitrogen and oxygen in the oxidant, respectively; $n_{i,\ fuel}$ and $n_{i,\ flue\ gas}$

are the molar flowrates of component *i* in the fuel and flue gas, respectively; h_i^0 is the molar enthalpy of formation of component *i* at 25 °C; T_{fuel}, $T_{oxidant}$, and T_{ad} are the fuel, oxidant, and adiabatic flame temperatures, respectively; and *C* is the fuel's molar flow of carbon.

The real flame temperature peaks around 1500 °C and is lower than T_{ad} because heat is transferred by radiation during combustion[183, 248]. However, it is useful to analyse T_{ad} because both flame temperatures follow similar trends[248]. This calculation does not consider dissociation of the products; therefore T_{ad} achieves a maximum value on stoichiometric combustion[248]. This assumption maximises the amount of NO_x formed during combustion[175] since it assumes that fuel-lean conditions are obtained throughout all combustion regions.

The hot flue gases transfer heat to the working fluid (steam) through radiation, convection, and conduction[183]. Heat transfer from radiation is primarily achieved through the triatomic gases and solid particles in the lower section of the furnace where flue gas can be at 1500 °C and water inside the cooled walls below 400 °C[183]. Heat transfer from radiation is proportional to the absolute temperature difference to the fourth power without requiring material contact[183]. This concept is known as the Stefan-Boltzmann law, where the total energy radiated per unit surface area of a black body, j (W/m^2), is calculated by Equation 3.36.

$$j = \sigma\, T^4 \tag{3.36}$$

Where σ is the Stefan-Boltzmann constant (5.670373×10^{-8} $W.m^{-2}.K^{-4}$), and T is the black body's temperature (K).

Conduction takes place when heat from a part of a body at higher temperature flows to a part at lower temperature, or from a body at a higher temperature to a body at a lower temperature[183]. This heat transfer process occurs in the tube walls inside the boiler[183]. Heat flux, q (W/m^2), is calculated using Fourier's law (Equation 3.37) through the product of thermal conductivity, k (W/(m.K)), with the negative temperature gradient, ∇T (K/m).

$$q = -k\, \nabla T \tag{3.37}$$

Convective heat transfer occurs in a moving fluid through the macroscopic motion of the fluid and the random motion of molecules[183]. Heat transfer is represented by Newton's law of cooling at the boundary layer close to the heat transfer surface[183]. Here, the heat transfer rate, Q (W) can be calculated using Equation 3.4. For convenience, the radiative heat transfer is lumped with the convective heat transfer at the boundary layer to simulate heat exchange from the furnace to the water walls[183].

3.2.2 Air Pre Heater

The air preheater (APH) is installed at the end of the boiler to increase the oxidant's temperature, stabilise fuel ignition, and improve combustion efficiency[69, 172, 183, 249–251]. Air preheaters and economisers recover low-grade heat from the flue gas, increasing the boiler's efficiency by 1 % for every 20 °C that the flue gas is cooled[183]. Regenerative air heaters are generally used in supercritical power plants to preheat air[183, 250–253]. These air heaters are generally smaller, their heat exchange surfaces are more straightforward to replace, and they achieve lower metal temperatures in the cold end than recuperative air heaters[183]. However, regenerative air heaters risk failure of their moving parts, air leakage into the flue gas and vice-versa, and increased pressure losses from solids deposition[183].

Ljungström regenerators are commonly used as APH in supercritical plants because they provide adequate heat exchange between the hot flue gas leaving the boiler and incoming cold oxidant[250–253]. These heat exchangers have a slow-moving rotor between two sealed peripheral housings separated in the middle of the equipment[250–253]. Hot flue gas passes in one side and cold gas in the other, achieving a heating efficiency of 85 – 90 %[250–253]. Heat is absorbed by metal plates when in contact with the hot flue gas and subsequently released when these plates contact the cold oxidant gas, in what is termed a regenerative process[250–253]. This equipment can have up to 6 m in diameter and 0.2 to 0.91 m height and can withstand gas temperatures up to 982 °C flowing at 2.5 m/s[250–253].

A plate's residence time should be considered in this heat transfer method since they alternate between contacting the hot and cold streams[250, 251]. However, this equipment can be simulated using a simple recuperator theory by assuming a sufficiently fast rotational speed[250, 251]. Ljungström heat exchangers can operate with small hydraulic diameters and enable higher amounts of heat transfer between flue gas and oxidant than other recuperative processes[250, 251].

3.2.3 Boiler

Feedwater enters the boiler from the economiser and exits from the second superheater (SH2) towards the high-pressure turbine (HP turb) at 600 °C and 300 bar[254]. This temperature and pressure are within the range of ultra-supercritical power plants[173, 178], limiting the choice of materials used in the exchanger tubes and turbines (See Tables A.1 and A.2 in the appendix for possible materials for a range of operating temperatures). The pressure drop of the flue gas inside the boiler was assumed to be 2.1 mbar, whilst feedwater had a pressure drop of 24.1 bar for the economiser, evaporator, and superheaters sections, and 5 bar for the reheater section[77]. These units were simulated as heat exchangers with steam flowing on the tube-side and flue

Table 3.5: Fractions and conditions of steam bled from the HP, IP and LP turbines, based on turbine feed to reach feedwater temperature of 300 °C.

Turbine	bleed no	w_n (%)	T (°C)	P (bar)
HP	1	9.30	365	75
IP	1	7.45	558	48
	2	4.81	460	25
	3	4.54	381	14
	4	4.82	297	7
LP	1	9.60	200	2.8
	2	5.60	102	0.9
	3	4.64	65	0.25

gas flowing on the shell-side[183].

Steam is expanded in three turbines until it reaches low pressure, generally below atmospheric, and condensed against liquid water[254]. The amount of steam bled from each turbine, along with their conditions, is presented in Table 3.5.

Steam exits the boiler from the second reheater (RH2) at 620 °C into an intermediate-pressure turbine (IP turb) followed by a low-pressure turbine (LP turb), exiting at 0.04 bar. The steam exiting the LP Turb is condensed, pumped to the boiler's operating pressure, and heated to 300 °C in the feedwater heating train before being recycled to the boiler[254].

The amount of steam generated depends on the amount of fuel and oxidant fed to the furnace[254]. A throttle valve located at the turbine's inlet allows adjusting the amount of electricity generated by varying the amount of steam expanded in the turbine, allowing the plant to adjust its output according to demand[254].

The overall plant efficiency, η_o, can be defined as the ratio of the specific net work produced, W_{net}, to the amount of heat released during combustion (CV) of the fuel as seen on Equation 3.38.

$$\eta_o = \frac{W_{net}}{CV} \tag{3.38}$$

Where $CV \equiv (H_R - H_P)_T$, and H_R and H_P are the enthalpies of the reactants and products, respectively, at temperature T. The characteristics of the fuels used in this thesis, bituminous Eastern Australian coal and clean wood chips sourced in the UK, are detailed in Table 3.6. Bituminous Eastern Australian coal was chosen to use a similar coal to Callide Oxyfuel project. The validation exercises against IECM and Kunzeman's work were made with the composition of an Appalachian medium sulfur bituminous coal (Table C.1) and the composition specified in [172], respectively. Clean wood chips were selected as a biomass feedstock to mitigate slagging and corrosion[255].

Table 3.6: Fuel composition, heating value, supply chain emissions (SCE), grindability parameters, and cost.

Fuel Component (wt%)[84, 150]	**Coal**	**Wood chips**
C	64.6	47.6
H	4.4	5.1
S	0.9	0.05
O	7.0	40.2
N	1.4	0.3
H_2O	9.5	4.8
Ash	12.2	1.95
HHV_{ar} (MJ/kg)[84, 150]	34.6	19.5
SCE (kg_{CO_2}/MWh_{th})[217, 256]	307	84 - 136
F_{80} (μm)[243]	2709	8400
P_{80} (μm)[243]	77	786
G (g/rev)[243]	0.664	0.053
Cost ($/t)[84, 150]	86	117
Supply chain emissions (kg_{CO_2}/MWh_{th})[217, 256]	307	110

Table 3.7: Boiler and flue gas pre-treatment operating conditions.

Parameter	**Unit**	**Value**
Feedwater temperature	°C	300
Steam temperature at superheater exit	°C	600
Reheated steam temperature at reheater exit	°C	620
Steam pressure at superheater exit	bar	300
Reheated steam pressure at reheater exit	bar	70
Excess air ratio		1.04
Amount of ash in coal	wt%	30
Amount of fly ash in total ash	wt%	75
Isentropic efficiency of fans	%	85
Isentropic efficiency of compressors	%	75

The impact of ash in coal was evaluated by increasing its content up to 30 % of the fuel's mass, following a high-ash coal similar to Kunzemann [172].
The operating parameters of the power plant are presented in Table 3.7.
The assumptions for the heat transfer coefficient (U), feedwater outlet temperature (T_{out}) and pressure drop (Δp) are represented in Table 3.8.

3.3 Gas processing unit

The gas processing unit (GPU) was adapted from the work of Kolster et al. [66] and Posch and Haider [208]. The operating conditions of heat exchangers and compressors were changed due to the different flue gas conditions obtained in this work. Flue gas at 26 °C and 1.01 bar is compressed to 28 bar in a three-staged compressor with inter-

Table 3.8: Operating conditions of the boiler simulated in this thesis.

Heat exchanger	U (W/(m^2 K))	T_{out} (°C)	Δp (bar)
Evaporator	80	401	5
Radiant superheater	50	500	5
Superheater 1	50	450	5
Superheater 2	50	600	4
Reheater 1	50	450	0.9
Reheater 2	50	620	3
Economiser	100	399	5

and after-cooling at 25 °C, removing all condensation[64, 66, 208, 210, 257].
Compressed flue gas is dehydrated before being cooled to −31 °C in a multiple-stream heat exchanger (MHX) against cold distillation products[66, 208]. This stream is mixed with the recycle stream and sent to the distillation column. Here, a stream with 99.96 wt% CO_2 is produced, similar to the purity obtained at the Callide Oxyfuel project[70]. The gas leaving the distillation column has low CO_2 concentration, warmed in the MHX, and flashed (flash-4)[66, 208]. The CO_2-rich liquid from this flash separation is recycled to the distillation column whilst the gas phase is sent to the stack[66, 208].
The CO_2 stream leaving the distillation column is warmed in the MHX and compressed to 68 bar and 1 °C using a two-staged compressor (HP Comp1 and 2) with inter- and after-cooling (HX5 and HX6)[66, 208]. This results in a supercritical fluid that is pumped (P-1) to pipeline pressure, assumed to be 120 bar, and sent for storage in a suitable reservoir (Figure 2.12)[66, 208]. The operating parameters of the GPU are presented in Table 3.9.
The work required to separate CO_2 from a gas decreases as inlet CO_2 concentration increases(Figure D.5). Indeed, high CO_2 concentrations between 75 wt% and 90 wt% exiting the power plant is an advantageous feature of oxy-combustion.
The separation efficiency can be defined using Equation 3.39.

$$\eta_{sep} = \frac{m_{\mathrm{CO_2},product}}{m_{\mathrm{CO_2},in}} \tag{3.39}$$

Where η_{sep} is the separation efficiency; $m_{\mathrm{CO_2},product}$ is the mass flow of CO_2 leaving the system; and $m_{\mathrm{CO_2},in}$ is the mass flow of CO_2 into the system.
A specific power consumption of 139.6 kWh/t_{CO_2} with a separation efficiency of 97 wt% was obtained for the GPU. However, a thermodynamic analysis of this unit revealed that it operates with a 5 % thermodynamic efficiency (Figure D.5).
A sensitivity analysis was also performed on the fraction sent to the GPU and the direct contact cooler (DCC). It was found that T_{ad} increases when more flue gas is sent to the

Table 3.9: Operating conditions of the GPU simulated in this thesis.

Parameter	Unit	Value
Flue gas inlet pressure	bar	1.01
Flue gas inlet temperature	°C	25
LP comp, 1st stage compression ratio		9.9
LP comp, 2nd stage compression ratio		2
LP comp, 3rd stage compression ratio		1.4
LP comp intercooling temperature	°C	25
Recycle compressor discharge pressure	bar	28
Recycle cooler temperature	°C	-35
HP comp, 1st stage discharge pressure	bar	40
HP comp, 2nd stage discharge pressure	bar	68
HP comp intercooling temperature	°C	25
Pump discharge pressure	bar	110

GPU, as can be seen in Figure D.6.
Increasing the cooling water in the DCC reduces the flue gas temperature and humidity. Reducing the amount of water sent to the GPU improves the plant's efficiency (Figure D.7) by reducing the volume required to be compressed.

3.4 Determining power plant efficiency

The net power generated (W_{net}) by the plant must deduct the parasitic power consumption of other units (W_{cons}) from the gross power generated by the turbines (W_g) according to Equation 3.40.

$$W_{net} = W_g - \sum W_{cons} \tag{3.40}$$

The net efficiency (η_{net}) (%) allows a direct comparison between power generating technologies[1] and can be calculated using Equation 3.41.

$$\eta_{net} = 100 \times \frac{W_{net}}{m_{fuel} \times HV_{fuel}} \tag{3.41}$$

Where $m_{fuel} \times HV_{fuel}$ is the amount of heat available during combustion. This equation can also be used to evaluate the plant's gross efficiency.

[1]Only used for electricity generated by heat. Comparing the efficiency of a fossil-fueled process with a renewable process (such as wind or PV) must consider other factors, such as fuel cost/availability, amongst others.

3.5 Techno-economic analysis

Economic evaluation is a decision tool that enables the choice between mutually exclusive projects[258]. The internal rate of return (IRR) is a general method employed for project evaluation[258]. The abated plant was assumed to be an nth of a kind (NOAK) to simplify the comparison with an unabated plant. In reality, the costs of a first of a kind (FOAK) plant will be higher due to technology uncertainty and material/equipment costs. The base year assumed in this study was 2015 and all costs were scaled using the respective CEPCI values (Table E.1).
Cash flows (CF) cannot be directly compared at different years because money is time-dependant; hence, it is necessary to translate these values to a common point in time, typically chosen at the present in the form of present value[258]. The net present value (NPV) is the summation of all cash flows during the project's lifetime, according to Equation 3.42[258].

$$NPV = \sum_{n=0}^{N} \frac{CF_n}{(1+i)^n} \tag{3.42}$$

Where i is the discount rate. Coal-fired power plants are generally built for over 40 years of operation[188]. The IRR can be determined by equating the NPV to zero via Equation 3.43[258] and following the procedure by Ward [258] and Katell and Wellman [259].

$$0 = \sum_{n=0}^{N} \frac{CF_n}{(1+IRR)^n} \tag{3.43}$$

Both capital (CAPEX) and operational (OPEX) expenditure were obtained from Aspen HYSYS, which has a built-in library to estimate these costs. Table 3.10[150, 260] shows the assumptions used to perform an economic evaluation of the process. The plant was assumed to need 2 % of the total plant cost and three months of operating and maintenance labour costs as a start-up cost, operate at 25 % capacity during the first month, and operate at 65 % capacity during the first year[150]. During the second year, it was assumed that the plant operates at 85 % capacity from accumulated operational experience, and at 90 % from the third year until the project's lifetime[150]. The oxy-combustion model has a general nature and can be applied anywhere with an accuracy between - 25 % to + 30 %[260].

Table 3.10: Assumptions used for the techno-economic analysis of the proposed framework.

Parameter	Value	Units
Currency	US Dollar	$
Year	2015	
Contingency[150]	10 % Fixed capital	$
CO_2 emissions cost[150]	25	$/$t_{CO_2}$
CO_2 T&S costs[150]	13	$/$t_{CO_2}$
Economic calculation	Discounted cash flows	
Number of operators (NO)[260]	5 $\times$ Labourers per shift	
Operating labour (OL)[150]	79800 $\times$ NO	$
Supervision[150]	30 % OL costs	$
Maintenance[150]	10 % Fixed capital	$
Royalty[260]	1 % Sales	$
Indirect expenses[260]	3 % Fixed capital	$
Interest rate (r)[150]	8	%
Inflation during construction[150]	8	%
Economic lifetime[150]	25	years
Construction time[150]	3	years
Yearly operating hours[150]	7885	h

Chapter 4

A methodological approach for achieving $/MWh cost reduction of CO_2 capture and storage (CCS) processes

The work detailed in this Chapter was partly published in Applied Energy[103].

4.1 Introduction

Oxy-combustion requires an air separation unit (ASU) to produce oxygen (O_2) and a gas processing unit (GPU) to capture CO_2 from the flue gas, adding an 8 – 12 % efficiency penalty[49]. Heat integration offers the potential to reduce this parasitic energy consumption by minimising process inefficiencies[232]. Analysing the unit operation's exergy destruction (ED), or lost work (LW), will identify these inefficiencies[232, 261]. Several studies investigated different ASU and GPU types to reduce this parasitic power consumption[111, 114, 115]. Skorek-Osikowska et al. [111] remarked that low-grade heat of compression could be used to pre-heat the boiler's feedwater and reduce the number of heat exchangers in the feedwater heating train.

Increased capital costs arising from improving this process's performance should be avoided to prevent an unsustainable increase in the cost per MWh of the low carbon electricity generated. This possibility creates the requirement to evaluate the efficacy of a process modification in this context.

Hence, a methodological approach using a rational analysis of the 1st and 2nd laws of thermodynamics linked with the project's capital expenditure (CAPEX) was developed to identify process improvements. The methodology proposed in this study is presented in Figure 4.1. It is well-suited to other CCS technologies and complex industrial processes, such as liquefied natural gas, because the analysis intends to reduce process

inefficiencies. The user starts by proposing a process flow diagram (PFD) and simulates the process. The user then performs a thermodynamic analysis and calculates the exergy destruction (ED) of each unit operation. The user determines the capital cost (CAPEX) and plots the first point in an efficiency (η) vs CAPEX figure.
The user then determines the minimum CAPEX, which would be an unabated ultra-supercritical coal power plant for this case, and calculates its maximum efficiency (η^{max}). These points will serve as boundary conditions for the analysis.
Following the thermodynamic analysis, the user can then propose new PFDs until a lower ED and CAPEX are obtained. The new point can then be added to the η vs CAPEX plot and compared with the original PFD.

4.2 Methods

4.2.1 General model

All models in this study were implemented in Aspen HYSYS v8.4, detailed in Chapter 3, using the Peng-Robinson equation of state.

4.2.2 Power plant

The pulverised coal-fired power plant was first simulated in air-fired mode (detailed in Appendix B.3) following the data from Spero et al. [70] and Spliethoff [174], according to Figure 4.2. This plant is assumed to have a two-pass once-through boiler[262], a turbine island, a feedwater heating train, and a flue gas pre-treatment unit.

4.2.3 Oxy-combustion

An oxy-combustion process was modelled following the work of Spero et al. [70] and Stanger et al. [102] by adapting the power plant model developed previously with a primary and secondary recycle flue gas (RFG) to the furnace. Medium-purity O_2 is mixed with the secondary RFG to maintain O_2 concentration below 40 % and avoid using construction materials specific for pure O_2[77].
52 % of the total flue gas leaving the regenerative heat exchanger (RHX) flow through a baghouse filter to remove fly ash and is recycled, mixed with medium-purity O_2 in what is generally called the secondary recycle, and sent back to the furnace[1, 49, 64, 70]. The remaining flue gas is sent to a spray dryer (SD) to remove SO_x, passed through a baghouse filter to remove fly ash, and cooled in a direct contact cooler (DCC)[1, 49, 64, 70]. 37 % of this flue gas is recycled as the primary RFG and used to pulverise coal to the furnace[70, 102] whilst the non-recycled flue gas is purified and compressed to transport specifications[263] on the GPU[66, 70]. The resulting PFD of the boiler operating in oxy-mode is presented in Figure 4.2.

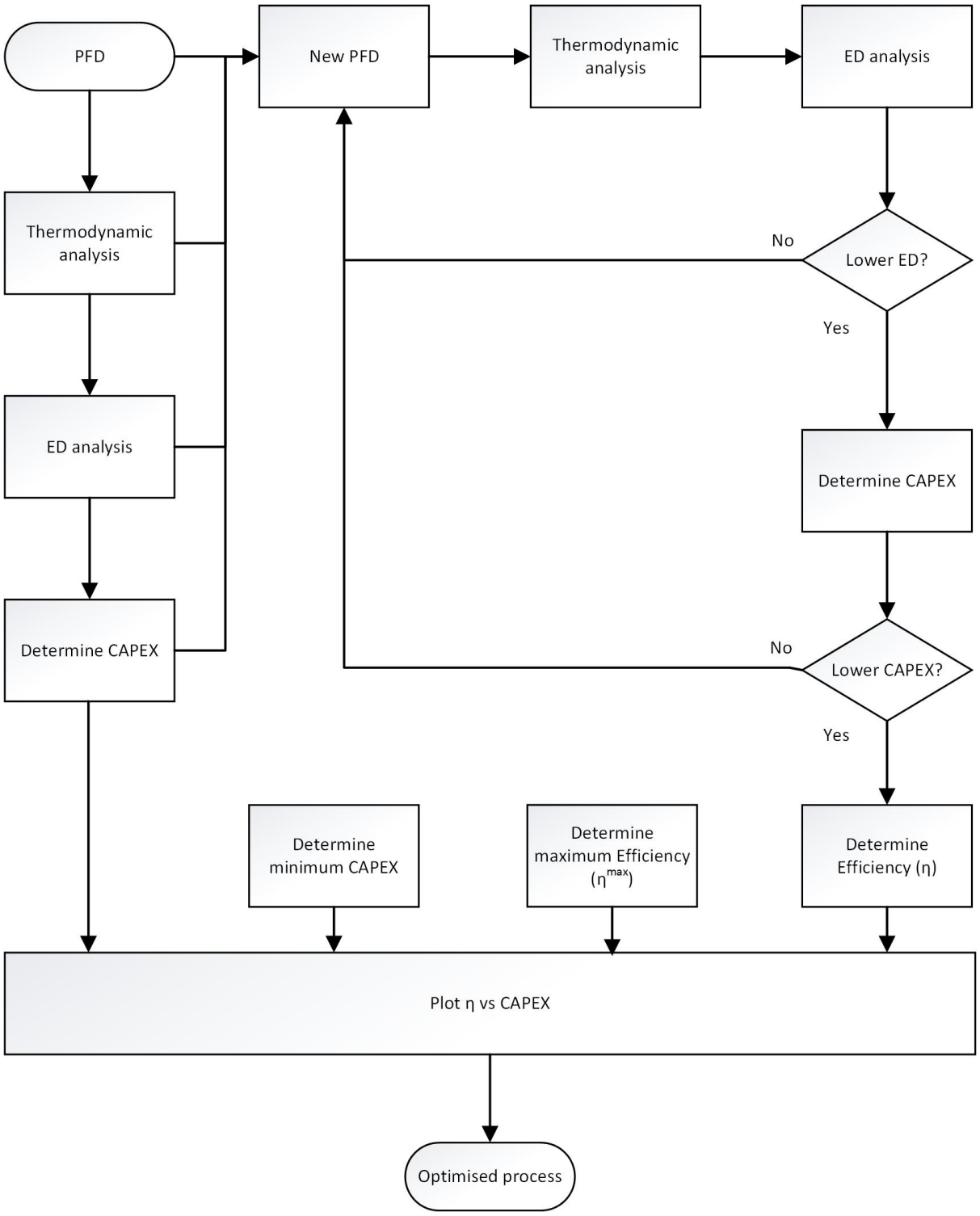


Figure 4.1: Methodology proposed for process improvement using a combination of first and second laws of thermodynamics with a CAPEX analysis, as published by Cabral and Mac Dowell [103].

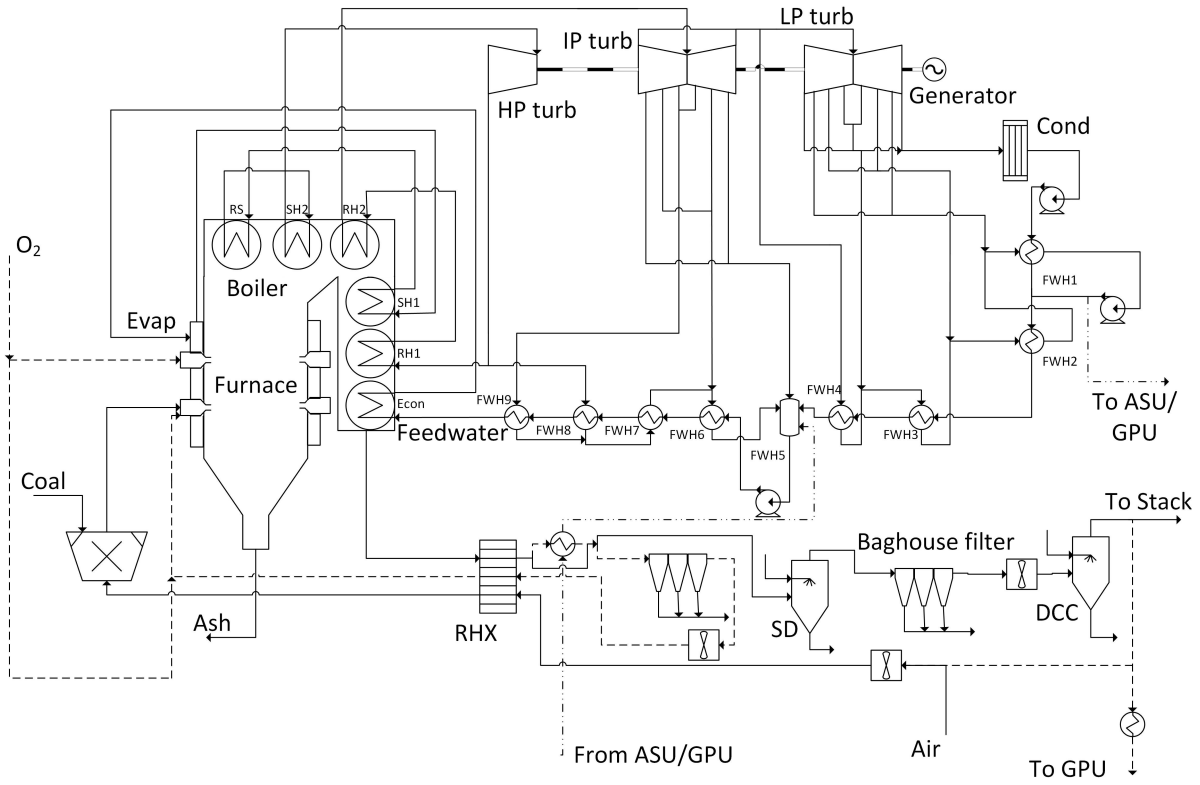


Figure 4.2: Process Flow Diagram (PFD) of the power plant complete with coal mill, boiler, turbine, feedwater heating train, ash collection and flue gas desulphurisation, as published by Cabral and Mac Dowell [103]. The boiler is divided into two sections: the furnace, where combustion takes place, and the boiler, where heat increases the temperature of feedwater and generate supercritical steam. Solid lines represent the flow paths in air- and oxy-modes, except for air inlet which is present in air-mode only. Dashed lines represent the extra flow paths in oxy-mode for O_2 feed and RFG. Dashed and dotted lines represent the heat integration pathways between the feedwater heating train and the compressors from the ASU and GPU. Feedwater heaters 1 to 4 can be bypassed with heat integration. HP turb - High pressure turbine; IP turb - Intermediate pressure turbine; LP turb - Low pressure turbine; Cond - Condenser; Econ - Economiser; Evap - Evaporator; SH1 and SH2 - Superheater 1 and 2; RS - Radiant superheater; RH1 and RH2 - Reheater 1 and 2, FWH1 to FWH9 - Feedwater heater 1 to 9; RHX - Regenerative heat exchanger; SD - Spray dryer for desulphurization.

4.2.4 Heat integration

This work did not focus on performing a full heat integration analysis, which would be adequately conducted by performing a pinch analysis and a heat exchanger network (HEN) analysis[264]. Instead, this work focuses on suggesting heat integration opportunities based on literature and evaluate the thermodynamic benefits of such an approach to test the methodology developed.

Low-grade heat of compression from the ASU and GPU has been suggested as potential heat integration strategies[111, 115]. The condensed water leaving the turbines had enough flowrate and was sufficiently cold to satisfy some compressors' cooling demand. Adopting this strategy will require changes to the inter- and after-coolers used in those

Table 4.1: Fractions and conditions of steam bled from the HP and IP turbines, based on turbine feed to reach feedwater temperature of 299 °C after heat integration.

Turbine	bleed no	w_n (%)	T (°C)	P (bar)
HP	1	9.30	365	75
IP	1	7.45	558	48
	2	4.81	460	25
	3	9.96	381	14

compressors, which will require custom-built units to support these changes. If this is conceivable, then the heat demand required by the condensate in feedwater heaters 1 to 4 can be satisfied using the low-grade heat of compression from the ASU and GPU, reducing the overall number of equipment. Another potential benefit of this strategy is that more electricity can be generated because more steam is available to expand in the turbines. These changes in the feedwater heating train will require different bleed fractions to satisfy its heat demand, detailed in Table 4.1. It is expected that the turbine manufacturer can perform the required changes to the turbines.

After the boiler, the heat transfer equipment was designed to maintain the flue gas above the acid dew point at the baghouse filters, which is 150 °C under oxy-combustion conditions[200]. There is also potential to further increase the feedwater temperature leaving the ASU by using some residual heat from the flue gas after the RHX. The dash-dotted lines in Figure 4.2 identify the changes to the power plant section by using this heat integration approach.

4.2.5 Thermodynamics analysis

Equations 3.22 and 3.20 calculate the maximum amount of power generated by the turbines ($P^{Max}_{Rankine}$) from a Rankine cycle. In this work, gross and net efficiencies were determined on a lower heating value (LHV) basis.

The net efficiency was compared against the maximum thermodynamic efficiency of an ideal Rankine cycle and the minimum thermodynamic separation work for both ASU and GPU. The ideal Rankine cycle is calculated using Equation 3.20.

The minimum separation work (W_{min}) relates the component's molar flow to be separated from the inlet with the outlet streams at a specific operating temperature. The minimum thermodynamic work to separate O_2 from air and CO_2 from flue gas is given by Equations 4.1 and 4.2 based on the first and second laws of thermodynamics[1].

$$\begin{aligned} W_{min}^{O_2}(kJ/mol) = RT\left(n_{Oxy}^{O_2}\ln(y_{Oxy}^{O_2}) - n_{Oxy}^{Oxy-O_2}\ln(y_{Oxy}^{Oxy-O_2})\right) \\ +RT\left(n_{Nit}^{O_2}\ln(y_{Nit}^{O_2}) - n_{Nit}^{Nit-O_2}\ln(y_{Nit}^{Nit-O_2})\right) \\ -RT\left(n_{Air}^{O_2}\ln(y_{Air}^{O_2}) - n_{Air}^{Air-O_2}\ln(y_{Air}^{Air-O_2})\right) \end{aligned} \tag{4.1}$$

$$\begin{aligned} W_{min}^{CO_2}(kJ/mol) = RT\left(n_{Final}^{CO_2}\ln(y_{Final}^{CO_2}) - n_{Final}^{Final-CO_2}\ln(y_{Final}^{Final-CO_2})\right) \\ +RT\left(n_{Waste}^{CO_2}\ln(y_{Waste}^{CO_2}) - n_{Waste}^{Waste-CO_2}\ln(y_{Waste}^{Waste-CO_2})\right) \\ -RT\left(n_{FlueGas}^{CO_2}\ln(y_{FlueGas}^{CO_2}) - n_{FlueGas}^{FlueGas-CO_2}\ln(y_{FlueGas}^{FlueGas-CO_2})\right) \end{aligned} \tag{4.2}$$

Where *Oxy* refers to the stream rich in O_2; *Nit* is the stream rich in N_2; *Air* is the air inlet stream; *Final* is the stream rich in CO_2; *Waste* is the stream sent to the stack; $FlueGas$ is the flue gas to be separated; T is the stream's temperature; and R is the gas constant, 8.314 kJ/(K kmol).

The potential to improve a process can be analysed from the Second Law efficiency.

$$\eta_{2^{nd}} = \frac{W_{min}}{W_{real}} \tag{4.3}$$

The maximum thermodynamic efficiency of oxy-combustion can be calculated using the maximum power produced by a Rankine cycle and the minimum separation work.

$$\eta_{net}^{Max} = \frac{P_{turbines}^{Max} - n_{Oxy}^{O_2}W_{min}^{O_2} - n_{Final}^{CO_2}W_{min}^{CO_2}}{\dot{m}_{fuel}LHV} \tag{4.4}$$

4.2.6 Exergy analysis

The exergy destruction (ED) of a unit operation is given by Equation 4.5[114].

$$ED = \sum_{In}\left[n(h - T_0 s) + Q\left(1 - \frac{T_0}{T_s}\right) + W_s\right] - \sum_{Out}\left[n(h - T_0 s) + Q\left(1 - \frac{T_0}{T_s}\right) + W_s\right] \tag{4.5}$$

Where n is the molar flow (mol/s); h is the specific molar enthalpy (kJ/mol); s is the specific entropy (kJ/(mol K)); Q is heat flow (kJ); T_0 is ambient temperature (K); T_s is the system temperature (K); and W_s is the work done by or to the system (kW). Performing this analysis to each unit operation of oxy-combustion identifies the most suitable candidates for process improvement.

Table 4.2: Comparison of the simulation data with data from the IECM and the Callide oxyfuel project[70].

Parameter	This work	IECM	Callide[117]
Gross power (MW)	509	517	500
Net power (MW)	373	396	345
$\eta_{\text{gross}}^{\text{LHV}}$ **(%)**	47	46	46
$\eta_{\text{net}}^{\text{LHV}}$ **(%)**	34	35	32
$\mathbf{O_2}$ **demand (kg/MWh)**	605	653	632
Fuel burned (kg/s)	40	46	54

4.3 Results and Discussion

4.3.1 Oxy-combustion

The oxy-combustion process was modelled based on the Callide Oxyfuel project[70] and the overview by Stanger et al. [102]. Part of the oxidant delivered by the ASU is mixed with the secondary RFG whilst the rest is mixed in the burner and the combustion chamber as oxygen lances[70, 102]. The resulting PFD can be found in Figure B.5.
This process requires 7400 tpd of oxidant to operate a 509 MW gross pulverised coal power plant and maintain 3.4 wt% of O_2 in the flue gas. Two ASU trains are required, one with 4000 tpd and another with 3400 tpd, to satisfy the power station's oxygen demand. This process has a coal consumption of 0.39 kg_{coal}/kWh, similar to the value reported by the U.S. Energy Information Administration[265]. Fly ash was assumed to be 75 % of total ash, and T_{ad} was 2176 °C, similar to the value of 2180 °C reported by Sharifi et al. [248] for anthracite. Grinding coal to 90 μm consumes 22 kWh/t_{coal}.

4.3.2 Simulation and model validation

The simulated oxy-combustion process has a gross efficiency of 47.2 % and a net efficiency of 34.6 %, resulting in a 12 % efficiency loss compared to the unabated plant.
The grand composite curve of the oxy-combustion process without heat integration is represented in Figure 4.3. The minimum temperature difference is found in the cryogenic sections, where they can be as low as 2 °C.
The results from this simulation were validated against data from the Integrated Environmental Control Model (IECM)[266] and from the Callide Oxyfuel project[117] in Table 4.2. The complete combustion assumption used in this work led to the disagreement observed for O_2 demand and fuel consumption.
The parasitic power consumption of the ASU, GPU, and other equipment from the power plant agree with the work of Tranier et al. [137] (Table 4.3).
The stream tables of the oxy-combustion can be found in Table B.1, the heat tables are

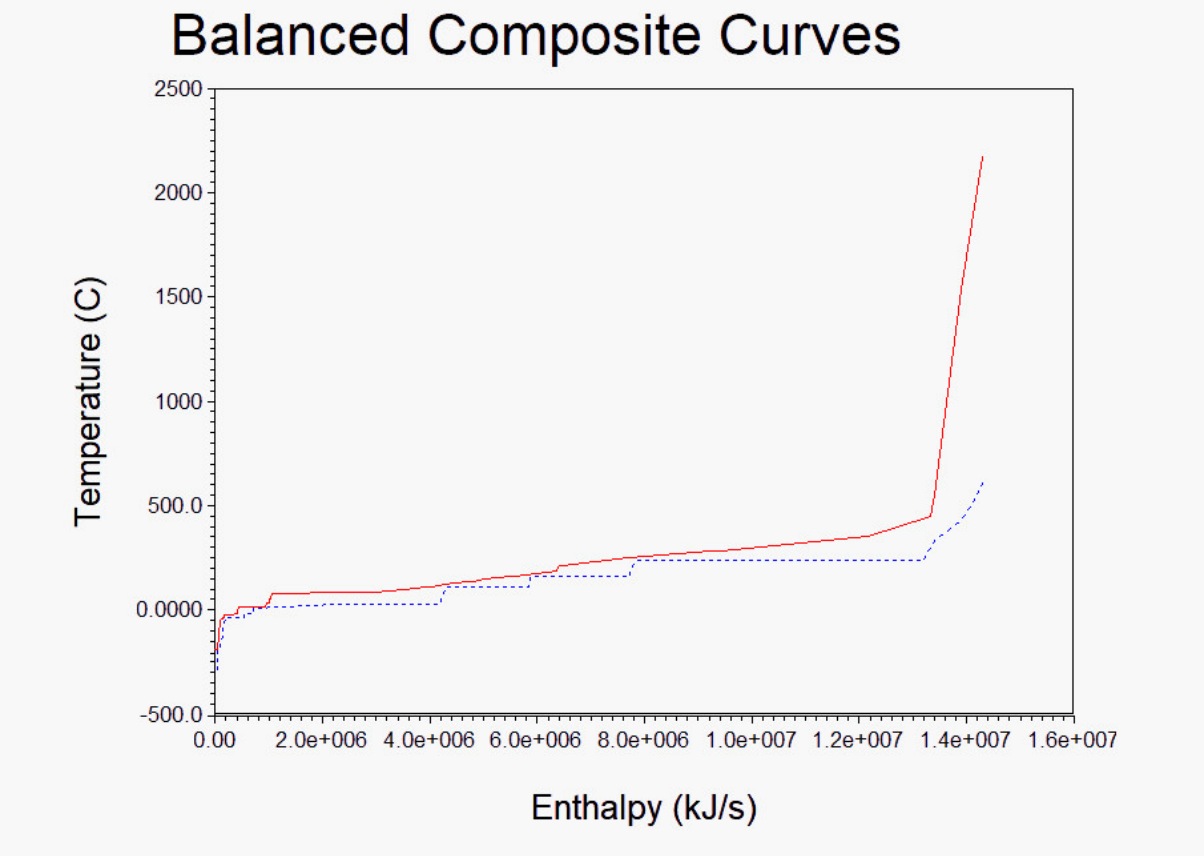


Figure 4.3: Grand composite curve of the oxy-combustion process without heat integration obtained from Aspen Energy Analyzer. The red solid line represents the hot composite curve whilst the blue dotted line represents the cold composite curve.

in Table B.2, the work tables in Table B.3, the carbon balance in Table B.4, and the energy balance in Table B.5.

4.3.3 Thermodynamic analysis

The minimum thermodynamic separation work (W_{min}) of the ASU and GPU is 5.8 kJ/mol_{O_2} (49.9 kWh/t_{O_2}) and 0.8 kJ/mol_{CO_2} (5.4 kWh/t_{CO_2}), respectively. The real separation work (W_{real}) of O_2 and CO_2 is 24 kJ/mol_{O_2} (206 kWh/t_{O_2}) and 23.3 kJ/mol_{CO_2} (156 kWh/t_{CO_2}).

Improving the thermodynamic efficiency of the ASU, GPU, and boiler reduces the parasitic power consumption (Figure 4.4). A 5 % increase of the ASU's thermodynamic efficiency reduces the overall power consumption by 17 % whilst a similar GPU increase reduces the power consumption by 46 %. Figure 4.4 demonstrates that the optimal path to improve the overall process starts by improving the GPU's efficiency to 22 % rather than trying to improve the more established ASU.

Table 4.3: Parasitic energy losses from ASU, GPU, and power plant from this simulation and from Tranier et al. [137].

	This work	Tranier, J. P.[137]
ASU	46.2 %	43.5 %
GPU	33.6 %	35.8 %
Power plant	20.1 %	20.7 %

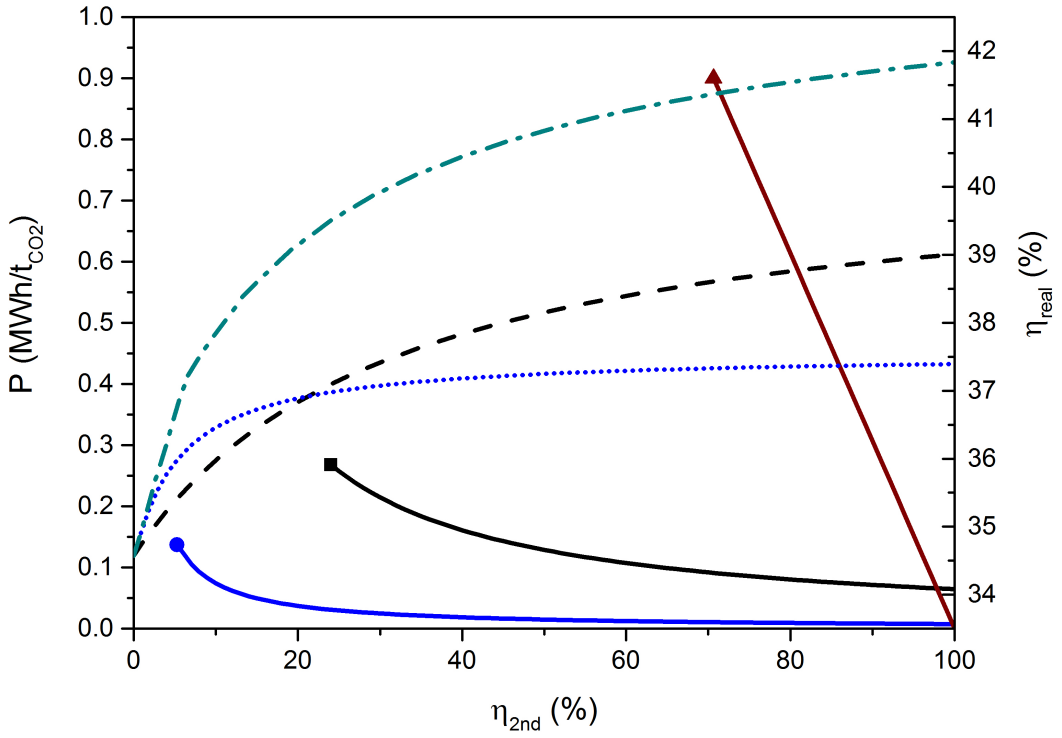


Figure 4.4: Effect of thermodynamic efficiency (η_{2nd}) on power needed for the ASU (black line) and GPU (blue line) and for the power lost by the boiler(red line), as published by Cabral and Mac Dowell [103]. The starting points for the ASU, GPU, and Boiler were obtained through this simulation and are represented as ■, ●, and ▲ respectively. The dashed lines represent the effect on the real efficiency of the oxy-combustion by increasing the thermodynamic efficiency of the ASU (black dashed line), the GPU (dotted blue line), and both (dash-dot cyan line). Improving the GPU will lead to the greatest improvement of the overall process.

4.3.4 Process improvement and heat integration

The maximum thermodynamic efficiency and power output were determined by relating the maximum Rankine power with both the minimum thermodynamic separation work for O_2 and CO_2 using Equations 3.20, 4.1, and 4.2, respectively. The net efficiency of the simulated power plant was 34.6 %. Then, assuming an ideal separation of O_2 from air and CO_2 from the flue gas, the net efficiency improves to 43.1 %. This shows that improving the separation processes can increase the plant efficiency by up to 8 %. Tranier et al. [137] stated that Air Liquide could improve the separation efficiency of

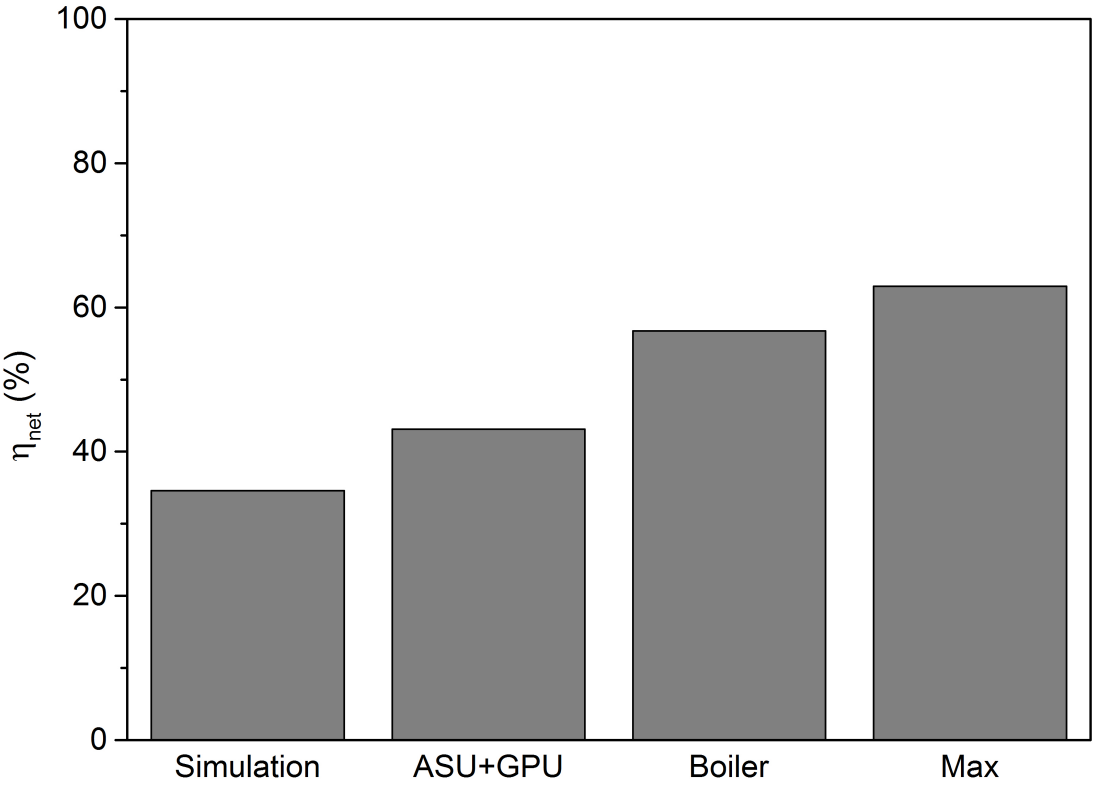


Figure 4.5: Comparison of the simulated oxy-combustion efficiency with the process if the ASU and GPU operate at the minimum thermodynamic separation work (ASU+GPU), if the boiler could achieve the maximum Rankine efficiency (Boiler), and the maximum thermodynamic efficiency of the oxy-combustion process (Max), as published by Cabral and Mac Dowell [103].

the ASU by 10 %. However, there is a more considerable potential to improve the boiler, with a maximum possible improvement of around 21 % relative to the simulation case. This could be a good starting point to improve the technology; however, coal boilers are a very mature technology, with decades of experience and improvement, making it an unlikely candidate for process design changes.

The power plant's maximum theoretical power output is 720 MW, achieving 63 % thermodynamic efficiency at the minimum separation work of O_2 and CO_2 of 24 kJ/mol and 16 kJ/mol, respectively. Oxy-combustion achieves a maximum theoretical efficiency of 67 % by excluding the power required to separate O_2 and CO_2 (Figure 4.5).

Increasing the boiler conditions to advanced ultra-supercritical steam parameters operating up to 700 °C and 350 bar is part of current development[184, 186]. These power plants can achieve net efficiencies up to 52 % on an LHV basis, but traditional materials cannot operate under such high temperatures, so more expensive nickel alloys must be used[184]. This indicates that increasing the efficiency of power plants is limited to current material selection[184, 186].

Low-grade heat of compression from the ASU and GPU was used to pre-heat the boiler's

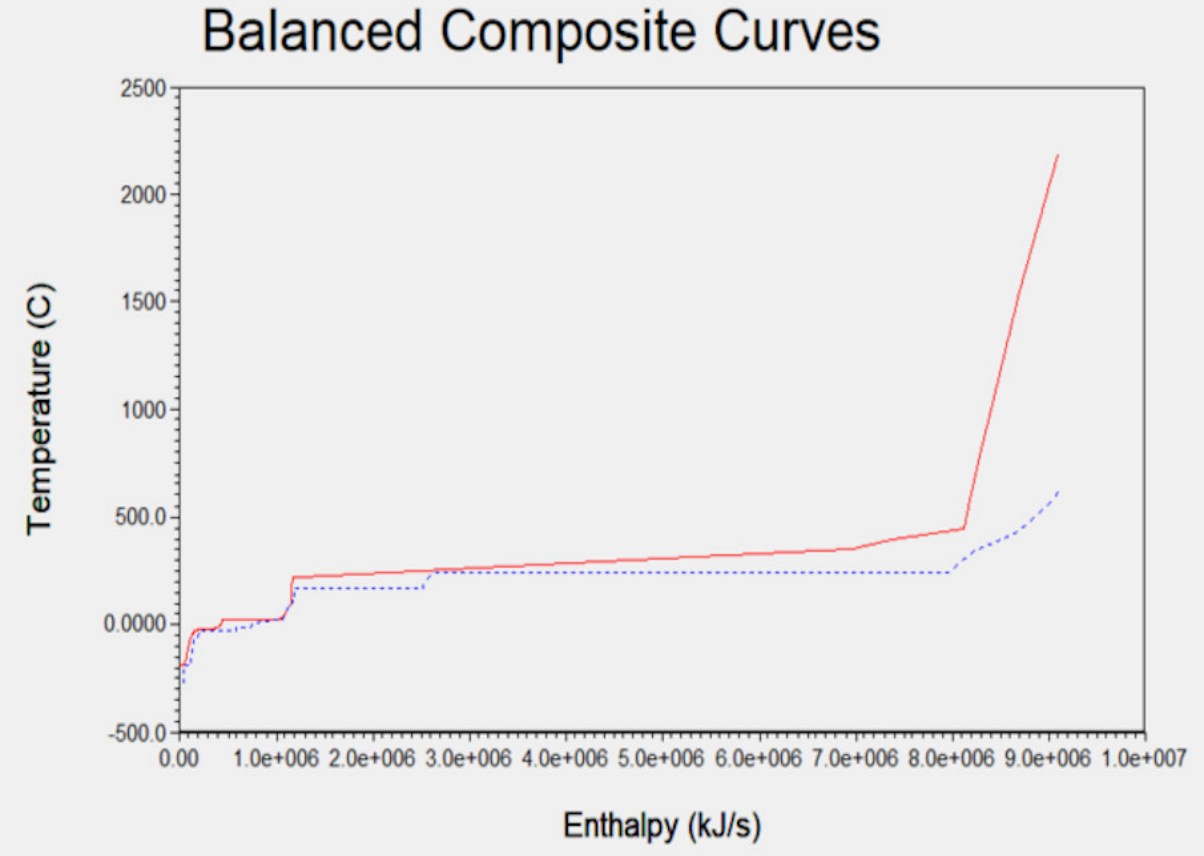


Figure 4.6: Grand composite curve of the oxy-combustion process with heat integration obtained from Aspen Energy Analyzer. The red solid line represents the hot composite curve whilst the blue dotted line represents the cold composite curve.

feedwater following the dashed lines from Figure 4.2 (A more detailed PFD is represented in Figure B.6). The grand composite curve of the oxy-combustion process with heat integration is represented in Figure 4.6.

The stream tables of this configuration can be found in Table B.7, the heat tables are in Table B.8, the work tables in Table B.9, the carbon balance in Table B.10, and the energy balance in Table B.11.

There is no need to have an O_2 purity greater than 95 %, which can be achieved by reducing the number of stages of the distillation columns[77, 114]. Reducing the amount of compression done by the booster can be another way of reducing the ASU's parasitic losses. These strategies offer the possibility to reduce the plant's capital cost.

The grand composite curve of the oxy-combustion process with heat integration and smaller ASU is represented in Figure 4.7. The grand composite curves indicate that there is still opportunity to improve the process by increasing the amount of heat integration. However, a HEN analysis is not the focus of this analysis and was not pursued.

The stream tables of this improved configuration can be found in Table B.13, the heat tables are in Table B.14, the work tables in Table B.15, the carbon balance in Table B.16, and the energy balance in Table B.17.

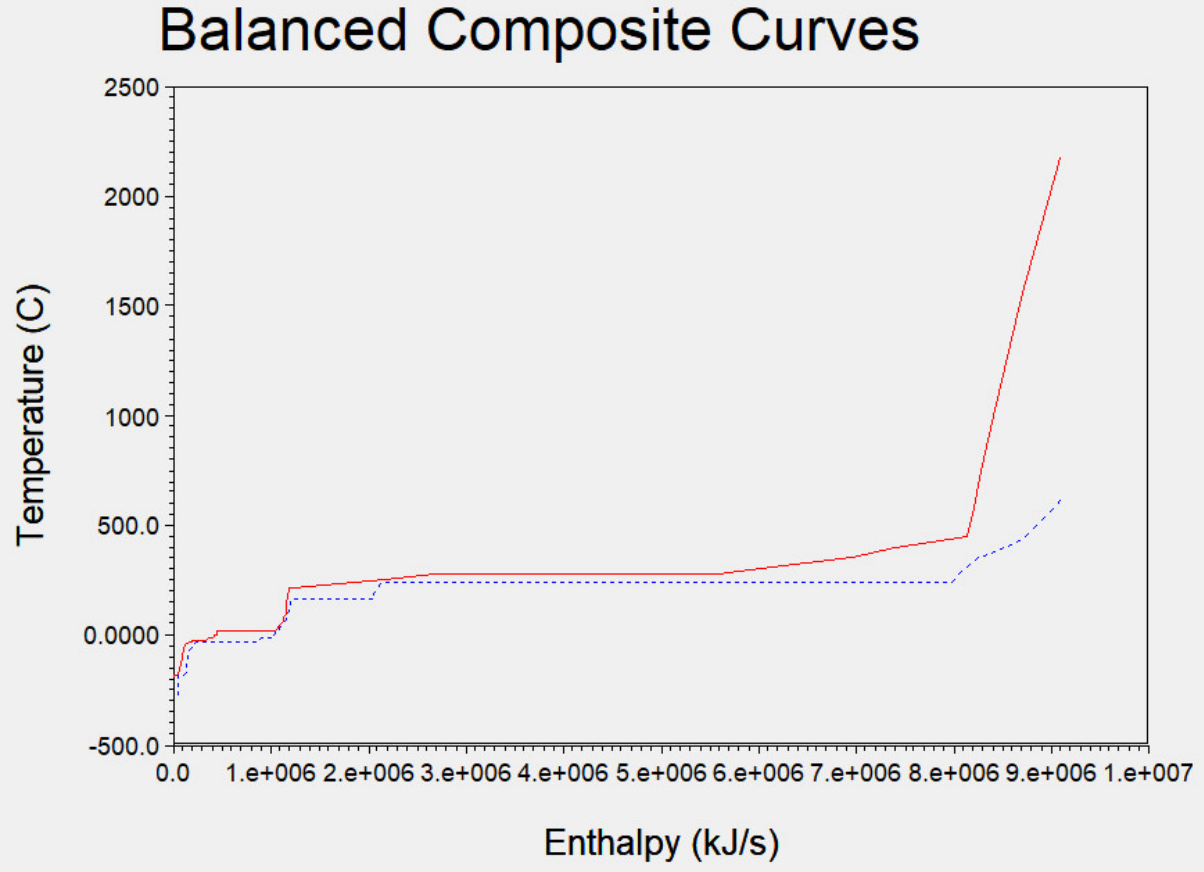


Figure 4.7: Grand composite curve of the oxy-combustion process with heat integration and smaller ASU obtained from Aspen Energy Analyzer. The red solid line represents the hot composite curve whilst the blue dotted line represents the cold composite curve.

An exergy analysis was performed to the oxy-combustion process, and the boiler demonstrated the most significant losses due to inefficiencies associated with large temperature differences. Due to material limitations, it is currently impossible to improve this section; however, the feedwater heating train shows the potential to reduce the plant's inefficiencies. Here, feedwater heaters 1 to 4 were determined as providing most of the inefficiencies from this section. This proves to be an excellent point to increase the feedwater's temperature using low-grade heat of compression from both the ASU and GPU. The feedwater's temperature increased sufficiently to bypass feedwater heaters 1 to 4 in the improved process after using this low-grade heat of compression.

An exergetic analysis was performed after process improvement and compared against the results obtained previously to check for any inefficiency reduction. The results obtained this way identified a pathway to improve the oxy-combustion process by minimising its main inefficiencies. The boiler has a 1.7 % exergy destruction increase, as shown in Figure 4.8, due to increased oxidant mass flow from the lower O_2 purity. The power plant's significant losses occur in the boiler, carrying over 40% of exergy destruction, of which the economiser and the superheater are the leading causes. This is

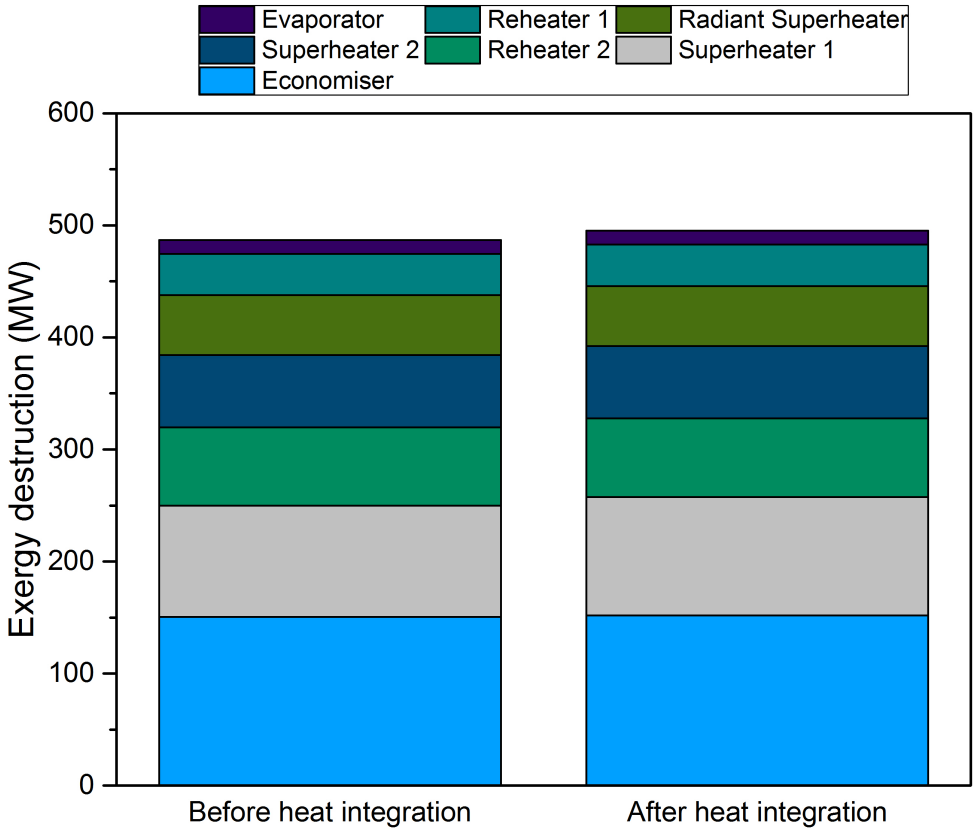


Figure 4.8: Exergy destruction of the boiler in oxy-combustion process before and after heat integration. The small increase of exergy destruction observed after heat integration is because of a lower O_2 purity. This increases the mass in the oxidiser, and so more losses are encountered in this unit.

due to the large temperature difference between the hot flue gas and the water/ steam exchanging heat in these sections. Thus, it may be advantageous to reduce feedwater heating on both the economiser and superheater and increase it on the evaporator, which in a supercritical plant can be called steam generator because no evaporation occurs. Throughout this work, the steam generator will be called evaporator, as this is a commonly used term in the industry, even when no evaporation occurs, such as in supercritical plants. This will result in a larger evaporator surface area whilst reducing that of both the economiser and the superheater. However, the adoption of this strategy is limited by the materials available, as this equipment could be seriously damaged by the very high-temperatures present in these sections[173, 174, 183]. Furthermore, it is unlikely that a boiler optimisation will significantly improve these sections' exergy destruction because there will always be a high-temperature difference between the flue gas and steam/water. Some considerable losses occur in the combustion chamber and the feedwater heating train, where the most significant loss is in the condenser.
It was found that the extra flue gas cooling was the leading cause of exergy destruction

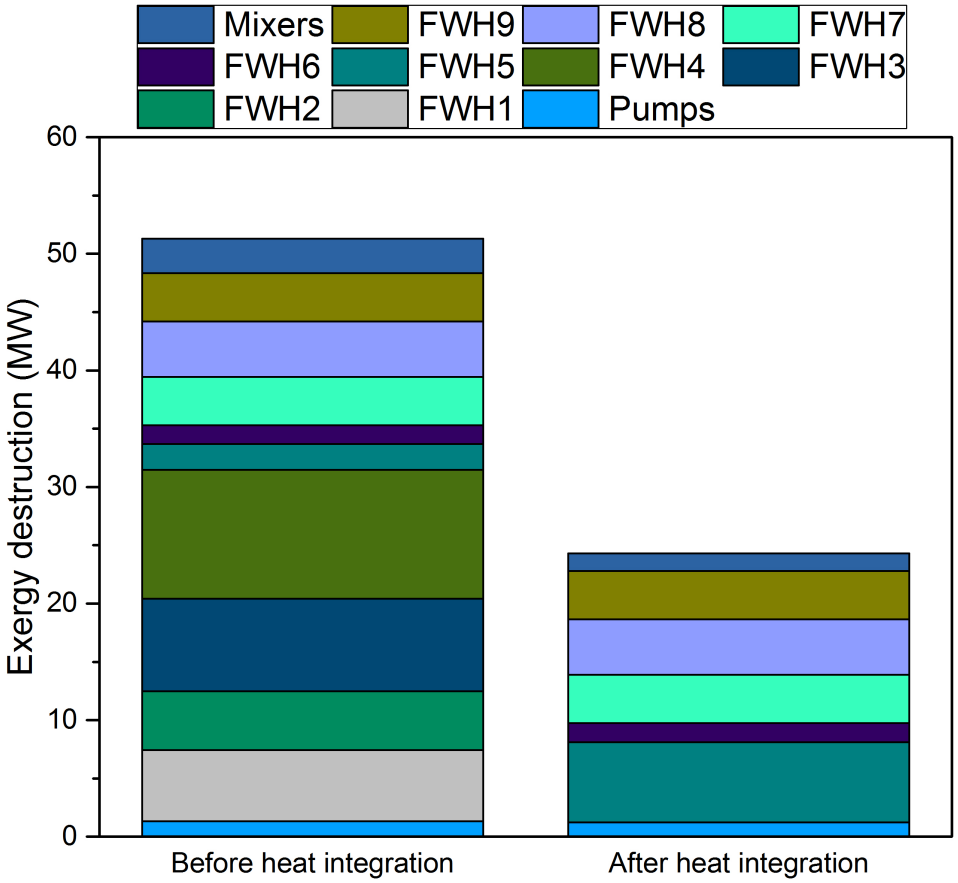


Figure 4.9: Exergy destruction of feedwater heating train in oxy-combustion process before and after heat integration, as published by Cabral and Mac Dowell [103]. The reduction of exergy destruction after heat integration is because feedwater heaters FWH1 to FWH4 are removed.

before entering the baghouse filters for fly ash removal. This heat can be integrated and recovered elsewhere, such as heating the feedwater.

Considerable exergy destruction was detected on feedwater heater 4, where the last bleed of the intermediate pressure turbine is condensed against colder feedwater. The exergy destruction associated with the feedwater heating train has been significantly reduced by 53 %, as shown in Figure 4.9. This reduction occurs because the low-pressure heaters, FWH1 to 4, are removed from the process after heat integration. However, this does not imply that all exergy destruction from FWH1 to 4 is prevented. Indeed, this exergy destruction is merely shifted to the ASU and GPU, where the heating previously provided by these units is satisfied by low-grade heat of compression, explaining the higher losses from the compressors in Figure 4.10. The smaller losses from the GPU compressors observed in Figure 4.11 come from optimising these units, rather than from using feedwater to cool the gas. The smaller exergy destruction in the feedwater heating train reduces the heat requirement from coal, reducing its consumption to 0.36 kg_{coal}/kWh, and increasing the gross and net efficiencies to 49 and 38 %, respectively.

The main heat exchanger (MHX) has the most exergy losses, also identified by Taniguchi as responsible for more than half of the exergy destroyed in the ASU[267]. This exergy destruction is due to the high heat duty and temperature difference. The difference between air pressure, at 4.2 bar, with the products' pressure, at 1.2 bar, also contribute to the exergy destruction of this unit. Reducing the air's temperature at the MHX inlet may be a good way to reduce this unit's losses; however, that also reduces the O_2 temperature leaving the heat exchanger. Although this negatively affects the combustion efficiency, which is not a concern for oxy-combustion, it will increase the operational safety of the process[110, 114]. Pre-heating pure oxygen on the flue gas cooler can be dangerous for the same reasons, as a spark might combust any deposited material.
The main air compressor (MAC) was a reliable operation for heat integration because compressed air is discharged at high temperatures, despite having small losses (4 %). A good alternative is to use adiabatic compressors with one inter- and one after-cooler instead of isothermal compressors. Feedwater can be used to cool this air stream whilst increasing its temperature, potentially reducing capital costs and cooling water[114].
Decreasing the temperature of the air flowing into the MHX led to a reduction of this unit's exergy destruction, as shown in Figure 4.10. Changing the MAC from an isothermal compressor to a two-staged adiabatic compressor increased the exergy destruction and power consumption. However, this change enables using the low-grade heat of compression to pre-heat a portion of the feedwater whilst cooling the compressed air stream. This strategy reduces the number of feedwater heaters, as previously described. The second stage of the booster was removed because the required compression could be provided using the work obtained by the expander. The HP column's number of stages was reduced to 10, and the LP column was reduced to 23 stages, decreasing the oxygen purity to 97 wt%. This strategy reduced the unit's power consumption to 197 kWh/t_{O_2}, similar to other authors' reports[111, 114, 115, 137, 138].
The power consumption of both the ASU and GPU is primarily associated with the compression work. It will be unlikely that major improvements in thermodynamic efficiency will come from them as the compressors are operating at 90 % adiabatic efficiency. One possible way to reduce the ASU's power consumption is by discharging more compressed air to the expansion turbine. This provides part of the power required to run the booster compressor, which accounts for 20 % of the power consumption and the rest being done mainly by the main air compressor.
The MHX has the GPU's highest exergy destruction, similar to the ASU. Low grade heat of the compressed gases can be used to pre-heat feedwater[70, 111, 114, 115]; however, Spero et al. [70] stated that some care must be taken when employing this strategy. This caution was expressed because the GPU only starts when CO_2 concentrations of the flue gas are high enough to allow a successful separation. Furthermore,

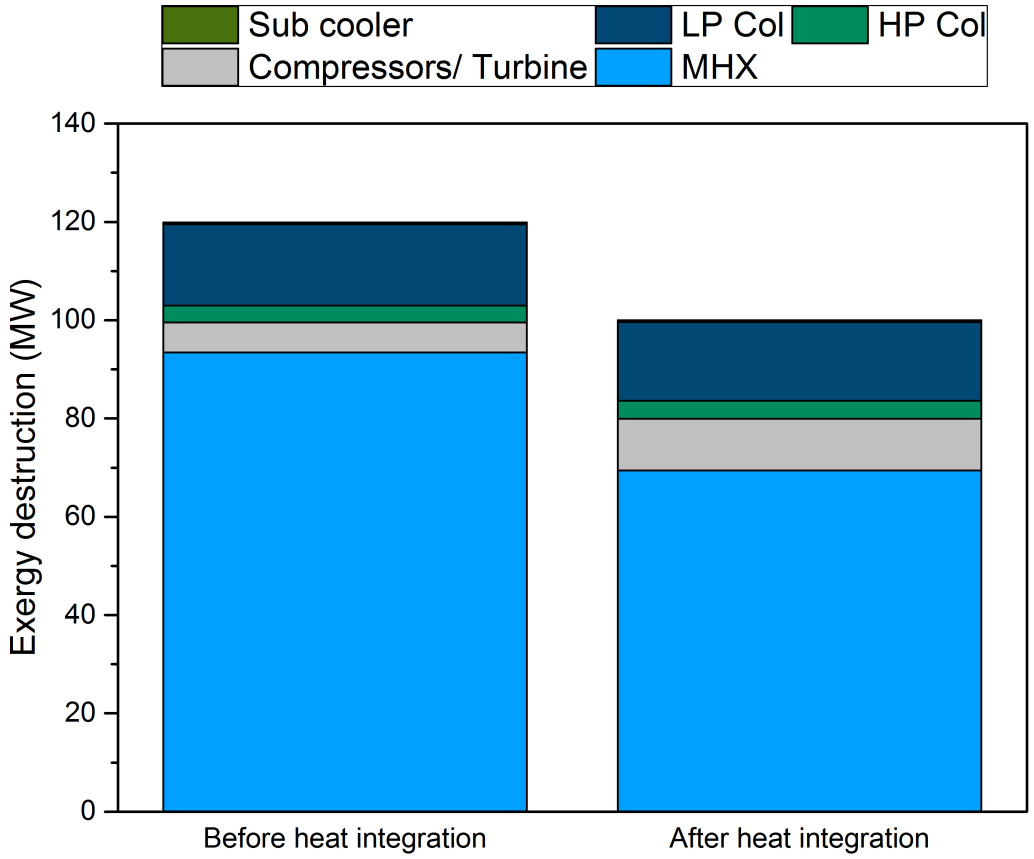


Figure 4.10: Exergy destruction of the ASU in the oxy-combustion process before and after heat integration, as published by Cabral and Mac Dowell [103]. An increase of the compressors' exergy destruction occurred from changing the MAC from isothermal to adiabatic. On the other hand, reducing the inlet temperature of air to the main heat exchanger reduces the exergy destroyed in this unit. Overall, a reduction of exergy destruction of the ASU is observed.

the GPU could be put at risk if a high concentration of impurities is present in the flue gas. One possible way of avoiding this issue is to use heat from the low-pressure compression train, and send the flue gas to the stack whilst CO_2 concentrations are not sufficiently high to run the GPU. Skorek-Osikowska et al. [111] has shown that this approach increases the plant's net efficiency.

Changing the first compressor from a one-stage to a two-staged compressor with intercooling reduced the unit's exergy destruction, as shown in Figure 4.11. This strategy also reduces the compressor's power and avoids increasing the gas temperature to levels that could reduce the equipment lifetime. Low-grade heat of compression is used to pre-heat another portion of the feedwater and cool the compressed flue gas. The second compressor uses the rest of the feedwater to cool the compressed flue gas, whilst using its heat to increase the feedwater temperature. This strategy reduced the exergy destruction of the GPU by 6.4 %.

In order to improve this process, new strategies might be needed for separating and

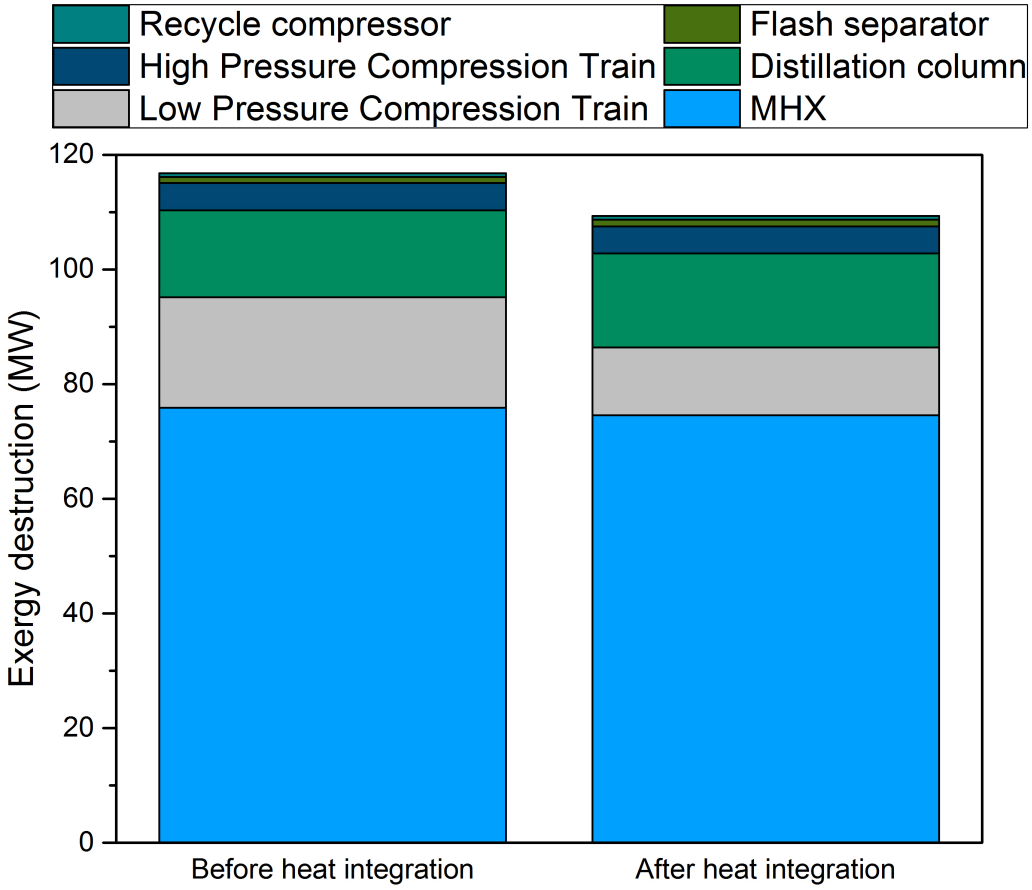


Figure 4.11: Exergy destruction of the GPU in the oxy-combustion process before and after heat integration. Adding one stage with inter-cooling to the first compressor reduces the exergy destroyed in this compression step.

purifying CO_2. For example, the power consumption would decrease if the distillation column could be operated at lower pressures and only compress the purified CO_2 stream to pipeline pressure. If lower O_2 purities are used, more compression work must be done to separate CO_2 due to higher concentrations of argon (Ar) and N_2 present in the flue gas[268].

Overall, a 4 % exergy destruction decrease was observed (Figure 4.12) from optimising the process and using the proposed heat integration.

4.3.5 Techno-economic analysis

The oxy-combustion efficiency was plotted against CAPEX (Figure 4.13) to evaluate the changes proposed from the thermodynamic and exergetic analysis. The CAPEX of an unabated power plant and the maximum thermodynamic efficiency of oxy-combustion were used to define the optimum boundaries of the process. Integrating the units as suggested increased the plant's efficiency from 34 % to 37 % and reduced the CAPEX from \$566M to \$480M, resulting in a 13 % decrease of \$/MWh.

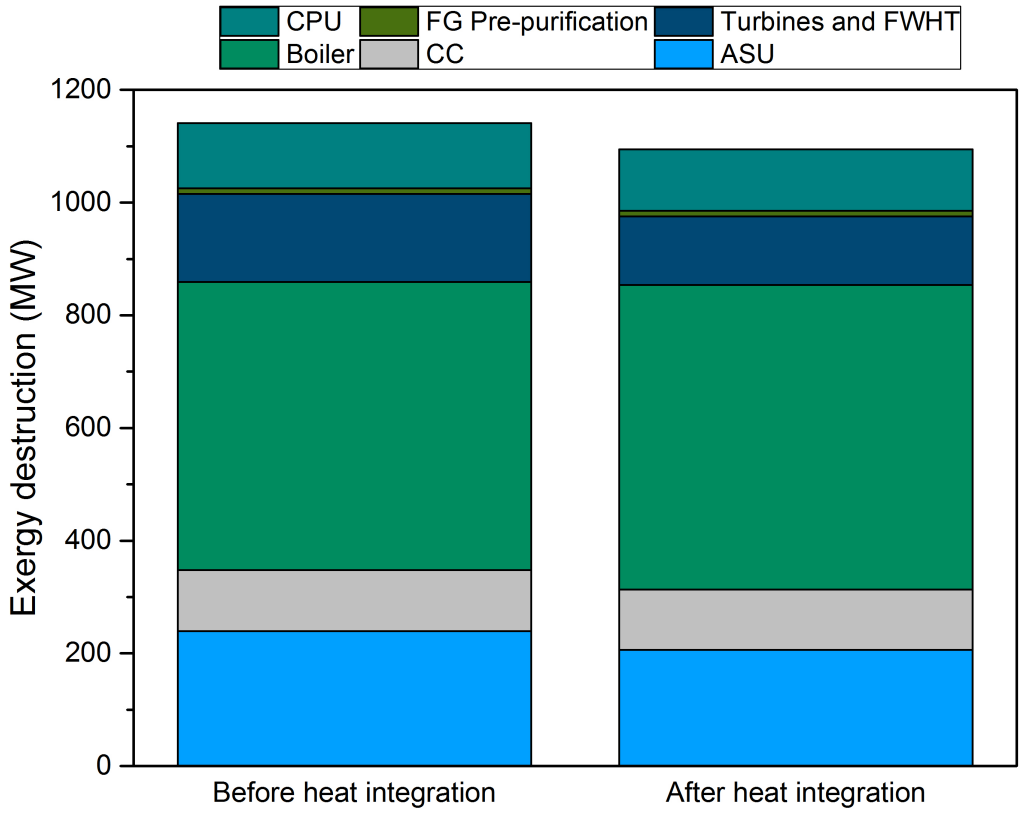


Figure 4.12: Exergy destruction of the oxy-combustion process before and after heat integration. A reduction of exergy destruction is observed after heat integration, showing a higher efficiency of the improved process.

4.4 Conclusions

This methodology enabled a rational approach towards process improvement via heat integration. This approach increased the oxy-combustion plant's net efficiency by 3 % whilst reducing the number of equipment required, reducing capital cost by 15 %, thus reducing the $/MWh by 13 %.

Specifically, minimising the exergy destruction by using low-grade heat of compression from the ASU and GPU to heat low-pressure feedwater reduces the number of feedwater heaters. Thus, fewer bleeds are required from the turbines, allowing more steam to generate electricity. This strategy would require turbines specifically designed to have fewer bleeds, but this will reduce the design's complexity, making it easier to implement. A more detailed pinch analysis and HEN analysis would likely lead to more optimal heat integration strategies. These analyses could be coupled with the methodology proposed here to aid in project selection.

It was determined that it is better to focus on improving the GPU design since this is the least thermodynamically efficient unit and would provide the most significant benefits

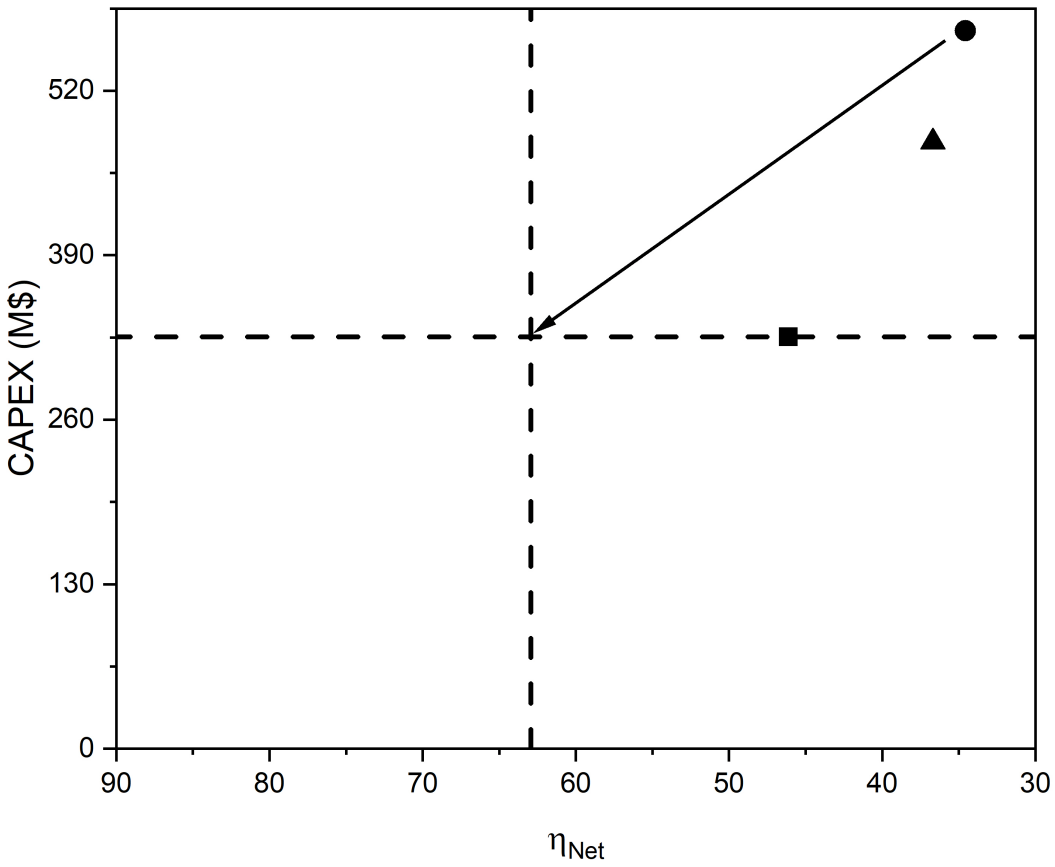


Figure 4.13: Plant efficiency plotted against CAPEX, ■ represents the unabated power plant, ● the oxy-combustion before process improvement and ▲ after process improvement, as published by Cabral and Mac Dowell [103]. The horizontal dashed line represents the CAPEX of the unabated power plant, and the vertical dashed line the maximum thermodynamic efficiency. The desired direction of process improvement is represented by the arrow, showing both an efficiency increase and a CAPEX reduction. The process improvement using this analysis reduced CAPEX and increased efficiency, but showed a sharper CAPEX reduction than efficiency increase.

to the entire power plant. Indeed, the GPU is less mature than the other technologies which may provide more opportunities for improvement.

Chapter 5

A techno-economic analysis of a novel solvent-based oxy-combustion CO_2 capture process

The work detailed in this Chapter was published in Industrial & Engineering Chemistry Research[269].

5.1 Introduction

The gas processing unit (GPU) was identified in Chapter 4 as the least thermodinamically efficient unit[103]. This led to the idea of replacing the traditional cryogenic GPU with a solvent-based capture process to improve the thermodynamic efficiency of the CO_2 separation step. The new process is illustrated in Figure 5.1 (full process) and Figure 5.4 a (GPU).

Several authors aimed to reduce the GPU's parasitic power consumption by proposing either different process configurations[66, 208, 270, 271] or alternative methods to purify CO_2[60, 61]. One of the proposed methods was adding membranes with high CO_2 selectivity downstream of a cryogenic GPU to increase its capture amount to 98 % and reduce the costs per ton of CO_2 of this unit by 5 – 10 %[270, 271]. Other researchers aimed to improve the economic attractiveness of CCS by using an MEA-based approach to capture CO_2 from a partial oxy-combustion process[60, 61]. However, the extra costs associated with O_2 production increased the levelised cost of electricity (LCOE) by 7 %, making this idea worse than either the base cases of post-combustion or oxy-combustion[61].

The increased CO_2 concentrations present in the flue gas from an oxy-combustion process offer the potential to investigate alternative processes or solvents to capture CO_2. Indeed, this already high CO_2 concentration significantly reduces the energy required for compression; therefore, it may become advantageous to select a high-pressure cap-

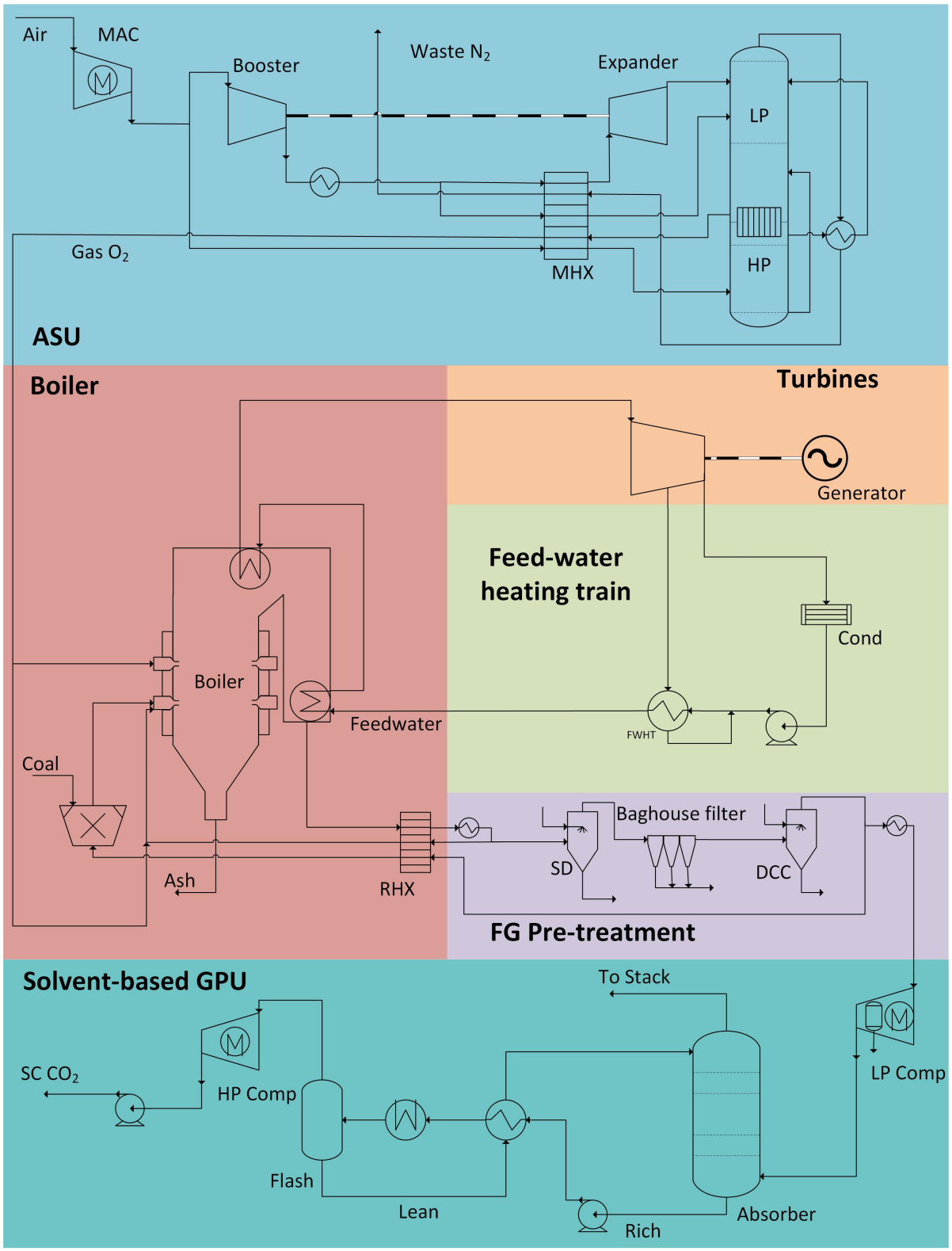


Figure 5.1: Simplified process flow diagram (PFD) of the oxy-combustion process with a solvent-based GPU, as published by Cabral et al. [269].

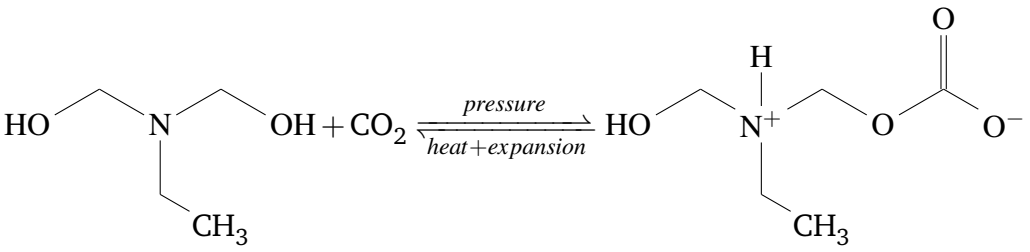


Figure 5.2: Reaction of EDEA with CO_2. Applying pressure favours the direct reaction to form the zwitterion EDEA-CO_2. Adding heat and reducing pressure favours the reverse reaction, releasing CO_2 and regenerating EDEA.

ture process, favouring a different class of solvents than tested by other authors[60, 61]. In this work, we propose a novel solvent-based GPU to treat the flue gas from oxy-combustion, illustrated in Figure 5.1. Here, flue gas is first compressed to the absorber's operating pressure using a 3-stage compressor with intercoolers at 25 °C[272]. Any resulting condensation is removed before the compressed gas is directed to an absorption column[272–277].

A stream essentially stripped of CO_2 is discharged from the top of the absorber and sent to the stack. From the bottom of the absorber, a CO_2-rich solvent is pumped to a heat exchanger to recover some heat from the incoming lean solvent stream[272–277]. Additional heat is added to promote CO_2 desorption and this stream is subsequently flashed, recovering a CO_2-rich gaseous product whilst the CO_2-lean solvent is recycled to the absorber[272–277]. The CO_2-rich gas is compressed to pipeline pressure and sent for storage in any suitable reservoir, *e.g.*, deep saline aquifer[76].

N-Ethyldiethanolamine (EDEA) is a tertiary alkanolamine[278] used in this work as a solvent to capture CO_2 originating from an oxy-combustion process. This amine reacts with CO_2 under pressure to create a zwitterionic ammonium alkylcarbonate ionic liquid and reverts to EDEA and CO_2 via expansion (Figure 5.2)[278].

This solvent demonstrated a selectivity to hydrogen sulfide (H_2S) and CO_2 similar to Selexol, and more reliable H_2S and CO_2 absorption than aqueous MDEA[278]. The versatility of capturing both H_2S and CO_2 can potentiate the use of EDEA across sectors, increasing its market demand and reducing its unit cost. Several configurations of the EDEA-based CO_2 capture process using varying degrees of heat integration will be evaluated, and their economic potential compared against previous results obtained for a cryogenic distillation GPU.

5.2 Model description

5.2.1 Oxy-combustion model

The traditional cryogenic distillation GPU[103] was replaced with a solvent-based capture unit with the operating conditions outlined in Table 5.1. The minimum thermo-

Table 5.1: Operating conditions of the absorber, flash unit, main heat exchanger (MHX), and CO_2 pump for the solvent-based GPU.

Unit	Parameter	Value
Absorber	T_{in} (°C)	25
	p_{in} (kPa)	2200
	Capture amount (%)	90
Flash	T_{in} (°C)	44
	Δp (kPa)	2100
MHX	Approach temperature (°C)	5
CO_2 pump	p_{out} (MPa)	11

Table 5.2: Chemical and physical properties of EDEA[282].

Property	Value
Molecular weight (g/mol)	133.2
Density at 20 °C (kg/m^3)	1013.5
Boiling point (°C)	247
Melting point (°C)	- 50
Flash point (°C)	138
Water solubility at 25 °C (mg/L)	1×10^6
Viscosity (pure) at 30 °C (mPa.s)[283]	47650
Viscosity (water, 5 mol%) at 30 °C (mPa.s)[284]	2.433

dynamic separation work of CO_2 was calculated according to Equations 4.1 and 4.2, enabling the calculation of a second-law efficiency with Equation 4.3.

5.2.2 EDEA

The model used the electrolyte NRTL equation of state with phase equilibrium data for EDEA obtained from Mathias et al. [278]. The electrolyte NRTL is a property method that can handle electrolytes in aqueous and mixed solvent mixtures[279]. All of the vapour-phase properties are determined using the Redlich-Kwong equation of state[279]. At the time of writing, small amounts of EDEA used for laboratory experiments are sold at $4180/kg[280].

Physical properties such as density and viscosity must be considered because they impact equipment size, which directly relates to capital costs[281]. It is vital to operate the process between the melting and boiling points to avoid solid formation or excessive solvent evaporation. It is also sensible to operate the process below the flash point to avoid combustion from any sparks that originate in the GPU. Chemical and physical properties of EDEA[282] relevant to this work are presented in Table 5.2.

Table 5.3: Breakdown of the specific power consumption (kWh/t_{CO_2}) of scenario 1.

Component	Value (kWh/t_{CO_2})
Main compressor	77
Recycle pumping	9
Post-compression	120
Heat requirement	27

5.2.3 Economic model

The economic evaluation was performed using the internal Aspen HYSYS cost estimator using a constant 2015 cost level and an exchange rate of 1.5 US dollars per British pound[66, 285]. The capital and operational expenditure (CAPEX and OPEX, respectively) were extracted from Aspen HYSYS, assuming a 25-year plant's lifetime[150]. The levelised cost of electricity (LCOE), a metric used to compare the economic attractiveness between power generating units, was subsequently calculated using Equation 5.1[286].

$$LCOE = \frac{CAPEX + \sum_{n=0}^{lt} \left[\frac{OPEX_n}{(1+r)^n} \right]}{\sum_{n=0}^{lt} \left[\frac{MWh_n}{(1+r)^n} \right]} \tag{5.1}$$

Where $CAPEX$ is the plant's capital cost in \$; $OPEX_n$ is the operating expenditure for year n in \$/kWh; lt is the plant's lifetime (years); r is the interest rate, here assumed to be the IRR; and MWh_n is the electricity generated in year n.

5.3 Results

5.3.1 Model output

The new solvent-based gas processing unit (Scenario 1) can capture 90 wt% of CO_2 at 95 wt% quality. This plant requires 230 kWh/t_{CO_2}, amounting to almost 50 % more power consumption than a traditional cryogenic distillation unit for CO_2 purification. Gas compression is the main contributor to this power consumption. However, efficiency losses are also attributed to the additional heat required from this unit, satisfied by low-pressure steam[273] (*i.e.*, requiring additional bleed from the turbines). The power consumption breakdown is detailed in Table 5.3.

CO_2 compression after flash consumes the most power within this unit and can be attributed to the high solvent expansion of 2100 kPa in the flash unit. Reducing this unit's pressure drop decreases power consumption but requires more heat to maintain adequate CO_2 purity (Figure 5.3).

Flue gas must be compressed from atmospheric pressure to 2200 kPa in the main compressor, making this step the second most energy-intensive. Reducing the absorber's operating pressure can decrease this unit's power consumption; however, this will reduce the amount of CO_2 captured[278]. Furthermore, flue gas from the oxy-combustion process already has high CO_2 concentration, reducing the benefits from this approach. The additional heat required from the steam turbine for solvent regeneration is the third most energy-intensive step, similar to what is observed in other ionic liquids[272]. The heat required depends on the pressure drop inside the flash unit, leading to water build-up if insufficient heat is added to the vessel, preventing solvent regeneration and increasing equipment size. Alternatively, there is a large amount of solvent evaporation at sufficiently high temperatures, thus requiring additional solvent make-up, consequently increasing the operating expenditure (OPEX).

5.3.2 Heat requirement leads to heat integration

A sensitivity analysis on the flash inlet temperature and pressure drop was performed to investigate their influence on the GPU's performance. The rich solvent's temperature at flash inlet was varied between 44 and 52 °C, and the pressure drop during flash was varied between 300 and 2100 kPa, maintaining the solvent with low viscosity[278].
Additional heat is required after the main heat exchanger, generating considerable efficiency penalties to the process[51]. Indeed, it becomes apparent that heat demand is inversely proportional to the pressure drop in the flash unit because water builds-up in the process at lower pressure drops (Figure 5.3).
Low-grade heat of compression can be used to satisfy some, or all, of the heat demand because only low temperatures are required (Figure 5.3). Scrutinising the initial process (Figure 5.4 a) for opportunities to use low-grade heat of compression led to the new process configurations proposed in Figures 5.4 b and c.

5.3.3 Dropping below the power consumption baseline

Several operating conditions were tested for each configuration, detailed in Table 5.4, to reduce this process's specific power requirement. Reducing pressure drop during flash increases heat demand, increasing the process' complexity by requiring additional heat integration between units. Scenario 1 and scenario 2 relate to the process represented in Figure 5.4 a; scenario 3, scenario 4, scenario 5, and scenario 6 are represented in Figure 5.4 b; and scenario 7 and scenario 8 are represented in Figure 5.4 c. The Aspen flowsheet of scenarios 1 and 2 is illustrated in Figure B.7, the stream tables are in Tables B.19 and B.22, the heat tables in Tables B.20 and B.23, and the work tables in Tables B.21 and B.24. The Aspen flowsheet of scenarios 3, 4, 5, and 6 is illustrated in Figure B.8, the stream tables are in Tables B.25, B.28, B.31, and B.34, the heat tables in Tables B.26, B.29, B.32, and B.35, and the work tables in Tables B.27, B.30, B.33,

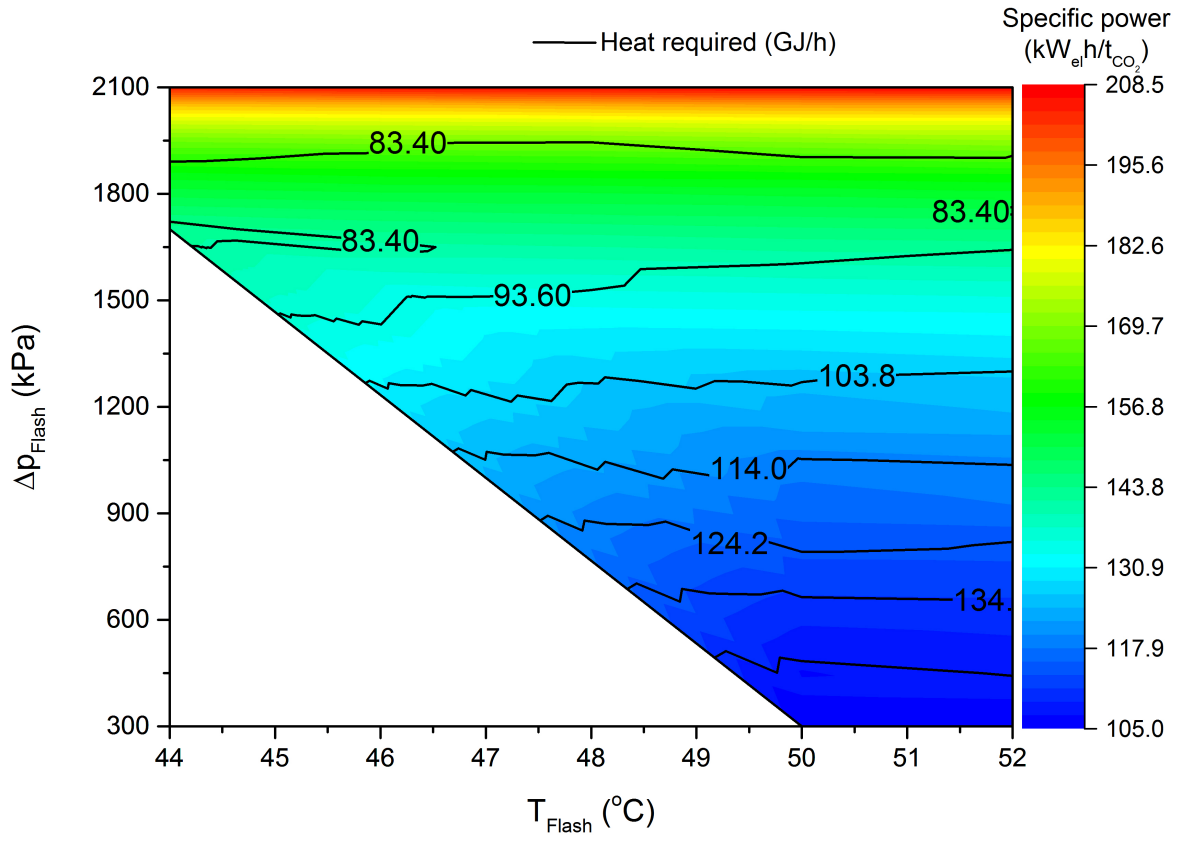


Figure 5.3: Specific electricity consumption of the GPU as a function of flash inlet temperature and pressure drop, as published by Cabral et al. [269]. The heat required to regenerate the solvent is superposed as a contour plot. The bottom left part of the figure has no data because water started to accumulate in the lean solvent. It is striking to observe that the amount of extra heat required is a function of pressure drop on the flash unit, but not its inlet temperature. This suggests that the amount of heat recovered in the main heat exchanger is proportional to the flash operating temperature.

and B.36. The Aspen flowsheet of scenarios 7 and 8 is illustrated in Figure B.9, the stream tables are in Tables B.37 and B.40, the heat tables in Tables B.38 and B.41, and the work tables in Tables B.39 and B.42.

Table 5.4 and Figure 5.5 show a potential energy efficiency improvement, where scenario 5 achieves a lower power consumption than a cryogenic GPU. Furthermore, it is possible to recover all heat from this scenario, from scenario 3, and scenario 4; however, these later two scenarios require more power than a cryogenic GPU.

Increasing the temperature can reduce the overall energy consumption despite requiring extra bleeds from the turbine (Figure 5.5, scenario 6, scenario 7, and scenario 8). Hence, a trade-off between a higher operating temperature of the flash unit and the amount of steam extracted from the turbine should be carefully analysed to optimise the process.

Scenario 8 was the most energy-efficient configuration with a power consumption of 125 kWh/t_{CO_2}. This power consumption is lower than a double flash GPU process with

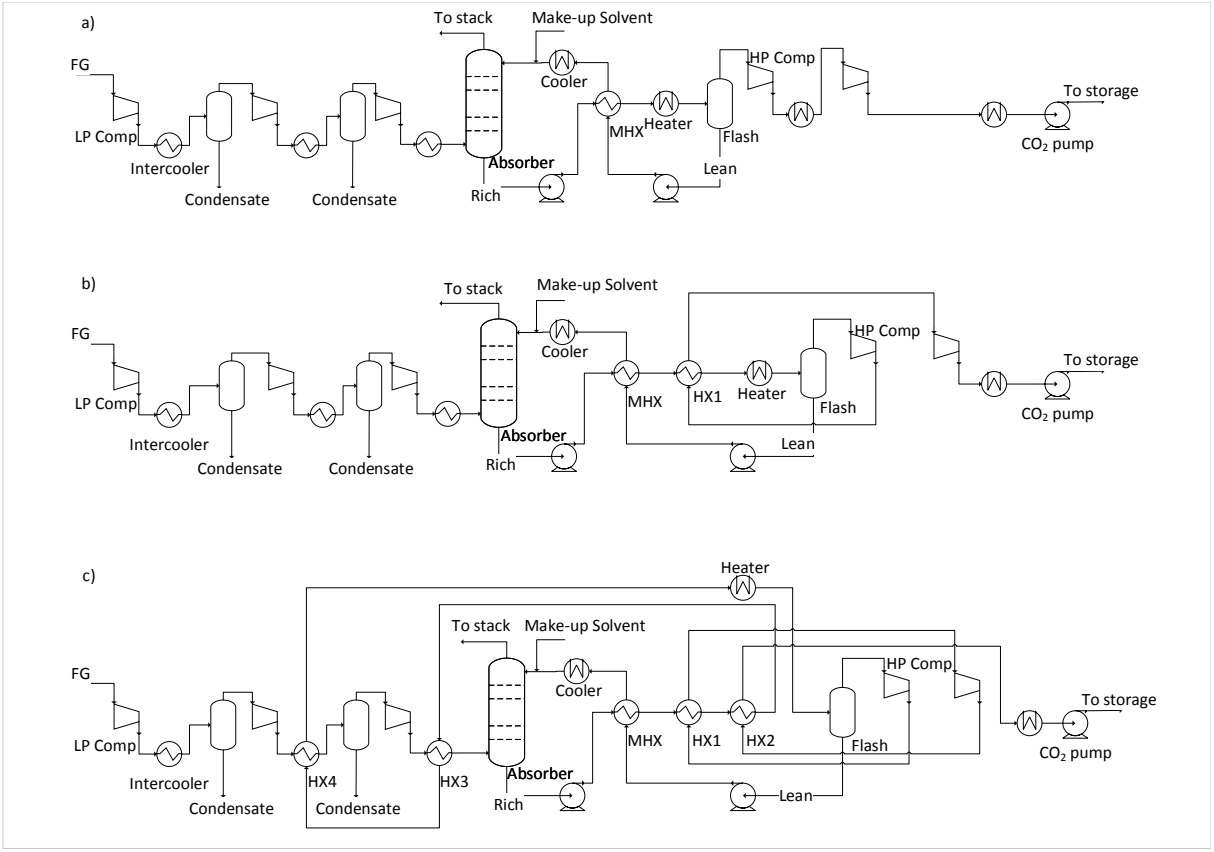


Figure 5.4: PFD of the solvent-based GPU a. without heat integration, b. with heat integration, c. with increased amounts of heat integration, as published by Cabral et al. [269].

similar capture rates and CO_2 purity[51, 66, 103, 115, 136, 150, 151].

5.3.4 Efficiency and CAPEX

Increasing the heat integration amount of this process reduces CAPEX and improves the plant's net efficiency (Figure 5.6). Calculating the second law efficiency of scenario 8 demonstrates a 1 % improvement relative to the cryogenic GPU.
Increasing the amount of heat integration also increases the number of heat exchangers in the process. The counter-intuitive CAPEX reduction observed in Figure 5.6 can be attributed to a smaller flash unit's size from a lower pressure drop.

5.3.5 Reformulating the analysis: efficiency and LCOE

A solvent-based capture process has higher OPEX than a traditional cryogenic process due to the additional solvent required to make-up for any losses[61, 150]. Indeed, replenishing the solvent increases OPEX compared with the base oxy-combustion plant, approaching a post-combustion CCS plant's cost breakdown[61, 150]. This adds another level of complexity to the previous analysis performed in Chapter 4[103], demanding that all costs are accounted for by calculating the LCOE.
Solvent cost significantly affects OPEX (Figure 5.7), but this effect can be reduced by

Table 5.4: Pressure drop in the flash unit and rich stream outlet temperature in the heat exchangers.

Configuration	Δp_{flash} (kPa)	$T^{out}_{Rich\ stream}$ (°C)					
		MHX	HX1	HX2	HX3	HX4	Heater
Scenario 1	2100	36	-	-	-	-	44
Scenario 2	950	37	-	-	-	-	48
Scenario 3	2100	35	44	-	-	-	-
Scenario 4	1900	36	44	-	-	-	-
Scenario 5	1700	38	48	-	-	-	-
Scenario 6	1200	37	44	-	-	-	48
Scenario 7	900	39	42	45	48	49	50
Scenario 8	800	39	41	45	47	49	50

applying a proper heat integration strategy which, as seen in Figure 5.6, can also reduce CAPEX. EDEA is currently sold at $4000/kg by Sigma-Aldrich[280], but costs are expected to decrease as manufacturing experience and product demand increases.

The lower bound for solvent cost in this sensitivity analysis was set at $1.3/kg, twice the ammonia price[287]. This shows good potential for this system, as the OPEX drops below that of a cryogenic distillation GPU. Hence, a lower LCOE can be expected if CAPEX, OPEX, and specific power consumption are lower in this process than for a conventional GPU.

Small quantities of monoethanolamine (MEA) are sold at $26/kg[288], reduced to $1/kg – $1.3/kg at bulk quantities[75, 289, 290]. Comparatively, ammonia costs $0.7/kg when purchased at bulk quantities[287].

EDEA is synthesised from ethylamine and ethylene oxide[291]. Ethylamine must be previously synthesised from acetaldehyde, ammonia, and hydrogen[292]. Contrastingly, MEA is synthesised in one step by reacting ammonia with ethylene oxide[293]. The extra step required to synthesise EDEA will make it more expensive than MEA, pointing that EDEA can cost between two to ten times that of MEA. However, this would require economies of scale from large-scale production of EDEA.

Looking at the US production volumes, between 10000 and 500000 pounds of EDEA was produced in 1994, with no further data beyond this year[291]. Comparatively, ethanolamine production ranged between 100 million and 500 million pounds in the same year[293]. This is one thousand times the production capacity of EDEA, making it unlikely to reach the large-scale production capacity of MEA in the short-term.

The large difference in the production capacity between EDEA and MEA stems from the wide range of uses for MEA (agriculture, automotive use, aquaculture, chemical industry, construction, consumer use, amongst others)[293] whilst EDEA has a short range of applications (chemical warfare, inert, pesticide)[291]. Thus, it is likely that bulk-orders of EDEA will be more than ten times the cost of MEA in the short-term.

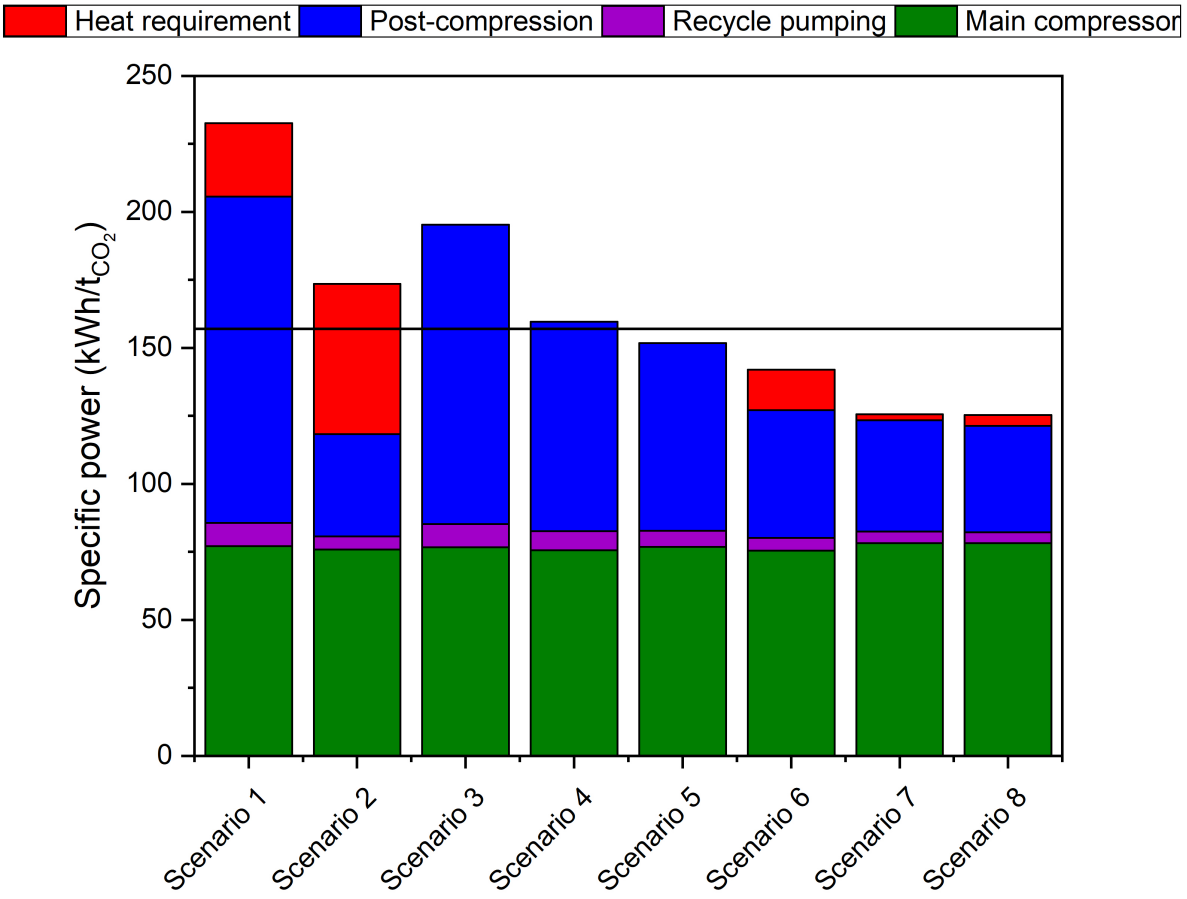


Figure 5.5: The specific power consumption is broken down into its components. Scenario 3 has the highest power consumption of all cases (it represents the point T = 44 °C and Δp_{Flash} = 2100 kPa in Figure 5.3 but includes heat requirement). The requirement of integrating low-grade heat of compression to reduce the specific power consumption from the capture unit is evident.

The EDEA make-up required as a function of flash temperature and pressure drop can be determined from Figure 5.8. Operating the flash unit at a lower pressure drop reduces EDEA lost from evaporation, leading to smaller make-up requirement, consequently reducing the OPEX. Temperature appears to have a marginal effect on EDEA make-up, becoming more pronounced at higher pressure drops inside the flash unit by increasing solvent evaporation.

The OPEX increase from high solvent make-up makes scenario 1 and scenario 3 uneconomical, obtaining LCOE above $520/MWh. Scenario 6 and scenario 8 have the lowest LCOE of all configurations studied, $158/MWh and $157/MWh, respectively (Figure 5.9), but are still less attractive than a traditional oxy-combustion or a post-capture process, with LCOE of $60/MWh – $130/MWh[51, 111, 117, 120, 150, 266, 294–296].

EDEA was chosen as a first-of-a-kind solvent to capture CO_2 from oxy-combustion using a solvent-based GPU, and may not necessarily be the best solvent for this purpose. Indeed, several commercial tertiary amines could have more suitable properties for

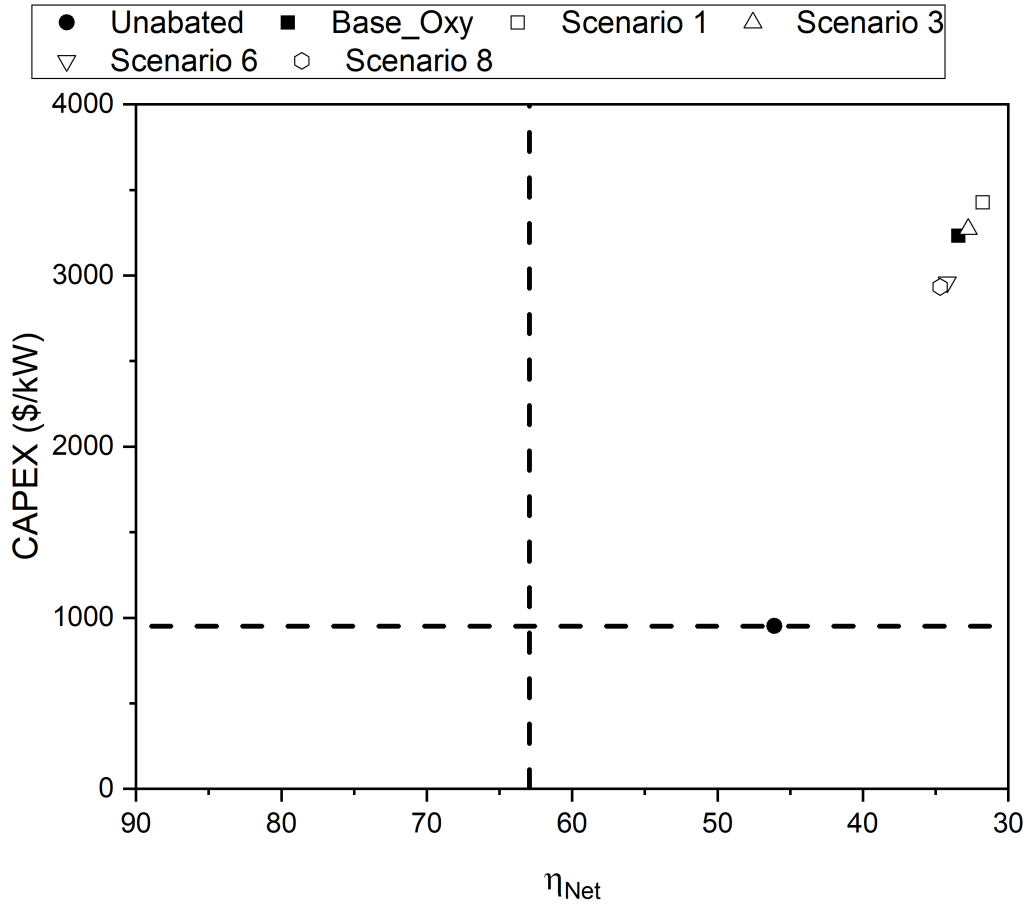


Figure 5.6: Net efficiency plotted against CAPEX for several process configurations, as published by Cabral et al. [269]. The horizontal dashed line represents the minimum CAPEX that can be achieved (*i.e.* unabated plant), whilst the vertical dashed line represents the maximum thermodynamic efficiency of an oxy-combustion process. We can observe a reduction of CAPEX for the cases with heat integration despite the increased number of equipment, due to lower water build-up in the lean solvent, reducing equipment size, ultimately decreasing costs. Here we can observe a sharp CAPEX reduction but only a marginal increase of net efficiency (η) by comparing with the base case scenario.

this capture type. It must be noted that pure EDEA is nine times less viscous than pure triethanolamine (TEA) at the same conditions[283, 297]. However, they possess similar viscosities at an aqueous solution of 5 mol% at 30 °C[284, 298]. On the other hand, EDEA is approximately three times more viscous than MEA under the same conditions[284, 298, 299]. Therefore, larger columns would be required for EDEA than MEA because higher viscosity reduces the mass transfer between gas and liquid.

5.3.6 Potential of oxy-solvent hybrid CCS

The LCOE directly relates to EDEA cost, with Figure 5.10 displaying promising economic potential if solvent costs fall below \$320 – 400 /kg. Indeed, scenario 6 and scenario 8 demonstrate high sensitivity for EDEA price between \$260/kg and 4180/kg (Figure 5.10).

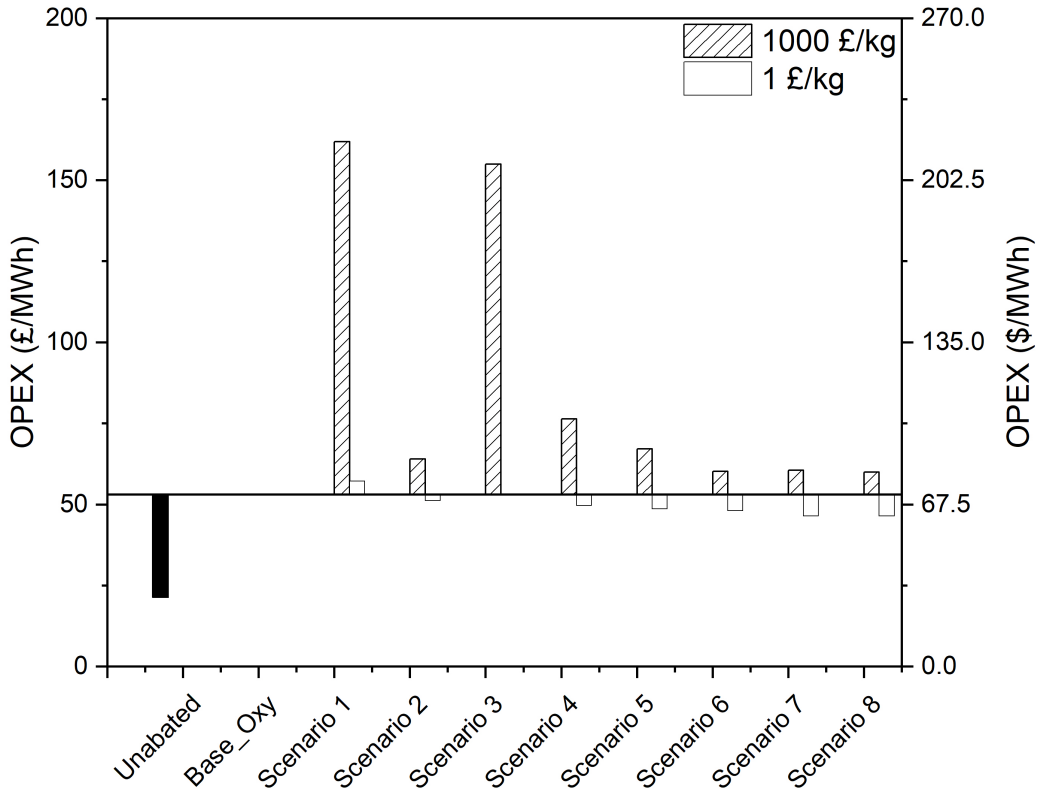


Figure 5.7: OPEX for different case scenarios are compared against the oxy-combustion with cryogenic distillation scenario, represented by the horizontal line. It can be observed that the unabated plant has the lowest OPEX, since it does not have any of the additional units required for CCS. For each of the tested plant configurations, several operating conditions of the flash unit were tested along with 3 different solvent costs. It is easy to observe that solvent cost directly affects OPEX, but what is more striking is that for the lower bound (twice the current cost of ammonia[287]) the OPEX is lower than the cryogenic distillation GPU.

A key observation is that the impact of solvent costs on process economics are subject to strongly diminishing returns once they fall below \$130/kg. A cross-over of the LCOE between these two configurations can be observed, highlighting the importance of performing a sensitivity analysis on LCOE when solvent make-up is required.
However, the CO_2 capture rate of this technology is set to 90 % whilst the cryogenic distillation GPU captures over 96 % of CO_2. Furthermore, the CO_2 purity from a cryogenic distillation GPU is over 99.9 % whilst the EDEA-based GPU yields a final CO_2 purity of 95 % with the remainder being O_2 and Ar. There is additional value created from a cryogenic distillation GPU, since this CO_2 can have other uses besides EOR. Therefore, it is better to compare the EDEA-based GPU with a double-flash GPU, where similar capture rates and CO_2 purity are obtained. As seen from Figure 5.10, a double-flash GPU is better suited to treat the flue gas from oxy-combustion than the EDEA-based

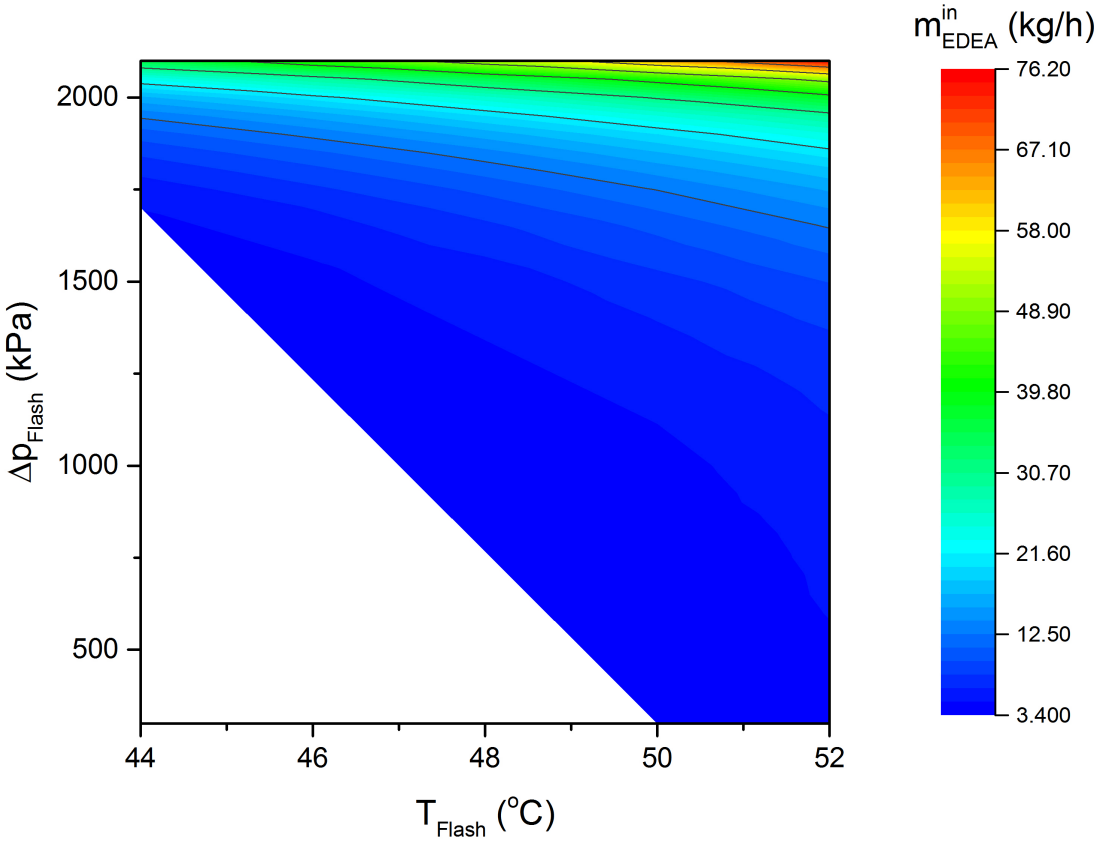


Figure 5.8: EDEA make-up is plotted against flash inlet temperature and pressure drop because OPEX is directly related to solvent make-up, as published by Cabral et al. [269]. Decreasing pressure drop lowers the amount of EDEA make-up required because less EDEA evaporates during flash.

GPU because EDEA's price needs to be below \$70/kg to manifest a better LCOE.

5.4 Conclusion

It is possible to reduce the GPU's power consumption by using a solvent-based capture unit, simultaneously reducing the capital cost and improving the oxy-combustion's efficiency. This economic potential was best represented by scenario 8, which possessed the highest net efficiency and lowest LCOE amongst the simulated processes.

The flash unit's operating conditions must be carefully chosen to optimise the process and minimise solvent make-up. Another consequence of optimising this unit pertains to reducing water build-up, which reduces both heat requirement and equipment size.

The high viscosity of EDEA will result in larger absorbers than other commercial amines, such as MEA, which will increase the equipment cost. Carefully designing a solvent to capture CO_2 from oxy-combustion can potentially improve the process. Such solvents must consider high CO_2 selectivity and low vapour pressure at the operating conditions whilst being cheap to manufacture.

EDEA price has a marginal effect on the LCOE if it falls below \$260/kg, at which point

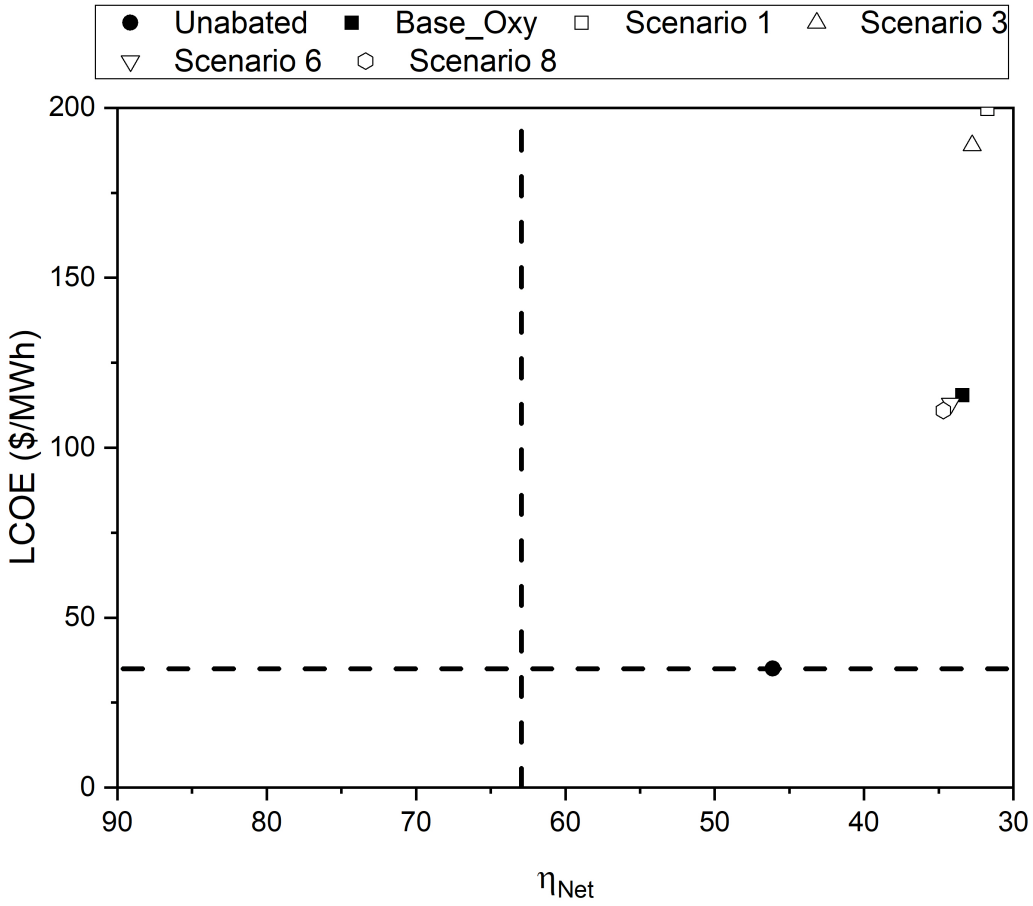


Figure 5.9: Net efficiency is plotted against LCOE for several configurations. The horizontal dashed line represents the minimum LCOE that can be achieved, *i.e.* unabated plant, whilst the vertical dashed line represents the same as in Figure 5.6. We can observe that using the current price of EDEA (extracted from Sigma Aldrich) yields high LCOEs, even for the cases with high heat integration (scenario 6 and scenario 8). Indeed in cases where no heat integration (scenario 1) and low heat integration (scenario 3) occurs, the resulting LCOE is more than 4 times higher than the oxy-combustion case, beyond any economical interest.

this process becomes more competitive than a traditional cryogenic GPU. Considering the current EDEA's market price for small purchases and comparing it to the price difference between small and bulk purchases of MEA, we can estimate current bulk EDEA price in the order of \$200/kg – \$400/kg. Therefore, an oxy-combustion process using EDEA to capture CO_2 can be more economical than using a traditional cryogenic distillation GPU (\$115/MWh) by purchasing EDEA at bulk. However, EDEA price would need to reduce below \$70/kg for the LCOE of the EDEA-based GPU to become lower than the LCOE of a double flash GPU (\$110/MWh), which yields similar capture rates and concentrations to the EDEA-based GPU. Bulk orders could increase the solvent's production rate and promote cost reduction by taking advantage of economy of scale. However, an increase in the production capacity of EDEA is unlikely due to its current limited use, making its cost reduction unlikely in the short term.

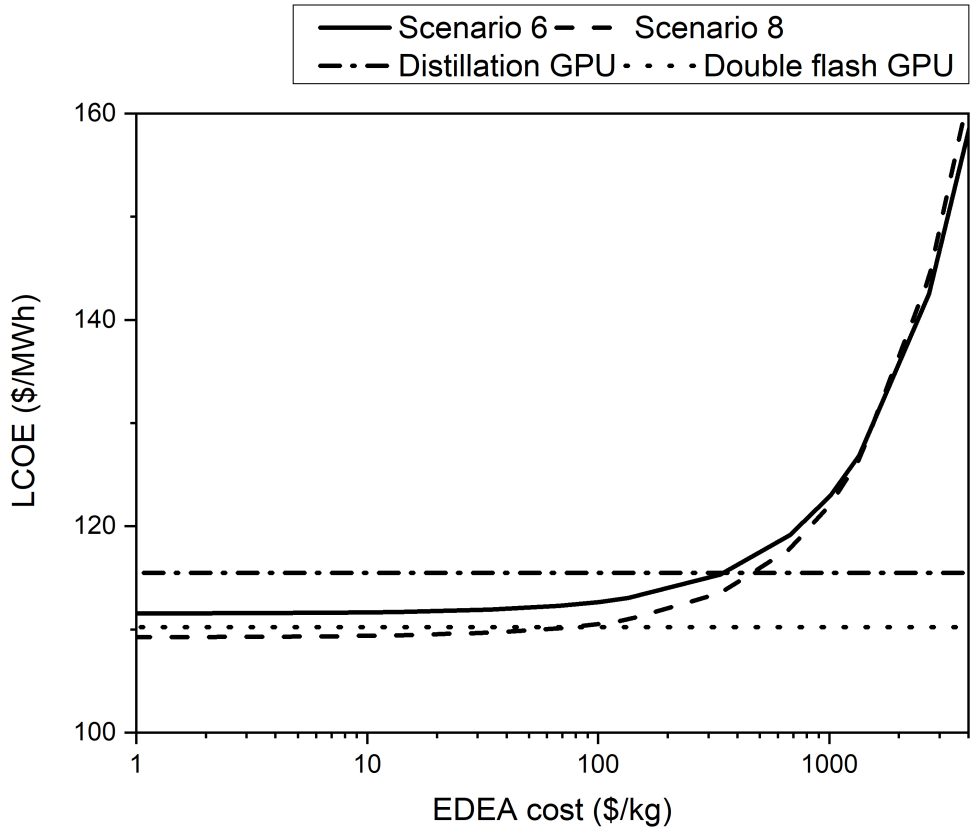


Figure 5.10: LCOE has a linear relationship with EDEA cost, as published by Cabral et al. [269]. Interestingly, a cross-over between the cases with high heat integration can be observed. Indeed, scenario 8 becomes more economical at EDEA costs lower than $1660/kg. Below EDEA costs of $350/kg (500 times the current cost of ammonia[287]) both configurations produce LCOE below oxy-combustion with cryogenic distillation GPU but not below that of a double flash GPU. LCOE is marginally affected by EDEA at costs below $130/kg.

The exhaust of oxy-combustion is composed primarily of CO_2 with some amount of water vapour and other gases. Therefore, it may be more economical to design a capture system to remove water vapour and the remaining gases from the exhaust stream instead of capturing CO_2. In such a scenario, it may even be more advantageous to produce a pure oxygen stream from the air separation unit instead of 95 % purity, which would reduce the amount of nitrogen and argon in the system. This scenario may be even more economical if nitrogen and argon can be sold.

Therefore, whilst a solvent-based approach to concentrate CO_2 from the exhaust of an oxy-combustion process appears to show some promise, the solvent and configurations proposed herein are far from optimal. A pinch analysis and a heat exchanger network (HEN) analysis would identify further heat integration opportunities and should be considered if this strategy is subjected to further analysis. However, improvements of the cryogenic-based GPU will likely deliver a similar LCOE cost-reduction, showing that EDEA will be unsuitable to capture CO_2 from an oxy-combustion flue gas.

Chapter 6

Valuing negative emissions through credits

The work detailed in this Chapter was published in the International Journal of Greenhouse Gas Control[300].

6.1 Introduction

All sectors must reduce their emissions to meet the 1.5 °C target and curb climate change[21]. However, other sectors do not have a renewable alternative making carbon capture and storage (CCS) the only viable method for decarbonisation[301, 302].
The substantial heterogeneity of CO_2 concentrations from industrial activity presents issues towards CCS application since each point source requires careful consideration, translating into high costs[26, 75, 301–303]. Some of these processes can be decarbonised by changing their feedstock, but this is expensive and poses technical issues due to fuel quality and competition with fossil fuels for energy production or raw materials[304–306]. However, such practises have been considered an acceptable means to reduce the carbon intensity of industries that require large quantities of energy whilst reducing waste[305, 307]. Indeed, biomass is already used by some operators for this end[305, 307].
Bioenergy with CCS (BECCS) can play an essential role to decarbonise the power and industrial sectors[29] by displacing fossil fuel use whilst removing atmospheric CO_2[216]. However, the successful implementation of this technology is likely to require governmental incentives that value negative emissions[50, 86, 216, 308–310].
This Chapter proposes a framework to auction negative emissions created by a BECCS plant in the form of credits to help decarbonise other sectors. Here, industry was chosen as a representative sector that could benefit from this scheme, but this framework's general nature allows it to be used in other sectors, such as aviation.

6.1.1 Industrial CO_2 emissions

Industrial CO_2 emissions are distributed in the same regions as the power sector, as evidenced in Figure 6.1. This implies that transporting CO_2 from both sectors would use the same pipelines. However, capturing CO_2 from industrial activity may prove cumbersome due to the considerable CO_2 variation at each point source within each process[301–303].

This leads to a wide range of CO_2 avoidance costs[311, 312] ranging from \$10/t_{CO_2} to \$170/t_{CO_2} (Figure 6.2)[301, 303]. Capturing industrial CO_2 emissions with CCS from most processes would likely cost more than \$80/t_{CO_2}.

Industrial activity accounts for 30 % of total global anthropogenic CO_2 emissions[2], representing 17 % of UK emissions[315]. In a global perspective, these emissions are mostly from iron and steel (28 %), cement (27 %), and chemical production and refining processes (13 %)[316]. In the UK, chemical production and refining amount to 50 % of industrial emissions, followed by iron and steel (29 %), and cement (11 %)[314], totalling 18 Mt_{CO_2} in 2015[315]. This demonstrates the variability of industrial activity throughout each region/ country.

Most CO_2 is used for enhanced oil recovery (EOR)[308, 312] and comes from high-purity sources (90 – 99 %) where CCS is fitted at low cost, mostly from natural gas sweetening, ammonia, or ethylene oxide synthesis[301–303, 308, 312]. Emissions from high-purity sources and high-concentration (30 – 90 %) only amount to 25 % of the industrial sector's CO_2 emissions, with CCS being expensive to apply to the remaining industrial activity[301–303, 308, 312]. However, EOR is not an option for countries without oil production capability[317], leaving these countries' industries without a means to recover the extra investment from capturing CO_2. It may become more economical to offset industrial CO_2 emissions by buying emission credits than applying CCS directly to these CO_2 emission sources. Hence, a direct trade scheme between these hard-to-decarbonise industrial sectors and BECCS via negative emission credits (NEC) may provide a cost-effective way to reduce global CO_2 emissions.

6.2 Framework for negative emissions generation

6.2.1 Oxy-BECCS model description

Oxy-combustion with 500 MW_{net} capacity was simulated in gPROMS using the methodology provided in the previous Chapters[134]. All unit operations used the Peng-Robinson equation of state except in the steam cycle, where SAFT-γ Mie group contribution equation of state was used[318]. The net power produced was maintained constant at all co-firing rates to provide a direct comparison between each simulation's results. The framework to generate and auction NEC is represented in Figure 6.3.

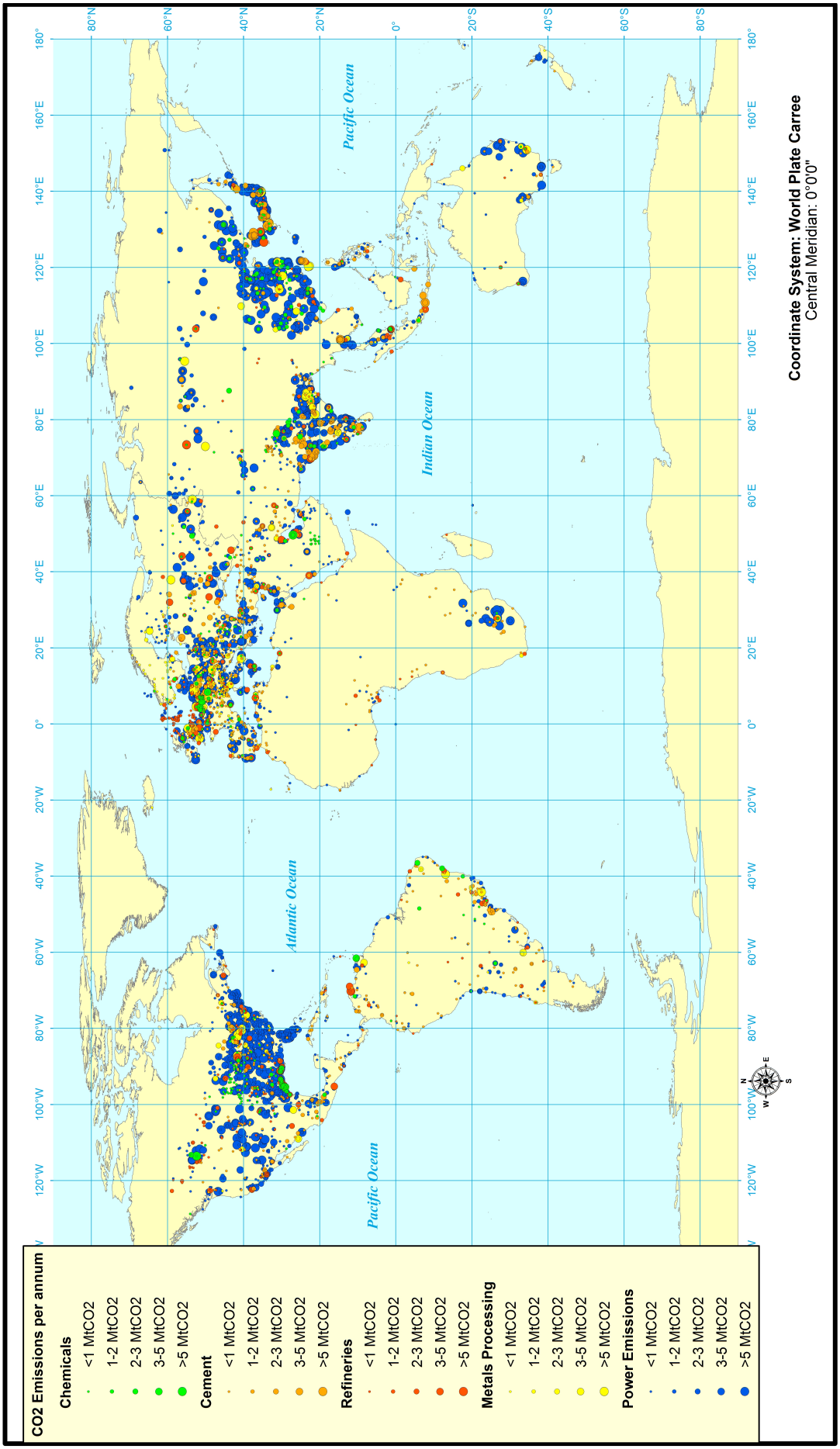


Figure 6.1: Global distribution of anthropogenic CO_2 emissions from chemicals, cement, refineries, metal processing, and power sector, as published by Cabral et al. [300]. The image was generated by Imperial College London using data sourced from IEA GHG CO_2 emissions database[313].

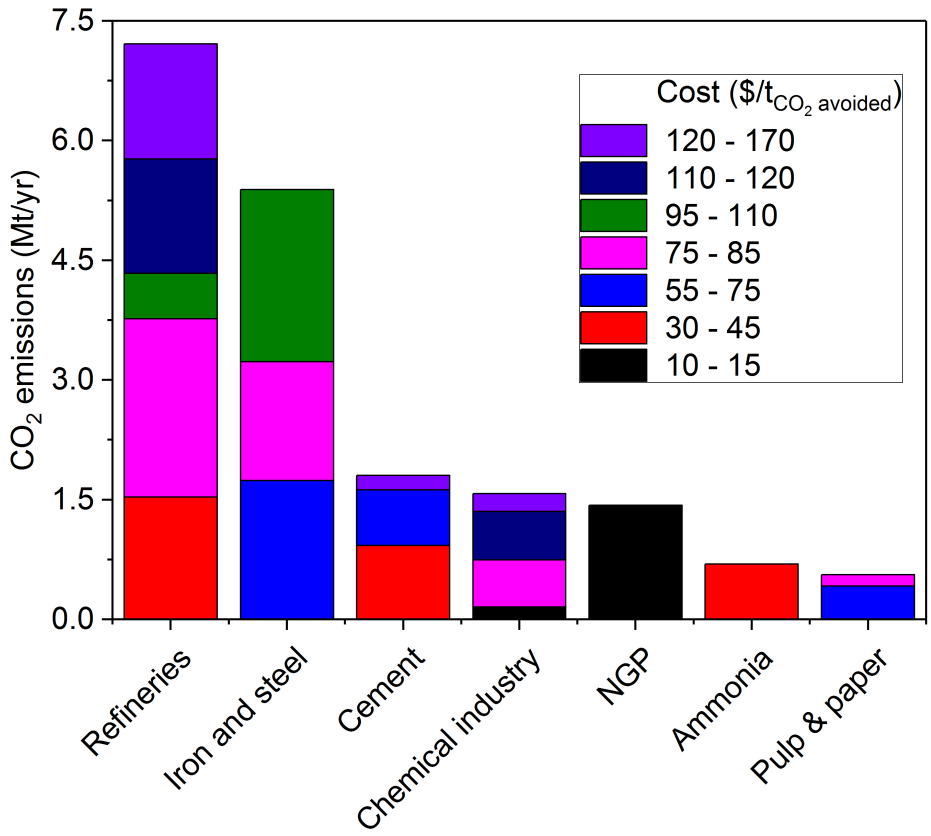


Figure 6.2: Amount of CO_2 emitted annually in the UK from the industrial sector, as published by Cabral et al. [300]. The costs associated with applying CCS for each point source are classified in ranges, represented by the different colours. Data sourced from[301, 303, 314].

6.2.2 Achieving negative emissions

A BECCS process achieves negative emissions when more biogenic CO_2 is captured than all other CO_2 emissions associated with the process activity, *e.g.* coal co-fired. Biogenic CO_2 emissions ($e^{biogenic}_{CO_2}$) (kg/h) are carbon neutral because it is assumed that biomass uses atmospheric CO_2 as the primary source of carbon. The actual CO_2 emissions ($e^{actual}_{CO_2}$) are obtained by subtracting the biogenic CO_2 emissions from the total amount of CO_2 released ($e^{total}_{CO_2}$) according to Equation 6.1.

$$e^{actual}_{CO_2} = e^{total}_{CO_2} - e^{biogenic}_{CO_2} \tag{6.1}$$

Similarly, the amount of biogenic CO_2 captured ($c^{biogenic}_{CO_2}$) (kg/h) is the total CO_2 captured ($c^{total}_{CO_2}$) without CO_2 from fossil-fuel sources ($c^{fossil}_{CO_2}$) (considering supply chain emissions) according to Equation 6.2.

$$c^{biogenic}_{CO_2} = c^{total}_{CO_2} - c^{fossil}_{CO_2} \tag{6.2}$$

Carbon intensity (CI) provides a quantitative information on CO_2 emissions from a

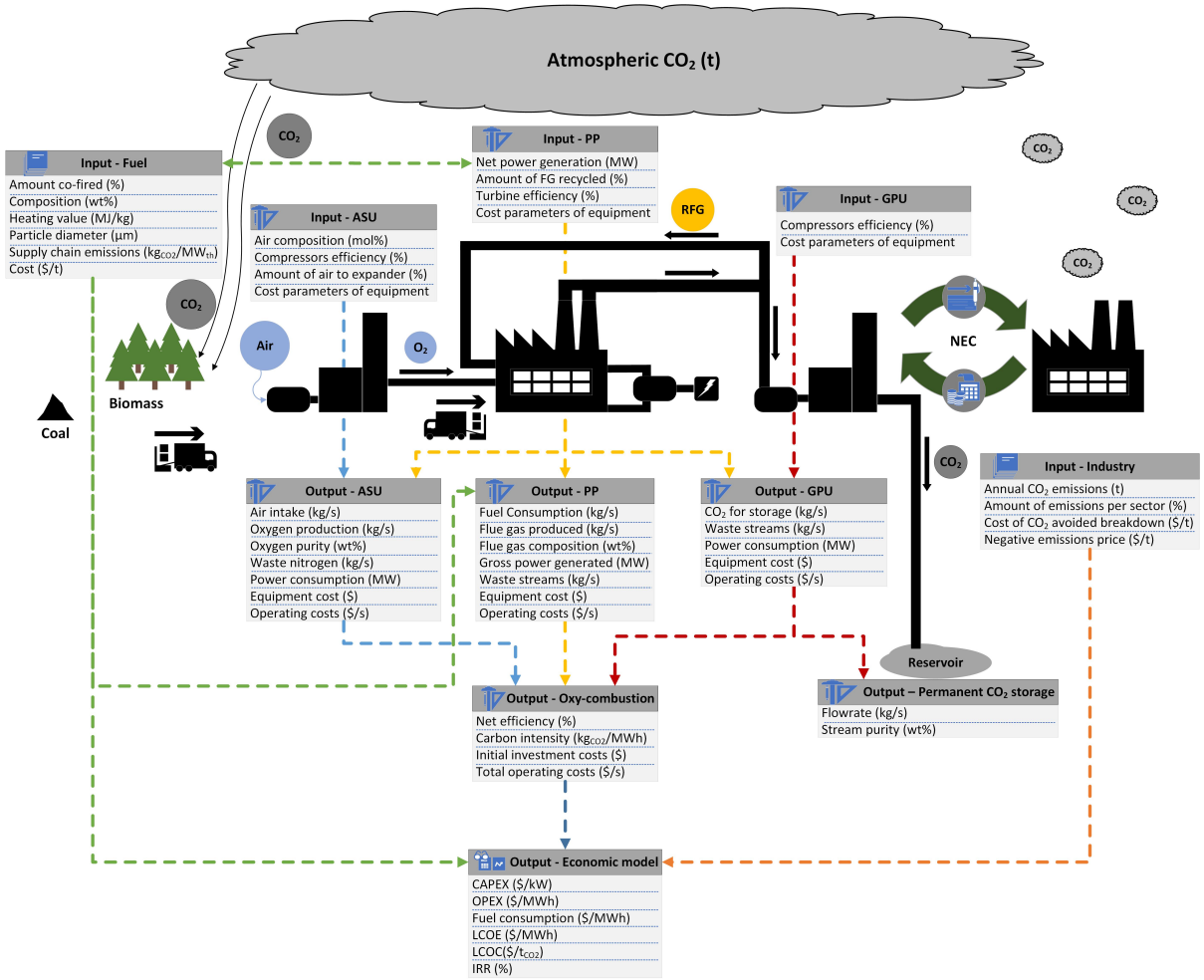


Figure 6.3: Process flow diagram of the proposed approach to offset industrial CO_2 emissions, as published by Cabral et al. [300]. Biomass captures atmospheric CO_2 for its growth before being harvested, pelletised and used as fuel in the power plant (PP) to generate electricity. The oxygen required to burn the fuel is produced by an air separation unit (ASU). Part of the flue gas generated from the combustion process is recycled to the furnace, whilst the remaining is sent to a gas processing unit (GPU). Here, CO_2 is purified and compressed to pipeline specifications. Negative emissions from storing biogenic CO_2 in a reservoir are auctioned as negative emission credits (NECs) to offset industrial emissions. The cycle is then closed by CO_2 emitted from industrial processes being captured again by biomass. Black lines represent mass flows between each process with arrows indicating the direction of flow. Dashed arrows represent the flow of information between the inputs and outputs from each process in the model.

power generation activity according to Equation 6.3.

$$CI = \frac{e_{CO_2}^{actual} - c_{CO_2}^{biogenic}}{Power_{net}} \tag{6.3}$$

Where a process is carbon-positive when CI is positive, carbon-negative when CI is negative, and carbon-neutral when CI is zero. Auctioning negative emissions is only possible for carbon-negative processes since all residual emissions from its activity must be offset before effectively reducing atmospheric CO_2.
The number of BECCS plants for a given net capacity required to offset global industrial CO_2 emissions ($e_{CO_2}^{gi}$) can then be calculated by Equation 6.4.

$$No.\ plants = \frac{e_{CO_2}^{gi}}{-CI \times Power_{net}} = \frac{e_{CO_2}^{gi}}{c_{CO_2}^{biogenic} - e_{CO_2}^{actual}} \tag{6.4}$$

6.2.3 Fuel

The characteristics of the fuels used, bituminous Eastern Australian coal and clean wood chips sourced in the UK are detailed in Table 3.6.

6.2.4 Economic model

Equipment cost, labourers per shift, and techno-economic analysis were obtained following the procedure described by Couper et al. [260, 281] with the assumptions described in Table 3.10[150, 260].

6.2.5 The cost of electricity

The levelised cost of electricity (LCOE) is calculated using Equation 5.1. It becomes crucial to analyse how much it costs to operate the plant, which can be done by calculating the marginal cost of electricity (MCOE) using Equation 6.5.

$$MCOE = \frac{\sum_{n=0}^{lt} \left[\frac{OPEX_n}{(1+r)^n}\right]}{\sum_{n=0}^{lt} \left[\frac{MWh_n}{(1+r)^n}\right]} \tag{6.5}$$

The cost of storing CO_2 was assessed by calculating the levelised cost of carbon (LCOC) using Equation 6.6.

$$LCOC = \frac{CAPEX + \sum_{n=0}^{lt}\left[\frac{OPEX_n}{(1+r)^n}\right]}{\sum_{n=0}^{lt}\left[\frac{\mathrm{CO_2\ stored}}{(1+r)^n}\right]} \tag{6.6}$$

These equations can be easily solved by assuming a constant OPEX, electricity generation, and the amount of CO_2 stored throughout the time frame considered. The approximation shown in Equation 6.7 assumes that this power plant has the same annual operating hours as a typical coal-fired power plant[150].

$$\sum_{n=0}^{lt}\left[\frac{\alpha_n}{(1+r)^n}\right] = \alpha \times \left(\left[\frac{1-\left(\frac{1}{1+r}\right)^{lt}}{1-\left(\frac{1}{1-r}\right)}\right] - \left[\frac{1-\left(\frac{1}{1+r}\right)^{ct}}{1-\left(\frac{1}{1-r}\right)}\right]\right) \tag{6.7}$$

Where α is the OPEX, electricity generation, or the amount of CO_2 stored; lt is the plant's lifetime; ct is the construction period; and r is the discount rate.
It is vital to operate the first two years at reduced capacities in this analysis. The NPV and IRR were calculated according to Equations 3.42 and 3.43.

6.2.6 CO_2 avoided costs

The CO_2 avoided costs ($/$t_{CO_2}$) was calculated according to Equation 6.8[150].

$$CO_2^{Avo}\ costs = \frac{LCOE_{CCS} - LCOE_{Reference}}{\mathrm{CO_2}^{Emission}_{Reference} - \mathrm{CO_2}^{Emission}_{CCS}} \tag{6.8}$$

Where $LCOE_{CCS}$ is the LCOE calculated from the simulation; $LCOE_{Reference}$ is the LCOE of an unabated plant of the same type; $\mathrm{CO_2}^{Emission}_{Reference}$ is the emission of the same unabated plant; and $\mathrm{CO_2}^{Emission}_{CCS}$ is the emission of the simulated plant. The CO_2 avoided cost evaluates the relative cost of applying a CCS option to a plant and is a useful metric to support project selection. However, this metric does not regard the profitability of a process, and it should come accompanied by a more rigorous economic analysis.

6.3 Analysing the synergy between BECCS and industry

6.3.1 Model validation

The simulated oxy-combustion plant had 32 % net efficiency and a CAPEX of $4400/kW, with OPEX, fuel consumption, LCOE of $56, $33, and $120 per MWh, respectively, and a CO_2 avoidance cost of $72/$t_{CO_2}$. These results exhibit good agreement with existing literature by falling within high-density points in Figure 6.4, representing estimates in the same order of magnitude[47, 51, 106, 111, 117, 120, 150, 266, 294–296, 319]. Literature data were scaled to the common year of 2015 using the respective CEPCI

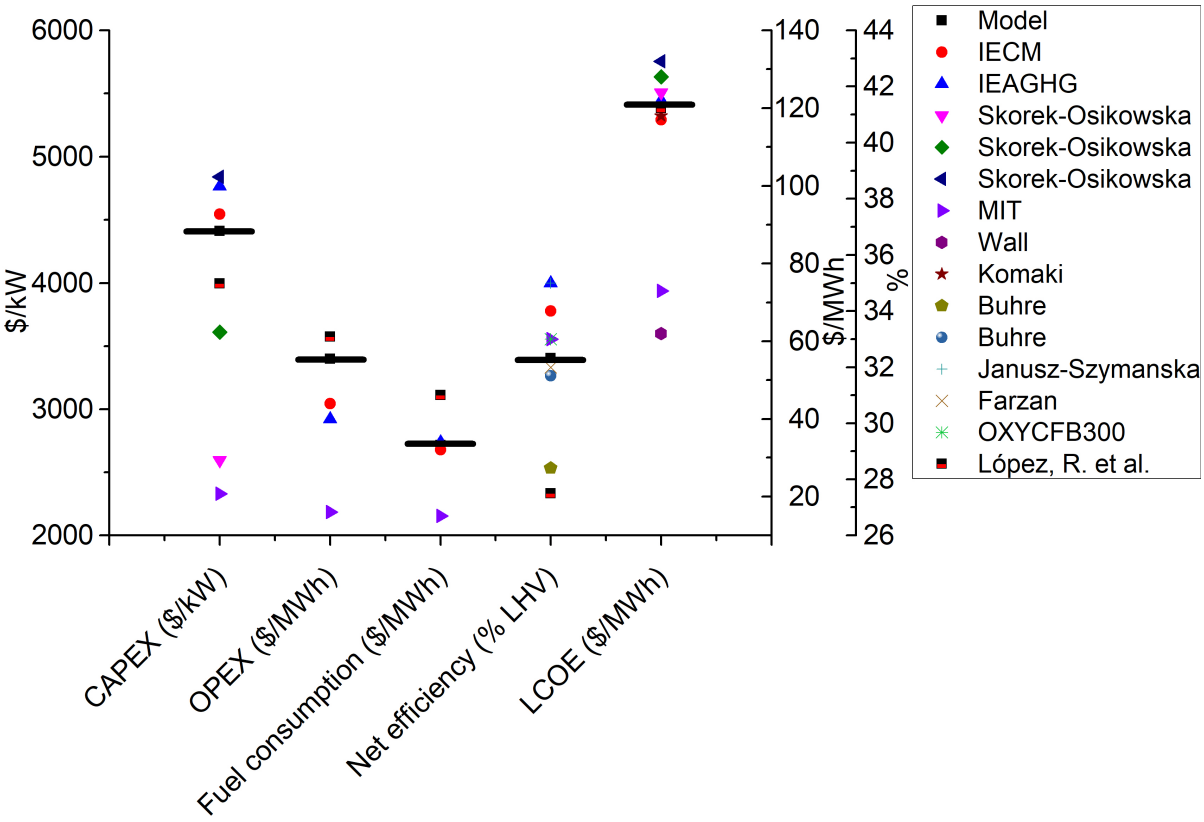


Figure 6.4: Validation of the oxy-combustion model against the main performance indicators capital cost (CAPEX), operating cost (OPEX), fuel consumption, net power generation, efficiency and levelised cost of electricity (LCOE)[47, 51, 106, 111, 117, 120, 150, 266, 294, 296, 319], as published by Cabral et al. [300]. The horizontal lines represent this model's values.

values (Table E.1). Different economic assumptions and operating parameters used in each study could explain the variability observed in Figure 6.4.

The normality of the LCOE values was assessed using D'Agostino and Pearson's test[320] with the SciPy library from Python 3.6. However, the data extracted from the literature was not enough to perform this analysis. Hence, a wide array of LCOEs ($/MWh) was calculated using the methodology described in sections 6.2.4 and 6.2.5. Here we used combinations of CAPEX, OPEX, fuel consumption, and plant efficiency obtained from literature to provide 400 LCOE values. The probability density function (PDF) follows a normal distribution curve with a mean (μ) of \$111/MWh and a standard deviation (σ) of \$23/MWh with a p-value of 0.04 (Figure 6.5). The LCOE of the simulated process is within 68 % of the confidence interval of the PDF.

The CAPEX and OPEX outliers (Figure 6.4) could have shifted the mean towards 110 \$/MWh, as seen by the higher than expected bars at 60 and 90 \$/MWh (Figure 6.5). This shift is reflected in the high standard deviation observed, suggesting that more data on oxy-combustion should be obtained to reduce the uncertainty of this analysis. These outliers do not imply that those figures are incorrect, but instead demonstrate

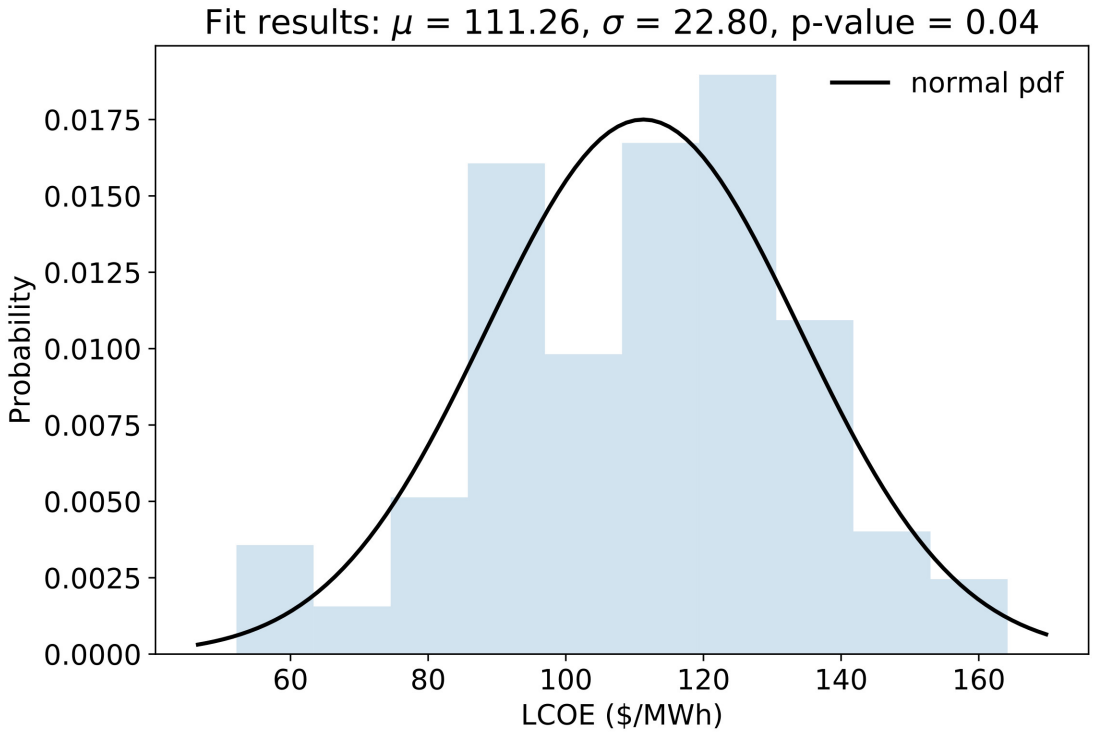


Figure 6.5: Normal probability density function (PDF) of LCOE, as published by Cabral et al. [300]. The amount of data required to construct the PDF was obtained by calculating the LCOE from combinations of CAPEX, OPEX, and net power efficiency from literature (See Fig 6.4).

that they belong to a different group, most likely from different assumptions.
Nonetheless, the high confidence interval obtained suggests that the LCOE from this study has a high likelihood of belonging to the same group as the LCOEs obtained from the reported literature. This reiterates the model's validity already suggested by direct comparison with the data points from the reported literature. More clarity in each study's techno-economic assumptions is required, hence a standard method to report these assumptions would be incredibly beneficial[321].

6.3.2 Economic impact of BECCS-generated electricity

A non-linear increase in CAPEX, OPEX, fuel consumption and LCOE, followed by reduced plant efficiency can be observed in Figure 6.6 by increasing the amount of biomass co-fired. The small discontinuities observed in Figure 6.6 are from artefacts encountered during the simulation of the oxy-combustion process.
Switching from coal to biomass imposes an efficiency penalty of up to 3 %, considering that 150 % more fuel is required to generate the same amount of power (Figure 6.6 and Table 6.1). This effect is explained by the lower heating values, higher moisture, and higher ash content of this biomass than bituminous coal (Table 3.6). These characteristics require a higher fuel consumption to achieve the same power output and, combined with the higher costs of wood-chips (Table 3.6), substantially increase OPEX, nearly doubling it (Table 6.1). Another factor influencing the OPEX is the higher

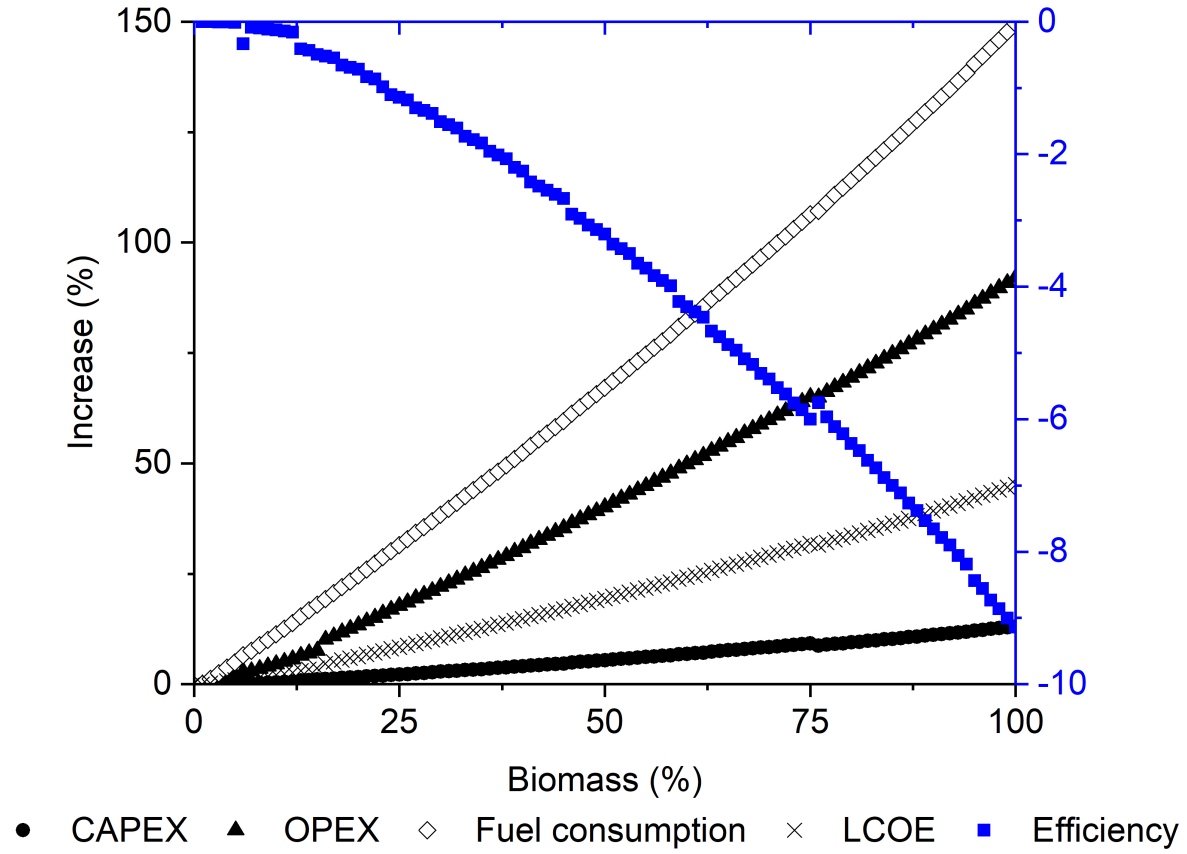


Figure 6.6: Amount of CAPEX, OPEX, fuel consumption, LCOE (black), and efficiency (blue) increase due to increased amounts of biomass co-fired, as published by Cabral et al. [300].

bond work index (BWI) of biomass[243], resulting in higher power consumption to grind the fuel. This penalty is intensified by the larger flowrates required when firing biomass for the same power output, increasing the equipment size, resulting in a 14 % higher CAPEX.

Equations 6.9, 6.10, 6.11, 6.12, and 6.13 represent the effect of biomass on CAPEX ($/kW), OPEX ($/year), fuel consumption (kg/kWh), LCOE ($/MWh), and net efficiency (η_{net}, in %) as a function of biomass fraction ($f_{biomass}$, in %).

$$CAPEX\ [\$/kW] = 0.015 f_{biomass}^2 + 4.408 f_{biomass} + 4397.922 \tag{6.9}$$

$$OPEX\ [\$/year] = 5607.21 f_{biomass}^2 + 1551256.26 f_{biomass} + 2.3 \times 10^8 \tag{6.10}$$

$$Fuel\ [kg/kWh] = 6.4 \times 10^{-6} f_{biomass}^2 + 0.0022 f_{biomass} + 0.42 \tag{6.11}$$

$$LCOE\ [\$/MWh] = 0.001 f_{biomass}^2 + 0.44 f_{biomass} + 119.06 \tag{6.12}$$

Table 6.1: CAPEX, OPEX, fuel consumption cost, LCOE, and LCOC for oxy-combustion using coal and wood-chips.

Parameter	Coal	Wood chips	Units
CAPEX	4400	5000	\$/kW
OPEX	56	107	\$/MWh
Fuel consumption	33	83	\$/MWh
LCOE	120	175	\$/MWh
LCOC	115	150	$\$/t_{CO_2}$
η_{net}^{LHV}	32	29	%

$$\eta_{Net}\ [\%] = -0.00015 f_{biomass}^2 - 0.015 f_{biomass} + 32.40 \tag{6.13}$$

The coefficient of determination (R^2) for Equations 6.9, 6.10, 6.11, 6.12, and 6.13 are 0.9984, 0.9888, 0.9954, 0.9975, and 0.9978, respectively.

Firing wood-chips increases the LCOE by 45 % to \$175/MWh and the LCOC by 30 % to $\$150/t_{CO_2}$, as seen in Table 6.1. This increase is rational[74, 296, 322–324], since biomass is a worse fuel than coal, with some authors identifying up to 95 % LCOE increase for some biomass types[229]. This analysis did not include any means of valuing negative emissions; however, a BECCS plant can still offset the emissions of another sector and gain an additional revenue source by auctioning NEC.

6.3.3 Potential of NECs to offset global industrial emissions

The 500 MW_{net} dedicated oxy-BECCS plant simulated in this work generated 3 Mt/yr of negative emissions, similar to what Kemper [216] reported. This would offset the 18 Mt_{CO_2}/yr from the UK's industrial activity by operating six oxy-BECCS plants.

Global industrial activity amounts to 12 Gt_{CO_2}/yr[5], where 3 Gt_{CO_2}/yr could be readily captured using CCS. This results in 9 Gt_{CO_2}/yr that is hard-to-decarbonise, similar to the reported maximum amount of sustainable negative emissions achieved by operating BECCS plants (10 Gt_{CO_2}/yr)[73, 216, 325]. Offsetting these emissions using the proposed framework would require 3000 oxy-BECCS plants with 500 MW capacity. This is comparable with the 3400 CCS plants required by the BLUE Map scenario to meet the global targets[326]. Larger plants would reduce the number of projects required whilst taking advantage of economy of scale. However, deploying these plants must be strictly regulated by local and international authorities to prevent an unsustainable use of the local biomass resources.

BECCS can be deployed either by erecting new plants, referred to as greenfield, or by converting existing coal plants, referred to as brownfield. The greenfield approach would benefit from the higher efficiencies of designing a biomass-specific process[273, 327]. However, the brownfield approach offers the opportunity to reduce the BECCS plant's capital costs, albeit at higher operating costs from reduced efficiency[273, 327].

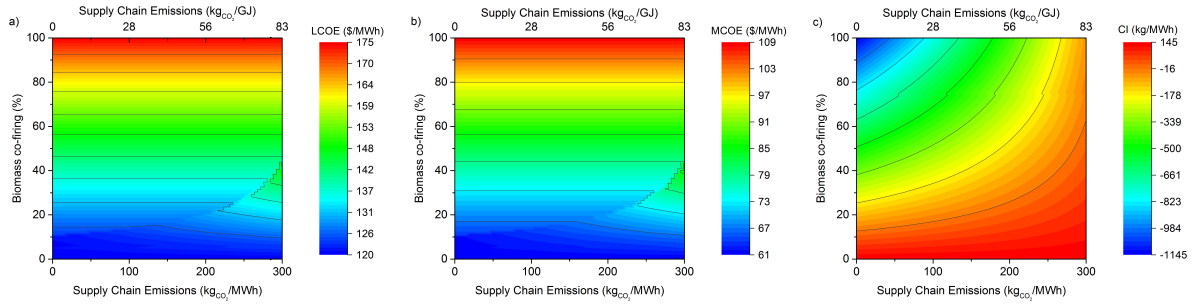


Figure 6.7: Effect of biomass co-firing (%) and supply chain emissions with $25/t carbon price[150] on a) Levelised cost of electricity (LCOE) ($/MWh), b) Marginal cost of electricity (MCOE) ($/MWh), and c) carbon intensity (CI) (kg_{CO_2}/MWh), as published by Cabral et al. [300]. Supply chain emissions can increase the LCOE and MCOE whilst carbon intensity is positive, characterised by the discontinuities observed in a and b. This corresponds to the point when CI = 0 kg_{CO_2}/MWh, *i.e.* the amount of biogenic CO_2 is not enough to displace total oxy-combustion emissions. This effect can be discerned by the cost increase from larger emissions associated with the supply chain for smaller amounts co-fired. Increasing the amount of biomass lets the process achieve net-negative emissions, at which point the supply chain ceases to have any detrimental effect on both LCOE and MCOE.

Capturing this amount of atmospheric CO_2 can be done sustainably using the existing global biomass (Table 2.4). Indeed, the amount of coal-fired plants worldwide[40] is comparable to the number of oxy-BECCS plants required; hence, it is possible to retrofit most of these plants to provide an early decarbonisation effort of both the power and industrial sectors. Such an approach would safeguard existing jobs whilst creating new job opportunities along the biomass supply chain[212].

This approach is instrumental in Asia, where a third of the newest coal power plant fleet is located[328–330]. These plants would reduce the costs associated with retrofitting by taking advantage of their increased efficiency. Indeed, half of the world's coal capacity is located in Asia, amounting to 310 GW of carbon-intensive electricity that could be made carbon-neutral, or even negative by employing BECCS. This approach also offers the opportunity to reduce local air pollution[328], a significant concern in this region, whilst displacing fossil fuel use with a renewable source.

6.3.4 How supply chain emissions impact the costs of BECCS

Varying both supply chain emissions and the amount of wood chips co-fired increases the LCOE and MCOE from 120 to 175 $/MWh and 60 to 108 $/MWh, respectively (Figure 6.7 a and b). This represents the potential variability of the biomass supply chain emissions[87–89], which are points of concern regarding the viability of BECCS to generate NEC.

Co-firing larger amounts of biomass imposes higher LCOE and MCOE by using a more expensive fuel with lower heating values than coal (Figure 6.7 a and b). This confirms the results experienced in Figure 6.6. Interestingly, the LCOE and MCOE are impacted

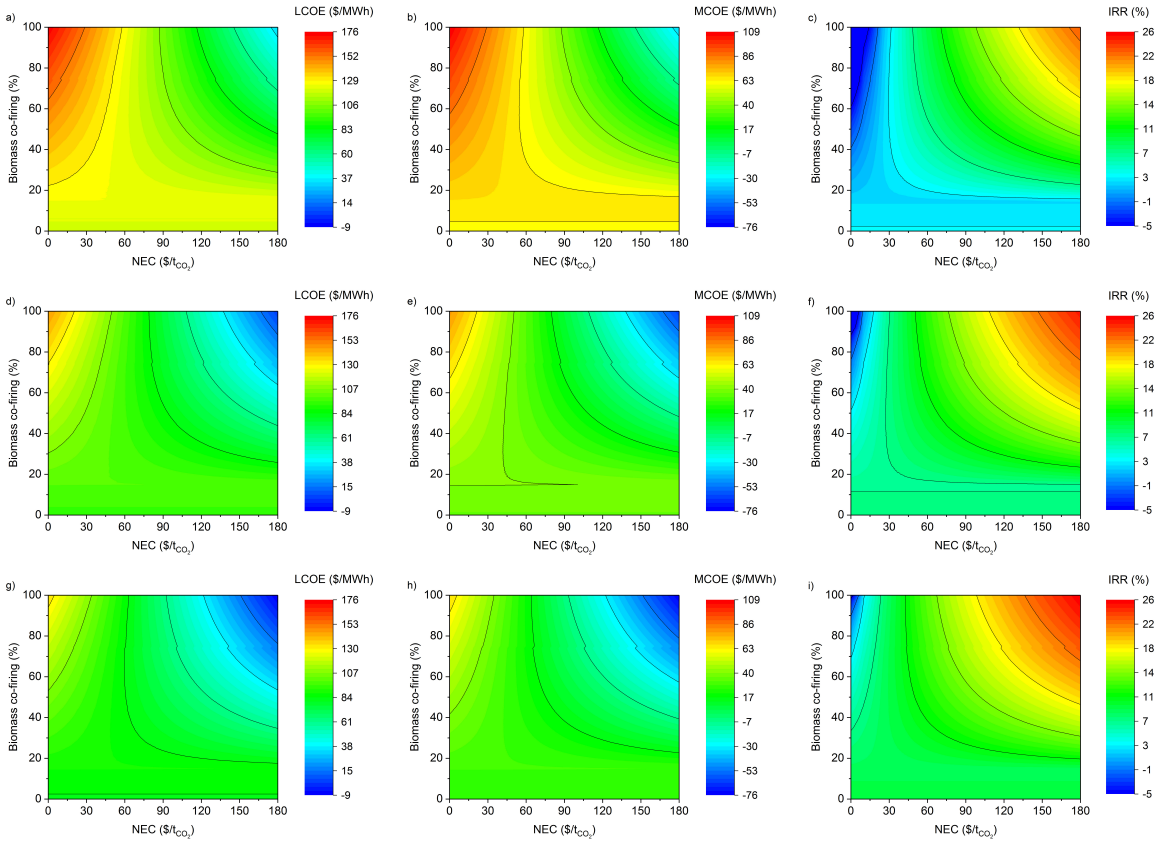


Figure 6.8: Effect of NEC and wood chips co-fired on a, d, g. LCOE ($/MWh); b, e, h. MCOE ($/MWh); and c, f, i. IRR (%); assuming supply chain emissions of 110 kg_{CO_2}/MWh for unsubsidised plants (a, b, and c), and subsidies of 35 (d, e, and f) and 50 (g, h, and i) $/$t_{CO_2}$, as published by Cabral et al. [300].

by supply chain emissions when co-firing small amounts of biomass. The process is carbon-positive at small biomass co-firing fractions and the plant operators would be required to pay for emissions if there is a carbon price in place. The process becomes carbon-neutral when the amount of captured biogenic CO_2 is adequate to meet the plant's residual emissions, and carbon-negative when these residual emissions are surpassed (Figure 6.7 c).

Carbon intensity (CI) is directly proportional to supply chain emissions. However, CI achieves negative values when large amounts of biomass are co-fired (Figure 6.7 c) because the biogenic CO_2 captured exceeds the supply chain emissions (Table 3.6). It is conspicuous that carbon negativity can be achieved even at high supply chain emissions for a biomass co-firing above 45 %.

6.3.5 Negative emission credits: paving the way for cost-competitive CCS

Auctioning the negative emissions generated by the plant in the form of credits provides a second source of revenue, potentially reducing the LCOE by up to 80 %(Figure 6.8).

This activity can also increase the IRR from 2 % for an oxy-coal plant to 23 % for an oxy-BECCS plant auctioning NEC at 180 $/t$_{CO_2}$ without government subsidies. However, this value is excessively high and unlikely to be purchased by an operator striving to reduce their carbon footprint in the absence of a higher carbon tax than this value. The LCOE is further reduced if governments decide to subsidize the plant.
Equations 6.14, 6.15, and 6.16 represent the effect of NEC price and the amount of wood-chips co-fired ($f_{biomass}$, in %) on the unsubsidised LCOE, MCOE, and IRR, respectively, at 110 kg$_{CO_2}$/MWh supply chain emissions.

$$LCOE\ [\$/MWh] = -0.78S + 0.09NEC + 0.53f_{biomass} - 0.009NEC \times f_{biomass} + 118.31 \tag{6.14}$$

$$MCOE\ [\$/MWh] = -0.78S + 0.09NEC + 0.45f_{biomass} - 0.009NEC \times f_{biomass} + 59.99 \tag{6.15}$$

$$\begin{aligned} IRR\ [\%] = {} & 2.4 \times 10^{-6} NEC^3 - 3.1 \times 10^{-5} f_{biomass}^3 - 0.0013NEC^2 + 0.004f_{biomass}^2 + \\ & + 0.14S + 0.12NEC - 0.25f_{biomass} + 0.0024NEC \times f_{biomass} + 2.82 \end{aligned} \tag{6.16}$$

Where S is the amount of subsidies awarded by a government in $/t$_{CO_2}$. The R^2 for Equations 6.14, 6.15, and 6.16 are 0.9931, 0.9931, and 0.9125, respectively.
It should be noted that the LCOE remains at approximately $115/MWh when co-firing more than 25 % biomass at an NEC of $75/t$_{CO_2}$, indicating that NEC is covering the marginal costs of switching the fuel. Interestingly, this value is similar to the potential economic threshold of a BECCS plant[325]. Above this NEC, it is possible to observe an LCOE increase until 17 % of biomass is co-fired, followed by an LCOE reduction at higher biomass fractions.
Co-firing more than 40 % of biomass and auctioning NEC at 70 $/t$_{CO_2}$ produces an IRR between 6 and 10 %. An IRR typical of public investments, generally 3 – 4 %[331], can be achieved by auctioning NECs between $30/t$_{CO_2}$ and $45/t$_{CO_2}$. Conversely, an IRR typically encountered in private investments, 11 – 14 %[331], is achieved by auctioning NEC above $90/t$_{CO_2}$. Indeed, typical LCOEs for photovoltaic panels (PV) and wind turbines of 51 – 115 $/MWh are achieved when NECs are auctioned between 90 and 135 $/t$_{CO_2}$[101, 332]. The results obtained from this analysis demonstrate that operating an oxy-BECCS plant with a framework that values negative emissions is more valuable than an oxy-coal combustion process.
Preliminary results demonstrate that a 14 % LCOE reduction could be achieved for a

coal-fired oxy-combustion process if the CAPEX is reduced by 25 %. Comparatively, only a 10 % LCOE decrease was observed for an oxy-BECCS plant if the CAPEX is reduced by 25 %. This highlights the impact that marginal cost has on the process, where both fuel and CO_2 transportation and storage costs have a substantial impact.
A less efficient plant, such as a supercritical or even a subcritical plant, could be more suitable if the plant's objective is to remove atmospheric CO_2 instead of power generation[331]. This would also lead to a reduced CAPEX and potentially smaller LCOE, but more detailed simulations would be required to evaluate this effect. Reducing plant costs would then allow NECs to be auctioned at lower prices, increasing this technology's economic potential.
The possibility of including H_2 production could further improve the economic potential of BECCS plants by introducing biofuel credits such as in California's low carbon fuel standard.[1]

6.3.6 BECCS and industry

A combination between BECCS and industry using the proposed framework could address the environmental issues of these sectors. Auctioning NECs this way reduces the burden of applying CCS to the electricity sector whilst offsetting industrial emissions that would otherwise have high costs of CO_2 capture. Furthermore, product quality is guaranteed since no change in the industrial process is required.
An early global-scale deployment of BECCS can increase the technical and operational knowledge of CCS, and build the required infrastructure for CO_2 transport. Costs associated with new CCS plants could then be reduced by building upon this newly-gained knowledge and using the already established infrastructure. Applying CCS directly to some industrial sectors could then become economically competitive, reducing the need to indirectly offset emissions via NECs.
BECCS plants could start effectively removing atmospheric CO_2 after widespread implementation of industrial CCS, assuming there is a vital requirement for negative emissions. If there is no requirement to achieve carbon negativity, or the policy framework does not justify this activity, plant operators could start co-firing fossil fuels to generate cheaper carbon-free electricity. Either way, new CCS plants can use the already existing infrastructure to reduce their costs.

6.4 Conclusions

Decarbonisation needs to accelerate across all sectors rapidly to achieve the target of 1.5 °C global warming. The greatest challenge is reducing CO_2 emissions in hard-to-reach sectors such as industry, transport, and aviation.

[1] California's low carbon fuel standard can grant credits as high as 200 $\$/t_{CO_2}$ for biofuels.

It has been demonstrated that repurposing the existing coal fleet to BECCS is both feasible and sustainable whilst preserving existing jobs and even promoting new jobs. The strategy presented here allows the electricity sector to be used as a proxy for industrial CCS development whilst decarbonising industry via NECs. This strategy allows industry to operate under business-as-usual, ensuring product quality, whilst curbing emissions at smaller costs than if CCS was directly applied.

If NECs cannot be auctioned, carbon-neutral electricity can be achieved at 18 % biomass co-firing, assuming a biomass supply chain emissions of 110 kg_{CO_2}/MWh_{th}. However, under the current CO_2 emissions cost of 25 $\$/t_{CO_2}$, it is still more economically attractive to operate a dedicated-coal oxy-combustion process. The higher costs of biomass compared to coal further accentuate that choice. Hence, achieving carbon-neutral electricity may be difficult to justify economically without either another source of revenue (such as NECs) or government subsidies.

The proposed framework enables the simultaneous decarbonisation of both industrial and electricity sectors cost-effectively. This would enable all sectors to achieve their targets whilst providing more time to develop new industrial decarbonisation strategies and improve CCS, driving its costs down, and implemented by industry at a later time. Another revenue source is introduced to an oxy-BECCS plant by auctioning NEC, thus improving the economics of the process, particularly above $\$75/t_{CO_2}$. This framework can offset 18 Mt/yr of the UK's industrial CO_2 emissions by operating five oxy-BECCS plants with 500 MW_{net}. Globally, this approach would require the 3000 plants to offset the industrial emissions, comparable to the number of CCS projects if they were directly applied to each emission source[326]. Indeed, the global coal power plant fleet is comparable to the number of oxy-BECCS projects required, suggesting a high potential for a brownfield approach to deploy BECCS. This approach would prevent job losses from the closure of these plants whilst promoting new jobs within the biomass supply chain[212] and achieve net-negative emissions beyond 2050[35, 37, 38].

Chapter 7

Demand-following oxy-combustion process for CCS with and without liquid oxygen storage

7.1 Introduction

Several technology solutions provide low carbon electricity, *e.g.*, nuclear power and bioenergy with carbon capture and storage (BECCS), that are an alternative to traditional fossil-fuel technologies[37, 333]. Not only are they more environmentally sustainable, but some authors argue that these solutions provide an economic incentive by creating more jobs than traditional fossil-fuel technologies[334–338].

Delaying the deployment of low-carbon power generating technologies will increase the costs of achieving the 1.5 °C target[21]. Such delay increases the reliance upon negative emissions technologies (NET) to remove the excess CO_2 that has since been emitted[21].

Operating the grid with a high penetration of variable renewable energy sources has yet to be performed, posing risks to system security and likely increasing costs[29, 30, 37, 38]. Hence, flexible plants able to adjust their power output according to demand are imperative to solve the intermittency issues of a high penetration of these energy sources[30, 37, 38]. These issues can be managed through electricity storage, increased interconnectivity, and flexible generation. Nowadays, these issues are mostly managed by dispatching flexible thermal power plants[30, 38, 90–93].

Improving the flexibility of power plants has been the focus of recent research, proposing methods such as dynamic data reconciliation[93], thermal energy storage[339, 340], and controlling water/fuel ratio[341, 342]. However, power plant flexibility must also be provided by other means to achieve the proposed targets.

Power plants fitted with carbon capture and storage (CCS) can provide flexible electric-

ity, maintaining grid stability whilst significantly reducing CO_2 emissions[38, 206, 277, 343–350]. Storing the solvent during peak electricity prices and regenerating it during off-peak electricity prices has been proposed to improve the economy of flexible post-combustion capture plants[347, 348, 351]. Detailed simulation of these plants witnessed only marginal economic benefits by storing the solvent; however, they observed increased profits at high peak/off-peak electricity price differences[347, 348, 351]. The flexibility of these plants can be improved by adopting a suitable control strategy whilst preserving a high degree of CO_2 capture[352]. Furthermore, post-combustion capture models have been experimentally validated at the UKCCSRC PACT pilot plant both in steady-state and ramping scenarios[277], demonstrating the feasibility of this operation.

Flexible operation of oxy-combustion has been researched despite post-combustion technology being identified as the most suitable for this type of operation[195]. The air separation unit (ASU), responsible for providing the required O_2 for the process, can be turned down to 50 % capacity with only 1 % O_2 purity variation[353], which is still suitable for oxy-combustion. Flexible operation of an ASU for industrial gas production with liquid oxygen (LOX) storage has significantly reduced costs whilst allowing the plant to engage in the ancillary services market[354]. This is a subset of cryogenic energy storage (CES) systems that store a cryogenic liquid (nitrogen, oxygen, argon) during off-peak electricity price periods, and discharge it when required[355–357].

Dubettier et al. [135] presented the concept of an oxy-combustion plant storing LOX during off-peak electricity price and discharging it during peak electricity prices to improve the plant's flexibility at reduced costs[138, 270]. This strategy was investigated for oxy-combustion of natural gas [350, 358] and coal[151, 152, 270, 359, 360], with net efficiency increasing between 6 and 10 % during LOX discharge[270, 358]. The authors concluded that a limited profit improvement could be obtained depending on the average electricity price and peak/off-peak electricity price difference, similar to post-combustion processes with solvent storage. However, Hanak et al. [151] witnessed a 1 % drop in the plant's average daily net efficiency by employing this strategy, attributed to the reduced equipment efficiency when operating at lower capacity[353, 359].

These studies generally assume enough LOX availability, requiring the ASU to be either a liquid oxygen plant or having an external O_2 liquefaction cycle[361]. However, Smith and Klosek [68] stated that obtaining a liquid product is two to three times more energy-intensive than producing a gaseous product; hence, typical ASUs designed for oxy-combustion favour the latter. Indeed Perrin et al. [270] determined that filling a LOX storage tank required 670 kWh/m^3 to separate and liquefy oxygen, resulting in a 50 – 91 % power consumption increase.

An indirect approach to improve oxy-combustion flexibility was proposed by Pacheco

et al. [355], opting for a CES strategy where liquid nitrogen (LIN) is stored at 200 bar during off-peak electricity prices instead of LOX. Then, pressurised LIN is discharged, evaporated, and expanded on a turbine to generate electricity during high-demand periods, taking advantage of high electricity prices[355]. The author noted that the power required to compress LIN to the desired pressure was five times higher than the amount generated, resulting in a 19 % net thermal efficiency of the CES cycle[355].
For a direct approach, Goloubev and Alekseev [361] demonstrated that it is possible to extract limited amounts of LOX directly from the low pressure (LP) column's sump during off-peak electricity prices with an 11 % power reduction at peak electricity price. This strategy has the advantage of using a traditional ASU without an external liquefaction process, potentially saving capital and operating costs. However, only limited amounts of LOX can be extracted from the LP column without compromising the plant's ability to separate air because LOX is required to cool incoming air to the ASU.
To the best of the author's knowledge, studies on oxy-biomass flexibility have yet to be performed. Hence, a flexible biomass-fired oxy-combustion model with LOX storage, represented in Figure 7.1, and the possibility of auctioning negative emission credits (NEC), as proposed in Chapter 6[300], was simulated to assess the potential economic benefits of this approach.

7.2 Model development

The model was developed in gPROMS using the assumptions outlined in Chapter 6.

7.2.1 Load changing rate

The oxy-combustion model described previously in Chapter 4[103] was used to assess the effects of varying the load according to demand. Typical load changing rates of a coal-fired boiler are 5 %/min at 50 – 90 % load and 4 %/min at 90 – 100 % load[359]. However, the oxy-combustion process requires an ASU, which only allows changing rates of 3 %/min[359], thus constraining the load changing rate of the whole process.

7.2.2 Daily electricity price

Daily electricity prices are detailed in Table 7.1[347, 348, 352], representing typical demand fluctuation patterns in the UK. They follow a similar pattern to what is found in the day ahead data extracted from the Nord Pool group, as depicted in Figures 7.2 and 7.3 for a representative hourly electricity price variation of a winter day and a summer day, respectively[362]. These two figures were generated by taking the average and standard deviation of the hourly electricity price throughout a representative month[362]. The data from Table 7.1 was used throughout this work to provide continuity from previous work[347, 348, 352]. This price variability translates to seven hours of peak-electricity price, eight hours of off-peak electricity price, and the remain-

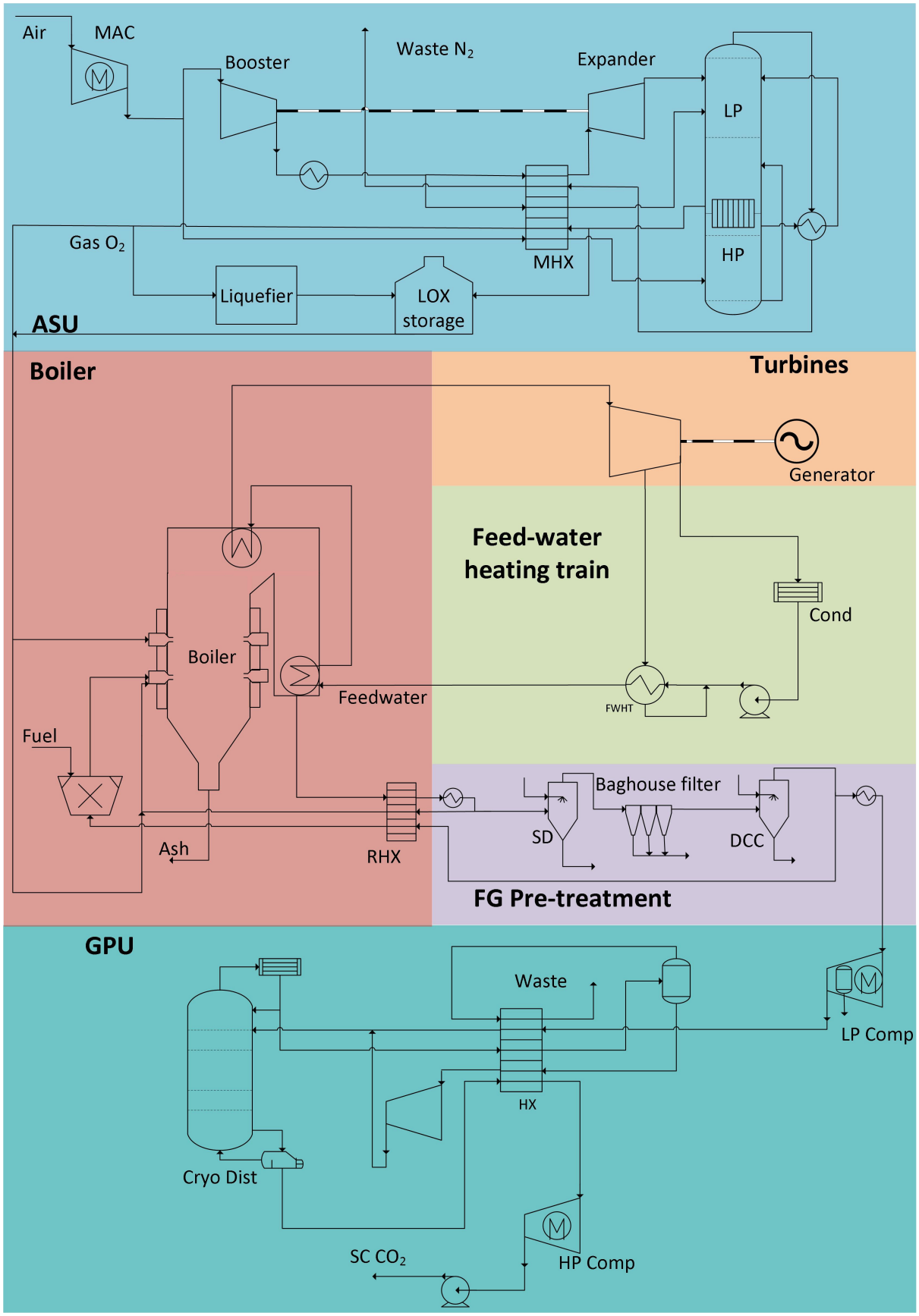


Figure 7.1: PFD of oxy-combustion with LOX storage for both schedules studied herein.

Table 7.1: Daily electricity price variation used in this work to determine the effects of flexible oxy-combustion operation[347, 348, 352].

Period	Electricity price ($/MWh)
00:00 – 06:00	80
06:00 – 10:00	140
10:00 – 16:00	90
16:00 – 19:00	140
19:00 – 22:00	90
22:00 – 24:00	80

Table 7.2: Assumptions required for the storage tank design.

Parameter	Value	Reference
Temperature (°C)	-196	[152]
Pressure (bar)	2.5	[359]
ρ_{LOX} (kg/m^3)	1204.3	[365]
$\rho_{\text{Expanded perlite}}$ (kg/m^3)	92.5	[366]
Height/ Diameter	0.58	[367, 368]
Annular space (m)	1.25	[363]
Perlite cost ($/t)	686	[369]
Inner wall thickness (mm)	19	[281]
Inner ceiling thickness (mm)	16	[281]

ing nine hours at an intermediate price.

The daily electricity price fluctuation provides the incentive for a flexible operation of the power plant[30, 37, 38] according to demand, either by ramping the plant up and down twice or in a day/night cycle with only one ramp up and down. This operation will require either 4 or 14 h of stored oxygen for the two ramps and one ramp, respectively, impacting the storage tank size and consequently its capital cost.

7.2.3 Storage tank design

The storage tank considered in this study was based on typical LNG tanks[363] due to their similarities. The tank consists of two vessels separated by perlite acting as an insulating material[152, 364]. Table 7.2 displays the storage tank's design parameters assumed in this work.

The mass balance of the storage tank is given by Equations 7.1 – 7.3.

$$\frac{dM_{i,Bulk}}{dt} = F_{i,in} - F_{i,out} \tag{7.1}$$

$$M_{Bulk} = \sum_{i} M_{i,Bulk} \tag{7.2}$$

$$x_{i,Bulk} = \frac{M_{i,Bulk}}{M_{Bulk}} \tag{7.3}$$

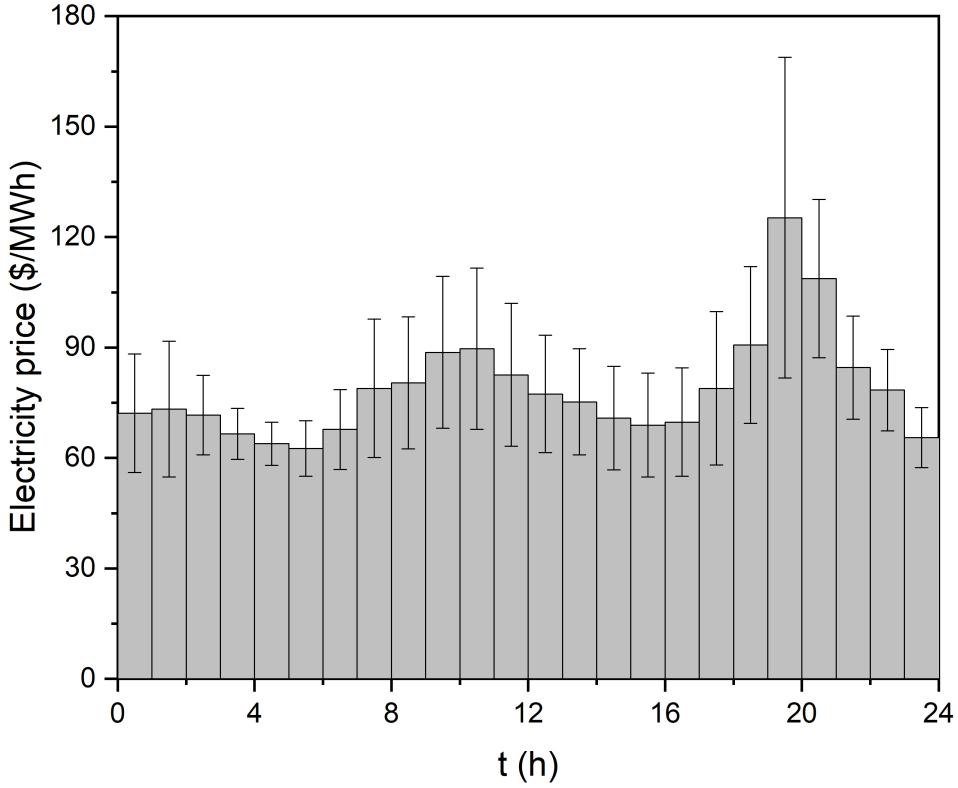


Figure 7.2: Daily electricity price variation of a representative winter month, extracted from Nord Pool group. The bars represent the average price for that time period with the corresponding standard deviation.

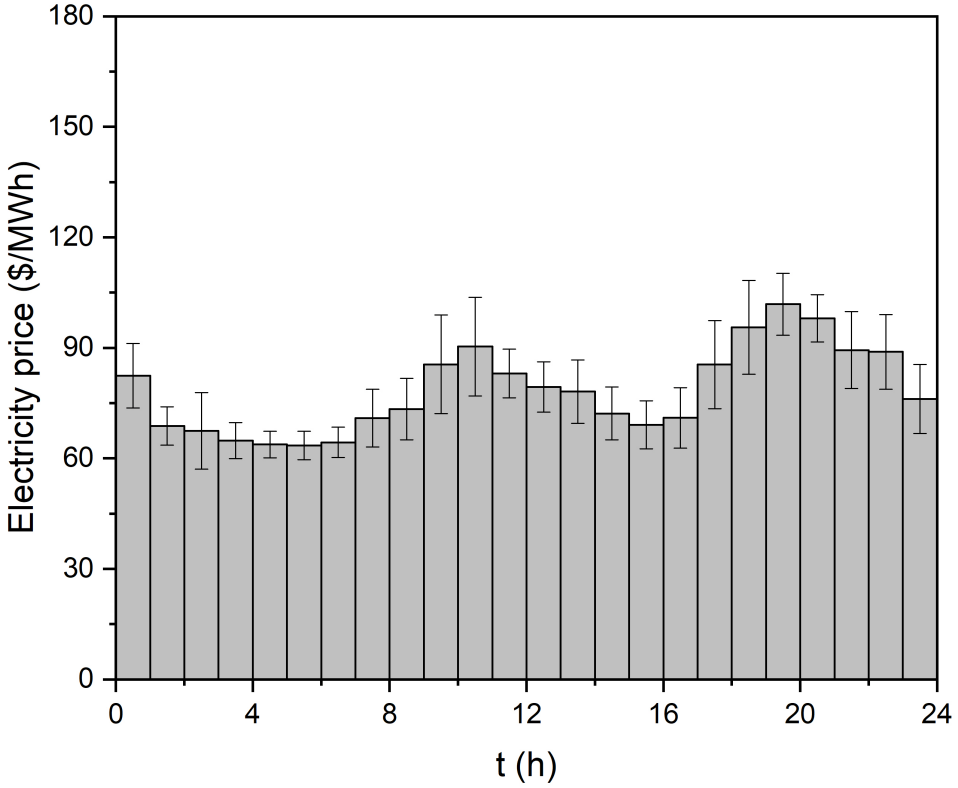


Figure 7.3: Daily electricity price variation of a representative summer month, extracted from Nord Pool group. The bars represent the average price for that time period with the corresponding standard deviation.

Where i can be either oxygen (O_2), nitrogen (N_2), or argon (Ar).
The storage tank is considered adiabatic, and no liquid evaporation is assumed during storage due to the short cycles proposed herein, as only up to 0.2 %/day of stored cryogenic liquids evaporate[357]. Nonetheless, the tank is sized with 10 % excess volume according to Equations 7.4 and 7.5 to accommodate for any possible evaporation that might occur.

$$V_{Tank} = \frac{F_{in} t_{res}}{0.9 \rho_{LOX}} \tag{7.4}$$

$$V_{Tank} = \pi r^2 H \tag{7.5}$$

Where V_{Tank} is the vessel volume (m^3); F_{in} is the mass flowrate of LOX during storage periods (kg/s); t_{res} is the residence time (s); ρ_{LOX} is LOX density (kg/m^3); r is the vessel radius (m); and H is the vessel height (m).
The height of liquid oxygen at any point in time is determined via Equation 7.6.

$$M_{Bulk} = \rho_{LOX} \pi r^2 h \tag{7.6}$$

The annular volume filled with expanded perlite is determined by subtracting the inner volume tank from the outer volume tank using Equation 7.7.

$$V_{Perlite} = V_{Outer\ tank} - V_{Inner\ tank} \tag{7.7}$$

The mass of perlite is then determined by multiplying the volume it occupies with its density.

7.2.4 Economic evaluation

The purchase cost (PC) of the storage tank was determined using the methodology described by Couper et al. [281] using Equation 7.8. It is assumed that the tank is field-erected and both inner and outer tanks are made from 340 austenitic steel ($F_M = 3$) and carbon steel ($F_M = 1.9$), respectively.

$$PC = 1.218 F_M e^{11.662 - 0.614 ln(V_{Tank}) + 0.04536 (ln(V_{Tank}))^2} \frac{CEPCI_{2015}}{CEPCI_{2003}}, \quad 95 < V_{Tank} < 50\,000\,\mathrm{m}^3 \tag{7.8}$$

Then, the installed cost was calculated by multiplying the inner and outer tank's PC by 1.5 and 2.3, respectively[281]. Finally, the total purchase/ installed cost were calculated by adding all purchase/ installed costs, respectively. The net present value (NPV) of the oxy-combustion process with and without LOX storage was calculated using the procedure detailed in the previous Chapters and Equation 5.1[300].

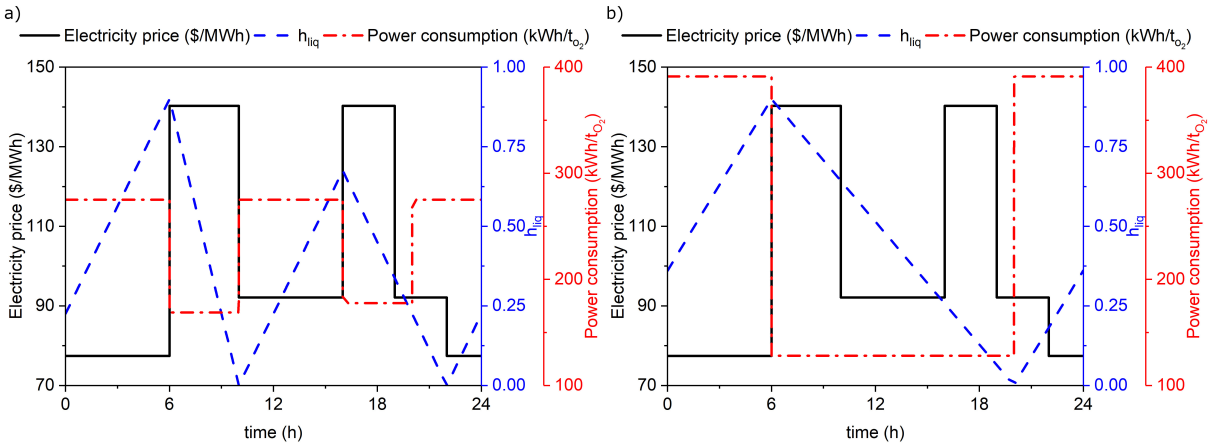


Figure 7.4: LOX storage schedules simulated for the daily electricity price variation detailed in Table 7.1. The storage tank is charged with LOX during both off-peak electricity prices and discharged during peak electricity prices (a); the storage tank is charged with LOX during night off-peak electricity price and discharged during the day (b).

7.3 Results and Discussion

7.3.1 Scheduling liquid oxygen storage

Liquid oxygen (LOX) is assumed to be evaporated against air before being discharged to the power plant. Figure 7.1 represents the configuration of the oxy-combustion process with LOX storage. In one schedule, LOX is stored during low electricity prices and discharged at high electricity prices, resulting in a double daily charge/ discharge cycles (Figure 7.4 a); in the other schedule, LOX is stored at night and subsequently discharged during the day, resulting in a single daily charge/ discharge cycle (Figure 7.4 b). Both schedules exploit the high electricity prices encountered during the day to reduce the parasitic power consumption of the ASU. However, there is an increased power consumption of the ASU during LOX charging period, associated with LOX production, that must be compensated to make this strategy attractive.

Operating with a double daily charge/ discharge cycles results in a smaller storage tank with $695000 installed cost. Here, LOX is extracted after the LP column, and thus only up to 11 % LOX can be extracted (Figure 7.5 a) due to the main heat exchanger (MHX) relying on vaporising and heating LOX to cool incoming air. Up to 3 % LOX can be extracted without any change in the ASU operating conditions; however, extracting more LOX will disturb the temperature of the LP column, preventing air separation. Maintaining the LP column's temperature can be accomplished by diverting more air to the expander (Figure 7.5 b). However, this limits the process to operate at a minimum 70 % capacity.

Operating with a single daily discharge increases the power consumption by 33 % during LOX charging relative to two daily discharges. During LOX discharge, the single

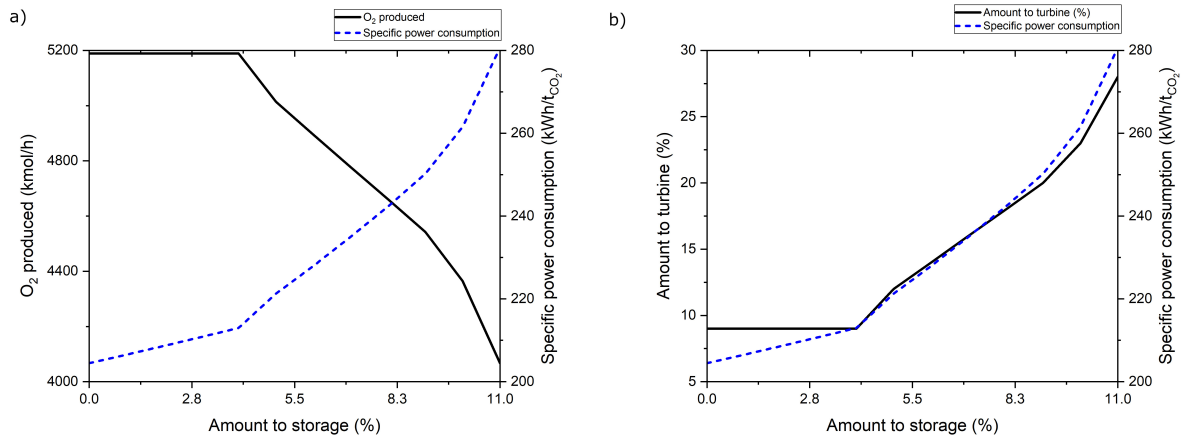


Figure 7.5: Amount of oxygen produced in the ASU and specific power consumption as function of the amount of LOX extracted from the LP column (a); and amount of air sent to the turbine and specific power consumption as function of the amount of LOX extracted from the LP column(b).

discharge cycle consumes 28 % less power than the schedule with a double discharge cycle. However, the single discharge schedule requires a larger storage tank, increasing its installed cost to M$1.7.

Using this stored LOX strategies reduces the power consumption during LOX discharge period, generating more net power during peak electricity prices. This operating cycle requires either a dedicated LOX plant or installing an external oxygen liquefaction process on an existing ASU. In this work, an external liquefaction process operating at the minimum possible power consumption (only the amount required to compress gaseous oxygen to storage pressure) has been assumed as an approximation to the power consumption of a dedicated LOX ASU.[1]

The daily cumulative profit can be observed in Figure 7.6 for the schedule with no LOX storage (full line), and with LOX storage following the schedules from Figure 7.4 a (dashed line) and b (dotted line), respectively. The cumulative profit was levelised for the daily power generated from each schedule to enable a direct comparison. Higher profit rates during peak electricity prices occur when LOX is discharged, resulting from more power being sold to the grid. However, lower profit rates during off-peak electricity prices, even close to zero, are observed because of the extra power required from the ASU to produce and store LOX. This increased power consumption can become detrimental if off-peak electricity prices are sufficiently large, as shown in 7.6 (dashed and dotted lines).

An oxy-coal power plant's profitability would be higher than an oxy-biomass power plant because coal is cheaper and has higher heating values[84, 300, 370]. However,

[1]Dedicated LOX ASU are being operated globaly. However, the technology is highly protected and the power consumption of such units is not available in the literature.

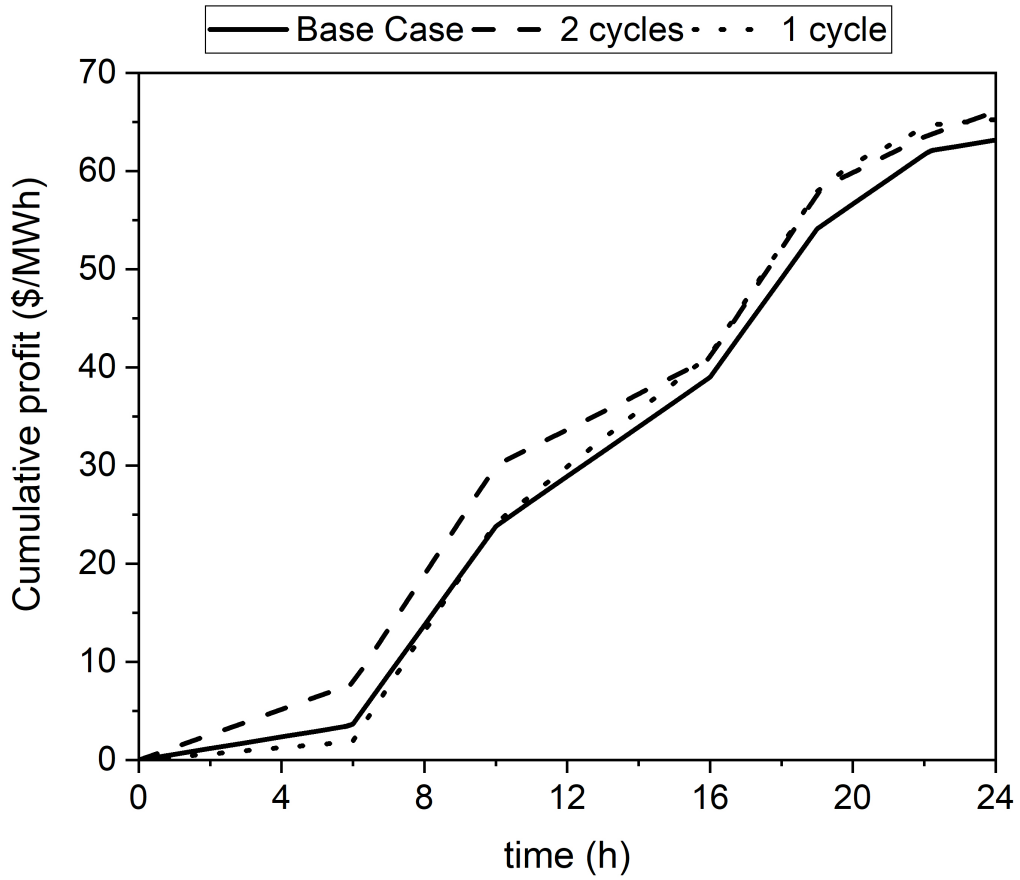


Figure 7.6: Cumulative profit levelised to the daily power output of an oxy-combustion process firing biomass without LOX storage for the schedule represented in Figure 7.4 b (Full line), with LOX storage for 2 cycles (dashed line) and for 1 cycle (dotted line) for the schedules represented in Figure 7.4 a and b, respectively.

an oxy-coal plant's residual CO_2 emissions can only be abated by adding a direct air capture (DAC) plant. This would significantly increase the project's capital costs because just the DAC plant can be 200 % more expensive than bioenergy with CCS (BECCS), assuming that DAC captures CO_2 at a rate of 1 – 2.5 Mt/year with a CAPEX of $16900/kW – $28200/kW[371, 372]. Furthermore, capturing a similar amount of atmospheric CO_2 using this approach would impose a 25 – 40 % power consumption penalty to the oxy-coal process, making it less attractive than a dedicated oxy-BECCS.

Whilst DAC will undoubtedly have a role in reducing atmospheric CO_2, it must be noted that it requires power to do so[371, 372]. This implies that the DAC plant might have to shut down during high electricity demand not satisfied by variable renewable sources. Hence, BECCS could be a potential candidate to reduce both atmospheric CO_2 and generate electricity in a flexible way, guaranteeing a firm power supply[35–39] if biomass can be sourced sustainably[73, 85–89].

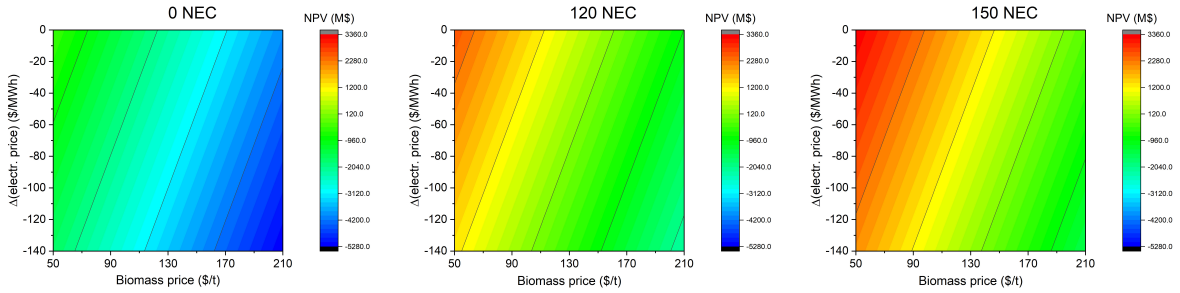


Figure 7.7: Sensitivity analysis on biomass price with NEC auctioned at different prices and difference between day off-peak electricity price and peak electricity price, analysing their effect on NPV for the schedule represented in Figure 7.4 a.

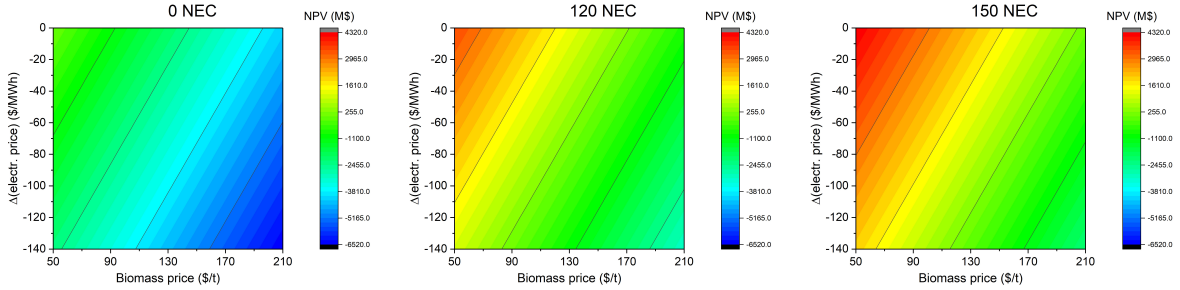


Figure 7.8: Sensitivity analysis on biomass price with NEC auctioned at different prices and difference between day off-peak electricity price and peak electricity price, analysing their effect on NPV for the schedule represented in Figure 7.4 b.

7.3.2 Sensitivity analysis

Understanding the effects of fuel cost and electricity price on the daily profit is necessary to estimate the benefits of implementing a LOX charge and discharge schedule. Extra profit from auctioning negative emission credits (NEC) at \$120/t_{CO_2} and \$150/t_{CO_2}, determined by Zhang et al. [370] to provide an IRR of 10 % and 15 %, respectively, is also assessed using the strategy proposed in Chapter 6[300].

Day off-peak electricity price variation

Day off-peak electricity price does not impact the daily profit relative to the case without LOX storage for the schedule with two LOX discharges, whilst fuel price does (Figure F.13). However, the trend appears to revert for the schedule with a single LOX discharge, demonstrating a significant impact from the day off-peak electricity price whilst fuel price has a marginal impact (Figure F.14). This is because oxy-combustion operates at part-load during day off-peak electricity price for the double LOX discharge schedule, making it resistant to fuel price fluctuation. However, the plant operates at full-load in the schedule with a single LOX discharge, making it susceptible to electricity price fluctuation.

Auctioning NEC above \$120/t_{CO_2} suggests that LOX storage is a more profitable option than following demand without storage. Increasing the NEC value enhances the

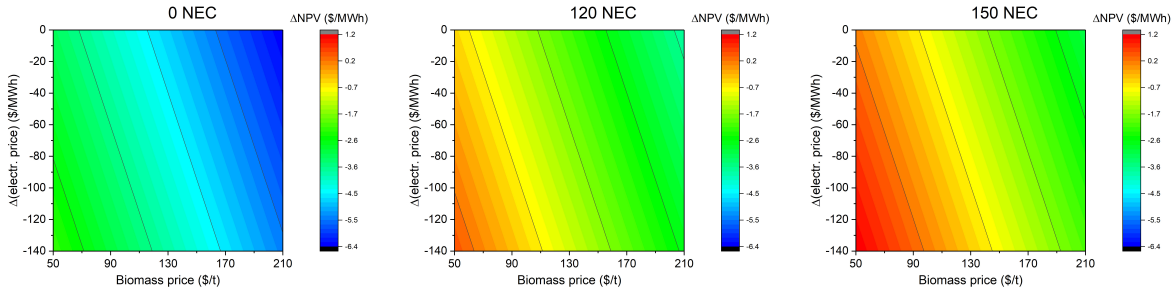


Figure 7.9: Sensitivity analysis on biomass price with NEC auctioned at different prices and difference between day off-peak electricity price and peak electricity price, analysing their effect on the NPV difference between the case with LOX storage and without LOX storage for the schedule represented in Figure 7.4 a.

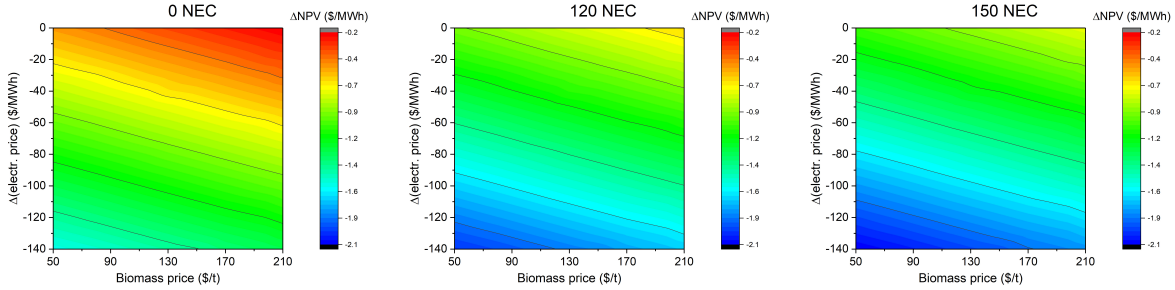


Figure 7.10: Sensitivity analysis on biomass price with NEC auctioned at different prices and difference between day off-peak electricity price and peak electricity price, analysing their effect on the NPV difference between the case with LOX storage and without LOX storage for the schedule represented in Figure 7.4 b.

profitability of operating with two LOX discharges (Figure F.13), whereas the single LOX discharge schedule follows the opposite trend (Figure F.14). This is because the plant operates at full-load during day off-peak electricity prices for the latter, capturing less biogenic CO_2, thus reducing its profits. Higher profitability obtained during the double daily discharge schedule arises from the plant operating at part-load during day off-peak electricity prices. This results from the increased power consumption whilst charging LOX, which captures more biogenic CO_2, thus generating more NEC than the scenario without storage.

However, profitability is not the only factor affecting a process's economic potential because capital costs should be considered for a more detailed evaluation of the process; hence, a net present value (NPV) analysis was performed on all simulations. Positive NPV can only be achieved by auctioning NEC (Figures 7.7 and 7.8), similar to what was concluded in Chapter 6[300].

The NPV of the schedule with two LOX discharges is represented by Equation 7.9 whilst the single discharge schedule is represented by Equation 7.10.

$$NPV[M\$] = 25.14NEC - 22.25Price_{Biomass} - 9.16\Delta Price_{electricity} + 688.28 \quad (7.9)$$

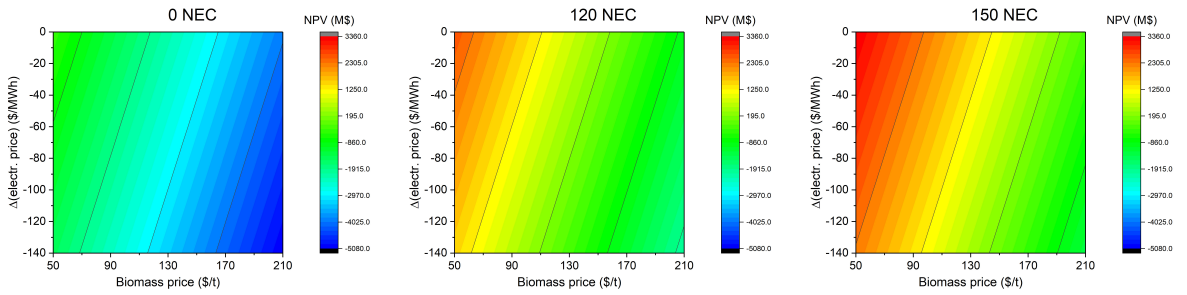


Figure 7.11: Sensitivity analysis on biomass price with NEC auctioned at different prices and the difference between night off-peak electricity price with peak electricity price, analysing the effect on NPV for the schedule represented in Figure 7.4 a.

$$NPV[M\$] = 28.51NEC - 26.30Price_{Biomass} - 16.70\Delta Price_{electricity} + 1350.78 \quad (7.10)$$

The equations were created by minimizing the sum of squares between the data obtained from the simulation and the calculated values. This is also true for the rest of the fitted equations throughout this chapter. Equations 7.9 and 7.10 have a coefficient of determination (R^2) of over 0.9999.

The effects observed for the NPV difference between the schedule with and without LOX storage are similar to the profit difference between the same cases. A higher NPV for both schedules with LOX storage than the case without storage is only obtained in extreme cases. A higher NPV occurs at fuel prices lower than \$100/t and at NEC higher than \$150/t_{CO_2} for the double LOX discharge schedule (Figure 7.9). Comparatively, a higher NPV occurs at high and flat daily electricity prices if no NEC are auctioned for the case with a single LOX discharge (Figure 7.10).

The NPV difference of the schedule with two LOX discharges is represented by Equation 7.11 and the single discharge by Equation 7.12.

$$\Delta NPV[\$/MWh] = 0.022NEC - 0.02Price_{Biomass} + 0.007\Delta Price_{electricity} - 2.217 \quad (7.11)$$

$$\Delta NPV[\$/MWh] = -0.004NEC + 0.002Price_{Biomass} - 0.008\Delta Price_{electricity} - 0.569 \quad (7.12)$$

Equations 7.11 and 7.12 have an R^2 of 0.9977 and 0.9951, respectively.

Night off-peak electricity price variation

The profitability of LOX storage is highly susceptible to the night off-peak electricity prices (Figures F.5, F.6, F.15, and F.16). Indeed, lower night off-peak electricity prices result in lower profits during this period. Hence it becomes advantageous to store

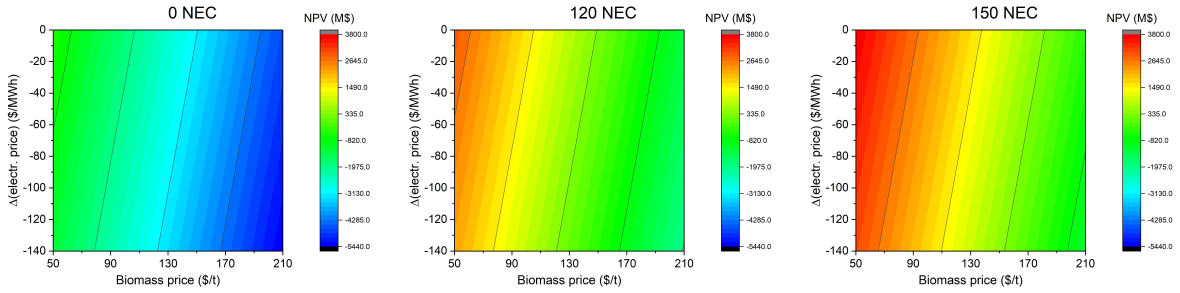


Figure 7.12: Sensitivity analysis on biomass price with NEC auctioned at different prices and the difference between night off-peak electricity price with peak electricity price, analysing the effect on NPV for the schedule represented in Figure 7.4 b.

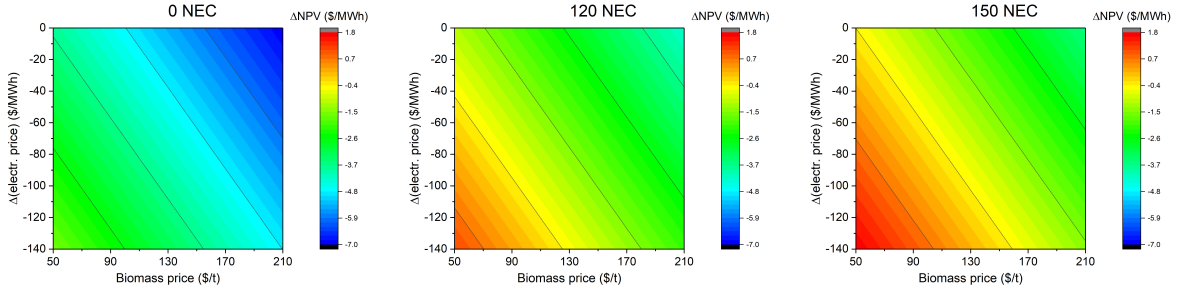


Figure 7.13: Sensitivity analysis on biomass price with NEC auctioned at different prices and the difference between night off-peak electricity price with peak electricity price, analysing their effect on the NPV difference between the case with LOX storage and without LOX storage for the schedule represented in Figure 7.4 a.

LOX during low electricity prices and discharge it during peak electricity prices. This parameter has a higher impact on the single daily discharge cycle, whilst the impact is shared with fuel price when two daily discharges are performed.

Auctioning NEC results in an increased profitability when LOX is stored, mainly for two daily discharges (Figures F.15 and F.16). This effect is observed because the plant can sell more electricity to the grid during high electricity prices. The plant can still produce sufficient revenue whilst storing LOX during day off-peak prices despite operating at a lower capacity. This effect is reversed for the single discharge cycle because it operates at full capacity during day off-peak electricity price, where prices are not sufficiently high to offset the losses incurred during storage.

Positive NPV can only be achieved by auctioning NEC above $\$120/t_{CO_2}$, following a similar trend when comparing it to daily profit, as observed by Figures F.7, 7.11, and 7.12. The NPV of the schedule with two LOX discharges is represented by Equation 7.13 and the single discharge by Equation 7.14.

$$NPV\,[M\$] = 25.14NEC - 22.25Price_{Biomass} - 7.82\Delta Price_{electricity} + 699.52 \tag{7.13}$$

$$NPV\,[M\$] = 28.52NEC - 26.31Price_{Biomass} - 5.27\Delta Price_{electricity} + 832.84 \tag{7.14}$$

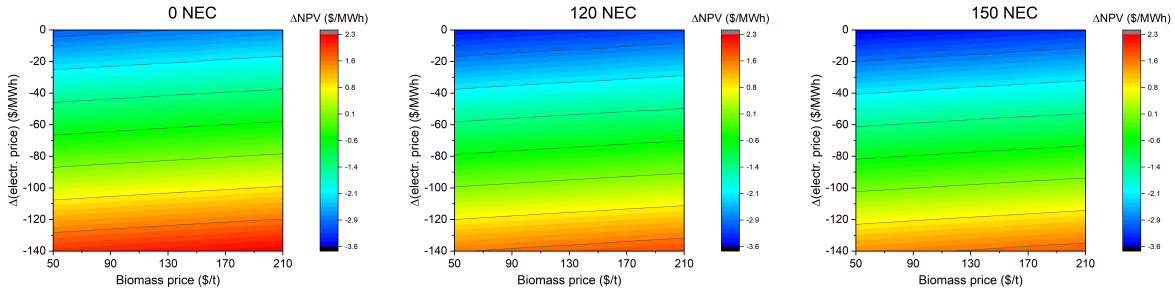


Figure 7.14: Sensitivity analysis on biomass price with NEC auctioned at different prices and the difference between night off-peak electricity price with peak electricity price, analysing their effect on the NPV difference between the case with LOX storage and without LOX storage for the schedule represented in Figure 7.4 b.

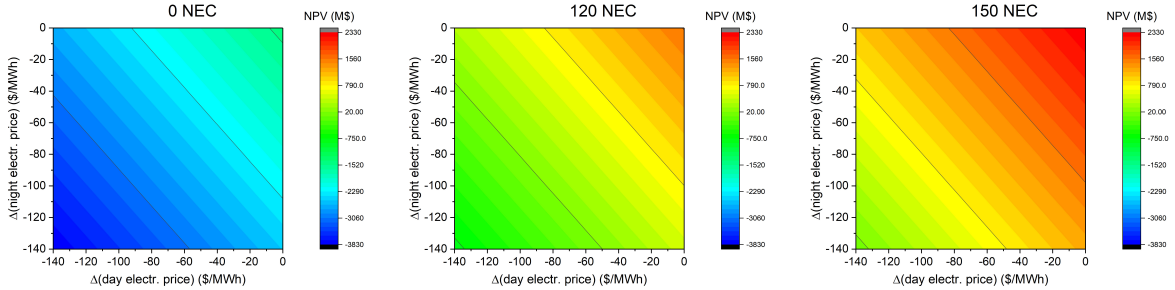


Figure 7.15: Sensitivity analysis on the difference between both night and day off-peak electricity prices with respect to peak electricity price and their effect on NPV for an oxy-combustion process firing biomass costing $117/t and auctioning NEC at different prices for the schedule represented in Figure 7.4 a.

Equations 7.13 and 7.14 have an R^2 over 0.9999.
However, storing LOX becomes less economical when considering the storage tank's cost (Figures 7.13 and 7.14). The NPV difference of the schedule with two LOX discharges is represented by Equation 7.15 and the single discharge by Equation 7.16.

$$\Delta NPV[\$/MWh] = 0.022NEC - 0.02Price_{Biomass} + 0.016\Delta Price_{electricity} - 2.786 \quad (7.15)$$

$$\Delta NPV[\$/MWh] = -0.004NEC + 0.002Price_{Biomass} + 0.036\Delta Price_{electricity} - 3.126 \quad (7.16)$$

Equations 7.15 and 7.16 have an R^2 of 0.9995 and 0.9997, respectively.
Whilst auctioning NEC improves the economic attractiveness of a double LOX daily discharge, this requires NEC above $\$150/t_{CO_2}$, a fuel cost below $90/t, and night off-peak electricity prices at least $110/MWh below peak electricity prices to become more attractive than not storing LOX (Figure 7.13). It becomes more attractive to discharge only once during the day than the case without LOX storage and no NEC (Figure 7.14) when the night off-peak electricity price difference is at least $100/MWh below peak

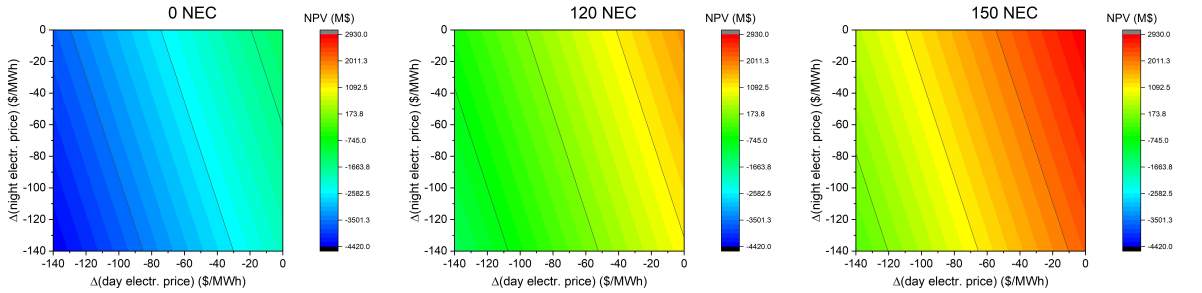


Figure 7.16: Sensitivity analysis on the difference between both night and day off-peak electricity prices with respect to peak electricity price and their effect on NPV for an oxy-combustion process firing biomass costing \$117/t and auctioning NEC at different prices for the schedule represented in Figure 7.4 b.

electricity price, regardless of fuel cost. Considering that a project would only be accepted with positive NPV, the single daily discharge option is only economically attractive if biomass can be sourced below \$130/t whilst valuing negative emissions via NEC above \$120/t_{CO_2}.

Day and night off-peak electricity price variation

Varying both day and night off-peak electricity price demonstrates that both schedules with LOX storage generate a higher revenue than without LOX storage at lower night off-peak electricity prices (Figures F.10, F.17, and F.18). Here, biomass price is set at \$117/t according to Chapter 6[300]. This practice takes advantage of the lower electricity prices during night off-peak period to store LOX which is subsequently discharged during the day at higher electricity prices.

The double daily discharge cycle has a higher revenue at lower day off-peak electricity price because the plant operates at lower capacity during this period whilst storing LOX. The single LOX discharge cycle contrasts with the previous schedule by providing more revenue than without storage at higher day off-peak electricity prices (Figure F.17). This occurs because the plant operates at full capacity during this period whilst discharging LOX, thus selling more electricity to the grid (Figure F.18). Auctioning NEC at higher prices improves the double discharge cycle's potential relative to the case without storage, whilst decreasing the single discharge cycle's potential with relation to no storage (Figures F.17 and F.18).

Positive NPV can be achieved if NEC are auctioned above \$120/t_{CO_2} and at high day off-peak prices for both storage cases studied herein (Figures 7.15 and 7.16).

The NPV of the schedule with two LOX discharges is represented by Equation 7.17 and the single LOX discharge by Equation 7.18.

$$NPV[M\$] = 25.14NEC - 9.16\Delta Price_{electricity,\ day} - 7.82\Delta Price_{electricity,\ night} - 1445.43 \tag{7.17}$$

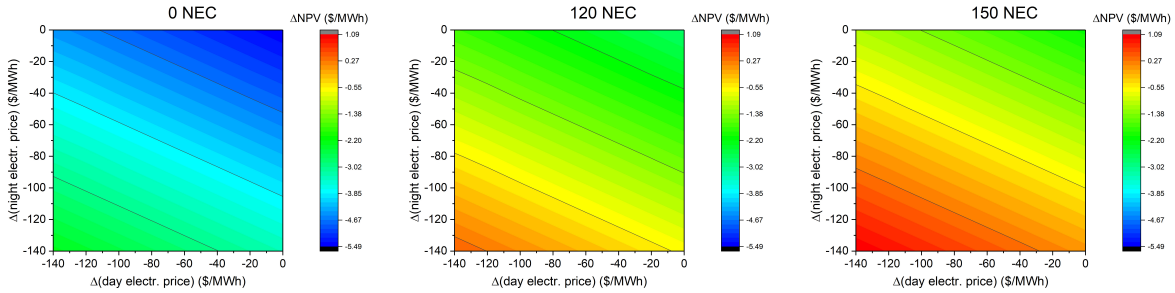


Figure 7.17: Sensitivity analysis on the difference between both night and day off-peak electricity prices with respect to peak electricity price. Their effect on NPV difference between the case of LOX storage with the case without LOX storage for an oxy-combustion process firing biomass costing $117/t and auctioning NEC at different prices for the schedule represented in Figure 7.4 a is assessed.

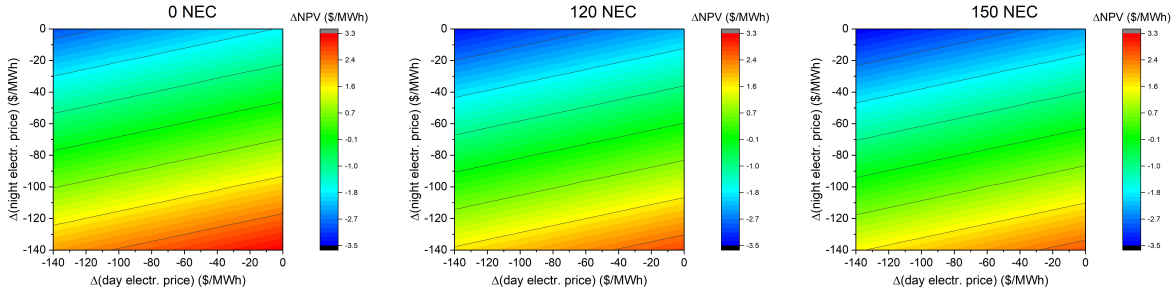


Figure 7.18: Sensitivity analysis on the difference between both night and day off-peak electricity prices with respect to peak electricity price. Their effect on NPV difference between the case of LOX storage with the case without LOX storage for an oxy-combustion process firing biomass costing $117/t and auctioning NEC at different prices for the schedule represented in Figure 7.4 b is assessed.

$$NPV[M\$] = 28.43NEC - 16.70\Delta Price_{electricity,\ day} - 5.28\Delta Price_{electricity,\ night} - 1341.12 \tag{7.18}$$

Equations 7.17 and 7.18 have an R^2 of over 0.9999.

A double LOX discharge schedule is more economically attractive than withour storage during low day and night off-peak electricity prices when auctioning NEC above $\$120/t_{CO_2}$ (Figure 7.17). Contrastingly, a single LOX discharge schedule is more economically attractive than without storage during low night off-peak electricity prices and high day off-peak electricity prices (Figure 7.18).

The NPV difference of the schedule with two LOX discharges is represented by Equation 7.19 and the single discharge by Equation 7.20.

$$\Delta NPV[\$/MWh] = 0.022NEC + 0.007\Delta Price_{electricity,\ day} + 0.016\Delta Price_{electricity,\ night} - 5.483 \tag{7.19}$$

$$\Delta NPV[\$/MWh] = -0.004NEC - 0.008\Delta Price_{electricity,\ day} + 0.036\Delta Price_{electricity,\ night} - 1.784 \tag{7.20}$$

Equations 7.19 and 7.20 have an R^2 of 0.9990 and 0.9999, respectively.

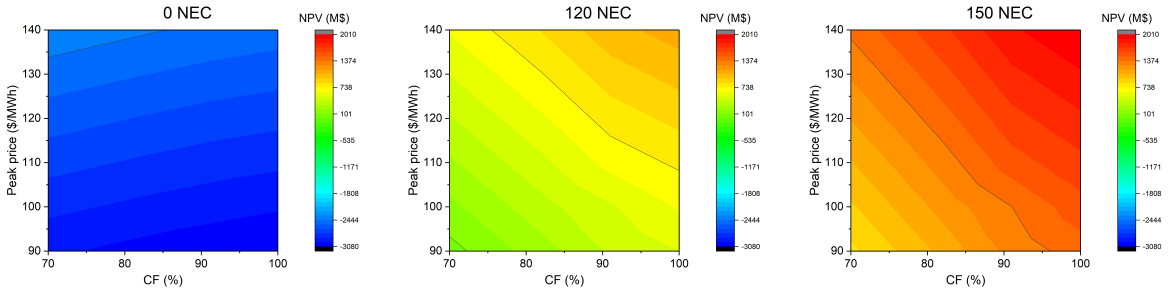


Figure 7.19: Sensitivity analysis of the capacity factor during off-peak electricity prices and peak electricity price variation, and their effect on NPV for an oxy-combustion process firing biomass costing $117/t for the schedule represented in Figure 7.4 a.

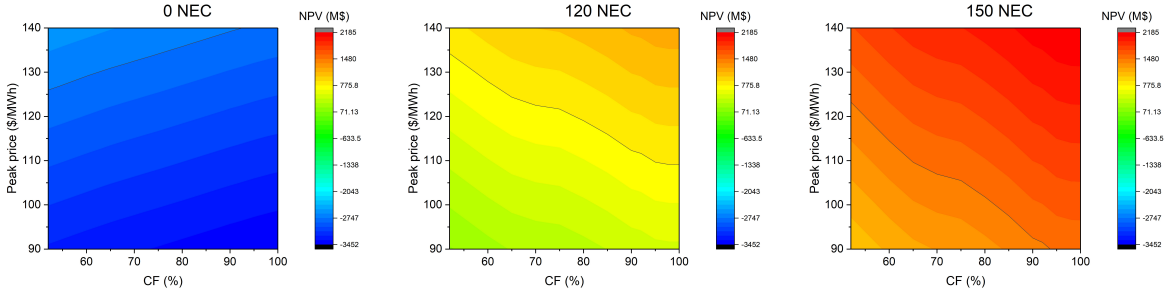


Figure 7.20: Sensitivity analysis of the capacity factor during off-peak electricity prices and peak electricity price variation, and their effect on NPV for an oxy-combustion process firing biomass costing $117/t for the schedule represented in Figure 7.4 b.

Peak electricity price and capacity factor variation

Decreasing peak electricity price, flattening electricity price throughout the day, will reduce the plant's revenue and consequently its NPV. Lower capacity factors during off-peak electricity increase the NPV if no NEC are auctioned; however, higher capacity factors are beneficial when auctioning NEC above $\$120/t_{CO_2}$ (Figures 7.19 and 7.20) because more biogenic fuel is consumed. Operating a flexible plant without LOX storage is more economical than operating one with LOX storage regardless if NEC are auctioned. However, plants with LOX storage become increasingly economical as NEC price increases (Figures 7.21 and 7.22). The decrease observed between a capacity factor (CF) of 65 % and 85 % suggests a non-linear relation between CF and peak electricity price on the potential of using LOX storage.

The NPV of the schedule with two LOX discharges is represented by Equation 7.21 and the single LOX discharge by Equation 7.22.

$$NPV[M\$] = -0.1CF^2 + 0.04\Delta Price^2_{electricity} + 27.88NEC + 27.88CF + \\ + 2.57\Delta Price_{electricity} - 5160.82 \quad (7.21)$$

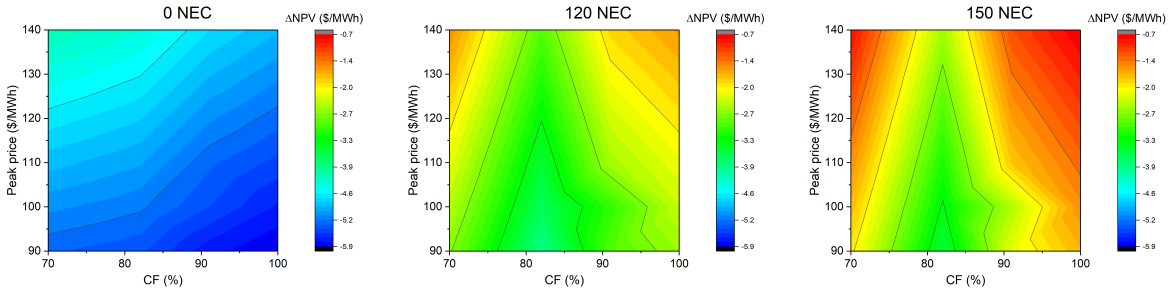


Figure 7.21: Sensitivity analysis of the capacity factor during off-peak electricity prices and peak electricity price variation, and their effect on NPV difference between the case of LOX storage with the case without LOX storage for an oxy-combustion process firing biomass costing $117/t for the schedule represented in Figure 7.4 a.

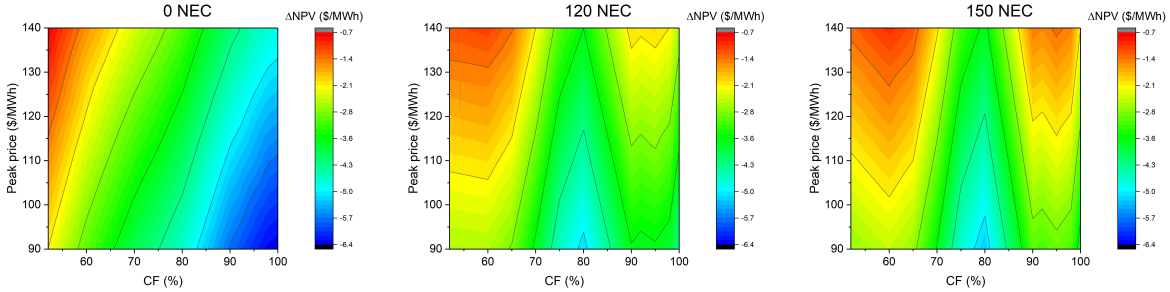


Figure 7.22: Sensitivity analysis of the capacity factor during off-peak electricity prices and peak electricity price variation, and their effect on NPV difference between the case of LOX storage with the case without LOX storage for an oxy-combustion process firing biomass costing $117/t for the schedule represented in Figure 7.4 b.

$$NPV[M\$] = -0.17CF^2 + 0.02\Delta Price^2_{electricity} + 31.35NEC + 30.03CF + \\ + 9.19\Delta Price_{electricity} - 5637.36 \quad (7.22)$$

Equations 7.21 and 7.22 have an R^2 of 0.9953 and 0.9975, respectively.
The NPV difference of the schedule with two LOX discharges is represented by Equation 7.23 and the single discharge by Equation 7.24.

$$\Delta NPV[\$/MWh] = -0.000309CF^3 + 0.08247CF^2 + 3.09 \times 10^{-5}\Delta Price^2_{electricity} + \\ + 10^{-5}CF \times \Delta Price_{electricity} + 0.00024NEC \times CF + 0.0007NEC - 7.28CF + \\ + 0.013\Delta Price_{electricity} + 205.18 \quad (7.23)$$

$$\Delta NPV[\$/MWh] = 1.24 \times 10^{-6}CF^3 + 1.17 \times 10^{-7}\Delta Price^3_{electricity} + 0.0012CF^2 + \\ - 2.56 \times 10^{-5}\Delta Price^2_{electricity} + 10^{-4}CF \times \Delta Price_{electricity} + 0.00053NEC \times CF + \\ - 0.034NEC - 0.306CF + 0.024\Delta Price_{electricity} + 8.36 \quad (7.24)$$

Equations 7.23 and 7.24 have an R^2 of 0.9562 and 0.8382, respectively.

7.3.3 To store, or not to store?

Storing LOX to enhance the flexibility of oxy-combustion is only advantageous under specific circumstances. This strategy requires night off-peak prices at least $80/MWh lower than peak electricity price regardless of the discharge cycle.
The single daily discharge cycle is more economically attractive when day off-peak prices are within $40/MWh of the peak electricity price since the plant operates at full capacity during this period. This operation mode increases the electricity sold to the grid during the day, when demand and electricity prices increase.
The double daily discharge cycle is more attractive when the day off-peak electricity prices are $80/MWh lower than the peak prices and biomass costs less than $90/t. This operation mode takes advantage of low day off-peak electricity prices to store LOX and discharge it during the second peak electricity price.
It is advantageous to operate with a single daily discharge in regions with flatter day electricity prices and low night electricity prices. Places with this electricity profile are Sweden, Norway, the Baltic states, France, and Switzerland during Summer[362, 373]. From these, the Baltic states achieve the highest peak/off-peak price difference, more than $40/MWh, which is still insufficient to make this practice economical. Hence, it may become advantageous for these regions to operate a flexible oxy-biomass plant without LOX storage. The electricity price profiles in most of these countries change during Winter, some to a two-peak profile, whilst others operate over a constant price[362, 373].
Regions with high electricity price variability throughout the day may benefit from implementing a double discharge cycle. This cycle takes advantage of existing low electricity prices to charge the storage tank, allowing it to be discharged during peak-times. This price variability is observed in Finland, Germany, and Austria during Summer; Sweden and the Baltic states during Winter; and the UK appears to peak twice throughout the year[362, 373]. The UK shows promise to use this storage option; however, Winter is more likely to provide a better revenue, since electricity is $40/MWh higher than during Summer[362]. Indeed, the afternoon peak-electricity price in the UK during Winter can be $88/MWh higher than the off-peak electricity price[362], making LOX storage more economical during this period. This double discharge operation mode has the benefit of requiring lower amounts of capital since the storage tank is smaller than the single discharge case. Indeed, multiple discharges throughout the day can be performed if the electricity price has a high daily fluctuation.

7.4 Conclusions

Flexible operation of oxy-combustion with LOX storage during off-peak electricity prices and discharge during peak electricity prices can be advantageous depending on the

region's electricity demand profile. Peak/ off-peak electricity price difference, fuel price, and capital availability are the primary factors affecting which mode of operation is more economically attractive.

A double discharge operation requires a smaller LOX tank, costing M$0.7 to erect, whilst a single discharge operation would require a M$1.7 tank. Hence, if access to capital is limited and the electricity price variation justifies LOX storage cycles, it is better to consider a multiple discharge option since it requires smaller storage tanks. However, it should be noted that the tanks are only 0.5 % and 1 % the total cost of the ASU for a double and single discharge operation, respectively. Supplying the required O_2 to burn the fuel whilst storing enough LOX to be used during peak times requires a larger ASU for the single discharge operation, increasing capital costs by 8 %.

The ASU's power consumption increases by 40 % when charging the LOX tank and decreases by 15 % during discharge for the double daily discharge cycle. During the single discharge cycle, the ASU's power consumption increases by 90 % when charging and decreases by 38 % when discharging. Hence, a high difference between peak and off-peak price must exist to make this operation economically attractive.

The single discharge cycle benefits from high, flat daily electricity prices, taking advantage of the large amounts of LOX stored overnight during low electricity prices. Night off-peak electricity prices must be $100/MWh lower than peak electricity prices to offset the higher power consumption during LOX charging.

The double discharge cycle benefits from a sizeable daily electricity price fluctuation, benefiting from low off-peak electricity prices to store LOX. However, this requires cheap off-peak electricity prices of at least $100/MWh lower than peak electricity prices to offset the increased power consumption of storing LOX.

Therefore, this strategy is unlikely to be used because of the extremely high electricity price difference that is required to offset the costs associated with the additional power consumed during LOX storage.

Chapter 8

Conclusions and future work recommendations

This work investigated oxy-combustion's potential to abate carbon dioxide (CO_2) emissions of an ultra-supercritical coal power plant. The model was developed in Aspen HYSYS and gPROMS based on the works of Raibhole and Sapali [147] for the air separation unit (ASU), Kunzemann [172] for the power plant, Posch and Haider [208] and Kolster et al. [66] for the gas processing unit (GPU), and Spero et al. [70] for the whole oxy-combustion process. An exergy destruction analysis was performed to identify thermodynamic inefficiencies and quantify the value of heat integration.

The high costs associated with carbon capture and storage (CCS) in the power sector result in high levelised costs of electricity. These costs make fossil fuel power plants fitted with CCS economically unattractive compared to other forms of electricity production. The thermodynamic and economic benefits of process integration were proven in Chapter 4. Here, the plant's thermodynamic efficiency improved whilst reducing the number of feedwater heaters. This strategy uses low-grade heat from the main compressors of the ASU and GPU instead of using cooling water, discarding it to the environment, thus reducing thermodynamic losses. Ultimately, this strategy improved the oxy-combustion's net efficiency by 3 % LHV whilst reducing CAPEX by 15 %.

However, it should be noted that a first-of-a-kind, large-capacity demonstration plant is unlikely to have such a high degree of heat integration. Indeed, this plant should operate more conservatively to provide both a safe operation and a more fundamental operational knowledge. Starting with this approach helps to identify critical aspects of the plant's operation, improving its efficiency and providing a safer path towards process integration.

The methodology proposed in Chapter 4 can be used in other power generation or storage technologies to provide a rational evaluation of heat integration strategies. Indeed, this methodology was later applied in Chapter 5, where the cryogenic-based GPU was

modified to a solvent-based capture unit using EDEA. This modification was proposed because the GPU was the least thermodynamically efficient unit.

Using EDEA to capture CO_2 from an oxy-combustion's exhaust was not a promising technology because it required low EDEA prices and a high degree of heat integration. The main compressor can provide low-grade heat to reduce the capture unit's operating costs; however, this low-grade heat will become unavailable to pre-heat the boiler's feedwater. Furthermore, some amount of steam must be extracted from the turbines to satisfy the required heat to regenerate EDEA, reducing the plant's gross power generation. Nonetheless, it was determined that this unit is 1 % more thermodynamically efficient than the cryogenic distillation GPU whilst reducing CAPEX by 9 %.

There are some caveats concerning this capture process. Firstly, it requires bulk EDEA cost dropping to one-tenth of the current price, approaching that of MEA. Secondly, the preliminary nature of this study indicates a higher error associated with the results. Thus, detailed kinetic studies are required to improve the techno-economical analysis of this option. However, the possible cost-reduction of cryogenic GPUs must also be considered, rendering the EDEA-based GPU less promising to reduce the LCOE of an oxy-combustion process than a cryogenic-based GPU. Furthermore, the higher capture rates and CO_2 purity obtained from a cryogenic distillation GPU makes it promising if there is a future market for high-purity CO_2.

The current plans for a decarbonised electricity system that favours renewable energy sources displace fossil fuel use. Indeed, coal plants are being substituted by cleaner natural gas plants, which are expected to be substituted by renewable sources over time. Hence, biomass is expected to play a crucial role by providing carbon-neutral thermal energy used as heat or converted to electricity.

Switching coal to biomass further increases the costs of an already expensive venture due to biomass's lower heating values and mineral composition. This fuel switch requires larger boilers for the same power output and changing the maintenance schedules to overcome the issues from biomass's different mineral composition. Nonetheless, Drax already operates dedicated biomass plants for power generation in North Yorkshire, proving the viability of this technology. However, this venture still requires government subsidies to be economically feasible.

Unlike the power sector, completely decarbonising industrial activity with CCS raises concerns regarding product quality. Applying CCS directly to an industrial process will be problematic due to the high variation of CO_2 concentration from several point sources. Furthermore, there may be space constraints which can complicate the erection of a CO_2 capture unit. Therefore, CO_2 emissions from this sector must be offset to achieve the 1.5 °C target by 2050.

Bioenergy with CCS (BECCS) captures biogenic CO_2 and stores it in a suitable reservoir,

effectively removing atmospheric CO_2. The services provided by BECCS were assessed in Chapter 6 for oxy-combustion by proposing the auction of negative emissions as credits to offset industrial emissions whilst simultaneously decarbonising electricity.
Burning biomass under oxy-combustion conditions has been proven[225, 226, 228–230], suggesting that biomass will behave similarly to coal under these conditions. Furthermore, the higher oxygen content generally contained in biomass demands a lower amount of oxygen than coal, reducing the ASU size. However, this effect is surpassed by larger fuel flowrates to generate the same amount of power, which increases the oxygen demand, increasing the ASU size. Nonetheless, oxy-combustion presents the opportunity to capture higher degrees of CO_2 than other capture technologies, making this venture particularly suited to auction negative emission credits (NEC).
Auctioning NEC above \$90/t_{CO2} provides subsidy-free, carbon-neutral electricity that is competitive with other renewable sources. This technology can offset 18 Mt/yr of industrial CO_2 emissions in the UK using five oxy-BECCS plants with a 500 MW net capacity. The number of oxy-BECCS plants required can be reduced if they possess larger capacity, which is consistent with the UK's active coal plants. Globally, this offset potential increases to 9 Gt_{CO_2}/yr of industrial emissions, requiring 3000 oxy-BECCS units at 500 MW_{Net}. The amount of biomass required to satisfy these units was determined to be within sustainable levels, but this should be strictly regulated by local and international authorities to prevent an unsustainable use of biomass resources. However, the NEC required to provide subsidy-free electricity is unlikely to be purchased by industry because it will still be more competitive to apply CCS directly to their processes. Hence, government subsidies of 35 – 50 \$/t_{CO_2} will be required to implement this scheme.
Re-furbishing the existing coal power plants to dedicated oxy-BECCS plants can reduce capital costs by using the existing infrastructure. Fitting oxy-combustion to existing plants was demonstrated by the Callide Oxyfuel project[70]; however, this results in more CO_2 leakages, reducing the benefit of auctioning NECs.
Operating an oxy-BECCS plant flexibly by following demand with and without liquid oxygen storage (LOX) was assessed in Chapter 7. This operation relies on daily electricity price fluctuation, posing considerable variations across countries/ regions. This is particularly true for LOX storage scenarios, requiring a peak/ off-peak price difference greater than \$80/MWh to become economically attractive.
Adding LOX storage will require a larger ASU to store sufficient oxygen during low electricity prices to satisfy the power plant's demand during high electricity prices. The tanks required to store LOX increase the CAPEX; however, they are marginal compared to the ASU's total cost. Nonetheless, erecting a LOX tank may require the availability of a large land area, depending on the charge/ discharge cycle chosen.
The UK appears to have a significant daily electricity price variation to justify the choice

of a double (or more) discharge cycle. However, this venture requires a very high peak/ off-peak electricity price difference to be attractive, which does not appear throughout the year. Indeed, high price differences are more common during Winter than Summer, making this option only beneficial during certain seasons.

Other countries that follow a flatter electricity price during the day may benefit from a single LOX discharge option. However, this venture will require a high peak/ off-peak electricity price difference to be attractive, similar to the double discharge case.

It is unlikely that a new-built plant would want to operate flexibly during its first years of operation, as high revenue during this period is critical to justify these ventures' high capital requirements. However, newly built plants will be expected to operate flexibly due to current electricity demand profiles, hindering the profitability of oxy-combustion plants. Hence, new business models that incentivise flexible operation are required to build new, high-efficiency plants for this type of operation.

There are two ways to achieve this flexibility without new business models. First, retrofitting existing plants that are already paid-for would enable them to continue operation without being prematurely decommissioned. This would allow the plant operators to get more profits whilst preventing loss of jobs, albeit at the cost of retrofitting the unit. However, this approach excludes new, high-efficiency plants that could provide a better service to the electricity system.

The second approach requires building new oxy-BECCS plants operated at base-load during the first years of operation. Then, the plant can start operating in a demand-following manner, dispatching electricity when required. LOX storage tanks can also be erected if the electricity price difference becomes sufficiently high to justify this venture.

The caveat of these approaches is that the ASU and GPU limit the flexible operation of oxy-combustion. It is possible to reduce the plant's capacity to 50 %, but it requires several compression trains to prevent excessive power consumption from recycling the gas back to the compressors. Another limitation of the ASU lies in the cold box, which requires enough air flow to produce the required oxygen.

There is an excellent opportunity to improve oxy-combustion efficiency through the concurrent application of the approaches studied herein. Coupling high degrees of heat integration with flexible operation may prove challenging; however, this may be managed by a careful design and a back-up plan.

It is recommended that oxy-combustion technology be built at commercial-scale to provide plant operators with the necessary insight to further improve the operational efficiency and detect improvement opportunities. Afterwards, process integration should be considered as a means to improve the plant's efficiency.

A successful and purposeful implementation of oxy-BECCS requires cradle-to-grave life-cycle assessments to consider all CO_2 equivalent emission sources from the operation.

This assessment would quantify the amount of negative emissions, if any, occurring during this plant's operation. Quantifying the NEC available for auction is thus intrinsically tied to the life-cycle assessment to prevent any misattributed credits. Hence, governments should carefully regulate oxy-BECCS plants to avoid such eventualities.
Carbon capture and utilisation (CCU) may provide additional benefits by converting CO_2 into products with high economic value. However, this option should be explored with extreme caution to avoid underestimating the CO_2 emissions associated with this new product's manufacture.
It may be valuable to perform computer simulations of oxy-combustion for industrial processes. This is particularly true for the cement sector, which may greatly benefit from updated process simulations following the success of the CEMCAP project. This venture demonstrated that oxy-combustion could be used in the cement process to capture CO_2 whilst maintaining the required product's properties[374]. Performing several computer simulation analyses would identify process improvement opportunities, further reduce costs, and make this technology closer to widespread deployment.
Surrogate models of oxy-combustion applied to the power sector can be developed using the results from this work, enabling efficient integration of this technology on whole system models of the electricity grid. This would identify possible cost-effective deployment strategies for CO_2 abatement at a country/ region level with greater degrees of confidence.

Bibliography

[1] Jennifer Wilcox. *Carbon Capture*. Springer-Verlag New York, New York, first edition, 2012. ISBN 978-1-4614-2215-0. URL https://link.springer.com/book/10.1007%2F978-1-4614-2215-0.

[2] Ottmar Edenhofer, Ramón Pichs-Madruga, Youba Sokona, Susanne Kadner, Jan C. Minx, Steffen Brunner, Shardul Agrawala, Giovanni Baiocchi, Igor Alexeyevich Bashmakov, Gabriel Blanco, John Broome, Thomas Bruckner, Mercedes Bustamante, Leon Clarke, Mariana Conte Grand, Felix Creutzig, Xochitl Cruz-Nú nez, Shobhakar Dhakal, Navroz K. Dubash, Patrick Eickemeier, Ellie Farahani, Manfred Fischedick, Marc Fleurbaey, Reyer Gerlag, Luis Gómez-Echeverri, Sujata Gupta, Jochen Harnisch, Kejun Jiang, Frank Jotzo, Sivan Kartha, Stephan Klasen, Charles Kolstad, Volker Krey, Howard Kunreuther, Oswaldo Lucon, Omar Masera, Yacob Mulugetta, Richard Norgaard, Anthony Patt, Nijavalli H. Ravindranath, Keywan Riahi, Joyashree Roy, Ambuj Sagar, Roberto Schaeffer, Steffen Schlömer, Karen Seto, Kristin Seyboth, Ralph Sims, Pete Smith, Eswaran Somanathan, Robert Stavins, Christoph von Stechow, Thomas Sterner, Taishi Sugiyama, Sangwon Suh, Kevin Urama, Diana Ürge Vorsatz, Anthony Venables, David G. Victor, Elke Weber, Dadi Zhou, Ji Zou, and Timm Zwickel. Climate Change 2014: Mitigation of Climate Change. Contribution of Working Group III to the Fifth Assessment Report of the Intergovernmental Panel on Climate Change. Technical summary, Cambridge University Press, Cambridge, United Kingdom and New York, NY, USA, 2014.

[3] C. Le Quéré, R. Moriarty, R. M. Andrew, J. G. Canadell, S. Sitch, J. I. Korsbakken, P. Friedlingstein, G. P. Peters, R. J. Andres, T. A. Boden, R. A. Houghton, J. I. House, R. F. Keeling, P. Tans, A. Arneth, D. C. E. Bakker, L. Barbero, L. Bopp, J. Chang, F. Chevallier, L. P. Chini, P. Ciais, M. Fader, R. A. Feely, T. Gkritzalis, I. Harris, J. Hauck, T. Ilyina, A. K. Jain, E. Kato, V. Kitidis, K. Klein Goldewijk, C. Koven, P. Landschützer, S. K. Lauvset, N. Lefèvre, A. Lenton, I. D. Lima, N. Metzl, F. Millero, D. R. Munro, A. Murata, J. E. M. S. Nabel, S. Nakaoka, Y. Nojiri, K. O'Brien, A. Olsen, T. Ono, F. F. Pérez, B. Pfeil, D. Pierrot, B. Poulter, G. Rehder, C. Rödenbeck, S. Saito, U. Schuster, J. Schwinger, R. Séférian, T. Steinhoff, B. D. Stocker, A. J. Sutton, T. Takahashi, B. Tilbrook, I. T. van der Laan-Luijkx, G. R. van der Werf, S. van Heuven, D. Vandemark, N. Viovy, A. Wiltshire, S. Zaehle, and N. Zeng. Global Carbon Budget 2015. *Earth System Science Data*, 7(2):349–396, 2015. doi: 10.5194/essd-7-349-2015. URL https://www.earth-syst-sci-data.net/7/349/2015/.

[4] Jos G. J. Olivier, Greet Janssens-Maenhout, Marilena Muntean, and Jeroen A. H. W. Peters. Trends in global CO_2 emissions. Report 2315, The Hague: PBL

Netherlands Environmental Assessment Agency, Ispra: European Commission, Joint Research Centre, 2016.

[5] C. Le Quéré, R. M. Andrew, P. Friedlingstein, S. Sitch, J. Pongratz, A. C. Manning, J. I. Korsbakken, G. P. Peters, J. G. Canadell, R. B. Jackson, T. A. Boden, P. P. Tans, O. D. Andrews, V. K. Arora, D. C. E. Bakker, L. Barbero, M. Becker, R. A. Betts, L. Bopp, F. Chevallier, L. P. Chini, P. Ciais, C. E. Cosca, J. Cross, K. Currie, T. Gasser, I. Harris, J. Hauck, V. Haverd, R. A. Houghton, C. W. Hunt, G. Hurtt, T. Ilyina, A. K. Jain, E. Kato, M. Kautz, R. F. Keeling, K. Klein Goldewijk, A. Körtzinger, P. Landschützer, N. Lefèvre, A. Lenton, S. Lienert, I. Lima, D. Lombardozzi, N. Metzl, F. Millero, P. M. S. Monteiro, D. R. Munro, J. E. M. S. Nabel, S.-I. Nakaoka, Y. Nojiri, X. A. Padin, A. Peregon, B. Pfeil, D. Pierrot, B. Poulter, G. Rehder, J. Reimer, C. Rödenbeck, J. Schwinger, R. Séférian, I. Skjelvan, B. D. Stocker, H. Tian, B. Tilbrook, F. N. Tubiello, I. T. van der Laan-Luijkx, G. R. van der Werf, S. van Heuven, N. Viovy, N. Vuichard, A. P. Walker, A. J. Watson, A. J. Wiltshire, S. Zaehle, and D. Zhu. Global Carbon Budget 2017. *Earth System Science Data*, 10(1):405 – 448, 2018. doi: 10.5194/essd-10-405-2018. URL https://www.earth-syst-sci-data.net/10/405/2018/.

[6] National Academies of Sciences, Engineering, and Medicine. *Negative Emissions Technologies and Reliable Sequestration: A Research Agenda*. The National Academies Press, Washington, DC, 2019. ISBN 978-0-309-48452-7. doi: 10.17226/25259. URL https://www.nap.edu/catalog/25259/negative-emissions-technologies-and-reliable-sequestration-a-research-agenda.

[7] Paul N. Pearson and Martin R. Palmer. Atmospheric carbon dioxide concentrations over the past 60 million years. *Nature*, 406:695, aug 2000. URL http://dx.doi.org/10.1038/3502100010.1038/35021000.

[8] WMO Statement on the state of the global climate in 2017. Technical Report WMO- No. 1212, World Meteorological Organization (WMO), 2018.

[9] L. Cirbus Sloan and D. K. Rea. Atmospheric carbon dioxide and early Eocene climate: A general circulation modeling sensitivity study. *Palaeogeography, Palaeoclimatology, Palaeoecology*, 119(3):275 – 292, 1996. ISSN 0031-0182. doi: https://doi.org/10.1016/0031-0182(95)00012-7. URL http://www.sciencedirect.com/science/article/pii/0031018295000127.

[10] National Academies. Joint science academies' statement: Global response to climate change, 2005. URL http://nationalacademies.org/onpi/06072005.pdf. Accessed 10 July 2019.

[11] American Association for the Advancement of Science. AAS Board statement on Climate Change, 2006. URL https://www.aaas.org/resources/aaas-board-releases-new-statement-climate-change. Accessed 10 July 2019.

[12] National Academy of Sciences. Understanding and Responding to Climate Change, 2008. URL http://dels.nas.edu/resources/static-assets/materials-based-on-reports/booklets/climate_change_2008_final.pdf. Accessed 10 July 2019.

[13] Svante Arrhenius. XXXI. On the influence of carbonic acid in the air upon the temperature of the ground. *The London, Edinburgh, and Dublin Philosophical Magazine and Journal of Science*, 41(251):237–276, 1896. doi: 10.1080/14786449608620846. URL https://doi.org/10.1080/14786449608620846.

[14] Adolf Stips, Diego Macias, Clare Coughlan, Elisa Garcia-Gorriz, and X San Liang. On the causal structure between CO_2 and global temperature. *Scientific Reports*, 6:21691, 2016. ISSN 2045-2322. doi: 10.1038/srep21691. URL http://www.ncbi.nlm.nih.gov/pmc/articles/PMC4761980/.

[15] Colin N. Waters, Jan Zalasiewicz, Colin Summerhayes, Anthony D. Barnosky, Clément Poirier, Agnieszka Gałuszka, Alejandro Cearreta, Matt Edgeworth, Erle C. Ellis, Michael Ellis, Catherine Jeandel, Reinhold Leinfelder, J. R. McNeill, Daniel deB. Richter, Will Steffen, James Syvitski, Davor Vidas, Michael Wagreich, Mark Williams, An Zhisheng, Jacques Grinevald, Eric Odada, Naomi Oreskes, and Alexander P. Wolfe. The Anthropocene is functionally and stratigraphically distinct from the Holocene. *Science*, 351(6269), 2016. ISSN 0036-8075. doi: 10.1126/science.aad2622. URL http://science.sciencemag.org/content/351/6269/aad2622.

[16] United Nations Framework Convention on Climate Change. Kyoto Protocol, 2015. URL http://unfccc.int/kyoto{_}protocol/items/2830.php.

[17] Laura Aylett, Tom Bain, Anindya Bhattacharya, Ephraim Broschkowski, Erin Cooper, Michel Cornet, Tom Counsell, Ruth Curran, Davide D'Ambrosio, Bernd Hezel, Nicole Kalas, Sophie Hartfield, Benoit Lefevre, Brijesh Manan, Kerenza McFaul, Julien Pestiaux, Anna Stephenson, Alexandre Strapasson, Erica Thompson, Jeremy Woods, Markus Wrobel, and Zhang Bo. The Global Calculator, 2015. URL http://globalcalculator.org/.

[18] European Commission. The Paris Protocol – A blueprint for tackling global climate change beyond 2020. Technical report, European Commission, 2015.

[19] Michael McCarthy. Was this the heatwave that finally ended climate denial? https://www.theguardian.com/commentisfree/2018/aug/01/heatwave-climate-denial-summer-2018-sceptics. Accessed October 2018.

[20] Kari Marie Norgaard. "We Don't Really Want to Know": Environmental Justice and Socially Organized Denial of Global Warming in Norway. *Organization & Environment*, 19(3):347–370, 2006. doi: 10.1177/1086026606292571. URL https://doi.org/10.1177/1086026606292571.

[21] V. Masson-Delmotte, P. Zhai, H. O. Pörtner, D. Roberts, J. Skea, P. R. Shukla, A. Pirani, Y. Chen, S. Connors, M. Gomis, E. Lonnoy, J. B. R. Matthews, W. Moufouma-Okia, C. Péan, R. Pidcock, N. Reay, M. Tignor, T. Waterfield, and X. Zhou. Global warming of 1.5 ^{o}C. An IPCC special report on the impacts of global warming of 1.5 ^{o}C above pre-industrial levels and related global greenhouse gas emission pathways, in the context of strengthening the global response to the threat of climate change, sustainable development, and efforts to eradicate poverty. Technical report, IPCC, 2018.

[22] International Energy Agency. World Energy Outlook 2017, 2017. URL https://www.oecd-ilibrary.org/content/publication/weo-2017-en.

[23] Sam Morgan. 18 EU countries now support 2050 carbon neutrality goal, June 2019. URL https://www.euractiv.com/section/climate-strategy-2050/news/18-eu-countries-sign-up-to-2050-carbon-neutrality-goal/. Accessed 30 June 2019.

[24] Jon Stone. EU member states swing behind 2050 carbon neutral target, June 2019. URL https://www.independent.co.uk/news/world/europe/eu-carbon-neutral-target-2050-climate-change-environment-a8962271.html. Accessed 30 June 2019.

[25] World Bank Group. Renewable energy consumption (% of total final energy consumption), 2019. URL https://data.worldbank.org/indicator/EG.FEC.RNEW.ZSl. Accessed 09 July 2019.

[26] Pathways from Paris: Assessing the INDC opportunity. Technical report, Energy Transitions Commission, 2016.

[27] Renewables 2018 Analysis and Forecasts to 2023. Technical report, IEA, 2018.

[28] UK climate action following the Paris Agreement. Technical report, Committee on Climate Change, 2016.

[29] Reducing UK emissions – 2018 Progress Report to Parliament. Technical report, Committee on Climate Change, 2018.

[30] National Infrastructure Assessment. Technical report, National Infrastructure Commission, 2018.

[31] GOV.UK. Press release - PM Theresa May: we will end UK contribution to climate change by 2050, June 2019. URL https://www.gov.uk/government/news/pm-theresa-may-we-will-end-uk-contribution-to-climate-change-by-2050.

[32] Sky News. UK to become first G7 nation to make zero net emissions law, June 2019. URL https://news.sky.com/story/uk-to-produce-net-zero-harmful-emissions-by-2050-theresa-may-will-pledge-11740022.

[33] Roger Harrabin. Climate change: UK government to commit to 2050 target, June 2019. URL https://www.bbc.co.uk/news/science-environment-48596775.

[34] The Guardian. The Guardian view on net zero emissions: better late than never, June 2019. URL https://www.theguardian.com/commentisfree/2019/jun/12/the-guardian-view-on-net-zero-emissions-better-late-than-never.

[35] Clara F. Heuberger, Iain Staffell, Nilay Shah, and Niall Mac Dowell. Quantifying the value of CCS for the future electricity system. *Energy & Environmental Science*, 9:2497–2510, 2016. doi: 10.1039/C6EE01120A. URL http://dx.doi.org/10.1039/C6EE01120A.

[36] Manfred Lenzen, Bonnie McBain, Ted Trainer, Silke Jütte, Olivier Rey-Lescure, and Jing Huang. Simulating low-carbon electricity supply for Australia. *Applied Energy*, 179:553 – 564, 2016. ISSN 0306-2619. doi: https://doi.org/10.1016/j.apenergy.2016.06.151. URL http://www.sciencedirect.com/science/article/pii/S0306261916309400.

[37] Clara F. Heuberger, Iain Staffell, Nilay Shah, and Niall Mac Dowell. A systems approach to quantifying the value of power generation and energy storage technologies in future electricity networks. *Computers & Chemical Engineering*, 107:247 – 256, 2017. ISSN 0098-1354. doi: https://doi.org/10.1016/j.compchemeng.2017.05.012. URL http://www.sciencedirect.com/science/article/pii/S0098135417302119.

[38] Clara Franziska Heuberger and Niall Mac Dowell. Real-World Challenges with a Rapid Transition to 100% Renewable Power Systems. *Joule*, 2(3):367 – 370, 2018. ISSN 2542-4351. doi: https://doi.org/10.1016/j.joule.2018.02.002. URL http://www.sciencedirect.com/science/article/pii/S2542435118300485.

[39] Nestor A. Sepulveda, Jesse D. Jenkins, Fernando J. de Sisternes, and Richard K. Lester. The role of firm low-carbon electricity resources in deep decarbonization of power generation. *Joule*, 2(11):2403 – 2420, 2018. ISSN 2542-4351. doi: https://doi.org/10.1016/j.joule.2018.08.006. URL http://www.sciencedirect.com/science/article/pii/S2542435118303866.

[40] BP Statistical Review of World Energy. Technical report, BP, June 2018.

[41] Coal Power Plant Post-Retirement Options. https://www.powermag.com/coal-power-plant-post-retirement-options/?pagenum=1. Accessed October 2018.

[42] S. Stoll-Kleemann, Tim O'Riordan, and Carlo C. Jaeger. The psychology of denial concerning climate mitigation measures: evidence from Swiss focus groups. *Global Environmental Change*, 11(2):107 – 117, 2001. ISSN 0959-3780. doi: https://doi.org/10.1016/S0959-3780(00)00061-3. URL http://www.sciencedirect.com/science/article/pii/S0959378000000613.

[43] Rachael Shwom, David Bidwell, Amy Dan, and Thomas Dietz. Understanding U.S. public support for domestic climate change policies. *Global Environmental Change*, 20(3):472 – 482, 2010. ISSN 0959-3780. doi: https://doi.org/10.1016/j.gloenvcha.2010.02.003. URL http://www.sciencedirect.com/science/article/pii/S0959378010000099. Governance, Complexity and Resilience.

[44] Flexibility in thermal power plants – With a focus on existing coal-fired power plants. Technical report, Agora Energiewende, 2017.

[45] Thermal Power Plant Flexibility. Technical report, Clean Energy Ministerial Campaign, 2018.

[46] Status of Power System Transformation. Technical report, IEA, 2018.

[47] B. J. P. Buhre, L. K. Elliott, C. D. Sheng, R. P. Gupta, and T. F. Wall. Oxy-fuel combustion technology for coal-fired power generation. *Progress in Energy and Combustion Science*, 31(4):283 – 307, 2005. ISSN 0360-1285. doi: https:

//doi.org/10.1016/j.pecs.2005.07.001. URL http://www.sciencedirect.com/science/article/pii/S0360128505000225.

[48] Niall Mac Dowell, Nick Florin, Antoine Buchard, Jason Hallett, Amparo Galindo, George Jackson, Claire S. Adjiman, Charlotte K. Williams, Nilay Shah, and Paul Fennell. An overview of CO_2 capture technologies. *Energy & Environmental Science*, 3:1645–1669, 2010. doi: 10.1039/C004106H. URL http://dx.doi.org/10.1039/C004106H.

[49] Matthew E. Boot-Handford, Juan C. Abanades, Edward J. Anthony, Martin J. Blunt, Stefano Brandani, Niall Mac Dowell, José R. Fernández, Maria-Chiara Ferrari, Robert Gross, Jason P. Hallett, R. Stuart Haszeldine, Philip Heptonstall, Anders Lyngfelt, Zen Makuch, Enzo Mangano, Richard T. J. Porter, Mohamed Pourkashanian, Gary T. Rochelle, Nilay Shah, Joseph G. Yao, and Paul S. Fennell. Carbon capture and storage update. *Energy & Environmental Science*, 7:130–189, 2014. doi: 10.1039/C3EE42350F. URL http://dx.doi.org/10.1039/C3EE42350F.

[50] Clara F Heuberger, Iain Staffell, Nilay Shah, and Niall Mac Dowell. Impact of myopic decision-making and disruptive events in power systems planning. *Nature Energy*, 2018. doi: https://doi.org/10.1038/s41560-018-0159-3.

[51] Terry F. Wall. Combustion processes for carbon capture. *Proceedings of the Combustion Institute*, 31(1):31 – 47, 2007. ISSN 1540-7489. doi: https://doi.org/10.1016/j.proci.2006.08.123. URL http://www.sciencedirect.com/science/article/pii/S1540748906003865.

[52] Martin Blunt. Carbon Dioxide Storage. Technical Report 4, Grantham Institute for Climate Change, 2010.

[53] S. M. Benson. Carbon Capture and Storage. In *Global Energy Assessment - Toward a Sustainable Future*, chapter 13, pages 993 – 1068. Cambridge University Press, Cambridge, UK and New York, NY, USA and the International Institute for Applied Systems Analysis, Laxenburg, Austria, Cambridge, UK, 2012. URL www.globalenergyassessment.org.

[54] The future of fossil fuels: How to steer fossil fuel use in a transition to a low-carbon energy system. Technical report, ETC, 2017.

[55] Just Transition of the Workforce, and the Creation of Decent Work and Quality Jobs. Technical report, UNFCCC, 2016.

[56] Richard Beavis, Jonathan Forsyth, Emma Roberts, Bai Song, Gary Combes, Jim Abbott, Norman Macleod, Elaine Vass, Mike Davies, and Ian Barton. A step-change sour shift process for improving the efficiency of IGCC with CCS. In *Energy Procedia 37*, pages 2256– 2264, 2013. doi: 10.1016/j.egypro.2013.06.106.

[57] Xiangping Zhang, Truls Gundersen, Simon Roussanaly, Amy L. Brunsvold, and Suojiang Zhang. Carbon chain analysis on a coal IGCC - CCS system with flexible multi-products. *Fuel Processing Technology*, 108(Special Issue of APCRE11):146–153, 2013. doi: 10.1016/j.fuproc.2012.05.012.

[58] Qin Chen, Ashok Rao, and Scott Samuelsen. H_2 coproduction in IGCC with CCS via coal and biomass mixture using advanced technologies. *Applied Energy*, 118: 258–270, 2014. doi: 10.1016/j.apenergy.2013.12.051.

[59] Sina Rezvani, Ye Huang, David McIlveen-Wright, Neil Hewitt, and Jayanta Deb Mondol. Comparative assessment of coal fired IGCC systems with CO_2 capture using physical absorption, membrane reactors and chemical looping. *Fuel*, 88 (12):2463–2472, 2009. doi: 10.1016/j.fuel.2009.04.021.

[60] F. Vega, A. Sanna, M. M. Maroto-Valer, B. Navarrete, and D. Abad-Correa. Study of the MEA degradation in a CO_2 capture process based on partial oxy-combustion approach. *International Journal of Greenhouse Gas Control*, 54:160 – 167, 2016. ISSN 1750-5836. doi: https://doi.org/10.1016/j.ijggc.2016.09.007. URL http://www.sciencedirect.com/science/article/pii/S1750583616305886.

[61] Giorgio Cau, Vittorio Tola, Francesca Ferrara, Andrea Porcu, and Alberto Pettinau. CO_2-free coal-fired power generation by partial oxy-fuel and post-combustion CO_2 capture: Techno-economic analysis. *Fuel*, 214:423 – 435, 2018. ISSN 0016-2361. doi: https://doi.org/10.1016/j.fuel.2017.10.023. URL http://www.sciencedirect.com/science/article/pii/S0016236117312693.

[62] Chungen Yin and Jinyue Yan. Oxy-fuel combustion of pulverized fuels: Combustion fundamentals and modeling. *Applied Energy*, 162:742 – 762, 2016. ISSN 0306-2619. doi: https://doi.org/10.1016/j.apenergy.2015.10.149. URL http://www.sciencedirect.com/science/article/pii/S0306261915013914.

[63] Oxyfuel Combustion of Pulverised Coals. Technical Report 2010/07, IEAGHG, .

[64] Terry Wall, Rohan Stanger, and Stanley Santos. Demonstrations of coal-fired oxy-fuel technology for carbon capture and storage and issues with commercial deployment. *International Journal of Greenhouse Gas Control*, 5:S5 – S15, 2011. ISSN 1750-5836. doi: https://doi.org/10.1016/j.ijggc.2011.03.014. URL http://www.sciencedirect.com/science/article/pii/S1750583611000442. Oxyfuel Combustion Technology - Working Toward Demonstration and Commercialisation.

[65] Chao Fu, Rahul Anantharaman, Kristin Jordal, and Truls Gundersen. Thermal efficiency of coal-fired power plants: From theoretical to practical assessments. *Energy Conversion and Management*, 105:530 – 544, 2015. ISSN 0196-8904. doi: https://doi.org/10.1016/j.enconman.2015.08.019. URL http://www.sciencedirect.com/science/article/pii/S0196890415007657.

[66] Clea Kolster, Evgenia Mechleri, Sam Krevor, and Niall Mac Dowell. The role of CO_2 purification and transport networks in carbon capture and storage cost reduction. *International Journal of Greenhouse Gas Control*, 58:127 – 141, 2017. ISSN 1750-5836. doi: https://doi.org/10.1016/j.ijggc.2017.01.014. URL http://www.sciencedirect.com/science/article/pii/S1750583617300658.

[67] Nicholas Florin and Paul Fennel. Carbon capture technology: future fossil fuel use and mitigating climate change. Technical Report 3, Grantham Institute for Climate Change, 2010.

[68] A. R. Smith and J. Klosek. A review of air separation technologies and their integration with energy conversion processes. *Fuel Processing Technology*, 70(2): 115 – 134, 2001. ISSN 0378-3820. doi: https://doi.org/10.1016/S0378-3820(01)00131-X. URL http://www.sciencedirect.com/science/article/pii/S037838200100131X.

[69] James G. Speight. *Coal-Fired Power Generation Handbook*. John Wiley & Sons, Inc. and Scrivener Publishing LLC., 2013.

[70] Chris Spero, Franco Montagner, Lyle Chapman, Doug Ranie, and Toshihiko Yamada. Callide Oxyfuel Project – Lessons Learned. Technical report, Global CCS Institute, 2014.

[71] Sabine Fuss, Josep G. Canadell, Glen P. Peters, Massimo Tavoni, Robbie M. Andrew, Philippe Ciais, Robert B. Jackson, Chris D. Jones, Florian Kraxner, Nebosja Nakicenovic, Corinne Le Quéré, Michael R. Raupach, Ayyoob Sharifi, Pete Smith, and Yoshiki Yamagata. Betting on negative emissions. *Nature Climate Change*, 4:850, Sep 2014. URL https://doi.org/10.1038/nclimate2392.

[72] Paweł Gładysz and Andrzej Ziębik. Environmental analysis of bio-CCS in an integrated oxy-fuel combustion power plant with CO_2 transport and storage. *Biomass and Bioenergy*, 85:109 – 118, 2016. ISSN 0961-9534. doi: https://doi.org/10.1016/j.biombioe.2015.12.008. URL http://www.sciencedirect.com/science/article/pii/S0961953415301811.

[73] Sabine Fuss, William F Lamb, Max W Callaghan, Jérôme Hilaire, Felix Creutzig, Thorben Amann, Tim Beringer, Wagner de Oliveira Garcia, Jens Hartmann, Tarun Khanna, Gunnar Luderer, Gregory F Nemet, Joeri Rogelj, Pete Smith, José Luis Vicente Vicente, Jennifer Wilcox, Maria del Mar Zamora Dominguez, and Jan C Minx. Negative emissions—part 2: Costs, potentials and side effects. *Environmental Research Letters*, 13(6):063002, may 2018. doi: 10.1088/1748-9326/aabf9f. URL https://doi.org/10.1088%2F1748-9326%2Faabf9f.

[74] Jan C Minx, William F Lamb, Max W Callaghan, Sabine Fuss, Jérôme Hilaire, Felix Creutzig, Thorben Amann, Tim Beringer, Wagner de Oliveira Garcia, Jens Hartmann, Tarun Khanna, Dominic Lenzi, Gunnar Luderer, Gregory F Nemet, Joeri Rogelj, Pete Smith, Jose Luis Vicente Vicente, Jennifer Wilcox, and Maria del Mar Zamora Dominguez. Negative emissions—part 1: Research landscape and synthesis. *Environmental Research Letters*, 13(6):063001, may 2018. doi: 10.1088/1748-9326/aabf9b. URL https://doi.org/10.1088%2F1748-9326%2Faabf9b.

[75] Mai Bui, Claire S. Adjiman, André Bardow, Edward J. Anthony, Andy Boston, Solomon Brown, Paul S. Fennell, Sabine Fuss, Amparo Galindo, Leigh A. Hackett, Jason P. Hallett, Howard J. Herzog, George Jackson, Jasmin Kemper, Samuel Krevor, Geoffrey C. Maitland, Michael Matuszewski, Ian S. Metcalfe, Camille Petit, Graeme Puxty, Jeffrey Reimer, David M. Reiner, Edward S. Rubin, Stuart A. Scott, Nilay Shah, Berend Smit, J. P. Martin Trusler, Paul Webley, Jennifer Wilcox, and Niall Mac Dowell. Carbon capture and storage (CCS): the way forward. *Energy & Environmental Science*, 11:1062–1176, 2018. doi: 10.1039/C7EE02342A. URL http://dx.doi.org/10.1039/C7EE02342A.

[76] Howard Herzog, Baldur Eliasson, and Olav Kaarstad. Capturing Greenhouse Gases. *Scientific American*, 282(2):72 – 79, 2000.

[77] D. J. Dillon, V. White, R. J. Allam, R. A. Wall, and J. Gibbins. Oxy Combustion Processes for CO_2 Capture from Power Plant. Technical Report 2005/9, Mitsui Babcock Energy Limited, 2005.

[78] Yann Le Moullec. Assessment of carbon capture thermodynamic limitation on coal-fired power plant efficiency. *International Journal of Greenhouse Gas Control*, 7:192 – 201, 2012. ISSN 1750-5836. doi: https://doi.org/10.1016/j.ijggc.2011.10.002. URL http://www.sciencedirect.com/science/article/pii/S1750583611001848.

[79] A. Chansomwong, K. E. Zanganeh, A. Shafeen, P. L. Douglas, E. Croiset, and L. A. Ricardez-Sandoval. Dynamic modelling of a CO_2 capture and purification unit for an oxy-coal-fired power plant. *International Journal of Greenhouse Gas Control*, 22:111 – 122, 2014. ISSN 1750-5836. doi: https://doi.org/10.1016/j.ijggc.2013.12.025. URL http://www.sciencedirect.com/science/article/pii/S1750583613004581.

[80] Berend Smit. Carbon Capture and Storage: introductory lecture. *Faraday Discuss.*, 192:9–25, 2016. doi: 10.1039/C6FD00148C. URL http://dx.doi.org/10.1039/C6FD00148C.

[81] Paul Upham and Thomas Roberts. Public perceptions of CCS in context: Results of NearCO2 focus groups in the UK, Belgium, the Netherlands, Germany, Spain and Poland. *Energy Procedia*, 4:6338 – 6344, 2011. ISSN 1876-6102. doi: https://doi.org/10.1016/j.egypro.2011.02.650. URL http://www.sciencedirect.com/science/article/pii/S1876610211009295. 10th International Conference on Greenhouse Gas Control Technologies.

[82] Vayos Karayannis, Georgios Charalampides, and Evangelia Lakioti. Socio-economic Aspects of CCS Technologies. *Procedia Economics and Finance*, 14:295 – 302, 2014. ISSN 2212-5671. doi: https://doi.org/10.1016/S2212-5671(14)00716-3. URL http://www.sciencedirect.com/science/article/pii/S2212567114007163. International Conference on Applied Economics, ICOAE 2014.

[83] Dimitrios Xenias and Lorraine Whitmarsh. Carbon capture and storage (CCS) experts' attitudes to and experience with public engagement. *International Journal of Greenhouse Gas Control*, 78:103 – 116, 2018. ISSN 1750-5836. doi: https://doi.org/10.1016/j.ijggc.2018.07.030. URL http://www.sciencedirect.com/science/article/pii/S1750583617308654.

[84] Mai Bui, Mathilde Fajardy, and Niall Mac Dowell. Bio-Energy with CCS (BECCS) performance evaluation: Efficiency enhancement and emissions reduction. *Applied Energy*, 195:289 – 302, 2017. ISSN 0306-2619. doi: https://doi.org/10.1016/j.apenergy.2017.03.063. URL http://www.sciencedirect.com/science/article/pii/S030626191730291X.

[85] Felix Creutzig, N. H. Ravindranath, Göran Berndes, Simon Bolwig, Ryan Bright, Francesco Cherubini, Helena Chum, Esteve Corbera, Mark Delucchi, Andre Faaij, Joseph Fargione, Helmut Haberl, Garvin Heath, Oswaldo Lucon, Richard Plevin, Alexander Popp, Carmenza Robledo-Abad, Steven Rose, Pete Smith, Anders Stromman, Sangwon Suh, and Omar Masera. Bioenergy and climate change mitigation: an assessment. *GCB Bioenergy*, 7(5):916–944, 2015. doi: 10.1111/gcbb.12205. URL https://onlinelibrary.wiley.com/doi/abs/10.1111/gcbb.12205.

[86] Holly Jean Buck. Rapid scale-up of negative emissions technologies: social barriers and social implications. *Climatic Change*, 139(2):155–167, Nov 2016. ISSN 1573-1480. doi: 10.1007/s10584-016-1770-6. URL https://doi.org/10.1007/s10584-016-1770-6.

[87] Mathilde Fajardy and Niall Mac Dowell. Can BECCS deliver sustainable and resource efficient negative emissions? *Energy Environ. Sci.*, 10:1389–1426, 2017. doi: 10.1039/C7EE00465F. URL http://dx.doi.org/10.1039/C7EE00465F.

[88] Mathilde Fajardy and Niall Mac Dowell. The energy return on investment of BECCS: is BECCS a threat to energy security? *Energy & Environmental Science*, 11:1581–1594, 2018. doi: 10.1039/C7EE03610H. URL http://dx.doi.org/10.1039/C7EE03610H.

[89] Mathilde Fajardy, Solene Chiquier, and Niall Mac Dowell. Investigating the BECCS resource nexus: delivering sustainable negative emissions. *Energy & Environmental Science*, 11:3408–3430, 2018. doi: 10.1039/C8EE01676C. URL http://dx.doi.org/10.1039/C8EE01676C.

[90] Michael Nimtz and Hans-Joachim Krautz. Flexible Operation of CCS Power Plants to Match Variable Renewable Energies. *Energy Procedia*, 40:294 – 303, 2013. ISSN 1876-6102. doi: https://doi.org/10.1016/j.egypro.2013.08.034. URL http://www.sciencedirect.com/science/article/pii/S1876610213016287. European Geosciences Union General Assembly 2013, EGUDivision Energy, Resources & the Environment, ERE.

[91] Falko Ueckerdt, Robert Brecha, Gunnar Luderer, Patrick Sullivan, Eva Schmid, Nico Bauer, Diana Böttger, and Robert Pietzcker. Representing power sector variability and the integration of variable renewables in long-term energy-economy models using residual load duration curves. *Energy*, 90:1799 – 1814, 2015. ISSN 0360-5442. doi: https://doi.org/10.1016/j.energy.2015.07.006. URL http://www.sciencedirect.com/science/article/pii/S0360544215008993.

[92] Jakob Kopiske, Sebastian Spieker, and George Tsatsaronis. Value of power plant flexibility in power systems with high shares of variable renewables: A scenario outlook for germany 2035. *Energy*, 137:823 – 833, 2017. ISSN 0360-5442. doi: https://doi.org/10.1016/j.energy.2017.04.138. URL http://www.sciencedirect.com/science/article/pii/S0360544217307065.

[93] Sisi Guo, Pei Liu, and Zheng Li. Enhancement of performance monitoring of a coal-fired power plant via dynamic data reconciliation. *Energy*, 151:203 – 210, 2018. ISSN 0360-5442. doi: https://doi.org/10.1016/j.energy.2018.03.039. URL http://www.sciencedirect.com/science/article/pii/S0360544218304419.

[94] Orhan Ekren and Banu Yetkin Ekren. Size optimization of a PV/wind hybrid energy conversion system with battery storage using response surface methodology. *Applied Energy*, 85(11):1086 – 1101, 2008. ISSN 0306-2619. doi: https://doi.org/10.1016/j.apenergy.2008.02.016. URL http://www.sciencedirect.com/science/article/pii/S0306261908000524.

[95] José L. Bernal-Agustín and Rodolfo Dufo-López. Simulation and optimization of stand-alone hybrid renewable energy systems. *Renewable and Sustainable Energy Reviews*, 13(8):2111 – 2118, 2009. ISSN 1364-0321. doi: https://doi.org/10.1016/j.rser.2009.01.010. URL http://www.sciencedirect.com/science/article/pii/S1364032109000215.

[96] R. Luna-Rubio, M. Trejo-Perea, D. Vargas-Vázquez, and G.J. Ríos-Moreno. Optimal sizing of renewable hybrids energy systems: A review of methodologies. *Solar Energy*, 86(4):1077 – 1088, 2012. ISSN 0038-092X. doi: https://doi.org/10.1016/j.solener.2011.10.016. URL http://www.sciencedirect.com/science/article/pii/S0038092X11003835. ISRES 2010.

[97] Orhan Ekren, Banu Y. Ekren, and Baris Ozerdem. Break-even analysis and size optimization of a PV/wind hybrid energy conversion system with battery storage – A case study. *Applied Energy*, 86(7):1043 – 1054, 2009. ISSN 0306-2619. doi: https://doi.org/10.1016/j.apenergy.2008.09.024. URL http://www.sciencedirect.com/science/article/pii/S0306261908002468.

[98] Manish Ram, Michael Child, Arman Aghahosseini, Dmitrii Bogdanov, Alena Lohrmann, and Christian Breyer. A comparative analysis of electricity generation costs from renewable, fossil fuel and nuclear sources in G20 countries for the period 2015-2030. *Journal of Cleaner Production*, 199:687 – 704, 2018. ISSN 0959-6526. doi: https://doi.org/10.1016/j.jclepro.2018.07.159. URL http://www.sciencedirect.com/science/article/pii/S0959652618321486.

[99] Michael Child, Claudia Kemfert, Dmitrii Bogdanov, and Christian Breyer. Flexible electricity generation, grid exchange and storage for the transition to a 100 % renewable energy system in Europe. *Renewable Energy*, 139:80 – 101, 2019. ISSN 0960-1481. doi: https://doi.org/10.1016/j.renene.2019.02.077. URL http://www.sciencedirect.com/science/article/pii/S0960148119302319.

[100] Francisco Díaz-González, Andreas Sumper, Oriol Gomis-Bellmunt, and Roberto Villafáfila-Robles. A review of energy storage technologies for wind power applications. *Renewable and Sustainable Energy Reviews*, 16(4):2154 – 2171, 2012. ISSN 1364-0321. doi: https://doi.org/10.1016/j.rser.2012.01.029. URL http://www.sciencedirect.com/science/article/pii/S1364032112000305.

[101] Daniel Hdidouan and Iain Staffell. The impact of climate change on the levelised cost of wind energy. *Renewable Energy*, 101:575 – 592, 2017. ISSN 0960-1481. doi: https://doi.org/10.1016/j.renene.2016.09.003. URL http://www.sciencedirect.com/science/article/pii/S0960148116307856.

[102] Rohan Stanger, Terry Wall, Reinhold Spörl, Manoj Paneru, Simon Grathwohl, Max Weidmann, Günter Scheffknecht, Denny McDonald, Kari Myöhänen, Jouni

Ritvanen, Sirpa Rahiala, Timo Hyppänen, Jan Mletzko, Alfons Kather, and Stanley Santos. Oxyfuel combustion for CO_2 capture in power plants. *International Journal of Greenhouse Gas Control*, 40:55 – 125, 2015. ISSN 1750-5836. doi: https://doi.org/10.1016/j.ijggc.2015.06.010. URL http://www.sciencedirect.com/science/article/pii/S1750583615002637. Special Issue commemorating the 10th year anniversary of the publication of the Intergovernmental Panel on Climate Change Special Report on CO2 Capture and Storage.

[103] Renato P. Cabral and Niall Mac Dowell. A novel methodological approach for achieving £/MWh cost reduction of CO_2 capture and storage (CCS) processes. *Applied Energy*, 205:529 – 539, 2017. ISSN 0306-2619. doi: https://doi.org/10.1016/j.apenergy.2017.08.003. URL http://www.sciencedirect.com/science/article/pii/S0306261917310188.

[104] Adriano Vinca, Marianna Rottoli, Giancomo Marangoni, and Massimo Tavoni. The role of carbon capture and storage electricity in attaining 15 and 2 ºC. *International Journal of Greenhouse Gas Control*, 78:148 – 159, 2018. ISSN 1750-5836. doi: https://doi.org/10.1016/j.ijggc.2018.07.020. URL http://www.sciencedirect.com/science/article/pii/S175058361730960X.

[105] ARC Gas & Supply LLC. Oxy-fuel welding and cutting. URL http://www.arcgassupply.com/Oxy-Fuel.html. Accessed 28 July 2017.

[106] H. Farzan, S. Vecci, D. McDonald, K. McCauley, Pavol Pranda, Rajani Varagani, Florian Gautier, Jean-Pierre Tranier, and N. Perrin. State of the art of oxy-coal combustion technology for CO_2 control from coal-fired boilers "are we ready for commercial installation? *24th Annual International Pittsburgh Coal Conference 2007, PCC 2007*, 1:340–360, 2007. URL http://www.canadiancleanpowercoalition.com/pdf/OS2%20-%20BR-1794.pdf.

[107] McDonald, D. K. and Moorman, S. and Darde, A. and de Limon, S. Oxy-Combustion: A Promising Technology for Coal-Fired Plants, 2011. URL http://www.powermag.com/oxy-combustion-a-promising-technology-for-coal-fired-plants/?printmode=1. Accessed 28 July 2017.

[108] Michael Matuszewski, Robert Brasington, and Mark Woods. Advancing Oxycombustion Technology for Bituminous Coal Power Plants: An R&D Guide. In *Carbon Management Technology Conference*, Orlando, Florida, USA, 2012.

[109] Min Zhao and Yanzhong Li. An effective layer pattern optimization model for multi-stream plate-fin heat exchanger using genetic algorithm. *International Journal of Heat and Mass Transfer*, 60:480 – 489, 2013. ISSN 0017-9310. doi: https://doi.org/10.1016/j.ijheatmasstransfer.2012.12.041. URL http://www.sciencedirect.com/science/article/pii/S0017931012009970.

[110] Terry Wall, Rohan Stanger, and Dennis McDonald. Coal-Fired Oxy-Fuel Technology for Carbon Capture and Storage. In *Oxygen-Enhanced Combustion*, Industrial Combustion, chapter 27, pages 631–648. CRC Press, New York; Boca Raton, Second edition, mar 2013. ISBN 978-1-4398-6228-5. URL https://doi.org/10.1201/b13974-28.

[111] Anna Skorek-Osikowska, Lukasz Bartela, Janusz Kotowicz, and Marcin Job. Thermodynamic and economic analysis of the different variants of a coal-fired, 460 MW power plant using oxy-combustion technology. *Energy Conversion and Management*, 76:109 – 120, 2013. ISSN 0196-8904. doi: https://doi.org/10.1016/j.enconman.2013.07.032. URL http://www.sciencedirect.com/science/article/pii/S0196890413004032.

[112] Anna Skorek-Osikowska, Łukasz Bartela, and Janusz Kotowicz. A comparative thermodynamic, economic and risk analysis concerning implementation of oxy-combustion power plants integrated with cryogenic and hybrid air separation units. *Energy Conversion and Management*, 92:421 – 430, 2015. ISSN 0196-8904. doi: https://doi.org/10.1016/j.enconman.2014.12.079. URL http://www.sciencedirect.com/science/article/pii/S0196890414011182.

[113] Anna Skorek-Osikowska, Łukasz Bartela, and Janusz Kotowicz. Thermodynamic and ecological assessment of selected coal-fired power plants integrated with carbon dioxide capture. *Applied Energy*, 200:73 – 88, 2017. ISSN 0306-2619. doi: https://doi.org/10.1016/j.apenergy.2017.05.055. URL http://www.sciencedirect.com/science/article/pii/S0306261917305238.

[114] Improved Oxygen Production Technologies. Technical Report 2007/14, IEA Greenhouse Gas R&D Programme (IEAGHG), .

[115] Hayato Hagi, Yann Le Moullec, Maroun Nemer, and Chakib Bouallou. Performance assessment of first generation oxy-coal power plants through an exergy-based process integration methodology. *Energy*, 69:272 – 284, 2014. ISSN 0360-5442. doi: https://doi.org/10.1016/j.energy.2014.03.008. URL http://www.sciencedirect.com/science/article/pii/S0360544214002618.

[116] Mathew Aneke and Meihong Wang. Process analysis of pressurized oxy-coal power cycle for carbon capture application integrated with liquid air power generation and binary cycle engines. *Applied Energy*, 154:556 – 566, 2015. ISSN 0306-2619. doi: https://doi.org/10.1016/j.apenergy.2015.05.030. URL http://www.sciencedirect.com/science/article/pii/S0306261915006406.

[117] Akihiro Komaki, Takahiro Gotou, Terutoshi Uchida, Toshihiko Yamada, Takashi Kiga, and Chris Spero. Operation Experiences of Oxyfuel Power Plant in Callide Oxyfuel Project. *Energy Procedia*, 63:490 – 496, 2014. ISSN 1876-6102. doi: https://doi.org/10.1016/j.egypro.2014.11.053. URL http://www.sciencedirect.com/science/article/pii/S1876610214018682. 12th International Conference on Greenhouse Gas Control Technologies, GHGT-12.

[118] Dunyu Liu, Terry Wall, and Rohan Stanger. CO_2 quality control in Oxy-fuel technology for CCS: SO_2 removal by the caustic scrubber in Callide Oxy-fuel Project. *International Journal of Greenhouse Gas Control*, 51:207 – 217, 2016. ISSN 1750-5836. doi: https://doi.org/10.1016/j.ijggc.2016.05.026. URL http://www.sciencedirect.com/science/article/pii/S1750583616302699.

[119] J. Monne, L. Jammes, E. Gaucher, N. Labat, C. Urbancyk, S. Thibeau, C. Prinet, X. Payre, T. Schuhler, D. Pourtoy, and D. Copin. Carbon Capture and Storage: the Lacq Pilot. Technical report, Total S. A., 2015.

[120] Endesa, Ciuden, Foster Wheeler, Briscnet Ibérica, Pablo Gutiérrez Cerezales, and Manuel Alonso Fernández. OXYCFB300 Compostilla, Carbon Capture and Storage Demonstration Project, Knowledge Sharing FEED Report. Technical report, Endesa, Madrid, 2013.

[121] Lars Strömberg, Göran Lindgren, Jürgen Jacoby, Rainer Giering, Marie Anheden, Uwe Burchhardt, Hubertus Altmann, Frank Kluger, and Georg-Nikolaus Stamatelopoulos. Update on Vattenfall's 30 MWth oxyfuel pilot plant in Schwarze Pumpe. *Energy Procedia*, 1(1):581 – 589, 2009. ISSN 1876-6102. doi: https://doi.org/10.1016/j.egypro.2009.01.077. URL http://www.sciencedirect.com/science/article/pii/S1876610209000782. Greenhouse Gas Control Technologies 9.

[122] M. Anheden, U. Burchhardt, H. Ecke, R. Faber, O. Jidinger, R. Giering, H. Kass, S. Lysk, E. Ramström, and J. Yan. Overview of operational experience and results from test activities in Vattenfall's 30 MWth oxyfuel pilot plant in Schwarze Pumpe. *Energy Procedia*, 4:941 – 950, 2011. ISSN 1876-6102. doi: https://doi.org/10.1016/j.egypro.2011.01.140. URL http://www.sciencedirect.com/science/article/pii/S1876610211001421. 10th International Conference on Greenhouse Gas Control Technologies.

[123] Linde AG. 125 years of Linde, A chronicle, 2004.

[124] Linde AG. Cryogenic air separation. History and technological progress, 2015.

[125] C. Linde. Process of producing low temperatures, the liquefaction of gases, and the separation of the constituents of gaseous mixtures, 1903. URL http://www.google.co.uk/patents/US727650. US Patent 727,650A.

[126] Randall F. Barron. *Cryogenic Systems*. Oxford University Press, New York, Oxford (Oxfordshire), Second edition, 1985. ISBN 9780195035674.

[127] Roger M. McGuinness and William T. Kleinberg. Oxygen Production. In Charles Edward Baukal, Jr., editor, *Oxygen-Enhanced Combustion*, Industrial Combustion, chapter 3, pages 43–76. CRC Press, New York; Boca Raton, Second edition, mar 2013. ISBN 978-1-4398-6228-5. URL https://doi.org/10.1201/b13974-4.

[128] D. M. Ruthven and S. Farooq. Air separation by pressure swing adsorption. *Gas Separation & Purification*, 4(3):141 – 148, 1990. ISSN 0950-4214. doi: https://doi.org/10.1016/0950-4214(90)80016-E. URL http://www.sciencedirect.com/science/article/pii/095042149080016E.

[129] Mai Xu, Han-Chun Wu, Y. S. Lin, and Shuguang Deng. Simulation and optimization of pressure swing adsorption process for high-temperature air separation by perovskite sorbents. *Chemical Engineering Journal*, 354:62 – 74, 2018. ISSN 1385-8947. doi: https://doi.org/10.1016/j.cej.2018.07.080. URL http://www.sciencedirect.com/science/article/pii/S1385894718313226.

[130] Neil A. Downie. *Industrial gases*. Springer, first edition, 1996. ISBN 978-0751403527.

[131] Mark J. Kirschner. Oxygen. In *Ullmann's Encyclopedia of Industrial Chemistry*. John Wiley and Sons, Inc., 2000. doi: 10.1002/14356007.a18_329.

[132] W. F. Castle. Air separation and liquefaction: recent developments and prospects for the beginning of the new millennium. *International Journal of Refrigeration*, 25(1):158 – 172, 2002. ISSN 0140-7007. doi: https://doi.org/10.1016/S0140-7007(01)00003-2. URL http://www.sciencedirect.com/science/article/pii/S0140700701000032.

[133] David R. Vinson. Air separation control technology. *Computers & Chemical Engineering*, 30(10):1436 – 1446, 2006. ISSN 0098-1354. doi: https://doi.org/10.1016/j.compchemeng.2006.05.038. URL http://www.sciencedirect.com/science/article/pii/S0098135406001554. Papers form Chemical Process Control VII.

[134] Don W. Green and Robert H. Perry. Cryogenic processes. In *Perry's Chemical Engineers' Handbook*. McGraw Hill Professional, Access Engineering, Eighth edition, 2008. ISBN 9780071422949.

[135] Richard Dubettier, A. Guillard, M. Cognard, Jean-Pierre Tranier, and Nicolas Perrin. Air separation Unit: Flexibility & Energy Storage. In *2nd Oxyfuel Combustion Conference*, Queensland, 2011.

[136] Arthur Darde, Rajeev Prabhakar, Jean-Pierre Tranier, and Nicolas Perrin. Air separation and flue gas compression and purification units for oxy-coal combustion systems. *Energy Procedia*, 1(1):527 – 534, 2009. ISSN 1876-6102. doi: https://doi.org/10.1016/j.egypro.2009.01.070. URL http://www.sciencedirect.com/science/article/pii/S187661020900071X. Greenhouse Gas Control Technologies 9.

[137] Jean-Pierre Tranier, Richard Dubettier, Arthur Darde, and Nicolas Perrin. Air separation, flue gas compression and purification units for oxy-coal combustion systems. *Energy Procedia*, 4:966 – 971, 2011. ISSN 1876-6102. doi: https://doi.org/10.1016/j.egypro.2011.01.143. URL http://www.sciencedirect.com/science/article/pii/S1876610211001457. 10th International Conference on Greenhouse Gas Control Technologies.

[138] Paul Higginbotham, Vince White, Kevin Fogash, and Galip Guvelioglu. Oxygen supply for oxyfuel CO_2 capture. *International Journal of Greenhouse Gas Control*, 5:S194 – S203, 2011. ISSN 1750-5836. doi: https://doi.org/10.1016/j.ijggc.2011.03.007. URL http://www.sciencedirect.com/science/article/pii/S1750583611000375. Oxyfuel Combustion Technology - Working Toward Demonstration and Commercialisation.

[139] Praxair. V120 XL-XXL, 2014.

[140] Cryogenmash. Cryogenmash. URL http://cryogenmash.ru/en/catalog/cryogenic-ASUs/.

[141] Salil U. Rege, Ralph T. Yang, and Mark A. Buzanowski. Sorbents for air prepurification in air separation. *Chemical Engineering Science*, 55(21):4827 – 4838,

2000. ISSN 0009-2509. doi: https://doi.org/10.1016/S0009-2509(00)00122-6. URL http://www.sciencedirect.com/science/article/pii/S0009250900001226.

[142] Salil U. Rege, Ralph T. Yang, Kangyi Qian, and Mark A. Buzanowski. Air-prepurification by pressure swing adsorption using single/layered beds. *Chemical Engineering Science*, 56(8):2745 – 2759, 2001. ISSN 0009-2509. doi: https://doi.org/10.1016/S0009-2509(00)00531-5. URL http://www.sciencedirect.com/science/article/pii/S0009250900005315.

[143] Mark W Ackley, Salil U Rege, and Himanshu Saxena. Application of natural zeolites in the purification and separation of gases. *Microporous and Mesoporous Materials*, 61(1):25 – 42, 2003. ISSN 1387-1811. doi: https://doi.org/10.1016/S1387-1811(03)00353-6. URL http://www.sciencedirect.com/science/article/pii/S1387181103003536. ZEOLITE '02 (Proceedings of the 6th Internationanl Conference on the Occurrence, Properties and Utilization of Natural Zeolites).

[144] Peiyuan Li and F. Handan Tezel. Adsorption separation of N_2, O_2, CO_2 and CH_4 gases by β-zeolite. *Microporous and Mesoporous Materials*, 98:94–101, 01 2007. doi: 10.1016/j.micromeso.2006.08.016.

[145] Ronny Pini, Stefan Ottiger, Arvind Rajendran, Giuseppe Storti, and Marco Mazzotti. Near-critical adsorption of CO_2 on 13X zeolite and N_2O on silica gel: lack of evidence of critical phenomena. *Adsorption*, 14(1):133 – 141, Feb 2008. ISSN 1572-8757. doi: 10.1007/s10450-007-9080-y. URL https://doi.org/10.1007/s10450-007-9080-y.

[146] Mohammad Ali Kalbassi, Anthony Finot, Timothy Christopher Golden, Christopher James Raiswell, and Ann Marie Botelho. Purification of Air, 2015. US Patent 9,108,145 B2.

[147] Vaijanath N. Raibhole and S. N. Sapali. Simulation and Parametric Analysis of Cryogenic Oxygen Plant for Biomass Gasification. *Mechanical Engineering Research*, 2(2):97–107, 2012. doi: 10.5539/mer.v2n2p97. URL http://dx.doi.org/10.5539/mer.v2n2p97.

[148] Zbigniew Tadeusz Fidkowski and Donn Michael Herron. Elevated pressure air separation process with use of waste expansion for compression of a process stream, 2000. US Patent 6,009,723.

[149] R. Ray and S. Ferguson. Assessing the cost reduction potential and competitiveness of novel (next generation) UK carbon capture technology. Benchmarking State-of-the-art and Next Generation Technologies. Technical Report 13333-8820-RP-001, BEIS, Wood, Amec Foster Wheeler Group, 2018.

[150] CO_2 Capture at Coal Based Power and Hydrogen Plants. Technical Report 2014/3, IEAGHG, May 2014.

[151] Dawid P. Hanak, Dante Powell, and Vasilije Manovic. Techno-economic analysis of oxy-combustion coal-fired power plant with cryogenic oxygen storage. *Applied Energy*, 191:193 – 203, 2017. ISSN 0306-2619. doi: https://doi.org/10.1016/

j.apenergy.2017.01.049. URL http://www.sciencedirect.com/science/article/pii/S0306261917300582.

[152] Yukun Hu, Xun Li, Hailong Li, and Jinyue Yan. Peak and off-peak operations of the air separation unit in oxy-coal combustion power generation systems. *Applied Energy*, 112:747 – 754, 2013. ISSN 0306-2619. doi: https://doi.org/10.1016/j.apenergy.2012.12.001. URL http://www.sciencedirect.com/science/article/pii/S0306261912008781.

[153] D. M. Herron and R. Agrawal. Air separation with intermediate pressure vaporization and expansion, 1999. URL https://www.google.com/patents/US5956973. US Patent 5,956,973.

[154] Jung-Tsai Chen, Chien-Chung Shih, Ywu-Jang Fu, Shu-Hsien Huang, Chien-Chieh Hu, Kueir-Rarn Lee, and Juin-Yih Lai. Zeolite-Filled Porous Mixed Matrix Membranes for Air Separation. *Industrial & Engineering Chemistry Research*, 53(7):2781 – 2789, 2014. doi: 10.1021/ie403833u. URL https://doi.org/10.1021/ie403833u.

[155] Jaap F. Vente, Wim. G. Haije, Ruud IJpelaan, and Frans T. Rusting. On the full-scale module design of an air separation unit using mixed ionic electronic conducting membranes. *Journal of Membrane Science*, 278(1):66 – 71, 2006. ISSN 0376-7388. doi: https://doi.org/10.1016/j.memsci.2005.10.044. URL http://www.sciencedirect.com/science/article/pii/S0376738805007763.

[156] Renzo Castillo. Thermodynamic analysis of a hard coal oxyfuel power plant with high temperature three-end membrane for air separation. *Applied Energy*, 88(5):1480 – 1493, 2011. ISSN 0306-2619. doi: https://doi.org/10.1016/j.apenergy.2010.10.044. URL http://www.sciencedirect.com/science/article/pii/S0306261910004599.

[157] S. S. Hashim, A. R. Mohamed, and S. Bhatia. Oxygen separation from air using ceramic-based membrane technology for sustainable fuel production and power generation. *Renewable and Sustainable Energy Reviews*, 15(2):1284 – 1293, 2011. ISSN 1364-0321. doi: https://doi.org/10.1016/j.rser.2010.10.002. URL http://www.sciencedirect.com/science/article/pii/S1364032110003424.

[158] Runze Wang, Bo Meng, Xiuxia Meng, Xiaoyao Tan, Jaka Sunarso, Lihong Liu, and Shaomin Liu. Highly stable $La_{0.6}Sr_{0.4}Co_{0.2}Fe_{0.8}O_{3-\delta}$ hollow fibre membrane for air separation swept by steam or steam mixture. *Journal of Membrane Science*, 479:232 – 239, 2015. ISSN 0376-7388. doi: https://doi.org/10.1016/j.memsci.2015.01.006. URL http://www.sciencedirect.com/science/article/pii/S0376738815000228.

[159] Khaled Mezghani and Amir Hamza. Application of $Ba_{0.5}Sr_{0.5}Co_{0.8}Fe_{0.2}O_{3-\delta}$ membranes in an oxy-fuel combustion reactor. *Journal of Membrane Science*, 518:254 – 262, 2016. ISSN 0376-7388. doi: https://doi.org/10.1016/j.memsci.2016.07.001. URL http://www.sciencedirect.com/science/article/pii/S0376738816308729.

[160] Kalpit Shah, Behdad Moghtaderi, and Terry Wall. Effect of flue gas impurities on the performance of a chemical looping based air separation process for oxy-fuel combustion. *Fuel*, 103:932 – 942, 2013. ISSN 0016-2361. doi: https://doi.org/10.1016/j.fuel.2012.09.018. URL http://www.sciencedirect.com/science/article/pii/S0016236112007314.

[161] Kun Wang, Qingbo Yu, and Qin Qin. Reduction Kinetics of Cu-Based Oxygen Carriers for Chemical Looping Air Separation. *Energy & Fuels*, 27(9):5466 – 5474, 2013. doi: 10.1021/ef401241r. URL https://doi.org/10.1021/ef401241r.

[162] Cheng Zhou, Kalpit Shah, and Behdad Moghtaderi. Techno-Economic Assessment of Integrated Chemical Looping Air Separation for Oxy-Fuel Combustion: An Australian Case Study. *Energy & Fuels*, 29(4):2074 – 2088, 2015. doi: 10.1021/ef5022076. URL https://doi.org/10.1021/ef5022076.

[163] R.M. Thorogood. Developments in air separation. *Gas Separation & Purification*, 5(2):83 – 94, 1991. ISSN 0950-4214. doi: https://doi.org/10.1016/0950-4214(91)80005-P. URL http://www.sciencedirect.com/science/article/pii/0950042149180005P.

[164] Yuanzhi Wang, Hongwei Cheng, Sha Chen, Hongbin Zhao, Xionggang Lu, and Qian Xu. CO_2-tolerance and oxygen permeability of novel cobalt-free mixed-conductor oxygen-permeable $Pr_{0.6}Sr_{0.4}Fe_{1-x}Nb_xO_{3-\delta}$ membranes. *Ceramics International*, 43(16):13791 – 13799, 2017. ISSN 0272-8842. doi: https://doi.org/10.1016/j.ceramint.2017.07.099. URL http://www.sciencedirect.com/science/article/pii/S0272884217315304.

[165] Jaka Sunarso, Siti Salwa Hashim, Na Zhu, and Wei Zhou. Perovskite oxides applications in high temperature oxygen separation, solid oxide fuel cell and membrane reactor: A review. *Progress in Energy and Combustion Science*, 61:57 – 77, 2017. ISSN 0360-1285. doi: https://doi.org/10.1016/j.pecs.2017.03.003. URL http://www.sciencedirect.com/science/article/pii/S0360128516300922.

[166] Ryan Falkenstein-Smith, Pingying Zeng, and Jeongmin Ahn. Investigation of oxygen transport membrane reactors for oxy-fuel combustion and carbon capture purposes. *Proceedings of the Combustion Institute*, 36(3):3969 – 3976, 2017. ISSN 1540-7489. doi: https://doi.org/10.1016/j.proci.2016.09.005. URL http://www.sciencedirect.com/science/article/pii/S1540748916304813.

[167] Yadi Hu, Ran An, Yuanyuan Chu, Xiaoyao Tan, Jaka Sunarso, Shaobin Wang, and Shaomin Liu. Perovskite hollow fiber membranes supported in a porous and catalytically active perovskite matrix for air separation. *Separation and Purification Technology*, 192:435 – 440, 2018. ISSN 1383-5866. doi: https://doi.org/10.1016/j.seppur.2017.10.037. URL http://www.sciencedirect.com/science/article/pii/S138358661732631X.

[168] Cyprien Marie Tessié du Motay and Charles Raphael Maréchal. Improved mode of producing oxygen gas, 1867.

[169] Eugene O Brimm. Chemical production of oxygen. U.S. Patent No. 2,427,707, 1942.

[170] Eugene O Brimm. Chemical production of oxygen. U.S. Patent No. 2,427,707, 1942.

[171] Behdad Moghtaderi. Review of the Recent Chemical Looping Process Developments for Novel Energy and Fuel Applications. *Energy & Fuels*, 26(1):15–40, 2012. doi: 10.1021/ef201303d. URL https://doi.org/10.1021/ef201303d.

[172] Paul Kunzemann. Modelling, development and validation of a supercritical decarbonised coal fired power plant model under different operating conditions in gproms. Master thesis, Chair of Technical Thermodynamics of RWTH Aachen University and Centre for Environmental Policy at Imperial College London, 2014.

[173] D. Zhang. *1 - Introduction to advanced and ultra-supercritical fossil fuel power plants*. Woodhead Publishing Series in Energy. Woodhead Publishing, 2013. ISBN 978-0-85709-116-1. doi: https://doi.org/10.1533/9780857097514.1. URL http://www.sciencedirect.com/science/article/pii/B9780857091161500015.

[174] Hartmut Spliethoff. *Power generation from solid fuels*. Springer-Verlag Berlin Heidelberg, first edition, 2010. ISBN 978-3-642-02855-7.

[175] B. Stanmore. 7 - Emissions from ultra-supercritical power plants and pollution control measures. In Dongke Zhang, editor, *Ultra-Supercritical Coal Power Plants*, Woodhead Publishing Series in Energy, pages 184 – 212. Woodhead Publishing, 2013. ISBN 978-0-85709-116-1. doi: https://doi.org/10.1533/9780857097514.2.184. URL http://www.sciencedirect.com/science/article/pii/B9780857091161500076.

[176] International Energy Agency. World Energy Outlook 2015. Technical report, International Energy Agency, 2015.

[177] B. Miller. 3 - Fuel considerations and burner design for ultra-supercritical power plants. In Dongke Zhang, editor, *Ultra-Supercritical Coal Power Plants*, Woodhead Publishing Series in Energy, pages 57 – 80. Woodhead Publishing, 2013. ISBN 978-0-85709-116-1. doi: https://doi.org/10.1533/9780857097514.1.57. URL http://www.sciencedirect.com/science/article/pii/B9780857091161500039.

[178] R.G. Narula, D. Koza, and H. Wen. 2 - Impacts of steam conditions on plant materials and operation in ultra-supercritical coal power plants. In Dongke Zhang, editor, *Ultra-Supercritical Coal Power Plants*, Woodhead Publishing Series in Energy, pages 23 – 56. Woodhead Publishing, 2013. ISBN 978-0-85709-116-1. doi: https://doi.org/10.1533/9780857097514.1.23. URL http://www.sciencedirect.com/science/article/pii/B9780857091161500027.

[179] D. Zhang. 6 - Ash fouling, deposition and slagging in ultra-supercritical coal power plants. In Dongke Zhang, editor, *Ultra-Supercritical Coal Power Plants*, Woodhead Publishing Series in Energy, pages 133 – 183. Woodhead Publishing, 2013. ISBN 978-0-85709-116-1. doi: https://doi.org/10.1533/9780857097514.2.133. URL http://www.sciencedirect.com/science/article/pii/B9780857091161500064.

[180] Prabir Basu. Chapter 2 - Biomass Characteristics. In Prabir Basu, editor, *Biomass Gasification and Pyrolysis*, pages 27 – 63. Academic Press, Boston, 2010. ISBN 978-0-12-374988-8. doi: https://doi.org/10.1016/B978-0-12-374988-8.00002-7. URL http://www.sciencedirect.com/science/article/pii/B9780123749888000027.

[181] Markus Preißinger, Sabrina Schatz, Anne Vogl, Andreas König-Haagen, and Dieter Brüggemann. Thermoeconomic analysis of configuration methods for modular Organic Rankine Cycle units in low-temperature applications. *Energy Conversion and Management*, 127:25–34, 2016. ISSN 01968904. doi: 10.1016/j.enconman.2016.08.092.

[182] J.M. Wheeldon and J.P. Shingledecker. 4 - Materials for boilers operating under supercritical steam conditions. In Dongke Zhang, editor, *Ultra-Supercritical Coal Power Plants*, Woodhead Publishing Series in Energy, pages 81 – 103. Woodhead Publishing, 2013. ISBN 978-0-85709-116-1. doi: https://doi.org/10.1533/9780857097514.1.81. URL http://www.sciencedirect.com/science/article/pii/B9780857091161500040.

[183] K. Zhang, Y. Zhang, Y. Guan, and D. Zhang. 5 - Boiler design for ultra-supercritical coal power plants. In Dongke Zhang, editor, *Ultra-Supercritical Coal Power Plants*, Woodhead Publishing Series in Energy, pages 104 – 130. Woodhead Publishing, 2013. ISBN 978-0-85709-116-1. doi: https://doi.org/10.1533/9780857097514.1.104. URL http://www.sciencedirect.com/science/article/pii/B9780857091161500052.

[184] Kyle Nicol. Status of advanced ultra-supercritical pulverised coal technology. Technical Report CCC/229, IEA Clean Coal Centre, 2013.

[185] Alexander Zoelle, Dale Keairns, Lora L Pinkerton, Marc J Turner, Mark Woods, Norma Kuehn, Vasant Shah, and Vincent Chou. Cost and performance baseline for fossil energy plants volume 1a: Bituminous coal (pc) and natural gas to electricity revision 3. doi: 10.2172/1480987.

[186] P. S. Weitzel, J. M. Tanzosh, B. Boring, N. Okita, T. Takahashi, and N. Ishikawa. Advanced Ultra-Supercritical Power Plant (700 to 760C) Design for Indian Coal. Technical Report BR-1884.

[187] Alstom. Major milestone achieved in the development of advanced ultra-supercritical steam power plants, December 2014. URL http://www.alstom.com/press-centre/2014/12/major-milestone-achieved-in-the-development-of-advanced-ultra-supercritical-steam-power-plants/.

[188] M.R. Hodkiewicz. 8 - Estimation, management and extension of the life of ultra-supercritical power plants. In Dongke Zhang, editor, *Ultra-Supercritical Coal Power Plants*, Woodhead Publishing Series in Energy, pages 213 – 228. Woodhead Publishing, 2013. ISBN 978-0-85709-116-1. doi: https://doi.org/10.1533/9780857097514.2.213. URL http://www.sciencedirect.com/science/article/pii/B9780857091161500088.

[189] Robert G. Mortimer. 10 - Gas Kinetic Theory. The Molecular Theory of Dilute Gases at Equilibrium. In Robert G. Mortimer, editor, *Physical Chemistry (Second Edition)*, pages 319 – 364. Academic Press, Burlington, second edition edition, 2000. ISBN 978-0-12-508345-4. doi: https://doi.org/10.1016/B978-0125083454-5/50013-7. URL http://www.sciencedirect.com/science/article/pii/B9780125083454500137.

[190] Nikita Vorobiev, Manfred Geier, Martin Schiemann, and Viktor Scherer. Experimentation for char combustion kinetics measurements: Bias from char preparation. *Fuel Processing Technology*, 151:155 – 165, 2016. ISSN 0378-3820. doi: https://doi.org/10.1016/j.fuproc.2016.05.005. URL http://www.sciencedirect.com/science/article/pii/S0378382016301898.

[191] A.E. Lear, T.C. Brown, and B.S. Haynes. Formation of metastable oxide complexes during the oxidation of carbons at low temperatures. *Symposium (International) on Combustion*, 23(1):1191 – 1197, 1991. ISSN 0082-0784. doi: https://doi.org/10.1016/S0082-0784(06)80380-2. URL http://www.sciencedirect.com/science/article/pii/S0082078406803802. Twenty-Third Symposium (International) on Combustion.

[192] Brian S. Haynes. A turnover model for carbon reactivity I. Development. *Combustion and Flame*, 126(1):1421 – 1432, 2001. ISSN 0010-2180. doi: https://doi.org/10.1016/S0010-2180(01)00263-2. URL http://www.sciencedirect.com/science/article/pii/S0010218001002632.

[193] Ethan S. Hecht, Christopher R. Shaddix, Manfred Geier, Alejandro Molina, and Brian S. Haynes. Effect of CO_2 and steam gasification reactions on the oxy-combustion of pulverized coal char. *Combustion and Flame*, 159(11):3437 – 3447, 2012. ISSN 0010-2180. doi: https://doi.org/10.1016/j.combustflame.2012.06.009. URL http://www.sciencedirect.com/science/article/pii/S0010218012001897.

[194] Osvalda Senneca. Oxidation of Carbon: What We Know and What We Still Need to Know. *Energy Procedia*, 120:62 – 74, 2017. ISSN 1876-6102. doi: https://doi.org/10.1016/j.egypro.2017.07.155. URL http://www.sciencedirect.com/science/article/pii/S1876610217327236. INFUB - 11th European Conference on Industrial Furnaces and Boilers, INFUB-11.

[195] M.R. Haines and J.E. Davison. Designing carbon capture power plants to assist in meeting peak power demand. *Energy Procedia*, 1(1):1457 – 1464, 2009. ISSN 1876-6102. doi: https://doi.org/10.1016/j.egypro.2009.01.191. URL http://www.sciencedirect.com/science/article/pii/S1876610209001921. Greenhouse Gas Control Technologies 9.

[196] Daehee Kim, Sangmin Choi, Christopher R. Shaddix, and Manfred Geier. Effect of CO_2 gasification reaction on char particle combustion in oxy-fuel conditions. *Fuel*, 120:130 – 140, 2014. ISSN 0016-2361. doi: https://doi.org/10.1016/j.fuel.2013.12.004. URL http://www.sciencedirect.com/science/article/pii/S0016236113011411.

[197] Oskar Karlström, Anders Brink, and Mikko Hupa. Desorption kinetics of CO in char oxidation and gasification in O_2, CO_2 and H_2O. *Combustion and Flame*, 162 (3):788 – 796, 2015. ISSN 0010-2180. doi: https://doi.org/10.1016/j.combustflame.2014.08.010. URL http://www.sciencedirect.com/science/article/pii/S0010218014002466.

[198] R. Payne, S. L. Chen, A. M. Wolsky, and W. F. Richter. CO_2 Recovery via Coal Combustion in Mixtures of Oxygen and Recycled Flue Gas. *Combustion Science and Technology*, 67(1-3):1–16, 1989. doi: 10.1080/00102208908924058. URL https://doi.org/10.1080/00102208908924058.

[199] K. Andersson, R. Johansson, and F. Johnsson. Thermal radiation in oxy-fuel flames. *International Journal of Greenhouse Gas Control*, 5:S58–S65, Jul 2011. ISSN 17505836. doi: 10.1016/j.ijggc.2011.05.018. URL http://www.sciencedirect.com/science/article/pii/S1750583611000788.

[200] Rohan Stanger, Lawrence Belo, Timothy Ting, Chris Spero, and Terry Wall. Mercury and SO_3 measurements on the fabric filter at the Callide Oxy-fuel Project during air and oxy-fuel firing transitions. *International Journal of Greenhouse Gas Control*, 47:221 – 232, 2016. ISSN 1750-5836. doi: https://doi.org/10.1016/j.ijggc.2016.01.049. URL http://www.sciencedirect.com/science/article/pii/S1750583616300494.

[201] Shiyuan Li, Haoyu Li, Wei Li, Mingxin Xu, Eric G. Eddings, Qiangqiang Ren, and Qinggang Lu. Coal combustion emission and ash formation characteristics at high oxygen concentration in a 1MWth pilot-scale oxy-fuel circulating fluidized bed. *Applied Energy*, 197:203 – 211, 2017. ISSN 0306-2619. doi: https://doi.org/10.1016/j.apenergy.2017.03.028. URL http://www.sciencedirect.com/science/article/pii/S0306261917302489.

[202] Rohan Stanger and Terry Wall. Sulphur impacts during pulverised coal combustion in oxy-fuel technology for carbon capture and storage. *Progress in Energy and Combustion Science*, 37(1):69 – 88, 2011. ISSN 0360-1285. doi: https://doi.org/10.1016/j.pecs.2010.04.001. URL http://www.sciencedirect.com/science/article/pii/S0360128510000365.

[203] B.O. Oboirien, V. Thulari, and B.C. North. Enrichment of trace elements in bottom ash from coal oxy-combustion: Effect of coal types. *Applied Energy*, 177:81 – 86, 2016. ISSN 0306-2619. doi: https://doi.org/10.1016/j.apenergy.2016.04.118. URL http://www.sciencedirect.com/science/article/pii/S0306261916306146.

[204] Prakash Mhaske, P. D. Siwal, and Bikash Chandra Mallick. Flexible operation of thermal power plant for integration of renewable generation. A Roadmap for Flexible Operation of Thermal, Gas and Hydro Power Stations to Facilitate Integration of Renewable Generation, 2019.

[205] M. Lucquiaud. 10 - CO_2 capture-ready ultra-supercritical coal power plants. In Dongke Zhang, editor, *Ultra-Supercritical Coal Power Plants*, Woodhead Publishing Series in Energy, pages 244 – 271. Woodhead Publishing, 2013. ISBN

978-0-85709-116-1. doi: https://doi.org/10.1533/9780857097514.2.244. URL http://www.sciencedirect.com/science/article/pii/B9780857091161500106.

[206] Niall Mac Dowell and Iain Staffell. The role of flexible CCS in the UK's future energy system. *International Journal of Greenhouse Gas Control*, 48:327 – 344, 2016. ISSN 1750-5836. doi: https://doi.org/10.1016/j.ijggc.2016.01.043. URL http://www.sciencedirect.com/science/article/pii/S1750583616300433. FLEXIBLE OPERATION OF CARBON CAPTURE PLANTS.

[207] Gabriele Pipitone and Olav Bolland. Power generation with CO_2 capture: Technology for CO_2 purification. *International Journal of Greenhouse Gas Control*, 3 (5):528 – 534, 2009. ISSN 1750-5836. doi: https://doi.org/10.1016/j.ijggc.2009.03.001. URL http://www.sciencedirect.com/science/article/pii/S1750583609000243.

[208] Sebastian Posch and Markus Haider. Optimization of CO_2 compression and purification units (CO_2CPU) for CCS power plants. *Fuel*, 101:254 – 263, 2012. ISSN 0016-2361. doi: https://doi.org/10.1016/j.fuel.2011.07.039. URL http://www.sciencedirect.com/science/article/pii/S0016236111004364. 8th European Conference on Coal Research and Its Applications.

[209] Rosa M. Cuéllar-Franca and Adisa Azapagic. Carbon capture, storage and utilisation technologies: A critical analysis and comparison of their life cycle environmental impacts. *Journal of CO2 Utilization*, 9:82 – 102, 2015. ISSN 2212-9820. doi: https://doi.org/10.1016/j.jcou.2014.12.001. URL http://www.sciencedirect.com/science/article/pii/S2212982014000626.

[210] Vince White, Laura Torrente-Murciano, David Sturgeon, and David Chadwick. Purification of oxyfuel-derived CO_2. *International Journal of Greenhouse Gas Control*, 4(2):137 – 142, 2010. ISSN 1750-5836. doi: https://doi.org/10.1016/j.ijggc.2009.07.004. URL http://www.sciencedirect.com/science/article/pii/S1750583609000814. The Ninth International Conference on Greenhouse Gas Control Technologies.

[211] Frederick Lockwood, Ludovic Granados, Mathieu Leclerc, Anne-Laure Lesort, Grégoire Beasse, Miguel A. Delgado, and Chris Spero. Oxy-combustion CPU – From Pilots Towards Industrial-scale Demonstration. *Energy Procedia*, 63:342 – 351, 2014. ISSN 1876-6102. doi: https://doi.org/10.1016/j.egypro.2014.11.037. URL http://www.sciencedirect.com/science/article/pii/S1876610214018529. 12th International Conference on Greenhouse Gas Control Technologies, GHGT-12.

[212] Piera Patrizio, Sylvain Leduc, Florian Kraxner, Sabine Fuss, Georg Kindermann, Sennai Mesfun, Kasparas Spokas, Alma Mendoza, Niall Mac Dowell, Elisabeth Wetterlund, Joakim Lundgren, Erik Dotzauer, Ping Yowargana, and Michael Obersteiner. Reducing US Coal Emissions Can Boost Employment. *Joule*, 2(12): 2633 – 2648, 2018. ISSN 2542-4351. doi: https://doi.org/10.1016/j.joule.2018.10.004. URL http://www.sciencedirect.com/science/article/pii/S2542435118304665.

[213] Nasim Pour, Paul A. Webley, and Peter J. Cook. Potential for using municipal solid waste as a resource for bioenergy with carbon capture and storage (BECCS). *International Journal of Greenhouse Gas Control*, 68:1 – 15, 2018. ISSN 1750-5836. doi: https://doi.org/10.1016/j.ijggc.2017.11.007. URL http://www.sciencedirect.com/science/article/pii/S1750583617301354.

[214] Killian Chary, Joël Aubin, Loïc Guindé, Jorge Sierra, and Jean-Marc Blazy. Cultivating biomass locally or importing it? LCA of biomass provision scenarios for cleaner electricity production in a small tropical island. *Biomass and Bioenergy*, 110:1 – 12, 2018. ISSN 0961-9534. doi: https://doi.org/10.1016/j.biombioe.2018.01.009. URL http://www.sciencedirect.com/science/article/pii/S0961953418300151.

[215] Andrew Welfle, Paul Gilbert, and Patricia Thornley. Increasing biomass resource availability through supply chain analysis. *Biomass and Bioenergy*, 70:249 – 266, 2014. ISSN 0961-9534. doi: https://doi.org/10.1016/j.biombioe.2014.08.001. URL http://www.sciencedirect.com/science/article/pii/S0961953414003730.

[216] Jasmin Kemper. Biomass and carbon dioxide capture and storage: A review. *International Journal of Greenhouse Gas Control*, 40:401 – 430, 2015. ISSN 1750-5836. doi: https://doi.org/10.1016/j.ijggc.2015.06.012. URL http://www.sciencedirect.com/science/article/pii/S1750583615002650. Special Issue commemorating the 10th year anniversary of the publication of the Intergovernmental Panel on Climate Change Special Report on CO2 Capture and Storage.

[217] Drax annual report and accounts. Technical report, Drax Group plc, 2015.

[218] Guangchao Ding, Boshu He, Yang Cao, Chaojun Wang, Liangbin Su, Zhipeng Duan, Jingge Song, Wenxiao Tong, and Xuezheng Li. Process simulation and optimization of municipal solid waste fired power plant with oxygen/carbon dioxide combustion for near zero carbon dioxide emission. *Energy Conversion and Management*, 157:157 – 168, 2018. ISSN 0196-8904. doi: https://doi.org/10.1016/j.enconman.2017.11.087. URL http://www.sciencedirect.com/science/article/pii/S0196890417311482.

[219] Ali Lewis and Jessica Gorton. Drax to pilot Europe's first carbon capture storage project. https://www.drax.com/press_release/drax-to-pilot-europes-first-carbon-capture-storage-project-beccs/3/, 2018. Accessed December 2018.

[220] Ben Doodley and Patrick E. Mason. Supply chain costs of biomass cofiring. Technical Report CCC/286, IEA CCC, April 2018.

[221] Raphael Slade, Ausilio Bauen, and Robert Gross. Global bioenergy resources. *Nature Climate Change*, 4:99 – 105, 2014. doi: 10.1038/nclimate2097.

[222] Naomi E Vaughan, Clair Gough, Sarah Mander, Emma W Littleton, Andrew Welfle, David E H J Gernaat, and Detlef P van Vuuren. Evaluating the use of biomass energy with carbon capture and storage in low emission scenarios. *Environmental Research Letters*, 13(4):044014, mar 2018. doi: 10.1088/1748-9326/aaaa02. URL https://doi.org/10.1088%2F1748-9326%2Faaaa02.

[223] Drax confirms £30m cost for fourth boiler conversion. https://www.endswasteandbioenergy.com/article/1484512/drax-confirms-30m-cost-fourth-boiler-conversion. Accessed October 2018.

[224] Jens Hetland, Ping Yowargana, Sylvain Leduc, and Florian Kraxner. Carbon-negative emissions: Systemic impacts of biomass conversion: A case study on CO_2 capture and storage options. *International Journal of Greenhouse Gas Control*, 49:330 – 342, 2016. ISSN 1750-5836. doi: https://doi.org/10.1016/j.ijggc.2016.03.017. URL http://www.sciencedirect.com/science/article/pii/S1750583616301220.

[225] N. Jurado, H.G. Darabkhani, E.J. Anthony, and J.E. Oakey. Oxy-combustion studies into the co –firing of coal and biomass blends: Effects on heat transfer, gas and ash compositions. *Energy Procedia*, 63:440 – 452, 2014. ISSN 1876-6102. doi: https://doi.org/10.1016/j.egypro.2014.11.047. URL http://www.sciencedirect.com/science/article/pii/S1876610214018621. 12th International Conference on Greenhouse Gas Control Technologies, GHGT-12.

[226] Ignacio Trabadela, Hannah Chalmers, and Jon Gibbins. Oxy-biomass Ignition in Air and Relevant Oxy-combustion Atmospheres for Safe Primary Recycle and Oxy-burner Development. *Energy Procedia*, 63:403 – 414, 2014. ISSN 1876-6102. doi: https://doi.org/10.1016/j.egypro.2014.11.042. URL http://www.sciencedirect.com/science/article/pii/S1876610214018578. 12th International Conference on Greenhouse Gas Control Technologies, GHGT-12.

[227] J. Riaza, M.V. Gil, L. Álvarez, C. Pevida, J.J. Pis, and F. Rubiera. Oxy-fuel combustion of coal and biomass blends. *Energy*, 41(1):429 – 435, 2012. ISSN 0360-5442. doi: https://doi.org/10.1016/j.energy.2012.02.057. URL http://www.sciencedirect.com/science/article/pii/S0360544212001715. 23rd International Conference on Efficiency, Cost, Optimization, Simulation and Environmental Impact of Energy Systems, ECOS 2010.

[228] Juan Riaza, Reza Khatami, Yiannis A. Levendis, Lucía Álvarez, María V. Gil, Covadonga Pevida, Fernando Rubiera, and José J. Pis. Combustion of single biomass particles in air and in oxy-fuel conditions. *Biomass and Bioenergy*, 64:162 – 174, 2014. ISSN 0961-9534. doi: https://doi.org/10.1016/j.biombioe.2014.03.018. URL http://www.sciencedirect.com/science/article/pii/S0961953414001366.

[229] Calin-Cristian Cormos. Oxy-combustion of coal, lignite and biomass: A techno-economic analysis for a large scale Carbon Capture and Storage (CCS) project in Romania. *Fuel*, 169:50 – 57, 2016. ISSN 0016-2361. doi: https://doi.org/10.1016/j.fuel.2015.12.005. URL http://www.sciencedirect.com/science/article/pii/S0016236115012582.

[230] Szabolcs Fogarasi and Calin-Cristian Cormos. Assessment of coal and sawdust co-firing power generation under oxy-combustion conditions with carbon capture and storage. *Journal of Cleaner Production*, 142:3527 – 3535, 2017. ISSN 0959-6526. doi: https://doi.org/10.1016/j.jclepro.2016.10.115. URL http://www.sciencedirect.com/science/article/pii/S0959652616317371.

[231] Yanqing Niu, Houzhang Tan, and Shi'en Hui. Ash-related issues during biomass combustion: Alkali-induced slagging, silicate melt-induced slagging (ash fusion), agglomeration, corrosion, ash utilization, and related countermeasures. *Progress in Energy and Combustion Science*, 52:1 – 61, 2016. ISSN 0360-1285. doi: https://doi.org/10.1016/j.pecs.2015.09.003. URL http://www.sciencedirect.com/science/article/pii/S0360128515300216.

[232] T. J. Kotas. Exergy concepts for thermal plant: First of two papers on exergy techniques in thermal plant analysis. *International Journal of Heat and Fluid Flow*, 2(3):105 – 114, 1980. ISSN 0142-727X. doi: https://doi.org/10.1016/0142-727X(80)90028-4. URL http://www.sciencedirect.com/science/article/pii/0142727X80900284.

[233] A.P. Hinderink, F.P.J.M. Kerkhof, A.B.K. Lie, J. De Swaan Arons, and H.J. Van Der Kooi. Exergy analysis with a flowsheeting simulator—i. theory; calculating exergies of material streams. *Chemical Engineering Science*, 51(20):4693 – 4700, 1996. ISSN 0009-2509. doi: https://doi.org/10.1016/0009-2509(96)00220-5. URL http://www.sciencedirect.com/science/article/pii/0009250996002205.

[234] Tyson Delmar Gray. An introduction to exergy and its evaluation using Aspen Plus. Kansas State University, 2019.

[235] *Aspen HYSYS User Operations Guide*. Aspen Technology Inc., 2011.

[236] A. W. Westerberg, H. P. Hutchison, R. L. Motard, and P. Winter. *Process flowsheeting*. Cambridge University Press, 1979.

[237] R. Krishnamurthy and R. Taylor. A nonequilibrium stage model of multicomponent separation processes. part i: Model description and method of solution. *AIChE Journal*, 31(3):449–456. doi: 10.1002/aic.690310312. URL https://onlinelibrary.wiley.com/doi/abs/10.1002/aic.690310312.

[238] J. Fair. Distillation. In *Kirk-Othmer Encyclopedia of Chemical Technology*, volume 8. John Wiley and Sons, Inc., 2001.

[239] Shivalingappa Sapali and V. N. Raibhole. Exergy Analysis of Cryogenic Air Separation Unit Integrated with Biomass Gasifier. volume 2, pages 621–625, 10 2013. ISBN 978-988-19253-1-2.

[240] Ding-Yu Peng and Donald B. Robinson. A New Two-Constant Equation of State. *Industrial & Engineering Chemistry Fundamentals*, 15:59–64, 2 1976. ISSN 0196-4313. doi: 10.1021/i160057a011. URL https://doi.org/10.1021/i160057a011.

[241] Hendrick C. Van Ness and Michael M. Abbott. Property calculations for gases and vapors. In *Perry's Chemical Engineers' Handbook*, chapter 4: Thermodynamics, pages 649 – 688. McGraw Hill Professional, Access Engineering, Eighth edition, 2008. ISBN 9780071422949.

[242] Robert James, Alexander Zoelle, Dale Keairns, Marc Turner, Mark Woods, and Norma Kuehn. Cost and performance baseline for fossil energy plants volume 1: Bituminous coal and natural gas to electricity. Technical Report NETL-PUB-22638, National Energy Technology Laboratory.

[243] Orla Williams, Carol Eastwick, Sam Kingman, Donald Giddings, Stephen Lormor, and Edward Lester. Investigation into the applicability of Bond Work Index (BWI) and Hardgrove Grindability Index (HGI) tests for several biomasses compared to Colombian La Loma coal. *Fuel*, 158:379 – 387, 2015. ISSN 0016-2361. doi: https://doi.org/10.1016/j.fuel.2015.05.027. URL http://www.sciencedirect.com/science/article/pii/S0016236115005232.

[244] Gebr. Pfeiffer SE. The versatile MPS vertical mill - with a fine tradition of quality grinding, 2017. URL http://www.gebr-pfeiffer.com/en/products/mps-vertical-roller-mill/?AppId=21.

[245] Yuming Gao, Indrek Külaots, Xu Chen, Eric M. Suuberg, Robert H. Hurt, and John M. Veranth. The effect of solid fuel type and combustion conditions on residual carbon properties and fly ash quality. *Proceedings of the Combustion Institute*, 29(1):475 – 483, 2002. ISSN 1540-7489. doi: https://doi.org/10.1016/S1540-7489(02)80062-1. URL http://www.sciencedirect.com/science/article/pii/S1540748902800621.

[246] Niko Hachenberg. Predictions of NOx emissions in pulverized coal combustion. University of Louisville. Electronic thesis and Dissertations. Paper 557, 2014.

[247] W. Richter, R. Payne, and M. P. Heap. Influence of thermal properties of wall deposits on performance of P. F. fired boiler combustion chambers. In *ACS Division of Fuel Chemistry, Preprints*, pages 249–261, 1984.

[248] Reza Sharifi, Sarma V. Pisupati, and Alan W. Scaroni. *Combustion Science and Technology*. American Cancer Society, 2000. ISBN 9780471238966. doi: 10.1002/0471238961.0315130219080118.a01. URL https://onlinelibrary.wiley.com/doi/abs/10.1002/0471238961.0315130219080118.a01.

[249] George Booras and Neville Holt. Pulverized coal and IGCC plant cost and performance estimates. In *Gasification Technologies*, Washington, DC, 2004.

[250] I. Warren. Ljungstrom heat exchangers for waste heat recovery. *Journal of Heat Recovery Systems*, 2(3):257 – 271, 1982. ISSN 0198-7593. doi: http://dx.doi.org/10.1016/0198-7593(82)90019-4. URL http://www.sciencedirect.com/science/article/pii/0198759382900194.

[251] Sreedhar Volloju, E. Manoj Kumar, M. Suresh Kumar, and K. Krishna Reddy. Analysis of Performance of Ljungstrom Air Preheater Elements. *International Journal of Current Engineering and Technology*, Special Issue-2:501 – 505, 2014.

[252] Don W. Green and Robert H. Perry. Energy recovery. In *Perry's Chemical Engineers' Handbook*, chapter 24: Energy Resources, Conversion, and Utilization. John Wiley and Sons, Inc., eighth edition, 2008.

[253] Tomme J. Lambertson. Performance of a Periodic-Flow Heat Exchanger. Master thesis, United States Naval Postgraduate School Monterey, California, 1957.

[254] R. W. Haywoo. *Analysis of Engineering Cycles: Power, Refrigerating and Gas Liquefaction Plant*. Pergamon Press plc., Headington Hill Hall, Oxford OX3 0BW, England, fourth edition, 1991.

[255] Mai Bui, Mathilde Fajardy, and Niall Mac Dowell. Bio-energy with carbon capture and storage (BECCS): Opportunities for performance improvement. *Fuel*, 213: 164 – 175, 2018. ISSN 0016-2361. doi: https://doi.org/10.1016/j.fuel.2017.10.100. URL http://www.sciencedirect.com/science/article/pii/S0016236117313583.

[256] Naser A. Odeh and Timothy T. Cockerill. Life cycle analysis of UK coal fired power plants. *Energy Conversion and Management*, 49(2):212 – 220, 2008. ISSN 0196-8904. doi: https://doi.org/10.1016/j.enconman.2007.06.014. URL http://www.sciencedirect.com/science/article/pii/S0196890407001756.

[257] Francisco Carrasco-Maldonado, Reinhold Spörl, Kristina Fleiger, Volker Hoenig, Jörg Maier, and Günter Scheffknecht. Oxy-fuel combustion technology for cement production – State of the art research and technology development. *International Journal of Greenhouse Gas Control*, 45:189 – 199, 2016. ISSN 1750-5836. doi: https://doi.org/10.1016/j.ijggc.2015.12.014. URL http://www.sciencedirect.com/science/article/pii/S1750583615301614.

[258] Thomas J. Ward. *Economic Evaluation*. John Wiley & Sons, Inc., 2000. ISBN 9780471238966. doi: 10.1002/0471238961.0503151423011804.a01.pub2. URL http://dx.doi.org/10.1002/0471238961.0503151423011804.a01.pub2.

[259] Sidney Katell and Paul Wellman. An evaluation of tonnage oxygen plants. *ACS Fuel Division Preprints*, 14(3):99–104, 1970.

[260] James R. Couper, Darryl W. Hertz, and Francis Lee Smith. Cash Flow. In *Perry's Chemical Engineers' Handbook*, chapter 9: Process economics. McGraw Hill Professional, Access Engineering, Eighth edition, 2008. ISBN 9780071422949.

[261] Farzad Abdollahi-Demneh, Mohammad Ali Moosavian, Mohammad Reza Omidkhah, and Hossein Bahmanyar. Calculating exergy in flowsheeting simulators: A HYSYS implementation. *Energy*, 36(8):5320 – 5327, 2011. ISSN 0360-5442. doi: https://doi.org/10.1016/j.energy.2011.06.040. URL http://www.sciencedirect.com/science/article/pii/S0360544211004269. PRES 2010.

[262] Jared Ciferno. Pulverized Coal Oxycombustion Power Plants. Technical Report DOE/NETL-2007/1291, National Energy Technology Laboratory.

[263] Richard T. J. Porter, Michael Fairweather, Clea Kolster, Niall Mac Dowell, Nilay Shah, and Robert M. Woolley. Cost and performance of some carbon capture technology options for producing different quality CO_2 product streams. *International Journal of Greenhouse Gas Control*, 57:185 – 195, 2017. ISSN 1750-5836. doi: https://doi.org/10.1016/j.ijggc.2016.11.020. URL http://www.sciencedirect.com/science/article/pii/S1750583616308398.

[264] Ludwig Heck, Nikolaus Poth, and Vipasha Soni. *Pinch Technology*. American Cancer Society, 2009. ISBN 9783527306732. doi: https://doi.org/10.1002/14356007.b03_13.pub2. URL https://onlinelibrary.wiley.com/doi/abs/10.1002/14356007.b03_13.pub2.

[265] U.S. Energy Information Administration. How much coal, natural gas, or petroleum is used to generate a kilowatthour of electricity?, February 2016. URL https://www.eia.gov/tools/faqs/faq.cfm?id=667&t=2.

[266] Edward S. Rubin, Haibo Zhai, Karen Kietzke, and Hari Mantripragada. Integrated Environmental Control Model, Version 9.2.1, Public Release; Carnegie Mellon University: Pittsburgh, PA. http://www.cmu.edu/epp/iecm/, 2016.

[267] M. Taniguchi, H. Asaoka, and T. Ayuhara. Energy saving air separation plant based on exergy analysis. *R and D: Research and Development Kobe Steel Engineering Reports*, 64:45–48, 04 2014.

[268] H. Li, J. Yan, J. Yan, and M. Anheden. Impurity impacts on the purification process in oxy-fuel combustion based CO_2 capture and storage system. *Applied Energy*, 86(2):202 – 213, 2009. ISSN 0306-2619. doi: https://doi.org/10.1016/j.apenergy.2008.05.006. URL http://www.sciencedirect.com/science/article/pii/S0306261908001281. IGEC III.

[269] Renato P. Cabral, David J. Heldebrant, and Niall Mac Dowell. A Techno-Economic Analysis of a Novel Solvent-Based Oxycombustion CO_2 Capture Process. *Industrial & Engineering Chemistry Research*, 58(16):6604–6612, 2019. doi: 10.1021/acs.iecr.9b00305. URL https://doi.org/10.1021/acs.iecr.9b00305.

[270] Nicolas Perrin, Richard Dubettier, Frederick Lockwood, Jean-Pierre Tranier, Claire Bourhy-Weber, and Paul Terrien. Oxycombustion for coal power plants: Advantages, solutions and projects. *Applied Thermal Engineering*, 74:75 – 82, 2015. ISSN 1359-4311. doi: https://doi.org/10.1016/j.applthermaleng.2014.03.074. URL http://www.sciencedirect.com/science/article/pii/S1359431114002750. 6th International Conference on Clean Coal Technologies CCT2013.

[271] Norfamila Che Mat and G. Glenn Lipscomb. Membrane process optimization for carbon capture. *International Journal of Greenhouse Gas Control*, 62:1 – 12, 2017. ISSN 1750-5836. doi: https://doi.org/10.1016/j.ijggc.2017.04.002. URL http://www.sciencedirect.com/science/article/pii/S1750583616308799.

[272] Maria T. Mota-Martinez, Patrick Brandl, Jason P. Hallett, and Niall Mac Dowell. Challenges and opportunities for the utilisation of ionic liquids as solvents for CO_2 capture. *Molecular Systems Design & Engineering*, 3:560–571, 2018. doi: 10.1039/C8ME00009C. URL http://dx.doi.org/10.1039/C8ME00009C.

[273] Anand B. Rao and Edward S. Rubin. A Technical, Economic, and Environmental Assessment of Amine-Based CO_2 Capture Technology for Power Plant Greenhouse Gas Control. *Environmental Science & Technology*, 36(20):4467–4475, 2002. doi: 10.1021/es0158861. URL https://doi.org/10.1021/es0158861. PMID: 12387425.

[274] Debangsu Bhattacharyya and David C Miller. Post-combustion CO_2 capture technologies — a review of processes for solvent-based and sorbent-based CO_2 capture. *Current Opinion in Chemical Engineering*, 17:78 – 92, 2017. ISSN 2211-3398. doi: https://doi.org/10.1016/j.coche.2017.06.005. URL http://www.sciencedirect.com/science/article/pii/S2211339817300205. Energy and Environmental Engineering / Reaction engineering and catalysis.

[275] J. de Riva, V. Ferro, C. Moya, M. A. Stadtherr, J. F. Brennecke, and J. Palomar. Aspen Plus supported analysis of the post-combustion CO_2 capture by chemical absorption using the [P2228][CNPyr] and [P66614][CNPyr]AHA Ionic Liquids. *International Journal of Greenhouse Gas Control*, 78:94 – 102, 2018. ISSN 1750-5836. doi: https://doi.org/10.1016/j.ijggc.2018.07.016. URL http://www.sciencedirect.com/science/article/pii/S1750583618301750.

[276] Qian Cui, Haoren Lu, Chufu Li, Surinder Singh, Liming Ba, Xinglei Zhao, and Anthony Y. Ku. China baseline coal-fired power plant with post-combustion CO_2 capture: 1. Definitions and performance. *International Journal of Greenhouse Gas Control*, 78:37 – 47, 2018. ISSN 1750-5836. doi: https://doi.org/10.1016/j.ijggc.2018.07.021. URL http://www.sciencedirect.com/science/article/pii/S1750583618300628.

[277] Mai Bui, Paul Tait, Mathieu Lucquiaud, and Niall Mac Dowell. Dynamic operation and modelling of amine-based CO_2 capture at pilot scale. *International Journal of Greenhouse Gas Control*, 79:134 – 153, 2018. ISSN 1750-5836. doi: https://doi.org/10.1016/j.ijggc.2018.08.016. URL http://www.sciencedirect.com/science/article/pii/S1750583618304250.

[278] Paul M. Mathias, Louis V. Jasperson, David VonNiederhausern, Mark D. Bearden, Phillip K. Koech, Charles J. Freeman, and David J. Heldebrant. Assessing anhydrous tertiary alkanolamines for high-pressure gas purifications. *Industrial & Engineering Chemistry Research*, 52(49):17562–17572, 2013. doi: 10.1021/ie4020974. URL https://doi.org/10.1021/ie4020974.

[279] Aspen Technology, Inc. Physical property methods and models, 2001.

[280] Sigma-Aldrich. N-Ethyldiethanolamine. https://www.sigmaaldrich.com/catalog/product/aldrich/112062?lang=en&region=GB, . Accessed: Oct. 2018.

[281] James R. Couper, W. Roy Penney, James R. Fair, and Stanley M. Walas. Chapter 21 - Costs of Individual Equipment. In *Chemical Process Equipment*, pages 717 – 726. Gulf Professional Publishing, Burlington, Second edition, 2010. ISBN 978-0-7506-7510-9.

[282] National Center for Biotechnology Information. PubChem Compound Database; CID=8769. N-Ethyldiethanolamine. https://pubchem.ncbi.nlm.nih.gov/compound/8769. Accessed: Nov. 2018.

[283] Ralph M. DiGuilio, Rong Jwyn Lee, Steven T. Schaeffer, Laura L. Brasher, and Amyn S. Teja. Densities and viscosities of the ethanolamines. *Journal of Chemical & Engineering Data*, 37(2):239–242, 1992. doi: 10.1021/je00006a028. URL https://doi.org/10.1021/je00006a028.

[284] Faisal Islam Chowdhury, Shamim Akhtar, and Muhammad A. Saleh. Viscosities and excess viscosities of aqueous solutions of some diethanolamines. *Journal of Molecular Liquids*, 155(1):1 – 7, 2010. ISSN 0167-7322. doi: https://doi.org/10.1016/j.molliq.2010.03.015. URL http://www.sciencedirect.com/science/article/pii/S0167732210001017.

[285] Aspen Technology, Inc. Aspen capital cost estimator version 8.0, 2012.

[286] UK Electricity Generation Costs Update. Technical report, Mott MacDonald, June 2010.

[287] Gary Schnitkey. Nitrogen Prices, Rates Cuts, and 2018 Fertilizer Costs. *farmdoc daily*, 8:58, 2018. URL https://farmdocdaily.illinois.edu/2018/04/nitrogen-prices-rates-cuts-and-2018-fertilizer-cost.html.

[288] Sigma-Aldrich. Ethanolamine. https://www.sigmaaldrich.com/catalog/product/aldrich/15014?lang=en&region=GB, . Accessed: Nov. 2018.

[289] Anand B. Rao. Details of a technical, economic and environmental assessment of amine-based CO_2 capture technology for power plant greenhouse gas control. Technical Report DE-FC26-00NT40935, United States Department of Energy, Carnegie Mellon University, 2002.

[290] R. K. Sinnott. 6.10.1 Cash Flow and Cash-Flow Diagrams. In *Coulson and Richardson's Chemical Engineering Volume 6 - Chemical Engineering Design*. Elsevier, Fourth edition, 2005. ISBN 978-0-7506-6538-4. URL https://app.knovel.com/hotlink/khtml/id:kt007SFMJ1/coulson-richardsons-chemical/cash-flow-cash-flow-diagrams.

[291] National Center for Biotechnology Information. Compound Summary for CID 8769, N-Ethyldiethanolamine, December 2019. URL https://pubchem.ncbi.nlm.nih.gov/compound/N-Ethyldiethanolamine. Accessed 21 December 2019.

[292] National Center for Biotechnology Information. PubChem Compound Summary for CID 6341, Ethylamine, December 2019. URL https://pubchem.ncbi.nlm.nih.gov/compound/Ethylamine. Accessed 21 December 2019.

[293] National Center for Biotechnology Information. PubChem Compound Summary for CID 700, Ethanolamine, December 2019. URL https://pubchem.ncbi.nlm.nih.gov/compound/Ethanolamine. Accessed 21 December 2019.

[294] James Katzer, Staphev Ansolabehere, Janos Beer, John Deutch, A. Denny Ellerman, S. Julio Friedmann, Howard Herzog, Henry D. Jacoby, Paul L. Joskow, Gregory McRae, Richard Lester, Ernest J. Moniz, and Edward Steinfeld. The future of coal. Technical report, MIT, 2007.

[295] Anna Hnydiuk-Stefan and Jan Składzień. Analysis of supercritical coal fired oxy combustion power plant with cryogenic oxygen unit and turbo-compressor. *Energy*, 128:271 – 283, 2017. ISSN 0360-5442. doi: https://doi.org/10.1016/j.energy.2017.04.021. URL http://www.sciencedirect.com/science/article/pii/S0360544217305868.

[296] R. López, M. Menéndez, C. Fernández, and A. Bernardo-Sánchez. The effects of scale-up and coal-biomass blending on supercritical coal oxy-combustion power plants. *Energy*, 148:571 – 584, 2018. ISSN 0360-5442. doi: https://doi.org/10.1016/j.energy.2018.01.179. URL http://www.sciencedirect.com/science/article/pii/S036054421830207X.

[297] Ch. Wohlfarth and B. Wohlfahrt. Pure Organic Liquids · C6: Datasheet from Landolt-Börnstein - Group IV Physical Chemistry · Volume 18B: "Pure Organic Liquids" in SpringerMaterials (https://doi.org/10.1007/10639283_7). URL https://materials.springer.com/lb/docs/sm_lbs_978-3-540-48513-1_7. Copyright 2002 Springer-Verlag Berlin Heidelberg.

[298] Y. Maham, C.-N. Liew, and A. E. Mather. Viscosities and Excess Properties of Aqueous Solutions of Ethanolamines from 25 to 80°C. *Journal of Solution Chemistry*, 31(9):743 – 756, 2002. ISSN 1572-8927.

[299] M. Nazrul Islam, M. Monirul Islam, and M.N. Yeasmin. Viscosity of aqueous solutions of 2-methoxyethanol, 2-ethoxyethanol, and ethanolamine. *The Journal of Chemical Thermodynamics*, 36(10):889 – 893, 2004. ISSN 0021-9614. doi: https://doi.org/10.1016/j.jct.2004.06.004. URL http://www.sciencedirect.com/science/article/pii/S002196140400117X.

[300] Renato P. Cabral, Mai Bui, and Niall Mac Dowell. A synergistic approach for the simultaneous decarbonisation of power and industry via bioenergy with carbon capture and storage (BECCS). *International Journal of Greenhouse Gas Control*, 87:221 – 237, 2019. ISSN 1750-5836. doi: https://doi.org/10.1016/j.ijggc.2019.05.020. URL http://www.sciencedirect.com/science/article/pii/S1750583619301422.

[301] Praveen Bains, Peter Psarras, and Jennifer Wilcox. CO_2 capture from the industry sector. *Progress in Energy and Combustion Science*, 63:146 – 172, 2017. ISSN 0360-1285. doi: https://doi.org/10.1016/j.pecs.2017.07.001. URL http://www.sciencedirect.com/science/article/pii/S0360128517300114.

[302] Peter C. Psarras, Stephen Comello, Praveen Bains, Panunya Charoensawadpong, Stefan Reichelstein, and Jennifer Wilcox. Carbon Capture and Utilization in the Industrial Sector. *Environmental Science & Technology*, 51(19):11440–11449, 2017. doi: 10.1021/acs.est.7b01723. URL https://doi.org/10.1021/acs.est.7b01723. PMID: 28858476.

[303] Duncan Leeson, Niall Mac Dowell, Nilay Shah, Camille Petit, and Paul S. Fennell. A Techno-economic analysis and systematic review of carbon capture and storage (CCS) applied to the iron and steel, cement, oil refining and pulp and paper industries, as well as other high purity sources. *International Journal of Greenhouse Gas Control*, 61:71 – 84, 2017. ISSN 1750-5836. doi: https://doi.org/10.1016/j.ijggc.2017.03.020. URL http://www.sciencedirect.com/science/article/pii/S175058361730289X.

[304] Elsayed Mousa, Chuan Wang, Johan Riesbeck, and Mikael Larsson. Biomass applications in iron and steel industry: An overview of challenges and opportunities. *Renewable and Sustainable Energy Reviews*, 65:1247 – 1266, 2016. ISSN 1364-0321. doi: https://doi.org/10.1016/j.rser.2016.07.061. URL http://www.sciencedirect.com/science/article/pii/S1364032116303896.

[305] Rahul Baidya, Sadhan Kumar Ghosh, and Ulhas V. Parlikar. Co-processing of Industrial Waste in Cement Kiln – A Robust System for Material and Energy

Recovery. *Procedia Environmental Sciences*, 31:309 – 317, 2016. ISSN 1878-0296. doi: https://doi.org/10.1016/j.proenv.2016.02.041. URL http://www.sciencedirect.com/science/article/pii/S1878029616000426. Selected Proceedings of the Tenth International Conference on Waste Management and Technology.

[306] Mohannad Mayyas, Rasoul Khayyam Nekouei, and Veena Sahajwalla. Valorization of lignin biomass as a carbon feedstock in steel industry: Iron oxide reduction, steel carburizing and slag foaming. *Journal of Cleaner Production*, 219:971 – 980, 2019. ISSN 0959-6526. doi: https://doi.org/10.1016/j.jclepro.2019.02.114. URL http://www.sciencedirect.com/science/article/pii/S0959652619305037.

[307] CEMEX UK Operations Limited. Alternative Fuels. URL https://www.cemex.co.uk/alternativefuels.aspx. Accessed 09 November 2020.

[308] Carbon Capture and Storage in Industrial Applications. Technical report, United Nations Industrial Development Organisation, November 2010.

[309] Karin Bäckstrand, James Meadowcroft, and Michael Oppenheimer. The politics and policy of carbon capture and storage: Framing an emergent technology. *Global Environmental Change*, 21(2):275 – 281, 2011. ISSN 0959-3780. doi: https://doi.org/10.1016/j.gloenvcha.2011.03.008. URL http://www.sciencedirect.com/science/article/pii/S0959378011000355. Special Issue on The Politics and Policy of Carbon Capture and Storage.

[310] Amit Bhave, Richard H.S. Taylor, Paul Fennell, William R. Livingston, Nilay Shah, Niall Mac Dowell, John Dennis, Markus Kraft, Mohammed Pourkashanian, Mathieu Insa, Jenny Jones, Nigel Burdett, Ausilio Bauen, Corinne Beal, Andrew Smallbone, and Jethro Akroyd. Screening and techno-economic assessment of biomass-based power generation with CCS technologies to meet 2050 CO_2 targets. *Applied Energy*, 190:481 – 489, 2017. ISSN 0306-2619. doi: https://doi.org/10.1016/j.apenergy.2016.12.120. URL http://www.sciencedirect.com/science/article/pii/S0306261916319043.

[311] John Davison. CCS in Industrial Processes. In *Workshop organized by the Swiss Federal Office of Energy*, 2014.

[312] Paul Zakkour and Greg Cook. CCS Roadmap for Industry: High-purity CO_2 sources. Technical Report 025, United Nations Industrial Development Organisation, September 2010.

[313] IEA GHG CO_2 Emissions Database. www.ieaghg.org/index.php?/20091223127/co2-emissions-database.html, . Accessed September 2018.

[314] 2016 UK Greenhouse gas emissions, final figures. Technical report, Department for Business, Energy, & Industrial Strategy, 2018.

[315] Ioannis Tsagatakis, Shaun Brace, Neil Passant, Ben Pearson, Ben Kiff, Joe Richardson, and Mark Ruddy. UK Emission Mapping Methodology. Technical Report ED62438203, Department for Business, Energy, & Industrial Strategy, October 2017.

[316] Energy Technology Perspectives 2017. Catalysing Energy Technology Transformations. Technical report, International Energy Agency, 2017.

[317] Niall Mac Dowell, Paul S. Fennell, Nilay Shah, and Geoffrey C. Maitland. The role of CO_2 capture and utilisation in mitigating climate change. *Nature Climate Change*, 7:243–249, Apr 2017. URL https://doi.org/10.1038/nclimate3231.

[318] Vasileios Papaioannou, Filipe Calado, Thomas Lafitte, Simon Dufal, Majid Sadeqzadeh, George Jackson, Claire S. Adjiman, and Amparo Galindo. Application of the SAFT-γ Mie group contribution equation of state to fluids of relevance to the oil and gas industry. *Fluid Phase Equilibria*, 416:104 – 119, 2016. ISSN 0378-3812. doi: https://doi.org/10.1016/j.fluid.2015.12.041. URL http://www.sciencedirect.com/science/article/pii/S0378381215302831. Special Issue: SAFT 2015.

[319] Katarzyna Janusz-Szymańska and Aleksandra Dryjańska. Possibilities for improving the thermodynamic and economic characteristics of an oxy-type power plant with a cryogenic air separation unit. *Energy*, 85:45 – 61, 2015. ISSN 0360-5442. doi: https://doi.org/10.1016/j.energy.2015.03.049. URL http://www.sciencedirect.com/science/article/pii/S0360544215003436.

[320] Asghar Ghasemi and Saleh Zahediasl. Normality tests for statistical analysis: a guide for non-statisticians. *International journal of endocrinology and metabolism*, 10(2):486–489, 2012. ISSN 1726-9148. URL https://www.ncbi.nlm.nih.gov/pubmed/23843808.

[321] Edward S. Rubin, Christopher Short, George Booras, John Davison, Clas Ekstrom, Michael Matuszewski, and Sean McCoy. A proposed methodology for CO_2 capture and storage cost estimates. *International Journal of Greenhouse Gas Control*, 17:488 – 503, 2013. ISSN 1750-5836. doi: https://doi.org/10.1016/j.ijggc.2013.06.004. URL http://www.sciencedirect.com/science/article/pii/S1750583613002521.

[322] R. López, C. Fernández, O. Martínez, and M.E. Sánchez. Techno-economic analysis of a 15 MW corn-rape oxy-combustion power plant. *Fuel Processing Technology*, 142:296 – 304, 2016. ISSN 0378-3820. doi: https://doi.org/10.1016/j.fuproc.2015.10.020. URL http://www.sciencedirect.com/science/article/pii/S0378382015302071.

[323] Duncan McLaren. A comparative global assessment of potential negative emissions technologies. *Process Safety and Environmental Protection*, 90(6):489 – 500, 2012. ISSN 0957-5820. doi: https://doi.org/10.1016/j.psep.2012.10.005. URL http://www.sciencedirect.com/science/article/pii/S0957582012001176. Special Issue: Negative emissions technology.

[324] Nasim Pour, Paul A. Webley, and Peter J. Cook. Opportunities for application of BECCS in the Australian power sector. *Applied Energy*, 224:615 – 635, 2018. ISSN 0306-2619. doi: https://doi.org/10.1016/j.apenergy.2018.04.117. URL http://www.sciencedirect.com/science/article/pii/S0306261918306846.

[325] Potential for Biomass and Carbon Dioxide Capture and Storage. Technical Report 2011/06, IEAGHG, July 2011.

[326] IEA. Carbon capture and storage roadmap, 2010.

[327] E. Kakaras, A. Koumanakos, A. Doukelis, D. Giannakopoulos, and I. Vorrias. Simulation of a Greenfield oxyfuel lignite-fired power plant. *Energy Conversion and Management*, 48(11):2879 – 2887, 2007. ISSN 0196-8904. doi: https://doi.org/10.1016/j.enconman.2007.07.017. URL http://www.sciencedirect.com/science/article/pii/S0196890407002075. 19th International Conference on Efficiency, Cost, Optimization, Simulation and Environmental Impact of Energy Systems.

[328] IEA. World Energy Investment, 2016.

[329] IEA. Coal 2017, 2017.

[330] Simon Evans, Rosamund Pearce, and Carbon Brief. Mapped: The world's coal power plants. https://www.carbonbrief.org/mapped-worlds-coal-power-plants. Accessed November 2018.

[331] Niall Mac Dowell and Mathilde Fajardy. Inefficient power generation as an optimal route to negative emissions via BECCS? *Environmental Research Letters*, 12(4):045004, apr 2017. doi: 10.1088/1748-9326/aa67a5. URL https://doi.org/10.1088%2F1748-9326%2Faa67a5.

[332] Sebastian Weida, Subhash Kumar, and Reinhard Madlener. Financial Viability of Grid-connected Solar PV and Wind Power Systems in Germany. *Energy Procedia*, 106:35 – 45, 2016. ISSN 1876-6102. doi: https://doi.org/10.1016/j.egypro.2016.12.103. URL http://www.sciencedirect.com/science/article/pii/S1876610216316617. Energy Economics Iberian Conference, EEIC 2016, 4-5 February 2016, Lisbon, Portugal.

[333] International Energy Agency. *World Energy Outlook 2014*. 2014. doi: https://doi.org/https://doi.org/10.1787/weo-2014-en. URL https://www.oecd-ilibrary.org/content/publication/weo-2014-en.

[334] J. Domac, K. Richards, and S. Risovic. Socio-economic drivers in implementing bioenergy projects. *Biomass and Bioenergy*, 28(2):97 – 106, 2005. ISSN 0961-9534. doi: https://doi.org/10.1016/j.biombioe.2004.08.002. URL http://www.sciencedirect.com/science/article/pii/S0961953404001485.

[335] Samuel Fankhauser, Friedel Sehlleier, and Nicholas Stern. Climate change, innovation and jobs. *Climate Policy*, 8:421 – 429, 2008. doi: 10.3763/cpol.2008.0513. URL https://doi.org/10.3763/cpol.2008.0513.

[336] Patricia Thornley, John Rogers, and Ye Huang. Quantification of employment from biomass power plants. *Renewable Energy*, 33(8):1922 – 1927, 2008. ISSN 0960-1481. doi: https://doi.org/10.1016/j.renene.2007.11.011. URL http://www.sciencedirect.com/science/article/pii/S0960148107003734.

[337] Clean Air – Clean Industry – Clean Growth, How Carbon Capture Will Boost the UK, Economy East Coast UK Carbon Capture and Storage Investment Study. Technical report, Summit Power, 2015.

[338] Max Wei, Shana Patadia, and Daniel M. Kammen. Putting renewables and energy efficiency to work: How many jobs can the clean energy industry generate in the US? *Energy Policy*, 38(2):919 – 931, 2010. ISSN 0301-4215. doi: https://doi.org/10.1016/j.enpol.2009.10.044. URL http://www.sciencedirect.com/science/article/pii/S0301421509007915.

[339] Oliver Garbrecht, Malte Bieber, and Reinhold Kneer. Increasing fossil power plant flexibility by integrating molten-salt thermal storage. *Energy*, 118:876 – 883, 2017. ISSN 0360-5442. doi: https://doi.org/10.1016/j.energy.2016.10.108. URL http://www.sciencedirect.com/science/article/pii/S0360544216315547.

[340] Marcel Richter, Gerd Oeljeklaus, and Klaus Görner. Improving the load flexibility of coal-fired power plants by the integration of a thermal energy storage. *Applied Energy*, 236:607 – 621, 2019. ISSN 0306-2619. doi: https://doi.org/10.1016/j.apenergy.2018.11.099. URL http://www.sciencedirect.com/science/article/pii/S0306261918318142.

[341] Chaoyang Wang, Yongliang Zhao, Ming Liu, Yongqiang Qiao, Daotong Chong, and Junjie Yan. Peak shaving operational optimization of supercritical coal-fired power plants by revising control strategy for water-fuel ratio. *Applied Energy*, 216:212 – 223, 2018. ISSN 0306-2619. doi: https://doi.org/10.1016/j.apenergy.2018.02.039. URL http://www.sciencedirect.com/science/article/pii/S0306261918301648.

[342] Yongliang Zhao, Ming Liu, Chaoyang Wang, Xin Li, Daotong Chong, and Junjie Yan. Increasing operational flexibility of supercritical coal-fired power plants by regulating thermal system configuration during transient processes. *Applied Energy*, 228:2375 – 2386, 2018. ISSN 0306-2619. doi: https://doi.org/10.1016/j.apenergy.2018.07.070. URL http://www.sciencedirect.com/science/article/pii/S0306261918310997.

[343] Mathieu Lucquiaud, Hannah Chalmers, and Jon Gibbins. Capture-ready supercritical coal-fired power plants and flexible post-combustion CO_2 capture. *Energy Procedia*, 1(1):1411 – 1418, 2009. ISSN 1876-6102. doi: https://doi.org/10.1016/j.egypro.2009.01.185. URL http://www.sciencedirect.com/science/article/pii/S1876610209001866. Greenhouse Gas Control Technologies 9.

[344] Hannah Chalmers, Mathieu Lucquiaud, Jon Gibbins, and Matt Leach. Flexible operation of coal fired power plants with postcombustion capture of carbon dioxide. *Journal of Environmental Engineering*, 135(6):449–458, 2009. doi: 10.1061/(ASCE)EE.1943-7870.0000007.

[345] John Davison. Flexible CCS plants–A key to near-zero emission electricity systems. *Energy Procedia*, 4:2548 – 2555, 2011. ISSN 1876-6102. doi: https://doi.org/10.1016/j.egypro.2011.02.152. URL http://www.sciencedirect.com/science/article/pii/S1876610211003493. 10th International Conference on Greenhouse Gas Control Technologies.

[346] Mai Bui, Indra Gunawan, Vincent Verheyen, Paul Feron, Erik Meuleman, and Sam Adeloju. Dynamic modelling and optimisation of flexible operation in post-combustion CO_2 capture plants—A review. *Computers & Chemical Engineering*, 61:245 – 265, 2014. ISSN 0098-1354. doi: https://doi.org/10.1016/j.compchemeng.2013.11.015. URL http://www.sciencedirect.com/science/article/pii/S0098135413003669.

[347] Niall Mac Dowell and Nilay Shah. The multi-period optimisation of an amine-based CO_2 capture process integrated with a super-critical coal-fired power station for flexible operation. *Computers & Chemical Engineering*, 74:169 – 183, 2015. ISSN 0098-1354. doi: https://doi.org/10.1016/j.compchemeng.2015.01.006. URL http://www.sciencedirect.com/science/article/pii/S0098135415000071.

[348] Evgenia Mechleri, Paul S. Fennell, and Niall Mac Dowell. Optimisation and evaluation of flexible operation strategies for coal- and gas-CCS power stations with a multi-period design approach. *International Journal of Greenhouse Gas Control*, 59:24 – 39, 2017. ISSN 1750-5836. doi: https://doi.org/10.1016/j.ijggc.2016.09.018. URL http://www.sciencedirect.com/science/article/pii/S1750583616303899.

[349] Abdirahman Mohamed Abdilahi and Mohd Wazir Mustafa. Carbon capture power plants: Decoupled emission and generation outputs for economic dispatch. *International Journal of Greenhouse Gas Control*, 63:12 – 19, 2017. ISSN 1750-5836. doi: https://doi.org/10.1016/j.ijggc.2017.05.001. URL http://www.sciencedirect.com/science/article/pii/S175058361730035X.

[350] Holger Teichgraeber, Philip G. Brodrick, and Adam R. Brandt. Optimal design and operations of a flexible oxyfuel natural gas plant. *Energy*, 141:506 – 518, 2017. ISSN 0360-5442. doi: https://doi.org/10.1016/j.energy.2017.09.087. URL http://www.sciencedirect.com/science/article/pii/S0360544217316067.

[351] Muhammad Zaman, Hong Jang, Muhammad Rizwan, and Jay H. Lee. Optimal design for flexible operation of the post-combustion CO_2 capture plant with uncertain economic factors. *Computers & Chemical Engineering*, 84:199 – 207, 2016. ISSN 0098-1354. doi: https://doi.org/10.1016/j.compchemeng.2015.09.002. URL http://www.sciencedirect.com/science/article/pii/S0098135415002938.

[352] Evgenia Mechleri, Adekola Lawal, Alfredo Ramos, John Davison, and Niall Mac Dowell. Process control strategies for flexible operation of post-combustion CO_2 capture plants. *International Journal of Greenhouse Gas Control*, 57:14 – 25, 2017. ISSN 1750-5836. doi: https://doi.org/10.1016/j.ijggc.2016.12.017. URL http://www.sciencedirect.com/science/article/pii/S1750583616306508.

[353] Gerhard Beysel. Enhanced cryogenic air separation - A proven process applied to oxyfuel, future prospects, 2009. Work presented at 1st Oxyfuel Combustion Conference, Cottbus.

[354] Qi Zhang, Ignacio E. Grossmann, Clara F. Heuberger, Arul Sundaramoorthy, and Jose M. Pinto. Air separation with cryogenic energy storage: Optimal scheduling

considering electric energy and reserve markets. *AIChE Journal*, 61(5):1547–1558, 2015. doi: 10.1002/aic.14730. URL https://aiche.onlinelibrary.wiley.com/doi/abs/10.1002/aic.14730.

[355] Kelvin André Pacheco, Yongliang Li, and Meihong Wang. Study of integration of cryogenic air energy storage and coal oxy-fuel combustion through modelling and simulation. In Jiří Jaromír Klemeš, Petar Sabev Varbanov, and Peng Yen Liew, editors, *24th European Symposium on Computer Aided Process Engineering*, volume 33 of *Computer Aided Chemical Engineering*, pages 1537 – 1542. Elsevier, 2014. doi: https://doi.org/10.1016/B978-0-444-63455-9.50091-X. URL http://www.sciencedirect.com/science/article/pii/B978044463455950091X.

[356] Rodrigo F. Abdo, Hugo T.C. Pedro, Ricardo N.N. Koury, Luiz Machado, Carlos F.M. Coimbra, and Matheus P. Porto. Performance evaluation of various cryogenic energy storage systems. *Energy*, 90:1024 – 1032, 2015. ISSN 0360-5442. doi: https://doi.org/10.1016/j.energy.2015.08.008. URL http://www.sciencedirect.com/science/article/pii/S0360544215010567.

[357] Sarah Hamdy, Tatiana Morosuk, and George Tsatsaronis. Cryogenics-based energy storage: Evaluation of cold exergy recovery cycles. *Energy*, 138:1069 – 1080, 2017. ISSN 0360-5442. doi: https://doi.org/10.1016/j.energy.2017.07.118. URL http://www.sciencedirect.com/science/article/pii/S0360544217312549.

[358] Charlotte Mitchell, Vitali Avagyan, Hannah Chalmers, and Mathieu Lucquiaud. An initial assessment of the value of Allam Cycle power plants with liquid oxygen storage in future GB electricity system. *International Journal of Greenhouse Gas Control*, 87:1 – 18, 2019. ISSN 1750-5836. doi: https://doi.org/10.1016/j.ijggc.2019.04.020. URL http://www.sciencedirect.com/science/article/pii/S17505836183077 6X.

[359] Operating Flexibility of Power Plants with CCS. Technical Report 2012/6, IEAGHG, June 2012.

[360] Yukun Hu, Anurag Tewari, Liz Varga, Hailong Li, and Jinyue Yan. System dynamics of oxyfuel power plants with liquid oxygen energy storage. *Energy Procedia*, 142:3727 – 3733, 2017. ISSN 1876-6102. doi: https://doi.org/10.1016/j.egypro.2017.12.268. URL http://www.sciencedirect.com/science/article/pii/S1876610217360022. Proceedings of the 9th International Conference on Applied Energy.

[361] Dimitri Goloubev and Alexander Alekseev. Integration of ASU in process of power generation, 20013. Work presented at 3rd Oxyfuel Combustion Conference, Ponferrada.

[362] NORD POOL. Day-ahead prices, June 2019. URL https://www.nordpoolgroup.com/Market-data1/Dayahead/Area-Prices/ALL1/Hourly/?view=table. Accessed 26 June 2019.

[363] Gas and LNG storage - The future of modular LNG tanks. Technical report, ARUP, 2017.

[364] Linde AG. Cryogenic standard tanks LITS 2, 2012.

[365] Eric W. Lemmon, Mark O. McLinden, and Daniel G. Friend. Thermophysical Properties of Fluid Systems. In P. J. Linstrom and Mallard W. G., editors, *NIST Chemistry WebBook, NIST Standard Reference Database Number 69*. National Institute of Standards and Technology, Gaithersburg MD, 20899, 2018. URL https://doi.org/10.18434/T4D303. Accessed 24 October 2018.

[366] IMERYS. Perlite, 2018.

[367] James R. Couper, W. Roy Penney, James R. Fair, and Stanley M. Walas. 18 - process vessels. In James R. Couper, W. Roy Penney, James R. Fair, and Stanley M. Walas, editors, *Chemical Process Equipment (Third Edition)*, pages 641 – 661. Butterworth-Heinemann, Boston, third edition edition, 2010. ISBN 978-0-12-396959-0. doi: https://doi.org/10.1016/B978-0-12-396959-0.00018-5. URL http://www.sciencedirect.com/science/article/pii/B9780123969590000185.

[368] Ruifu Zhang and Dagen Weng. Assessment of the seismic effect of insulation on extra-large cryogenic liquid natural gas storage tanks. *Journal of Loss Prevention in the Process Industries*, 30:9 – 16, 2014. ISSN 0950-4230. doi: https://doi.org/10.1016/j.jlp.2014.04.003. URL http://www.sciencedirect.com/science/article/pii/S0950423014000552.

[369] Shawnna M. Bennett. Perlite. In Wallace Bolen, editor, *2015 Minerals Yearbook*. USGS, 2017. URL https://s3-us-west-2.amazonaws.com/prd-wret/assets/palladium/production/mineral-pubs/perlite/myb1-2015-perli.pdf.

[370] Di Zhang, Mai Bui, Mathilde Fajardy, Piera Patrizio, Florian Kraxner, and Niall Mac Dowell. Unlocking the potential of BECCS with indigenous sources of biomass at a national scale. *Sustainable Energy Fuels*, 4:226–253, 2020. doi: 10.1039/C9SE00609E. URL http://dx.doi.org/10.1039/C9SE00609E.

[371] David W. Keith, Geoffrey Holmes, David St. Angelo, and Kenton Heidel. A Process for Capturing CO_2 from the Atmosphere. *Joule*, 2(8):1573 – 1594, 2018. ISSN 2542-4351. doi: https://doi.org/10.1016/j.joule.2018.05.006. URL http://www.sciencedirect.com/science/article/pii/S2542435118302253.

[372] Habiba Ahut Daggash and Niall Mac Dowell. The implications of delivering the UK's Paris Agreement commitments on the power sector. *International Journal of Greenhouse Gas Control*, 85:174 – 181, 2019. ISSN 1750-5836. doi: https://doi.org/10.1016/j.ijggc.2019.04.007. URL http://www.sciencedirect.com/science/article/pii/S175058361830731X.

[373] Epexspot. Day-ahead Auction, June 2019. URL http://www.epexspot.com/en/market-data/dayaheadauction/auction-table/2019-06-26/FR. Accessed 26 June 2019.

[374] Francisco M. Carrasco, Simon Grathwohl, Jörg Maier, Eike Wilms, and Johannes Ruppert. D7.2 Oxyfuel burner prototype performance tests, July 2018. URL https://doi.org/10.5281/zenodo.2597125.

[375] Arunim Bose. Simulation of air liquefaction using aspen plus. Bachelor thesis, Department of Chemical Engineering of National Institute of Technology Rourkela, 2011.

[376] Samantha Schmidt and Russell Clayton. Dynamic Design of a Cryogenic Air Separation Unit. Technical report, 2013.

[377] Armin Ebrahimi, Mousa Meratizaman, Hamed Akbarpour Reyhani, Omid Pourali, and Majid Amidpour. Energetic, exergetic and economic assessment of oxygen production from two columns cryogenic air separation unit. *Energy*, 90(9):1298–1316, 2015. doi: 10.1016/j.energy.2015.06.083.

Appendix A

Materials for components

Table A.1: Possible materials used in the construction of boiler tubes, headers, and pipings, adapted from Narula et al. [178].

Component	Steam temperature at turbine inlet				
	Up to 565 °C	Up to 593 °C	Up to 620 °C	Up to 650 °C	Up to 700 °C
Headers/pipes	P22, P91, P92	P91, P92, P122	P92, P122, E911	SAVE12, NF12	HR6W, Alloy 617, HR35
Superheater/Reheater – non-corrosive	T91, 304H, 347	Super304H, TP347HFG	Super304H, NF709	Inconel 617, NF709	HR6W, Alloy 617
Superheater/Reheater – corrosive	310 NbN	310 NbN, SS347/IN72	310 NbN, Super 304/IN72	310 NbN, NF 709/IN72	HR6W
Lower waterwall	C steel	T11, T12, T22	T11, T12, T22	T11, T12, T22	T23
Upper waterwall	T11, T12, T22	T23	T23	T23	T23, T92
Waterwall – corrosive	Clad>20%Cr	Clad>20%Cr	Clad>20%Cr	Clad>20%Cr	Clad>20–40%Cr

Table A.2: Possible materials used for the construction of steam turbine components, adapted from Narula et al. [178].

Component	Steam temperature at turbine inlet			
	Up to 565 °C	Up to 593 °C	Up to 620 °C	Up to 700 °C
Rotor	1 Cr-MoV forging, 11CrMoVTaN, 12CrMoVNbN	11CrMoVNbN, 10CrMoVWNbN	9–12CrWCo forging, 12CrMo1.84WVNbN, 18CrMoVNb Alloy B91	IN625/IN740, CCA617, Haynes 230
Nozzles/valves	CrMoV cast, 10CrMoVNb cast	9Cr1MoVNb cast, 10CrMoVNb, 12CrMoVNbN	9–10CrW, 12CrWCo	CCA617, IN625
Valve inner casing	1–2CrMo cast, CrMoV cast, 10CrMoVNb	9Cr1MoVNb, 10CrMoVNb	9–12CrW, Cast 12CrWCo, 19Cr12.5NiNbMoC	CCA 617, Inconel 625, Inconel 718
Blades	Type 422 Allow, 10CrMoVNbN	9 CrWCo	9–12CrWCo	Wrought Ni-based, 19Cr12.5NiNbMoC
Bolts	Type 422, 912 CrMoV, Nimonic80A	Nimonic 85A, Refractaloy26	9–12CrMoV, IN718, A286	Nimonic 105/115, Inconel718, Allvac718 Plus

Appendix B

Simulations

B.1 Single-column design

Air is compressed to 30 – 60 bar, if gaseous O_2 is required, or 200 bar if liquid O_2 is the required product in a single-column design[134]. Compressed air is sent through the main heat exchanger and cooled against cold O_2 and N_2 streams[134]. Chilled air is partially condensed through expansion to atmospheric pressure in Joule-Thomson valves before entering the distillation column[134]. This process produces high-purity O_2 with low efficiency, resulting in a highly impure N_2 stream[134].
A simple single-column design was modelled in Aspen HYSYS (Figure B.1) according to the work developed by Bose [375].
The simulation ran successfully using the Peng-Robinson Equation of State fluid package, with an average absolute deviation of 1 % from Bose's work, obtaining a stream of 2.9 t/h of oxygen (99 mol%) with 2466 kWh/t_{O_2} power consumption.

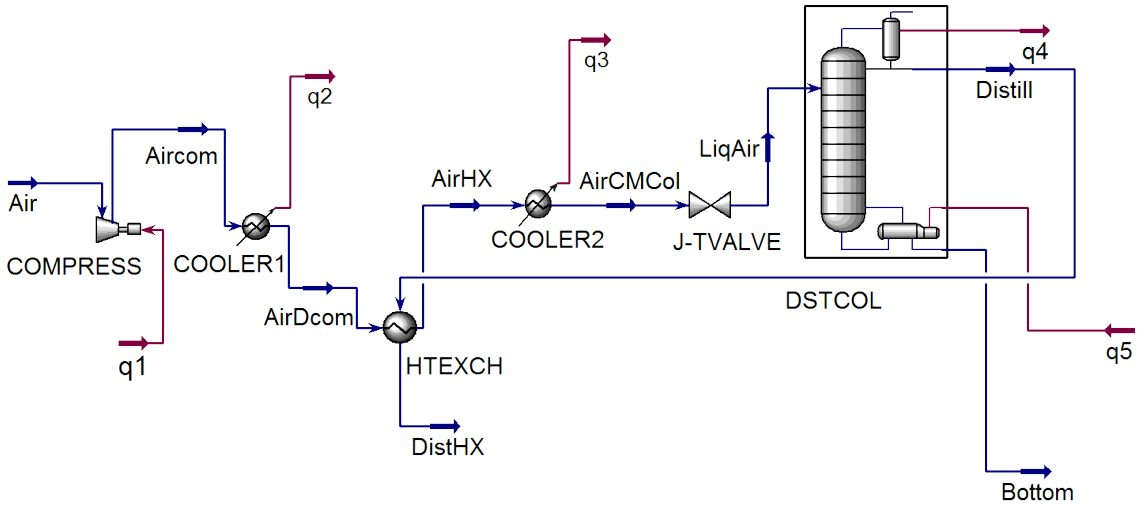


Figure B.1: Process Flow Diagram of a Single Column Cryogenic Air Separation Unit as described in Bose's bachelor thesis.

B.2 Double-column design

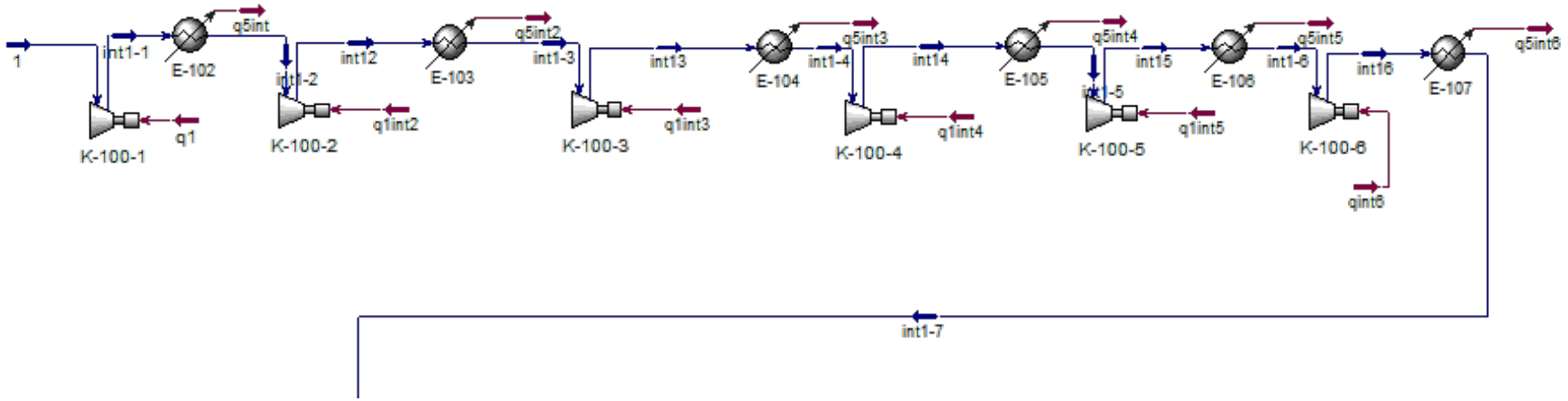
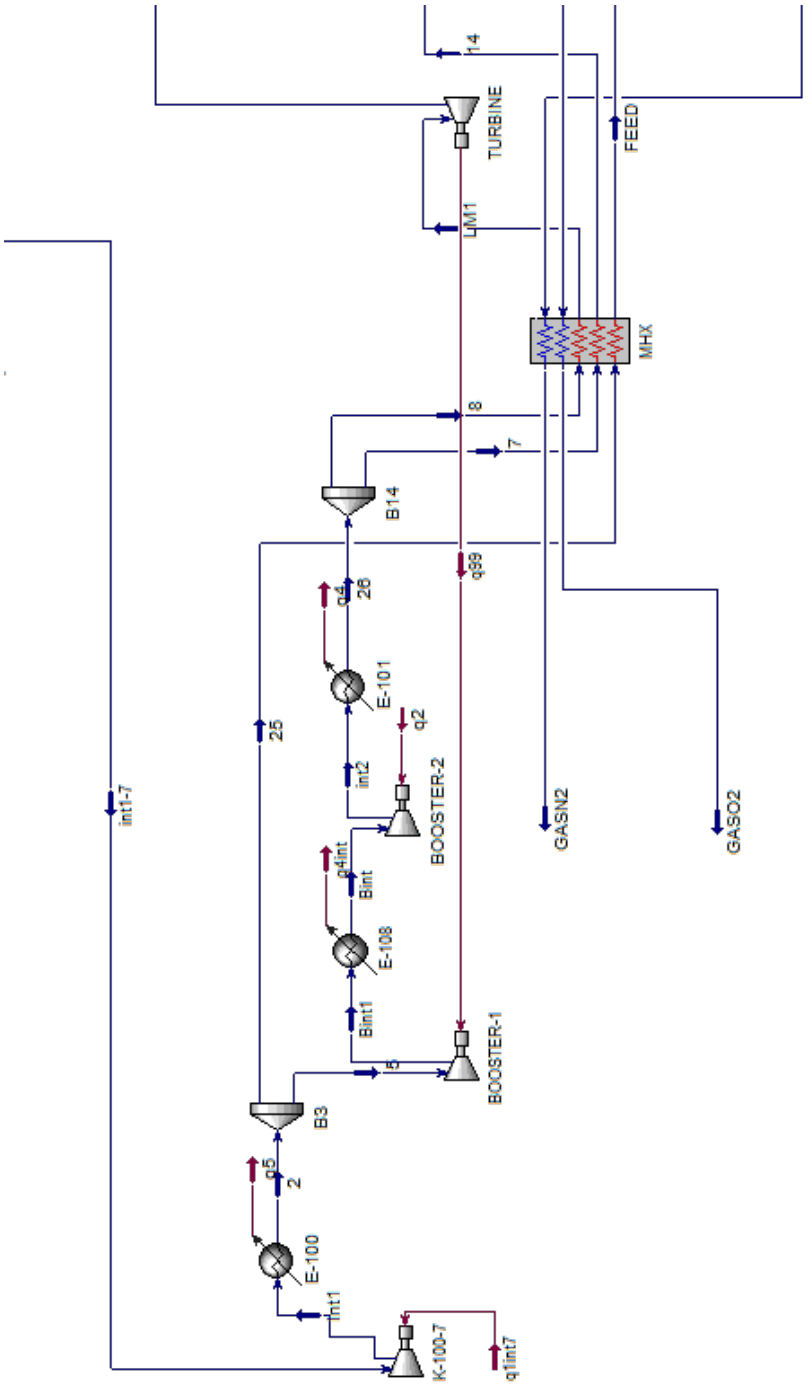
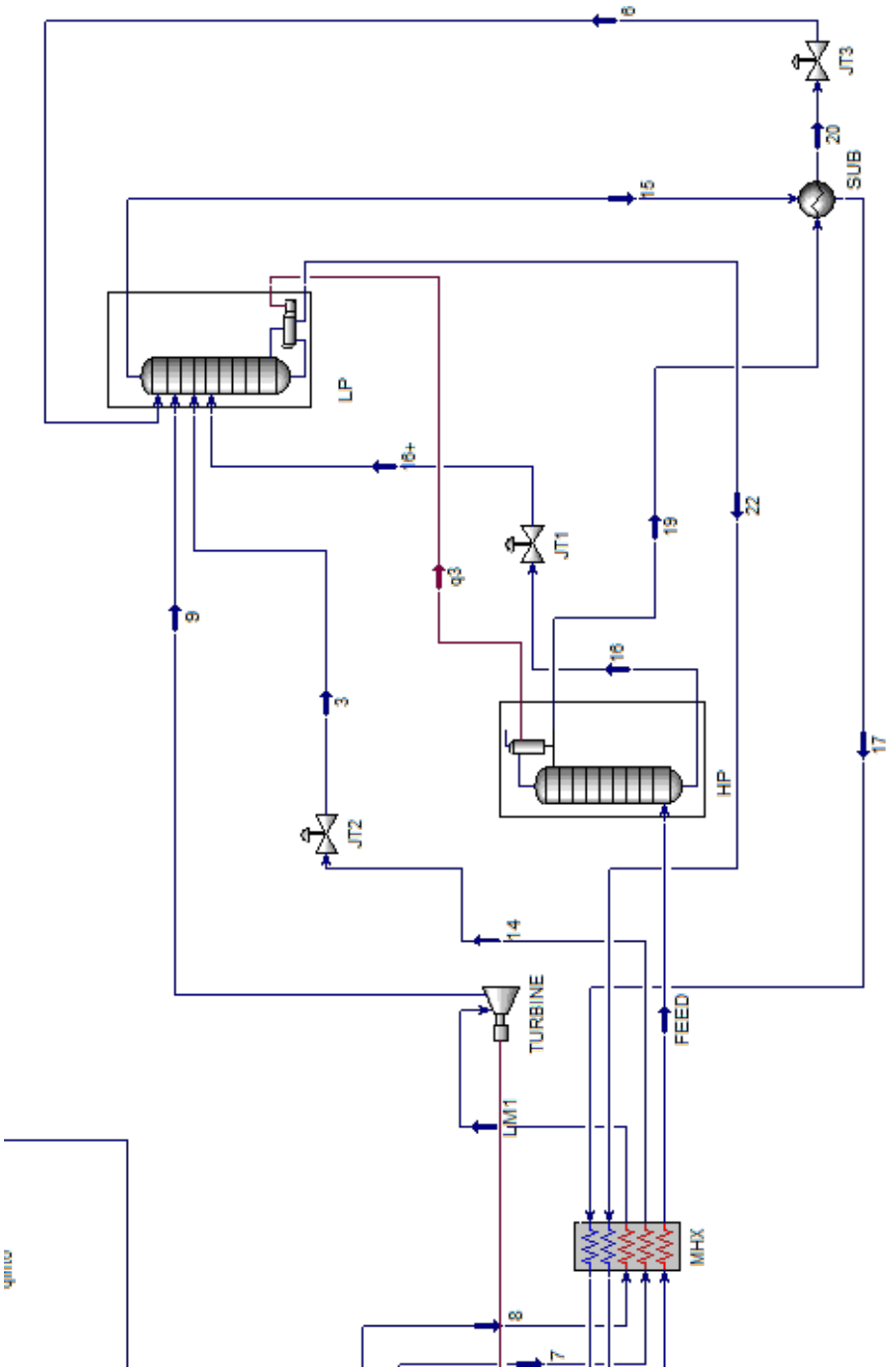


Figure B.2: Process Flow Diagram of a Double Column Cryogenic Air Separation Unit as described in Sapali and Raibhole's work.


14
TURBINE
FEED
LM1
MHX
8
7
B14
q99
q4
26
E-101
25
q2
int2
BOOSTER-2
GASN2
GASO2
int1-7
q4int
Bint
E-108
Bint1
BOOSTER-1
5
B3
q5
2
E-100
Int1
K-100-7
q1int7

Cont.


8
JT3
20
SUB
15
LP
16+
JT1
19
22
q3
9
16
3
17
HP
JT2
14
TURBINE
FEED
LIM1
MHX
8
7

Cont.

B.3 Air-fired power plant

The combustion chamber and boiler design were modelled in Aspen HYSYS according to the work developed by Kunzemann [172] using the Peng-Robinson Equation of State fluid package.
Coal temperature depends on the drying technology applied and whether the coal is stored or directly delivered to the combustion chamber after the being pulverised. For comparison purposes with the work of Kunzemann [172], it is assumed that coal is stored before entering the combustion chamber with a temperature of 15 °C, which represents the International Standard Atmosphere conditions.
Ash removal is crucial due to the problems caused as previously described, so equipment for ash disposal must be included, increasing capital and operation costs. Oxidation of ash components is not considered as this is highly complex, so ash was considered to come with coal in its oxidised form.
The boiler configuration follows the once-through Benson type boiler, where liquid feedwater transitions to supercritical state. The PFD can be seen in Figure B.3.
Coal enters the furnace where it burns in air previously heated to 268 °C against flue gas leaving the boiler at 381 °C in a regenerative heat exchanger (E-100). The combustion reactions take place inside the furnace, whose purpose is to absorb the heat of combustion and transfer it to the water inside the waterwalls[178].
Plant start-up was not simulated. A supercritical plant operates under subcritical regime at part-load, forcing it to operate with water recirculation, similar to a subcritical plant, until the water's pressure rises above the critical point[174, 183]. This is achieved by diverting the water-steam mixture to a phase separator during this transitional period[174]. At 75 – 80 % load the plant shifts operation to the supercritical regime, where there is no distinction between water and steam[183]. At this point, the valve to the phase separator is closed and the boiler operates in a once-through regime.
Unlike subcritical plants, the furnace's upper membrane walls also act as a superheater in supercritical plants because there is no distinction between water and steam[183]. During subcritical operation, the upper membrane walls of the furnace will "dry" which decreases tube cooling due to the lower density of steam relative to water or supercritical fluid[183]. This will increase the tube's metal temperature and lead to hot spots or overheating, which may lead to tube failure[183].
Flue gas is produced from the combustion reactions, leaving from the top alongside fly ash whilst bottom ash leaves from the bottom of the furnace. It was assumed that 90 % of ash is fly ash, as reported by Spero et al. [70]. Flue gas then enters the boiler section characterised by the heat exchangers Evaporator, Radiant Superheater, Superheater2, Reheater2, Superheater1, Reheater1, and Economiser, following the paths shown in Figure B.3. The reheaters are positioned after the superheater because steam in the reheater has a lower cooling ability due to its lower operating pressure[183]. Flue gas is then cooled against incoming air to 130 °C. These heat exchangers were modelled by specifying the temperatures according to Hagi et al. [115], Kunzemann [172], Ciferno [262]. This temperature is chosen to be above acid dew point[70, 77, 175] to allow a safe operation for baghouse filters[70].
Feedwater enters the boiler through the Economiser and exits the boiler as steam through the Superheater2, where it is sent to the high-pressure turbine (HPTurbine). Here, supercritical steam rotates the turbine shaft and generates electricity. Approximately 9% of steam is bled from the HP turbine to pre-heat the feedwater. The remain-

der is sent back to the boiler to be reheated in the reheater. The steam then leaves on Reheater2 into an intermediate pressure turbine, IPTurbines 1 to 4, to account for the bleeds that take place in this turbine. The steam not bled is then sent to a low-pressure turbine, represented by LPTurbine 1 to 4, for the same reasons as in the intermediate pressure turbine, where steam leaves the turbine partially condensed at 0.04 bar. This stream is sent to a condenser and pumped to the feedwater heating train, where it is heated from 24 °C to 299 °C against the bleeds previously mentioned, closing the water cycle.
The boiler provides supercritical steam at 600 °C and 30 bar entering the HP turbine. The steam is then reheated to obtain the same temperature conditions at the IP turbine inlet (620 °C and 70 bar). The total pressure drop on the flue gas side (shell-side in Figure B.3) was of 2.1 mbar, and on the tube side, the total pressure drop was 24.1 bar for the superheater and 5 bar for the reheater. These pressure drops were distributed amongst the several heat exchangers that comprise the boiler model. After the IP turbine expansion process, the steam then passes through the LP turbine. The turbine features steam extractions at different stages, used for feedwater heating in the feedwater heating chain.
The simulation was performed successfully with an absolute average deviation of 3 % from Kunzemann's thesis (the difference can be seen in Table C.2). This simulated supercritical coal power plant consumes approximately 53 kg/s of coal to generate 509 MW_e with a gross efficiency, (η_{gross}) of 47 % (LHV). This is still far from the maximum efficiency determined by the Rankine efficiency (Equation 3.20), determined to be 66 %. The most considerable difference between this work and Kunzemann's simulation was that slightly different bleeds were taken from the turbines. This is due to slight differences between the material's properties determined from Aspen's fluid package and gPROMS' fluid package that would not converge under the same circumstances.

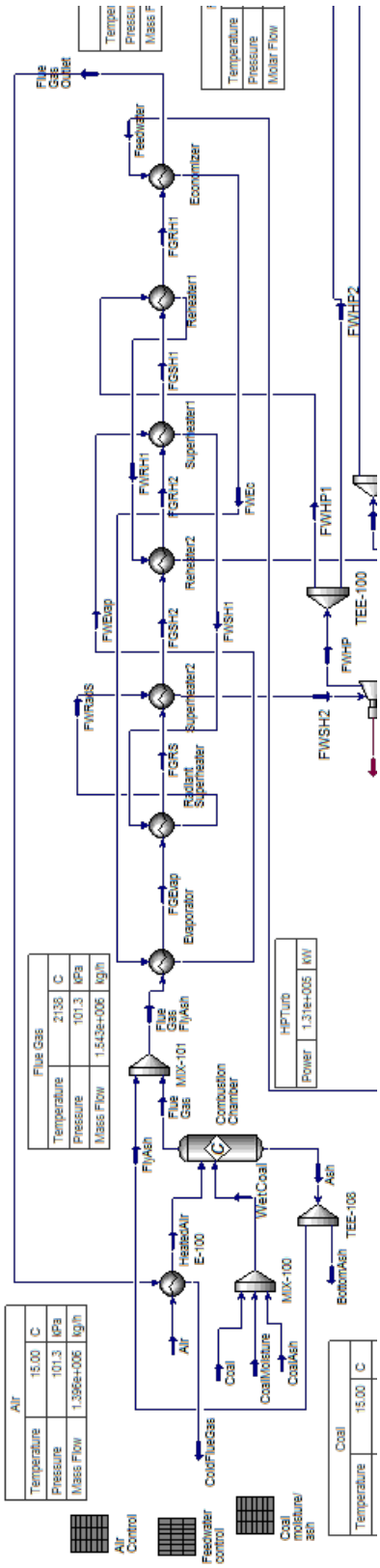
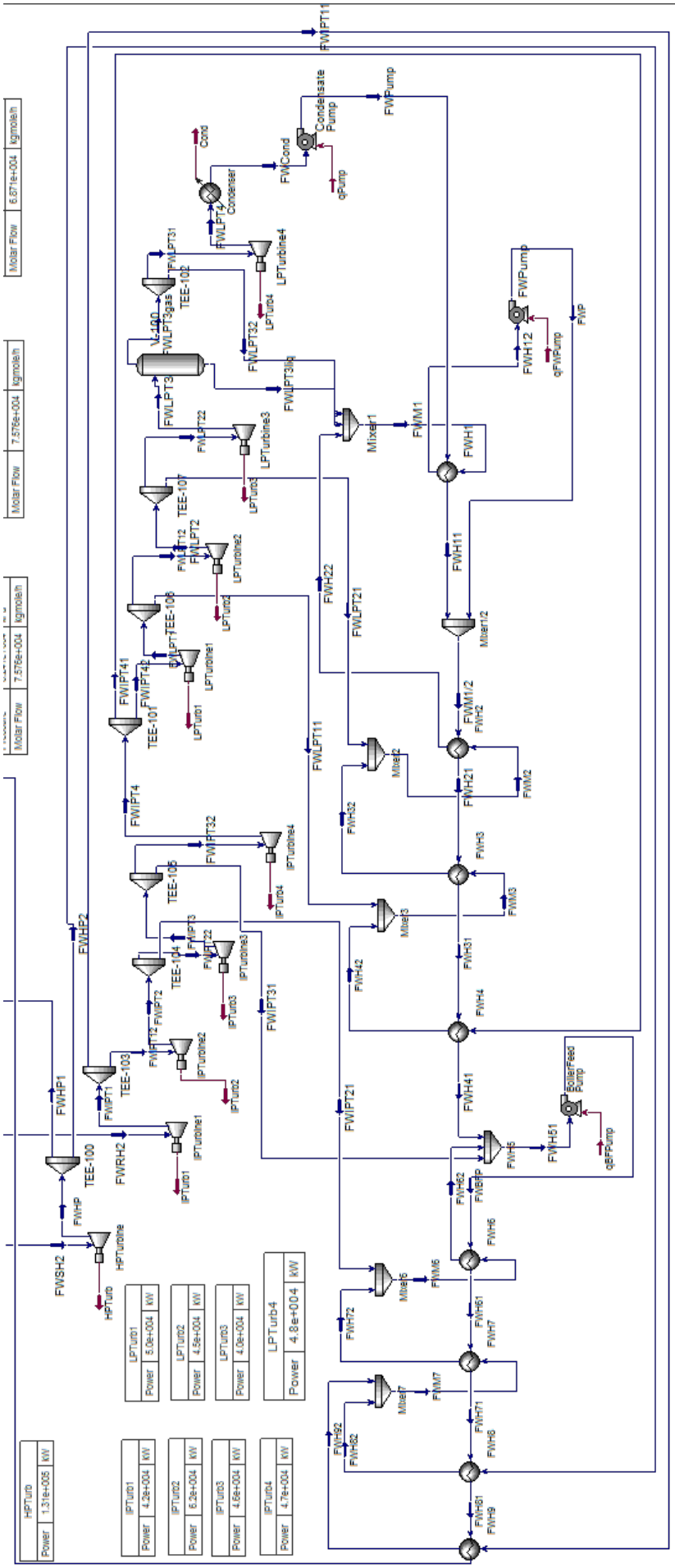


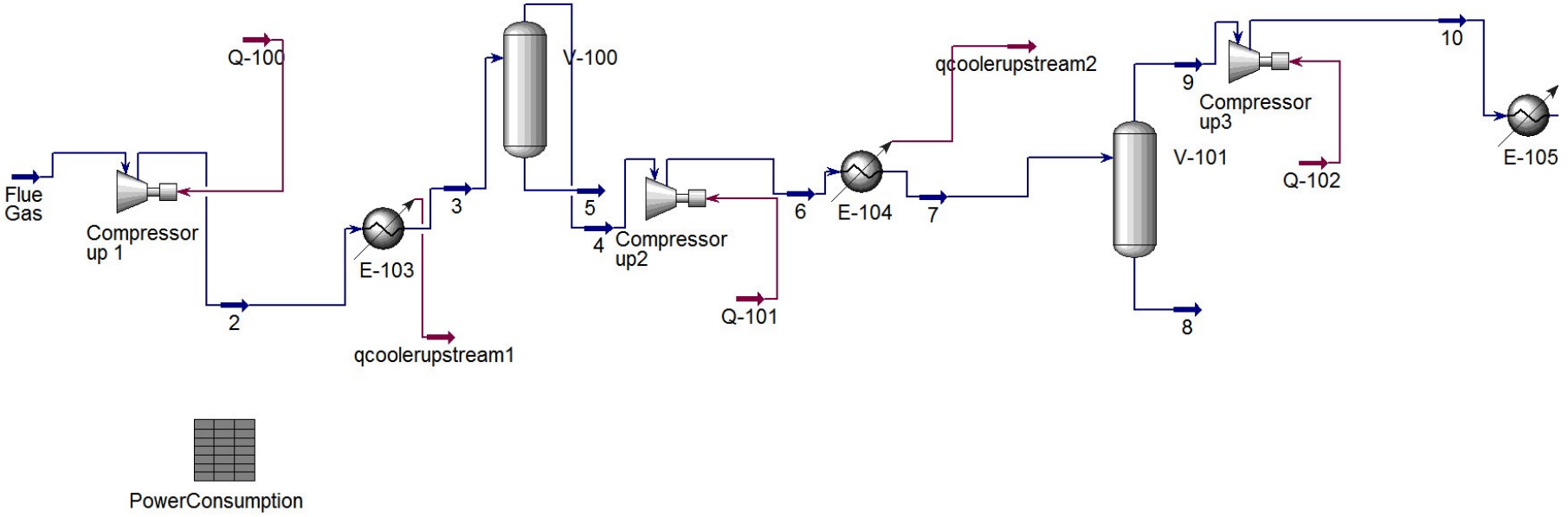
Figure B.3: Process Flow Diagram of a Coal Power Plant as described in Kunzemann's master thesis.


FWLPT11
Condensate Pump
FWPump
Cond
FWCond
qPump
Condenser
FWLPT4
FWLPT31
TEE-102
LPTurbine4
LPTurb4
FWLPT32
V-100
FWLPT3gas
FWLPT3liq
FWLPT3
FWLPT22
LPTurbine3
LPTurb3
TEE-107
FWLPT12
FWLPT2
LPTurbine2
LPTurb2
TEE-105
FWLPT1
LPTurbine1
LPTurb1
FWIPT41
FWIPT42
TEE-101
FWIPT4
FWIPT32
IPTurbine4
IPTurb4
TEE-106
FWIPT3
FWIPT22
IPTurbine3
IPTurb3
TEE-104
FWIPT2
FWIPT12
IPTurbine2
IPTurb2
FWIPT11
TEE-103
FWIPT1
IPTurbine1
IPTurb1
FWIPT31
FWHP2
FWHP1
TEE-100
FWRH2
FWHP
FWSH2
HPTurbine
HPTurb
Mixer1
FWM1
FWH1
FWH12
qFWPump
FWP
FWH11
FWH22
FWLPT21
Mixer1/2
FWM1/2
FWH2
Mixer2
FWH21
FWM2
FWH32
FWH3
FWM3
Mixer3
FWH31
FWH42
FWH4
FWH41
FWH5
FWH51
BoilerFeed Pump
qBFPump
FWH62
FWBFP
FWH6
Mixer6
FWM6
FWH72
FWH61
FWH7
Mixer7
FWM7
FWH82
FWH71
FWH8
FWH92
FWH81
FWH9
HPTurb
Power 1.31e+005 kW
IPTurb1
Power 4.2e+004 kW
IPTurb2
Power 6.2e+004 kW
IPTurb3
Power 4.6e+004 kW
IPTurb4
Power 4.7e+004 kW
LPTurb1
Power 5.0e+004 kW
LPTurb2
Power 4.5e+004 kW
LPTurb3
Power 4.0e+004 kW
LPTurb4
Power 4.8e+004 kW
Molar Flow 6.671e+004 kgmole/h
Molar Flow 7.576e+004 kgmole/h
Molar Flow 7.576e+004 kgmole/h
Molar Flow 7.576e+004 kgmole/h

Cont.

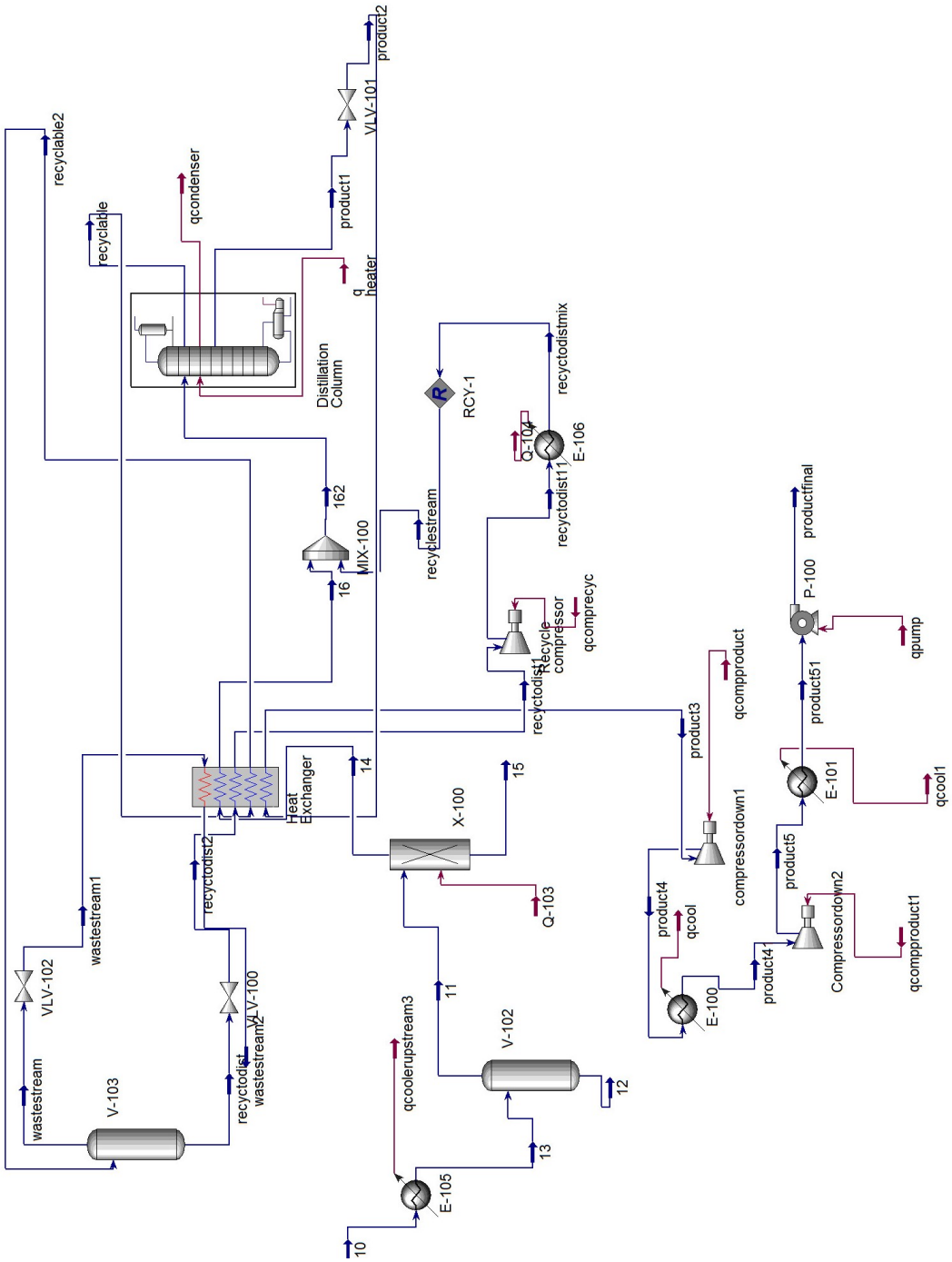
The air's, or the oxidant's, inlet temperature impacts the boiler's performance by increasing T_{ad} following Equation 3.35, which increases plant's efficiency by reducing fuel consumption as shown in Figure D.3.
These results suggest that we should pre-heat the air as much as possible before feeding it to the combustion chamber. However, one must be aware that we are limited in how much we can pre-heat the air because we use flue gas leaving the boiler for this end. We are also limited on how low we can decrease flue gas temperature because acid dew point is around 120 – 130 °C and boilers typically operate with flue gas exiting 10 °C above the acid dew point[175]. It is common practice to limit flue gas temperature to between 110 – 160 °C and select appropriate materials to prevent corrosion problems[77].
Increasing air to fuel ratio (λ) increases T_{ad} until stoichiometric combustion is achieved and then starts to decrease. For low λ, we can observe that lower T_{ad} occur from incomplete combustion. When O_2 in air is higher than the stoichiometry, T_{ad} decreases due to excess O_2 on exhaust gas. This tendency can be seen in Figure D.4, and it is also possible to see that O_2 is completely consumed until stoichiometry is achieved, following Sharifi et al. [248], at around $\lambda = 12$, after which it starts to build up. It is necessary to operate above the stoichiometric point to minimise incomplete combustion.
The T_{ad} obtained in this study was 2167 °C. This T_{ad} is similar to the 1926 – 2176 °C shown by Hecht et al. [193] for a sub-bituminous char, 2135 °C shown by Kim et al. [196] for a subbituminous coal char, and 2167 °C shown by Sharifi et al. [248] for anthracite. The similarities between the T_{ad} values from single-particle simulations[193, 196] and simulations using the heating value from the bulk of coal, such as found in this study and by Sharifi et al. [248], show evidence that both methods can estimate flame temperatures and heat flows from the combustion of solid fuels. This value is dependant on coal properties; however, this comparison is useful to have an idea of the range for T_{ad} during coal combustion.
A sensitivity analysis showed that T_{ad} increases with O_2 concentration in the oxidant until approximately 3000 °C, which could improve the plant's efficiency were it not for material restrictions limiting the boiler temperatures to similar values as in air fired conditions[65]. This is achieved by recirculating part of the flue gases back to the combustion chamber, further increasing the CO_2 concentration in the flue gas, allowing for a physical separation and purification of CO_2.

B.4 GPU



PowerConsumption		
Power consumption	8.586e+004	kW
Specific Power consumption (kW.h/tonneCO2)	232.8	

Figure B.4: CO_2 compression and purification unit with a 6-stage distillation colum PFD as described by Kolster.


recyclable2
recyclable
qcondenser
product1
VLV-101
product2
q heater
Distillation Column
RCY-1
recyctodistmix
Q-104
E-106
recyctodist11
162
MIX-100
16
recyclestream
productfinal
P-100
qpump
Recycle compressor
qcomprecyc
recyctodist1
product3
qcompproduct
compressordown1
product51
E-101
qcool1
Heat Exchanger
14
15
X-100
recyctodist2
Q-103
product5
Compressordown2
qcompproduct1
wastestream1
VLV-102
VLV-100
product4
qcool
E-100
11
qcoolerupstream3
V-102
12
wastestream
V-103
recyctodist
wastestream2
13
E-105
10

Cont.

B.5 Oxy-combustion power plant

B.5.1 Without heat integration

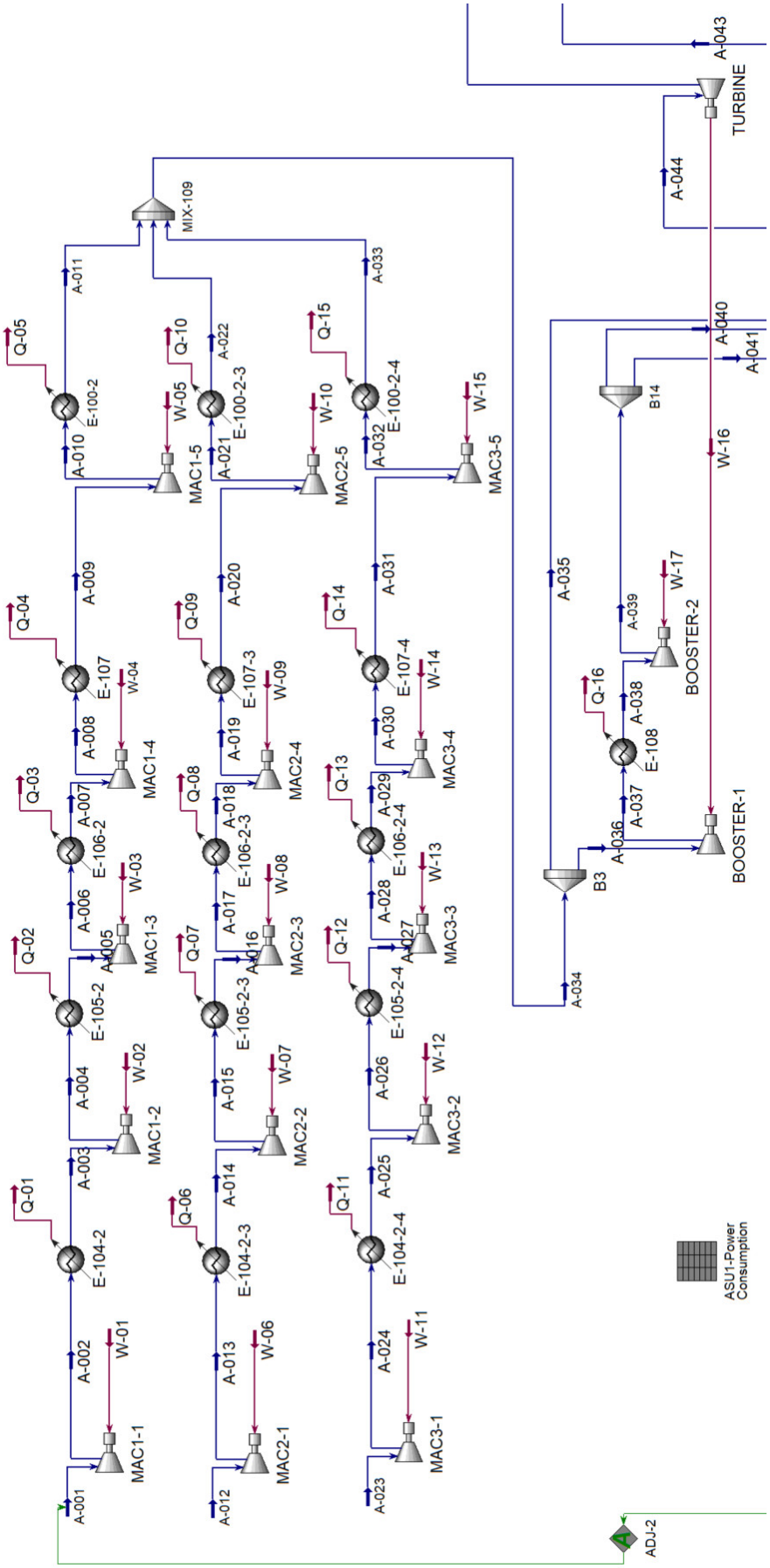
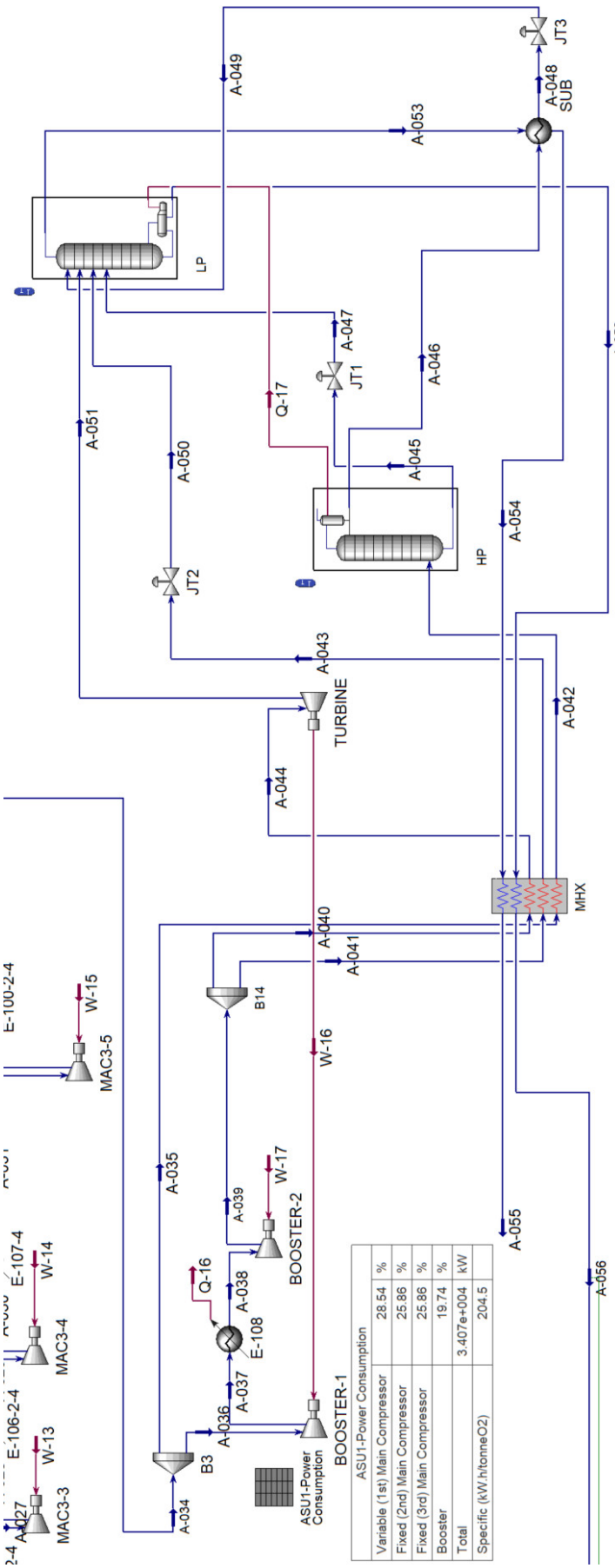
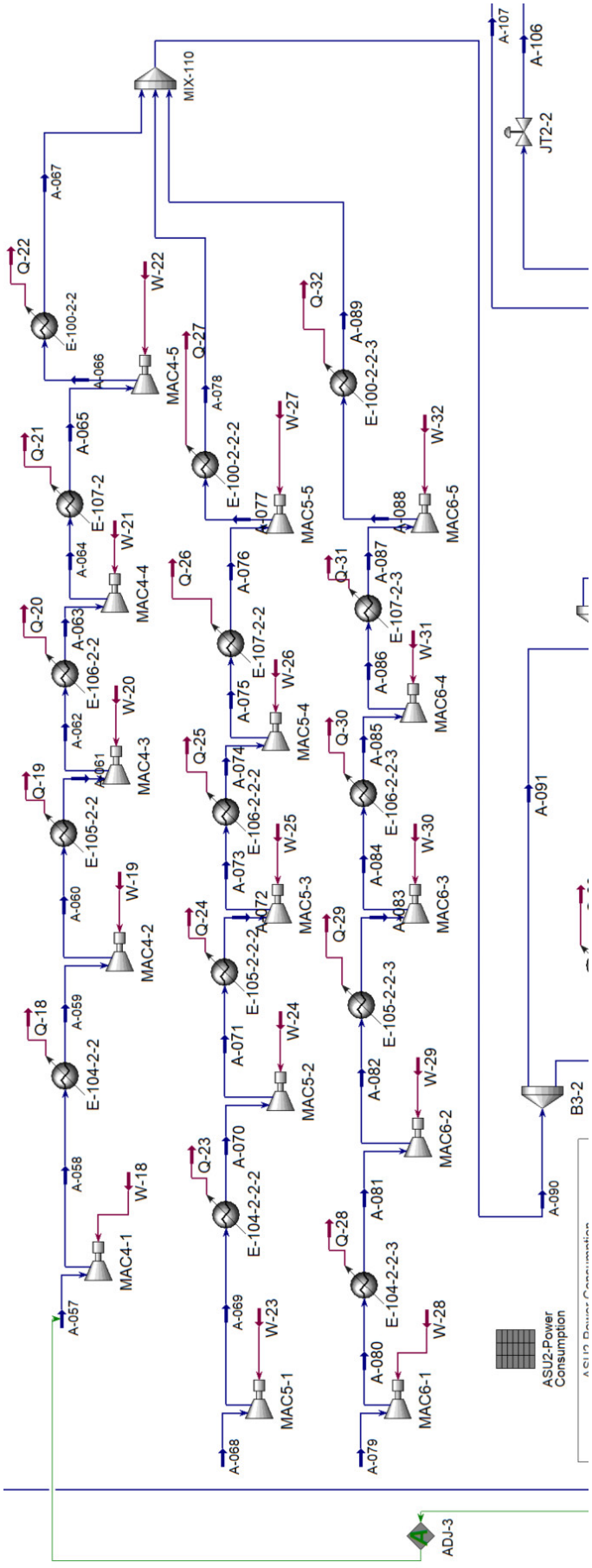


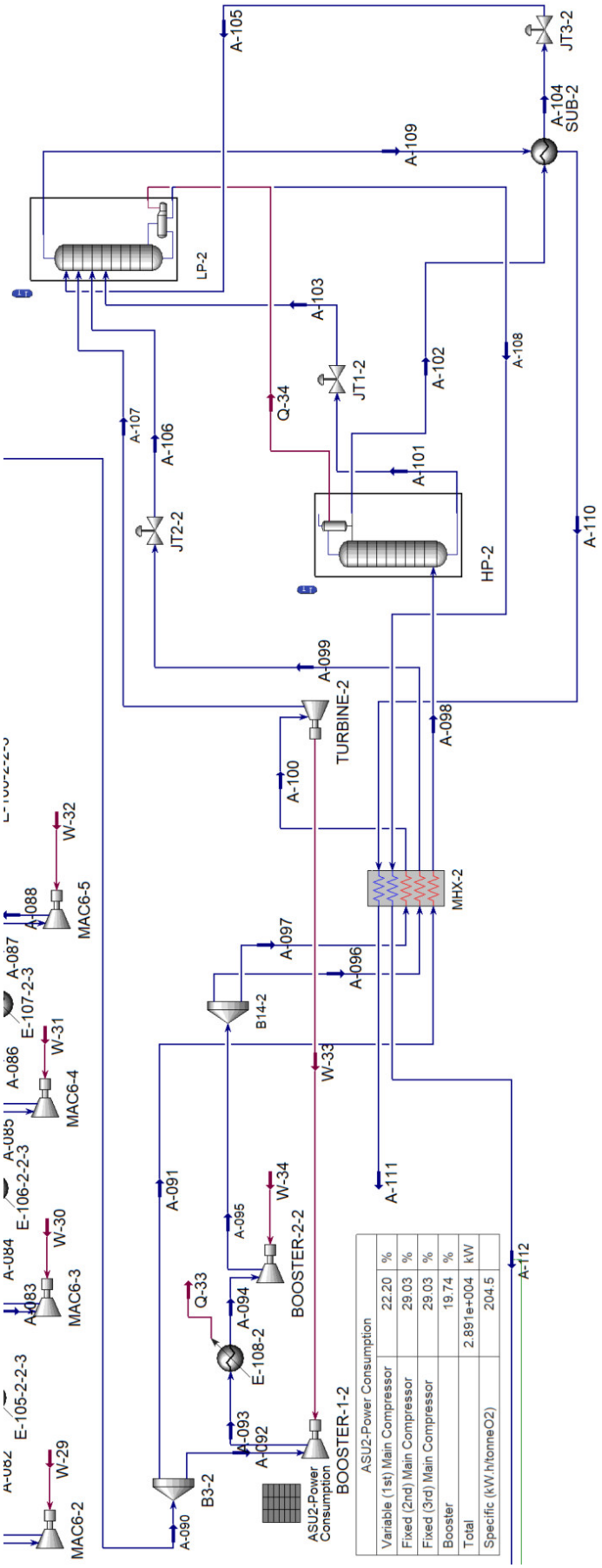
Figure B.5: Oxy-fuel combustion process developed according to the works of Spero and Stanger.


A-049
JT3
A-048
SUB
A-053
LP
A-047
JT1
A-046
Q-17
A-051
A-050
A-045
HP
A-054
JT2
A-043
TURBINE
A-042
A-044
MHX
A-040
A-041
B14
W-16
W-15
MAC3-5
A-035
A-039
W-17
BOOSTER-2
A-055
Q-16
A-038
E-108
E-107-4
W-14
MAC3-4
A-037
A-036
E-106-2-4
W-13
MAC3-3
B3
A-034
ASU1-Power Consumption
BOOSTER-1
A-056
ASU1-Power Consumption
Variable (1st) Main Compressor 28.54 %
Fixed (2nd) Main Compressor 25.86 %
Fixed (3rd) Main Compressor 25.86 %
Booster 19.74 %
Total 3.407e+004 kW
Specific (kW.h/tonneO2) 204.5

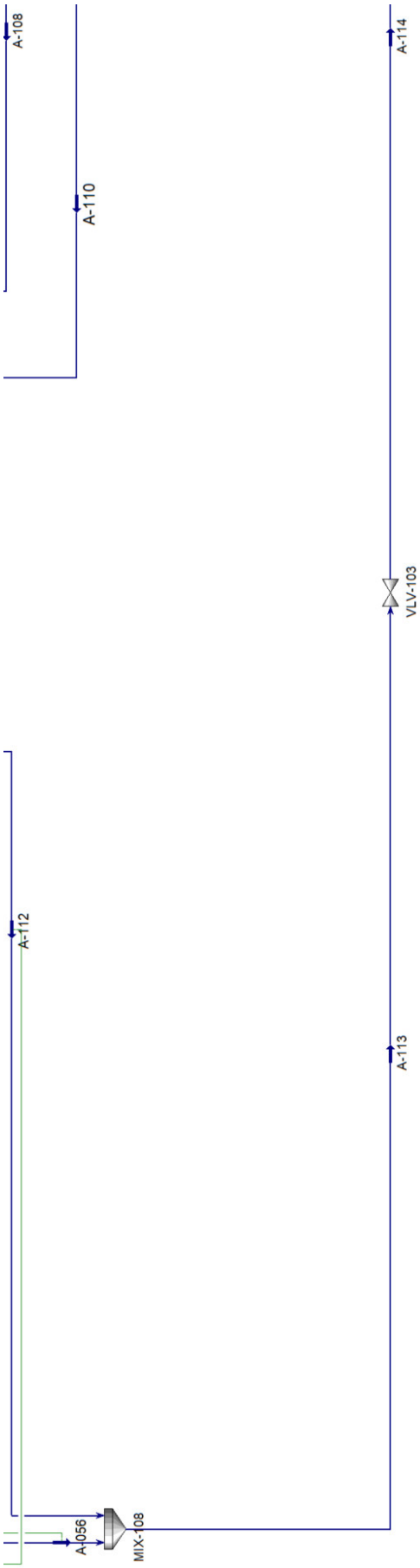
Cont.


MIX-110
A-107
A-106
JT2-2
A-067
Q-22
E-100-2-2
W-22
MAC4-5
Q-27
A-078
Q-32
A-089
E-100-2-2-3
A-066
Q-21
A-065
E-107-2
W-21
MAC4-4
W-27
E-100-2-2-2
A-077
MAC5-5
A-088
MAC6-5
W-32
A-064
Q-20
A-063
E-106-2-2
W-20
MAC4-3
Q-26
A-076
E-107-2-2
W-26
MAC5-4
Q-31
A-087
E-107-2-3
W-31
MAC6-4
A-086
A-062
A-061
Q-19
E-105-2-2
W-19
MAC4-2
Q-25
A-074
E-106-2-2-2
W-25
MAC5-3
Q-30
A-085
E-106-2-2-3
W-30
MAC6-3
A-084
A-060
A-073
A-072
Q-24
E-105-2-2-2
W-24
MAC5-2
Q-29
A-083
E-105-2-2-3
W-29
MAC6-2
A-082
A-059
A-071
Q-18
E-104-2-2
A-058
W-18
MAC4-1
Q-23
A-070
E-104-2-2-2
A-081
Q-28
E-104-2-2-3
A-057
A-069
W-23
MAC5-1
A-080
W-28
MAC6-1
A-068
A-079
A-091
B3-2
A-090
ASU2-Power Consumption
ADJ-3

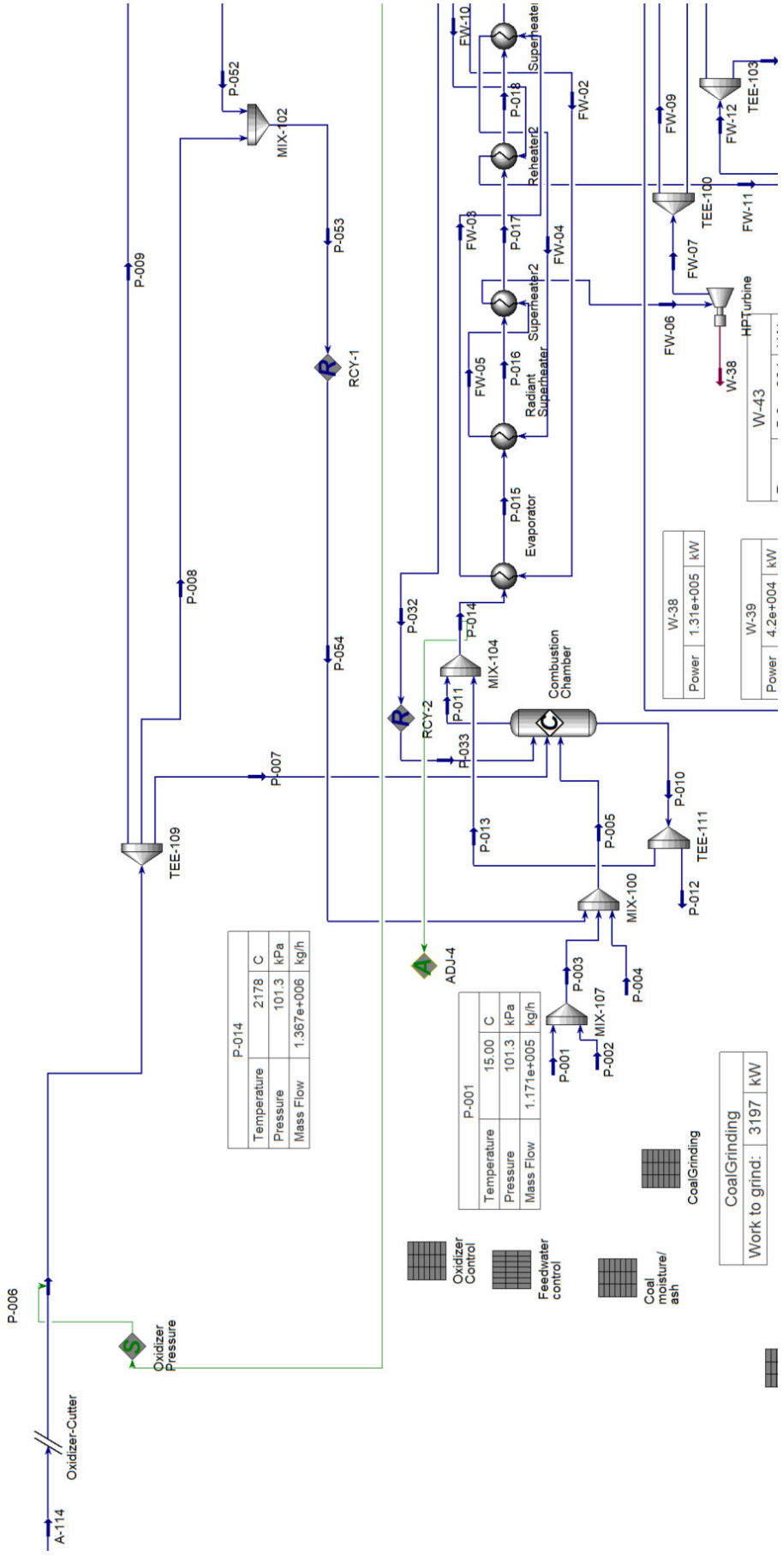
Cont.


A-105
JT3-2
A-104
SUB-2
A-109
LP-2
A-103
JT1-2
A-102
A-108
Q-34
A-107
A-106
JT2-2
A-101
HP-2
A-110
A-099
TURBINE-2
A-098
A-100
MHX-2
W-32
A-088
MAC6-5
A-087
E-107-2-3
A-097
A-096
B14-2
A-086
W-31
MAC6-4
W-33
A-085
E-106-2-2-3
A-091
A-095
W-34
A-111
A-084
W-30
A-083
MAC6-3
Q-33
A-094
BOOSTER-2-2
A-112
E-108-2
E-105-2-2-3
A-093
A-092
BOOSTER-1-2
W-29
B3-2
ASU2-Power Consumption
MAC6-2
A-090
ASU2-Power Consumption
Variable (1st) Main Compressor 22.20 %
Fixed (2nd) Main Compressor 29.03 %
Fixed (3rd) Main Compressor 29.03 %
Booster 19.74 %
Total 2.891e+004 kW
Specific (kW.h/tonneO2) 204.5

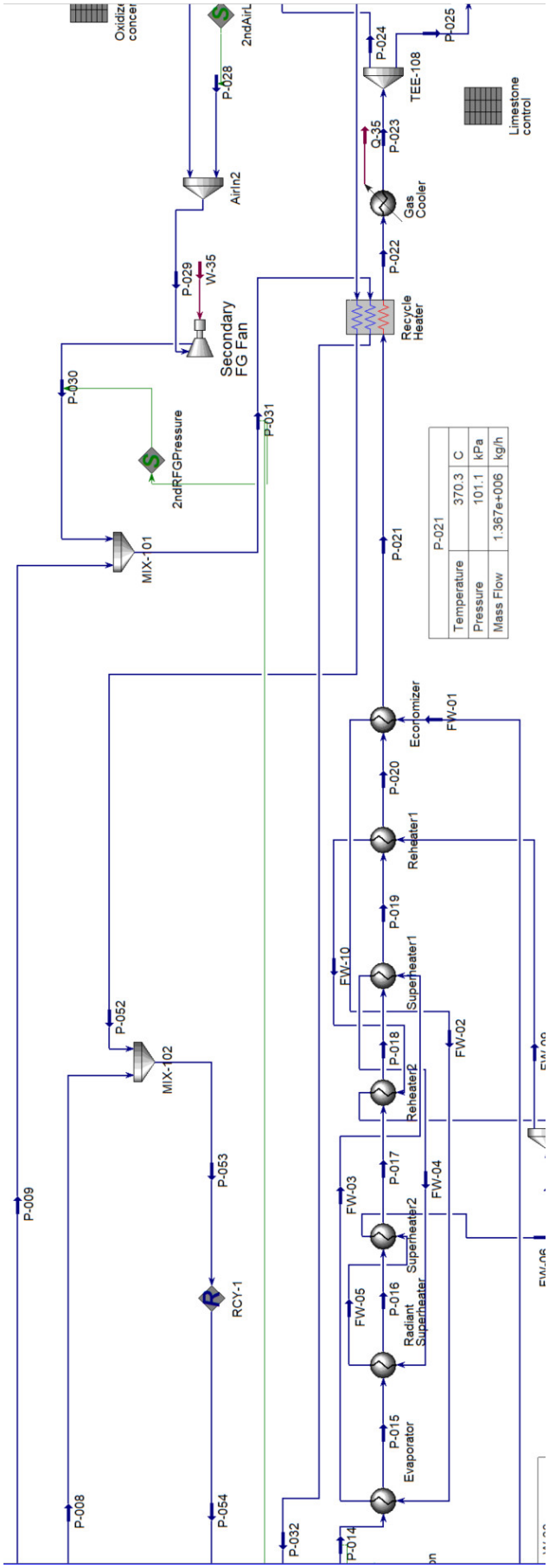
Cont.



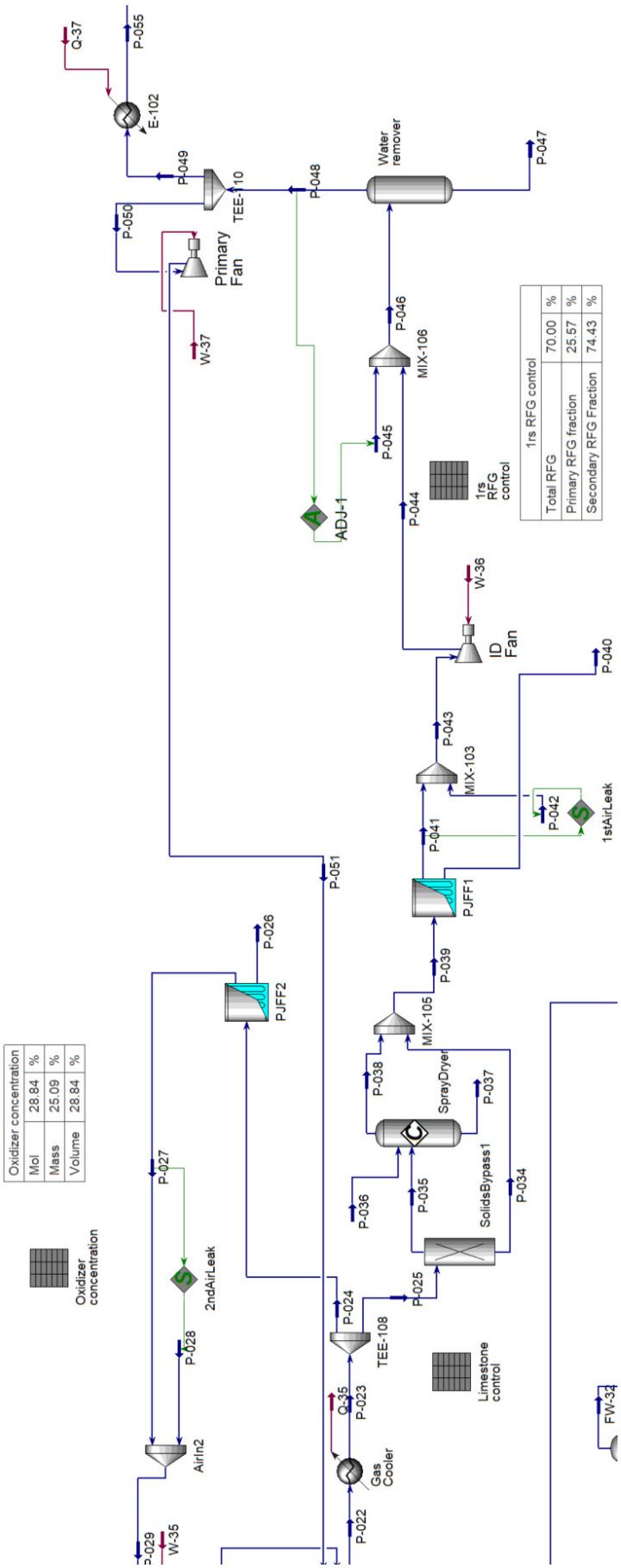
Cont.


A-114
Oxidizer-Cutter
P-006
Oxidizer Pressure
TEE-109
P-009
P-008
P-007
P-052
MIX-102
P-053
RCY-1
P-054
P-032
RCY-2
ADJ-4
P-033
P-011
MIX-104
P-014
P-015
Evaporator
Radiant Superheater
P-016
Superheater2
P-017
Reheater2
P-018
Superheater
FW-10
FW-02
FW-03
FW-04
FW-05
FW-06
FW-07
FW-09
FW-11
FW-12
TEE-100
TEE-103
HPTurbine
W-38
W-43
W-38
Power 1.31e+005 kW
W-39
Power 4.2e+004 kW
Combustion Chamber
P-010
TEE-111
P-012
P-005
P-013
MIX-100
P-003
P-004
MIX-107
P-001
P-002
P-014
Temperature 2178 C
Pressure 101.3 kPa
Mass Flow 1.367e+006 kg/h
P-001
Temperature 15.00 C
Pressure 101.3 kPa
Mass Flow 1.171e+005 kg/h
CoalGrinding
Work to grind: 3197 kW
CoalGrinding
Oxidizer Control
Feedwater control
Coal moisture/ ash

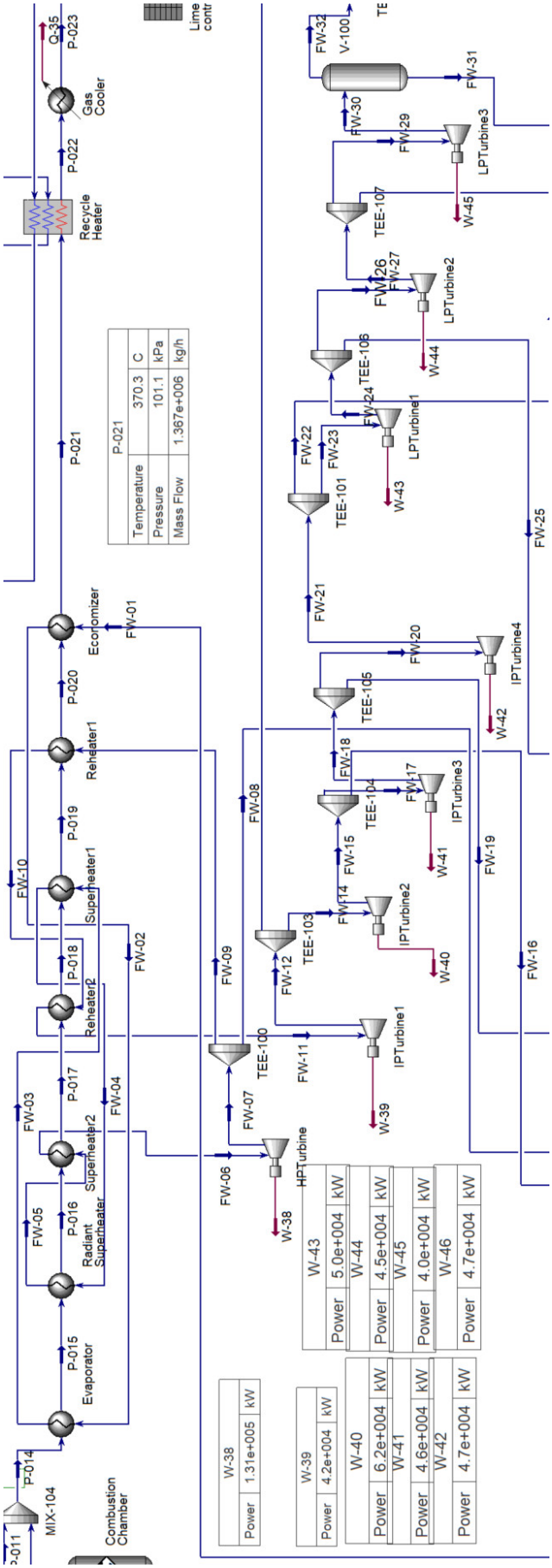
Cont.


2ndAirL
P-028
AirIn2
P-029
W-35
Secondary FG Fan
P-030
2ndRFGPressure
P-031
MIX-101
P-052
MIX-102
P-053
RCY-1
P-054
P-009
P-008
P-032
P-014
P-015
Evaporator
P-016
Radiant Superheater
FW-05
P-017
Superheater2
FW-03
FW-04
P-018
Reheater2
FW-10
P-019
Superheater1
FW-02
P-020
Reheater1
FW-01
Economizer
P-021
Recycle Heater
P-022
Gas Cooler
Q-35
P-023
TEE-108
P-024
P-025
Limestone control
P-021
Temperature 370.3 C
Pressure 101.1 kPa
Mass Flow 1.367e+006 kg/h

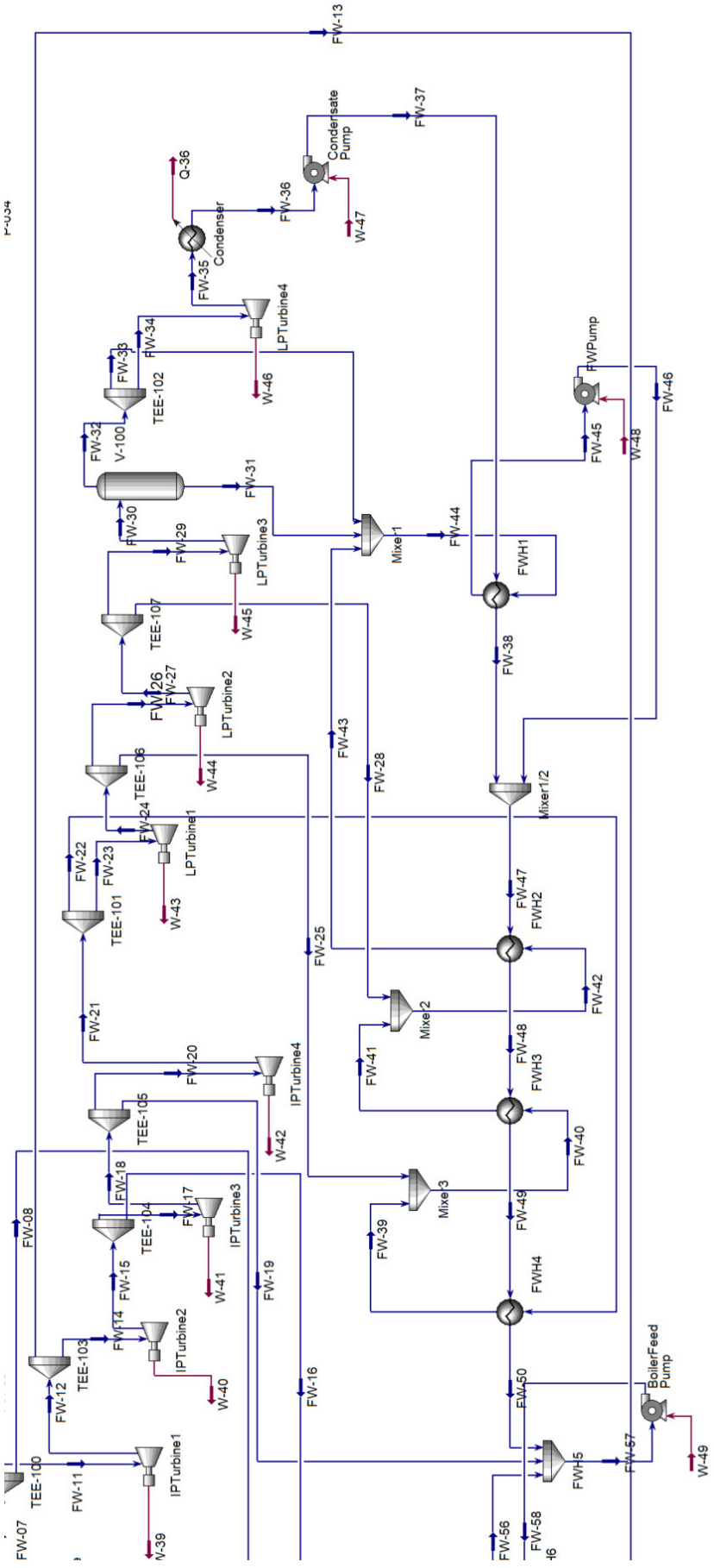
Cont.


Q-37
P-055
E-102
P-049
TEE-110
P-048
Water remover
P-047
P-050
Primary Fan
W-37
P-046
MIX-106
P-045
ADJ-1
P-044
1rs RFG control
1rs RFG control
Total RFG 70.00 %
Primary RFG fraction 25.57 %
Secondary RFG Fraction 74.43 %
W-36
ID Fan
P-040
P-043
MIX-103
P-042
1stAirLeak
P-041
P-051
PJFF1
P-026
PJFF2
P-039
MIX-105
P-038
SprayDryer
P-037
Oxidizer concentration
Mol 28.84 %
Mass 25.09 %
Volume 28.84 %
Oxidizer concentration
P-027
2ndAirLeak
P-028
P-036
P-035
SolidsBypass1
P-034
P-025
P-024
TEE-108
Limestone control
Q-35
P-023
Gas Cooler
AirIn2
P-022
P-029
W-35
FW-32

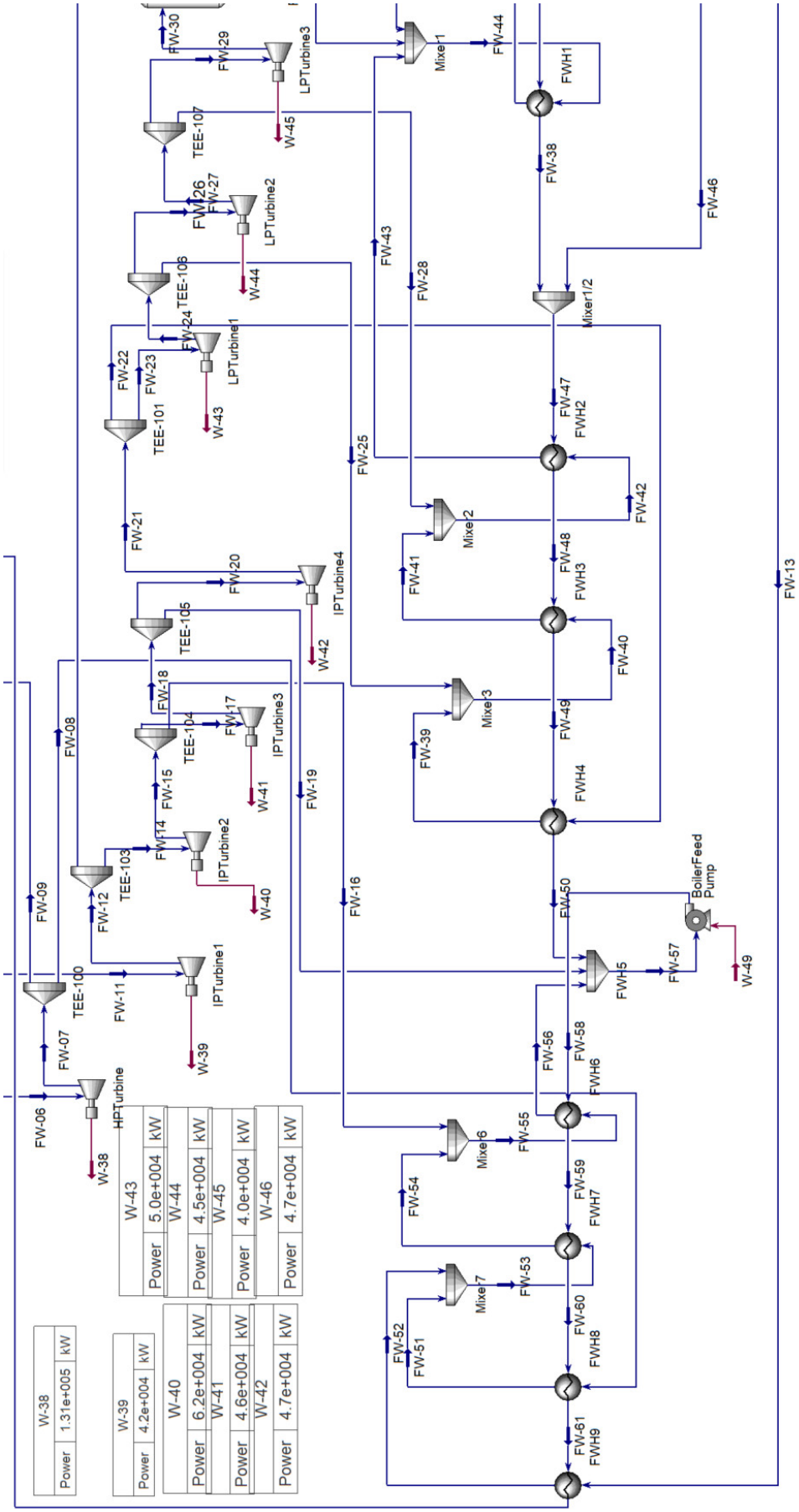
Cont.


Lime contr
Q-35
P-023
Gas Cooler
P-022
Recycle Heater
P-021
P-021
Temperature 370.3 C
Pressure 101.1 kPa
Mass Flow 1.367e+006 kg/h
Economizer
FW-01
P-020
Reheater1
P-019
Superheater1
FW-10
P-018
Reheater2
FW-02
FW-09
FW-08
FW-03
P-017
Superheater2
FW-04
FW-05
P-016
Radiant Superheater
FW-06
FW-07
TEE-100
FW-11
FW-12
TEE-103
FW-14
FW-15
TEE-104
FW-18
TEE-105
FW-20
FW-21
TEE-101
FW-22
FW-23
FW-24
TEE-106
FW-26
FW-27
TEE-107
FW-29
FW-30
V-100
FW-32
FW-31
FW-25
FW-16
FW-19
FW-17
P-015
Evaporator
P-014
MIX-104
Combustion Chamber
HPTurbine
IPTurbine1
IPTurbine2
IPTurbine3
IPTurbine4
LPTurbine1
LPTurbine2
LPTurbine3
W-38
W-39
W-40
W-41
W-42
W-43
W-44
W-45
W-46
W-38 Power 1.31e+005 kW
W-39 Power 4.2e+004 kW
W-40 Power 6.2e+004 kW
W-41 Power 4.6e+004 kW
W-42 Power 4.7e+004 kW
W-43 Power 5.0e+004 kW
W-44 Power 4.5e+004 kW
W-45 Power 4.0e+004 kW
W-46 Power 4.7e+004 kW

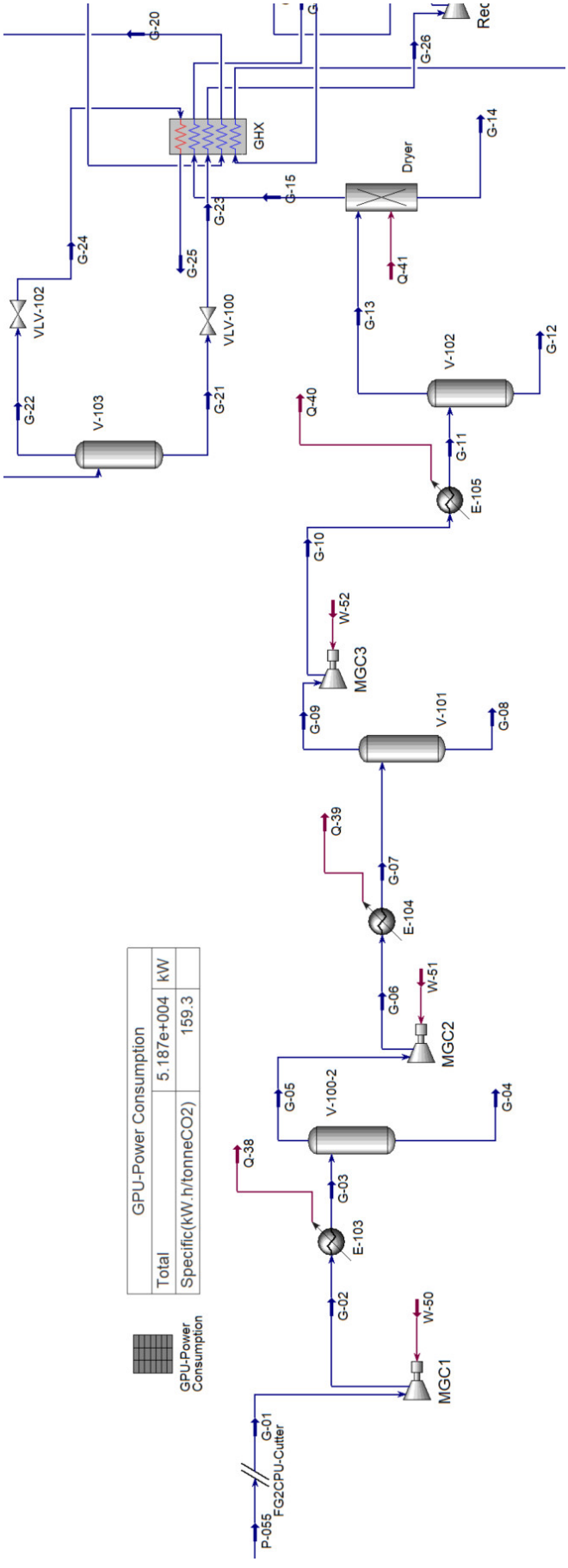
Cont.


FW-13
Condersate Pump
FW-37
Q-36
FW-36
Condenser
W-47
FW-35
LPTurbine4
FW-34
FW-33
TEE-102
W-46
FWPump
FW-46
FW-32
V-100
FW-45
W-48
FW-31
FW-30
FW-29
LPTurbine3
Mixer1
FW-44
FWH1
TEE-107
W-45
FW-38
FW-26
FW-27
LPTurbine2
FW-43
FW-28
TEE-106
W-44
Mixer1/2
FW-24
LPTurbine1
FW-22
FW-23
FW-47
FWH2
TEE-101
W-43
FW-25
FW-42
FW-21
Mixer2
FW-41
FW-48
FWH3
FW-20
IPTurbine4
TEE-105
W-42
FW-40
FW-18
Mixer3
FW-49
FW-17
IPTurbine3
TEE-104
FW-39
FW-08
FW-15
W-41
FW-19
FWH4
FW-14
IPTurbine2
TEE-103
FW-50
BoilerFeed Pump
FW-12
W-40
FW-16
FW-11
IPTurbine1
TEE-100
FW-07
FWH5
FW-57
W-49
FW-56
FW-58

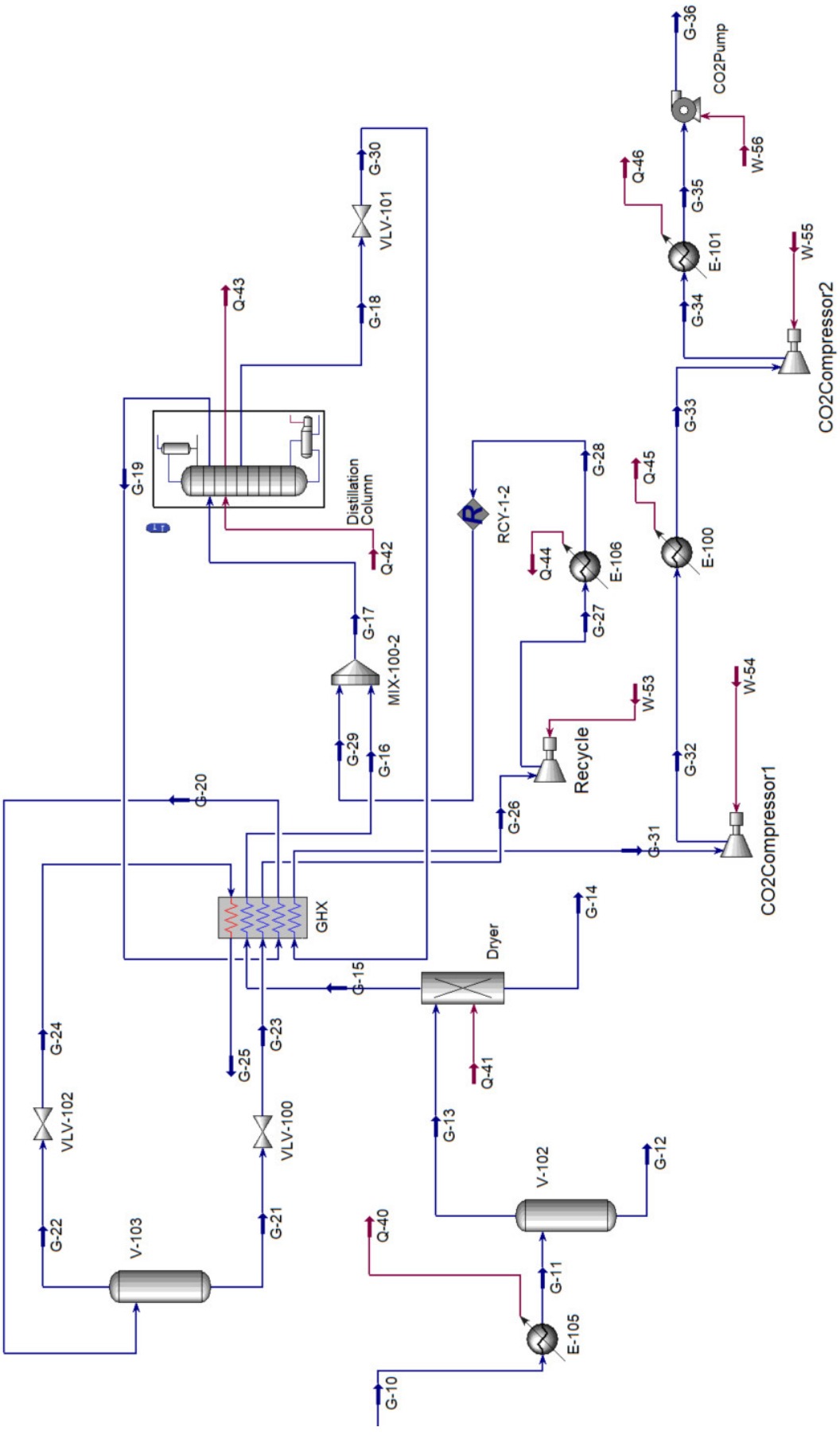
Cont.


FW-06
FW-07
FW-08
FW-09
FW-11
FW-12
FW-13
FW-14
FW-15
FW-16
FW-17
FW-18
FW-19
FW-20
FW-21
FW-22
FW-23
FW-24
FW-25
FW-26
FW-27
FW-28
FW-29
FW-30
FW-38
FW-39
FW-40
FW-41
FW-42
FW-43
FW-44
FW-45
FW-46
FW-47
FW-48
FW-49
FW-50
FW-51
FW-52
FW-53
FW-54
FW-55
FW-56
FW-57
FW-58
FW-59
FW-60
FW-61
HPTurbine
IPTurbine1
IPTurbine2
IPTurbine3
IPTurbine4
LPTurbine1
LPTurbine2
LPTurbine3
TEE-100
TEE-101
TEE-103
TEE-104
TEE-105
TEE-106
TEE-107
Mixer1
Mixer1/2
Mixer2
Mixer3
Mixer6
Mixer7
FWH1
FWH2
FWH3
FWH4
FWH5
FWH6
FWH7
FWH8
FWH9
BoilerFeed Pump
W-38 Power 1.31e+005 kW
W-39 Power 4.2e+004 kW
W-40 Power 6.2e+004 kW
W-41 Power 4.6e+004 kW
W-42 Power 4.7e+004 kW
W-43 Power 5.0e+004 kW
W-44 Power 4.5e+004 kW
W-45 Power 4.0e+004 kW
W-46 Power 4.7e+004 kW

Cont.


G-20
G-26
GHX
Dryer
G-14
G-15
G-23
G-24
G-25
Q-41
VLV-102
VLV-100
G-13
V-102
G-12
G-22
V-103
G-21
Q-40
G-11
E-105
G-10
W-52
MGC3
G-09
V-101
G-08
Q-39
G-07
E-104
W-51
G-06
MGC2
G-05
V-100-2
G-04
Q-38
G-03
E-103
G-02
W-50
MGC1
G-01
FG2CPU-Cutter
P-055
GPU-Power Consumption
GPU-Power Consumption
Total
5.187e+004
kW
Specific(kW.h/tonneCO2)
159.3

Cont.


G-36
CO2Pump
W-56
Q-46
G-35
E-101
W-55
G-34
CO2Compressor2
G-33
Q-45
E-100
G-32
W-54
CO2Compressor1
G-31
G-30
VLV-101
G-18
Q-43
G-19
Distillation Column
Q-42
G-17
MIX-100-2
G-29
G-16
G-28
RCY-1-2
Q-44
E-106
G-27
W-53
Recycle
G-26
G-20
GHX
G-14
Dryer
G-15
Q-41
G-24
VLV-102
G-25
G-23
VLV-100
G-13
V-102
G-12
G-22
V-103
G-21
Q-40
G-11
E-105
G-10

Cont.

Table B.1: Stream tables of the oxy-combustion process without heat integration.

Parameter	Units	A-001	A-002	A-003	A-004	A-005	A-006	A-007	A-008	A-009	A-010
Temperature	°C	10	40.51	22	40.72	21	41.36	21	45.35	21	64.93
Pressure	kPa	101.32	140	140	170	170	210	210	270	270	420
Mass Enthalpy	kJ/kg	-15.34	15.23	-3.41	15.37	-4.50	15.92	-4.61	19.81	-4.78	39.34
Mass Entropy	kJ/(kg.°C)	5.19	5.20	5.14	5.15	5.08	5.09	5.02	5.03	4.95	4.96
Mass Density	kg/m^3	1.25	1.56	1.65	1.89	2.02	2.33	2.49	2.96	3.20	4.33
Mass Flow	kg/h	253084	253084	253084	253084	253084	253084	253084	253084	253084	253084
Molar Flow	kmol/h	8737.5099	8737.8	8737.8	8737.8	8737.8	8737.8	8737.8	8737.8	8737.8	8737.8
Mole fraction											
C		0	0	0	0	0	0	0	0	0	0
H_2		0	0	0	0	0	0	0	0	0	0
S		0	0	0	0	0	0	0	0	0	0
Ar		0.0097	0.0097	0.0097	0.0097	0.0097	0.0097	0.0097	0.0097	0.0097	0.0097
O_2		0.2095	0.2095	0.2095	0.2095	0.2095	0.2095	0.2095	0.2095	0.2095	0.2095
N_2		0.7808	0.7808	0.7808	0.7808	0.7808	0.7808	0.7808	0.7808	0.7808	0.7808
CO_2		0	0	0	0	0	0	0	0	0	0
H_2O		0	0	0	0	0	0	0	0	0	0
SO_2		0	0	0	0	0	0	0	0	0	0
SiO_2		0	0	0	0	0	0	0	0	0	0
Al_2O_3		0	0	0	0	0	0	0	0	0	0
Fe_2O_3		0	0	0	0	0	0	0	0	0	0
CaO		0	0	0	0	0	0	0	0	0	0
MgO		0	0	0	0	0	0	0	0	0	0
Na_2O		0	0	0	0	0	0	0	0	0	0
K_2O		0	0	0	0	0	0	0	0	0	0
TiO_2		0	0	0	0	0	0	0	0	0	0
Mn_3O_4		0	0	0	0	0	0	0	0	0	0
P_2O_5		0	0	0	0	0	0	0	0	0	0
SO_3		0	0	0	0	0	0	0	0	0	0
$CaCO_3$		0	0	0	0	0	0	0	0	0	0
$CaSO_3$		0	0	0	0	0	0	0	0	0	0
Cl_2		0	0	0	0	0	0	0	0	0	0

Parameter	Units	A-011	A-012	A-013	A-014	A-015	A-016	A-017	A-018	A-019	A-020
Temperature	°C	45	10	40.51	22	40.72	21	41.36	21	45.35	21
Pressure	kPa	420	101.32	140	140	170	170	210	210	270	270
Mass Enthalpy	kJ/kg	19.09	-15.34	15.23	-3.41	15.37	-4.50	15.92	-4.61	19.81	-4.78
Mass Entropy	kJ/(kg. °C)	4.90	5.19	5.20	5.14	5.15	5.08	5.09	5.02	5.03	4.95
Mass Density	kg/m^3	4.61	1.25	1.56	1.65	1.89	2.02	2.33	2.49	2.96	3.20
Mass Flow	kg/h	253084	229279	229279	229279	229279	229279	229279	229279	229279	229279
Molar Flow	kmol/h	8737.9	7916.0	7916.0	7916.0	7916.0	7916.0	7916.0	7916.0	7916.0	7916.0
Mole fraction											
C		0	0	0	0	0	0	0	0	0	0
H_2		0	0	0	0	0	0	0	0	0	0
S		0	0	0	0	0	0	0	0	0	0
Ar		0.0097	0.0097	0.0097	0.0097	0.0097	0.0097	0.0097	0.0097	0.0097	0.0097
O_2		0.2095	0.2095	0.2095	0.2095	0.2095	0.2095	0.2095	0.2095	0.2095	0.2095
N_2		0.7808	0.7808	0.7808	0.7808	0.7808	0.7808	0.7808	0.7808	0.7808	0.7808
CO_2		0	0	0	0	0	0	0	0	0	0
H_2O		0	0	0	0	0	0	0	0	0	0
SO_2		0	0	0	0	0	0	0	0	0	0
SiO_2		0	0	0	0	0	0	0	0	0	0
Al_2O_3		0	0	0	0	0	0	0	0	0	0
Fe_2O_3		0	0	0	0	0	0	0	0	0	0
CaO		0	0	0	0	0	0	0	0	0	0
MgO		0	0	0	0	0	0	0	0	0	0
Na_2O		0	0	0	0	0	0	0	0	0	0
K_2O		0	0	0	0	0	0	0	0	0	0
TiO_2		0	0	0	0	0	0	0	0	0	0
Mn_3O_4		0	0	0	0	0	0	0	0	0	0
P_2O_5		0	0	0	0	0	0	0	0	0	0
SO_3		0	0	0	0	0	0	0	0	0	0
$CaCO_3$		0	0	0	0	0	0	0	0	0	0
$CaSO_3$		0	0	0	0	0	0	0	0	0	0
Cl_2		0	0	0	0	0	0	0	0	0	0

Parameter	Units	A-021	A-022	A-023	A-024	A-025	A-026	A-027	A-028	A-029	A-030
Temperature	°C	64.93	45	10	40.51	22	40.72	21	41.36	21	45.35
Pressure	kPa	420	420	101.32	140	140	170	170	210	210	270
Mass Enthalpy	kJ/kg	39.34	19.09	-15.34	15.23	-3.41	15.37	-4.50	15.92	-4.61	19.81
Mass Entropy	kJ/(kg. °C)	4.96	4.90	5.19	5.20	5.14	5.15	5.08	5.09	5.02	5.03
Mass Density	kg/m^3	4.33	4.61	1.25	1.56	1.65	1.89	2.02	2.33	2.49	2.96
Mass Flow	kg/h	229279	229279	229279	229279	229279	229279	229279	229279	229279	229279
Molar Flow	kmol/h	7916.0	7916.0	7916.0	7916.0	7916.0	7916.0	7916.0	7916.0	7916.0	7916.0
Mole fraction											
C		0	0	0	0	0	0	0	0	0	0
H_2		0	0	0	0	0	0	0	0	0	0
S		0	0	0	0	0	0	0	0	0	0
Ar		0.0097	0.0097	0.0097	0.0097	0.0097	0.0097	0.0097	0.0097	0.0097	0.0097
O_2		0.2095	0.2095	0.2095	0.2095	0.2095	0.2095	0.2095	0.2095	0.2095	0.2095
N_2		0.7808	0.7808	0.7808	0.7808	0.7808	0.7808	0.7808	0.7808	0.7808	0.7808
CO_2		0	0	0	0	0	0	0	0	0	0
H_2O		0	0	0	0	0	0	0	0	0	0
SO_2		0	0	0	0	0	0	0	0	0	0
SiO_2		0	0	0	0	0	0	0	0	0	0
Al_2O_3		0	0	0	0	0	0	0	0	0	0
Fe_2O_3		0	0	0	0	0	0	0	0	0	0
CaO		0	0	0	0	0	0	0	0	0	0
MgO		0	0	0	0	0	0	0	0	0	0
Na_2O		0	0	0	0	0	0	0	0	0	0
K_2O		0	0	0	0	0	0	0	0	0	0
TiO_2		0	0	0	0	0	0	0	0	0	0
Mn_3O_4		0	0	0	0	0	0	0	0	0	0
P_2O_5		0	0	0	0	0	0	0	0	0	0
SO_3		0	0	0	0	0	0	0	0	0	0
$CaCO_3$		0	0	0	0	0	0	0	0	0	0
$CaSO_3$		0	0	0	0	0	0	0	0	0	0
Cl_2		0	0	0	0	0	0	0	0	0	0

Parameter	Units	A-031	A-032	A-033	A-034	A-035	A-036	A-037	A-038	A-039	A-040
Temperature	°C	21	64.93	45	45	45	45	57.19	22	156.22	156.22
Pressure	kPa	270	420	420	420	420	420	473.03	473.03	1588	1588
Mass Enthalpy	kJ/kg	-4.78	39.34	19.09	19.09	19.09	19.09	31.35	-4.35	131.73	131.73
Mass Entropy	kJ/(kg.°C)	4.95	4.96	4.90	4.90	4.90	4.90	4.90	4.79	4.82	4.82
Mass Density	kg/m^3	3.20	4.33	4.61	4.61	4.61	4.61	4.99	5.60	12.85	12.85
Mass Flow	kg/h	229279	229279	229279	711642	533732	177911	177911	177911	177911	16012
Molar Flow	kmol/h	7916.0	7916.0	7916.0	24569.9	18427.4	6142.5	6142.5	6142.5	6142.5	552.8
Mole fraction											
C		0	0	0	0	0	0	0	0	0	0
H_2		0	0	0	0	0	0	0	0	0	0
S		0	0	0	0	0	0	0	0	0	0
Ar		0.0097	0.0097	0.0097	0.0097	0.0097	0.0097	0.0097	0.0097	0.0097	0.0097
O_2		0.2095	0.2095	0.2095	0.2095	0.2095	0.2095	0.2095	0.2095	0.2095	0.2095
N_2		0.7808	0.7808	0.7808	0.7808	0.7808	0.7808	0.7808	0.7808	0.7808	0.7808
CO_2		0	0	0	0	0	0	0	0	0	0
H_2O		0	0	0	0	0	0	0	0	0	0
SO_2		0	0	0	0	0	0	0	0	0	0
SiO_2		0	0	0	0	0	0	0	0	0	0
Al_2O_3		0	0	0	0	0	0	0	0	0	0
Fe_2O_3		0	0	0	0	0	0	0	0	0	0
CaO		0	0	0	0	0	0	0	0	0	0
MgO		0	0	0	0	0	0	0	0	0	0
Na_2O		0	0	0	0	0	0	0	0	0	0
K_2O		0	0	0	0	0	0	0	0	0	0
TiO_2		0	0	0	0	0	0	0	0	0	0
Mn_3O_4		0	0	0	0	0	0	0	0	0	0
P_2O_5		0	0	0	0	0	0	0	0	0	0
SO_3		0	0	0	0	0	0	0	0	0	0
$CaCO_3$		0	0	0	0	0	0	0	0	0	0
$CaSO_3$		0	0	0	0	0	0	0	0	0	0
Cl_2		0	0	0	0	0	0	0	0	0	0

Parameter	Units	A-041	A-042	A-043	A-044	A-045	A-046	A-047	A-048	A-049	A-050
Temperature	°C	156.22	-177.66	-179	10	-177.96	-181.58	-190.76	-187	-193.96	-192.21
Pressure	kPa	1588	410	1578	1578	410	410	125	410	125	125
Mass Enthalpy	kJ/kg	131.73	-225.17	-388.64	-19.82	-385.26	-397.05	-385.26	-408.28	-408.28	-388.64
Mass Entropy	kJ/(kg.°C)	4.82	3.48	1.74	4.39	1.72	1.67	1.74	1.54	1.55	1.78
Mass Density	kg/m^3	12.85	18.54	805.26	19.62	855.04	736.39	43.87	764.39	72.50	40.61
Mass Flow	kg/h	161899	533732	161899	16012	317914	215818	317914	215818	215818	161899
Molar Flow	kmol/h	5589.6	18427.4	5589.6	552.8	10723.7	7703.7	10723.7	7703.7	7703.7	5589.6
Mole fraction											
C		0	0	0	0	0	0	0	0	0	0
H_2		0	0	0	0	0	0	0	0	0	0
S		0	0	0	0	0	0	0	0	0	0
Ar		0.0097	0.0097	0.0097	0.0097	0.0165	0.0002	0.0165	0.0002	0.0002	0.0097
O_2		0.2095	0.2095	0.2095	0.2095	0.3600	0	0.3600	0	0	0.2095
N_2		0.7808	0.7808	0.7808	0.7808	0.6235	0.9998	0.6235	0.9998	0.9998	0.7808
CO_2		0	0	0	0	0	0	0	0	0	0
H_2O		0	0	0	0	0	0	0	0	0	0
SO_2		0	0	0	0	0	0	0	0	0	0
SiO_2		0	0	0	0	0	0	0	0	0	0
Al_2O_3		0	0	0	0	0	0	0	0	0	0
Fe_2O_3		0	0	0	0	0	0	0	0	0	0
CaO		0	0	0	0	0	0	0	0	0	0
MgO		0	0	0	0	0	0	0	0	0	0
Na_2O		0	0	0	0	0	0	0	0	0	0
K_2O		0	0	0	0	0	0	0	0	0	0
TiO_2		0	0	0	0	0	0	0	0	0	0
Mn_3O_4		0	0	0	0	0	0	0	0	0	0
P_2O_5		0	0	0	0	0	0	0	0	0	0
SO_3		0	0	0	0	0	0	0	0	0	0
$CaCO_3$		0	0	0	0	0	0	0	0	0	0
$CaSO_3$		0	0	0	0	0	0	0	0	0	0
Cl_2		0	0	0	0	0	0	0	0	0	0

Parameter	Units	A-051	A-052	A-053	A-054	A-055	A-056	A-057	A-058	A-059	A-060
Temperature	°C	-131.970498	-182.34	-194.84	-190.54	45.78	154	10	40.51	22	40.72
Pressure	kPa	125	111.33	111.33	111.33	101.33	101.33	101.32	140	140	170
Mass Enthalpy	kJ/kg	-156.01	-391.97	-225.15	-220.70	21.28	119.12	-15.34	15.23	-3.41	15.37
Mass Entropy	kJ/(kg.°C)	4.44	1.15	3.88	3.94	5.34	4.86	5.19	5.20	5.14	5.15
Mass Density	kg/m^3	3.12	1145.65	5.03	4.74	1.07	0.92	1.25	1.56	1.65	1.89
Mass Flow	kg/h	16012	166620	545023	545023	545023	166620	167064	167064	167064	167064
Molar Flow	kmol/h	552.8	5188.8	19381.1	19381.1	19381.1	5188.8	5768.0	5768.0	5768.0	5768.0
Mole fraction											
C		0	0	0	0	0	0	0	0	0	0
H_2		0	0	0	0	0	0	0	0	0	0
S		0	0	0	0	0	0	0	0	0	0
Ar		0.0097	0.0140	0.0085	0.0085	0.0085	0.0140	0.0097	0.0097	0.0097	0.0097
O_2		0.2095	0.9860	0.0016	0.0016	0.0016	0.9860	0.2095	0.2095	0.2095	0.2095
N_2		0.7808	0	0.9898	0.9898	0.9898	0	0.7808	0.7808	0.7808	0.7808
CO_2		0	0	0	0	0	0	0	0	0	0
H_2O		0	0	0	0	0	0	0	0	0	0
SO_2		0	0	0	0	0	0	0	0	0	0
SiO_2		0	0	0	0	0	0	0	0	0	0
Al_2O_3		0	0	0	0	0	0	0	0	0	0
Fe_2O_3		0	0	0	0	0	0	0	0	0	0
CaO		0	0	0	0	0	0	0	0	0	0
MgO		0	0	0	0	0	0	0	0	0	0
Na_2O		0	0	0	0	0	0	0	0	0	0
K_2O		0	0	0	0	0	0	0	0	0	0
TiO_2		0	0	0	0	0	0	0	0	0	0
Mn_3O_4		0	0	0	0	0	0	0	0	0	0
P_2O_5		0	0	0	0	0	0	0	0	0	0
SO_3		0	0	0	0	0	0	0	0	0	0
$CaCO_3$		0	0	0	0	0	0	0	0	0	0
$CaSO_3$		0	0	0	0	0	0	0	0	0	0
Cl_2		0	0	0	0	0	0	0	0	0	0

Parameter	Units	A-061	A-062	A-063	A-064	A-065	A-066	A-067	A-068	A-069	A-070
Temperature	°C	21	41.36	21	45.35	21	64.93	45	10	40.51	22
Pressure	kPa	170	210	210	270	270	420	420	101.32	140	140
Mass Enthalpy	kJ/kg	-4.50	15.92	-4.61	19.81	-4.78	39.34	19.09	-15.34	15.23	-3.41
Mass Entropy	kJ/(kg. °C)	5.08	5.09	5.02	5.03	4.95	4.96	4.90	5.19	5.20	5.14
Mass Density	kg/m^3	2.02	2.33	2.49	2.96	3.20	4.33	4.61	1.25	1.56	1.65
Mass Flow	kg/h	167064	167064	167064	167064	167064	167064	167064	218410	218410	218410
Molar Flow	kmol/h	5768.0	5768.0	5768.0	5768.0	5768.0	5768.0	5768.0	7540.7	7540.7	7540.7
Mole fraction											
C		0	0	0	0	0	0	0	0	0	0
H_2		0	0	0	0	0	0	0	0	0	0
S		0	0	0	0	0	0	0	0	0	0
Ar		0.0097	0.0097	0.0097	0.0097	0.0097	0.0097	0.0097	0.0097	0.0097	0.0097
O_2		0.2095	0.2095	0.2095	0.2095	0.2095	0.2095	0.2095	0.2095	0.2095	0.2095
N_2		0.7808	0.7808	0.7808	0.7808	0.7808	0.7808	0.7808	0.7808	0.7808	0.7808
CO_2		0	0	0	0	0	0	0	0	0	0
H_2O		0	0	0	0	0	0	0	0	0	0
SO_2		0	0	0	0	0	0	0	0	0	0
SiO_2		0	0	0	0	0	0	0	0	0	0
Al_2O_3		0	0	0	0	0	0	0	0	0	0
Fe_2O_3		0	0	0	0	0	0	0	0	0	0
CaO		0	0	0	0	0	0	0	0	0	0
MgO		0	0	0	0	0	0	0	0	0	0
Na_2O		0	0	0	0	0	0	0	0	0	0
K_2O		0	0	0	0	0	0	0	0	0	0
TiO_2		0	0	0	0	0	0	0	0	0	0
Mn_3O_4		0	0	0	0	0	0	0	0	0	0
P_2O_5		0	0	0	0	0	0	0	0	0	0
SO_3		0	0	0	0	0	0	0	0	0	0
$CaCO_3$		0	0	0	0	0	0	0	0	0	0
$CaSO_3$		0	0	0	0	0	0	0	0	0	0
Cl_2		0	0	0	0	0	0	0	0	0	0

Parameter	Units	A-071	A-072	A-073	A-074	A-075	A-076	A-077	A-078	A-079	A-080
Temperature	°C	40.72	21	41.36	21	45.35	21	64.93	45	10	40.51
Pressure	kPa	170	170	210	210	270	270	420	420	101.32	140
Mass Enthalpy	kJ/kg	15.37	-4.50	15.92	-4.61	19.81	-4.78	39.34	19.09	-15.34	15.23
Mass Entropy	kJ/(kg. °C)	5.15	5.08	5.09	5.02	5.03	4.95	4.96	4.90	5.19	5.20
Mass Density	kg/m^3	1.89	2.02	2.33	2.49	2.96	3.20	4.33	4.61	1.25	1.56
Mass Flow	kg/h	218410	218410	218410	218410	218410	218410	218410	218410	218410	218410
Molar Flow	kmol/h	7540.7	7540.7	7540.7	7540.7	7540.7	7540.7	7540.7	7540.7	7540.7	7540.7
Mole fraction											
C		0	0	0	0	0	0	0	0	0	0
H_2		0	0	0	0	0	0	0	0	0	0
S		0	0	0	0	0	0	0	0	0	0
Ar		0.0097	0.0097	0.0097	0.0097	0.0097	0.0097	0.0097	0.0097	0.0097	0.0097
O_2		0.2095	0.2095	0.2095	0.2095	0.2095	0.2095	0.2095	0.2095	0.2095	0.2095
N_2		0.7808	0.7808	0.7808	0.7808	0.7808	0.7808	0.7808	0.7808	0.7808	0.7808
CO_2		0	0	0	0	0	0	0	0	0	0
H_2O		0	0	0	0	0	0	0	0	0	0
SO_2		0	0	0	0	0	0	0	0	0	0
SiO_2		0	0	0	0	0	0	0	0	0	0
Al_2O_3		0	0	0	0	0	0	0	0	0	0
Fe_2O_3		0	0	0	0	0	0	0	0	0	0
CaO		0	0	0	0	0	0	0	0	0	0
MgO		0	0	0	0	0	0	0	0	0	0
Na_2O		0	0	0	0	0	0	0	0	0	0
K_2O		0	0	0	0	0	0	0	0	0	0
TiO_2		0	0	0	0	0	0	0	0	0	0
Mn_3O_4		0	0	0	0	0	0	0	0	0	0
P_2O_5		0	0	0	0	0	0	0	0	0	0
SO_3		0	0	0	0	0	0	0	0	0	0
$CaCO_3$		0	0	0	0	0	0	0	0	0	0
$CaSO_3$		0	0	0	0	0	0	0	0	0	0
Cl_2		0	0	0	0	0	0	0	0	0	0

Parameter	Units	A-081	A-082	A-083	A-084	A-085	A-086	A-087	A-088	A-089	A-090
Temperature	°C	22	40.72	21	41.36	21	45.35	21	64.93	45	45
Pressure	kPa	140	170	170	210	210	270	270	420	420	420
Mass Enthalpy	kJ/kg	-3.41	15.37	-4.50	15.92	-4.61	19.81	-4.78	39.34	19.09	19.09
Mass Entropy	kJ/(kg.°C)	5.14	5.15	5.08	5.09	5.02	5.03	4.95	4.96	4.90	4.90
Mass Density	kg/m^3	1.65	1.89	2.02	2.33	2.49	2.96	3.20	4.33	4.61	4.61
Mass Flow	kg/h	218410	218410	218410	218410	218410	218410	218410	218410	218410	603884
Molar Flow	kmol/h	7540.7	7540.7	7540.7	7540.7	7540.7	7540.7	7540.7	7540.7	7540.7	20849.4
Mole fraction											
C		0	0	0	0	0	0	0	0	0	0
H_2		0	0	0	0	0	0	0	0	0	0
S		0	0	0	0	0	0	0	0	0	0
Ar		0.0097	0.0097	0.0097	0.0097	0.0097	0.0097	0.0097	0.0097	0.0097	0.0097
O_2		0.2095	0.2095	0.2095	0.2095	0.2095	0.2095	0.2095	0.2095	0.2095	0.2095
N_2		0.7808	0.7808	0.7808	0.7808	0.7808	0.7808	0.7808	0.7808	0.7808	0.7808
CO_2		0	0	0	0	0	0	0	0	0	0
H_2O		0	0	0	0	0	0	0	0	0	0
SO_2		0	0	0	0	0	0	0	0	0	0
SiO_2		0	0	0	0	0	0	0	0	0	0
Al_2O_3		0	0	0	0	0	0	0	0	0	0
Fe_2O_3		0	0	0	0	0	0	0	0	0	0
CaO		0	0	0	0	0	0	0	0	0	0
MgO		0	0	0	0	0	0	0	0	0	0
Na_2O		0	0	0	0	0	0	0	0	0	0
K_2O		0	0	0	0	0	0	0	0	0	0
TiO_2		0	0	0	0	0	0	0	0	0	0
Mn_3O_4		0	0	0	0	0	0	0	0	0	0
P_2O_5		0	0	0	0	0	0	0	0	0	0
SO_3		0	0	0	0	0	0	0	0	0	0
$CaCO_3$		0	0	0	0	0	0	0	0	0	0
$CaSO_3$		0	0	0	0	0	0	0	0	0	0
Cl_2		0	0	0	0	0	0	0	0	0	0

Parameter	Units	A-091	A-092	A-093	A-094	A-095	A-096	A-097	A-098	A-099	A-100
Temperature	°C	45	45	57.19	22	156.22	156.22	156.22	-177.66	-179	10
Pressure	kPa	420	420	473.03	473.03	1588	1588	1588	410	1578	1578
Mass Enthalpy	kJ/kg	19.09	19.09	31.35	-4.35	131.73	131.73	131.73	-225.17	-388.64	-19.82
Mass Entropy	kJ/(kg.°C)	4.90	4.90	4.90	4.79	4.82	4.82	4.82	3.48	1.74	4.39
Mass Density	kg/m^3	4.61	4.61	4.99	5.60	12.85	12.85	12.85	18.54	805.26	19.62
Mass Flow	kg/h	452913	150971	150971	150971	150971	137384	13587	452913	137384	13587
Molar Flow	kmol/h	15637.1	5212.4	5212.4	5212.4	5212.4	4743.2	469.1	15637.1	4743.2	469.1
Mole fraction											
C		0	0	0	0	0	0	0	0	0	0
H_2		0	0	0	0	0	0	0	0	0	0
S		0	0	0	0	0	0	0	0	0	0
Ar		0.0097	0.0097	0.0097	0.0097	0.0097	0.0097	0.0097	0.0097	0.0097	0.0097
O_2		0.2095	0.2095	0.2095	0.2095	0.2095	0.2095	0.2095	0.2095	0.2095	0.2095
N_2		0.7808	0.7808	0.7808	0.7808	0.7808	0.7808	0.7808	0.7808	0.7808	0.7808
CO_2		0	0	0	0	0	0	0	0	0	0
H_2O		0	0	0	0	0	0	0	0	0	0
SO_2		0	0	0	0	0	0	0	0	0	0
SiO_2		0	0	0	0	0	0	0	0	0	0
Al_2O_3		0	0	0	0	0	0	0	0	0	0
Fe_2O_3		0	0	0	0	0	0	0	0	0	0
CaO		0	0	0	0	0	0	0	0	0	0
MgO		0	0	0	0	0	0	0	0	0	0
Na_2O		0	0	0	0	0	0	0	0	0	0
K_2O		0	0	0	0	0	0	0	0	0	0
TiO_2		0	0	0	0	0	0	0	0	0	0
Mn_3O_4		0	0	0	0	0	0	0	0	0	0
P_2O_5		0	0	0	0	0	0	0	0	0	0
SO_3		0	0	0	0	0	0	0	0	0	0
$CaCO_3$		0	0	0	0	0	0	0	0	0	0
$CaSO_3$		0	0	0	0	0	0	0	0	0	0
Cl_2		0	0	0	0	0	0	0	0	0	0

Parameter	Units	A-101	A-102	A-103	A-104	A-105	A-106	A-107	A-108	A-109	A-110
Temperature	°C	-177.96	-181.58	-190.76	-187	-193.96	-192.21	-131.97	-182.34	-194.84	-190.54
Pressure	kPa	410	410	125	410	125	125	125	111.33	111.33	111.33
Mass Enthalpy	kJ/kg	-385.26	-397.05	-385.26	-408.28	-408.28	-388.64	-156.01	-391.97	-225.15	-220.70
Mass Entropy	kJ/(kg.°C)	1.72	1.67	1.74	1.54	1.55	1.78	4.44	1.15	3.88	3.94
Mass Density	kg/m^3	855.04	736.39	43.87	764.39	72.50	40.61	3.12	1145.65	5.03	4.74
Mass Flow	kg/h	269772	183141	269772	183141	183141	137384	13587	141388	462496	462496
Molar Flow	kmol/h	9099.8	6537.2	9099.8	6537.2	6537.2	4743.2	469.1	4403.0	16446.4	16446.4
Mole fraction											
C		0	0	0	0	0	0	0	0	0	0
H_2		0	0	0	0	0	0	0	0	0	0
S		0	0	0	0	0	0	0	0	0	0
Ar		0.0165	0.0002	0.0165	0.0002	0.0002	0.0097	0.0097	0.0140	0.0085	0.0085
O_2		0.3600	0	0.3600	0	0	0.2095	0.2095	0.9860	0.0016	0.0016
N_2		0.6234	0.9998	0.6234	0.9998	0.9998	0.7808	0.7808	0	0.9898	0.9898
CO_2		0	0	0	0	0	0	0	0	0	0
H_2O		0	0	0	0	0	0	0	0	0	0
SO_2		0	0	0	0	0	0	0	0	0	0
SiO_2		0	0	0	0	0	0	0	0	0	0
Al_2O_3		0	0	0	0	0	0	0	0	0	0
Fe_2O_3		0	0	0	0	0	0	0	0	0	0
CaO		0	0	0	0	0	0	0	0	0	0
MgO		0	0	0	0	0	0	0	0	0	0
Na_2O		0	0	0	0	0	0	0	0	0	0
K_2O		0	0	0	0	0	0	0	0	0	0
TiO_2		0	0	0	0	0	0	0	0	0	0
Mn_3O_4		0	0	0	0	0	0	0	0	0	0
P_2O_5		0	0	0	0	0	0	0	0	0	0
SO_3		0	0	0	0	0	0	0	0	0	0
$CaCO_3$		0	0	0	0	0	0	0	0	0	0
$CaSO_3$		0	0	0	0	0	0	0	0	0	0
Cl_2		0	0	0	0	0	0	0	0	0	0

Parameter	Units	A-111	A-112	A-113	A-114	P-001	P-002	P-003	P-004	P-005	P-006
Temperature	°C	45.78	154	154	154	15	15	15.00	15	149.65	154
Pressure	kPa	101.33	101.33	101.33	101.32	101.32	101.32	101.32	101.32	101.32	101.32
Mass Enthalpy	kJ/kg	21.28	119.12	119.12	119.12	-924.92	-15930.96	-924.91	-78.55	-4098.50	119.12
Mass Entropy	kJ/(kg.°C)	5.34	4.86	4.86	4.86	4.17	2.83	4.17	5.20	5.00	4.86
Mass Density	kg/m^3	1.07	0.92	0.92	0.92	1.48	1014.81	1.48	3210.80	1.12	0.92
Mass Flow	kg/h	462496	141388	308008	308008	117066	0	117066	27511	455004	308008
Molar Flow	kmol/h	16446.4	4403.0	9591.8	9591.8	11470.0	0.0	11470.0	314.5	19821.8	9591.8
Mole fraction											
C		0	0	0	0	0.6758	0	0.6758	0	0.3911	0
H_2		0	0	0	0	0.2592	0	0.2592	0	0.1500	0
S		0	0	0	0	0.0023	0	0.0023	0	0.0013	0
Ar		0.0085	0.0140	0.0140	0.0140	0	0	0	0	0.0061	0.0140
O_2		0.0016	0.9860	0.9860	0.9860	0.0215	0	0.0215	0	0.1694	0.9860
N_2		0.9898	0	0	0	0.0057	0	0.0057	0	0.0075	0
CO_2		0	0	0	0	0	0	0	0	0.2301	0
H_2O		0	0	0	0	0.0354	1	0.0354	0	0.0285	0
SO_2		0	0	0	0	0	0	0	0	0.0001	0
SiO_2		0	0	0	0	0	0	0	0.5005	0.0079	0
Al_2O_3		0	0	0	0	0	0	0	0.3035	0.0048	0
Fe_2O_3		0	0	0	0	0	0	0	0.1327	0.0021	0
CaO		0	0	0	0	0	0	0	0.0131	0.0002	0
MgO		0	0	0	0	0	0	0	0.0090	0.0001	0
Na_2O		0	0	0	0	0	0	0	0.0010	0.0000	0
K_2O		0	0	0	0	0	0	0	0.0020	0.0000	0
TiO_2		0	0	0	0	0	0	0	0.0191	0.0003	0
Mn_3O_4		0	0	0	0	0	0	0	0.0030	0.0000	0
P_2O_5		0	0	0	0	0	0	0	0.0020	0.0000	0
SO_3		0	0	0	0	0	0	0	0.0141	0.0002	0
$CaCO_3$		0	0	0	0	0	0	0	0	0	0
$CaSO_3$		0	0	0	0	0	0	0	0	0	0
Cl_2		0	0	0	0	0.0001	0	0.0001	0	0.0001	0

Parameter	Units	P-007	P-008	P-009	P-010	P-011	P-012	P-013	P-014	P-015	P-016
Temperature	°C	154	154	154	2178.28	2178.28	2178.28	2178.28	2178.28	2149.96	2003.52
Pressure	kPa	101.32	101.32	101.32	101.32	101.32	101.32	101.32	101.32	101.29	101.26
Mass Enthalpy	kJ/kg	119.12	119.12	119.12	1955.34	-5866.73	1955.34	1955.34	-5750.16	-5799.61	-6047.38
Mass Entropy	kJ/(kg.°C)	4.86	4.86	4.86	7.20	7.36	7.20	7.20	7.36	7.34	7.23
Mass Density	kg/m^3	0.92	0.92	0.92	3240.65	0.19	3240.65	3240.65	0.19	0.19	0.21
Mass Flow	kg/h	3.1E9	9.2E9	1.8E10	2.7E9	1.3E11	6.8E8	2.0E9	1.4E11	1.4E11	1.4E11
Molar Flow	kmol/h	959.18	2877.55	5755.09	310.12	35514	77.53	232.59	35747	35747	35747
Mole fraction											
C		0	0	0	0	0	0	0	0	0	0
H_2		0	0	0	0	0	0	0	0	0	0
S		0	0	0	0	0	0	0	0	0	0
Ar		0.0140	0.0140	0.0140	0	0.0127	0	0	0.0126	0.0126	0.0126
O_2		0.9860	0.9860	0.9860	0	0.0426	0	0	0.0423	0.0423	0.0423
N_2		0.0000	0.0000	0.0000	0	0.0109	0	0	0.0109	0.0109	0.0109
CO_2		0	0	0	0	0.7238	0	0	0.7191	0.7191	0.7191
H_2O		0	0	0	0	0.2080	0	0	0.2067	0.2067	0.2067
SO_2		0	0	0	0	0.0016	0	0	0.0016	0.0016	0.0016
SiO_2		0	0	0	0.5076	0	0.5076	0.5076	0.0033	0.0033	0.0033
Al_2O_3		0	0	0	0.3078	0	0.3078	0.3078	0.0020	0.0020	0.0020
Fe_2O_3		0	0	0	0.1346	0	0.1346	0.1346	0.0009	0.0009	0.0009
CaO		0	0	0	0.0133	0	0.0133	0.0133	0.0001	0.0001	0.0001
MgO		0	0	0	0.0092	0	0.0092	0.0092	0.0001	0.0001	0.0001
Na_2O		0	0	0	0.0010	0	0.0010	0.0010	0.0000	0.0000	0.0000
K_2O		0	0	0	0.0020	0	0.0020	0.0020	0.0000	0.0000	0.0000
TiO_2		0	0	0	0.0194	0	0.0194	0.0194	0.0001	0.0001	0.0001
Mn_3O_4		0	0	0	0.0031	0	0.0031	0.0031	0.0000	0.0000	0.0000
P_2O_5		0	0	0	0.0020	0	0.0020	0.0020	0.0000	0.0000	0.0000
SO_3		0	0	0	0	0.0003	0	0	0.0003	0.0003	0.0003
$CaCO_3$		0	0	0	0	0	0	0	0	0	0
$CaSO_3$		0	0	0	0	0	0	0	0	0	0
Cl_2		0	0	0	0	0.0001	0	0	0.0001	0.0001	0.0001

Parameter	Units	P-017	P-018	P-019	P-020	P-021	P-022	P-023	P-024	P-025	P-026
Temperature	°C	1784.46	1541.61	1180.50	1043.03	370.35	253.21	150	150	150	150
Pressure	kPa	101.23	101.20	101.17	101.14	101.11	101.11	91.11	91.11	91.11	89.11
Mass Enthalpy	kJ/kg	-6398.74	-6769.69	-7296.80	-7490.55	-8360.50	-8493.20	-8603.98	-8603.98	-8603.98	113.51
Mass Entropy	kJ/(kg.°C)	7.07	6.88	6.56	6.42	5.50	5.27	5.06	5.06	5.06	5.61
Mass Density	kg/m^3	0.23	0.26	0.32	0.36	0.73	0.89	1.00	1.00	1.00	
Mass Flow	kg/h	1.4E11	1.4E11	1.4E11	1.4E11	1.4E11	1.4E11	1.4E11	712071	654612	10612
Molar Flow	kmol/h	35747	35747	35747	35747	35747	35747	35747	18625	17122	121.18
Mole fraction											
C		0	0	0	0	0	0	0	0	0	0
H_2		0	0	0	0	0	0	0	0	0	0
S		0	0	0	0	0	0	0	0	0	0
Ar		0.0126	0.0126	0.0126	0.0126	0.0126	0.0126	0.0126	0.0126	0.0126	0
O_2		0.0423	0.0423	0.0423	0.0423	0.0423	0.0423	0.0423	0.0423	0.0423	0
N_2		0.0109	0.0109	0.0109	0.0109	0.0109	0.0109	0.0109	0.0109	0.0109	0
CO_2		0.7191	0.7191	0.7191	0.7191	0.7191	0.7191	0.7191	0.7191	0.7191	0
H_2O		0.2067	0.2067	0.2067	0.2067	0.2067	0.2067	0.2067	0.2067	0.2067	0
SO_2		0.0016	0.0016	0.0016	0.0016	0.0016	0.0016	0.0016	0.0016	0.0016	0
SiO_2		0.0033	0.0033	0.0033	0.0033	0.0033	0.0033	0.0033	0.0033	0.0033	0.5076
Al_2O_3		0.0020	0.0020	0.0020	0.0020	0.0020	0.0020	0.0020	0.0020	0.0020	0.3078
Fe_2O_3		0.0009	0.0009	0.0009	0.0009	0.0009	0.0009	0.0009	0.0009	0.0009	0.1346
CaO		0.0001	0.0001	0.0001	0.0001	0.0001	0.0001	0.0001	0.0001	0.0001	0.0133
MgO		0.0001	0.0001	0.0001	0.0001	0.0001	0.0001	0.0001	0.0001	0.0001	0.0092
Na_2O		0.0000	0.0000	0.0000	0.0000	0	0	0	0	0	0.0010
K_2O		0.0000	0.0000	0.0000	0.0000	0	0	0	0	0	0.0020
TiO_2		0.0001	0.0001	0.0001	0.0001	0.0001	0.0001	0.0001	0.0001	0.0001	0.0194
Mn_3O_4		0.0000	0.0000	0.0000	0.0000	0	0	0	0	0	0.0031
P_2O_5		0.0000	0.0000	0.0000	0.0000	0	0	0	0	0	0.0020
SO_3		0.0003	0.0003	0.0003	0.0003	0.0003	0.0003	0.0003	0.0003	0.0003	0
$CaCO_3$		0	0	0	0	0	0	0	0	0	0
$CaSO_3$		0	0	0	0	0	0	0	0	0	0
Cl_2		0.0001	0.0001	0.0001	0.0001	0.0001	0.0001	0.0001	0.0001	0.0001	0

Parameter	Units	P-027	P-028	P-029	P-030	P-031	P-032	P-033	P-034	P-035	P-036
Temperature	°C	150	15	149.74	163.32	161.49	280	280	150	150	15
Pressure	kPa	89.11	101.32	89.11	101.32	101.32	101.32	101.32	91.11	91.11	101.32
Mass Enthalpy	kJ/kg	-8735.84	-10.33	-8718.43	-8704.24	-6867.30	-6741.52	-6741.53	111.95	-8671.42	-15545
Mass Entropy	kJ/(kg.°C)	5.06	5.21	5.06	5.07	5.12	5.38	5.38	5.53	5.06	3.02
Mass Density	kg/m^3	0.96	1.23	0.96	1.06	1.03	0.80	0.80	61.34	0.99	1082.54
Mass Flow	kg/h	701460	1403	702863	702863	887667	887667	887668	5026	649586	25777
Molar Flow	kmol/h	18504	48.45	18552	18552	24307	24307	24307	57.79	17064	1313.50
Mole fraction											
C		0	0	0	0	0	0	0	0	0	0
H_2		0	0	0	0	0	0	0	0	0	0
S		0	0	0	0	0	0	0	0	0	0
Ar		0.0127	0.0097	0.0127	0.0127	0.0130	0.0130	0.0130	0	0.0126	0
O_2		0.0426	0.2095	0.0430	0.0430	0.2663	0.2663	0.2663	0	0.0424	0
N_2		0.0109	0.7808	0.0130	0.0130	0.0099	0.0099	0.0099	0	0.0109	0
CO_2		0.7238	0	0.7219	0.7219	0.5510	0.5510	0.5510	0	0.7215	0
H_2O		0.2080	0	0.2075	0.2075	0.1584	0.1584	0.1584	0	0.2074	0.9804
SO_2		0.0016	0	0.0016	0.0016	0.0012	0.0012	0.0012	0	0.0016	0
SiO_2		0	0	0	0	0	0	0	0.4893	0.0017	0
Al_2O_3		0	0	0	0	0	0	0	0.2967	0.0010	0
Fe_2O_3		0	0	0	0	0	0	0	0.1297	0.0004	0
CaO		0	0	0	0	0	0	0	0.0128	0	0
MgO		0	0	0	0	0	0	0	0.0088	0	0
Na_2O		0	0	0	0	0	0	0	0.0010	0	0
K_2O		0	0	0	0	0	0	0	0.0020	0	0
TiO_2		0	0	0	0	0	0	0	0.0187	0.0001	0
Mn_3O_4		0	0	0	0	0	0	0	0.0029	0	0
P_2O_5		0	0	0	0	0	0	0	0.0020	0	0
SO_3		0.0003	0	0.0003	0.0003	0.0002	0.0002	0.0002	0	0.0003	0
$CaCO_3$		0	0	0	0	0	0	0	0	0	0.0196
$CaSO_3$		0	0	0	0	0	0	0	0	0	0
Cl_2		0.0001	0	0.0001	0.0001	0.0001	0.0001	0.0001	0.0362	0	0

Parameter	Units	P-037	P-038	P-039	P-040	P-041	P-042	P-043	P-044	P-045	P-046
Temperature	°C	63.90	63.90	64.46	64.46	64.46	15	64.36	75.86	15	24.82
Pressure	kPa	91.11	91.11	91.11	89.11	89.11	101.32	89.11	101.3	101.3	101.3
Mass Enthalpy	kJ/kg	-4768.05	-8987.48	-8919.40	35.83	-8984.88	-10.33	-8966.97	-8955.26	-15931	-15162
Mass Entropy	kJ/(kg.°C)	4.73	5.02	5.02	5.40	5.02	5.21	5.03	5.03	2.83	3.09
Mass Density	kg/m^3	1718.17	1.19	1.20	3240.65	1.16	1.23	1.16	1.28	1014.81	17.77
Mass Flow	kg/h	8613	666751	671777	4878	666899	1334	668233	668233	5397314	6065547
Molar Flow	kmol/h	121.29	18256	18314	55.70	18259	46.06	18305	18305	299599	317904
Mole fraction											
C		0	0	0	0	0	0	0	0	0	0
H_2		0	0	0	0	0	0	0	0	0	0
S		0	0	0	0	0	0	0	0	0	0
Ar		0	0.0118	0.0118	0	0.0118	0.0097	0.0118	0.0118	0	0.0007
O_2		0	0.0397	0.0395	0	0.0397	0.2095	0.0401	0.0401	0	0.0023
N_2		0	0.0102	0.0102	0	0.0102	0.7808	0.0121	0.0121	0	0.0007
CO_2		0	0.6756	0.6735	0	0.6755	0	0.6738	0.6738	0	0.0388
H_2O		0.3284	0.2622	0.2614	0	0.2622	0	0.2615	0.2615	1	0.9575
SO_2		0	0.0003	0.0003	0	0.0003	0	0.0003	0.0003	0	0
SiO_2		0.2331	0	0.0015	0.5076	0	0	0	0	0	0
Al_2O_3		0.1414	0	0.0009	0.3078	0	0	0	0	0	0
Fe_2O_3		0.0618	0	0.0004	0.1346	0	0	0	0	0	0
CaO		0.0061	0	0	0.0133	0	0	0	0	0	0
MgO		0.0042	0	0	0.0092	0	0	0	0	0	0
Na_2O		0.0005	0	0	0.0010	0	0	0	0	0	0
K_2O		0.0009	0	0	0.0020	0	0	0	0	0	0
TiO_2		0.0089	0	0.0001	0.0194	0	0	0	0	0	0
Mn_3O_4		0.0014	0	0	0.0031	0	0	0	0	0	0
P_2O_5		0.0009	0	0	0.0020	0	0	0	0	0	0
SO_3		0	0.0002	0.0002	0	0.0002	0	0.0002	0.0002	0	0
$CaCO_3$		0.0319	0	0	0	0	0	0	0	0	0
$CaSO_3$		0.1805	0	0	0	0	0	0	0	0	0
Cl_2		0	0	0.0001	0	0.0001	0	0.0001	0.0001	0	0

Parameter	Units	P-047	P-048	P-049	P-050	P-051	P-052	P-053	P-054	P-055	FW-01
Temperature	°C	24.90	24.90	24.90	24.90	24.92	350	295.35	295.35	26	298.97
Pressure	kPa	101.3	101.3	101.3	101.3	101.32	101.32	101.32	101.32	101.3	32407
Mass Enthalpy	kJ/kg	-15880	-8416.24	-8416.24	-8416.24	-8416.22	-8096.46	-5651.00	-5651.56	-8415.27	-14608
Mass Entropy	kJ/(kg·°C)	2.98	4.12	4.12	4.12	4.12	4.83	4.97	4.97	4.12	5.89
Mass Density	kg/m^3	1007.66	1.74	1.74	1.74	1.74	0.83	0.83	0.83	1.73	777.40
Mass Flow	kg/h	5482074	583473	365448	218025	218025	218025	310427	310427	365448	1364826
Molar Flow	kmol/h	304091	13808.6	8648.8	5159.8	5159.8	5159.8	8037.4	8037.2	8648.8	75760.1
Mole fraction											
C		0	0	0	0	0	0	0	0	0	0
H_2		0	0	0	0	0	0	0	0	0	0
S		0	0	0	0	0	0	0	0	0	0
Ar		0	0.0157	0.0157	0.0157	0.0157	0.0157	0.0151	0.0151	0.0157	0
O_2		0	0.0531	0.0531	0.0531	0.0531	0.0531	0.3871	0.3870	0.0531	0
N_2		0	0.0161	0.0161	0.0161	0.0161	0.0161	0.0103	0.0103	0.0161	0
CO_2		0.0004	0.8838	0.8838	0.8838	0.8838	0.8838	0.5674	0.5674	0.8838	0
H_2O		0.9995	0.0310	0.0310	0.0310	0.0310	0.0310	0.0199	0.0199	0.0310	1
SO_2		0	0.0002	0.0002	0.0002	0.0002	0.0002	0.0001	0.0001	0.0002	0
SiO_2		0	0	0	0	0	0	0	0	0	0
Al_2O_3		0	0	0	0	0	0	0	0	0	0
Fe_2O_3		0	0	0	0	0	0	0	0	0	0
CaO		0	0	0	0	0	0	0	0	0	0
MgO		0	0	0	0	0	0	0	0	0	0
Na_2O		0	0	0	0	0	0	0	0	0	0
K_2O		0	0	0	0	0	0	0	0	0	0
TiO_2		0	0	0	0	0	0	0	0	0	0
Mn_3O_4		0	0	0	0	0	0	0	0	0	0
P_2O_5		0	0	0	0	0	0	0	0	0	0
SO_3		0	0	0	0	0	0	0	0	0	0
$CaCO_3$		0	0	0	0	0	0	0	0	0	0
$CaSO_3$		0	0	0	0	0	0	0	0	0	0
Cl_2		0	0.0001	0.0001	0.0001	0.0001	0.0001	0.0001	0.0001	0.0001	0

Parameter	Units	FW-02	FW-03	FW-04	FW-05	FW-06	FW-07	FW-08	FW-09	FW-10	FW-11
Temperature	°C	399	401	450	500	600	365.10	365.10	365.10	450	620
Pressure	kPa	31907	31407	30907	30407	30000	7500	7500	7500	7300	7000
Mass Enthalpy	kJ/kg	-13737	-13688	-13160	-12912	-12560	-12904	-12904	-12904	-12690	-12281
Mass Entropy	kJ/(kg.°C)	7.27	7.35	8.11	8.45	8.89	8.97	8.97	8.97	9.29	9.82
Mass Density	kg/m^3	313.03	294.73	154.15	117.58	87.56	29.80	29.80	29.80	23.99	17.61
Mass Flow	kg/h	1364826	1364826	1364826	1364826	1364826	1364826	126929	1237897	1237897	1237897
Molar Flow	kmol/h	75760	75760	75760	75760	75760	75760	7045.7	68714	68714	68714
Mole fraction											
C		0	0	0	0	0	0	0	0	0	0
H_2		0	0	0	0	0	0	0	0	0	0
S		0	0	0	0	0	0	0	0	0	0
Ar		0	0	0	0	0	0	0	0	0	0
O_2		0	0	0	0	0	0	0	0	0	0
N_2		0	0	0	0	0	0	0	0	0	0
CO_2		0	0	0	0	0	0	0	0	0	0
H_2O		1	1	1	1	1	1	1	1	1	1
SO_2		0	0	0	0	0	0	0	0	0	0
SiO_2		0	0	0	0	0	0	0	0	0	0
Al_2O_3		0	0	0	0	0	0	0	0	0	0
Fe_2O_3		0	0	0	0	0	0	0	0	0	0
CaO		0	0	0	0	0	0	0	0	0	0
MgO		0	0	0	0	0	0	0	0	0	0
Na_2O		0	0	0	0	0	0	0	0	0	0
K_2O		0	0	0	0	0	0	0	0	0	0
TiO_2		0	0	0	0	0	0	0	0	0	0
Mn_3O_4		0	0	0	0	0	0	0	0	0	0
P_2O_5		0	0	0	0	0	0	0	0	0	0
SO_3		0	0	0	0	0	0	0	0	0	0
$CaCO_3$		0	0	0	0	0	0	0	0	0	0
$CaSO_3$		0	0	0	0	0	0	0	0	0	0
Cl_2		0	0	0	0	0	0	0	0	0	0

Parameter	Units	FW-12	FW-13	FW-14	FW-15	FW-16	FW-17	FW-18	FW-19	FW-20	FW-21
Temperature	°C	558.01	558.01	558.01	459.70	459.70	459.70	381.02	381.02	381.02	296.70
Pressure	kPa	4800	4800	4800	2500	2500	2500	1400	1400	1400	700
Mass Enthalpy	kJ/kg	-12404	-12404	-12404	-12598	-12598	-12598	-12751	-12751	-12751	-12914
Mass Entropy	kJ/(kg.°C)	9.84	9.84	9.84	9.89	9.89	9.89	9.93	9.93	9.93	9.97
Mass Density	kg/m^3	12.95	12.95	12.95	7.61	7.61	7.61	4.75	4.75	4.75	2.71
Mass Flow	kg/h	1237897	92222	1145675	1145675	59575	1086100	1086100	56238	1029862	1029862
Molar Flow	kmol/h	68714	5119.1	63595	63595	3307.0	60288	60288	3121.7	57167	57167
Mole fraction											
C		0	0	0	0	0	0	0	0	0	0
H_2		0	0	0	0	0	0	0	0	0	0
S		0	0	0	0	0	0	0	0	0	0
Ar		0	0	0	0	0	0	0	0	0	0
O_2		0	0	0	0	0	0	0	0	0	0
N_2		0	0	0	0	0	0	0	0	0	0
CO_2		0	0	0	0	0	0	0	0	0	0
H_2O		1	1	1	1	1	1	1	1	1	1
SO_2		0	0	0	0	0	0	0	0	0	0
SiO_2		0	0	0	0	0	0	0	0	0	0
Al_2O_3		0	0	0	0	0	0	0	0	0	0
Fe_2O_3		0	0	0	0	0	0	0	0	0	0
CaO		0	0	0	0	0	0	0	0	0	0
MgO		0	0	0	0	0	0	0	0	0	0
Na_2O		0	0	0	0	0	0	0	0	0	0
K_2O		0	0	0	0	0	0	0	0	0	0
TiO_2		0	0	0	0	0	0	0	0	0	0
Mn_3O_4		0	0	0	0	0	0	0	0	0	0
P_2O_5		0	0	0	0	0	0	0	0	0	0
SO_3		0	0	0	0	0	0	0	0	0	0
$CaCO_3$		0	0	0	0	0	0	0	0	0	0
$CaSO_3$		0	0	0	0	0	0	0	0	0	0
Cl_2		0	0	0	0	0	0	0	0	0	0

Parameter	Units	FW-22	FW-23	FW-24	FW-25	FW-26	FW-27	FW-28	FW-29	FW-30	FW-31
Temperature	°C	296.70	296.70	199.91	199.91	199.91	101.50	101.50	101.50	65.07	65.07
Pressure	kPa	700	700	280	280	280	90	90	90	25	25
Mass Enthalpy	kJ/kg	-12914	-12914	-13098.2	-13098.2	-13098.2	-13282.7	-13282.7	-13282.7	-13455.7	-15714.8
Mass Entropy	kJ/(kg.°C)	9.97	9.97	10.04	10.04	10.04	10.12	10.12	10.12	10.21	3.53
Mass Density	kg/m^3	2.71	2.71	1.30	1.30	1.30	0.52	0.52	0.52	0.17	976.39
Mass Flow	kg/h	59753	970109	970109	93130	876979	876979	54373	822606	822606	37110
Molar Flow	kmol/h	3316.8	53850	53850	5169.6	48680	48680	3018.2	45662	45662	2059.9
Mole fraction											
C		0	0	0	0	0	0	0	0	0	0
H_2		0	0	0	0	0	0	0	0	0	0
S		0	0	0	0	0	0	0	0	0	0
Ar		0	0	0	0	0	0	0	0	0	0
O_2		0	0	0	0	0	0	0	0	0	0
N_2		0	0	0	0	0	0	0	0	0	0
CO_2		0	0	0	0	0	0	0	0	0	0
H_2O		1	1	1	1	1	1	1	1	1	1
SO_2		0	0	0	0	0	0	0	0	0	0
SiO_2		0	0	0	0	0	0	0	0	0	0
Al_2O_3		0	0	0	0	0	0	0	0	0	0
Fe_2O_3		0	0	0	0	0	0	0	0	0	0
CaO		0	0	0	0	0	0	0	0	0	0
MgO		0	0	0	0	0	0	0	0	0	0
Na_2O		0	0	0	0	0	0	0	0	0	0
K_2O		0	0	0	0	0	0	0	0	0	0
TiO_2		0	0	0	0	0	0	0	0	0	0
Mn_3O_4		0	0	0	0	0	0	0	0	0	0
P_2O_5		0	0	0	0	0	0	0	0	0	0
SO_3		0	0	0	0	0	0	0	0	0	0
$CaCO_3$		0	0	0	0	0	0	0	0	0	0
$CaSO_3$		0	0	0	0	0	0	0	0	0	0
Cl_2		0	0	0	0	0	0	0	0	0	0

Parameter	Units	FW-32	FW-33	FW-34	FW-35	FW-36	FW-37	FW-38	FW-39	FW-40	FW-41
Temperature	°C	65.07	65.07	65.07	29.68	24.76	24.98	61	138.48	131.15	96.68
Pressure	kPa	25	25	25	4.1	3.1	2300	2100	400	280	90
Mass Enthalpy	kJ/kg	-13349	-13349	-13349	-13568.2	-15888.9	-15885.8	-15730.5	-15390.7	-13994.2	-15182.4
Mass Entropy	kJ/(kg.°C)	10.52	10.52	10.52	10.64	2.98	2.98	3.47	4.39	7.85	4.98
Mass Density	kg/m^3	0.16	0.16	0.16	0.03	1007.49	1008.01	980.34	914.35	2.34	3.07
Mass Flow	kg/h	785496	7854.96	777641	777641	777641	777641	777641	59753	152884	152884
Molar Flow	kmol/h	43602	436.02	43166	43166	43166	43166	43166	3316.8	8486.4	8486.4
Mole fraction											
C		0	0	0	0	0	0	0	0	0	0
H_2		0	0	0	0	0	0	0	0	0	0
S		0	0	0	0	0	0	0	0	0	0
Ar		0	0	0	0	0	0	0	0	0	0
O_2		0	0	0	0	0	0	0	0	0	0
N_2		0	0	0	0	0	0	0	0	0	0
CO_2		0	0	0	0	0	0	0	0	0	0
H_2O		1	1	1	1	1	1	1	1	1	1
SO_2		0	0	0	0	0	0	0	0	0	0
SiO_2		0	0	0	0	0	0	0	0	0	0
Al_2O_3		0	0	0	0	0	0	0	0	0	0
Fe_2O_3		0	0	0	0	0	0	0	0	0	0
CaO		0	0	0	0	0	0	0	0	0	0
MgO		0	0	0	0	0	0	0	0	0	0
Na_2O		0	0	0	0	0	0	0	0	0	0
K_2O		0	0	0	0	0	0	0	0	0	0
TiO_2		0	0	0	0	0	0	0	0	0	0
Mn_3O_4		0	0	0	0	0	0	0	0	0	0
P_2O_5		0	0	0	0	0	0	0	0	0	0
SO_3		0	0	0	0	0	0	0	0	0	0
$CaCO_3$		0	0	0	0	0	0	0	0	0	0
$CaSO_3$		0	0	0	0	0	0	0	0	0	0
Cl_2		0	0	0	0	0	0	0	0	0	0

Parameter	Units	FW-42	FW-43	FW-44	FW-45	FW-46	FW-47	FW-48	FW-49	FW-50	FW-51
Temperature	°C	96.68	85.94	65.07	60.78	61	61	87	127	158.72	287.86
Pressure	kPa	90	60	25	25	2100	2100	1900	1700	1400	7300
Mass Enthalpy	kJ/kg	-14684	-15244.5	-15254.6	-15733.4	-15730.5	-15730.5	-15617.8	-15441.4	-15297.7	-14496.8
Mass Entropy	kJ/(kg.°C)	6.33	4.84	4.89	3.47	3.47	3.47	3.80	4.26	4.61	6.16
Mass Density	kg/m^3	1.36	2.21	0.83	979.78	980.34	980.34	959.44	925.38	896.04	260.36
Mass Flow	kg/h	207256	207256	252221	252221	252221	1029862	1029862	1029862	1029862	126929
Molar Flow	kmol/h	11504.6	11504.6	14000.5	14000.5	14000.5	57166.6	57166.6	57166.6	57166.6	7045.7
Mole fraction											
C		0	0	0	0	0	0	0	0	0	0
H_2		0	0	0	0	0	0	0	0	0	0
S		0	0	0	0	0	0	0	0	0	0
Ar		0	0	0	0	0	0	0	0	0	0
O_2		0	0	0	0	0	0	0	0	0	0
N_2		0	0	0	0	0	0	0	0	0	0
CO_2		0	0	0	0	0	0	0	0	0	0
H_2O		1	1	1	1	1	1	1	1	1	1
SO_2		0	0	0	0	0	0	0	0	0	0
SiO_2		0	0	0	0	0	0	0	0	0	0
Al_2O_3		0	0	0	0	0	0	0	0	0	0
Fe_2O_3		0	0	0	0	0	0	0	0	0	0
CaO		0	0	0	0	0	0	0	0	0	0
MgO		0	0	0	0	0	0	0	0	0	0
Na_2O		0	0	0	0	0	0	0	0	0	0
K_2O		0	0	0	0	0	0	0	0	0	0
TiO_2		0	0	0	0	0	0	0	0	0	0
Mn_3O_4		0	0	0	0	0	0	0	0	0	0
P_2O_5		0	0	0	0	0	0	0	0	0	0
SO_3		0	0	0	0	0	0	0	0	0	0
$CaCO_3$		0	0	0	0	0	0	0	0	0	0
$CaSO_3$		0	0	0	0	0	0	0	0	0	0
Cl_2		0	0	0	0	0	0	0	0	0	0

Parameter	Units	FW-52	FW-53	FW-54	FW-55	FW-56	FW-57	FW-58	FW-59	FW-60	FW-61
Temperature	°C	293.32	262.31	224.74	224.55	220.10	195.32	202.64	224	259.7	292
Pressure	kPa	4781.3	4781.3	4581.3	2500	2300	1400	32650	32600	32550	32500
Mass Enthalpy	kJ/kg	-13018	-13874	-14978	-14469	-14965	-15125	-15076	-14975	-14798	-14650
Mass Entropy	kJ/(kg.°C)	8.96	7.36	5.29	6.32	5.32	4.99	5.00	5.21	5.56	5.81
Mass Density	kg/m^3	21.20	42.40	828.52	42.83	344.09	858.85	877.24	857.36	821.75	785.97
Mass Flow	kg/h	92222	219150	219150	278725	278725	1364826	1364826	1364826	1364826	1364826
Molar Flow	kmol/h	5119.1	12164.8	12164.8	15471.8	15471.8	75760.1	75760.1	75760.1	75760.1	75760.1
Mole fraction											
C		0	0	0	0	0	0	0	0	0	0
H_2		0	0	0	0	0	0	0	0	0	0
S		0	0	0	0	0	0	0	0	0	0
Ar		0	0	0	0	0	0	0	0	0	0
O_2		0	0	0	0	0	0	0	0	0	0
N_2		0	0	0	0	0	0	0	0	0	0
CO_2		0	0	0	0	0	0	0	0	0	0
H_2O		1	1	1	1	1	1	1	1	1	1
SO_2		0	0	0	0	0	0	0	0	0	0
SiO_2		0	0	0	0	0	0	0	0	0	0
Al_2O_3		0	0	0	0	0	0	0	0	0	0
Fe_2O_3		0	0	0	0	0	0	0	0	0	0
CaO		0	0	0	0	0	0	0	0	0	0
MgO		0	0	0	0	0	0	0	0	0	0
Na_2O		0	0	0	0	0	0	0	0	0	0
K_2O		0	0	0	0	0	0	0	0	0	0
TiO_2		0	0	0	0	0	0	0	0	0	0
Mn_3O_4		0	0	0	0	0	0	0	0	0	0
P_2O_5		0	0	0	0	0	0	0	0	0	0
SO_3		0	0	0	0	0	0	0	0	0	0
$CaCO_3$		0	0	0	0	0	0	0	0	0	0
$CaSO_3$		0	0	0	0	0	0	0	0	0	0
Cl_2		0	0	0	0	0	0	0	0	0	0

Parameter	Units	G-01	G-02	G-03	G-04	G-05	G-06	G-07	G-08	G-09	G-10
Temperature	°C	26	255.12	25	25	25	84.08	25	25	25	53.47
Pressure	kPa	101.3	1001.3	1000.3	1000.3	1000.3	2000.3	2000	2000	2000	2800
Mass Enthalpy	kJ/kg	-8417.37	-8200.91	-8455.13	-15813.69	-8367.04	-8318.78	-8378.28	-15745	-8373.59	-8352.33
Mass Entropy	kJ/(kg.°C)	4.12	4.21	3.56	2.98	3.57	3.59	3.41	2.98	3.41	3.42
Mass Density	kg/m^3	1.73	9.68	18.46	1009.40	18.24	30.59	38.67	1011.37	38.65	49.57
Mass Flow	kg/h	365357	365357	365357	4322.1	361034	361034	361034	229.89	360804	360804
Molar Flow	kmol/h	8647.51	8647.51	8647.51	238.41	8409.10	8409.10	8409.10	12.61	8396.49	8396.49
Mole fraction											
C		0	0	0	0	0	0	0	0	0	0
H_2		0	0	0	0	0	0	0	0	0	0
S		0	0	0	0	0	0	0	0	0	0
Ar		0.0157	0.0157	0.0157	0	0.0161	0.0161	0.0161	0	0.0161	0.0161
O_2		0.0531	0.0531	0.0531	0	0.0546	0.0546	0.0546	0	0.0547	0.0547
N_2		0.0161	0.0161	0.0161	0	0.0165	0.0165	0.0165	0	0.0166	0.0166
CO_2		0.8839	0.8839	0.8839	0.0043	0.9088	0.9088	0.9088	0.0083	0.9102	0.9102
H_2O		0.0310	0.0310	0.0310	0.9957	0.0036	0.0036	0.0036	0.9916	0.0022	0.0022
SO_2		0.0002	0.0002	0.0002	0.0001	0.0002	0.0002	0.0002	0.0001	0.0002	0.0002
SiO_2		0	0	0	0	0	0	0	0	0	0
Al_2O_3		0	0	0	0	0	0	0	0	0	0
Fe_2O_3		0	0	0	0	0	0	0	0	0	0
CaO		0	0	0	0	0	0	0	0	0	0
MgO		0	0	0	0	0	0	0	0	0	0
Na_2O		0	0	0	0	0	0	0	0	0	0
K_2O		0	0	0	0	0	0	0	0	0	0
TiO_2		0	0	0	0	0	0	0	0	0	0
Mn_3O_4		0	0	0	0	0	0	0	0	0	0
P_2O_5		0	0	0	0	0	0	0	0	0	0
SO_3		0	0	0	0	0	0	0	0	0	0
$CaCO_3$		0	0	0	0	0	0	0	0	0	0
$CaSO_3$		0	0	0	0	0	0	0	0	0	0
Cl_2		0	0	0	0	0	0	0	0	0	0

Parameter	Units	G-11	G-12	G-13	G-14	G-15	G-16	G-17	G-18	G-19	G-20
Temperature	°C	25	25	25	25	25	-31.1	-33.89	-7.48	-10.81	-54
Pressure	kPa	2800	2800	2800	2800	2800	2800	2800	2800	2800	2800
Mass Enthalpy	kJ/kg	-8382.4	-15694	-8381.2	-15885	-8377.3	-8685.4	-8931.4	-9272.7	-8540.6	-8875.9
Mass Entropy	kJ/(kg.°C)	3.32	2.98	3.32	2.98	3.31	2.12	2.00	2.11	3.15	1.82
Mass Density	kg/m^3	56.94	1012.84	56.94	1008.14	56.95	368.51	637.34	971.00	73.41	777.33
Mass Flow	kg/h	360804	58.32	360746	269.10	360477	360477	1615734	325737	1289997	1289997
Molar Flow	kmol/h	8396.5	3.18	8393.3	14.94	8378.4	8378.4	37245.0	7400.5	29844.4	29844.4
Mole fraction											
C		0	0	0	0	0	0	0	0	0	0
H_2		0	0	0	0	0	0	0	0	0	0
S		0	0	0	0	0	0	0	0	0	0
Ar		0.0161	0	0.0161	0	0.0162	0.0162	0.0100	0	0.0125	0.0125
O_2		0.0547	0	0.0547	0	0.0548	0.0548	0.0372	0	0.0465	0.0465
N_2		0.0166	0	0.0166	0	0.0166	0.0166	0.0089	0	0.0111	0.0111
CO_2		0.9102	0.0113	0.9105	0	0.9121	0.9121	0.9438	0.9997	0.9300	0.9300
H_2O		0.0022	0.9886	0.0018	1	0	0	0	0	0	0
SO_2		0.0002	0.0001	0.0002	0	0.0002	0.0002	0.0001	0.0003	0	0
SiO_2		0	0	0	0	0	0	0	0	0	0
Al_2O_3		0	0	0	0	0	0	0	0	0	0
Fe_2O_3		0	0	0	0	0	0	0	0	0	0
CaO		0	0	0	0	0	0	0	0	0	0
MgO		0	0	0	0	0	0	0	0	0	0
Na_2O		0	0	0	0	0	0	0	0	0	0
K_2O		0	0	0	0	0	0	0	0	0	0
TiO_2		0	0	0	0	0	0	0	0	0	0
Mn_3O_4		0	0	0	0	0	0	0	0	0	0
P_2O_5		0	0	0	0	0	0	0	0	0	0
SO_3		0	0	0	0	0	0	0	0	0	0
$CaCO_3$		0	0	0	0	0	0	0	0	0	0
$CaSO_3$		0	0	0	0	0	0	0	0	0	0
Cl_2		0	0	0	0	0	0	0	0	0	0

Parameter	Units	G-21	G-22	G-23	G-24	G-25	G-26	G-27	G-28	G-29	G-30
Temperature	°C	-54	-54	-55.15	-66.35	-34.87	-5	22.42	-35	-35	-54.31
Pressure	kPa	2800	2800	1980	1300	1300	1980	2800	2800	2800	550
Mass Enthalpy	kJ/kg	-9043	-2868	-9043	-2868	-2840	-8680.4	-8662	-9002.3	-9002.1	-9272.7
Mass Entropy	kJ/(kg.°C)	1.78	3.39	1.78	3.55	3.67	3.26	3.27	1.96	1.96	2.17
Mass Density	kg/m^3	1141.29	62.35	754.99	28.83	24.38	45.71	59.08	790.35	790.02	49.10
Mass Flow	kg/h	1255092	34905	1255092	34905	34905	1255092	1255092	1255092	1255257	325737
Molar Flow	kmol/h	28862	982.15	28862	982.15	982.15	28862	28862	28862	28867	7400.5
Mole fraction											
C		0	0	0	0	0	0	0	0	0	0
H_2		0	0	0	0	0	0	0	0	0	0
S		0	0	0	0	0	0	0	0	0	0
Ar		0.0083	0.1358	0.0083	0.1358	0.1358	0.0083	0.0083	0.0083	0.0082	0
O_2		0.0319	0.4739	0.0319	0.4739	0.4739	0.0319	0.0319	0.0319	0.0321	0
N_2		0.0067	0.1392	0.0067	0.1392	0.1392	0.0067	0.0067	0.0067	0.0066	0
CO_2		0.9531	0.2511	0.9531	0.2511	0.2511	0.9531	0.9531	0.9531	0.9530	0.9997
H_2O		0	0	0	0	0	0	0	0	0	0
SO_2		0	0	0	0	0	0	0	0	0	0.0003
SiO_2		0	0	0	0	0	0	0	0	0	0
Al_2O_3		0	0	0	0	0	0	0	0	0	0
Fe_2O_3		0	0	0	0	0	0	0	0	0	0
CaO		0	0	0	0	0	0	0	0	0	0
MgO		0	0	0	0	0	0	0	0	0	0
Na_2O		0	0	0	0	0	0	0	0	0	0
K_2O		0	0	0	0	0	0	0	0	0	0
TiO_2		0	0	0	0	0	0	0	0	0	0
Mn_3O_4		0	0	0	0	0	0	0	0	0	0
P_2O_5		0	0	0	0	0	0	0	0	0	0
SO_3		0	0	0	0	0	0	0	0	0	0
$CaCO_3$		0	0	0	0	0	0	0	0	0	0
$CaSO_3$		0	0	0	0	0	0	0	0	0	0
Cl_2		0	0	0	0	0	0	0	0	0	0

Parameter	Units	G-31	G-32	G-33	G-34	G-35	G-36
Temperature	°C	-34	139.78	49.78	98.53	26.03	39.18
Pressure	kPa	550	4000	4000	6800	6800	12000
Mass Enthalpy	kJ/kg	-9003.7	-8863.8	-8962.1	-8929.1	-9162.4	-9153.1
Mass Entropy	kJ/(kg.°C)	3.39	3.48	3.21	3.22	2.48	2.49
Mass Density	kg/m^3	12.95	55.18	80.40	118.26	654.83	674.49
Mass Flow	kg/h	325737	325737	325737	325737	325737	325737
Molar Flow	kmol/h	7400.5	7400.5	7400.5	7400.5	7400.5	7400.5
Mole fraction							
C		0	0	0	0	0	0
H_2		0	0	0	0	0	0
S		0	0	0	0	0	0
Ar		0	0	0	0	0	0
O_2		0	0	0	0	0	0
N_2		0	0	0	0	0	0
CO_2		0.9997	0.9997	0.9997	0.9997	0.9997	0.9997
H_2O		0	0	0	0	0	0
SO_2		0.0003	0.0003	0.0003	0.0003	0.0003	0.0003
SiO_2		0	0	0	0	0	0
Al_2O_3		0	0	0	0	0	0
Fe_2O_3		0	0	0	0	0	0
CaO		0	0	0	0	0	0
MgO		0	0	0	0	0	0
Na_2O		0	0	0	0	0	0
K_2O		0	0	0	0	0	0
TiO_2		0	0	0	0	0	0
Mn_3O_4		0	0	0	0	0	0
P_2O_5		0	0	0	0	0	0
SO_3		0	0	0	0	0	0
$CaCO_3$		0	0	0	0	0	0
$CaSO_3$		0	0	0	0	0	0
Cl_2		0	0	0	0	0	0

Table B.2: Heat tables of the oxy-combustion process without heat integration.

Unit	Heat Flow (GJ/h)	Utility (kg/h)
Q-01	-4.718	225581
Q-02	-5.029	240462
Q-03	-5.196	248453
Q-04	-6.224	297567
Q-05	-5.126	245094
Q-06	-4.274	204363
Q-07	-4.556	217845
Q-08	-4.708	225085
Q-09	-5.638	269579
Q-10	-4.644	222041
Q-11	-4.274	204363
Q-12	-4.556	217845
Q-13	-4.708	225085
Q-14	-5.638	269579
Q-15	-4.644	222041
Q-16	-6.351	303665
Q-17	-87.989	0
Q-18	-3.114	148909
Q-19	-3.320	158732
Q-20	-3.430	164007
Q-21	-4.108	196428
Q-22	-3.384	161790
Q-23	-4.072	194675
Q-24	-4.340	207518
Q-25	-4.484	214414
Q-26	-5.371	256800
Q-27	-4.424	211515
Q-28	-4.072	194675
Q-29	-4.340	207518
Q-30	-4.484	214414
Q-31	-5.371	256800
Q-32	-4.424	211515
Q-33	-5.389	257683
Q-34	-74.666	0
Q-35	-151.392	7238418
Q-36	-1804.668	86285810
Q-37	0.356	162
Q-38	-92.882	4440917
Q-39	-21.481	1027054
Q-40	-10.848	518683
Q-41	0.611	0
Q-42	505.868	126467037
Q-43	-112.943	28235727
Q-44	-427.223	318613442
Q-45	-32.020	1530953
Q-46	-76.005	3634000

Table B.3: Power table of the oxy-combustion process without heat integration.

	W-01	W-02	W-03	W-04	W-05	W-06	W-07	W-08	W-09	W-10
Work (kW)	2149.39	1320.31	1435.40	1716.74	3102.37	1947.22	1196.12	1300.40	1555.27	2810.57
	W-11	W-12	W-13	W-14	W-15	W-16	W-17	W-18	W-19	W-20
Work (kW)	1947.22	1196.12	1300.40	1555.27	2810.57	605.77	6725.04	1418.84	871.55	947.53
	W-21	W-22	W-23	W-24	W-25	W-26	W-27	W-28	W-29	W-30
Work (kW)	1133.24	2047.92	1854.91	1139.42	1238.75	1481.54	2677.33	1854.91	1139.42	1238.75
	W-31	W-32	W-33	W-34	W-35	W-36	W-37	W-38	W-39	W-40
Work (kW)	1481.54	2677.33	514.04	5706.72	2769.16	2172.61	1.03	-130615.9	-42341.5	-61643.2
	W-41	W-42	W-43	W-44	W-45	W-46	W-47	W-48	W-49	W-50
Work (kW)	-46317.1	-46557.0	-49622.2	-44942.8	-39543.4	-47341.5	656.29	197.72	18392.74	21968.43
	W-51	W-52	W-53	W-54	W-55	W-56				
Work (kW)	4839.42	2130.90	6441.69	12658.02	2988.02	845.31				

Table B.4: Overall carbon balance of the oxy-combustion process without heat integration.

Carbon In		Carbon Out	
	kg/h		kg/h
Coal	93019.2	Spray dryer out	46.43
Limestone	309.0	DCC out	1567.87
		Dissolved in GPU compression	13.86
		Stack	2959.04
		Storage	88782.0
Total	93328.3	Total	93369.2
		Balance	40.88
		Error (%)	0.04

Table B.5: Energy balance of the oxy-combustion process without heat integration. Energy in.

	HHV (GJ/h)	Sensible + Latent (GJ/h)	Power (GJ/h)	Total (GJ/h)
ASU1 - MAC1	0	0	35.01	35.01
ASU1 - MAC2	0	0	31.71	31.71
ASU1 - MAC3	0	0	31.71	31.71
ASU1 - Booster 1	0	0	2.18	2.18
ASU1 - Booster 2	0	0	24.21	24.21
ASU1 - LP Reboiler	0	87.99	0	87.99
ASU2 - MAC1	0	0	23.11	23.11
ASU2 - MAC2	0	0	30.21	30.21
ASU2 - MAC3	0	0	30.21	30.21
ASU2 - Booster 1	0	0	1.85	1.85
ASU2 - Booster 2	0	0	20.54	20.54
ASU2 - LP reboiler	0	74.67	0	74.67
Coal	3919.06	0	0	3919.06
Limestone	52.81	0	0	52.81
ID fan	0	0	7.82	7.82
Primary fan	0	0	0.00	0.00
Secondary FG fan	0	0	9.97	9.97
Condensate pump	0	0	2.36	2.36
FW pump	0	0	0.71	0.71
Boiler feed pump	0	0	66.21	66.21
Water	12286.57	0	0	12286.57
Gas heater	0	0.36	0	0.36
GPU - Main compressor	0	0	104.18	104.18
GPU - Gas dryer	0	0.61	0	0.61
GPU - Reboiler	0	505.87	0	505.87
GPU - Recycle compressor	0	0	23.19	23.19
GPU - CO_2 compressor	0	0	56.33	56.33
GPU - CO_2 pump	0	0	3.04	3.04
Total	16258.45	669.49	504.57	17432.51

Table B.6: Energy balance of the oxy-combustion process without heat integration. Energy out.

	HHV (GJ/h)	Sensible + Latent (GJ/h)	Power (GJ/h)	Total (GJ/h)
ASU1 - MAC1 cooling	0	26.29	0	26.29
ASU1 - MAC2 cooling	0	23.82	0	23.82
ASU1 - MAC3 cooling	0	23.82	0	23.82
ASU1 - Turbine	0	2.18	0	2.18
ASU1 - Booster cooling	0	6.35	0	6.35
ASU1 - HP condenser	0	87.99	0	87.99
ASU2 - MAC1 cooling	0	17.36	0	17.36
ASU2 - MAC2 cooling	0	22.69	0	22.69
ASU2 - MAC3 cooling	0	22.69	0	22.69
ASU2 - Turbine	0	1.85	0	1.85
ASU2 - Booster cooling	0	5.39	0	5.39
ASU2 - HP condenser	0	74.67	0	74.67
Gas cooler	0	151.39	0	151.39
Slurry	1.63	0	0	1.63
Water	12465.38	0	0	12465.38
HP turbine	0	0	470.22	470.22
IP turbine	0	0	708.69	708.69
LP turbine	0	0	653.22	653.22
Condenser	0	1804.67	0	1804.67
GPU - Main comp. cooling	0	125.21	0	125.21
GPU - Condensate	10.38	0	0	10.38
GPU - Water	0.61	0	0	0.61
GPU - Condenser	0	112.94	0	112.94
GPU - Gas cooler	0	427.22	0	427.22
GPU - CO_2 comp. cooling	0	108.03	0	108.03
CO_2 for storage	0.02	0	0	0.02
Unaccounted energy				77.81
Unaccounted energy (%)				0.45

B.5.2 With heat integration

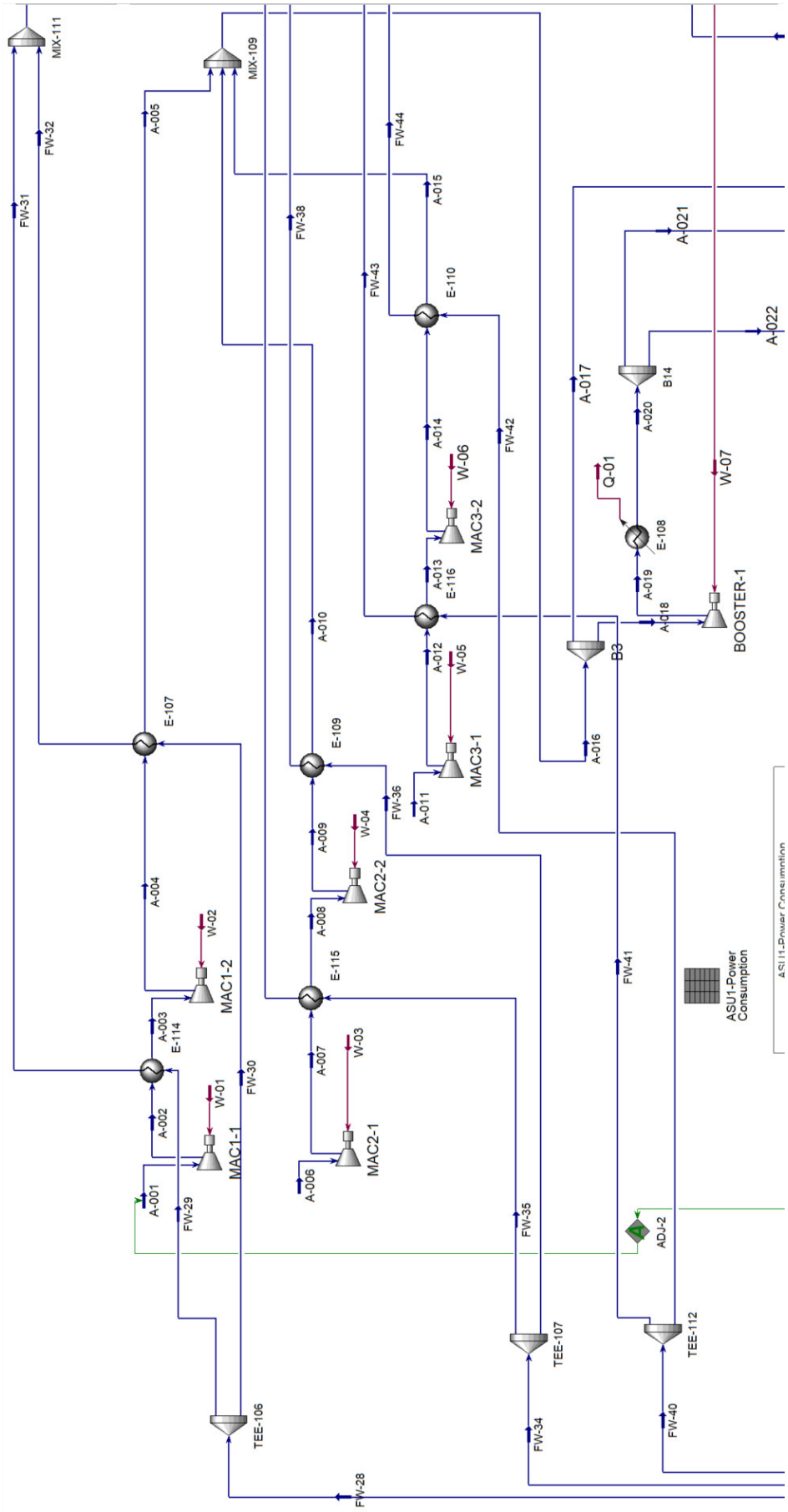
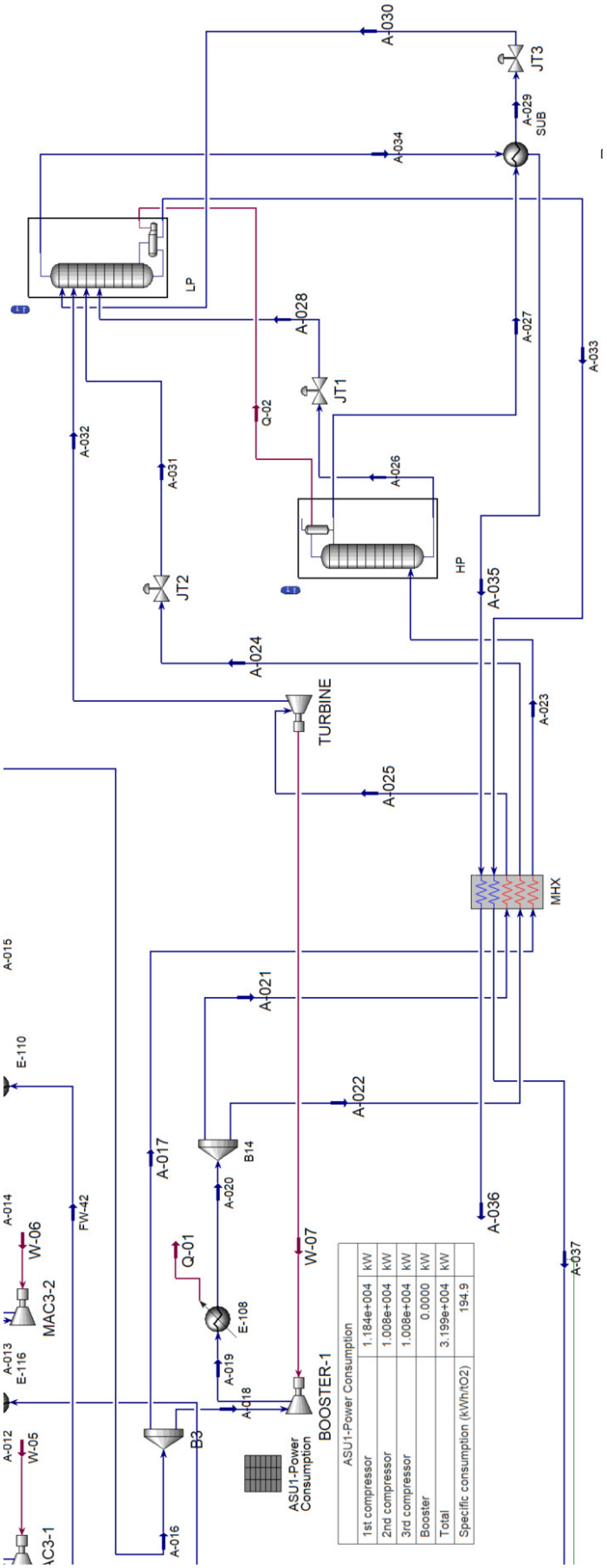
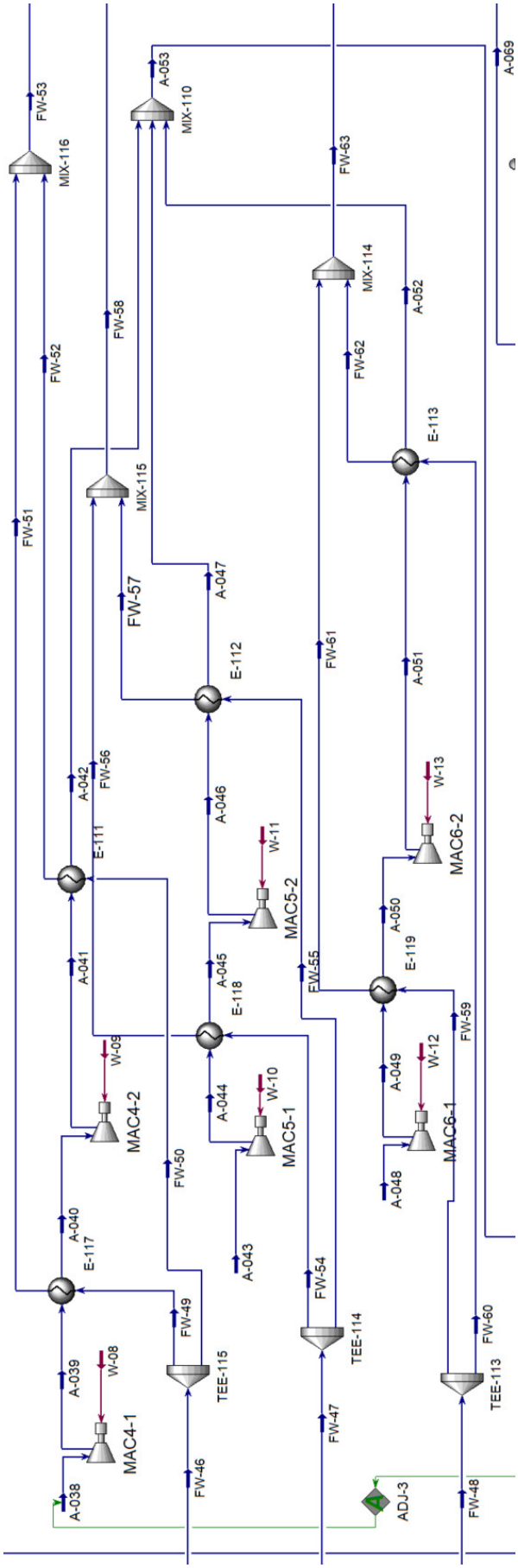


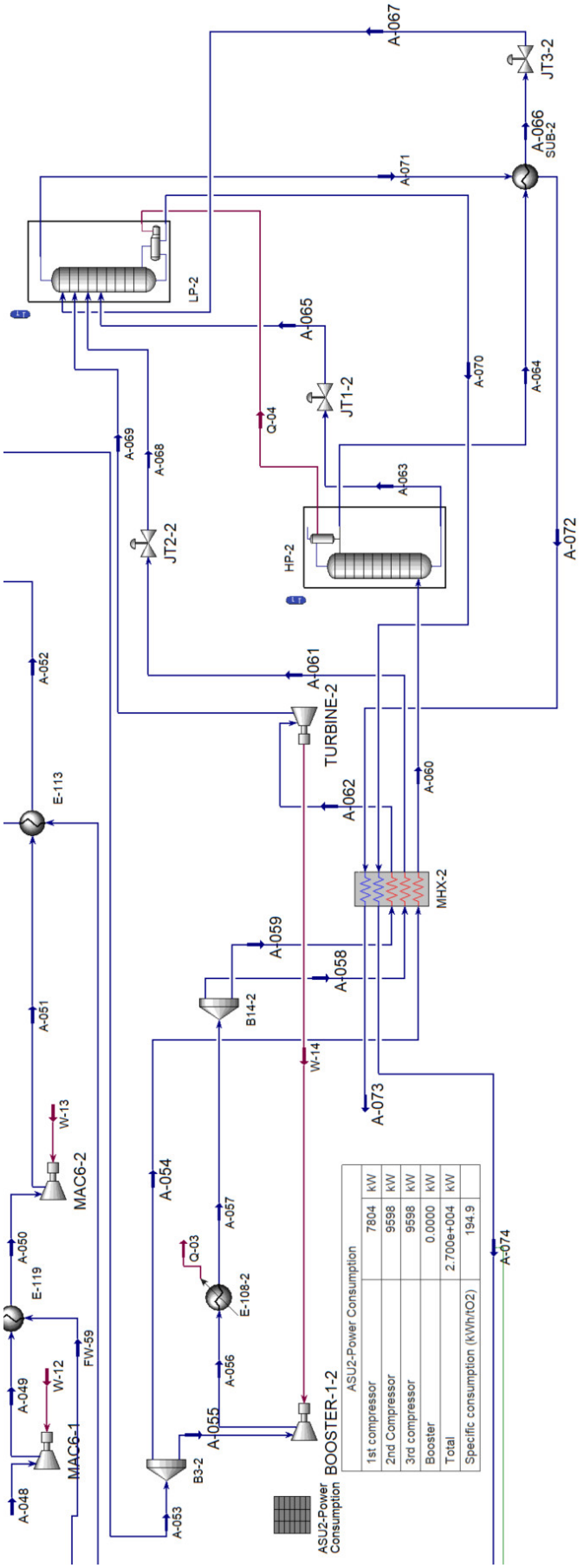
Figure B.6: Oxy-fuel combustion process after heat integration.


A-030
JT3
A-029
SUB
A-034
LP
A-028
JT1
A-027
A-033
Q-02
A-032
A-031
A-026
HP
JT2
A-035
A-024
TURBINE
A-023
A-025
MHX
A-021
A-022
E-110
A-017
B14
A-020
A-036
A-037
A-015
A-014
W-06
FW-42
Q-01
W-07
MAC3-2
A-013
E-116
E-108
A-019
A-018
BOOSTER-1
A-012
W-05
B3
A-016
ASU1-Power Consumption
ASU1-Power Consumption
1st compressor 1.184e+004 kW
2nd compressor 1.008e+004 kW
3rd compressor 1.008e+004 kW
Booster 0.0000 kW
Total 3.199e+004 kW
Specific consumption (kWh/tO2) 194.9

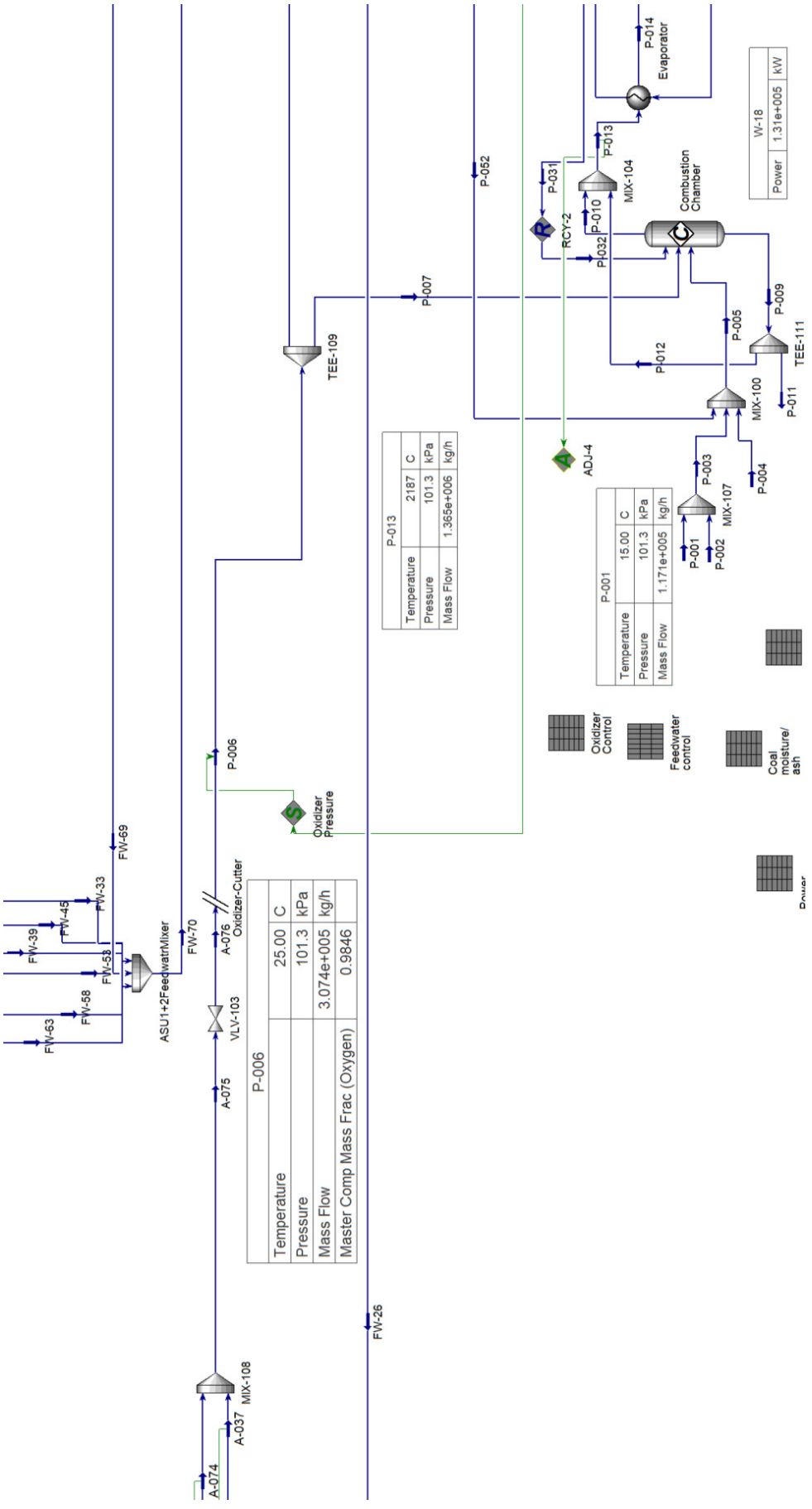
Cont.


FW-53
MIX-116
A-053
MIX-110
A-069
FW-63
MIX-114
FW-58
A-052
FW-52
FW-62
E-113
FW-51
MIX-115
FW-57
A-047
E-112
FW-61
A-051
A-042
FW-56
A-046
W-13
W-11
MAC6-2
E-111
MAC5-2
A-050
A-041
A-045
E-118
FW-55
E-119
FW-59
W-09
W-12
A-049
A-044
W-10
MAC4-2
MAC5-1
MAC6-1
FW-50
A-048
A-040
E-117
A-043
FW-54
TEE-114
FW-49
FW-60
A-039
W-08
TEE-115
TEE-113
FW-47
MAC4-1
FW-46
A-038
ADJ-3
FW-48

Cont.


A-067
JT3-2
A-066
SUB-2
A-071
LP-2
A-065
JT1-2
Q-04
A-070
A-064
A-069
A-068
A-063
JT2-2
HP-2
A-072
A-052
A-061
TURBINE-2
E-113
A-062
A-060
MHX-2
A-059
A-058
B14-2
W-14
A-073
A-051
W-13
MAC6-2
A-054
A-057
Q-03
A-050
E-119
E-108-2
A-074
FW-59
W-12
A-049
A-056
A-055
MAC6-1
BOOSTER-1-2
B3-2
A-048
A-053
ASU2-Power Consumption
ASU2-Power Consumption
1st compressor 7804 kW
2nd Compressor 9598 kW
3rd compressor 9598 kW
Booster 0.0000 kW
Total 2.700e+004 kW
Specific consumption (kWh/tO2) 194.9

Cont.

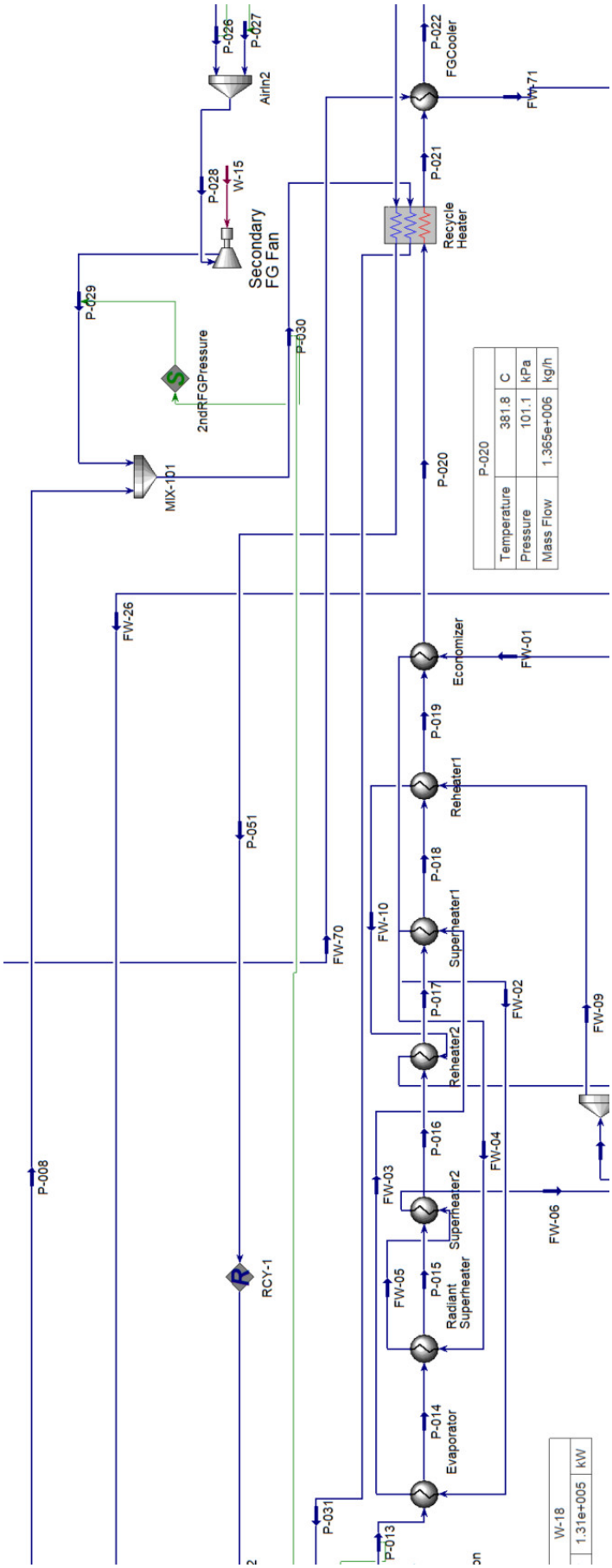


P-006		
Temperature	25.00	C
Pressure	101.3	kPa
Mass Flow	3.074e+005	kg/h
Master Comp Mass Frac (Oxygen)	0.9846	

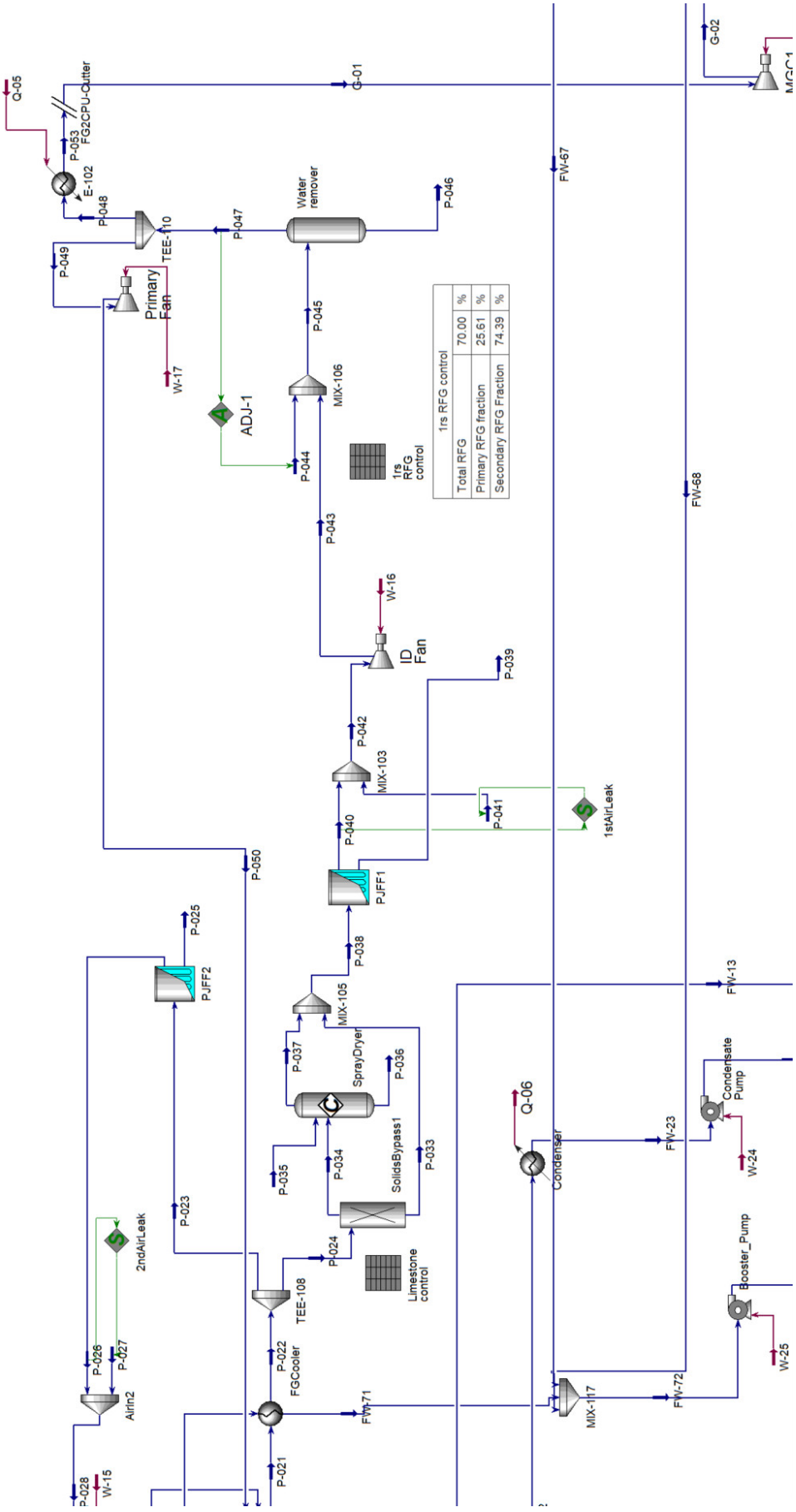
P-013		
Temperature	2187	C
Pressure	101.3	kPa
Mass Flow	1.365e+006	kg/h

P-001		
Temperature	15.00	C
Pressure	101.3	kPa
Mass Flow	1.171e+005	kg/h

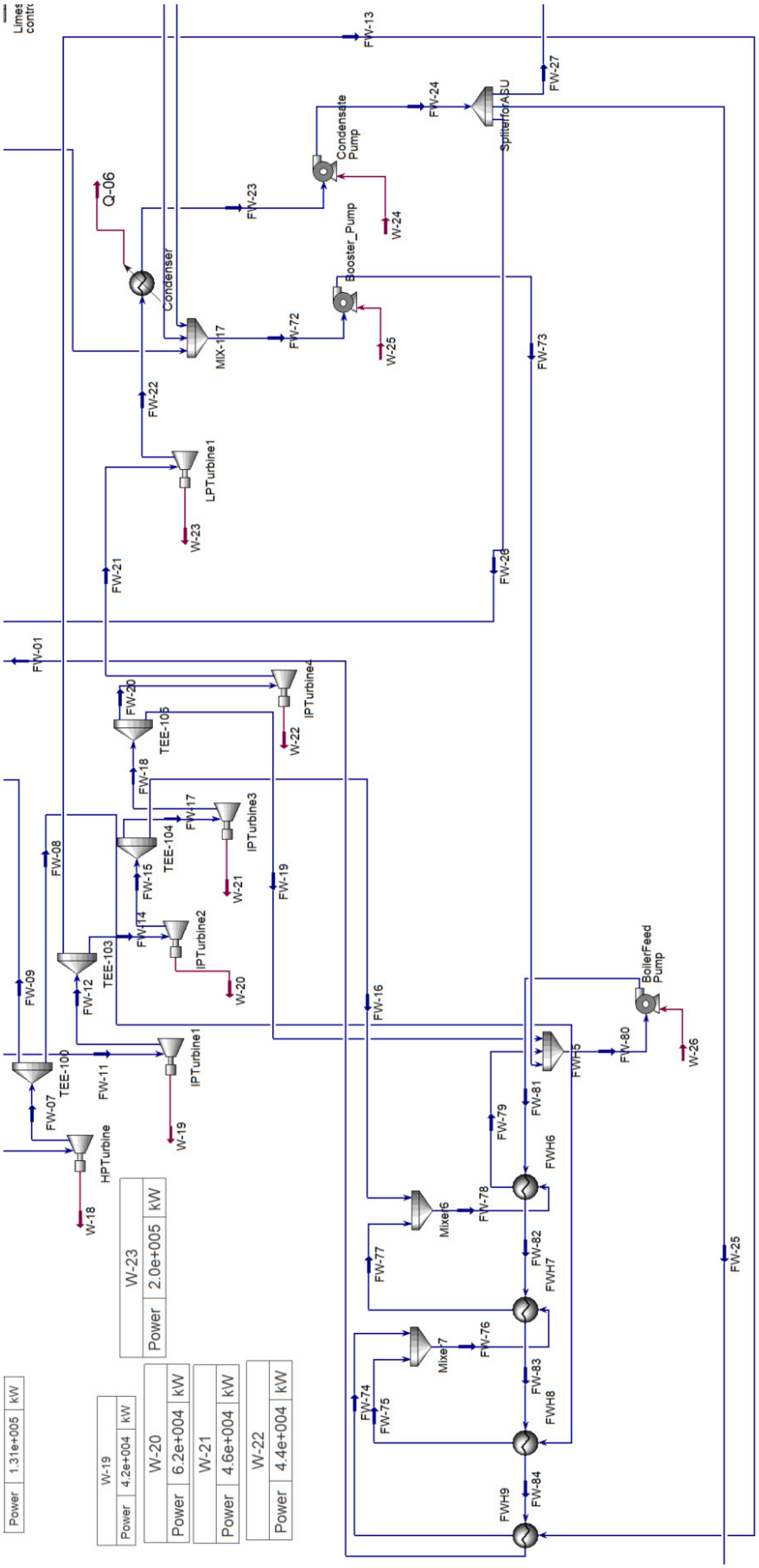
Cont.


P-026
P-027
Airin2
P-028
W-15
Secondary FG Fan
P-029
2ndRFGPressure
MIX-101
P-030
P-051
FW-26
FW-70
P-008
RCY-1
P-031
P-013
P-014
Evaporator
P-015
Radiant Superheater
FW-05
FW-03
Superheater2
P-016
FW-04
FW-06
Reheater2
P-017
FW-02
FW-09
FW-10
Superheater1
P-018
Reheater1
P-019
Economizer
FW-01
P-020
P-021
Recycle Heater
P-022
FGCooler
FW-71
P-020
Temperature 381.8 C
Pressure 101.1 kPa
Mass Flow 1.365e+006 kg/h
W-18
1.31e+005 kW

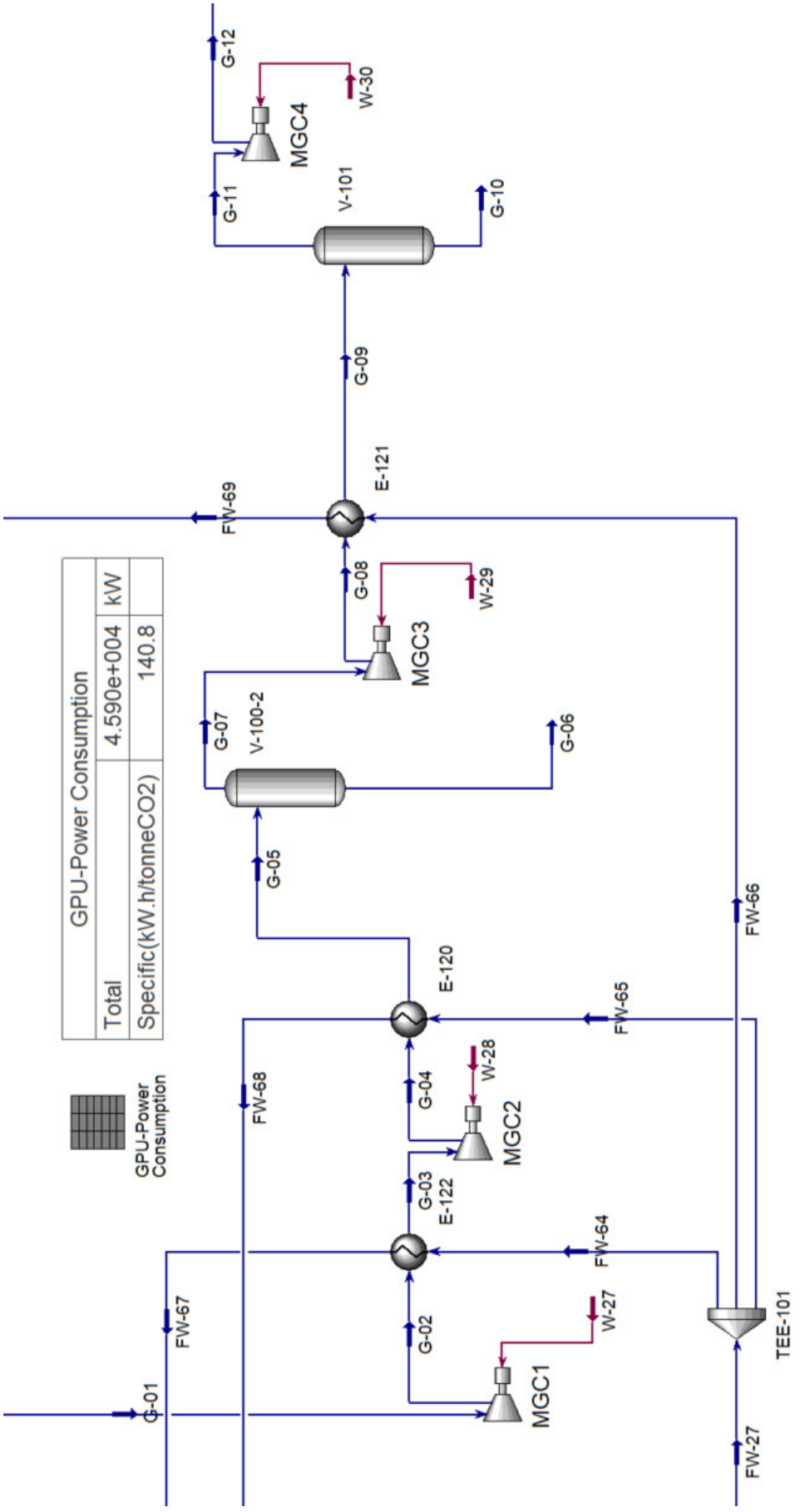
Cont.


Q-05
FG2CPU-Cutter
P-053
E-102
P-048
TEE-110
P-047
Water remover
P-046
G-01
G-02
FW-67
P-049
Primary Fan
W-17
P-045
MIX-106
ADJ-1
P-044
1rs RFG control
1rs RFG control
Total RFG 70.00 %
Primary RFG fraction 25.61 %
Secondary RFG Fraction 74.39 %
P-043
FW-68
W-16
ID Fan
P-039
P-042
MIX-103
P-041
1stAirLeak
P-040
P-050
PJFF1
P-025
PJFF2
P-038
MIX-105
FW-13
P-037
SprayDryer
P-036
Q-06
Condenser
Condensate Pump
FW-23
W-24
P-035
P-034
SolidsBypass1
P-033
P-023
2ndAirLeak
P-024
Limestone control
Booster_Pump
W-25
P-026
P-027
TEE-108
P-022
FGCooler
Airin2
FW-71
MIX-117
FW-72
P-028
W-15
P-021

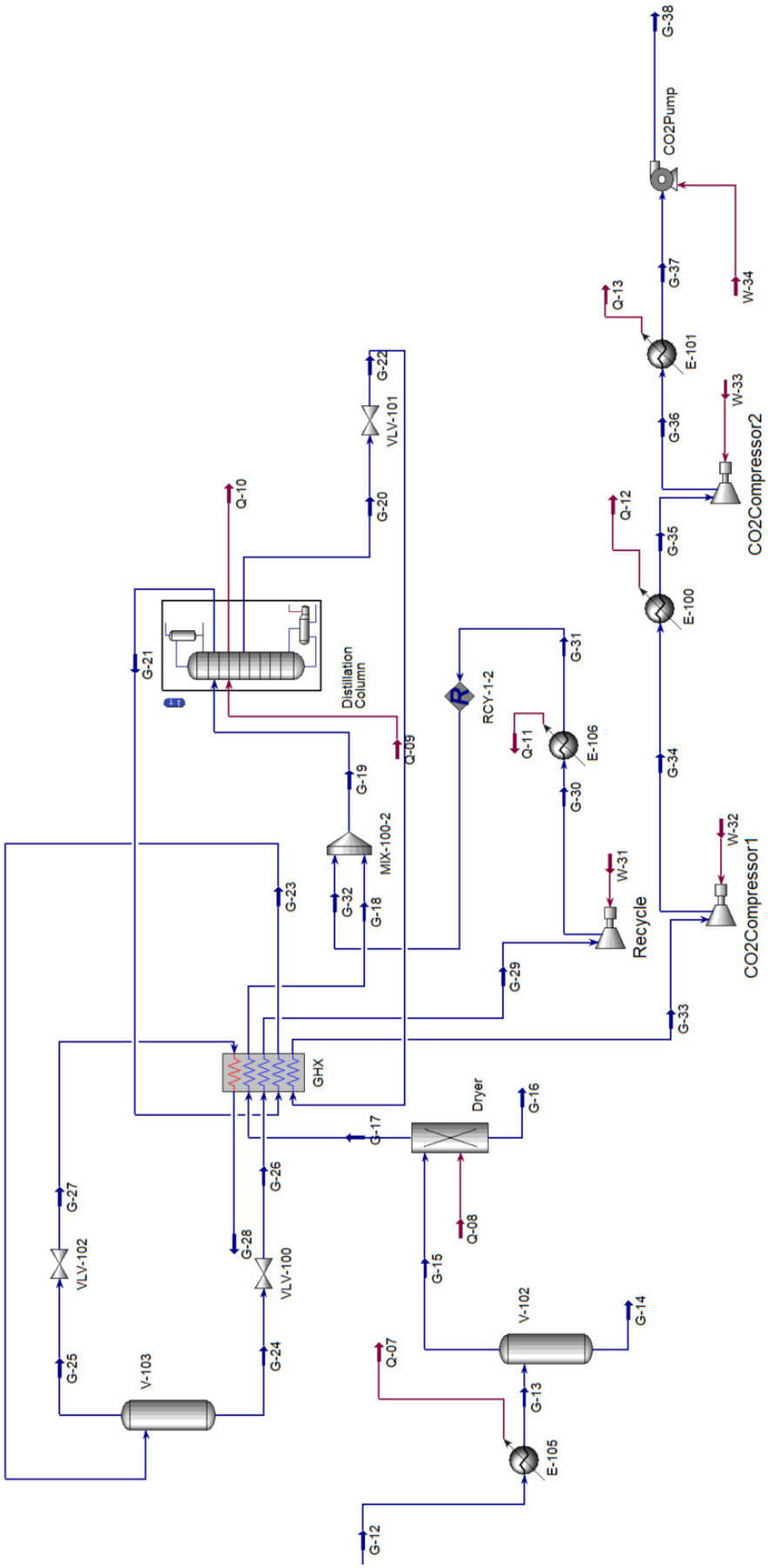
Cont.


FW-13
FW-27
FW-24
Splitter for ASU
Condensate Pump
W-24
Booster_Pump
W-25
Q-06
Condenser
FW-23
MIX-117
FW-72
FW-73
FW-22
LPTurbine1
W-23
FW-21
FW-26
FW-01
FW-20
IPTurbine4
W-22
TEE-105
FW-18
FW-17
IPTurbine3
W-21
TEE-104
FW-15
FW-19
FW-08
FW-14
IPTurbine2
W-20
TEE-103
FW-12
FW-09
FW-16
BoilerFeed Pump
W-26
FW-80
FW-5
FW-81
FW-79
FWH6
FW-78
Mixer6
FW-77
FW-82
FWH7
Mixer7
FW-76
FW-74
FW-75
FW-83
FWH8
FW-84
FWH9
FW-25
FW-07
TEE-100
FW-11
IPTurbine1
W-19
HPTurbine
W-18
W-23
Power 2.0e+005 kW
W-19
Power 4.2e+004 kW
W-20
Power 6.2e+004 kW
W-21
Power 4.6e+004 kW
W-22
Power 4.4e+004 kW
Power 1.31e+005 kW

Cont.


G-12
W-30
MGC4
G-11
V-101
G-10
G-09
E-121
FW-69
G-08
W-29
MGC3
G-07
V-100-2
G-06
G-05
FW-66
E-120
FW-65
W-28
FW-68
G-04
MGC2
G-03
E-122
FW-64
FW-67
W-27
G-02
TEE-101
G-01
MGC1
FW-27
GPU-Power Consumption
Total
4.590e+004
kW
Specific(kW.h/tonneCO2)
140.8
GPU-Power Consumption

Cont.


G-38
CO2Pump
G-37
W-34
Q-13
E-101
G-36
W-33
CO2Compressor2
Q-12
G-35
E-100
G-34
W-32
CO2Compressor1
G-33
G-22
VLV-101
G-20
Q-10
G-21
Distillation Column
LT
Q-09
G-19
MIX-100-2
G-32
G-18
G-23
RCY-1-2
G-31
Q-11
E-106
G-30
W-31
Recycle
G-29
GHX
G-17
Dryer
G-16
Q-08
G-15
V-102
G-14
Q-07
G-13
E-105
G-12
G-27
VLV-102
G-25
V-103
G-26
G-28
VLV-100
G-24

Cont.

Table B.7: Stream tables of the oxy-combustion process with heat integration.

Parameter	Units	A-001	A-002	A-003	A-004	A-005	A-006	A-007	A-008	A-009	A-010
Temperature	°C	10	88.31	28	106.42	28	10	88.31	28	106.42	28
Pressure	kPa	101.32	210	210	420	420	101.32	210	210	420	420
Mass Enthalpy	kJ/kg	-15.34	63.57	2.44	81.73	1.87	-15.34	63.57	2.44	81.73	1.87
Mass Entropy	kJ/(kg.°C)	5.19	5.23	5.04	5.08	4.84	5.19	5.23	5.04	5.08	4.84
Mass Density	kg/m^3	1.25	2.02	2.43	3.85	4.87	1.25	2.02	2.43	3.85	4.87
Mass Flow	kg/h	269353	269353	269353	269353	269353	229279	229279	229279	229279	229279
Molar Flow	kmol/h	9300	9300	9300	9300	9300	7916	7916	7916	7916	7916
Mole fraction											
C		0	0	0	0	0	0	0	0	0	0
H_2		0	0	0	0	0	0	0	0	0	0
S		0	0	0	0	0	0	0	0	0	0
Ar		0.0097	0.0097	0.0097	0.0097	0.0097	0.0097	0.0097	0.0097	0.0097	0.0097
O_2		0.2095	0.2095	0.2095	0.2095	0.2095	0.2095	0.2095	0.2095	0.2095	0.2095
N_2		0.7808	0.7808	0.7808	0.7808	0.7808	0.7808	0.7808	0.7808	0.7808	0.7808
CO_2		0	0	0	0	0	0	0	0	0	0
H_2O		0	0	0	0	0	0	0	0	0	0
SO_2		0	0	0	0	0	0	0	0	0	0
SiO_2		0	0	0	0	0	0	0	0	0	0
Al_2O_3		0	0	0	0	0	0	0	0	0	0
Fe_2O_3		0	0	0	0	0	0	0	0	0	0
CaO		0	0	0	0	0	0	0	0	0	0
MgO		0	0	0	0	0	0	0	0	0	0
Na_2O		0	0	0	0	0	0	0	0	0	0
K_2O		0	0	0	0	0	0	0	0	0	0
TiO_2		0	0	0	0	0	0	0	0	0	0
Mn_3O_4		0	0	0	0	0	0	0	0	0	0
P_2O_5		0	0	0	0	0	0	0	0	0	0
SO_3		0	0	0	0	0	0	0	0	0	0
$CaCO_3$		0	0	0	0	0	0	0	0	0	0
$CaSO_3$		0	0	0	0	0	0	0	0	0	0
H_2SO_4		0	0	0	0	0	0	0	0	0	0
Cl_2		0	0	0	0	0	0	0	0	0	0

Parameter	Units	A-011	A-012	A-013	A-014	A-015	A-016	A-017	A-018	A-019	A-020
Temperature	°C	10	88.31	28	106.42	28	28	28	28	35.86	28
Pressure	kPa	101.32	210	210	420	420	420	420	420	455.5	455.5
Mass Enthalpy	kJ/kg	-15.34	63.57	2.44	81.73	1.87	1.87	1.87	1.87	9.74	1.77
Mass Entropy	kJ/(kg.°C)	5.19	5.23	5.04	5.08	4.84	4.84	4.84	4.84	4.84	4.82
Mass Density	kg/m^3	1.25	2.02	2.43	3.85	4.87	4.87	4.87	4.87	5.15	5.28
Mass Flow	kg/h	229279	229279	229279	229279	229279	727912	545934	181978	181978	181978
Molar Flow	kmol/h	7916	7916	7916	7916	7916	25132	18849	6283	6283	6283
Mole fraction											
C		0	0	0	0	0	0	0	0	0	0
H_2		0	0	0	0	0	0	0	0	0	0
S		0	0	0	0	0	0	0	0	0	0
Ar		0.0097	0.0097	0.0097	0.0097	0.0097	0.0097	0.0097	0.0097	0.0097	0.0097
O_2		0.2095	0.2095	0.2095	0.2095	0.2095	0.2095	0.2095	0.2095	0.2095	0.2095
N_2		0.7808	0.7808	0.7808	0.7808	0.7808	0.7808	0.7808	0.7808	0.7808	0.7808
CO_2		0	0	0	0	0	0	0	0	0	0
H_2O		0	0	0	0	0	0	0	0	0	0
SO_2		0	0	0	0	0	0	0	0	0	0
SiO_2		0	0	0	0	0	0	0	0	0	0
Al_2O_3		0	0	0	0	0	0	0	0	0	0
Fe_2O_3		0	0	0	0	0	0	0	0	0	0
CaO		0	0	0	0	0	0	0	0	0	0
MgO		0	0	0	0	0	0	0	0	0	0
Na_2O		0	0	0	0	0	0	0	0	0	0
K_2O		0	0	0	0	0	0	0	0	0	0
TiO_2		0	0	0	0	0	0	0	0	0	0
Mn_3O_4		0	0	0	0	0	0	0	0	0	0
P_2O_5		0	0	0	0	0	0	0	0	0	0
SO_3		0	0	0	0	0	0	0	0	0	0
$CaCO_3$		0	0	0	0	0	0	0	0	0	0
$CaSO_3$		0	0	0	0	0	0	0	0	0	0
H_2SO_4		0	0	0	0	0	0	0	0	0	0
Cl_2		0	0	0	0	0	0	0	0	0	0

Parameter	Units	A-021	A-022	A-023	A-024	A-025	A-026	A-027	A-028	A-029	A-030
Temperature	°C	28	28	-177.66	-179	10	-177.96	-181.58	-190.76	-187	-193.96
Pressure	kPa	455.5	455.5	410	445.5	445.5	410	410	125	410	125
Mass Enthalpy	kJ/kg	1.77	1.77	-225.17	-388.95	-16.398	-385.26	-397.05	-385.26	-408.28	-408.28
Mass Entropy	kJ/(kg.°C)	4.82	4.82	3.48	1.75	4.76	1.72	1.67	1.74	1.54	1.55
Mass Density	kg/m^3	5.28	5.28	18.54	800.73	5.50	855.04	736.39	43.87	764.39	72.50
Mass Flow	kg/h	16378	165600	545934	165600	16378	325182	220752	325182	220752	220752
Molar Flow	kmol/h	565.46	5717	18849	5717	565.46	10969	7880	10969	7880	7880
Mole fraction											
C		0	0	0	0	0	0	0	0	0	0
H_2		0	0	0	0	0	0	0	0	0	0
S		0	0	0	0	0	0	0	0	0	0
Ar		0.0097	0.0097	0.0097	0.0097	0.0097	0.0165	0.0002	0.0165	0.0002	0.0002
O_2		0.2095	0.2095	0.2095	0.2095	0.2095	0.36	0	0.36	0	0
N_2		0.7808	0.7808	0.7808	0.7808	0.7808	0.6235	0.9998	0.6235	0.9998	0.9998
CO_2		0	0	0	0	0	0	0	0	0	0
H_2O		0	0	0	0	0	0	0	0	0	0
SO_2		0	0	0	0	0	0	0	0	0	0
SiO_2		0	0	0	0	0	0	0	0	0	0
Al_2O_3		0	0	0	0	0	0	0	0	0	0
Fe_2O_3		0	0	0	0	0	0	0	0	0	0
CaO		0	0	0	0	0	0	0	0	0	0
MgO		0	0	0	0	0	0	0	0	0	0
Na_2O		0	0	0	0	0	0	0	0	0	0
K_2O		0	0	0	0	0	0	0	0	0	0
TiO_2		0	0	0	0	0	0	0	0	0	0
Mn_3O_4		0	0	0	0	0	0	0	0	0	0
P_2O_5		0	0	0	0	0	0	0	0	0	0
SO_3		0	0	0	0	0	0	0	0	0	0
$CaCO_3$		0	0	0	0	0	0	0	0	0	0
$CaSO_3$		0	0	0	0	0	0	0	0	0	0
H_2SO_4		0	0	0	0	0	0	0	0	0	0
Cl_2		0	0	0	0	0	0	0	0	0	0

Parameter	Units	A-031	A-032	A-033	A-034	A-035	A-036	A-037	A-038	A-039	A-040
Temperature	°C	-192.21	-78.99	-182.33	-194.71	-190.43	25.20	25	10	88.31	28
Pressure	kPa	125	112.17	111.33	111.33	111.33	101.33	101.33	101.32	210	210
Mass Enthalpy	kJ/kg	-388.95	-103.83	-392.22	-224.75	-220.34	-0.07	-0.30	-15.34	63.57	2.44
Mass Entropy	kJ/(kg.°C)	1.78	4.79	1.15	3.89	3.94	5.28	4.52	5.19	5.23	5.04
Mass Density	kg/m^3	41.08	2.02	1145	5.02	4.74	1.15	1.31	1.25	2.02	2.43
Mass Flow	kg/h	165600	16378	166685	561228	561228	561228	166685	177571	177571	177571
Molar Flow	kmol/h	5717	565.46	5193	19939	19939	19939	5193	6131	6131	6131
Mole fraction											
C		0	0	0	0	0	0	0	0	0	0
H_2		0	0	0	0	0	0	0	0	0	0
S		0	0	0	0	0	0	0	0	0	0
Ar		0.0097	0.0097	0.0124	0.009	0.009	0.009	0.0124	0.0097	0.0097	0.0097
O_2		0.2095	0.2095	0.9876	0.0069	0.0069	0.0069	0.9876	0.2095	0.2095	0.2095
N_2		0.7808	0.7808	0	0.9842	0.9842	0.9842	0	0.7808	0.7808	0.7808
CO_2		0	0	0	0	0	0	0	0	0	0
H_2O		0	0	0	0	0	0	0	0	0	0
SO_2		0	0	0	0	0	0	0	0	0	0
SiO_2		0	0	0	0	0	0	0	0	0	0
Al_2O_3		0	0	0	0	0	0	0	0	0	0
Fe_2O_3		0	0	0	0	0	0	0	0	0	0
CaO		0	0	0	0	0	0	0	0	0	0
MgO		0	0	0	0	0	0	0	0	0	0
Na_2O		0	0	0	0	0	0	0	0	0	0
K_2O		0	0	0	0	0	0	0	0	0	0
TiO_2		0	0	0	0	0	0	0	0	0	0
Mn_3O_4		0	0	0	0	0	0	0	0	0	0
P_2O_5		0	0	0	0	0	0	0	0	0	0
SO_3		0	0	0	0	0	0	0	0	0	0
$CaCO_3$		0	0	0	0	0	0	0	0	0	0
$CaSO_3$		0	0	0	0	0	0	0	0	0	0
H_2SO_4		0	0	0	0	0	0	0	0	0	0
Cl_2		0	0	0	0	0	0	0	0	0	0

Parameter	Units	A-041	A-042	A-043	A-044	A-045	A-046	A-047	A-048	A-049	A-050
Temperature	°C	106.42	28	10	88.31	28	106.42	28	10	88.31	28
Pressure	kPa	420	420	101.32	210	210	420	420	101.32	210	210
Mass Enthalpy	kJ/kg	81.73	1.87	-15.34	63.57	2.44	81.73	1.87	-15.34	63.57	2.44
Mass Entropy	kJ/(kg.°C)	5.08	4.84	5.19	5.23	5.04	5.08	4.84	5.19	5.23	5.04
Mass Density	kg/m^3	3.85	4.87	1.25	2.02	2.43	3.85	4.87	1.25	2.02	2.43
Mass Flow	kg/h	177571	177571	218410	218410	218410	218410	218410	218410	218410	218410
Molar Flow	kmol/h	6131	6131	7541	7541	7541	7541	7541	7541	7541	7541
Mole fraction											
C		0	0	0	0	0	0	0	0	0	0
H_2		0	0	0	0	0	0	0	0	0	0
S		0	0	0	0	0	0	0	0	0	0
Ar		0.0097	0.0097	0.0097	0.0097	0.0097	0.0097	0.0097	0.0097	0.0097	0.0097
O_2		0.2095	0.2095	0.2095	0.2095	0.2095	0.2095	0.2095	0.2095	0.2095	0.2095
N_2		0.7808	0.7808	0.7808	0.7808	0.7808	0.7808	0.7808	0.7808	0.7808	0.7808
CO_2		0	0	0	0	0	0	0	0	0	0
H_2O		0	0	0	0	0	0	0	0	0	0
SO_2		0	0	0	0	0	0	0	0	0	0
SiO_2		0	0	0	0	0	0	0	0	0	0
Al_2O_3		0	0	0	0	0	0	0	0	0	0
Fe_2O_3		0	0	0	0	0	0	0	0	0	0
CaO		0	0	0	0	0	0	0	0	0	0
MgO		0	0	0	0	0	0	0	0	0	0
Na_2O		0	0	0	0	0	0	0	0	0	0
K_2O		0	0	0	0	0	0	0	0	0	0
TiO_2		0	0	0	0	0	0	0	0	0	0
Mn_3O_4		0	0	0	0	0	0	0	0	0	0
P_2O_5		0	0	0	0	0	0	0	0	0	0
SO_3		0	0	0	0	0	0	0	0	0	0
$CaCO_3$		0	0	0	0	0	0	0	0	0	0
$CaSO_3$		0	0	0	0	0	0	0	0	0	0
H_2SO_4		0	0	0	0	0	0	0	0	0	0
Cl_2		0	0	0	0	0	0	0	0	0	0

Parameter	Units	A-051	A-052	A-053	A-054	A-055	A-056	A-057	A-058	A-059	A-060
Temperature	°C	106.42	28	28	28	28	35.86	28	28	28	-177.66
Pressure	kPa	420	420	420	420	420	455.5	455.5	455.5	455.5	410
Mass Enthalpy	kJ/kg	81.73	1.87	1.87	1.87	1.87	9.74	1.77	1.77	1.77	-225.17
Mass Entropy	kJ/(kg.°C)	5.08	4.84	4.84	4.84	4.84	4.84	4.82	4.82	4.82	3.48
Mass Density	kg/m^3	3.85	4.87	4.87	4.87	4.87	5.15	5.28	5.28	5.28	18.54
Mass Flow	kg/h	218410	218410	614391	460794	153598	153598	153598	139774	13824	460794
Molar Flow	kmol/h	7541	7541	21212	15909	5303	5303	5303	4826	477.27	15909
Mole fraction											
C		0	0	0	0	0	0	0	0	0	0
H_2		0	0	0	0	0	0	0	0	0	0
S		0	0	0	0	0	0	0	0	0	0
Ar		0.0097	0.0097	0.0097	0.0097	0.0097	0.0097	0.0097	0.0097	0.0097	0.0097
O_2		0.2095	0.2095	0.2095	0.2095	0.2095	0.2095	0.2095	0.2095	0.2095	0.2095
N_2		0.7808	0.7808	0.7808	0.7808	0.7808	0.7808	0.7808	0.7808	0.7808	0.7808
CO_2		0	0	0	0	0	0	0	0	0	0
H_2O		0	0	0	0	0	0	0	0	0	0
SO_2		0	0	0	0	0	0	0	0	0	0
SiO_2		0	0	0	0	0	0	0	0	0	0
Al_2O_3		0	0	0	0	0	0	0	0	0	0
Fe_2O_3		0	0	0	0	0	0	0	0	0	0
CaO		0	0	0	0	0	0	0	0	0	0
MgO		0	0	0	0	0	0	0	0	0	0
Na_2O		0	0	0	0	0	0	0	0	0	0
K_2O		0	0	0	0	0	0	0	0	0	0
TiO_2		0	0	0	0	0	0	0	0	0	0
Mn_3O_4		0	0	0	0	0	0	0	0	0	0
P_2O_5		0	0	0	0	0	0	0	0	0	0
SO_3		0	0	0	0	0	0	0	0	0	0
$CaCO_3$		0	0	0	0	0	0	0	0	0	0
$CaSO_3$		0	0	0	0	0	0	0	0	0	0
H_2SO_4		0	0	0	0	0	0	0	0	0	0
Cl_2		0	0	0	0	0	0	0	0	0	0

Parameter	Units	A-061	A-062	A-063	A-064	A-065	A-066	A-067	A-068	A-069	A-070
Temperature	°C	-179	10	-177.96	-181.58	-190.76	-187	-193.96	-192.21	-78.99	-182.33
Pressure	kPa	445.5	445.5	410	410	125	410	125	125	112.17	111.33
Mass Enthalpy	kJ/kg	-388.95	-16.398	-385.26	-397.05	-385.26	-408.28	-408.28	-388.95	-103.83	-392.22
Mass Entropy	kJ/(kg·°C)	1.75	4.76	1.72	1.67	1.74	1.54	1.55	1.78	4.79	1.15
Mass Density	kg/m^3	800.73	5.50	855.04	736.39	43.87	764.39	72.50	41.08	2.02	1145
Mass Flow	kg/h	139774	13824	274466	186327	274466	186327	186327	139774	13824	140685
Molar Flow	kmol/h	4826	477.27	9258	6651	9258	6651	6651	4826	477.27	4383
Mole fraction											
C		0	0	0	0	0	0	0	0	0	0
H_2		0	0	0	0	0	0	0	0	0	0
S		0	0	0	0	0	0	0	0	0	0
Ar		0.0097	0.0097	0.0165	0.0002	0.0165	0.0002	0.0002	0.0097	0.0097	0.0124
O_2		0.2095	0.2095	0.36	0	0.36	0	0	0.2095	0.2095	0.9876
N_2		0.7808	0.7808	0.6234	0.9998	0.6234	0.9998	0.9998	0.7808	0.7808	0
CO_2		0	0	0	0	0	0	0	0	0	0
H_2O		0	0	0	0	0	0	0	0	0	0
SO_2		0	0	0	0	0	0	0	0	0	0
SiO_2		0	0	0	0	0	0	0	0	0	0
Al_2O_3		0	0	0	0	0	0	0	0	0	0
Fe_2O_3		0	0	0	0	0	0	0	0	0	0
CaO		0	0	0	0	0	0	0	0	0	0
MgO		0	0	0	0	0	0	0	0	0	0
Na_2O		0	0	0	0	0	0	0	0	0	0
K_2O		0	0	0	0	0	0	0	0	0	0
TiO_2		0	0	0	0	0	0	0	0	0	0
Mn_3O_4		0	0	0	0	0	0	0	0	0	0
P_2O_5		0	0	0	0	0	0	0	0	0	0
SO_3		0	0	0	0	0	0	0	0	0	0
$CaCO_3$		0	0	0	0	0	0	0	0	0	0
$CaSO_3$		0	0	0	0	0	0	0	0	0	0
H_2SO_4		0	0	0	0	0	0	0	0	0	0
Cl_2		0	0	0	0	0	0	0	0	0	0

Parameter	Units	A-071	A-072	A-073	A-074	A-075	A-076	P-001	P-002	P-003	P-004
Temperature	°C	-194.71	-190.43	25.20	25	25	24.99998	15	15	15.00	15
Pressure	kPa	111.33	111.33	101.33	101.33	101.33	101.32	101.32	101.32	101.32	101.32
Mass Enthalpy	kJ/kg	-224.75	-220.34	-0.07	-0.30	-0.30	-0.30	-924.92	-15931	-924.91	-78.55
Mass Entropy	kJ/(kg·°C)	3.89	3.94	5.28	4.52	4.52	4.52	4.17	2.83	4.17	5.20
Mass Density	kg/m^3	5.02	4.74	1.15	1.31	1.31	1.31	1.48	1015	1.48	3211
Mass Flow	kg/h	473706	473706	473706	140685	307370	307370	117066	0	117066	27511
Molar Flow	kmol/h	16829	16829	16829	4383	9576	9576	11470	0	11470	314.54
Mole fraction											
C		0	0	0	0	0	0	0.6758	0	0.6758	0
H_2		0	0	0	0	0	0	0.2592	0	0.2592	0
S		0	0	0	0	0	0	0.0023	0	0.0023	0
Ar		0.009	0.009	0.009	0.0124	0.0124	0.0124	0	0	0	0
O_2		0.0069	0.0069	0.0069	0.9876	0.9876	0.9876	0.0215	0	0.0215	0
N_2		0.9841	0.9841	0.9841	0	0	0	0.0057	0	0.0057	0
CO_2		0	0	0	0	0	0	0	0	0	0
H_2O		0	0	0	0	0	0	0.0354	1	0.0354	0
SO_2		0	0	0	0	0	0	0	0	0	0
SiO_2		0	0	0	0	0	0	0	0	0	0.5005
Al_2O_3		0	0	0	0	0	0	0	0	0	0.3035
Fe_2O_3		0	0	0	0	0	0	0	0	0	0.1327
CaO		0	0	0	0	0	0	0	0	0	0.0131
MgO		0	0	0	0	0	0	0	0	0	0.009
Na_2O		0	0	0	0	0	0	0	0	0	0.001
K_2O		0	0	0	0	0	0	0	0	0	0.002
TiO_2		0	0	0	0	0	0	0	0	0	0.0191
Mn_3O_4		0	0	0	0	0	0	0	0	0	0.003
P_2O_5		0	0	0	0	0	0	0	0	0	0.002
SO_3		0	0	0	0	0	0	0	0	0	0.0141
$CaCO_3$		0	0	0	0	0	0	0	0	0	0
$CaSO_3$		0	0	0	0	0	0	0	0	0	0
H_2SO_4		0	0	0	0	0	0	0	0	0	0
Cl_2		0	0	0	0	0	0	0.0001	0	0.0001	0

Parameter	Units	P-005	P-006	P-007	P-008	P-009	P-010	P-011	P-012	P-013	P-014
Temperature	°C	148.92	24.99998	25	24.99998	2187	2187	2187	2187	2187	2159
Pressure	kPa	101.32	101.32	101.32	101.32	101.32	101.32	101.325	101.32	101.32	101.29
Mass Enthalpy	kJ/kg	-5181	-0.30	-0.30	-0.3	1963	-5861	1963	1963	-5744	-5794
Mass Entropy	kJ/(kg.°C)	4.93	4.52	4.52	4.52	7.2	7.37	7.2	7.2	7.37	7.35
Mass Density	kg/m^3	1.18	1.31	1.31	1.31	3241	0.19	3241	3241	0.19	0.19
Mass Flow	kg/h	362673	307370	30737	276633	27156	1344140	6789	20367	1364507	1364507
Molar Flow	kmol/h	16946	9576	957.58	8618	310.12	35457	77.53	232.59	35690	35690
Mole fraction											
C		0.4574	0	0	0	0	0	0	0	0	0
H_2		0.1754	0	0	0	0	0	0	0	0	0
S		0.0015	0	0	0	0	0	0	0	0	0
Ar		0.0042	0.0124	0.0124	0.0124	0	0.0112	0	0	0.0112	0.0112
O_2		0.0308	0.9876	0.9876	0.9876	0	0.0427	0	0	0.0425	0.0425
N_2		0.0088	0	0	0	0	0.011	0	0	0.0109	0.0109
CO_2		0.2696	0	0	0	0	0.7249	0	0	0.7202	0.7202
H_2O		0.0334	0	0	0	0	0.2082	0	0	0.2068	0.2068
SO_2		0.0001	0	0	0	0	0.0016	0	0	0.0016	0.0016
SiO_2		0.0093	0	0	0	0.5076	0	0.5076	0.5076	0.0033	0.0033
Al_2O_3		0.0056	0	0	0	0.3078	0	0.3078	0.3078	0.002	0.002
Fe_2O_3		0.0025	0	0	0	0.1346	0	0.1346	0.1346	0.0009	0.0009
CaO		0.0002	0	0	0	0.0133	0	0.0133	0.0133	0.0001	0.0001
MgO		0.0002	0	0	0	0.0092	0	0.0092	0.0092	0.0001	0.0001
Na_2O		0	0	0	0	0.001	0	0.001	0.001	0	0
K_2O		0	0	0	0	0.002	0	0.002	0.002	0	0
TiO_2		0.0004	0	0	0	0.0194	0	0.0194	0.0194	0.0001	0.0001
Mn_3O_4		0.0001	0	0	0	0.0031	0	0.0031	0.0031	0	0
P_2O_5		0	0	0	0	0.002	0	0.002	0.002	0	0
SO_3		0.0003	0	0	0	0	0.0003	0	0	0.0003	0.0003
$CaCO_3$		0	0	0	0	0	0	0	0	0	0
$CaSO_3$		0	0	0	0	0	0	0	0	0	0
H_2SO_4		0	0	0	0	0	0	0	0	0	0
Cl_2		0.0001	0	0	0	0	0.0001	0	0	0.0001	0.0001

Parameter	Units	P-015	P-016	P-017	P-018	P-019	P-020	P-021	P-022	P-023	P-024
Temperature	°C	2013	1794	1551	1190	1053	381.79	223.06	150	150	150
Pressure	kPa	101.26	101.23	101.2	101.17	101.14	101.11	101.11	101.11	101.11	101.11
Mass Enthalpy	kJ/kg	-6042	-6394	-6766	-7294	-7488	-8359	-8538	-8616	-8616	-8616
Mass Entropy	kJ/(kg.°C)	7.24	7.08	6.89	6.57	6.43	5.52	5.21	5.04	5.04	5.04
Mass Density	kg/m^3	0.21	0.23	0.26	0.32	0.35	0.71	0.94	1.11	1.11	1.11
Mass Flow	kg/h	1364507	1364507	1364507	1364507	1364507	1364507	1364507	1364507	710542	653965
Molar Flow	kmol/h	35690	35690	35690	35690	35690	35690	35690	35690	18585	17105
Mole fraction											
C		0	0	0	0	0	0	0	0	0	0
H_2		0	0	0	0	0	0	0	0	0	0
S		0	0	0	0	0	0	0	0	0	0
Ar		0.0112	0.0112	0.0112	0.0112	0.0112	0.0112	0.0112	0.0112	0.0112	0.0112
O_2		0.0425	0.0425	0.0425	0.0425	0.0425	0.0425	0.0425	0.0425	0.0425	0.0425
N_2		0.0109	0.0109	0.0109	0.0109	0.0109	0.0109	0.0109	0.0109	0.0109	0.0109
CO_2		0.7202	0.7202	0.7202	0.7202	0.7202	0.7202	0.7202	0.7202	0.7202	0.7202
H_2O		0.2068	0.2068	0.2068	0.2068	0.2068	0.2068	0.2068	0.2068	0.2068	0.2068
SO_2		0.0016	0.0016	0.0016	0.0016	0.0016	0.0016	0.0016	0.0016	0.0016	0.0016
SiO_2		0.0033	0.0033	0.0033	0.0033	0.0033	0.0033	0.0033	0.0033	0.0033	0.0033
Al_2O_3		0.002	0.002	0.002	0.002	0.002	0.002	0.002	0.002	0.002	0.002
Fe_2O_3		0.0009	0.0009	0.0009	0.0009	0.0009	0.0009	0.0009	0.0009	0.0009	0.0009
CaO		0.0001	0.0001	0.0001	0.0001	0.0001	0.0001	0.0001	0.0001	0.0001	0.0001
MgO		0.0001	0.0001	0.0001	0.0001	0.0001	0.0001	0.0001	0.0001	0.0001	0.0001
Na_2O		0	0	0	0	0	0	0	0	0	0
K_2O		0	0	0	0	0	0	0	0	0	0
TiO_2		0.0001	0.0001	0.0001	0.0001	0.0001	0.0001	0.0001	0.0001	0.0001	0.0001
Mn_3O_4		0	0	0	0	0	0	0	0	0	0
P_2O_5		0	0	0	0	0	0	0	0	0	0
SO_3		0.0003	0.0003	0.0003	0.0003	0.0003	0.0003	0.0003	0.0003	0.0003	0.0003
$CaCO_3$		0	0	0	0	0	0	0	0	0	0
$CaSO_3$		0	0	0	0	0	0	0	0	0	0
H_2SO_4		0	0	0	0	0	0	0	0	0	0
Cl_2		0.0001	0.0001	0.0001	0.0001	0.0001	0.0001	0.0001	0.0001	0.0001	0.0001

Parameter	Units	P-025	P-026	P-027	P-028	P-029	P-030	P-031	P-032	P-033	P-034
Temperature	°C	150	150	15	149.74	152.05	119.06	290	290	150	150
Pressure	kPa	99.11	99.11	101.32	99.11	101.32	101.32	101.32	101.32	101.11	101.11
Mass Enthalpy	kJ/kg	113.51	-8748	-10.33	-8731	-8728	-6260	-6081	-6080	111.95	-8684
Mass Entropy	kJ/(kg.°C)	5.61	5.04	5.21	5.04	5.04	5.02	5.40	5.40	5.53	5.04
Mass Density	kg/m^3	3241	1.07	1.23	1.07	1.09	1.12	0.78	0.78	67.96	1.10
Mass Flow	kg/h	10606	699936	1400	701336	701336	977969	977969	977887	5029	648936
Molar Flow	kmol/h	121.12	18464	48.34	18512	18512	27130	27130	27128	57.83	17047
Mole fraction											
C		0	0	0	0	0	0	0	0	0	0
H_2		0	0	0	0	0	0	0	0	0	0
S		0	0	0	0	0	0	0	0	0	0
Ar		0	0.0112	0.0097	0.0112	0.0112	0.0116	0.0116	0.0116	0	0.0112
O_2		0	0.0427	0.2095	0.0432	0.0432	0.3432	0.3432	0.3432	0	0.0426
N_2		0	0.011	0.7808	0.013	0.013	0.0089	0.0089	0.0089	0	0.0109
CO_2		0	0.7249	0	0.723	0.723	0.4933	0.4933	0.4933	0	0.7226
H_2O		0	0.2082	0	0.2076	0.2076	0.1417	0.1417	0.1416	0	0.2075
SO_2		0	0.0016	0	0.0016	0.0016	0.0011	0.0011	0.0011	0	0.0016
SiO_2		0.5076	0	0	0	0	0	0	0	0.4893	0.0017
Al_2O_3		0.3078	0	0	0	0	0	0	0	0.2967	0.001
Fe_2O_3		0.1346	0	0	0	0	0	0	0	0.1297	0.0004
CaO		0.0133	0	0	0	0	0	0	0	0.0128	0
MgO		0.0092	0	0	0	0	0	0	0	0.0088	0
Na_2O		0.001	0	0	0	0	0	0	0	0.001	0
K_2O		0.002	0	0	0	0	0	0	0	0.002	0
TiO_2		0.0194	0	0	0	0	0	0	0	0.0187	0.0001
Mn_3O_4		0.0031	0	0	0	0	0	0	0	0.0029	0
P_2O_5		0.002	0	0	0	0	0	0	0	0.002	0
SO_3		0	0.0003	0	0.0003	0.0003	0.0002	0.0002	0.0002	0	0.0003
$CaCO_3$		0	0	0	0	0	0	0	0	0	0
$CaSO_3$		0	0	0	0	0	0	0	0	0	0
H_2SO_4		0	0	0	0	0	0	0	0	0	0
Cl_2		0	0.0001	0	0.0001	0.0001	0.0001	0.0001	0.0001	0.0362	0

Parameter	Units	P-035	P-036	P-037	P-038	P-039	P-040	P-041	P-042	P-043	P-044
Temperature	°C	15	66.08	66.08	66.63	66.63	66.63	15	66.53	68.48	15
Pressure	kPa	101.32	101.11	101.11	101.11	99.11	99.11	101.32	99.11	101.3	101.3
Mass Enthalpy	kJ/kg	-15544.5	-5567	-8993	-8925	37.80	-8991	-10.33	-8973	-8971	-15931
Mass Entropy	kJ/(kg.°C)	3.02	4.65	4.99	5	5.41	5	5.21	5	5	2.83
Mass Density	kg/m^3	1083	1627	1.32	1.33	3241	1.29	1.23	1.29	1.31	1015
Mass Flow	kg/h	25783	9298	665421	670450	4881	665569	1331	666901	666901	5199100
Molar Flow	kmol/h	1314	159.17	18202	18260	55.74	18204	45.97	18250	18250	288597
Mole fraction											
C		0	0	0	0	0	0	0	0	0	0
H_2		0	0	0	0	0	0	0	0	0	0
S		0	0	0	0	0	0	0	0	0	0
Ar		0	0	0.0105	0.0105	0	0.0105	0.0097	0.0105	0.0105	0
O_2		0	0	0.0399	0.0398	0	0.0399	0.2095	0.0403	0.0403	0
N_2		0	0	0.0102	0.0102	0	0.0102	0.7808	0.0122	0.0122	0
CO_2		0	0.0001	0.6780	0.6758	0	0.6779	0	0.6762	0.6762	0
H_2O		0.9804	0.4879	0.2608	0.2600	0	0.2608	0	0.2602	0.2602	1
SO_2		0	0	0.0003	0.0003	0	0.0003	0	0.0003	0.0003	0
SiO_2		0	0.1778	0	0.0015	0.5076	0	0	0	0	0
Al_2O_3		0	0.1078	0	0.0009	0.3078	0	0	0	0	0
Fe_2O_3		0	0.0471	0	0.0004	0.1346	0	0	0	0	0
CaO		0	0.0046	0	0	0.0133	0	0	0	0	0
MgO		0	0.0032	0	0	0.0092	0	0	0	0	0
Na_2O		0	0.0004	0	0	0.001	0	0	0	0	0
K_2O		0	0.0007	0	0	0.002	0	0	0	0	0
TiO_2		0	0.0068	0	0.0001	0.0194	0	0	0	0	0
Mn_3O_4		0	0.0011	0	0	0.0031	0	0	0	0	0
P_2O_5		0	0.0007	0	0	0.002	0	0	0	0	0
SO_3		0	0	0.0002	0.0002	0	0.0002	0	0.0002	0.0002	0
$CaCO_3$		0.0196	0.0243	0	0	0	0	0	0	0	0
$CaSO_3$		0	0.1376	0	0	0	0	0	0	0	0
H_2SO_4		0	0	0	0	0	0	0	0	0	0
Cl_2		0	0	0	0.0001	0	0.0001	0	0.0001	0.0001	0

Parameter	Units	P-045	P-046	P-047	P-048	P-049	P-050	P-051	P-052	P-053	FW-01
Temperature	°C	24.88	24.93	24.93	24.93	24.93	24.95	350	350	26	298.97
Pressure	kPa	101.3	101.3	101.3	101.3	101.3	101.32	101.32	101.32	101.3	32407
Mass Enthalpy	kJ/kg	-15140	-15880	-8430	-8430	-8430	-8430	-8110	-8110	-8429	-14608
Mass Entropy	kJ/(kg.°C)	3.09	2.98	4.12	4.12	4.12	4.12	4.84	4.84	4.12	5.89
Mass Density	kg/m^3	17.20	1008	1.74	1.74	1.74	1.74	0.83	0.83	1.73	777.4
Mass Flow	kg/h	5866001	5282948	583053	364964	218088.5	218088.5	218088.5	218095.5	364964.2	1364825.8
Molar Flow	kmol/h	306847	293045	13798	8637	5160.9	5160.9	5160.9	5161.1	8636.7	75760.1
Mole fraction											
C		0	0	0	0	0	0	0	0	0	0
H_2		0	0	0	0	0	0	0	0	0	0
S		0	0	0	0	0	0	0	0	0	0
Ar		0.0006	0	0.0139	0.0139	0.0139	0.0139	0.0139	0.0139	0.0139	0
O_2		0.0024	0	0.0533	0.0533	0.0533	0.0533	0.0533	0.0534	0.0533	0
N_2		0.0007	0	0.0161	0.0161	0.0161	0.0161	0.0161	0.0161	0.0161	0
CO_2		0.0402	0.0004	0.8853	0.8853	0.8853	0.8853	0.8853	0.8852	0.8853	0
H_2O		0.9560	0.9995	0.031	0.031	0.031	0.031	0.031	0.031	0.031	1
SO_2		0	0	0.0002	0.0002	0.0002	0.0002	0.0002	0.0002	0.0002	0
SiO_2		0	0	0	0	0	0	0	0	0	0
Al_2O_3		0	0	0	0	0	0	0	0	0	0
Fe_2O_3		0	0	0	0	0	0	0	0	0	0
CaO		0	0	0	0	0	0	0	0	0	0
MgO		0	0	0	0	0	0	0	0	0	0
Na_2O		0	0	0	0	0	0	0	0	0	0
K_2O		0	0	0	0	0	0	0	0	0	0
TiO_2		0	0	0	0	0	0	0	0	0	0
Mn_3O_4		0	0	0	0	0	0	0	0	0	0
P_2O_5		0	0	0	0	0	0	0	0	0	0
SO_3		0	0	0	0	0	0	0	0	0	0
$CaCO_3$		0	0	0	0	0	0	0	0	0	0
$CaSO_3$		0	0	0	0	0	0	0	0	0	0
H_2SO_4		0	0	0	0	0	0	0	0	0	0
Cl_2		0	0	0.0001	0.0001	0.0001	0.0001	0.0001	0.0001	0.0001	0

Parameter	Units	FW-02	FW-03	FW-04	FW-05	FW-06	FW-07	FW-08	FW-09	FW-10	FW-11
Temperature	°C	399	401	450	500	600	365.1	365.1	365.1	450	620
Pressure	kPa	31907	31407	30907	30407	30000	7500	7500	7500	7300	7000
Mass Enthalpy	kJ/kg	-13737	-13688	-13160	-12912	-12560	-12904	-12904	-12904	-12690	-12281
Mass Entropy	kJ/(kg.°C)	7.27	7.35	8.11	8.45	8.89	8.97	8.97	8.97	9.29	9.82
Mass Density	kg/m^3	313.03	294.73	154.15	117.58	87.56	29.8	29.8	29.8	23.99	17.61
Mass Flow	kg/h	1364826	1364826	1364826	1364826	1364826	1364826	126929	1237897	1237897	1237897
Molar Flow	kmol/h	75760	75760	75760	75760	75760	75760	7046	68714	68714	68714
Mole fraction											
C		0	0	0	0	0	0	0	0	0	0
H_2		0	0	0	0	0	0	0	0	0	0
S		0	0	0	0	0	0	0	0	0	0
Ar		0	0	0	0	0	0	0	0	0	0
O_2		0	0	0	0	0	0	0	0	0	0
N_2		0	0	0	0	0	0	0	0	0	0
CO_2		0	0	0	0	0	0	0	0	0	0
H_2O		1	1	1	1	1	1	1	1	1	1
SO_2		0	0	0	0	0	0	0	0	0	0
SiO_2		0	0	0	0	0	0	0	0	0	0
Al_2O_3		0	0	0	0	0	0	0	0	0	0
Fe_2O_3		0	0	0	0	0	0	0	0	0	0
CaO		0	0	0	0	0	0	0	0	0	0
MgO		0	0	0	0	0	0	0	0	0	0
Na_2O		0	0	0	0	0	0	0	0	0	0
K_2O		0	0	0	0	0	0	0	0	0	0
TiO_2		0	0	0	0	0	0	0	0	0	0
Mn_3O_4		0	0	0	0	0	0	0	0	0	0
P_2O_5		0	0	0	0	0	0	0	0	0	0
SO_3		0	0	0	0	0	0	0	0	0	0
$CaCO_3$		0	0	0	0	0	0	0	0	0	0
$CaSO_3$		0	0	0	0	0	0	0	0	0	0
H_2SO_4		0	0	0	0	0	0	0	0	0	0
Cl_2		0	0	0	0	0	0	0	0	0	0

Parameter	Units	FW-12	FW-13	FW-14	FW-15	FW-16	FW-17	FW-18	FW-19	FW-20	FW-21
Temperature	°C	558.01	558.01	558.01	459.70	459.70023	459.70	381.02	381.02	381.02	296.7
Pressure	kPa	4800	4800	4800	2500	2500	2500	1400	1400	1400	700
Mass Enthalpy	kJ/kg	-12404	-12404	-12404	-12598	-12598	-12598	-12751	-12751	-12751	-12914
Mass Entropy	kJ/(kg.°C)	9.84	9.84	9.84	9.89	9.89	9.89	9.93	9.93	9.93	9.97
Mass Density	kg/m^3	12.95	12.95	12.95	7.61	7.61	7.61	4.75	4.75	4.75	2.71
Mass Flow	kg/h	1237897	92222	1145675	1145675	59575	1086100	1086100	122295	963805	963805
Molar Flow	kmol/h	68714	5119	63595	63595	3307	60288	60288	6788	53500	53500
Mole fraction											
C		0	0	0	0	0	0	0	0	0	0
H_2		0	0	0	0	0	0	0	0	0	0
S		0	0	0	0	0	0	0	0	0	0
Ar		0	0	0	0	0	0	0	0	0	0
O_2		0	0	0	0	0	0	0	0	0	0
N_2		0	0	0	0	0	0	0	0	0	0
CO_2		0	0	0	0	0	0	0	0	0	0
H_2O		1	1	1	1	1	1	1	1	1	1
SO_2		0	0	0	0	0	0	0	0	0	0
SiO_2		0	0	0	0	0	0	0	0	0	0
Al_2O_3		0	0	0	0	0	0	0	0	0	0
Fe_2O_3		0	0	0	0	0	0	0	0	0	0
CaO		0	0	0	0	0	0	0	0	0	0
MgO		0	0	0	0	0	0	0	0	0	0
Na_2O		0	0	0	0	0	0	0	0	0	0
K_2O		0	0	0	0	0	0	0	0	0	0
TiO_2		0	0	0	0	0	0	0	0	0	0
Mn_3O_4		0	0	0	0	0	0	0	0	0	0
P_2O_5		0	0	0	0	0	0	0	0	0	0
SO_3		0	0	0	0	0	0	0	0	0	0
$CaCO_3$		0	0	0	0	0	0	0	0	0	0
$CaSO_3$		0	0	0	0	0	0	0	0	0	0
H_2SO_4		0	0	0	0	0	0	0	0	0	0
Cl_2		0	0	0	0	0	0	0	0	0	0

Parameter	Units	FW-22	FW-23	FW-24	FW-25	FW-26	FW-27	FW-28	FW-29	FW-30	FW-31
Temperature	°C	29.68	24.95	24.99	24.99	24.99	24.99	24.99	24.99	24.99	84.67
Pressure	kPa	4.1	3.1	250	250	250	250	250	250	250	250
Mass Enthalpy	kJ/kg	-13659	-15888	-15888	-15888	-15888	-15888	-15888	-15888	-15888	-15629
Mass Entropy	kJ/(kg.°C)	10.34	2.98	2.98	2.98	2.98	2.98	2.98	2.98	2.98	3.77
Mass Density	kg/m^3	0.03	1007	1007	1007	1007	1007	1007	1007	1007	960.67
Mass Flow	kg/h	963805	963805	963805	380703	322875	260227	141622	63730	77892	63730
Molar Flow	kmol/h	53500	53500	53500	21132	17922	14445	7861	3538	4324	3538
Mole fraction											
C		0	0	0	0	0	0	0	0	0	0
H_2		0	0	0	0	0	0	0	0	0	0
S		0	0	0	0	0	0	0	0	0	0
Ar		0	0	0	0	0	0	0	0	0	0
O_2		0	0	0	0	0	0	0	0	0	0
N_2		0	0	0	0	0	0	0	0	0	0
CO_2		0	0	0	0	0	0	0	0	0	0
H_2O		1	1	1	1	1	1	1	1	1	1
SO_2		0	0	0	0	0	0	0	0	0	0
SiO_2		0	0	0	0	0	0	0	0	0	0
Al_2O_3		0	0	0	0	0	0	0	0	0	0
Fe_2O_3		0	0	0	0	0	0	0	0	0	0
CaO		0	0	0	0	0	0	0	0	0	0
MgO		0	0	0	0	0	0	0	0	0	0
Na_2O		0	0	0	0	0	0	0	0	0	0
K_2O		0	0	0	0	0	0	0	0	0	0
TiO_2		0	0	0	0	0	0	0	0	0	0
Mn_3O_4		0	0	0	0	0	0	0	0	0	0
P_2O_5		0	0	0	0	0	0	0	0	0	0
SO_3		0	0	0	0	0	0	0	0	0	0
$CaCO_3$		0	0	0	0	0	0	0	0	0	0
$CaSO_3$		0	0	0	0	0	0	0	0	0	0
H_2SO_4		0	0	0	0	0	0	0	0	0	0
Cl_2		0	0	0	0	0	0	0	0	0	0

Parameter	Units	FW-32	FW-33	FW-34	FW-35	FW-36	FW-37	FW-38	FW-39	FW-40	FW-41
Temperature	°C	88.74	86.91	24.99	24.99	24.99	85.17	89.28	87.43	24.99	24.99
Pressure	kPa	250	250	250	250	250	250	250	250	250	250
Mass Enthalpy	kJ/kg	-15612	-15620	-15888	-15888	-15888	-15627	-15609	-15617	-15888	-15888
Mass Entropy	kJ/(kg.°C)	3.82	3.80	2.98	2.98	2.98	3.78	3.83	3.8	2.98	2.98
Mass Density	kg/m^3	957.33	958.84	1007	1007	1007	960.26	956.89	958.41	1007	1007
Mass Flow	kg/h	77892	141622	119541	53793	65747	53793	65747	119541	119541	53793
Molar Flow	kmol/h	4324	7861	6636	2986	3650	2986	3650	6636	6636	2986
Mole fraction											
C		0	0	0	0	0	0	0	0	0	0
H_2		0	0	0	0	0	0	0	0	0	0
S		0	0	0	0	0	0	0	0	0	0
Ar		0	0	0	0	0	0	0	0	0	0
O_2		0	0	0	0	0	0	0	0	0	0
N_2		0	0	0	0	0	0	0	0	0	0
CO_2		0	0	0	0	0	0	0	0	0	0
H_2O		1	1	1	1	1	1	1	1	1	1
SO_2		0	0	0	0	0	0	0	0	0	0
SiO_2		0	0	0	0	0	0	0	0	0	0
Al_2O_3		0	0	0	0	0	0	0	0	0	0
Fe_2O_3		0	0	0	0	0	0	0	0	0	0
CaO		0	0	0	0	0	0	0	0	0	0
MgO		0	0	0	0	0	0	0	0	0	0
Na_2O		0	0	0	0	0	0	0	0	0	0
K_2O		0	0	0	0	0	0	0	0	0	0
TiO_2		0	0	0	0	0	0	0	0	0	0
Mn_3O_4		0	0	0	0	0	0	0	0	0	0
P_2O_5		0	0	0	0	0	0	0	0	0	0
SO_3		0	0	0	0	0	0	0	0	0	0
$CaCO_3$		0	0	0	0	0	0	0	0	0	0
$CaSO_3$		0	0	0	0	0	0	0	0	0	0
H_2SO_4		0	0	0	0	0	0	0	0	0	0
Cl_2		0	0	0	0	0	0	0	0	0	0

Parameter	Units	FW-42	FW-43	FW-44	FW-45	FW-46	FW-47	FW-48	FW-49	FW-50	FW-51
Temperature	°C	24.99	85.17	89.28	87.43	24.99	24.99	24.99	24.99	24.99	84.5
Pressure	kPa	250	250	250	250	250	250	250	250	250	250
Mass Enthalpy	kJ/kg	-15888	-15627	-15609	-15617	-15888	-15888	-15888	-15888	-15888	-15630
Mass Entropy	kJ/(kg.°C)	2.98	3.78	3.83	3.8	2.98	2.98	2.98	2.98	2.98	3.77
Mass Density	kg/m^3	1007	960.26	956.89	958.41	1007	1007	1007	1007	1007	960.81
Mass Flow	kg/h	65747	53793	65747	119541	93634	114621	114621	42135	51499	42135
Molar Flow	kmol/h	3650	2986	3650	6636	5198	6362	6362	2339	2859	2339
Mole fraction											
C		0	0	0	0	0	0	0	0	0	0
H_2		0	0	0	0	0	0	0	0	0	0
S		0	0	0	0	0	0	0	0	0	0
Ar		0	0	0	0	0	0	0	0	0	0
O_2		0	0	0	0	0	0	0	0	0	0
N_2		0	0	0	0	0	0	0	0	0	0
CO_2		0	0	0	0	0	0	0	0	0	0
H_2O		1	1	1	1	1	1	1	1	1	1
SO_2		0	0	0	0	0	0	0	0	0	0
SiO_2		0	0	0	0	0	0	0	0	0	0
Al_2O_3		0	0	0	0	0	0	0	0	0	0
Fe_2O_3		0	0	0	0	0	0	0	0	0	0
CaO		0	0	0	0	0	0	0	0	0	0
MgO		0	0	0	0	0	0	0	0	0	0
Na_2O		0	0	0	0	0	0	0	0	0	0
K_2O		0	0	0	0	0	0	0	0	0	0
TiO_2		0	0	0	0	0	0	0	0	0	0
Mn_3O_4		0	0	0	0	0	0	0	0	0	0
P_2O_5		0	0	0	0	0	0	0	0	0	0
SO_3		0	0	0	0	0	0	0	0	0	0
$CaCO_3$		0	0	0	0	0	0	0	0	0	0
$CaSO_3$		0	0	0	0	0	0	0	0	0	0
H_2SO_4		0	0	0	0	0	0	0	0	0	0
Cl_2		0	0	0	0	0	0	0	0	0	0

Parameter	Units	FW-52	FW-53	FW-54	FW-55	FW-56	FW-57	FW-58	FW-59	FW-60	FW-61
Temperature	°C	88.56	86.73	24.99	24.99	84.78	88.86	87.03	24.99	24.99	84.78
Pressure	kPa	250	250	250	250	250	250	250	250	250	250
Mass Enthalpy	kJ/kg	-15612	-15620	-15888	-15888	-15629	-15611	-15619	-15888	-15888	-15629
Mass Entropy	kJ/(kg.°C)	3.82	3.8	2.98	2.98	3.77	3.82	3.80	2.98	2.98	3.77
Mass Density	kg/m^3	957.48	958.98	1007	1007	960.58	957.23	958.74	1007	1007	960.58
Mass Flow	kg/h	51499	93634	51579	63041	51579	63041	114621	51579	63041	51579
Molar Flow	kmol/h	2859	5198	2863	3499	2863	3499	6362	2863	3499	2863
Mole fraction											
C		0	0	0	0	0	0	0	0	0	0
H_2		0	0	0	0	0	0	0	0	0	0
S		0	0	0	0	0	0	0	0	0	0
Ar		0	0	0	0	0	0	0	0	0	0
O_2		0	0	0	0	0	0	0	0	0	0
N_2		0	0	0	0	0	0	0	0	0	0
CO_2		0	0	0	0	0	0	0	0	0	0
H_2O		1	1	1	1	1	1	1	1	1	1
SO_2		0	0	0	0	0	0	0	0	0	0
SiO_2		0	0	0	0	0	0	0	0	0	0
Al_2O_3		0	0	0	0	0	0	0	0	0	0
Fe_2O_3		0	0	0	0	0	0	0	0	0	0
CaO		0	0	0	0	0	0	0	0	0	0
MgO		0	0	0	0	0	0	0	0	0	0
Na_2O		0	0	0	0	0	0	0	0	0	0
K_2O		0	0	0	0	0	0	0	0	0	0
TiO_2		0	0	0	0	0	0	0	0	0	0
Mn_3O_4		0	0	0	0	0	0	0	0	0	0
P_2O_5		0	0	0	0	0	0	0	0	0	0
SO_3		0	0	0	0	0	0	0	0	0	0
$CaCO_3$		0	0	0	0	0	0	0	0	0	0
$CaSO_3$		0	0	0	0	0	0	0	0	0	0
H_2SO_4		0	0	0	0	0	0	0	0	0	0
Cl_2		0	0	0	0	0	0	0	0	0	0

Parameter	Units	FW-62	FW-63	FW-64	FW-65	FW-66	FW-67	FW-68	FW-69	FW-70	FW-71
Temperature	°C	88.86	87.03	24.99	24.99	24.99	123.41	127.37	86.05	86.99	117.66
Pressure	kPa	250	250	250	250	250	250	250	250	250	250
Mass Enthalpy	kJ/kg	-15611	-15619	-15888	-15888	-15888	-15459	-15412	-15623	-15619	-15484
Mass Entropy	kJ/(kg.°C)	3.82	3.8	2.98	2.98	2.98	4.22	4.34	3.79	3.8	4.16
Mass Density	kg/m^3	957.23	958.74	1007	1007	1007	927.79	95.27	959.54	958.77	932.83
Mass Flow	kg/h	63041	114621	65057	111898	83273	65057	111898	83273	786851	786851
Molar Flow	kmol/h	3499	6362	3611	6211	4622	3611	6211	4622	43677	43677
Mole fraction											
C		0	0	0	0	0	0	0	0	0	0
H_2		0	0	0	0	0	0	0	0	0	0
S		0	0	0	0	0	0	0	0	0	0
Ar		0	0	0	0	0	0	0	0	0	0
O_2		0	0	0	0	0	0	0	0	0	0
N_2		0	0	0	0	0	0	0	0	0	0
CO_2		0	0	0	0	0	0	0	0	0	0
H_2O		1	1	1	1	1	1	1	1	1	1
SO_2		0	0	0	0	0	0	0	0	0	0
SiO_2		0	0	0	0	0	0	0	0	0	0
Al_2O_3		0	0	0	0	0	0	0	0	0	0
Fe_2O_3		0	0	0	0	0	0	0	0	0	0
CaO		0	0	0	0	0	0	0	0	0	0
MgO		0	0	0	0	0	0	0	0	0	0
Na_2O		0	0	0	0	0	0	0	0	0	0
K_2O		0	0	0	0	0	0	0	0	0	0
TiO_2		0	0	0	0	0	0	0	0	0	0
Mn_3O_4		0	0	0	0	0	0	0	0	0	0
P_2O_5		0	0	0	0	0	0	0	0	0	0
SO_3		0	0	0	0	0	0	0	0	0	0
$CaCO_3$		0	0	0	0	0	0	0	0	0	0
$CaSO_3$		0	0	0	0	0	0	0	0	0	0
H_2SO_4		0	0	0	0	0	0	0	0	0	0
Cl_2		0	0	0	0	0	0	0	0	0	0

Parameter	Units	FW-72	FW-73	FW-74	FW-75	FW-76	FW-77	FW-78	FW-79	FW-80	FW-81
Temperature	°C	119.93	120.09	293.32	287.86	262.31	224.74	224.55	220.10	195.32	202.64
Pressure	kPa	250	1700	4781	7300	4781	4581	2500	2300	1400	32650
Mass Enthalpy	kJ/kg	-15474	-15472	-13018	-14497	-13874	-14978	-14469	-14965	-15125	-15076
Mass Entropy	kJ/(kg.°C)	4.18	4.18	8.96	6.16	7.36	5.29	6.32	5.32	4.99	5
Mass Density	kg/m^3	930.85	931.45	21.20	260.36	42.4	828.52	42.83	344.09	858.85	877.24
Mass Flow	kg/h	963805	963805	92222	126929	219150	219150	278725	278725	1364826	1364826
Molar Flow	kmol/h	53500	53500	5119	7046	12165	12165	15472	15472	75760	75760
Mole fraction											
C		0	0	0	0	0	0	0	0	0	0
H_2		0	0	0	0	0	0	0	0	0	0
S		0	0	0	0	0	0	0	0	0	0
Ar		0	0	0	0	0	0	0	0	0	0
O_2		0	0	0	0	0	0	0	0	0	0
N_2		0	0	0	0	0	0	0	0	0	0
CO_2		0	0	0	0	0	0	0	0	0	0
H_2O		1	1	1	1	1	1	1	1	1	1
SO_2		0	0	0	0	0	0	0	0	0	0
SiO_2		0	0	0	0	0	0	0	0	0	0
Al_2O_3		0	0	0	0	0	0	0	0	0	0
Fe_2O_3		0	0	0	0	0	0	0	0	0	0
CaO		0	0	0	0	0	0	0	0	0	0
MgO		0	0	0	0	0	0	0	0	0	0
Na_2O		0	0	0	0	0	0	0	0	0	0
K_2O		0	0	0	0	0	0	0	0	0	0
TiO_2		0	0	0	0	0	0	0	0	0	0
Mn_3O_4		0	0	0	0	0	0	0	0	0	0
P_2O_5		0	0	0	0	0	0	0	0	0	0
SO_3		0	0	0	0	0	0	0	0	0	0
$CaCO_3$		0	0	0	0	0	0	0	0	0	0
$CaSO_3$		0	0	0	0	0	0	0	0	0	0
H_2SO_4		0	0	0	0	0	0	0	0	0	0
Cl_2		0	0	0	0	0	0	0	0	0	0

Parameter	Units	FW-82	FW-83	FW-84	G-01	G-02	G-03	G-04	G-05	G-06	G-07
Temperature	°C	224	259.7	292	26	127	45	151.27	28	28	28
Pressure	kPa	32600	32550	32500	101.3	318.44	318.44	1001	1001	1001	1001
Mass Enthalpy	kJ/kg	-14975	-14798	-14650	-8431	-8339	-8416	-8320	-8465	-15806	-8380
Mass Entropy	kJ/(kg·°C)	5.21	5.56	5.81	4.12	4.16	3.95	3.99	3.57	3.03	3.58
Mass Density	kg/m^3	857.36	821.75	785.97	1.73	4.07	5.16	12.17	18.25	1007	18.04
Mass Flow	kg/h	1364826	1364826	1364826	364873	364873	364873	364873	364873	4215	360658
Molar Flow	kmol/h	75760	75760	75760	8635	8635	8635	8635	8635	232.60	8403
Mole fraction											
C		0	0	0	0	0	0	0	0	0	0
H_2		0	0	0	0	0	0	0	0	0	0
S		0	0	0	0	0	0	0	0	0	0
Ar		0	0	0	0.0139	0.0139	0.0139	0.0139	0.0139	0	0.0142
O_2		0	0	0	0.0533	0.0533	0.0533	0.0533	0.0533	0	0.0548
N_2		0	0	0	0.0161	0.0161	0.0161	0.0161	0.0161	0	0.0166
CO_2		0	0	0	0.8854	0.8854	0.8854	0.8854	0.8854	0.004	0.9098
H_2O		1	1	1	0.031	0.031	0.031	0.031	0.031	0.996	0.0043
SO_2		0	0	0	0.0002	0.0002	0.0002	0.0002	0.0002	0.0001	0.0002
SiO_2		0	0	0	0	0	0	0	0	0	0
Al_2O_3		0	0	0	0	0	0	0	0	0	0
Fe_2O_3		0	0	0	0	0	0	0	0	0	0
CaO		0	0	0	0	0	0	0	0	0	0
MgO		0	0	0	0	0	0	0	0	0	0
Na_2O		0	0	0	0	0	0	0	0	0	0
K_2O		0	0	0	0	0	0	0	0	0	0
TiO_2		0	0	0	0	0	0	0	0	0	0
Mn_3O_4		0	0	0	0	0	0	0	0	0	0
P_2O_5		0	0	0	0	0	0	0	0	0	0
SO_3		0	0	0	0	0	0	0	0	0	0
$CaCO_3$		0	0	0	0	0	0	0	0	0	0
$CaSO_3$		0	0	0	0	0	0	0	0	0	0
H_2SO_4		0	0	0	0	0	0	0	0	0	0
Cl_2		0	0	0	0	0	0	0	0	0	0

Parameter	Units	G-08	G-09	G-10	G-11	G-12	G-13	G-14	G-15	G-16	G-17
Temperature	°C	88.13	27.83	27.83	27.83	55.28	25	25	25	25	25
Pressure	kPa	2001	2001	2001	2001	2801	2801	2801	2801	2800	2800
Mass Enthalpy	kJ/kg	-8330	-8391	-15741	-8385	-8365	-8397	-15694	-8395	-15885	-8391
Mass Entropy	kJ/(kg.°C)	3.6	3.42	3.02	3.42	3.42	3.32	2.98	3.32	2.98	3.31
Mass Density	kg/m^3	30.19	38.20	1009	38.18	49.21	57.01	1013	56.99	1008	56.98
Mass Flow	kg/h	360658	360658	278.55	360379	360379	360379	115.88	360263	268.85	359994
Molar Flow	kmol/h	8403	8403	15.29	8388	8388	8388	6.33	8381	14.92	8366
Mole fraction											
C		0	0	0	0	0	0	0	0	0	0
H_2		0	0	0	0	0	0	0	0	0	0
S		0	0	0	0	0	0	0	0	0	0
Ar		0.0142	0.0142	0	0.0143	0.0143	0.0143	0	0.0143	0	0.0143
O_2		0.0548	0.0548	0	0.0549	0.0549	0.0549	0	0	0	0.0551
N_2		0.0166	0.0166	0	0.0166	0.0166	0.0166	0	0.0166	0	0.0166
CO_2		0.9098	0.9098	0.0078	0.9114	0.9114	0.9114	0.0113	0.9121	0	0.9137
H_2O		0.0043	0.0043	0.9921	0.0025	0.0025	0.0025	0.9885	0.0018	1	0
SO_2		0.0002	0.0002	0.0001	0.0002	0.0002	0.0002	0.0001	0.0002	0	0.0002
SiO_2		0	0	0	0	0	0	0	0	0	0
Al_2O_3		0	0	0	0	0	0	0	0	0	0
Fe_2O_3		0	0	0	0	0	0	0	0	0	0
CaO		0	0	0	0	0	0	0	0	0	0
MgO		0	0	0	0	0	0	0	0	0	0
Na_2O		0	0	0	0	0	0	0	0	0	0
K_2O		0	0	0	0	0	0	0	0	0	0
TiO_2		0	0	0	0	0	0	0	0	0	0
Mn_3O_4		0	0	0	0	0	0	0	0	0	0
P_2O_5		0	0	0	0	0	0	0	0	0	0
SO_3		0	0	0	0	0	0	0	0	0	0
$CaCO_3$		0	0	0	0	0	0	0	0	0	0
$CaSO_3$		0	0	0	0	0	0	0	0	0	0
H_2SO_4		0	0	0	0	0	0	0	0	0	0
Cl_2		0	0	0	0	0	0	0	0	0	0

Parameter	Units	G-18	G-19	G-20	G-21	G-22	G-23	G-24	G-25	G-26	G-27
Temperature	°C	-31.1	-33.9	-7.48	-10.79	-54.31	-54	-54	-54	-55.15	-66.32
Pressure	kPa	2800	2800	2800	2800	550	2800	2800	2800	1980	1300
Mass Enthalpy	kJ/kg	-8700	-8936	-9273	-8546	-9273	-8882	-9045	-2878	-9045	-2878
Mass Entropy	kJ/(kg.°C)	2.12	1.99	2.11	3.15	2.17	1.82	1.78	3.4	1.78	3.57
Mass Density	kg/m^3	375.44	642.2	971	73.41	49.1	782.64	1141	62.16	755.19	28.74
Mass Flow	kg/h	359994	1615951	325952	1289999	325952	1289999	1255962	34037	1255962	34037
Molar Flow	kmol/h	8366	37252	7405	29847	7405	29847	28886	960.72	28886	960.72
Mole fraction											
C		0	0	0	0	0	0	0	0	0	0
H_2		0	0	0	0	0	0	0	0	0	0
S		0	0	0	0	0	0	0	0	0	0
Ar		0.0143	0.0091	0	0.0114	0	0.0114	0.0076	0.1246	0.0076	0.1246
O_2		0.0551	0.0374	0	0.0467	0	0.0467	0.0323	0.4794	0.0323	0.4794
N_2		0.0166	0.0091	0	0.0114	0	0.0114	0	0.1448	0	0.1448
CO_2		0.9137	0.9443	0.9997	0.9305	0.9997	0.9305	0.9531	0.2511	0.9531	0.2511
H_2O		0	0	0	0	0	0	0	0	0	0
SO_2		0.0002	0.0001	0.0003	0	0.0003	0	0	0	0	0
SiO_2		0	0	0	0	0	0	0	0	0	0
Al_2O_3		0	0	0	0	0	0	0	0	0	0
Fe_2O_3		0	0	0	0	0	0	0	0	0	0
CaO		0	0	0	0	0	0	0	0	0	0
MgO		0	0	0	0	0	0	0	0	0	0
Na_2O		0	0	0	0	0	0	0	0	0	0
K_2O		0	0	0	0	0	0	0	0	0	0
TiO_2		0	0	0	0	0	0	0	0	0	0
Mn_3O_4		0	0	0	0	0	0	0	0	0	0
P_2O_5		0	0	0	0	0	0	0	0	0	0
SO_3		0	0	0	0	0	0	0	0	0	0
$CaCO_3$		0	0	0	0	0	0	0	0	0	0
$CaSO_3$		0	0	0	0	0	0	0	0	0	0
H_2SO_4		0	0	0	0	0	0	0	0	0	0
Cl_2		0	0	0	0	0	0	0	0	0	0

Parameter	Units	G-28	G-29	G-30	G-31	G-32	G-33	G-34	G-35	G-36	G-37	G-38
Temperature	°C	-28.77	-5	21.34	-35	-35	-34	117.84	27.84	73.46	26.03	39.05
Pressure	kPa	1300	1980	2800	2800	2800	550	4000	4000	6800	6800	12000
Mass Enthalpy	kJ/kg	-2844	-8682	-8665	-9004	-9004	-9004	-8887	-8989	-8962	-9162	-9154
Mass Entropy	kJ/(kg.°C)	3.71	3.26	3.26	1.96	1.96	3.39	3.42	3.13	3.13	2.48	2.49
Mass Density	kg/m^3	23.61	45.7	59.44	790.52	790.56	12.95	59.38	93.14	137.39	654.7	676.04
Mass Flow	kg/h	34037	1255962	1255962	1255962	1255957	325952	325952	325952	325952	325952	325952
Molar Flow	kmol/h	960.72	28886	28886	28886	28886	7405	7405	7405	7405	7405	7405
Mole fraction												
C		0	0	0	0	0	0	0	0	0	0	0
H_2		0	0	0	0	0	0	0	0	0	0	0
S		0	0	0	0	0	0	0	0	0	0	0
Ar		0.1246	0.0076	0.0076	0.0076	0.0076	0	0	0	0	0	0
O_2		0.4794	0.0323	0.0323	0.0323	0.0323	0	0	0	0	0	0
N_2		0.1448	0	0	0	0	0	0	0	0	0	0
CO_2		0.2511	0.9531	0.9531	0.9531	0.9531	0.9997	0.9997	0.9997	0.9997	0.9997	0.9997
H_2O		0	0	0	0	0	0	0	0	0	0	0
SO_2		0	0	0	0	0	0.0003	0.0003	0.0003	0.0003	0.0003	0.0003
SiO_2		0	0	0	0	0	0	0	0	0	0	0
Al_2O_3		0	0	0	0	0	0	0	0	0	0	0
Fe_2O_3		0	0	0	0	0	0	0	0	0	0	0
CaO		0	0	0	0	0	0	0	0	0	0	0
MgO		0	0	0	0	0	0	0	0	0	0	0
Na_2O		0	0	0	0	0	0	0	0	0	0	0
K_2O		0	0	0	0	0	0	0	0	0	0	0
TiO_2		0	0	0	0	0	0	0	0	0	0	0
Mn_3O_4		0	0	0	0	0	0	0	0	0	0	0
P_2O_5		0	0	0	0	0	0	0	0	0	0	0
SO_3		0	0	0	0	0	0	0	0	0	0	0
$CaCO_3$		0	0	0	0	0	0	0	0	0	0	0
$CaSO_3$		0	0	0	0	0	0	0	0	0	0	0
H_2SO_4		0	0	0	0	0	0	0	0	0	0	0
Cl_2		0	0	0	0	0	0	0	0	0	0	0

Table B.8: Heat tables of the oxy-combustion process with heat integration.

Unit	Heat Flow (GJ/h)	Utility (kg/h)
Q-01	-1.449	69302
Q-02	-90.001	0
Q-03	-1.223	58494
Q-04	-75.965	0
Q-05	0.347	158
Q-06	-2148.850	102742037
Q-07	-11.650	557009
Q-08	-0.606	151497
Q-09	506.502	126625601
Q-10	-112.923	28230703
Q-11	-426.144	317780448
Q-12	-33.165	1585705
Q-13	-65.346	16336583

Table B.9: Power tables of the oxy-combustion process with heat integration.

	W-01	W-02	W-03	W-04	W-05	W-06	W-07	W-08	W-09	W-10
Work (kW)	5904.35	5932.93	5025.91	5050.24	5025.91	5050.24	397.77	3892.44	3911.28	4787.65
	W-11	W-12	W-13	W-14	W-15	W-16	W-17	W-18	W-19	W-20
Work (kW)	4810.83	4787.65	4810.83	335.73	469.16	366.41	1.03	-130616	-42341	-61643
	W-21	W-22	W-23	W-24	W-25	W-26	W-27	W-28	W-29	W-30
Work (kW)	-46317	-43571	199312	87.49	490.32	18392.7	9289.06	9776.89	4958.87	2035.01
	W-31	W-32	W-33	W-34						
Work (kW)	6040.54	10555	2441.73	799.04						

Table B.10: Overall carbon balance of the oxy-combustion process with heat integration.

Carbon In		Carbon Out	
	kg/h		kg/h
Coal	93019.2	Spray dryer out	46.52
Limestone	309.1	DCC out	1512.6
		Dissolved in GPU compression	13.38
		Stack	2895.2
		Storage	88839.9
Total	93328.4	Total	93307.6
		Balance	20.78
		Error (%)	0.02

Table B.11: Energy balance of the oxy-combustion process with heat integration. Energy in.

	HHV	Sensible + Latent	Power	Total
ASU1 - Turbine	0	0	397.77	397.77
ASU1 - Booster cooling	0	1.45	0	1.45
ASU1 - HP condenser	0	90	0	90
ASU2 - Turbine	0	0	1.21	1.21
ASU2 - Booster cooling	0	1.22	0	1.22
ASU2 - HP condenser	0	75.97	0	75.97
Slurry	1.76	0	0	1.76
Water	12012.55	0	0	12012.55
HP turbine	0	0	470.22	470.22
IP turbine	0	0	697.94	697.94
LP turbine	0	0	717.52	717.52
Condenser	0	2148.85	0	2148.85
GPU - Main compressor cooling	0	11.65	0	11.65
GPU - Main compressor condensate	10.38	0	0	10.38
GPU - Water	0.61	0	0	0.61
GPU - Condenser	0	112.92	0	112.92
GPU - Gas cooler	0	426.14	0	426.14
GPU - CO_2 compressor intercooling	0	98.51	0	98.51
Stack	0	0	0	0
CO_2 for storage	0.02	0	0	0.02
Unaccounted energy	12025.32	2966.72	2284.65	51.84
Unaccounted energy (%)				0.30

Table B.12: Energy balance of the oxy-combustion process with heat integration. Energy out.

	HHV (GJ/h)	Sensible + Latent (GJ/h)	Power (GJ/h)	Total (GJ/h)
ASU1 - Turbine	0	0	397.77	397.77
ASU1 - Booster cooling	0	1.45	0	1.45
ASU1 - HP condenser	0	90	0	90
ASU2 - Turbine	0	0	1.21	1.21
ASU2 - Booster cooling	0	1.22	0	1.22
ASU2 - HP condenser	0	75.97	0	75.97
Slurry	1.76	0	0	1.76
Water	12012.55	0	0	12012.55
HP turbine	0	0	470.22	470.22
IP turbine	0	0	697.94	697.94
LP turbine	0	0	717.52	717.52
Condenser	0	2148.85	0	2148.85
GPU - Main comp cooling	0	11.65	0	11.65
GPU - Comp condensate	10.38	0	0	10.38
GPU - Water	0.61	0	0	0.61
GPU - Condenser	0	112.92	0	112.92
GPU - Gas cooler	0	426.14	0	426.14
GPU - CO_2 comp cooling	0	98.51	0	98.51
Stack	0	0	0	0
CO_2 for storage	0.02	0	0	0.02
Unaccounted energy				51.84
Unaccounted energy (%)				0.30

B.5.3 With heat integration and smaller ASU

This simulation used the same PFD represented in Figure B.6.

Table B.13: Stream tables of the oxy-combustion process with heat integration and smaller ASU.

Parameter	Units	A-001	A-002	A-003	A-004	A-005	A-006	A-007	A-008	A-009	A-010
Temperature	°C	10	88.31	28	106.42	28	10	88.31	28	106.42	28
Pressure	kPa	101.32	210	210	420	420	101.32	210	210	420	420
Mass Enthalpy	kJ/kg	-15.34	63.57	2.44	81.73	1.87	-15.34	63.57	2.44	81.73	1.87
Mass Entropy	kJ/(kg.°C)	5.19	5.23	5.04	5.08	4.84	5.19	5.23	5.04	5.08	4.84
Mass Density	kg/m^3	1.25	2.02	2.43	3.85	4.87	1.25	2.02	2.43	3.85	4.87
Mass Flow	kg/h	264962	264962	264962	264962	264962	229279	229279	229279	229279	229279
Molar Flow	kmol/h	9148	9148	9148	9148	9148	7916	7916	7916	7916	7916
Mole fraction											
C		0	0	0	0	0	0	0	0	0	0
H_2		0	0	0	0	0	0	0	0	0	0
S		0	0	0	0	0	0	0	0	0	0
Ar		0.0097	0.0097	0.0097	0.0097	0.0097	0.0097	0.0097	0.0097	0.0097	0.0097
O_2		0.2095	0.2095	0.2095	0.2095	0.2095	0.2095	0.2095	0.2095	0.2095	0.2095
N_2		0.7808	0.7808	0.7808	0.7808	0.7808	0.7808	0.7808	0.7808	0.7808	0.7808
CO_2		0	0	0	0	0	0	0	0	0	0
H_2O		0	0	0	0	0	0	0	0	0	0
SO_2		0	0	0	0	0	0	0	0	0	0
SiO_2		0	0	0	0	0	0	0	0	0	0
Al_2O_3		0	0	0	0	0	0	0	0	0	0
Fe_2O_3		0	0	0	0	0	0	0	0	0	0
CaO		0	0	0	0	0	0	0	0	0	0
MgO		0	0	0	0	0	0	0	0	0	0
Na_2O		0	0	0	0	0	0	0	0	0	0
K_2O		0	0	0	0	0	0	0	0	0	0
TiO_2		0	0	0	0	0	0	0	0	0	0
Mn_3O_4		0	0	0	0	0	0	0	0	0	0
P_2O_5		0	0	0	0	0	0	0	0	0	0
SO_3		0	0	0	0	0	0	0	0	0	0
$CaCO_3$		0	0	0	0	0	0	0	0	0	0
$CaSO_3$		0	0	0	0	0	0	0	0	0	0
H_2SO_4		0	0	0	0	0	0	0	0	0	0
Cl_2		0	0	0	0	0	0	0	0	0	0

Parameter	Units	A-011	A-012	A-013	A-014	A-015	A-016	A-017	A-018	A-019	A-020
Temperature	°C	10	88.31	28	106.42	28	28	28	28	35.86	28
Pressure	kPa	101.32	210	210	420	420	420	420	420	455.5	455.5
Mass Enthalpy	kJ/kg	-15.34	63.57	2.44	81.73	1.87	1.87	1.87	1.87	9.74	1.77
Mass Entropy	kJ/(kg.°C)	5.19	5.23	5.04	5.08	4.84	4.84	4.84	4.84	4.84	4.82
Mass Density	kg/m^3	1.25	2.02	2.43	3.85	4.87	4.87	4.87	4.87	5.15	5.28
Mass Flow	kg/h	229279	229279	229279	229279	229279	723521	542641	180880	180880	180880
Molar Flow	kmol/h	7916	7916	7916	7916	7916	24980	18735	6245	6245	6245
Mole fraction											
C		0	0	0	0	0	0	0	0	0	0
H_2		0	0	0	0	0	0	0	0	0	0
S		0	0	0	0	0	0	0	0	0	0
Ar		0.0097	0.0097	0.0097	0.0097	0.0097	0.0097	0.0097	0.0097	0.0097	0.0097
O_2		0.2095	0.2095	0.2095	0.2095	0.2095	0.2095	0.2095	0.2095	0.2095	0.2095
N_2		0.7808	0.7808	0.7808	0.7808	0.7808	0.7808	0.7808	0.7808	0.7808	0.7808
CO_2		0	0	0	0	0	0	0	0	0	0
H_2O		0	0	0	0	0	0	0	0	0	0
SO_2		0	0	0	0	0	0	0	0	0	0
SiO_2		0	0	0	0	0	0	0	0	0	0
Al_2O_3		0	0	0	0	0	0	0	0	0	0
Fe_2O_3		0	0	0	0	0	0	0	0	0	0
CaO		0	0	0	0	0	0	0	0	0	0
MgO		0	0	0	0	0	0	0	0	0	0
Na_2O		0	0	0	0	0	0	0	0	0	0
K_2O		0	0	0	0	0	0	0	0	0	0
TiO_2		0	0	0	0	0	0	0	0	0	0
Mn_3O_4		0	0	0	0	0	0	0	0	0	0
P_2O_5		0	0	0	0	0	0	0	0	0	0
SO_3		0	0	0	0	0	0	0	0	0	0
$CaCO_3$		0	0	0	0	0	0	0	0	0	0
$CaSO_3$		0	0	0	0	0	0	0	0	0	0
H_2SO_4		0	0	0	0	0	0	0	0	0	0
Cl_2		0	0	0	0	0	0	0	0	0	0

Parameter	Units	A-021	A-022	A-023	A-024	A-025	A-026	A-027	A-028	A-029	A-030
Temperature	°C	28	28	-177.66	-179	10	-177.97	-181.49	-190.77	-187	-193.89
Pressure	kPa	455.5	455.5	410	445.5	445.5	410	410	125	410	125
Mass Enthalpy	kJ/kg	1.77	1.77	-225.17	-388.95	-16.4	-385.55	-396.36	-385.55	-407.72	-407.72
Mass Entropy	kJ/(kg.°C)	4.82	4.82	3.48	1.75	4.76	1.72	1.68	1.74	1.55	1.57
Mass Density	kg/m^3	5.28	5.28	18.54	800.73	5.5	854.23	739.84	43.83	768.29	73.42
Mass Flow	kg/h	16279	164601	542641	164601	16279	317792	224848	317792	224848	224848
Molar Flow	kmol/h	562.05	5683	18735	5683	562.05	10726	8009	10726	8009	8009
Mole fraction											
C		0	0	0	0	0	0	0	0	0	0
H_2		0	0	0	0	0	0	0	0	0	0
S		0	0	0	0	0	0	0	0	0	0
Ar		0.0097	0.0097	0.0097	0.0097	0.0097	0.015	0.0026	0.015	0.0026	0.0026
O_2		0.2095	0.2095	0.2095	0.2095	0.2095	0.36	0.0079	0.36	0.0079	0.0079
N_2		0.7808	0.7808	0.7808	0.7808	0.7808	0.625	0.9895	0.625	0.9895	0.9895
CO_2		0	0	0	0	0	0	0	0	0	0
H_2O		0	0	0	0	0	0	0	0	0	0
SO_2		0	0	0	0	0	0	0	0	0	0
SiO_2		0	0	0	0	0	0	0	0	0	0
Al_2O_3		0	0	0	0	0	0	0	0	0	0
Fe_2O_3		0	0	0	0	0	0	0	0	0	0
CaO		0	0	0	0	0	0	0	0	0	0
MgO		0	0	0	0	0	0	0	0	0	0
Na_2O		0	0	0	0	0	0	0	0	0	0
K_2O		0	0	0	0	0	0	0	0	0	0
TiO_2		0	0	0	0	0	0	0	0	0	0
Mn_3O_4		0	0	0	0	0	0	0	0	0	0
P_2O_5		0	0	0	0	0	0	0	0	0	0
SO_3		0	0	0	0	0	0	0	0	0	0
$CaCO_3$		0	0	0	0	0	0	0	0	0	0
$CaSO_3$		0	0	0	0	0	0	0	0	0	0
H_2SO_4		0	0	0	0	0	0	0	0	0	0
Cl_2		0	0	0	0	0	0	0	0	0	0

Parameter	Units	A-031	A-032	A-033	A-034	A-035	A-036	A-037	A-038	A-039	A-040
Temperature	°C	-192.21	-78.99	-182.39	-194.70	-190.26	25.2	25	10	88.31	28
Pressure	kPa	125	112.17	111.33	111.33	111.33	101.33	101.33	101.32	210	210
Mass Enthalpy	kJ/kg	-388.95	-103.83	-390.39	-225.15	-220.56	-0.07	-0.3	-15.34	63.57	2.44
Mass Entropy	kJ/(kg·°C)	1.78	4.79	1.16	3.89	3.95	5.29	4.51	5.19	5.23	5.04
Mass Density	kg/m^3	41.08	2.02	1148.33	5.02	4.72	1.15	1.32	1.25	2.02	2.43
Mass Flow	kg/h	164601	16279	166739	556782	556782	556782	166739	193605	193605	193605
Molar Flow	kmol/h	5683	562.05	5179	19801	19801	19801	5179	6684	6684	6684
Mole fraction											
C		0	0	0	0	0	0	0	0	0	0
H_2		0	0	0	0	0	0	0	0	0	0
S		0	0	0	0	0	0	0	0	0	0
Ar		0.0097	0.0097	0.0243	0.0059	0.0059	0.0059	0.0243	0.0097	0.0097	0.0097
O_2		0.2095	0.2095	0.9757	0.0091	0.0091	0.0091	0.9757	0.2095	0.2095	0.2095
N_2		0.7808	0.7808	0	0.985	0.985	0.985	0	0.7808	0.7808	0.7808
CO_2		0	0	0	0	0	0	0	0	0	0
H_2O		0	0	0	0	0	0	0	0	0	0
SO_2		0	0	0	0	0	0	0	0	0	0
SiO_2		0	0	0	0	0	0	0	0	0	0
Al_2O_3		0	0	0	0	0	0	0	0	0	0
Fe_2O_3		0	0	0	0	0	0	0	0	0	0
CaO		0	0	0	0	0	0	0	0	0	0
MgO		0	0	0	0	0	0	0	0	0	0
Na_2O		0	0	0	0	0	0	0	0	0	0
K_2O		0	0	0	0	0	0	0	0	0	0
TiO_2		0	0	0	0	0	0	0	0	0	0
Mn_3O_4		0	0	0	0	0	0	0	0	0	0
P_2O_5		0	0	0	0	0	0	0	0	0	0
SO_3		0	0	0	0	0	0	0	0	0	0
$CaCO_3$		0	0	0	0	0	0	0	0	0	0
$CaSO_3$		0	0	0	0	0	0	0	0	0	0
H_2SO_4		0	0	0	0	0	0	0	0	0	0
Cl_2		0	0	0	0	0	0	0	0	0	0

Parameter	Units	A-041	A-042	A-043	A-044	A-045	A-046	A-047	A-048	A-049	A-050
Temperature	°C	106.42	28	10	88.31	28	106.42	28	10	88.31	28
Pressure	kPa	420	420	101.32	210	210	420	420	101.32	210	210
Mass Enthalpy	kJ/kg	81.73	1.87	-15.34	63.57	2.44	81.73	1.87	-15.34	63.57	2.44
Mass Entropy	kJ/(kg.°C)	5.08	4.84	5.19	5.23	5.04	5.08	4.84	5.19	5.23	5.04
Mass Density	kg/m^3	3.85	4.87	1.25	2.02	2.43	3.85	4.87	1.25	2.02	2.43
Mass Flow	kg/h	193605	193605	218410	218410	218410	218410	218410	218410	218410	218410
Molar Flow	kmol/h	6684	6684	7541	7541	7541	7541	7541	7541	7541	7541
Mole fraction											
C		0	0	0	0	0	0	0	0	0	0
H_2		0	0	0	0	0	0	0	0	0	0
S		0	0	0	0	0	0	0	0	0	0
Ar		0.0097	0.0097	0.0097	0.0097	0.0097	0.0097	0.0097	0.0097	0.0097	0.0097
O_2		0.2095	0.2095	0.2095	0.2095	0.2095	0.2095	0.2095	0.2095	0.2095	0.2095
N_2		0.7808	0.7808	0.7808	0.7808	0.7808	0.7808	0.7808	0.7808	0.7808	0.7808
CO_2		0	0	0	0	0	0	0	0	0	0
H_2O		0	0	0	0	0	0	0	0	0	0
SO_2		0	0	0	0	0	0	0	0	0	0
SiO_2		0	0	0	0	0	0	0	0	0	0
Al_2O_3		0	0	0	0	0	0	0	0	0	0
Fe_2O_3		0	0	0	0	0	0	0	0	0	0
CaO		0	0	0	0	0	0	0	0	0	0
MgO		0	0	0	0	0	0	0	0	0	0
Na_2O		0	0	0	0	0	0	0	0	0	0
K_2O		0	0	0	0	0	0	0	0	0	0
TiO_2		0	0	0	0	0	0	0	0	0	0
Mn_3O_4		0	0	0	0	0	0	0	0	0	0
P_2O_5		0	0	0	0	0	0	0	0	0	0
SO_3		0	0	0	0	0	0	0	0	0	0
$CaCO_3$		0	0	0	0	0	0	0	0	0	0
$CaSO_3$		0	0	0	0	0	0	0	0	0	0
H_2SO_4		0	0	0	0	0	0	0	0	0	0
Cl_2		0	0	0	0	0	0	0	0	0	0

Parameter	Units	A-051	A-052	A-053	A-054	A-055	A-056	A-057	A-058	A-059	A-060
Temperature	°C	106.42	28	28	28	28	35.86	28	28	28	-177.66
Pressure	kPa	420	420	420	420	420	455.5	455.5	455.5	455.5	410
Mass Enthalpy	kJ/kg	81.73	1.87	1.87	1.87	1.87	9.74	1.77	1.77	1.77	-225.17
Mass Entropy	kJ/(kg.°C)	5.08	4.84	4.84	4.84	4.84	4.84	4.82	4.82	4.82	3.48
Mass Density	kg/m^3	3.85	4.87	4.87	4.87	4.87	5.15	5.28	5.28	5.28	18.54
Mass Flow	kg/h	218410	218410	630425	472819	157606	157606	157606	14185	143422	472819
Molar Flow	kmol/h	7541	7541	21766	16324	5441	5441	5441	489.73	4952	16324
Mole fraction											
C		0	0	0	0	0	0	0	0	0	0
H_2		0	0	0	0	0	0	0	0	0	0
S		0	0	0	0	0	0	0	0	0	0
Ar		0.0097	0.0097	0.0097	0.0097	0.0097	0.0097	0.0097	0.0097	0.0097	0.0097
O_2		0.2095	0.2095	0.2095	0.2095	0.2095	0.2095	0.2095	0.2095	0.2095	0.2095
N_2		0.7808	0.7808	0.7808	0.7808	0.7808	0.7808	0.7808	0.7808	0.7808	0.7808
CO_2		0	0	0	0	0	0	0	0	0	0
H_2O		0	0	0	0	0	0	0	0	0	0
SO_2		0	0	0	0	0	0	0	0	0	0
SiO_2		0	0	0	0	0	0	0	0	0	0
Al_2O_3		0	0	0	0	0	0	0	0	0	0
Fe_2O_3		0	0	0	0	0	0	0	0	0	0
CaO		0	0	0	0	0	0	0	0	0	0
MgO		0	0	0	0	0	0	0	0	0	0
Na_2O		0	0	0	0	0	0	0	0	0	0
K_2O		0	0	0	0	0	0	0	0	0	0
TiO_2		0	0	0	0	0	0	0	0	0	0
Mn_3O_4		0	0	0	0	0	0	0	0	0	0
P_2O_5		0	0	0	0	0	0	0	0	0	0
SO_3		0	0	0	0	0	0	0	0	0	0
$CaCO_3$		0	0	0	0	0	0	0	0	0	0
$CaSO_3$		0	0	0	0	0	0	0	0	0	0
H_2SO_4		0	0	0	0	0	0	0	0	0	0
Cl_2		0	0	0	0	0	0	0	0	0	0

Parameter	Units	A-061	A-062	A-063	A-064	A-065	A-066	A-067	A-068	A-069	A-070
Temperature	°C	-179	10	-177.97	-181.49	-190.77	-187	-193.89	-192.21	-78.99	-182.39
Pressure	kPa	445.5	445.5	410	410	125	410	125	125	112.17	111.33
Mass Enthalpy	kJ/kg	-388.95	-16.4	-385.55	-396.36	-385.55	-407.72	-407.72	-388.95	-103.83	-390.39
Mass Entropy	kJ/(kg.°C)	1.75	4.76	1.72	1.68	1.74	1.55	1.57	1.78	4.79	1.16
Mass Density	kg/m^3	800.73	5.5	854.23	739.84	43.83	768.29	73.42	41.08	2.02	1148.32
Mass Flow	kg/h	143422	14185	276901	195918	276901	195918	195918	143422	14185	145279
Molar Flow	kmol/h	4952	489.73	9346	6978	9346	6978	6978	4952	489.73	4513
Mole fraction											
C		0	0	0	0	0	0	0	0	0	0
H_2		0	0	0	0	0	0	0	0	0	0
S		0	0	0	0	0	0	0	0	0	0
Ar		0.0097	0.0097	0.015	0.0026	0.015	0.0026	0.0026	0.0097	0.0097	0.0243
O_2		0.2095	0.2095	0.36	0.0079	0.36	0.0079	0.0079	0.2095	0.2095	0.9757
N_2		0.7808	0.7808	0.625	0.9895	0.625	0.9895	0.9895	0.7808	0.7808	0
CO_2		0	0	0	0	0	0	0	0	0	0
H_2O		0	0	0	0	0	0	0	0	0	0
SO_2		0	0	0	0	0	0	0	0	0	0
SiO_2		0	0	0	0	0	0	0	0	0	0
Al_2O_3		0	0	0	0	0	0	0	0	0	0
Fe_2O_3		0	0	0	0	0	0	0	0	0	0
CaO		0	0	0	0	0	0	0	0	0	0
MgO		0	0	0	0	0	0	0	0	0	0
Na_2O		0	0	0	0	0	0	0	0	0	0
K_2O		0	0	0	0	0	0	0	0	0	0
TiO_2		0	0	0	0	0	0	0	0	0	0
Mn_3O_4		0	0	0	0	0	0	0	0	0	0
P_2O_5		0	0	0	0	0	0	0	0	0	0
SO_3		0	0	0	0	0	0	0	0	0	0
$CaCO_3$		0	0	0	0	0	0	0	0	0	0
$CaSO_3$		0	0	0	0	0	0	0	0	0	0
H_2SO_4		0	0	0	0	0	0	0	0	0	0
Cl_2		0	0	0	0	0	0	0	0	0	0

Parameter	Units	A-071	A-072	A-073	A-074	A-075	A-076	P-001	P-002	P-003	P-004
Temperature	°C	-194.7	-190.26	25.2	25	25	25	15	15	15	15
Pressure	kPa	111.33	111.33	101.33	101.33	101.33	101.32	101.32	101.32	101.32	101.32
Mass Enthalpy	kJ/kg	-225.15	-220.56	-0.07	-0.3	-0.3	-0.3	-924.92	-15931	-924.91	-78.55
Mass Entropy	kJ/(kg.°C)	3.89	3.95	5.29	4.51	4.51	4.51	4.17	2.83	4.17	5.2
Mass Density	kg/m^3	5.02	4.72	1.15	1.32	1.32	1.32	1.48	1014.81	1.48	3210.8
Mass Flow	kg/h	485147	485147	485147	145279	312018	312018	117066	0	117066	27511
Molar Flow	kmol/h	17253	17253	17253	4513	9692	9692	11470	0	11470	314.54
Mole fraction											
C		0	0	0	0	0	0	0.6758	0	0.6758	0
H_2		0	0	0	0	0	0	0.2592	0	0.2592	0
S		0	0	0	0	0	0	0.0023	0	0.0023	0
Ar		0.0059	0.0059	0.0059	0.0243	0.0243	0.0243	0	0	0	0
O_2		0.0091	0.0091	0.0091	0.9757	0.9757	0.9757	0.0215	0	0.0215	0
N_2		0.985	0.985	0.985	0	0	0	0.0057	0	0.0057	0
CO_2		0	0	0	0	0	0	0	0	0	0
H_2O		0	0	0	0	0	0	0.0354	1	0.0354	0
SO_2		0	0	0	0	0	0	0	0	0	0
SiO_2		0	0	0	0	0	0	0	0	0	0.5005
Al_2O_3		0	0	0	0	0	0	0	0	0	0.3035
Fe_2O_3		0	0	0	0	0	0	0	0	0	0.1327
CaO		0	0	0	0	0	0	0	0	0	0.0131
MgO		0	0	0	0	0	0	0	0	0	0.009
Na_2O		0	0	0	0	0	0	0	0	0	0.001
K_2O		0	0	0	0	0	0	0	0	0	0.002
TiO_2		0	0	0	0	0	0	0	0	0	0.0191
Mn_3O_4		0	0	0	0	0	0	0	0	0	0.003
P_2O_5		0	0	0	0	0	0	0	0	0	0.002
SO_3		0	0	0	0	0	0	0	0	0	0.0141
$CaCO_3$		0	0	0	0	0	0	0	0	0	0
$CaSO_3$		0	0	0	0	0	0	0	0	0	0
H_2SO_4		0	0	0	0	0	0	0	0	0	0
Cl_2		0	0	0	0	0	0	0.0001	0	0.0001	0

Parameter	Units	P-005	P-006	P-007	P-008	P-009	P-010	P-011	P-012	P-013	P-014
Temperature	°C	148.42	25	25	25	2178	2178	2178	2178	2178	2150
Pressure	kPa	101.32	101.32	101.32	101.32	101.32	101.32	101.32	101.32	101.32	101.29
Mass Enthalpy	kJ/kg	-5120.73	-0.3	-0.3	-0.3	1955	-5797	1955	1955	-5683	-5732
Mass Entropy	kJ/(kg.°C)	4.92	4.51	4.51	4.51	7.2	7.34	7.2	7.2	7.34	7.32
Mass Density	kg/m^3	1.18	1.32	1.32	1.32	3241	0.19	3241	3241	0.19	0.19
Mass Flow	kg/h	362892	312018	31202	280816	27156	1361074	6789	20367	1381441	1381441
Molar Flow	kmol/h	16956	9692	969.22	8723	310.12	35901	77.53	232.59	36134	36134
Mole fraction											
C		0.4572	0	0	0	0	0	0	0	0	0
H_2		0.1753	0	0	0	0	0	0	0	0	0
S		0.0015	0	0	0	0	0	0	0	0	0
Ar		0.0082	0.0243	0.0243	0.0243	0	0.022	0	0	0.0219	0.0219
O_2		0.0306	0.9757	0.9757	0.9757	0	0.0421	0	0	0.0418	0.0418
N_2		0.0088	0	0	0	0	0.011	0	0	0.0109	0.0109
CO_2		0.2663	0	0	0	0	0.7163	0	0	0.7117	0.7117
H_2O		0.0334	0	0	0	0	0.2067	0	0	0.2053	0.2053
SO_2		0.0001	0	0	0	0	0.0016	0	0	0.0016	0.0016
SiO_2		0.0093	0	0	0	0.5076	0	0.5076	0.5076	0.0033	0.0033
Al_2O_3		0.0056	0	0	0	0.3078	0	0.3078	0.3078	0.002	0.002
Fe_2O_3		0.0025	0	0	0	0.1346	0	0.1346	0.1346	0.0009	0.0009
CaO		0.0002	0	0	0	0.0133	0	0.0133	0.0133	0.0001	0.0001
MgO		0.0002	0	0	0	0.0092	0	0.0092	0.0092	0.0001	0.0001
Na_2O		0	0	0	0	0.001	0	0.001	0.001	0	0
K_2O		0	0	0	0	0.002	0	0.002	0.002	0	0
TiO_2		0.0004	0	0	0	0.0194	0	0.0194	0.0194	0.0001	0.0001
Mn_3O_4		0.0001	0	0	0	0.0031	0	0.0031	0.0031	0	0
P_2O_5		0	0	0	0	0.002	0	0.002	0.002	0	0
SO_3		0.0003	0	0	0	0	0.0003	0	0	0.0003	0.0003
$CaCO_3$		0	0	0	0	0	0	0	0	0	0
$CaSO_3$		0	0	0	0	0	0	0	0	0	0
H_2SO_4		0	0	0	0	0	0	0	0	0	0
Cl_2		0.0001	0	0	0	0	0.0001	0	0	0.0001	0.0001

Parameter	Units	P-015	P-016	P-017	P-018	P-019	P-020	P-021	P-022	P-023	P-024
Temperature	°C	2004	1786	1545	1186	1049	381.3	222.66	150	150	150
Pressure	kPa	101.26	101.23	101.2	101.17	101.14	101.11	101.11	101.11	101.11	101.11
Mass Enthalpy	kJ/kg	-5977	-6324	-6691	-7213	-7405	-8265	-8443	-8520	-8520	-8520
Mass Entropy	kJ/(kg.°C)	7.21	7.05	6.86	6.54	6.41	5.51	5.20	5.03	5.03	5.03
Mass Density	kg/m^3	0.21	0.23	0.26	0.32	0.35	0.72	0.94	1.11	1.11	1.11
Mass Flow	kg/h	1381441	1381441	1381441	1381441	1381441	1381441	1381441	1381441	659000	722441
Molar Flow	kmol/h	36134	36134	36134	36134	36134	36134	36134	36134	17237	18897
Mole fraction											
C		0	0	0	0	0	0	0	0	0	0
H_2		0	0	0	0	0	0	0	0	0	0
S		0	0	0	0	0	0	0	0	0	0
Ar		0.0219	0.0219	0.0219	0.0219	0.0219	0.0219	0.0219	0.0219	0.0219	0.0219
O_2		0.0418	0.0418	0.0418	0.0418	0.0418	0.0418	0.0418	0.0418	0.0418	0.0418
N_2		0.0109	0.0109	0.0109	0.0109	0.0109	0.0109	0.0109	0.0109	0.0109	0.0109
CO_2		0.7117	0.7117	0.7117	0.7117	0.7117	0.7117	0.7117	0.7117	0.7117	0.7117
H_2O		0.2053	0.2053	0.2053	0.2053	0.2053	0.2053	0.2053	0.2053	0.2053	0.2053
SO_2		0.0016	0.0016	0.0016	0.0016	0.0016	0.0016	0.0016	0.0016	0.0016	0.0016
SiO_2		0.0033	0.0033	0.0033	0.0033	0.0033	0.0033	0.0033	0.0033	0.0033	0.0033
Al_2O_3		0.002	0.002	0.002	0.002	0.002	0.002	0.002	0.002	0.002	0.002
Fe_2O_3		0.0009	0.0009	0.0009	0.0009	0.0009	0.0009	0.0009	0.0009	0.0009	0.0009
CaO		0.0001	0.0001	0.0001	0.0001	0.0001	0.0001	0.0001	0.0001	0.0001	0.0001
MgO		0.0001	0.0001	0.0001	0.0001	0.0001	0.0001	0.0001	0.0001	0.0001	0.0001
Na_2O		0	0	0	0	0	0	0	0	0	0
K_2O		0	0	0	0	0	0	0	0	0	0
TiO_2		0.0001	0.0001	0.0001	0.0001	0.0001	0.0001	0.0001	0.0001	0.0001	0.0001
Mn_3O_4		0	0	0	0	0	0	0	0	0	0
P_2O_5		0	0	0	0	0	0	0	0	0	0
SO_3		0.0003	0.0003	0.0003	0.0003	0.0003	0.0003	0.0003	0.0003	0.0003	0.0003
$CaCO_3$		0	0	0	0	0	0	0	0	0	0
$CaSO_3$		0	0	0	0	0	0	0	0	0	0
H_2SO_4		0	0	0	0	0	0	0	0	0	0
Cl_2		0.0001	0.0001	0.0001	0.0001	0.0001	0.0001	0.0001	0.0001	0.0001	0.0001

Parameter	Units	P-025	P-026	P-027	P-028	P-029	P-030	P-031	P-032	P-033	P-034
Temperature	°C	150	150	15	149.74	152.06	119.14	290	290	150	150
Pressure	kPa	99.11	99.11	101.32	99.11	101.32	101.32	101.32	101.32	101.11	101.11
Mass Enthalpy	kJ/kg	113.51	-8649	-10.33	-8632	-8630	-6192	-6014	-6014	111.95	-8586
Mass Entropy	kJ/(kg.°C)	5.61	5.03	5.21	5.03	5.03	5.01	5.39	5.39	5.53	5.03
Mass Density	kg/m^3	-	1.07	1.23	1.07	1.09	1.12	0.78	0.78	67.93	1.1
Mass Flow	kg/h	10651	711790	1424	713214	713214	994030	994030	994136	5006	653994
Molar Flow	kmol/h	121.63	18775	49.16	18824	18824	27547	27547	27550	57.56	17180
Mole fraction											
C		0	0	0	0	0	0	0	0	0	0
H_2		0	0	0	0	0	0	0	0	0	0
S		0	0	0	0	0	0	0	0	0	0
Ar		0	0.022	0.0097	0.022	0.022	0.0227	0.0227	0.0227	0	0.0219
O_2		0	0.0421	0.2095	0.0425	0.0425	0.338	0.338	0.338	0	0.042
N_2		0	0.011	0.7808	0.013	0.013	0.0089	0.0089	0.0089	0	0.0109
CO_2		0	0.7163	0	0.7144	0.7144	0.4882	0.4882	0.4882	0	0.7141
H_2O		0	0.2067	0	0.2061	0.2061	0.1409	0.1409	0.1408	0	0.206
SO_2		0	0.0016	0	0.0016	0.0016	0.0011	0.0011	0.0011	0	0.0016
SiO_2		0.5076	0	0	0	0	0	0	0	0.4893	0.0016
Al_2O_3		0.3078	0	0	0	0	0	0	0	0.2967	0.001
Fe_2O_3		0.1346	0	0	0	0	0	0	0	0.1297	0.0004
CaO		0.0133	0	0	0	0	0	0	0	0.0128	0
MgO		0.0092	0	0	0	0	0	0	0	0.0088	0
Na_2O		0	0	0	0	0	0	0	0	0.001	0
K_2O		0	0	0	0	0	0	0	0	0.002	0
TiO_2		0.0194	0	0	0	0	0	0	0	0.0187	0.0001
Mn_3O_4		0.0031	0	0	0	0	0	0	0	0.0029	0
P_2O_5		0	0	0	0	0	0	0	0	0.002	0
SO_3		0	0.0003	0	0.0003	0.0003	0.0002	0.0002	0.0002	0	0.0003
$CaCO_3$		0	0	0	0	0	0	0	0	0	0
$CaSO_3$		0	0	0	0	0	0	0	0	0	0
H_2SO_4		0	0	0	0	0	0	0	0	0	0
Cl_2		0	0.0001	0	0.0001	0.0001	0.0001	0.0001	0.0001	0.0362	0

Parameter	Units	P-035	P-036	P-037	P-038	P-039	P-040	P-041	P-042	P-043	P-044
Temperature	°C	15	65.95	65.95	66.5	66.5	66.5	15	66.4	68.35	15
Pressure	kPa	101.32	101.11	101.11	101.11	99.11	99.11	101.32	99.11	101.30	101.3
Mass Enthalpy	kJ/kg	-15545	-5450	-8897	-8830	37.68	-8894	-10.33	-8876	-8874	-15931
Mass Entropy	kJ/(kg.°C)	3.02	4.66	4.99	4.99	5.41	4.99	5.21	5	5	2.83
Mass Density	kg/m^3	1083	1639	1.32	1.33	3241	1.29	1.23	1.29	1.31	1015
Mass Flow	kg/h	25790	9158	670627	675633	4858	670775	1342	672117	672117	5199100
Molar Flow	kmol/h	1314	152.32	18341	18399	55.48	18344	46.33	18390	18390	288597
Mole fraction											
C		0	0	0	0	0	0	0	0	0	0
H_2		0	0	0	0	0	0	0	0	0	0
S		0	0	0	0	0	0	0	0	0	0
Ar		0	0	0.0205	0.0205	0	0.0205	0.0097	0.0205	0.0205	0
O_2		0	0	0.0393	0.0392	0	0.0393	0.2095	0.0397	0.0397	0
N_2		0	0	0.0102	0.0102	0	0.0102	0.7808	0.0122	0.0122	0
CO_2		0	0.0001	0.6701	0.668	0	0.67	0	0.6683	0.6683	0
H_2O		0.9804	0.4666	0.2593	0.2585	0	0.2593	0	0.2587	0.2587	1
SO_2		0	0	0.0003	0.0003	0	0.0003	0	0.0003	0.0003	0
SiO_2		0	0.1849	0	0.0015	0.5076	0	0	0	0	0
Al_2O_3		0	0.1121	0	0.0009	0.3078	0	0	0	0	0
Fe_2O_3		0	0.049	0	0.0004	0.1346	0	0	0	0	0
CaO		0	0.0048	0	0	0.0133	0	0	0	0	0
MgO		0	0.0033	0	0	0.0092	0	0	0	0	0
Na_2O		0	0.0004	0	0	0.001	0	0	0	0	0
K_2O		0	0.0007	0	0	0.002	0	0	0	0	0
TiO_2		0	0.0071	0	0.0001	0.0194	0	0	0	0	0
Mn_3O_4		0	0.0011	0	0	0.0031	0	0	0	0	0
P_2O_5		0	0.0007	0	0	0.002	0	0	0	0	0
SO_3		0	0	0.0002	0.0002	0	0.0002	0	0.0002	0.0002	0
$CaCO_3$		0.0196	0.0254	0	0	0	0	0	0	0	0
$CaSO_3$		0	0.1438	0	0	0	0	0	0	0	0
H_2SO_4		0	0	0	0	0	0	0	0	0	0
Cl_2		0	0	0	0.0001	0	0.0001	0	0.0001	0.0001	0

Parameter	Units	P-045	P-046	P-047	P-048	P-049	P-050	P-051	P-052	P-053	FW-01
Temperature	°C	24.89	24.93	24.93	24.93	24.93	24.95	350	350	26	299
Pressure	kPa	101.3	101.3	101.3	101.3	101.3	101.32	101.32	101.32	101.3	32407
Mass Enthalpy	kJ/kg	-15123	-15880	-8324	-8324	-8324	-8324	-8006	-8006	-8323	-14608
Mass Entropy	kJ/(kg.°C)	3.09	2.98	4.12	4.12	4.12	4.12	4.83	4.83	4.12	5.89
Mass Density	kg/m^3	17.05	1008	1.73	1.73	1.73	1.73	0.83	0.83	1.73	777.36
Mass Flow	kg/h	5871217	5282955	588262	369947	218315	218315	218315	218315	369947	1364826
Molar Flow	kmol/h	306987	293048	13935	8763	5171	5171	5171	5171	8763	75760
Mole fraction											
C		0	0	0	0	0	0	0	0	0	0
H_2		0	0	0	0	0	0	0	0	0	0
S		0	0	0	0	0	0	0	0	0	0
Ar		0.0012	0	0.0271	0.0271	0.0271	0.0271	0.0271	0.0270	0.0271	0
O_2		0.0024	0	0.0524	0.0524	0.0524	0.0524	0.0524	0.0525	0.0524	0
N_2		0.0007	0	0.0161	0.0161	0.0161	0.0161	0.0161	0.0161	0.0161	0
CO_2		0.04	0.0004	0.873	0.873	0.873	0.873	0.873	0.873	0.873	0
H_2O		0.9556	0.9996	0.031	0.031	0.031	0.031	0.031	0.031	0.031	1
SO_2		0	0	0.0002	0.0002	0.0002	0.0002	0.0002	0.0002	0.0002	0
SiO_2		0	0	0	0	0	0	0	0	0	0
Al_2O_3		0	0	0	0	0	0	0	0	0	0
Fe_2O_3		0	0	0	0	0	0	0	0	0	0
CaO		0	0	0	0	0	0	0	0	0	0
MgO		0	0	0	0	0	0	0	0	0	0
Na_2O		0	0	0	0	0	0	0	0	0	0
K_2O		0	0	0	0	0	0	0	0	0	0
TiO_2		0	0	0	0	0	0	0	0	0	0
Mn_3O_4		0	0	0	0	0	0	0	0	0	0
P_2O_5		0	0	0	0	0	0	0	0	0	0
SO_3		0	0	0	0	0	0	0	0	0	0
$CaCO_3$		0	0	0	0	0	0	0	0	0	0
$CaSO_3$		0	0	0	0	0	0	0	0	0	0
H_2SO_4		0	0	0	0	0	0	0	0	0	0
Cl_2		0	0	0.0001	0.0001	0.0001	0.0001	0.0001	0.0001	0.0001	0

Parameter	Units	FW-02	FW-03	FW-04	FW-05	FW-06	FW-07	FW-08	FW-09	FW-10	FW-11
Temperature	°C	399	401	450	500	600	365.1	365.1	365.1	450	620
Pressure	kPa	31907	31407	30907	30407	30000	7500	7500	7500	7300	7000
Mass Enthalpy	kJ/kg	-13737	-13688	-13160	-12912	-12560	-12904	-12904	-12904	-12690	-12281
Mass Entropy	kJ/(kg.°C)	7.27	7.35	8.11	8.45	8.89	8.97	8.97	8.97	9.29	9.82
Mass Density	kg/m^3	313.03	294.73	154.15	117.58	87.56	29.8	29.8	29.8	23.99	17.61
Mass Flow	kg/h	1364826	1364826	1364826	1364826	1364826	1364826	126929	1237897	1237897	1237897
Molar Flow	kmol/h	75760	75760	75760	75760	75760	75760	7046	68714	68714	68714
Mole fraction											
C		0	0	0	0	0	0	0	0	0	0
H_2		0	0	0	0	0	0	0	0	0	0
S		0	0	0	0	0	0	0	0	0	0
Ar		0	0	0	0	0	0	0	0	0	0
O_2		0	0	0	0	0	0	0	0	0	0
N_2		0	0	0	0	0	0	0	0	0	0
CO_2		0	0	0	0	0	0	0	0	0	0
H_2O		1	1	1	1	1	1	1	1	1	1
SO_2		0	0	0	0	0	0	0	0	0	0
SiO_2		0	0	0	0	0	0	0	0	0	0
Al_2O_3		0	0	0	0	0	0	0	0	0	0
Fe_2O_3		0	0	0	0	0	0	0	0	0	0
CaO		0	0	0	0	0	0	0	0	0	0
MgO		0	0	0	0	0	0	0	0	0	0
Na_2O		0	0	0	0	0	0	0	0	0	0
K_2O		0	0	0	0	0	0	0	0	0	0
TiO_2		0	0	0	0	0	0	0	0	0	0
Mn_3O_4		0	0	0	0	0	0	0	0	0	0
P_2O_5		0	0	0	0	0	0	0	0	0	0
SO_3		0	0	0	0	0	0	0	0	0	0
$CaCO_3$		0	0	0	0	0	0	0	0	0	0
$CaSO_3$		0	0	0	0	0	0	0	0	0	0
H_2SO_4		0	0	0	0	0	0	0	0	0	0
Cl_2		0	0	0	0	0	0	0	0	0	0

Parameter	Units	FW-12	FW-13	FW-14	FW-15	FW-16	FW-17	FW-18	FW-19	FW-20	FW-21
Temperature	°C	558.01	558.01	558.01	459.7	459.7	459.7	381.02	381.02	381.02	296.7
Pressure	kPa	4800	4800	4800	2500	2500	2500	1400	1400	1400	700
Mass Enthalpy	kJ/kg	-12404	-12404	-12404	-12598	-12598	-12598	-12751	-12751	-12751	-12914
Mass Entropy	kJ/(kg.°C)	9.84	9.84	9.84	9.89	9.89	9.89	9.93	9.93	9.93	9.97
Mass Density	kg/m^3	12.95	12.95	12.95	7.61	7.61	7.61	4.75	4.75	4.75	2.71
Mass Flow	kg/h	1237897	92223	1145674	1145674	60721	1084953	1084953	121298	963655	963655
Molar Flow	kmol/h	68714	5119	63595	63595	3371	60225	60225	6733	53492	53492
Mole fraction											
C		0	0	0	0	0	0	0	0	0	0
H_2		0	0	0	0	0	0	0	0	0	0
S		0	0	0	0	0	0	0	0	0	0
Ar		0	0	0	0	0	0	0	0	0	0
O_2		0	0	0	0	0	0	0	0	0	0
N_2		0	0	0	0	0	0	0	0	0	0
CO_2		0	0	0	0	0	0	0	0	0	0
H_2O		1	1	1	1	1	1	1	1	1	1
SO_2		0	0	0	0	0	0	0	0	0	0
SiO_2		0	0	0	0	0	0	0	0	0	0
Al_2O_3		0	0	0	0	0	0	0	0	0	0
Fe_2O_3		0	0	0	0	0	0	0	0	0	0
CaO		0	0	0	0	0	0	0	0	0	0
MgO		0	0	0	0	0	0	0	0	0	0
Na_2O		0	0	0	0	0	0	0	0	0	0
K_2O		0	0	0	0	0	0	0	0	0	0
TiO_2		0	0	0	0	0	0	0	0	0	0
Mn_3O_4		0	0	0	0	0	0	0	0	0	0
P_2O_5		0	0	0	0	0	0	0	0	0	0
SO_3		0	0	0	0	0	0	0	0	0	0
$CaCO_3$		0	0	0	0	0	0	0	0	0	0
$CaSO_3$		0	0	0	0	0	0	0	0	0	0
H_2SO_4		0	0	0	0	0	0	0	0	0	0
Cl_2		0	0	0	0	0	0	0	0	0	0

Parameter	Units	FW-22	FW-23	FW-24	FW-25	FW-26	FW-27	FW-28	FW-29	FW-30	FW-31
Temperature	°C	29.68	24.95	24.99	24.99	24.99	24.99	24.99	24.99	24.99	24.99
Pressure	kPa	4.1	3.1	250	250	250	250	250	250	250	250
Mass Enthalpy	kJ/kg	-13659	-15888	-15888	-15888	-15888	-15888	-15888	-15888	-15888	-15888
Mass Entropy	kJ/(kg.°C)	10.34	2.98	2.98	2.98	2.98	2.98	2.98	2.98	2.98	2.98
Mass Density	kg/m^3	0.03	1007.35	1007.39	1007.39	1007.39	1007.39	1007.39	1007.39	1007.39	1007.39
Mass Flow	kg/h	963655	963655	963655	380644	322825	260187	141600	119522	119522	63720
Molar Flow	kmol/h	53492	53492	53492	21129	17920	14443	7860	6635	6635	3537
Mole fraction											
C		0	0	0	0	0	0	0	0	0	0
H_2		0	0	0	0	0	0	0	0	0	0
S		0	0	0	0	0	0	0	0	0	0
Ar		0	0	0	0	0	0	0	0	0	0
O_2		0	0	0	0	0	0	0	0	0	0
N_2		0	0	0	0	0	0	0	0	0	0
CO_2		0	0	0	0	0	0	0	0	0	0
H_2O		1	1	1	1	1	1	1	1	1	1
SO_2		0	0	0	0	0	0	0	0	0	0
SiO_2		0	0	0	0	0	0	0	0	0	0
Al_2O_3		0	0	0	0	0	0	0	0	0	0
Fe_2O_3		0	0	0	0	0	0	0	0	0	0
CaO		0	0	0	0	0	0	0	0	0	0
MgO		0	0	0	0	0	0	0	0	0	0
Na_2O		0	0	0	0	0	0	0	0	0	0
K_2O		0	0	0	0	0	0	0	0	0	0
TiO_2		0	0	0	0	0	0	0	0	0	0
Mn_3O_4		0	0	0	0	0	0	0	0	0	0
P_2O_5		0	0	0	0	0	0	0	0	0	0
SO_3		0	0	0	0	0	0	0	0	0	0
$CaCO_3$		0	0	0	0	0	0	0	0	0	0
$CaSO_3$		0	0	0	0	0	0	0	0	0	0
H_2SO_4		0	0	0	0	0	0	0	0	0	0
Cl_2		0	0	0	0	0	0	0	0	0	0

Parameter	Units	FW-32	FW-33	FW-34	FW-35	FW-36	FW-37	FW-38	FW-39	FW-40	FW-41
Temperature	°C	24.99	83.71	87.72	85.92	24.99	24.99	85.18	89.29	87.44	24.99
Pressure	kPa	250	250	250	250	250	250	250	250	250	250
Mass Enthalpy	kJ/kg	-15888	-15634	-15616	-15624	-15888	-15888	-15627	-15609	-15617	-15888
Mass Entropy	kJ/(kg.°C)	2.98	3.76	3.81	3.79	2.98	2.98	3.78	3.83	3.8	2.98
Mass Density	kg/m^3	1007.39	961.46	958.17	959.65	1007	1007	960.26	956.88	958.4	1007
Mass Flow	kg/h	77880	63720	77880	141600	53785	65737	53785	65737	119522	53785
Molar Flow	kmol/h	4323	3537	4323	7860	2986	3649	2986	3649	6635	2986
Mole fraction											
C		0	0	0	0	0	0	0	0	0	0
H_2		0	0	0	0	0	0	0	0	0	0
S		0	0	0	0	0	0	0	0	0	0
Ar		0	0	0	0	0	0	0	0	0	0
O_2		0	0	0	0	0	0	0	0	0	0
N_2		0	0	0	0	0	0	0	0	0	0
CO_2		0	0	0	0	0	0	0	0	0	0
H_2O		1	1	1	1	1	1	1	1	1	1
SO_2		0	0	0	0	0	0	0	0	0	0
SiO_2		0	0	0	0	0	0	0	0	0	0
Al_2O_3		0	0	0	0	0	0	0	0	0	0
Fe_2O_3		0	0	0	0	0	0	0	0	0	0
CaO		0	0	0	0	0	0	0	0	0	0
MgO		0	0	0	0	0	0	0	0	0	0
Na_2O		0	0	0	0	0	0	0	0	0	0
K_2O		0	0	0	0	0	0	0	0	0	0
TiO_2		0	0	0	0	0	0	0	0	0	0
Mn_3O_4		0	0	0	0	0	0	0	0	0	0
P_2O_5		0	0	0	0	0	0	0	0	0	0
SO_3		0	0	0	0	0	0	0	0	0	0
$CaCO_3$		0	0	0	0	0	0	0	0	0	0
$CaSO_3$		0	0	0	0	0	0	0	0	0	0
H_2SO_4		0	0	0	0	0	0	0	0	0	0
Cl_2		0	0	0	0	0	0	0	0	0	0

Parameter	Units	FW-42	FW-43	FW-44	FW-45	FW-46	FW-47	FW-48	FW-49	FW-50	FW-51
Temperature	°C	24.99	85.18	89.29	87.44	24.99	24.99	24.99	24.99	24.99	85.05
Pressure	kPa	250	250	250	250	250	250	250	250	250	250
Mass Enthalpy	kJ/kg	-15888	-15627	-15609	-15617	-15888	-15888	-15888	-15888	-15888	-15628
Mass Entropy	kJ/(kg.°C)	2.98	3.78	3.83	3.8	2.98	2.98	2.98	2.98	2.98	3.78
Mass Density	kg/m^3	1007	960.26	956.88	958.4	1007	1007	1007	1007	1007	960.37
Mass Flow	kg/h	65737	53785	65737	119522	96847	112989	112989	45518	51329	45518
Molar Flow	kmol/h	3649	2986	3649	6635	5376	6272	6272	2527	2849	2527
Mole fraction											
C		0	0	0	0	0	0	0	0	0	0
H_2		0	0	0	0	0	0	0	0	0	0
S		0	0	0	0	0	0	0	0	0	0
Ar		0	0	0	0	0	0	0	0	0	0
O_2		0	0	0	0	0	0	0	0	0	0
N_2		0	0	0	0	0	0	0	0	0	0
CO_2		0	0	0	0	0	0	0	0	0	0
H_2O		1	1	1	1	1	1	1	1	1	1
SO_2		0	0	0	0	0	0	0	0	0	0
SiO_2		0	0	0	0	0	0	0	0	0	0
Al_2O_3		0	0	0	0	0	0	0	0	0	0
Fe_2O_3		0	0	0	0	0	0	0	0	0	0
CaO		0	0	0	0	0	0	0	0	0	0
MgO		0	0	0	0	0	0	0	0	0	0
Na_2O		0	0	0	0	0	0	0	0	0	0
K_2O		0	0	0	0	0	0	0	0	0	0
TiO_2		0	0	0	0	0	0	0	0	0	0
Mn_3O_4		0	0	0	0	0	0	0	0	0	0
P_2O_5		0	0	0	0	0	0	0	0	0	0
SO_3		0	0	0	0	0	0	0	0	0	0
$CaCO_3$		0	0	0	0	0	0	0	0	0	0
$CaSO_3$		0	0	0	0	0	0	0	0	0	0
H_2SO_4		0	0	0	0	0	0	0	0	0	0
Cl_2		0	0	0	0	0	0	0	0	0	0

Parameter	Units	FW-52	FW-53	FW-54	FW-55	FW-56	FW-57	FW-58	FW-59	FW-60	FW-61
Temperature	°C	94.47	90.04	24.99	24.99	85.64	89.78	87.91	24.99	24.99	85.64
Pressure	kPa	250	250	250	250	250	250	250	250	250	250
Mass Enthalpy	kJ/kg	-15586	-15606	-15888	-15888	-15625	-15607	-15615	-15888	-15888	-15625
Mass Entropy	kJ/(kg.°C)	3.89	3.84	2.98	2.98	3.78	3.83	3.81	2.98	2.98	3.78
Mass Density	kg/m^3	952.58	956.25	1007	1007	959.88	956.48	958.01	1007	1007	959.88
Mass Flow	kg/h	51329	96847	50845	62144	50845	62144	112989	50845	62144	50845
Molar Flow	kmol/h	2849	5376	2822	3450	2822	3450	6272	2822	3450	2822
Mole fraction											
C		0	0	0	0	0	0	0	0	0	0
H_2		0	0	0	0	0	0	0	0	0	0
S		0	0	0	0	0	0	0	0	0	0
Ar		0	0	0	0	0	0	0	0	0	0
O_2		0	0	0	0	0	0	0	0	0	0
N_2		0	0	0	0	0	0	0	0	0	0
CO_2		0	0	0	0	0	0	0	0	0	0
H_2O		1	1	1	1	1	1	1	1	1	1
SO_2		0	0	0	0	0	0	0	0	0	0
SiO_2		0	0	0	0	0	0	0	0	0	0
Al_2O_3		0	0	0	0	0	0	0	0	0	0
Fe_2O_3		0	0	0	0	0	0	0	0	0	0
CaO		0	0	0	0	0	0	0	0	0	0
MgO		0	0	0	0	0	0	0	0	0	0
Na_2O		0	0	0	0	0	0	0	0	0	0
K_2O		0	0	0	0	0	0	0	0	0	0
TiO_2		0	0	0	0	0	0	0	0	0	0
Mn_3O_4		0	0	0	0	0	0	0	0	0	0
P_2O_5		0	0	0	0	0	0	0	0	0	0
SO_3		0	0	0	0	0	0	0	0	0	0
$CaCO_3$		0	0	0	0	0	0	0	0	0	0
$CaSO_3$		0	0	0	0	0	0	0	0	0	0
H_2SO_4		0	0	0	0	0	0	0	0	0	0
Cl_2		0	0	0	0	0	0	0	0	0	0

Parameter	Units	FW-62	FW-63	FW-64	FW-65	FW-66	FW-67	FW-68	FW-69	FW-70	FW-71
Temperature	°C	89.78	87.91	24.99	24.99	24.99	125.06	127.37	80.92	86.93	117.65
Pressure	kPa	250	250	250	250	250	250	250	250	250	250
Mass Enthalpy	kJ/kg	-15607	-15615	-15888	-15888	-15888	-15451	-15405	-15646	-15619	-15484
Mass Entropy	kJ/(kg.°C)	3.83	3.81	2.98	2.98	2.98	4.24	4.36	3.72	3.8	4.16
Mass Density	kg/m^3	956.48	958.01	1007	1007	1007	926.33	78.58	963.74	958.82	932.84
Mass Flow	kg/h	62144	112989	65047	111880	83260	65047	111880	83260	786728	786728
Molar Flow	kmol/h	3450	6272	3611	6210	4622	3611	6210	4622	43670	43670
Mole fraction											
C		0	0	0	0	0	0	0	0	0	0
H_2		0	0	0	0	0	0	0	0	0	0
S		0	0	0	0	0	0	0	0	0	0
Ar		0	0	0	0	0	0	0	0	0	0
O_2		0	0	0	0	0	0	0	0	0	0
N_2		0	0	0	0	0	0	0	0	0	0
CO_2		0	0	0	0	0	0	0	0	0	0
H_2O		1	1	1	1	1	1	1	1	1	1
SO_2		0	0	0	0	0	0	0	0	0	0
SiO_2		0	0	0	0	0	0	0	0	0	0
Al_2O_3		0	0	0	0	0	0	0	0	0	0
Fe_2O_3		0	0	0	0	0	0	0	0	0	0
CaO		0	0	0	0	0	0	0	0	0	0
MgO		0	0	0	0	0	0	0	0	0	0
Na_2O		0	0	0	0	0	0	0	0	0	0
K_2O		0	0	0	0	0	0	0	0	0	0
TiO_2		0	0	0	0	0	0	0	0	0	0
Mn_3O_4		0	0	0	0	0	0	0	0	0	0
P_2O_5		0	0	0	0	0	0	0	0	0	0
SO_3		0	0	0	0	0	0	0	0	0	0
$CaCO_3$		0	0	0	0	0	0	0	0	0	0
$CaSO_3$		0	0	0	0	0	0	0	0	0	0
H_2SO_4		0	0	0	0	0	0	0	0	0	0
Cl_2		0	0	0	0	0	0	0	0	0	0

Parameter	Units	FW-72	FW-73	FW-74	FW-75	FW-76	FW-77	FW-78	FW-79	FW-80	FW-81
Temperature	°C	120.21	120.37	292.16	266.21	262.3	224.52	224.54	220	193.62	200.63
Pressure	kPa	250	1700	4781	7300	4781	4581	2500	2300	1400	32650
Mass Enthalpy	kJ/kg	-15473	-15471	-13021	-14755	-14025	-14979	-14462	-15002	-15133	-15086
Mass Entropy	kJ/(kg.°C)	4.19	4.19	8.95	5.71	7.08	5.29	6.33	5.25	4.97	4.98
Mass Density	kg/m^3	930.6	931.21	21.26	776.8	50.35	828.8	42.3	831.7	860.67	879.06
Mass Flow	kg/h	963655	963655	92223	126929	219152	219152	279873	279873	1364826	1364826
Molar Flow	kmol/h	53492	53492	5119	7046	12165	12165	15535	15535	75760	75760
Mole fraction											
C		0	0	0	0	0	0	0	0	0	0
H_2		0	0	0	0	0	0	0	0	0	0
S		0	0	0	0	0	0	0	0	0	0
Ar		0	0	0	0	0	0	0	0	0	0
O_2		0	0	0	0	0	0	0	0	0	0
N_2		0	0	0	0	0	0	0	0	0	0
CO_2		0	0	0	0	0	0	0	0	0	0
H_2O		1	1	1	1	1	1	1	1	1	1
SO_2		0	0	0	0	0	0	0	0	0	0
SiO_2		0	0	0	0	0	0	0	0	0	0
Al_2O_3		0	0	0	0	0	0	0	0	0	0
Fe_2O_3		0	0	0	0	0	0	0	0	0	0
CaO		0	0	0	0	0	0	0	0	0	0
MgO		0	0	0	0	0	0	0	0	0	0
Na_2O		0	0	0	0	0	0	0	0	0	0
K_2O		0	0	0	0	0	0	0	0	0	0
TiO_2		0	0	0	0	0	0	0	0	0	0
Mn_3O_4		0	0	0	0	0	0	0	0	0	0
P_2O_5		0	0	0	0	0	0	0	0	0	0
SO_3		0	0	0	0	0	0	0	0	0	0
$CaCO_3$		0	0	0	0	0	0	0	0	0	0
$CaSO_3$		0	0	0	0	0	0	0	0	0	0
H_2SO_4		0	0	0	0	0	0	0	0	0	0
Cl_2		0	0	0	0	0	0	0	0	0	0

Parameter	Units	FW-82	FW-83	FW-84	FW-85	G-01	G-02	G-03	G-04	G-05	G-06
Temperature	°C	224	255	292	299	26	127.69	45	151.99	28	28
Pressure	kPa	32600	32550	32500	32406.92	101.3	318.44	318.44	1001	1001	1001
Mass Enthalpy	kJ/kg	-14975	-14822	-14650	-14608	-8325	-8233	-8310	-8213	-8359	-15806
Mass Entropy	kJ/(kg.°C)	5.21	5.51	5.81	5.89	4.12	4.16	3.94	3.98	3.57	3.03
Mass Density	kg/m^3	857.36	826.62	785.97	777.36	1.73	4.06	5.15	12.13	18.22	1006.99
Mass Flow	kg/h	1364826	1364826	1364826	1364826	369855	369855	369855	369855	369855	4276
Molar Flow	kmol/h	75760	75760	75760	75760	8762	8762	8762	8762	8762	236.01
Mole fraction											
C		0	0	0	0	0	0	0	0	0	0
H_2		0	0	0	0	0	0	0	0	0	0
S		0	0	0	0	0	0	0	0	0	0
Ar		0	0	0	0	0.0271	0.0271	0.0271	0.0271	0.0271	0
O_2		0	0	0	0	0.0524	0.0524	0.0524	0.0524	0.0524	0
N_2		0	0	0	0	0.0161	0.0161	0.0161	0.0161	0.0161	0
CO_2		0	0	0	0	0.8732	0.8732	0.8732	0.8732	0.8732	0.0039
H_2O		1	1	1	1	0.031	0.031	0.031	0.031	0.031	0.996
SO_2		0	0	0	0	0.0002	0.0002	0.0002	0.0002	0.0002	0.0001
SiO_2		0	0	0	0	0	0	0	0	0	0
Al_2O_3		0	0	0	0	0	0	0	0	0	0
Fe_2O_3		0	0	0	0	0	0	0	0	0	0
CaO		0	0	0	0	0	0	0	0	0	0
MgO		0	0	0	0	0	0	0	0	0	0
Na_2O		0	0	0	0	0	0	0	0	0	0
K_2O		0	0	0	0	0	0	0	0	0	0
TiO_2		0	0	0	0	0	0	0	0	0	0
Mn_3O_4		0	0	0	0	0	0	0	0	0	0
P_2O_5		0	0	0	0	0	0	0	0	0	0
SO_3		0	0	0	0	0	0	0	0	0	0
$CaCO_3$		0	0	0	0	0	0	0	0	0	0
$CaSO_3$		0	0	0	0	0	0	0	0	0	0
H_2SO_4		0	0	0	0	0	0	0	0	0	0
Cl_2		0	0	0	0	0	0	0	0	0	0

Parameter	Units	G-07	G-08	G-09	G-10	G-11	G-12	G-13	G-14	G-15	G-16
Temperature	°C	28	88.48	33.01	33.01	33.01	60.87	25	25	25	25
Pressure	kPa	1001	2001	2001	2001	2001	2801	2801	2801	2801	2800
Mass Enthalpy	kJ/kg	-8272	-8223	-8278	-15735	-8275	-8254	-8292	-15696	-8287	-15885
Mass Entropy	kJ/(kg.°C)	3.58	3.6	3.43	3.1	3.43	3.44	3.32	2.98	3.32	2.98
Mass Density	kg/m^3	18.01	30.09	37.19	1004.65	37.17	47.90	56.78	1012.78	56.74	1008.14
Mass Flow	kg/h	365578	365578	365578	154	365424	365424	365424	247	365177	271
Molar Flow	kmol/h	8526	8526	8526	8	8518	8518	8518	13.52	8504	15.06
Mole fraction											
C		0	0	0	0	0	0	0	0	0	0
H_2		0	0	0	0	0	0	0	0	0	0
S		0	0	0	0	0	0	0	0	0	0
Ar		0.0278	0.0278	0.0278	0	0.0278	0.0278	0.0278	0	0.0279	0
O_2		0.0539	0.0539	0.0539	0	0.0539	0.0539	0.0539	0	0.054	0
N_2		0.0165	0.0165	0.0165	0	0.0165	0.0165	0.0165	0	0.0166	0
CO_2		0.8972	0.8972	0.8972	0.0068	0.8981	0.8981	0.8981	0.0111	0.8995	0
H_2O		0.0043	0.0043	0.0043	0.9931	0.0033	0.0033	0.0033	0.9887	0.0018	1
SO_2		0.0002	0.0002	0.0002	0.0001	0.0002	0.0002	0.0002	0.0001	0.0002	0
SiO_2		0	0	0	0	0	0	0	0	0	0
Al_2O_3		0	0	0	0	0	0	0	0	0	0
Fe_2O_3		0	0	0	0	0	0	0	0	0	0
CaO		0	0	0	0	0	0	0	0	0	0
MgO		0	0	0	0	0	0	0	0	0	0
Na_2O		0	0	0	0	0	0	0	0	0	0
K_2O		0	0	0	0	0	0	0	0	0	0
TiO_2		0	0	0	0	0	0	0	0	0	0
Mn_3O_4		0	0	0	0	0	0	0	0	0	0
P_2O_5		0	0	0	0	0	0	0	0	0	0
SO_3		0	0	0	0	0	0	0	0	0	0
$CaCO_3$		0	0	0	0	0	0	0	0	0	0
$CaSO_3$		0	0	0	0	0	0	0	0	0	0
H_2SO_4		0	0	0	0	0	0	0	0	0	0
Cl_2		0	0	0	0	0	0	0	0	0	0

Parameter	Units	G-17	G-18	G-19	G-20	G-21	G-22	G-23	G-24	G-25	G-26	G-27
Temperature	°C	25	-31.1	-33.82	-7.47	-54.31	-10.94	-53.5	-53.5	-53.5	-54.67	-66.09
Pressure	kPa	2800	2800	2800	2800	550	2800	2800	2800	2800	1980	1300
Mass Enthalpy	kJ/kg	-8283	-8584	-8904	-9273	-9273	-8509	-8842	-9037	-2862	-9037	-2862
Mass Entropy	kJ/(kg.°C)	3.31	2.15	2	2.11	2.17	3.15	1.83	1.78	3.29	1.78	3.45
Mass Density	kg/m^3	56.73	327.06	610.93	971.01	49.1	73.43	742.35	1140.77	63.47	753.62	29.38
Mass Flow	kg/h	364906	364906	1614126	324126	324126	1290000	1290000	1249208	40792	1249208	40792
Molar Flow	kmol/h	8489	8489	37186	7364	7364	29822	29822	28697	1125	28697	1125
Mole fraction												
C		0	0	0	0	0	0	0	0	0	0	0
H_2		0	0	0	0	0	0	0	0	0	0	0
S		0	0	0	0	0	0	0	0	0	0	0
Ar		0.0279	0.0279	0.0163	0	0	0.0204	0.0204	0.0129	0.2109	0.0129	0.2109
O_2		0.0541	0.0541	0.0336	0	0	0.0418	0.0418	0.0275	0.4082	0.0275	0.4082
N_2		0.0166	0.0166	0.0084	0	0	0.0105	0.0105	0.006	0.1251	0.006	0.1251
CO_2		0.9011	0.9011	0.9416	0.9997	0.9997	0.9272	0.9272	0.9536	0.2558	0.9536	0.2558
H_2O		0	0	0	0	0	0	0	0	0	0	0
SO_2		0.0002	0.0002	0.0001	0.0003	0.0003	0	0	0	0	0	0
SiO_2		0	0	0	0	0	0	0	0	0	0	0
Al_2O_3		0	0	0	0	0	0	0	0	0	0	0
Fe_2O_3		0	0	0	0	0	0	0	0	0	0	0
CaO		0	0	0	0	0	0	0	0	0	0	0
MgO		0	0	0	0	0	0	0	0	0	0	0
Na_2O		0	0	0	0	0	0	0	0	0	0	0
K_2O		0	0	0	0	0	0	0	0	0	0	0
TiO_2		0	0	0	0	0	0	0	0	0	0	0
Mn_3O_4		0	0	0	0	0	0	0	0	0	0	0
P_2O_5		0	0	0	0	0	0	0	0	0	0	0
SO_3		0	0	0	0	0	0	0	0	0	0	0
$CaCO_3$		0	0	0	0	0	0	0	0	0	0	0
$CaSO_3$		0	0	0	0	0	0	0	0	0	0	0
H_2SO_4		0	0	0	0	0	0	0	0	0	0	0
Cl_2		0	0	0	0	0	0	0	0	0	0	0

Parameter	Units	G-28	G-29	G-30	G-31	G-32	G-33	G-34	G-35	G-36	G-37	G-38
Temperature	°C	-59.89	-5	21.37	-35	-35	-34	117.84	27.84	73.46	0.96	5.75
Pressure	kPa	1300	1980	2800	2800	2800	550	4000	4000	6800	6800	12000
Mass Enthalpy	kJ/kg	-2857	-8676	-8659	-8997.65	-8997	-9003.65	-8887	-8988	-8961	-9255	-9249
Mass Entropy	kJ/(kg.°C)	3.47	3.25	3.26	1.95	1.95	3.39	3.42	3.13	3.13	2.16	2.16
Mass Density	kg/m^3	28.35	45.76	59.51	797.31	797.33	12.95	59.38	93.14	137.39	949.79	958.86
Mass Flow	kg/h	40792	1249208	1249208	1249208	1249220	324126	324126	324126	324126	324126	324126
Molar Flow	kmol/h	1125	28697	28697	28697	28697	7364	7364	7364	7364	7364	7364
Mole fraction												
C		0	0	0	0	0	0	0	0	0	0	0
H_2		0	0	0	0	0	0	0	0	0	0	0
S		0	0	0	0	0	0	0	0	0	0	0
Ar		0.2109	0.0129	0.0129	0.0129	0.0129	0	0	0	0	0	0
O_2		0.4082	0.0275	0.0275	0.0275	0.0275	0	0	0	0	0	0
N_2		0.1251	0.006	0.006	0.006	0.006	0	0	0	0	0	0
CO_2		0.2558	0.9536	0.9536	0.9536	0.9536	0.9997	0.9997	0.9997	0.9997	0.9997	0.9997
H_2O		0	0	0	0	0	0	0	0	0	0	0
SO_2		0	0	0	0	0	0.0003	0.0003	0.0003	0.0003	0.0003	0.0003
SiO_2		0	0	0	0	0	0	0	0	0	0	0
Al_2O_3		0	0	0	0	0	0	0	0	0	0	0
Fe_2O_3		0	0	0	0	0	0	0	0	0	0	0
CaO		0	0	0	0	0	0	0	0	0	0	0
MgO		0	0	0	0	0	0	0	0	0	0	0
Na_2O		0	0	0	0	0	0	0	0	0	0	0
K_2O		0	0	0	0	0	0	0	0	0	0	0
TiO_2		0	0	0	0	0	0	0	0	0	0	0
Mn_3O_4		0	0	0	0	0	0	0	0	0	0	0
P_2O_5		0	0	0	0	0	0	0	0	0	0	0
SO_3		0	0	0	0	0	0	0	0	0	0	0
$CaCO_3$		0	0	0	0	0	0	0	0	0	0	0
$CaSO_3$		0	0	0	0	0	0	0	0	0	0	0
H_2SO_4		0	0	0	0	0	0	0	0	0	0	0
Cl_2		0	0	0	0	0	0	0	0	0	0	0

Table B.14: Heat tables of the oxy-combustion process with heat integration and smaller ASU.

Unit	Heat Flow (GJ/h)	Utility (kg/h)
Q-01	-1.441	68884
Q-02	-89.460	0
Q-03	-1.255	60021
Q-04	-77.951	0
Q-05	0.350	159.43
Q-06	-2148.515	102726025
Q-07	-14.101	674202
Q-08	0.612	153124
Q-09	502.927	125731700
Q-10	-113.040	28259982
Q-11	-423.592	315877983
Q-12	-32.979	1576826
Q-13	-95.270	23817528

Table B.15: Power tables of the oxy-combustion process with heat integration and smaller ASU.

	W-01	W-02	W-03	W-04	W-05	W-06	W-07	W-08	W-09	W-10
Work(kW)	5808.09	5836.21	5025.91	5050.24	5025.91	5050.24	395.37	4243.91	4264.45	4787.65
	W-11	W-12	W-13	W-14	W-15	W-16	W-17	W-18	W-19	W-20
Work(kW)	4810.83	4787.65	4810.83	344.49	477.09	369.10	1.03	-130616	-42341	-61643
	W-21	W-22	W-23	W-24	W-25	W-26	W-27	W-28	W-29	W-30
Work(kW)	-46268	-43564	-199281	87.48	490.37	17969.95	9434.99	9932.02	5039.56	2119.80
	W-31	W-32	W-33	W-34						
Work(kW)	6000.69	10496.13	2428.05	547.70						

Table B.16: Overall carbon balance of the oxy-combustion process with heat integration and smaller ASU.

Carbon In		Carbon Out	
	kg/h		kg/h
Coal	93019.2	Spray dryer out	46.52
Limestone	309.2	DCC out	1491.6
		Dissolved in GPU compression	13.60
		Stack	3454.7
		Storage	88341.8
Total	93328.5	Total	93348.3
		Balance	19.81
		Error (%)	0.02

Table B.17: Energy balance of the oxy-combustion process with heat integration and small ASU. Energy in.

	HHV (GJ/h)	Sensible + Latent (GJ/h)	Power (GJ/h)	Total (GJ/h)
ASU1 - MAC1	0	0	41.92	41.92
ASU1 - MAC2	0	0	36.27	36.27
ASU1 - MAC3	0	0	36.27	36.27
ASU1 - Booster	0	0	1.42	1.42
ASU1 - LP Reboiler	0	89	0	89.46
ASU2 - MAC1	0	0	30.63	30.63
ASU2 - MAC2	0	0	34.55	34.55
ASU2 - MAC3	0	0	34.55	34.55
ASU2 - Booster	0	0	1.24	1.24
ASU2 - LP reboiler	0	77.95	0	77.95
Coal	3919.06	0	0	3919.06
Limestone	52.84	0	0	52.84
ID fan	0	0	1.33	1.33
Primary fan	0	0	0	0.00
Secondary FG fan	0	0	1.72	1.72
Condensate pump	0	0	0.31	0.31
Booster pump	0	0	1.77	1.77
Boiler feed pump	0	0	64.69	64.69
Water	11835.35	0	0	11835.35
Gas heater	0	0.35	0	0.35
GPU - Main compressor	0	0	95.49	95.49
GPU - Gas dryer	0	0.61	0	0.61
GPU - Reboiler	0	502.93	0	502.93
GPU - Recycle compressor	0	0	21.60	21.60
GPU - CO2 compressor	0	0	46.53	46.53
GPU - CO2 pump	0	0	1.97	1.97
Total	15807.26	671.30	452.29	16930.85

Table B.18: Energy balance of the oxy-combustion process with heat integration and small ASU. Energy out.

	HHV (GJ/h)	Sensible + Latent (GJ/h)	Power (GJ/h)	Total (GJ/h)
ASU1 - Turbine	0	0	1.42	1.42
ASU1 - Booster cooling	0	1.44	0	1.44
ASU1 - HP condenser	0	89.46	0	89.46
ASU2 - Turbine	0	0	1.24	1.24
ASU2 - Booster cooling	0	1.26	0	1.26
ASU2 - HP condenser	0	77.95	0	77.95
Slurry	1.74	0	0	1.74
Water	12013	0	0	12012.74
HP turbine	0	0	470.22	470.22
IP turbine	0	0	697.74	697.74
LP turbine	0	0	717.41	717.41
Condenser	0	2149	0	2148.51
GPU - Main comp cooling	0	14.1	0	14.1
GPU - Condensate	10.53	0	0	10.53
GPU - Water	0.62	0	0	0.62
GPU - Condenser	0	113.04	0	113.04
GPU - Gas cooler	0	423.59	0	423.59
GPU - CO2 comp cooling	0	128.25	0	128.25
Stack	0	0	0	0
CO2 for storage	0.02	0	0	0.02
Unaccounted energy				19.56
Unaccounted energy (%)				0.12

B.6 EDEA for oxy-combustion

B.6.1 Scenarios 1 and 2

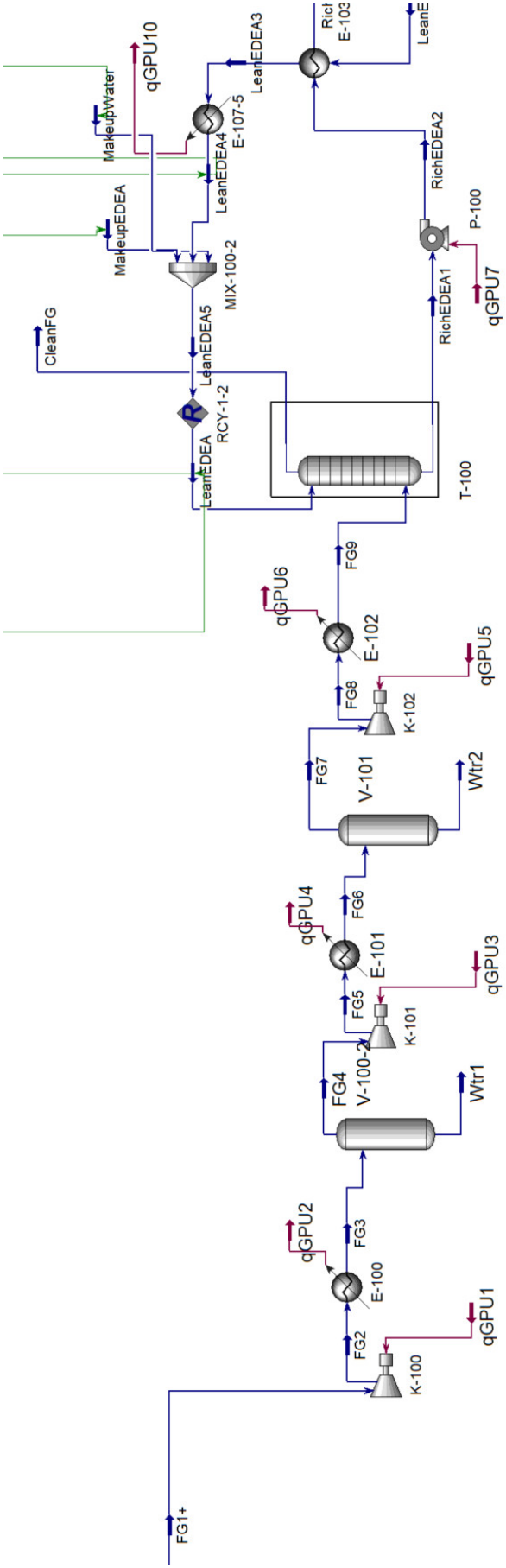
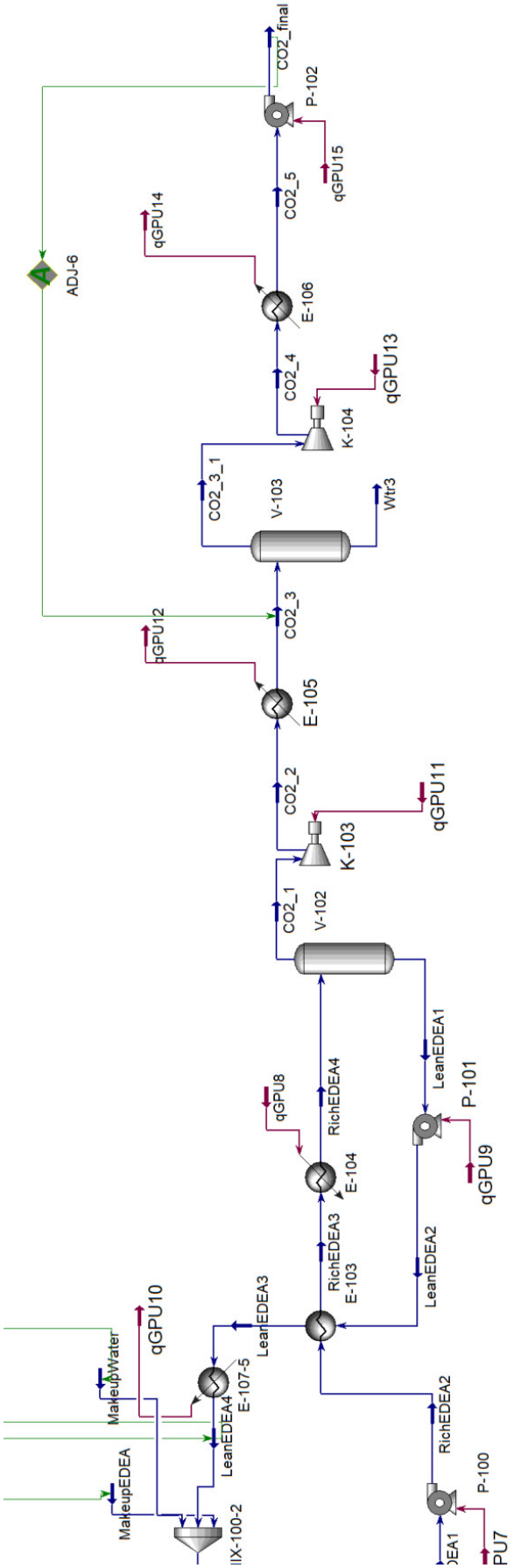


Figure B.7: PFD of the EDEA-based GPU for scenarios 1 and 2.


CO2_final
P-102
qGPU15
CO2_5
qGPU14
ADJ-6
E-106
CO2_4
qGPU13
K-104
CO2_3_1
V-103
Wtr3
CO2_3
qGPU12
E-105
CO2_2
qGPU11
K-103
CO2_1
V-102
LeanEDEA1
P-101
qGPU9
qGPU8
RichEDEA4
E-104
RichEDEA3
E-103
LeanEDEA2
LeanEDEA3
qGPU10
E-107-5
MakeupWater
LeanEDEA4
MakeupEDEA
IIX-100-2
RichEDEA2
P-100
PU7

Cont.

Table B.19: Stream tables of the capture plant using EDEA for a flue gas obtained from oxy-combustion of coal. Scenario 1.

Parameter	Units	FG1+	FG2	FG3	Wtr1	FG4	FG5	FG6	Wtr2	FG7	FG8
Temperature	°C	27	116	25	25	25	113	25	25	25	115
Pressure	kPa	101.3	282.6	282.6	282.6	282.6	788.5	788.5	788.5	788.5	2200
Mass Enthalpy	kJ/kg	-8457	-8378	-8493	-13545	-8408	-8331	-8422	-12284	-8397	-8322
Mass Entropy	kJ/(kg.°C)	0.13	0.16	-0.19	-7.08	-0.07	-0.04	-0.31	-5.75	-0.28	-0.25
Mass Density	kg/m^3	1.73	3.72	5.04	859.23	4.95	10.70	14.30	804.06	14.21	30.76
Viscosity	cP	0.02	0.02	<empty>	0.51	0.02	0.02	<empty>	0.33	0.02	0.02
Mass Flow	kg/h	370642	370642	370642	6127	364515	364515	364515	2378	362138	362138
Molar Flow	kmol/h	8755	8755	8755	258	8496	8496	8496	85	8411	8411
Mole fraction											
H_2O		0.0310	0.0310	0.0310	0.7804	0.0082	0.0082	0.0082	0.6180	0.0021	0.0021
EDEA		0	0	0	0	0	0	0	0	0	0
CO_2		0.8907	0.8907	0.8907	0.2187	0.9112	0.9112	0.9112	0.3796	0.9166	0.9166
H_2S		0	0	0	0	0	0	0	0	0	0
N_2		0.0165	0.0165	0.0165	0.0001	0.0170	0.0170	0.0170	0.0002	0.0172	0.0172
Ar		0.0157	0.0157	0.0157	0.0002	0.0161	0.0161	0.0161	0.0004	0.0163	0.0163
O_2		0.0457	0.0457	0.0457	0.0005	0.0471	0.0471	0.0471	0.0014	0.0475	0.0475
NO_2		0	0	0	0	0	0	0	0	0	0
SO_2		0.0002	0.0002	0.0002	0.0001	0.0002	0.0002	0.0002	0.0003	0.0002	0.0002
SO_3		0	0	0	0	0	0	0	0	0	0
Cl_2		0.0002	0.0002	0.0002	0.0000	0.0002	0.0002	0.0002	0.0001	0.0002	0.0002

Parameter	Units	FG9	LeanEDEA	CleanFG	RichEDEA1	RichEDEA2	RichEDEA3	RichEDEA4	LeanEDEA1
Temperature	°C	25	25	29	30	30	36	44	42
Pressure	kPa	2200	2100	2100	2200	2300	2250	2200	100
Mass Enthalpy	kJ/kg	-8412	-3709	-6642	-4140	-4140	-4123	-4104	-3668
Mass Entropy	kJ/(kg.°C)	-0.51	-7.30	-0.40	-6.69	-6.69	-6.63	-6.57	-7.17
Mass Density	kg/m^3	42.84	863.22	35.79	889.72	890.61	854.23	705.48	852.36
Viscosity	cP	<empty>	51.89	0.02	<empty>	8.85	<empty>	<empty>	20.97
Mass Flow	kg/h	362138	3283225	45352	3600010	3600010	3600010	3600010	3283147
Molar Flow	kmol/h	8411	25503	1132	32782	32782	32782	32782	25501
Mole fraction									
H_2O		0.0021	0.0300	0	0.0239	0.0239	0.0239	0.0239	0.0300
EDEA		0	0.9588	0	0.7459	0.7459	0.7459	0.7459	0.9589
CO_2		0.9166	0.0109	0.6752	0.2203	0.2203	0.2203	0.2203	0.0109
H_2S		0	0	0	0	0	0	0	0
N_2		0.0172	0.0000	0.1248	0.0001	0.0001	0.0001	0.0001	0
Ar		0.0163	0.0000	0.0564	0.0023	0.0023	0.0023	0.0023	0
O_2		0.0475	0.0001	0.1436	0.0073	0.0073	0.0073	0.0073	0.0001
NO_2		0	0	0	0	0	0	0	0
SO_2		0.0002	0.0000	0.0000	0.0001	0.0001	0.0001	0.0001	0
SO_3		0	0	0	0	0	0	0	0
Cl_2		0.0002	0.0000	0.0000	0.0001	0.0001	0.0001	0.0001	0

Parameter	Units	CO2_1	LeanEDEA2	LeanEDEA3	LeanEDEA4	MakeupEDEA	MakeupWater	LeanEDEA5
Temperature	°C	42	43	35	25	25	25	25
Pressure	kPa	100	2200	2150	2100	2100	2100	2100
Mass Enthalpy	kJ/kg	-8628	-3665	-3684	-3709	-3671	-15864	-3709
Mass Entropy	kJ/(kg.°C)	0.15	-7.16	-7.22	-7.30	-7.33	-9.06	-7.30
Mass Density	kg/m^3	1.67	851.63	856.73	863.21	861.57	998.06	863.21
Viscosity	cP	0.02	19.89	29.39	51.90	58.47	0.91	51.90
Mass Flow	kg/h	316863	3283147	3283147	3283147	35	0	3283183
Molar Flow	kmol/h	7281	25501	25501	25501	0	0	25501
Mole fraction								
H_2O		0.0025	0.0300	0.0300	0.0300	0.02	1	0.0300
EDEA		0	0.9589	0.9589	0.9589	0.98	0	0.9589
CO_2		0.9540	0.0109	0.0109	0.0109	0	0	0.0109
H_2S		0	0	0	0	0	0	0
N_2		0.0004	0	0	0	0	0	0
Ar		0.0101	0	0	0	0	0	0
O_2		0.0326	0.0001	0.0001	0.0001	0	0	0.0001
NO_2		0	0	0	0	0	0	0
SO_2		0.0003	0	0	0	0	0	0
SO_3		0	0	0	0	0	0	0
Cl_2		0.0002	0	0	0	0	0	0

Parameter	Units	CO2_2	CO2_3	Wtr3	CO2_3_1	CO2_4	CO2_5	CO2_final
Temperature	°C	409	50	50	50	114	20	37
Pressure	kPa	3400	3400	3400	3400	6800	6800	11000
Mass Enthalpy	kJ/kg	-8265	-8647	-10052	-8645	-8598	-8797	-8790
Mass Entropy	kJ/(kg.°C)	0.24	-0.56	-3.95	-0.55	-0.53	-1.22	-1.17
Mass Density	kg/m^3	26.26	63.78	879.52	63.72	107.78	705.49	549.13
Viscosity	cP	0.03	<empty>	0.13	0.02	0.02	0.07	<empty>
Mass Flow	kg/h	316863	316863	325	316538	316538	316538	316538
Molar Flow	kmol/h	7281	7281	9	7272	7272	7272	7272
Mole fraction								
H_2O		0.0025	0.0025	0.4091	0.0020	0.0020	0.0020	0.0020
EDEA		0	0	0.0286	0	0	0	0
CO_2		0.9540	0.9540	0.5564	0.9545	0.9545	0.9545	0.9545
H_2S		0	0	0	0	0	0	0
N_2		0.0004	0.0004	0	0.0004	0.0004	0.0004	0.0004
Ar		0.0101	0.0101	0.0010	0.0101	0.0101	0.0101	0.0101
O_2		0.0326	0.0326	0.0036	0.0326	0.0326	0.0326	0.0326
NO_2		0	0	0	0	0	0	0
SO_2		0.0003	0.0003	0.0008	0.0003	0.0003	0.0003	0.0003
SO_3		0	0	0.0001	0	0	0	0
Cl_2		0.0002	0.0002	0.0003	0.0002	0.0002	0.0002	0.0002

Table B.20: Heat tables of the capture plant using EDEA for a flue gas obtained from oxy-combustion of coal. Scenario 1.

Unit	Heat Flow (GJ/h)
qGPU2	42.60
qGPU4	33.31
qGPU6	32.69
qGPU8	66.91
qGPU10	81.17
qGPU12	120.96
qGPU14	62.87

Table B.21: Work tables of the capture plant using EDEA for a flue gas obtained from oxy-combustion of coal. Scenario 1.

	Unit	qGPU1	qGPU3	qGPU5	qGPU7	qGPU9	qGPU11	qGPU13	qGPU15
Work	kW	8183	7819	7545	125	2497	31938	4108	582

Table B.22: Stream tables of the capture plant using EDEA for a flue gas obtained from oxy-combustion of coal. Scenario 2.

Parameter	Units	FG1+	FG2	FG3	Wtr1	FG4	FG5	FG6	Wtr2	FG7	FG8
Temperature	°C	27	116	25	25	25	113	25	25	25	115
Pressure	kPa	101.3	282.6	282.6	282.6	282.6	788.5	788.5	788.5	788.5	2200
Mass Enthalpy	kJ/kg	-8457	-8378	-8493	-13545	-8408	-8331	-8422	-12284	-8397	-8322
Molar Entropy	kJ/(kmol.°C)	5.42	6.74	-7.94	-167.91	-3.08	-1.77	-13.43	-160.71	-11.94	-10.67
Mass Density	kg/m^3	1.73	3.72	5.04	859.23	4.95	10.70	14.30	804.06	14.21	30.76
Viscosity	cP	0.02	0.02	<empty>	0.51	0.02	0.02	<empty>	0.33	0.02	0.02
Mass Flow	kg/h	370642	370642	370642	6127	364515	364515	364515	2378	362138	362138
Molar Flow	kmol/h	8755	8755	8755	258	8496	8496	8496	85	8411	8411
Mole fraction											
H_2O		0.0310	0.0310	0.0310	0.7804	0.0082	0.0082	0.0082	0.6180	0.0021	0.0021
EDEA		0	0	0	0	0	0	0	0	0	0
CO_2		0.8907	0.8907	0.8907	0.2187	0.9112	0.9112	0.9112	0.3796	0.9166	0.9166
H_2S		0	0	0	0	0	0	0	0	0	0
N_2		0.0165	0.0165	0.0165	0.0001	0.0170	0.0170	0.0170	0.0002	0.0172	0.0172
Ar		0.0157	0.0157	0.0157	0.0002	0.0161	0.0161	0.0161	0.0004	0.0163	0.0163
O_2		0.0457	0.0457	0.0457	0.0005	0.0471	0.0471	0.0471	0.0014	0.0475	0.0475
NO_2		0	0	0	0	0	0	0	0	0	0
SO_2		0.0002	0.0002	0.0002	0.0001	0.0002	0.0002	0.0002	0.0003	0.0002	0.0002
SO_3		0	0	0	0	0	0	0	0.0001	0	0
Cl_2		0.0002	0.0002	0.0002	0.0000	0.0002	0.0002	0.0002	0.0001	0.0002	0.0002

Parameter	Units	FG9	LeanEDEA	CleanFG	RichEDEA1	RichEDEA2	RichEDEA3	RichEDEA4
Temperature	°C	25	25	28	30	30	37	48
Pressure	kPa	2200	2100	2100	2200	2300	2250	2200
Mass Enthalpy	kJ/kg	-8412	-4264	-6913	-4587	-4587	-4562	-4532
Molar Entropy	kJ/(kmol.°C)	-22.12	-727.73	-16.51	-613.65	-613.61	-605.99	-597.25
Mass Density	kg/m^3	42.84	886.67	36.25	906.17	906.15	769.38	516.66
Viscosity	cP	<empty>	13.02	0.02	4.36	4.35	<empty>	<empty>
Mass Flow	kg/h	362138	4008206	38665	4331678	4331678	4331678	4331678
Molar Flow	kmol/h	8411	38442	961	45893	45893	45893	45893
Mole fraction								
H_2O		0.0021	0.1401	0.0002	0.1177	0.1177	0.1177	0.1177
EDEA		0	0.7166	0	0.6003	0.6003	0.6003	0.6003
CO_2		0.9166	0.1400	0.7059	0.2705	0.2705	0.2705	0.2705
H_2S		0	0	0	0	0	0	0
N_2		0.0172	0.0000	0.1433	0.0002	0.0002	0.0002	0.0002
Ar		0.0163	0.0006	0.0434	0.0026	0.0026	0.0026	0.0026
O_2		0.0475	0.0020	0.1071	0.0081	0.0081	0.0081	0.0081
NO_2		0	0	0	0	0	0	0
SO_2		0.0002	0.0004	0.0001	0.0004	0.0004	0.0004	0.0004
SO_3		0	0.0001	0	0.0001	0.0001	0.0001	0.0001
Cl_2		0.0002	0.0002	0.0001	0.0002	0.0002	0.0002	0.0002

Parameter	Units	LeanEDEA1	CO2_1	LeanEDEA2	LeanEDEA3	LeanEDEA4	MakeupEDEA	MakeupWater
Temperature	°C	46	46	46	35	25	25	25
Pressure	kPa	1250	1250	2200	2150	2100	2100	2100
Mass Enthalpy	kJ/kg	-4206	-8558	-4205	-4233	-4264	-3671	-15864
Molar Entropy	kJ/(kmol.°C)	-709.00	-14.41	-708.63	-717.50	-728.00	-958.77	-163.23
Mass Density	kg/m^3	872.66	21.54	872.33	879.97	886.59	861.57	998.06
Viscosity	cP	5.26	0.02	5.16	8.20	13.05	58.47	0.91
Mass Flow	kg/h	4007363	324315	4007363	4007363	4007363	5	0
Molar Flow	kmol/h	38428	7465	38428	38428	38428	0	0
Mole fraction								
H_2O		0.1404	0.0011	0.1404	0.1404	0.1404	0.02	1
EDEA		0.7169	0	0.7169	0.7169	0.7169	0.98	0
CO_2		0.1395	0.9449	0.1395	0.1395	0.1395	0	0
H_2S		0	0	0	0	0	0	0
N_2		0	0.0009	0	0	0	0	0
Ar		0.0006	0.0128	0.0006	0.0006	0.0006	0	0
O_2		0.0020	0.0398	0.0020	0.0020	0.0020	0	0
NO_2		0	0	0	0	0	0	0
SO_2		0.0004	0.0003	0.0004	0.0004	0.0004	0	0
SO_3		0.0001	0.0000	0.0001	0.0001	0.0001	0	0
Cl_2		0.0002	0.0002	0.0002	0.0002	0.0002	0	0

Parameter	Units	LeanEDEA5	CO2_2	CO2_3	Wtr3	CO2_3_1	CO2_4	CO2_5	CO2_final
Temperature	°C	25	137	50	50	50	114	18	36
Pressure	kPa	2100	3400	3400	3400	3400	6800	6800	11000
Mass Enthalpy	kJ/kg	-4264	-8482	-8570	-6084	-8570	-8523	-8729	-8722
Molar Entropy	kJ/(kmol.°C)	-728.00	-13.18	-23.72	-360.09	-23.72	-22.92	-53.65	-51.32
Mass Density	kg/m^3	886.59	46.12	63.44	940.74	63.44	107.18	707.83	552.08
Viscosity	cP	13.05	0.02	0.02	0.50	0.02	0.02	0.07	<empty>
Mass Flow	kg/h	4007368	324315	324315	3	324312	324312	324312	324312
Molar Flow	kmol/h	38428	7465	7465	0	7465	7465	7465	7465
Mole fraction									
H_2O		0.1404	0.0011	0.0011	0.2715	0.0011	0.0011	0.0011	0.0011
EDEA		0.7169	0	0	0.3085	0	0	0	0
CO_2		0.1395	0.9449	0.9449	0.4115	0.9449	0.9449	0.9449	0.9449
H_2S		0	0	0	0	0	0	0	0
N_2		0	0.0009	0.0009	0	0.0009	0.0009	0.0009	0.0009
Ar		0.0006	0.0128	0.0128	0.0016	0.0128	0.0128	0.0128	0.0128
O_2		0.0020	0.0398	0.0398	0.0054	0.0398	0.0398	0.0398	0.0398
NO_2		0	0	0	0	0	0	0	0
SO_2		0.0004	0.0003	0.0003	0.0010	0.0003	0.0003	0.0003	0.0003
SO_3		0.0001	0	0	0.0001	0	0	0	0
Cl_2		0.0002	0.0002	0.0002	0.0004	0.0002	0.0002	0.0002	0.0002

Table B.23: Heat tables of the capture plant using EDEA for a flue gas obtained from oxy-combustion of coal. Scenario 2.

Unit	Heat Flow (GJ/h)
qGPU2	42.60
qGPU4	33.31
qGPU6	32.69
qGPU8	127.87
qGPU10	124.70
qGPU12	28.68
qGPU14	66.64

Table B.24: Work tables of the capture plant using EDEA for a flue gas obtained from oxy-combustion of coal. Scenario 2.

	Unit	qGPU1	qGPU3	qGPU5	qGPU7	qGPU9	qGPU11	qGPU13	qGPU15
Work	kW	8183	7819	7545	148	1346	6841	4230	594

B.6.2 Scenarios 3, 4, 5, and 6

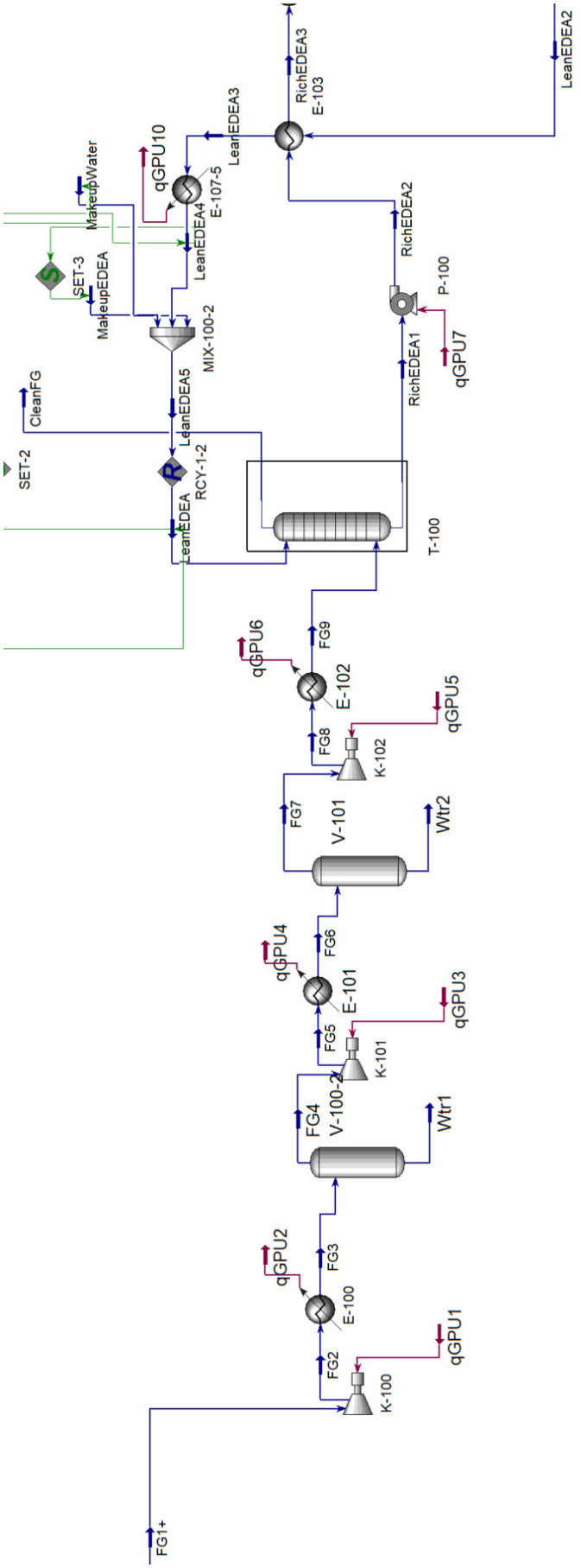
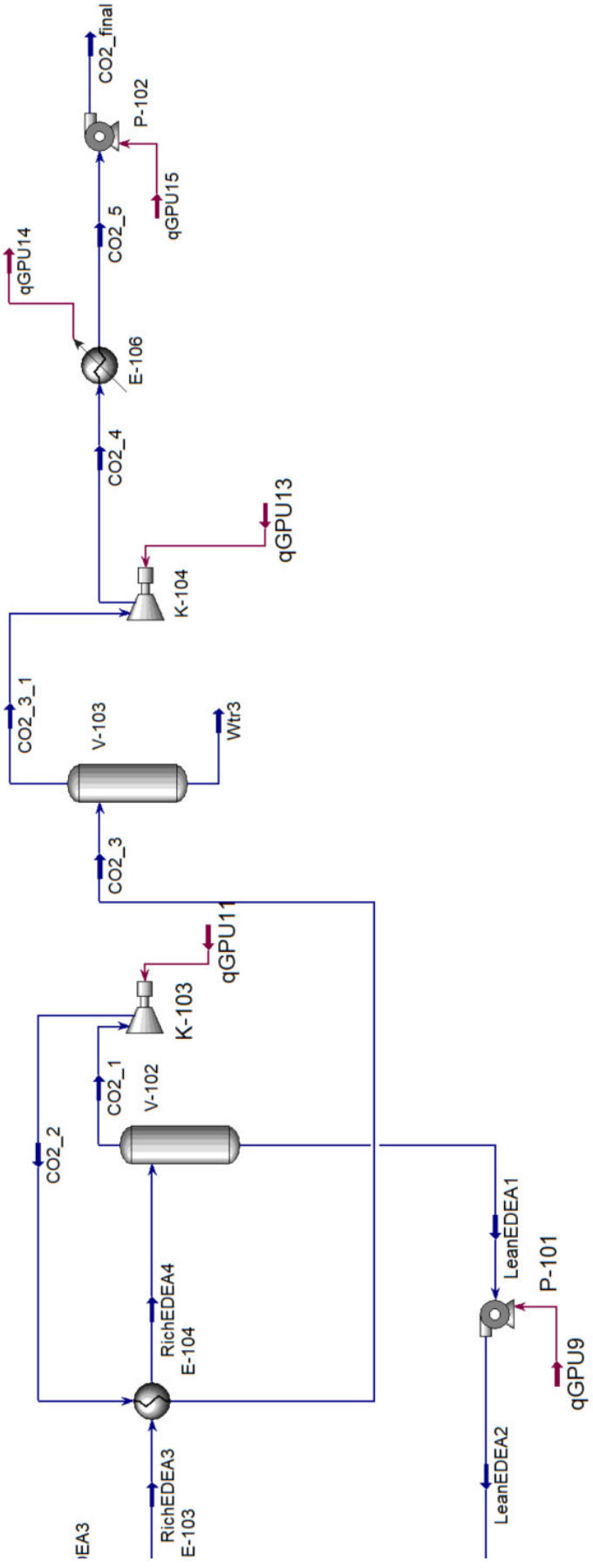


Figure B.8: PFD of the EDEA-based GPU for scenarios 3, 4, 5, and 6.


CO2_final
P-102
qGPU15
CO2_5
qGPU14
E-106
CO2_4
qGPU13
K-104
CO2_3_1
V-103
Wtr3
CO2_3
qGPU11
K-103
CO2_1
V-102
CO2_2
RichEDEA4
E-104
LeanEDEA1
P-101
qGPU9
LeanEDEA2
RichEDEA3
E-103
IEA3

Cont.

Table B.25: Stream tables of the capture plant using EDEA for a flue gas obtained from oxy-combustion of coal. Scenario 3.

Parameter	Units	FG1+	FG2	FG3	Wtr1	FG4	FG5	FG6	Wtr2	FG7	FG8
Temperature	°C	27	116	25	25	25	113	25	25	25	115
Pressure	kPa	101.3	282.6	282.6	282.6	282.6	788.5	788.5	788.5	788.5	2200
Mass Enthalpy	kJ/kg	-8457	-8378	-8493	-13545	-8408	-8331	-8422	-12284	-8397	-8322
Mass Entropy	kJ/(kg.°C)	0.13	0.16	-0.19	-7.08	-0.07	-0.04	-0.31	-5.75	-0.28	-0.25
Mass Density	kg/m^3	1.73	3.72	5.04	859.23	4.95	10.70	14.30	804.06	14.21	30.76
Viscosity	cP	0.02	0.02	<empty>	0.51	0.02	0.02	<empty>	0.33	0.02	0.02
Mass Flow	kg/h	370642	370642	370642	6127	364515	364515	364515	2378	362138	362138
Molar Flow	kmol/h	8755	8755	8755	258	8496	8496	8496	85	8411	8411
Mole fraction											
H_2O		0.0310	0.0310	0.0310	0.7804	0.0082	0.0082	0.0082	0.6180	0.0021	0.0021
EDEA		0	0	0	0	0	0	0	0	0	0
CO_2		0.8907	0.8907	0.8907	0.2187	0.9112	0.9112	0.9112	0.3796	0.9166	0.9166
H_2S		0	0	0	0	0	0	0	0	0	0
N_2		0.0165	0.0165	0.0165	0.0001	0.0170	0.0170	0.0170	0.0002	0.0172	0.0172
Ar		0.0157	0.0157	0.0157	0.0002	0.0161	0.0161	0.0161	0.0004	0.0163	0.0163
O_2		0.0457	0.0457	0.0457	0.0005	0.0471	0.0471	0.0471	0.0014	0.0475	0.0475
NO_2		0	0	0	0	0	0	0	0	0	0
SO_2		0.0002	0.0002	0.0002	0.0001	0.0002	0.0002	0.0002	0.0003	0.0002	0.0002
SO_3		0	0	0	0	0	0	0	0.0001	0	0
Cl_2		0.0002	0.0002	0.0002	0.0000	0.0002	0.0002	0.0002	0.0001	0.0002	0.0002

Parameter	Units	FG9	LeanEDEA	CleanFG	RichEDEA1	RichEDEA2	RichEDEA3	RichEDEA4	LeanEDEA1
Temperature	°C	25	25	28	29	29	35	44	42
Pressure	kPa	2200	2100	2100	2200	2300	2250	2200	100
Mass Enthalpy	kJ/kg	-8412	-3710	-6604	-4149	-4149	-4129	-4108	-3669
Mass Entropy	kJ/(kg.°C)	-0.51	-7.30	-0.40	-6.70	-6.69	-6.63	-6.57	-7.17
Mass Density	kg/m^3	42.84	863.22	35.83	891.63	891.61	857.09	696.03	852.38
Viscosity	cP	<empty>	51.78	0.02	9.23	9.21	<empty>	<empty>	20.96
Mass Flow	kg/h	362138	3269840	43610	3588367	3588367	3588367	3588367	3269781
Molar Flow	kmol/h	8411	25410	1091	32730	32730	32730	32730	25408
Mole fraction									
H_2O		0.0021	0.0305	0	0.0242	0.0242	0.0242	0.0242	0.0305
EDEA		0	0.9584	0	0.7440	0.7440	0.7440	0.7440	0.9584
CO_2		0.9166	0.0109	0.6700	0.2216	0.2216	0.2216	0.2216	0.0109
H_2S		0	0	0	0	0	0	0	0
N_2		0.0172	0	0.1295	0.0001	0.0001	0.0001	0.0001	0
Ar		0.0163	0	0.0568	0.0023	0.0023	0.0023	0.0023	0
O_2		0.0475	0.0001	0.1437	0.0075	0.0075	0.0075	0.0075	0.0001
NO_2		0	0	0	0	0	0	0	0
SO_2		0.0002	0.0000	0	0.0001	0.0001	0.0001	0.0001	0
SO_3		0	0.0000	0	0	0	0	0	0
Cl_2		0.0002	0.0000	0	0.0001	0.0001	0.0001	0.0001	0

Parameter	Units	CO2_1	LeanEDEA2	LeanEDEA3	LeanEDEA4	MakeupEDEA	MakeupWater	LeanEDEA5
Temperature	°C	42	43	34	25	25	25	25
Pressure	kPa	100	2200	2150	2100	2100	2100	2100
Mass Enthalpy	kJ/kg	-8622	-3666	-3687	-3710	-3671	-15864	-3710
Mass Entropy	kJ/(kg.°C)	0.15	-7.16	-7.23	-7.30	-7.33	-9.06	-7.30
Mass Density	kg/m^3	1.67	851.66	857.42	863.22	861.57	998.06	863.22
Viscosity	cP	0.02	19.87	31.01	51.79	58.47	0.91	51.79
Mass Flow	kg/h	318586	3269781	3269781	3269781	35	0	3269817
Molar Flow	kmol/h	7322	25408	25408	25408	0	0	25409
Mole fraction								
H_2O		0.0025	0.0305	0.0305	0.0305	0.02	1	0.0305
EDEA		0	0.9584	0.9584	0.9584	0.98	0	0.9584
CO_2		0.9531	0.0109	0.0109	0.0109	0	0	0.0109
H_2S		0	0	0	0	0	0	0
N_2		0.0004	0	0	0	0	0	0
Ar		0.0103	0	0	0	0	0	0
O_2		0.0332	0.0001	0.0001	0.0001	0	0	0.0001
NO_2		0	0	0	0	0	0	0
SO_2		0.0003	0	0	0	0	0	0
SO_3		0	0	0	0	0	0	0
Cl_2		0.0002	0	0	0	0	0	0

Parameter	Units	CO2_2	CO2_3	Wtr3	CO2_3_1	CO2_4	CO2_5	CO2_final
Temperature	°C	282	45	45	45	216	20	37
Pressure	kPa	1200	1150	1150	1150	6800	6800	11000
Mass Enthalpy	kJ/kg	-8393	-8627	-4851	-8627	-8481	-8794	-8790
Mass Entropy	kJ/(kg.°C)	0.22	-0.32	-6.73	-0.32	-0.27	-1.22	-1.17
Mass Density	kg/m^3	11.38	19.79	886.57	19.79	77.53	704.97	549.13
Viscosity	cP	0.03	<empty>	2.63	0.02	0.02	0.07	<empty>
Mass Flow	kg/h	318586	318586	37	318549	318549	318549	318549
Molar Flow	kmol/h	7322	7322	0	7322	7322	7322	7322
Mole fraction								
H_2O		0.0025	0.0025	0.2999	0.0025	0.0025	0.0025	0.0025
EDEA		0	0	0.5366	0	0	0	0
CO_2		0.9531	0.9531	0.1608	0.9532	0.9532	0.9532	0.9532
H_2S		0	0	0	0	0	0	0
N_2		0.0004	0.0004	0	0.0004	0.0004	0.0004	0.0004
Ar		0.0103	0.0103	0.0004	0.0103	0.0103	0.0103	0.0103
O_2		0.0332	0.0332	0.0015	0.0332	0.0332	0.0332	0.0332
NO_2		0	0	0	0	0	0	0
SO_2		0.0003	0.0003	0.0004	0.0003	0.0003	0.0003	0.0003
SO_3		0	0	0.0001	0	0	0	0
Cl_2		0.0002	0.0002	0.0002	0.0002	0.0002	0.0002	0.0002

Table B.26: Heat tables of the capture plant using EDEA for a flue gas obtained from oxy-combustion of coal. Scenario 3.

Unit	Heat Flow (GJ/h)
qGPU2	42.60
qGPU4	33.31
qGPU6	32.69
qGPU10	72.49
qGPU14	99.78

Table B.27: Work tables of the capture plant using EDEA for a flue gas obtained from oxy-combustion of coal. Scenario 3.

	Unit	qGPU1	qGPU3	qGPU5	qGPU7	qGPU9	qGPU11	qGPU13	qGPU15
Work	kW	8183	7819	7545	124	2486	20288	12957	586

Table B.28: Stream tables of the capture plant using EDEA for a flue gas obtained from oxy-combustion of coal. Scenario 4.

Parameter	Units	FG1+	FG2	FG3	Wtr1	FG4	FG5	FG6	Wtr2	FG7	FG8
Temperature	°C	27	116	25	25	25	113	25	25	25	115
Pressure	kPa	101.3	282.6	282.6	282.6	282.6	788.5	788.5	788.5	788.5	2200
Mass Enthalpy	kJ/kg	-8457	-8378	-8493	-13545	-8408	-8331	-8422	-12284	-8397	-8322
Mass Entropy	kJ/(kg.°C)	0.13	0.16	-0.19	-7.08	-0.07	-0.04	-0.31	-5.75	-0.28	-0.25
Mass Density	kg/m^3	1.73	3.72	5.04	859.23	4.95	10.70	14.30	804.06	14.21	30.76
Viscosity	cP	0.02	0.02	<empty>	0.51	0.02	0.02	<empty>	0.33	0.02	0.02
Mass Flow	kg/h	370642	370642	370642	6127	364515	364515	364515	2378	362138	362138
Molar Flow	kmol/h	8755	8755	8755	258	8496	8496	8496	85	8411	8411
Mole fraction											
H_2O		0.0310	0.0310	0.0310	0.7804	0.0082	0.0082	0.0082	0.6180	0.0021	0.0021
EDEA		0	0	0	0	0	0	0	0	0	0
CO_2		0.8907	0.8907	0.8907	0.2187	0.9112	0.9112	0.9112	0.3796	0.9166	0.9166
H_2S		0	0	0	0	0	0	0	0	0	0
N_2		0.0165	0.0165	0.0165	0.0001	0.0170	0.0170	0.0170	0.0002	0.0172	0.0172
Ar		0.0157	0.0157	0.0157	0.0002	0.0161	0.0161	0.0161	0.0004	0.0163	0.0163
O_2		0.0457	0.0457	0.0457	0.0005	0.0471	0.0471	0.0471	0.0014	0.0475	0.0475
NO_2		0	0	0	0	0	0	0	0	0	0
SO_2		0.0002	0.0002	0.0002	0.0001	0.0002	0.0002	0.0002	0.0003	0.0002	0.0002
SO_3		0	0	0	0	0	0	0	0.0001	0	0
Cl_2		0.0002	0.0002	0.0002	0.0000	0.0002	0.0002	0.0002	0.0001	0.0002	0.0002

Parameter	Units	FG9	LeanEDEA	CleanFG	RichEDEA1	RichEDEA2	RichEDEA3	RichEDEA4	LeanEDEA1
Temperature	°C	30	30	32	34	34	36	44	40
Pressure	kPa	2200	2100	2100	2200	2300	2250	2200	300
Mass Enthalpy	kJ/kg	-8406	-3888	-6235	-4341	-4340	-4335	-4315	-3862
Mass Entropy	kJ/(kg.°C)	-0.50	-7.20	-0.38	-6.57	-6.57	-6.55	-6.49	-7.12
Mass Density	kg/m^3	41.84	865.34	34.63	894.82	894.78	886.79	683.46	858.90
Viscosity	cP	<empty>	24.53	0.02	5.36	5.35	<empty>	<empty>	15.10
Mass Flow	kg/h	362138	3086438	39818	3408758	3408758	3408758	3408758	3086196
Molar Flow	kmol/h	8411	26092	1009	33494	33494	33494	33494	26087
Mole fraction									
H_2O		0.0021	0.1001	0.0002	0.0785	0.0785	0.0785	0.0785	0.1001
EDEA		0	0.8621	0	0.6716	0.6716	0.6716	0.6716	0.8623
CO_2		0.9166	0.0371	0.6248	0.2402	0.2402	0.2402	0.2402	0.0369
H_2S		0	0	0	0	0	0	0	0
N_2		0.0172	0	0.1394	0.0001	0.0001	0.0001	0.0001	0
Ar		0.0163	0.0001	0.0660	0.0022	0.0022	0.0022	0.0022	0.0001
O_2		0.0475	0.0003	0.1696	0.0071	0.0071	0.0071	0.0071	0.0004
NO_2		0	0	0	0	0	0	0	0
SO_2		0.0002	0.0001	0	0.0002	0.0002	0.0002	0.0002	0.0001
SO_3		0	0	0	0	0	0	0	0
Cl_2		0.0002	0.0001	0	0.0001	0.0001	0.0001	0.0001	0.0001

Parameter	Units	CO2_1	LeanEDEA2	LeanEDEA3	LeanEDEA4	MakeupEDEA	MakeupWater	LeanEDEA5
Temperature	°C	40	41	39	30	25	25	30
Pressure	kPa	300	2200	2150	2100	2100	2100	2100
Mass Enthalpy	kJ/kg	-8648	-3860	-3866	-3887	-3671	-15864	-3887
Mass Entropy	kJ/(kg.°C)	-0.07	-7.11	-7.13	-7.20	-7.33	-9.06	-7.20
Mass Density	kg/m^3	5.08	858.26	859.75	865.30	861.57	998.06	865.30
Viscosity	cP	0.02	14.42	16.04	24.56	58.47	0.91	24.56
Mass Flow	kg/h	322562	3086196	3086196	3086196	9	0	3086206
Molar Flow	kmol/h	7408	26087	26087	26087	0	0	26087
Mole fraction								
H_2O		0.0024	0.1001	0.1001	0.1001	0.02	1	0.1001
EDEA		0	0.8623	0.8623	0.8623	0.98	0	0.8623
CO_2		0.9564	0.0369	0.0369	0.0369	0	0	0.0369
H_2S		0	0	0	0	0	0	0
N_2		0.0005	0	0	0	0	0	0
Ar		0.0095	0.0001	0.0001	0.0001	0	0	0.0001
O_2		0.0307	0.0004	0.0004	0.0004	0	0	0.0004
NO_2		0	0	0	0	0	0	0
SO_2		0.0003	0.0001	0.0001	0.0001	0	0	0.0001
SO_3		0	0	0	0	0	0	0
Cl_2		0.0002	0.0001	0.0001	0.0001	0	0	0.0001

Parameter	Units	CO2_2	CO2_3	Wtr3	CO2_3_1	CO2_4	CO2_5	CO2_final
Temperature	°C	255	48	48	48	130	20	37
Pressure	kPa	2850	2800	2800	2800	6800	6800	11000
Mass Enthalpy	kJ/kg	-8449	-8660	-10470	-8660	-8598	-8813	-8807
Mass Entropy	kJ/(kg.°C)	-0.01	-0.51	-4.27	-0.51	-0.49	-1.21	-1.16
Mass Density	kg/m^3	28.85	51.54	874.51	51.52	101.21	705.49	551.11
Viscosity	cP	0.03	<empty>	0.15	0.02	0.02	0.07	<empty>
Mass Flow	kg/h	322562	322562	103	322459	322459	322459	322459
Molar Flow	kmol/h	7408	7408	3	7405	7405	7405	7405
Mole fraction								
H_2O		0.0024	0.0024	0.4621	0.0022	0.0022	0.0022	0.0022
EDEA		0	0	0.0225	0	0	0	0
CO_2		0.9564	0.9564	0.5106	0.9566	0.9566	0.9566	0.9566
H_2S		0	0	0	0	0	0	0
N_2		0.0005	0.0005	0	0.0005	0.0005	0.0005	0.0005
Ar		0.0095	0.0095	0.0008	0.0095	0.0095	0.0095	0.0095
O_2		0.0307	0.0307	0.0028	0.0307	0.0307	0.0307	0.0307
NO_2		0	0	0	0	0	0	0
SO_2		0.0003	0.0003	0.0008	0.0003	0.0003	0.0003	0.0003
SO_3		0	0	0.0001	0	0	0	0
Cl_2		0.0002	0.0002	0.0003	0.0002	0.0002	0.0002	0.0002

Table B.29: Heat tables of the capture plant using EDEA for a flue gas obtained from oxy-combustion of coal. Scenario 4.

Unit	Heat Flow (GJ/h)
qGPU2	42.60
qGPU4	33.31
qGPU6	30.64
qGPU10	66.83
qGPU14	69.49

Table B.30: Work tables of the capture plant using EDEA for a flue gas obtained from oxy-combustion of coal. Scenario 4.

	Unit	qGPU1	qGPU3	qGPU5	qGPU7	qGPU9	qGPU11	qGPU13	qGPU15
Work	kW	8183	7819	7545	118	2107	17843	5567	592

Table B.31: Stream tables of the capture plant using EDEA for a flue gas obtained from oxy-combustion of coal. Scenario 5.

Parameter	Units	FG1+	FG2	FG3	Wtr1	FG4	FG5	FG6	Wtr2	FG7	FG8
Temperature	°C	27	116	25	25	25	113	25	25	25	115
Pressure	kPa	101.3	282.6	282.6	282.6	282.6	788.5	788.5	788.5	788.5	2200
Mass Enthalpy	kJ/kg	-8457	-8378	-8493	-13545	-8408	-8331	-8422	-12284	-8397	-8322
Mass Entropy	kJ/(kg.°C)	0.13	0.16	-0.19	-7.08	-0.07	-0.04	-0.31	-5.75	-0.28	-0.25
Mass Density	kg/m^3	1.73	3.72	5.04	859.23	4.95	10.70	14.30	804.06	14.21	30.76
Viscosity	cP	0.02	0.02	<empty>	0.51	0.02	0.02	<empty>	0.33	0.02	0.02
Mass Flow	kg/h	370642	370642	370642	6127	364515	364515	364515	2378	362138	362138
Molar Flow	kmol/h	8755	8755	8755	258	8496	8496	8496	85	8411	8411
Mole fraction											
H_2O		0.0310	0.0310	0.0310	0.7804	0.0082	0.0082	0.0082	0.6180	0.0021	0.0021
EDEA		0	0	0	0	0	0	0	0	0	0
CO_2		0.8907	0.8907	0.8907	0.2187	0.9112	0.9112	0.9112	0.3796	0.9166	0.9166
H_2S		0	0	0	0	0	0	0	0	0	0
N_2		0.0165	0.0165	0.0165	0.0001	0.0170	0.0170	0.0170	0.0002	0.0172	0.0172
Ar		0.0157	0.0157	0.0157	0.0002	0.0161	0.0161	0.0161	0.0004	0.0163	0.0163
O_2		0.0457	0.0457	0.0457	0.0005	0.0471	0.0471	0.0471	0.0014	0.0475	0.0475
NO_2		0	0	0	0	0	0	0	0	0	0
SO_2		0.0002	0.0002	0.0002	0.0001	0.0002	0.0002	0.0002	0.0003	0.0002	0.0002
SO_3		0	0	0	0	0	0	0	0.0001	0	0
Cl_2		0.0002	0.0002	0.0002	0	0.0002	0.0002	0.0002	0.0001	0.0002	0.0002

Parameter	Units	FG9	LeanEDEA	CleanFG	RichEDEA1	RichEDEA2	RichEDEA3	RichEDEA4	LeanEDEA1
Temperature	°C	30	30	34	36	36	38	48	42
Pressure	kPa	2200	2100	2100	2200	2300	2250	2200	500
Mass Enthalpy	kJ/kg	-8406	-4130	-6249	-4594	-4594	-4590	-4563	-4098
Mass Entropy	kJ/(kg.°C)	-0.50	-7.14	-0.37	-6.47	-6.47	-6.45	-6.37	-7.04
Mass Density	kg/m^3	41.84	871.95	34.51	900.20	900.60	893.23	591.27	864.02
Viscosity	cP	<empty>	15.07	0.02	3.38	3.37	<empty>	<empty>	8.72
Mass Flow	kg/h	362138	2818592	42787	3137943	3137943	3137943	3137943	2818600
Molar Flow	kmol/h	8411	26249	1082	33578	33578	33578	33578	26247
Mole fraction									
H_2O		0.0021	0.1728	0.0003	0.1356	0.1356	0.1356	0.1356	0.1727
EDEA		0	0.7609	0	0.5948	0.5948	0.5948	0.5948	0.7610
CO_2		0.9166	0.0652	0.6274	0.2604	0.2604	0.2604	0.2604	0.0653
H_2S		0	0	0	0	0	0	0	0
N_2		0.0172	0	0.1293	0.0001	0.0001	0.0001	0.0001	0
Ar		0.0163	0.0001	0.0671	0.0020	0.0020	0.0020	0.0020	0.0002
O_2		0.0475	0.0005	0.1758	0.0067	0.0067	0.0067	0.0067	0.0006
NO_2		0	0	0	0	0	0	0	0
SO_2		0.0002	0.0002	0.0001	0.0002	0.0002	0.0002	0.0002	0.0002
SO_3		0	0	0	0	0	0	0	0
Cl_2		0.0002	0.0001	0	0.0001	0.0001	0.0001	0.0001	0.0001

Parameter	Units	CO2_1	LeanEDEA2	LeanEDEA3	LeanEDEA4	MakeupEDEA	MakeupWater	LeanEDEA5
Temperature	°C	42	43	41	30	25	25	30
Pressure	kPa	500	2200	2150	2100	2100	2100	2100
Mass Enthalpy	kJ/kg	-8669	-4096	-4100	-4130	-3671	-15864	-4130
Mass Entropy	kJ/(kg.°C)	-0.16	-7.03	-7.04	-7.14	-7.33	-9.06	-7.14
Mass Density	kg/m^3	8.48	863.47	864.61	871.95	861.57	998.06	871.95
Viscosity	cP	0.02	8.42	9.04	15.07	58.47	0.91	15.07
Mass Flow	kg/h	319343	2818600	2818600	2818600	7	0	2818607
Molar Flow	kmol/h	7331	26247	26247	26247	0	0	26247
Mole fraction								
H_2O		0.0028	0.1727	0.1727	0.1727	0.02	1	0.1727
EDEA		0	0.7610	0.7610	0.7610	0.98	0	0.7610
CO_2		0.9589	0.0653	0.0653	0.0653	0	0	0.0653
H_2S		0	0	0	0	0	0	0
N_2		0.0006	0	0	0	0	0	0.0000
Ar		0.0088	0.0002	0.0002	0.0002	0	0	0.0002
O_2		0.0284	0.0006	0.0006	0.0006	0	0	0.0006
NO_2		0	0	0	0	0	0	0
SO_2		0.0003	0.0002	0.0002	0.0002	0	0	0.0002
SO_3		0	0	0	0	0	0	0
Cl_2		0.0002	0.0001	0.0001	0.0001	0	0	0.0001

Parameter	Units	CO2_2	CO2_3	Wtr3	CO2_3_1	CO2_4	CO2_5	CO2_final
Temperature	°C	287	51	51	51	63	21	41
Pressure	kPa	6000	5950	5950	5950	6800	6800	11000
Mass Enthalpy	kJ/kg	-8444	-8711	-9613	-8702	-8695	-8824	-8818
Mass Entropy	kJ/(kg.°C)	-0.10	-0.73	-1.94	-0.71	-0.71	-1.20	-1.15
Mass Density	kg/m^3	58.01	130.57	493.94	129.58	143.03	707.59	515.14
Viscosity	cP	0.03	<empty>	0.06	0.02	0.02	0.07	<empty>
Mass Flow	kg/h	319343	319343	3305	316038	316038	316038	316038
Molar Flow	kmol/h	7331	7331	84	7247	7247	7247	7247
Mole fraction								
H_2O		0.0028	0.0028	0.1808	0.0007	0.0007	0.0007	0.0007
EDEA		0	0	0.0006	0	0	0	0
CO_2		0.9589	0.9589	0.8103	0.9607	0.9607	0.9607	0.9607
H_2S		0	0	0	0	0	0	0
N_2		0.0006	0.0006	0	0.0006	0.0006	0.0006	0.0006
Ar		0.0088	0.0088	0.0015	0.0088	0.0088	0.0088	0.0088
O_2		0.0284	0.0284	0.0052	0.0287	0.0287	0.0287	0.0287
NO_2		0	0	0	0	0	0	0
SO_2		0.0003	0.0003	0.0010	0.0003	0.0003	0.0003	0.0003
SO_3		0	0	0.0001	0	0	0	0
Cl_2		0.0002	0.0002	0.0004	0.0002	0.0002	0.0002	0.0002

Table B.32: Heat tables of the capture plant using EDEA for a flue gas obtained from oxy-combustion of coal. Scenario 5.

Unit	Heat Flow (GJ/h)
qGPU2	42.60
qGPU4	33.31
qGPU6	30.64
qGPU10	82.96
qGPU14	40.93

Table B.33: Work tables of the capture plant using EDEA for a flue gas obtained from oxy-combustion of coal. Scenario 5.

	Unit	qGPU1	qGPU3	qGPU5	qGPU7	qGPU9	qGPU11	qGPU13	qGPU15
Work	kW	8183	7819	7545	108	1712	19910	642	579

Table B.34: Stream tables of the capture plant using EDEA for a flue gas obtained from oxy-combustion of coal. Scenario 6.

Parameter	Units	FG1+	FG2	FG3	Wtr1	FG4	FG5	FG6	Wtr2	FG7	FG8
Temperature	°C	27	116	25	25	25	113	25	25	25	115
Pressure	kPa	101.3	282.6	282.6	282.6	282.6	788.5	788.5	788.5	788.5	2200
Mass Enthalpy	kJ/kg	-8457	-8378	-8493	-13545	-8408	-8331	-8422	-12284	-8397	-8322
Mass Entropy	kJ/(kg.°C)	0.13	0.16	-0.19	-7.08	-0.07	-0.04	-0.31	-5.75	-0.28	-0.25
Mass Density	kg/m^3	1.73	3.72	5.04	859.23	4.95	10.70	14.30	804.06	14.21	30.76
Viscosity	cP	0.02	0.02	<empty>	0.51	0.02	0.02	<empty>	0.33	0.02	0.02
Mass Flow	kg/h	370642	370642	370642	6127	364515	364515	364515	2378	362138	362138
Molar Flow	kmol/h	8755	8755	8755	258	8496	8496	8496	85	8411	8411
Mole fraction											
H_2O		0.0310	0.0310	0.0310	0.7804	0.0082	0.0082	0.0082	0.6180	0.0021	0.0021
EDEA		0	0	0	0	0	0	0	0	0	0
CO_2		0.8907	0.8907	0.8907	0.2187	0.9112	0.9112	0.9112	0.3796	0.9166	0.9166
H_2S		0	0	0	0	0	0	0	0	0	0
N_2		0.0165	0.0165	0.0165	0.0001	0.0170	0.0170	0.0170	0.0002	0.0172	0.0172
Ar		0.0157	0.0157	0.0157	0.0002	0.0161	0.0161	0.0161	0.0004	0.0163	0.0163
O_2		0.0457	0.0457	0.0457	0.0005	0.0471	0.0471	0.0471	0.0014	0.0475	0.0475
NO_2		0	0	0	0	0	0	0	0	0	0
SO_2		0.0002	0.0002	0.0002	0.0001	0.0002	0.0002	0.0002	0.0003	0.0002	0.0002
SO_3		0	0	0	0	0	0	0	0.0001	0	0
Cl_2		0.0002	0.0002	0.0002	0.0000	0.0002	0.0002	0.0002	0.0001	0.0002	0.0002

Parameter	Units	FG9	LeanEDEA	CleanFG	RichEDEA1	RichEDEA2	RichEDEA3	RichEDEA4	RichEDEA5
Temperature	°C	25	25	30	31	31	37	44	48
Pressure	kPa	2200	2100	2100	2200	2300	2250	2200	2150
Mass Enthalpy	kJ/kg	-8412	-4341	-6399	-4763	-4763	-4744	-4724	-4713
Mass Entropy	kJ/(kg.°C)	-0.51	-7.04	-0.39	-6.41	-6.41	-6.35	-6.28	-6.25
Mass Density	kg/m^3	42.84	885.16	35.25	911.23	911.23	766.50	548.17	462.82
Viscosity	cP	<empty>	12.44	0.02	3.28	3.28	<empty>	<empty>	<empty>
Mass Flow	kg/h	362138	2979462	37833	3303767	3303767	3303767	3303767	3303767
Molar Flow	kmol/h	8411	29544	955	37001	37001	37001	37001	37001
Mole fraction									
H_2O		0.0021	0.1868	0.0003	0.1496	0.1496	0.1496	0.1496	0.1496
EDEA		0	0.6918	0	0.5524	0.5524	0.5524	0.5524	0.5524
CO_2		0.9166	0.1191	0.6433	0.2869	0.2869	0.2869	0.2869	0.2869
H_2S		0	0	0	0	0	0	0	0
N_2		0.0172	0	0.1448	0.0002	0.0002	0.0002	0.0002	0.0002
Ar		0.0163	0.0004	0.0599	0.0025	0.0025	0.0025	0.0025	0.0025
O_2		0.0475	0.0014	0.1515	0.0080	0.0080	0.0080	0.0080	0.0080
NO_2		0	0	0	0	0	0	0	0
SO_2		0.0002	0.0004	0.0001	0.0003	0.0003	0.0003	0.0003	0.0003
SO_3		0	0.0001	0	0	0	0	0	0
Cl_2		0.0002	0.0001	0.0001	0.0001	0.0001	0.0001	0.0001	0.0001

Parameter	Units	LeanEDEA1	CO2_1	LeanEDEA2	LeanEDEA3	LeanEDEA4	MakeupEDEA	MakeupWater	LeanEDEA5
Temperature	°C	44	44	44	36	25	25	25	25
Pressure	kPa	950	950	2200	2150	2100	2100	2100	2100
Mass Enthalpy	kJ/kg	-4289	-8612	-4287	-4308	-4341	-3671	-15864	-4341
Mass Entropy	kJ/(kg.°C)	-6.87	-0.28	-6.87	-6.93	-7.04	-7.33	-9.06	-7.04
Mass Density	kg/m^3	872.74	16.31	872.33	877.92	885.20	861.57	998.06	885.20
Viscosity	cP	5.49	0.02	5.36	7.51	12.42	58.47	0.91	12.42
Mass Flow	kg/h	2979795	323972	2979795	2979795	2979795	4	0	2979800
Molar Flow	kmol/h	29554	7447	29554	29554	29554	0	0	29554
Mole fraction									
H_2O		0.1869	0.0017	0.1869	0.1869	0.1869	0.02	1	0.1869
EDEA		0.6916	0	0.6916	0.6916	0.6916	0.98	0	0.6916
CO_2		0.1193	0.9519	0.1193	0.1193	0.1193	0	0	0.1193
H_2S		0	0	0	0	0	0	0	0
N_2		0	0.0008	0	0	0	0	0	0.0000
Ar		0.0004	0.0108	0.0004	0.0004	0.0004	0	0	0.0004
O_2		0.0013	0.0344	0.0013	0.0013	0.0013	0	0	0.0013
NO_2		0	0	0	0	0	0	0	0
SO_2		0.0004	0.0003	0.0004	0.0004	0.0004	0	0	0.0004
SO_3		0.0001	0	0.0001	0.0001	0.0001	0	0	0.0001
Cl_2		0.0001	0.0002	0.0001	0.0001	0.0001	0	0	0.0001

Parameter	Units	CO2_2	CO2_3	CO2_5	CO2_final
Temperature	°C	223	43	15	37
Pressure	kPa	6150	6100	6100	11000
Mass Enthalpy	kJ/kg	-8456	-8662	-8802	-8795
Mass Entropy	kJ/(kg.°C)	-0.24	-0.76	-1.29	-1.17
Mass Density	kg/m^3	68.54	142.35	760.66	549.13
Viscosity	cP	0.02	<empty>	0.07	<empty>
Mass Flow	kg/h	323972	323972	323972	323972
Molar Flow	kmol/h	7447	7447	7447	7447
Mole fraction					
H_2O		0.0017	0.0017	0.0017	0.0017
EDEA		0	0	0	0
CO_2		0.9519	0.9519	0.9519	0.9519
H_2S		0	0	0	0
N_2		0.0008	0.0008	0.0008	0.0008
Ar		0.0108	0.0108	0.0108	0.0108
O_2		0.0344	0.0344	0.0344	0.0344
NO_2		0	0	0	0
SO_2		0.0003	0.0003	0.0003	0.0003
SO_3		0	0	0	0
Cl_2		0.0002	0.0002	0.0002	0.0002

Table B.35: Heat tables of the capture plant using EDEA for a flue gas obtained from oxy-combustion of coal. Scenario 6.

Unit	Heat Flow (GJ/h)
qGPU2	42.60
qGPU4	33.31
qGPU6	32.69
qGPU10	99.89
qGPU12	37.59
qGPU14	45.20

Table B.36: Work tables of the capture plant using EDEA for a flue gas obtained from oxy-combustion of coal. Scenario 6.

	Unit	qGPU1	qGPU3	qGPU5	qGPU7	qGPU9	qGPU11	qGPU13
Work	kW	8183	7819	7545	112	1317	14032	644

B.6.3 Scenarios 7 and 8

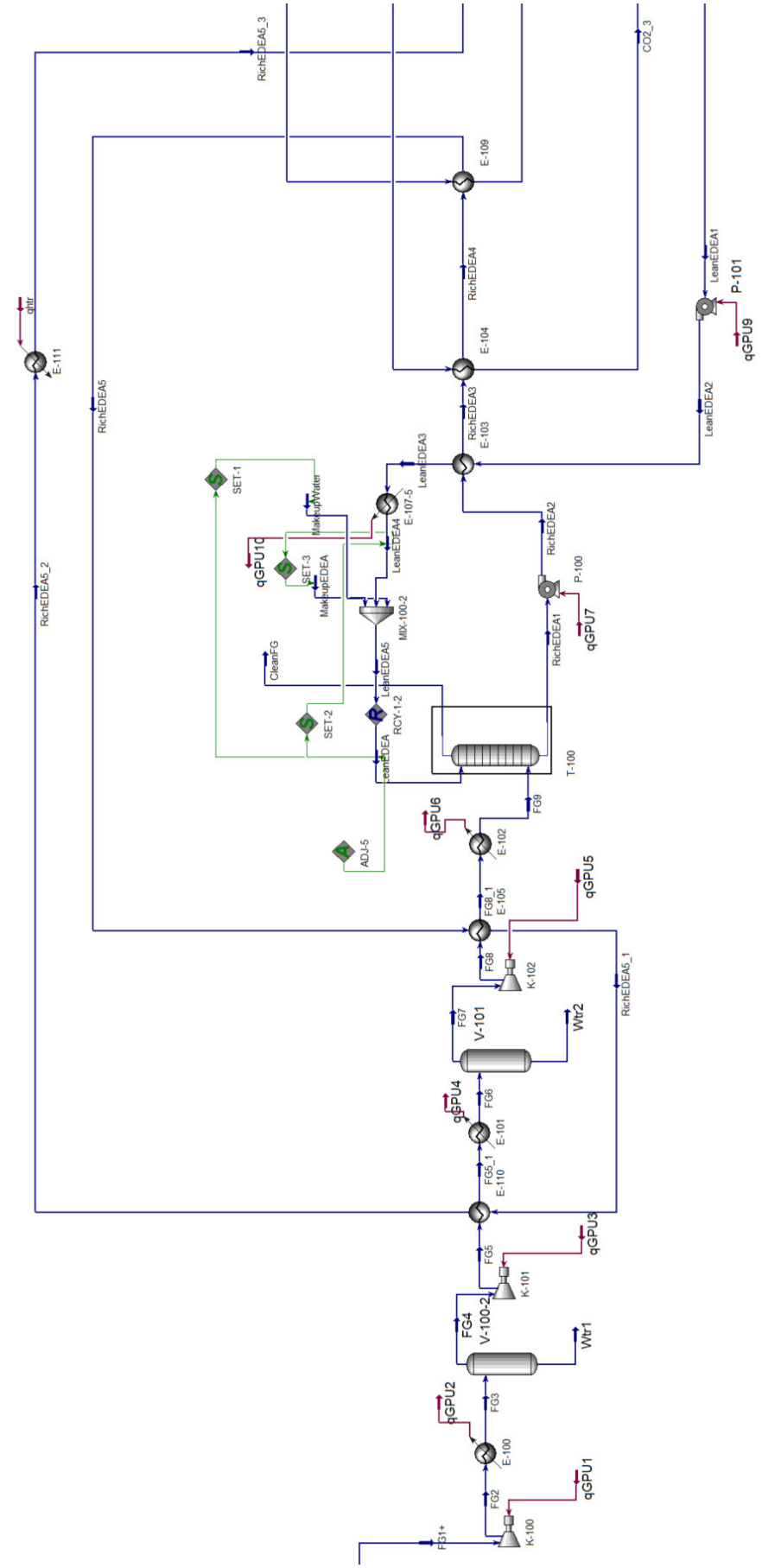


Figure B.9: PFD of the EDEA-based GPU for scenarios 7, and 8.

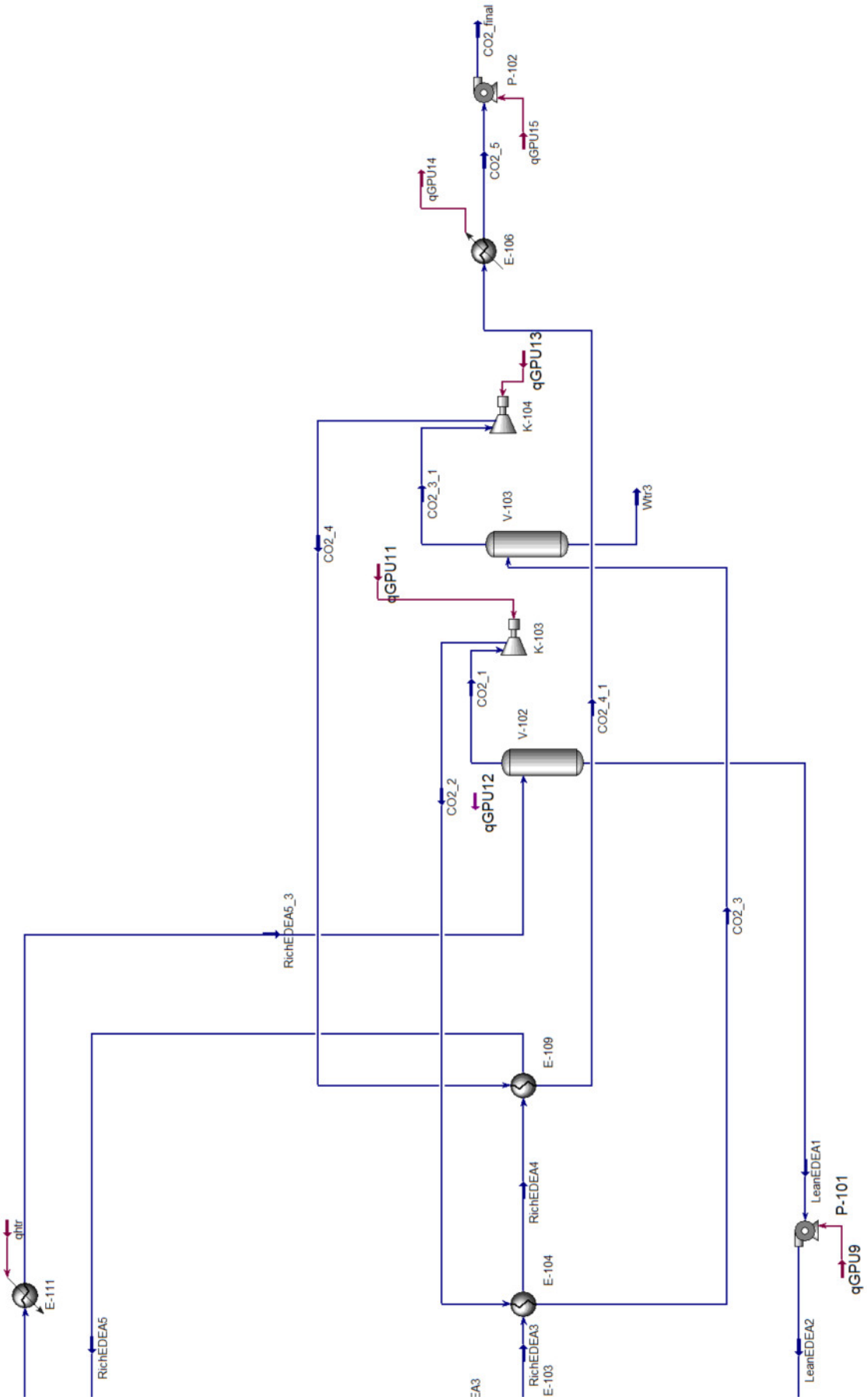

CO2_final
P-102
qGPU15
CO2_5
qGPU14
E-106
qGPU13
K-104
CO2_3_1
V-103
Wtr3
CO2_4
qGPU11
K-103
CO2_1
V-102
CO2_4_1
CO2_2
qGPU12
RichEDEA5_3
CO2_3
E-109
RichEDEA4
E-104
LeanEDEA1
P-101
qGPU9
qhtr
E-111
RichEDEA5
RichEDEA3
E-103
LeanEDEA2

Table B.37: Stream tables of the capture plant using EDEA for a flue gas obtained from oxy-combustion of coal. Scenario 7.

Parameter	Units	FG1+	FG2	FG3	Wtr1	FG4	FG5	FG5_1	FG6	Wtr2	FG7
Temperature	°C	27	116	25	25	25	114	55	25	25	25
Pressure	kPa	101.3	284.8	284.8	284.8	284.8	800.4	750.4	750.4	750.4	750.4
Mass Enthalpy	kJ/kg	-8457	-8377	-8493	-13536	-8408	-8330	-8384	-8421	-12349	-8397
Mass Entropy	kJ/(kg.°C)	0.13	0.16	-0.19	-7.07	-0.07	-0.04	-0.18	-0.30	-5.83	-0.27
Mass Density	kg/m^3	1.73	3.75	5.08	858.82	4.99	10.85	12.12	13.57	806.66	13.49
Viscosity	cP	0.02	0.02	<empty>	0.51	0.02	0.02	0.02	<empty>	0.34	0.02
Mass Flow	kg/h	370642	370642	370642	6161	364481	364481	364481	364481	2235	362246
Molar Flow	kmol/h	8755	8755	8755	259	8495	8495	8495	8495	81	8415
Mole fraction											
H_2O		0.0310	0.0310	0.0310	0.7794	0.0081	0.0081	0.0081	0.0081	0.6273	0.0022
EDEA		0	0	0	0	0	0	0	0	0	0
CO_2		0.8907	0.8907	0.8907	0.2196	0.9112	0.9112	0.9112	0.9112	0.3704	0.9164
H_2S		0	0	0	0	0	0	0	0	0	0
N_2		0.0165	0.0165	0.0165	0.0001	0.0170	0.0170	0.0170	0.0170	0.0002	0.0172
Ar		0.0157	0.0157	0.0157	0.0002	0.0161	0.0161	0.0161	0.0161	0.0004	0.0163
O_2		0.0457	0.0457	0.0457	0.0005	0.0471	0.0471	0.0471	0.0471	0.0013	0.0475
NO_2		0	0	0	0	0	0	0	0	0	0
SO_2		0.0002	0.0002	0.0002	0.0001	0.0002	0.0002	0.0002	0.0002	0.0003	0.0002
SO_3		0	0	0	0	0	0	0	0	0.0001	0
Cl_2		0.0002	0.0002	0.0002	0.0000	0.0002	0.0002	0.0002	0.0002	0.0001	0.0002

Parameter	Units	FG8	FG8_1	FG9	LeanEDEA	CleanFG	RichEDEA1	RichEDEA2	RichEDEA3
Temperature	°C	121	51	25	25	29	31	31	39
Pressure	kPa	2250	2200	2200	2100	2100	2200	2300	2250
Mass Enthalpy	kJ/kg	-8316	-8384	-8413	-4368	-6566	-4771	-4771	-4745
Mass Entropy	kJ/(kg.°C)	-0.24	-0.42	-0.51	-7.01	-0.39	-6.41	-6.41	-6.33
Mass Density	kg/m^3	30.87	38.26	42.86	886.91	35.57	911.59	911.58	697.38
Viscosity	cP	0.02	0.02	<empty>	11.66	0.02	3.27	3.27	<empty>
Mass Flow	kg/h	362246	362246	362246	3094419	39833	3416833	3416833	3416833
Molar Flow	kmol/h	8415	8415	8415	30915	999	38330	38330	38330
Mole fraction									
H_2O		0.0022	0.0022	0.0022	0.1855	0.0003	0.1501	0.1501	0.1501
EDEA		0	0	0	0.6830	0	0.5509	0.5509	0.5509
CO_2		0.9164	0.9164	0.9164	0.1290	0.6642	0.2879	0.2879	0.2879
H_2S		0	0	0	0	0	0	0	0
N_2		0.0172	0.0172	0.0172	0	0.1382	0.0002	0.0002	0.0002
Ar		0.0163	0.0163	0.0163	0.0004	0.0559	0.0025	0.0025	0.0025
O_2		0.0475	0.0475	0.0475	0.0015	0.1414	0.0079	0.0079	0.0079
NO_2		0	0	0	0	0	0	0	0
SO_2		0.0002	0.0002	0.0002	0.0004	0.0001	0.0004	0.0004	0.0004
SO_3		0	0	0	0.0001	0	0	0	0
Cl_2		0.0002	0.0002	0.0002	0.0002	0.0001	0.0002	0.0002	0.0002

Parameter	Units	RichEDEA4	RichEDEA5	RichEDEA5_1	RichEDEA5_2	RichEDEA5_3	LeanEDEA1	CO2_1	LeanEDEA2
Temperature	°C	42	45	48	50	50	47	47	47
Pressure	kPa	2200	2150	2100	2050	2000	1100	1100	2200
Mass Enthalpy	kJ/kg	-4737	-4727	-4720	-4714	-4712	-4306	-8605	-4304
Mass Entropy	kJ/(kg.°C)	-6.30	-6.27	-6.25	-6.23	-6.22	-6.82	-0.30	-6.82
Mass Density	kg/m^3	595.52	502.57	446.05	405.35	383.60	872.15	18.78	871.79
Viscosity	cP	<empty>	<empty>	<empty>	<empty>	<empty>	4.60	0.02	4.50
Mass Flow	kg/h	3416833	3416833	3416833	3416833	3416833	3093987	322845	3093987
Molar Flow	kmol/h	38330	38330	38330	38330	38330	30908	7422	30908
Mole fraction									
H_2O		0.1501	0.1501	0.1501	0.1501	0.1501	0.1857	0.0018	0.1857
EDEA		0.5509	0.5509	0.5509	0.5509	0.5509	0.6832	0	0.6832
CO_2		0.2879	0.2879	0.2879	0.2879	0.2879	0.1286	0.9511	0.1286
H_2S		0	0	0	0	0	0	0	0
N_2		0.0002	0.0002	0.0002	0.0002	0.0002	0	0.0009	0
Ar		0.0025	0.0025	0.0025	0.0025	0.0025	0.0004	0.0110	0.0004
O_2		0.0079	0.0079	0.0079	0.0079	0.0079	0.0015	0.0349	0.0015
NO_2		0	0	0	0	0	0	0	0
SO_2		0.0004	0.0004	0.0004	0.0004	0.0004	0.0004	0.0003	0.0004
SO_3		0	0	0	0	0	0.0001	0	0.0001
Cl_2		0.0002	0.0002	0.0002	0.0002	0.0002	0.0002	0.0002	0.0002

Parameter	Units	LeanEDEA3	LeanEDEA4	MakeupEDEA	MakeupWater	LeanEDEA5	CO2_2	CO2_3	Wtr3
Temperature	°C	36	25	25	25	25	130	48	48
Pressure	kPa	2150	2100	2100	2100	2100	2760	2710	2710
Mass Enthalpy	kJ/kg	-4333	-4367	-3671	-15864	-4367	-8535	-8616	-7120
Mass Entropy	kJ/(kg.°C)	-6.91	-7.02	-7.33	-9.06	-7.02	-0.28	-0.50	-5.51
Mass Density	kg/m^3	879.61	886.86	861.57	998.06	886.86	37.80	49.39	960.45
Viscosity	cP	7.12	11.68	58.47	0.91	11.68	0.02	0.02	0.38
Mass Flow	kg/h	3093987	3093987	5	0	3093992	322845	322845	6
Molar Flow	kmol/h	30908	30908	0	0	30908	7422	7422	0
Mole fraction									
H_2O		0.1857	0.1857	0.02	1	0.1857	0.0018	0.0018	0.3827
EDEA		0.6832	0.6832	0.98	0	0.6832	0	0	0.2090
CO_2		0.1286	0.1286	0	0	0.1286	0.9511	0.9511	0.4026
H_2S		0	0	0	0	0	0	0	0
N_2		0	0	0	0	0	0.0009	0.0009	0
Ar		0.0004	0.0004	0	0	0.0004	0.0110	0.0110	0.0010
O_2		0.0015	0.0015	0	0	0.0015	0.0349	0.0349	0.0035
NO_2		0	0	0	0	0	0	0	0
SO_2		0.0004	0.0004	0	0	0.0004	0.0003	0.0003	0.0008
SO_3		0.0001	0.0001	0	0	0.0001	0	0	0.0001
Cl_2		0.0002	0.0002	0	0	0.0002	0.0002	0.0002	0.0003

Parameter	Units	CO2_3_1	CO2_4	CO2_4_1	CO2_5	CO2_final
Temperature	°C	48	134	49	19	36
Pressure	kPa	2710	6800	6750	6750	11000
Mass Enthalpy	kJ/kg	-8616	-8550	-8657	-8776	-8770
Mass Entropy	kJ/(kg.°C)	-0.50	-0.47	-0.77	-1.23	-1.18
Mass Density	kg/m_3	49.39	99.43	158.37	711.73	559.51
Viscosity	cP	0.02	0.02	<empty>	0.07	<empty>
Mass Flow	kg/h	322839	322839	322839	322839	322839
Molar Flow	kmol/h	7422	7422	7422	7422	7422
Mole fraction						
H_2O		0.0018	0.0018	0.0018	0.0018	0.0018
EDEA		0	0	0	0	0
CO_2		0.9511	0.9511	0.9511	0.9511	0.9511
H_2S		0	0	0	0	0
N_2		0.0009	0.0009	0.0009	0.0009	0.0009
Ar		0.0110	0.0110	0.0110	0.0110	0.0110
O_2		0.0349	0.0349	0.0349	0.0349	0.0349
NO_2		0	0	0	0	0
SO_2		0.0003	0.0003	0.0003	0.0003	0.0003
SO_3		0	0	0	0	0
Cl_2		0.0002	0.0002	0.0002	0.0002	0.0002

Table B.38: Heat tables of the capture plant using EDEA for a flue gas obtained from oxy-combustion of coal. Scenario 7.

Unit	Heat Flow (GJ/h)
qGPU2	42.90
qGPU4	13.30
qGPU6	10.32
qGPU10	104.69
qGPU14	38.52
qhtr	5.96

Table B.39: Work tables of the capture plant using EDEA for a flue gas obtained from oxy-combustion of coal. Scenario 7.

	Unit	qGPU1	qGPU3	qGPU5	qGPU7	qGPU9	qGPU11	qGPU13	qGPU15
Work	kW	8250	7881	8157	116	1204	6264	5857	595

Table B.40: Stream tables of the capture plant using EDEA for a flue gas obtained from oxy-combustion of coal. Scenario 8.

Parameter	Units	FG1+	FG2	FG3	Wtr1	FG4	FG5	FG5_1	FG6	Wtr2	FG7
Temperature	°C	27	116	25	25	25	114	52	25	25	25
Pressure	kPa	101.3	284.8	284.8	284.8	284.8	800.4	750.4	750.4	750.4	750.4
Mass Enthalpy	kJ/kg	-8457	-8377	-8493	-13536	-8408	-8330	-8387	-8421	-12349	-8397
Mass Entropy	kJ/(kg.°C)	0.13	0.16	-0.19	-7.07	-0.07	-0.04	-0.19	-0.30	-5.83	-0.27
Mass Density	kg/m^3	1.73	3.75	5.08	858.82	4.99	10.85	12.23	13.57	806.66	13.49
Viscosity	cP	0.02	0.02	<empty>	0.51	0.02	0.02	0.02	<empty>	0.34	0.02
Mass Flow	kg/h	370642	370642	370642	6161	364481	364481	364481	364481	2235	362246
Molar Flow	kmol/h	8755	8755	8755	259	8495	8495	8495	8495	81	8415
Mole fraction											
H_2O		0.0310	0.0310	0.0310	0.7794	0.0081	0.0081	0.0081	0.0081	0.6273	0.0022
EDEA		0	0	0	0	0	0	0	0	0	0
CO_2		0.8907	0.8907	0.8907	0.2196	0.9112	0.9112	0.9112	0.9112	0.3704	0.9164
H_2S		0	0	0	0	0	0	0	0	0	0
N_2		0.0165	0.0165	0.0165	0.0001	0.0170	0.0170	0.0170	0.0170	0.0002	0.0172
Ar		0.0157	0.0157	0.0157	0.0002	0.0161	0.0161	0.0161	0.0161	0.0004	0.0163
O_2		0.0457	0.0457	0.0457	0.0005	0.0471	0.0471	0.0471	0.0471	0.0013	0.0475
NO_2		0	0	0	0	0	0	0	0	0	0
SO_2		0.0002	0.0002	0.0002	0.0001	0.0002	0.0002	0.0002	0.0002	0.0003	0.0002
SO_3		0	0	0	0	0	0	0	0	0.0001	0
Cl_2		0.0002	0.0002	0.0002	0.0000	0.0002	0.0002	0.0002	0.0002	0.0001	0.0002

Parameter	Units	FG8	FG8_1	FG9	LeanEDEA	CleanFG	RichEDEA1	RichEDEA2	RichEDEA3
Temperature	°C	121	47	25	25	29	31	31	39
Pressure	kPa	2250	2200	2200	2100	2100	2200	2300	2250
Mass Enthalpy	kJ/kg	-8316	-8387	-8413	-4408	-6637	-4794	-4794	-4766
Mass Entropy	kJ/(kg.°C)	-0.24	-0.43	-0.51	-6.99	-0.40	-6.40	-6.40	-6.32
Mass Density	kg/m^3	30.87	38.74	42.86	888.97	35.71	912.42	912.41	693.50
Viscosity	cP	0.02	0.02	<empty>	10.72	0.02	3.19	3.19	<empty>
Mass Flow	kg/h	362246	362246	362246	3210923	39654	3533515	3533515	3533515
Molar Flow	kmol/h	8415	8415	8415	32474	993	39896	39896	39896
Mole fraction									
H_2O		0.0022	0.0022	0.0022	0.1878	0.0003	0.1533	0.1533	0.1533
EDEA		0	0	0	0.6700	0	0.5454	0.5454	0.5454
CO_2		0.9164	0.9164	0.9164	0.1394	0.6727	0.2900	0.2900	0.2900
H_2S		0	0	0	0	0	0	0	0
N_2		0.0172	0.0172	0.0172	0	0.1387	0.0002	0.0002	0.0002
Ar		0.0163	0.0163	0.0163	0.0005	0.0535	0.0025	0.0025	0.0025
O_2		0.0475	0.0475	0.0475	0.0017	0.1347	0.0080	0.0080	0.0080
NO_2		0	0	0	0	0	0	0	0
SO_2		0.0002	0.0002	0.0002	0.0004	0.0001	0.0004	0.0004	0.0004
SO_3		0	0	0	0.0001	0	0.0001	0.0001	0.0001
Cl_2		0.0002	0.0002	0.0002	0.0002	0.0001	0.0002	0.0002	0.0002

Parameter	Units	RichEDEA4	RichEDEA5	RichEDEA5_1	RichEDEA5_2	RichEDEA5_3	LeanEDEA1	CO2_1	LeanEDEA2
Temperature	°C	41	44.5	47	49	50	47	47	48
Pressure	kPa	2200	2150	2100	2050	2000	1200	1200	2200
Mass Enthalpy	kJ/kg	-4760	-4750	-4742	-4736	-4733	-4345	-8595	-4343
Mass Entropy	kJ/(kg.°C)	-6.29	-6.26	-6.24	-6.22	-6.21	-6.79	-0.32	-6.78
Mass Density	kg/m^3	600.89	504.84	446.79	405.21	378.69	873.88	20.54	873.55
Viscosity	cP	<empty>	<empty>	<empty>	<empty>	<empty>	4.21	0.02	4.13
Mass Flow	kg/h	3533515	3533515	3533515	3533515	3533515	3210467	323048	3210467
Molar Flow	kmol/h	39896	39896	39896	39896	39896	32468	7429	32468
Mole fraction									
H_2O		0.1533	0.1533	0.1533	0.1533	0.1533	0.1880	0.0017	0.1880
EDEA		0.5454	0.5454	0.5454	0.5454	0.5454	0.6702	0	0.6702
CO_2		0.2900	0.2900	0.2900	0.2900	0.2900	0.1391	0.9498	0.1391
H_2S		0	0	0	0	0	0	0	0
N_2		0.0002	0.0002	0.0002	0.0002	0.0002	0	0.0009	0
Ar		0.0025	0.0025	0.0025	0.0025	0.0025	0.0005	0.0113	0.0005
O_2		0.0080	0.0080	0.0080	0.0080	0.0080	0.0017	0.0359	0.0017
NO_2		0	0	0	0	0	0	0	0
SO_2		0.0004	0.0004	0.0004	0.0004	0.0004	0.0004	0.0003	0.0004
SO_3		0.0001	0.0001	0.0001	0.0001	0.0001	0.0001	0	0.0001
Cl_2		0.0002	0.0002	0.0002	0.0002	0.0002	0.0002	0.0002	0.0002

Parameter	Units	LeanEDEA3	LeanEDEA4	MakeupEDEA	MakeupWater	LeanEDEA5	CO2_2	CO2_3	Wtr3
Temperature	°C	36	25	25	25	25	122	50	50
Pressure	kPa	2150	2100	2100	2100	2100	2760	2710	2710
Mass Enthalpy	kJ/kg	-4373	-4408	-3671	-15864	-4408	-8533	-8604	-6066
Mass Entropy	kJ/(kg.°C)	-6.88	-6.99	-7.33	-9.06	-6.99	-0.30	-0.49	-5.89
Mass Density	kg/m^3	881.68	888.92	861.57	998.06	888.92	38.67	48.94	932.03
Viscosity	cP	6.60	10.74	58.47	0.91	10.74	0.02	0.02	0.62
Mass Flow	kg/h	3210467	3210467	5	0	3210472	323048	323048	3
Molar Flow	kmol/h	32468	32468	0	0	32468	7429	7429	0
Mole fraction									
H_2O		0.1880	0.1880	0.02	1	0.1880	0.0017	0.0017	0.3284
EDEA		0.6702	0.6702	0.98	0	0.6702	0	0	0.3190
CO_2		0.1391	0.1391	0	0	0.1391	0.9498	0.9498	0.3466
H_2S		0	0	0	0	0	0	0	0
N_2		0	0	0	0	0	0.0009	0.0009	0
Ar		0.0005	0.0005	0	0	0.0005	0.0113	0.0113	0.0011
O_2		0.0017	0.0017	0	0	0.0017	0.0359	0.0359	0.0037
NO_2		0	0	0	0	0	0	0	0
SO_2		0.0004	0.0004	0	0	0.0004	0.0003	0.0003	0.0008
SO_3		0.0001	0.0001	0	0	0.0001	0	0	0.0001
Cl_2		0.0002	0.0002	0	0	0.0002	0.0002	0.0002	0.0003

Parameter	Units	CO2_3_1	CO2_4	CO2_4_1	CO2_5	CO2_final
Temperature	°C	50	137	47	19	36
Pressure	kPa	2710	6800	6750	6750	11000
Mass Enthalpy	kJ/kg	-8604	-8538	-8649	-8767	-8761
Mass Entropy	kJ/(kg.°C)	-0.49	-0.47	-0.78	-1.23	-1.18
Mass Density	kg/m^3	48.94	98.53	160.28	711.95	560.41
Viscosity	cP	0.02	0.02	<empty>	0.07	<empty>
Mass Flow	kg/h	323045	323045	323045	323045	323045
Molar Flow	kmol/h	7429	7429	7429	7429	7429
Mole fraction						
H_2O		0.0017	0.0017	0.0017	0.0017	0.0017
EDEA		0	0	0	0	0
CO_2		0.9498	0.9498	0.9498	0.9498	0.9498
H_2S		0	0	0	0	0
N_2		0.0009	0.0009	0.0009	0.0009	0.0009
Ar		0.0113	0.0113	0.0113	0.0113	0.0113
O_2		0.0359	0.0359	0.0359	0.0359	0.0359
NO_2		0	0	0	0	0
SO_2		0.0003	0.0003	0.0003	0.0003	0.0003
SO_3		0	0	0	0	0
Cl_2		0.0002	0.0002	0.0002	0.0002	0.0002

Table B.41: Heat tables of the capture plant using EDEA for a flue gas obtained from oxy-combustion of coal. Scenario 8.

Unit	Heat Flow (GJ/h)
qGPU2	42.90
qGPU4	12.41
qGPU6	9.22
qGPU10	110.29
qGPU14	38.19
qhtr	11.06

Table B.42: Work tables of the capture plant using EDEA for a flue gas obtained from oxy-combustion of coal. Scenario 8.

	Unit	qGPU1	qGPU3	qGPU5	qGPU7	qGPU9	qGPU11	qGPU13	qGPU15
Work	kW	8250	7881	8157	120	1134	5608	5914	595

Appendix C

Validation exercises

Table C.1: Composition of Appalachian medium sulfur bituminous coal used in this work, extracted from IECM[266].

Fuel Component	Mass Fraction (w_i as received)
C	0.74
H	0.05
S	0.02
O	0.05
N	0.01
H_2O	0.05
Cl_2	6×10^{-4}
Ash	0.07
Fuel HHV (MJ/kg)	33.48

Table C.2: Validation exercise between this work and Kunzemann's work.

	Kunzemann's Thesis			This work			Absolute Percentage Error		
Flow no.	**p (bar)**	**T (°C)**	**m (kg/s)**	**p (bar)**	**T (°C)**	**m (kg/s)**	**p (bar)**	**T (°C)**	**m (kg/s)**
FWSH2	300	600	379	300	600	379	0 %	0 %	0 %
FWHP2	75	382	30	75	365	35	0 %	4 %	18 %
FWHP1	75	382	339	75	365	344	0 %	4 %	1 %
FWRH2	70	620	335	70	620	344	0 %	0 %	3 %
FWIPT11	48	559	26	48	558	26	0 %	0 %	1 %
FWIPT21	25	460	14	25	460	17	0 %	0 %	18 %
FWIPT31	14	375	16	14	381	16	0 %	2 %	2 %
FWIPT41	7	288	17	7	297	17	0 %	3 %	2 %
FWIPT42	7	289	245	7	297	269	0 %	3 %	10 %
FWLPT11	2.8	188	16	2.8	200	26	0 %	6 %	62 %
FWLPT21	0.9	97	15	0.9	102	15	0 %	5 %	1 %
FWLPT3Liq+31	0.2	64	12	0.25	65	13	5 %	2 %	6 %
FWLPT4	0.04	27	201	0.04	29	216	0 %	8 %	7 %
FWCond	0.03	28	231	0.03	24	216	0 %	14 %	7 %
FWPump	23	30	231	23	24	216	0 %	19 %	7 %
FWH11	21	61	292	21	61	286	0 %	0 %	2 %
FWH21	19	94	292	19	87	286	0 %	7 %	2 %
FWH31	17	127	292	17	127	286	0 %	0 %	2 %
FWH41	14	161	292	14	159	286	0 %	1 %	2 %
FWH51	14	194	379	14	195	379	0 %	1 %	0 %
FWBFP	326	201	379	327	203	379	0 %	1 %	0 %
FWH61	326	226	379	326	224	379	0 %	1 %	0 %
FWH71	325	259	379	326	260	379	0 %	0 %	0 %
FWH81	325	292	379	325	292	379	0 %	0 %	0 %
Feedwater	324	300	379	324	299	379	0 %	0 %	0 %

Appendix D

Sensitivity analysis

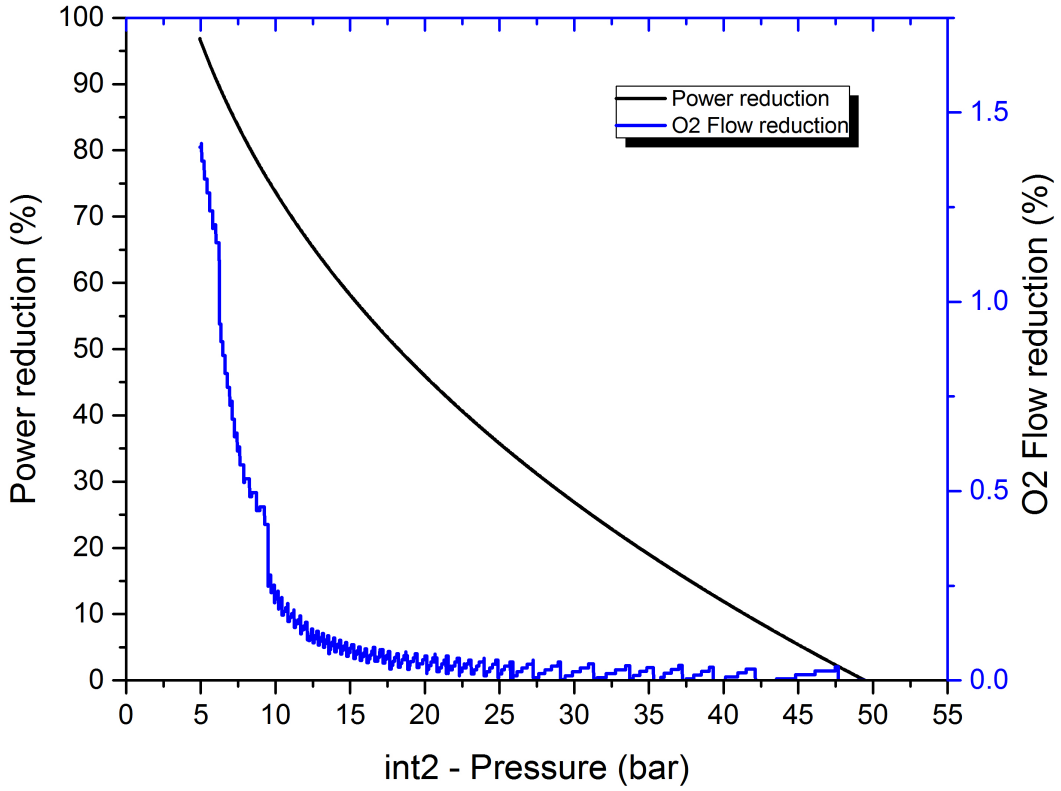


Figure D.1: Effect of booster outlet pressure on power consumption and O_2 flow reduction.

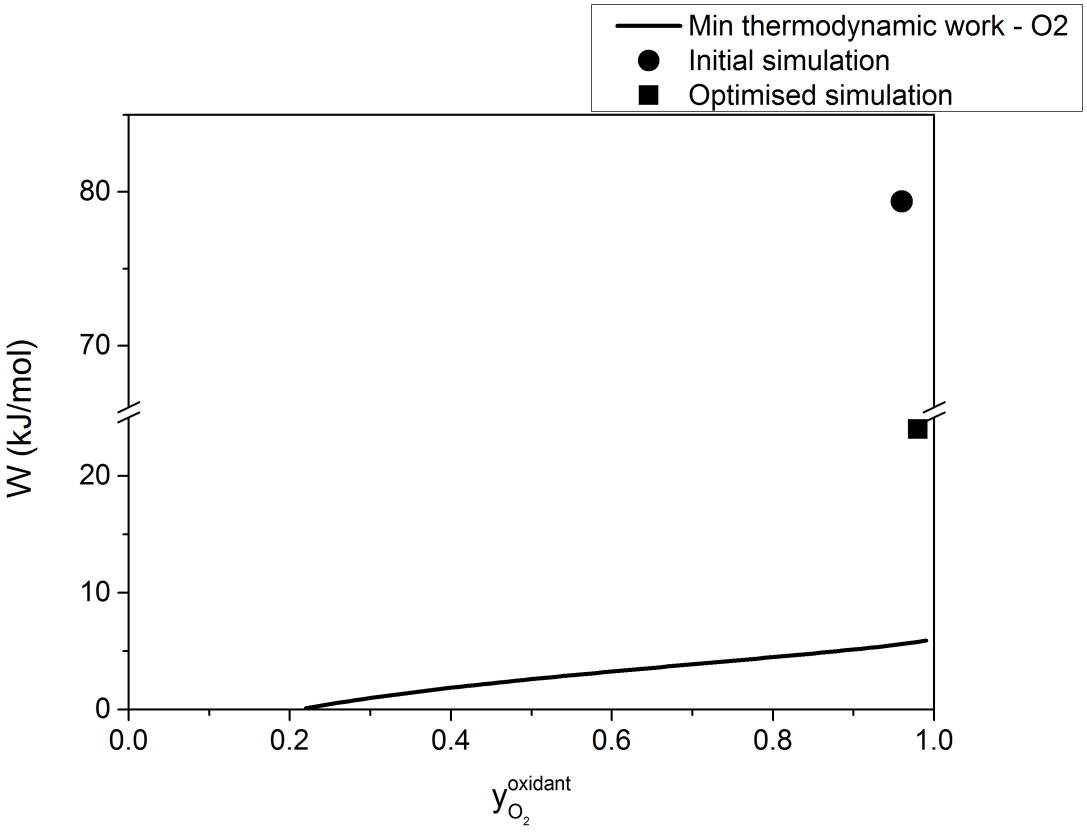


Figure D.2: Actual work from initial simulation (●) and optimised simulation (■) against minimum thermodynamic work required for air separation. The initial model has a thermodynamic efficiency of 19% while the optimised model is increased to 25%.

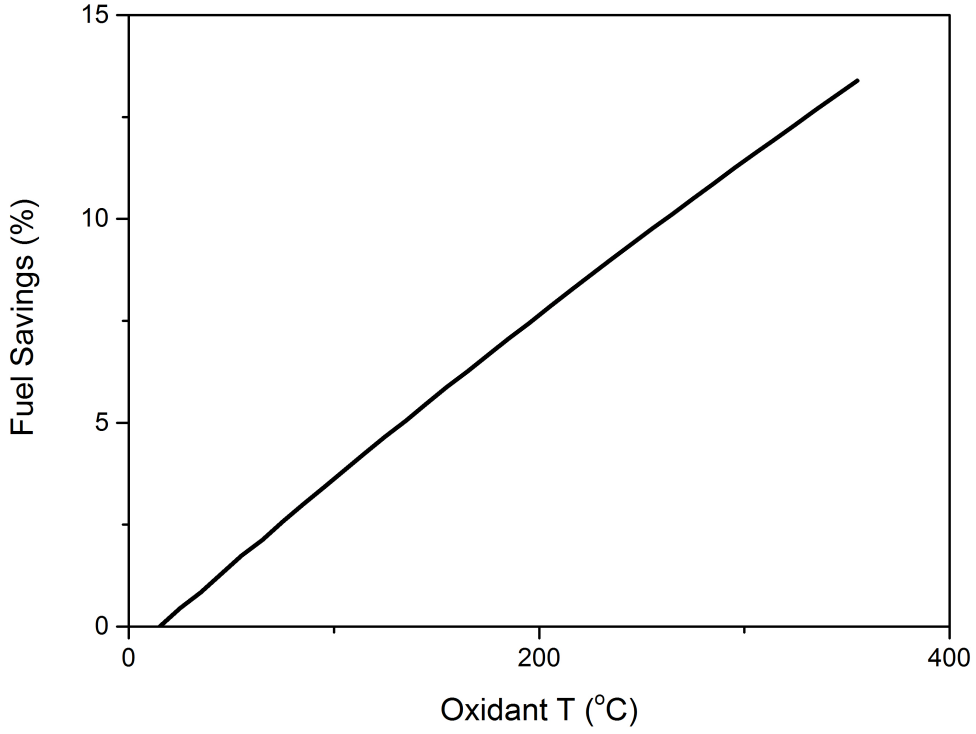


Figure D.3: Fuel savings potential based on air inlet temperature.

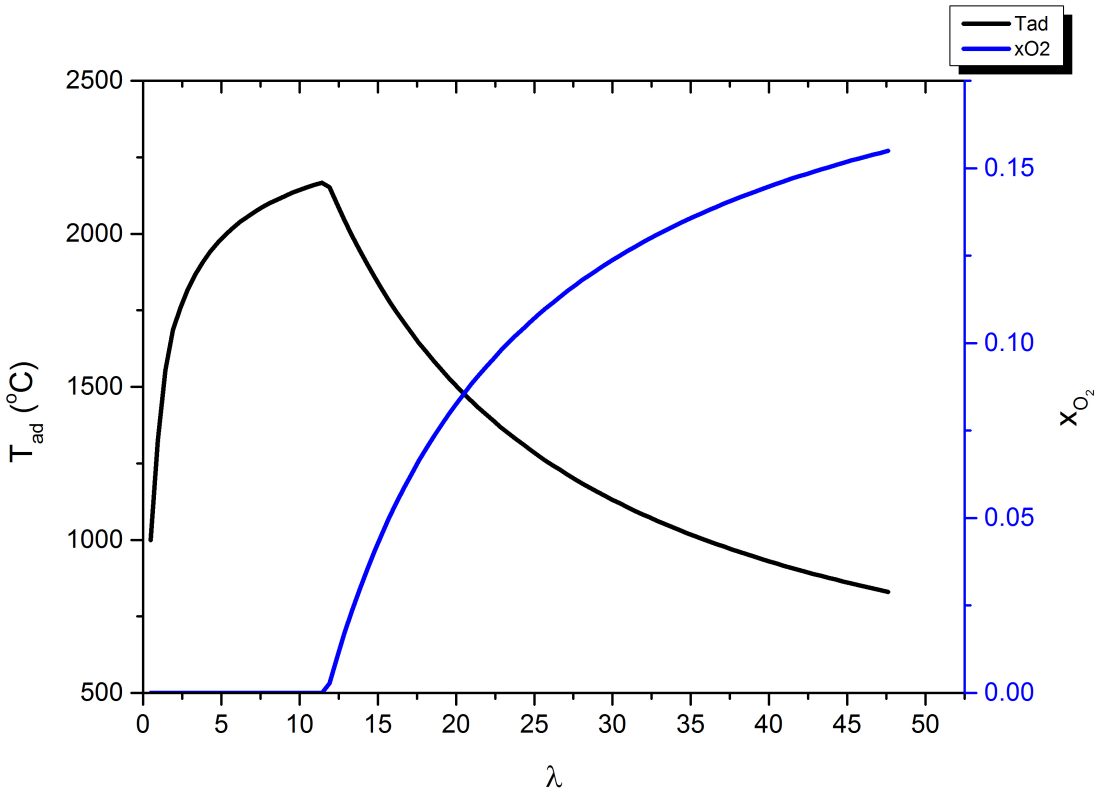


Figure D.4: Adiabatic flame temperature and fraction of O_2 in flue gas based on air to fuel ratio.

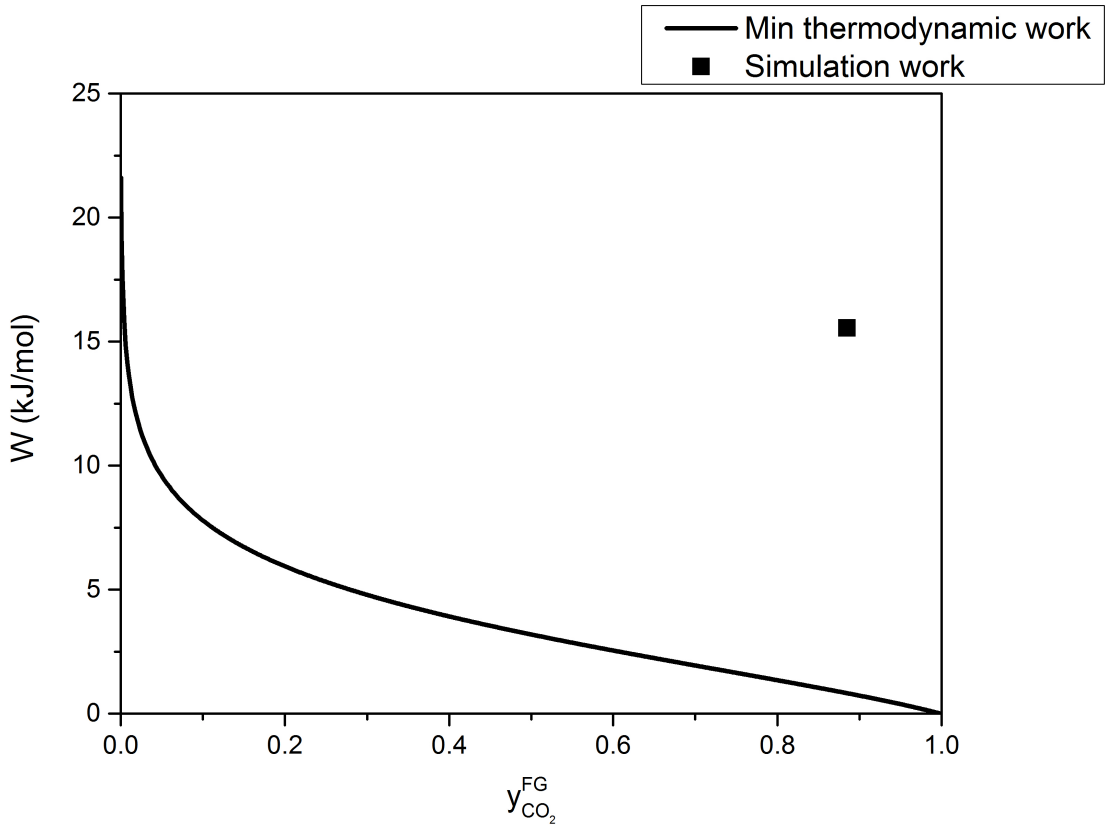


Figure D.5: Minimum thermodynamic separation work of CO_2 from a gas mixture for different CO_2 concentrations in the flue gas (FG).

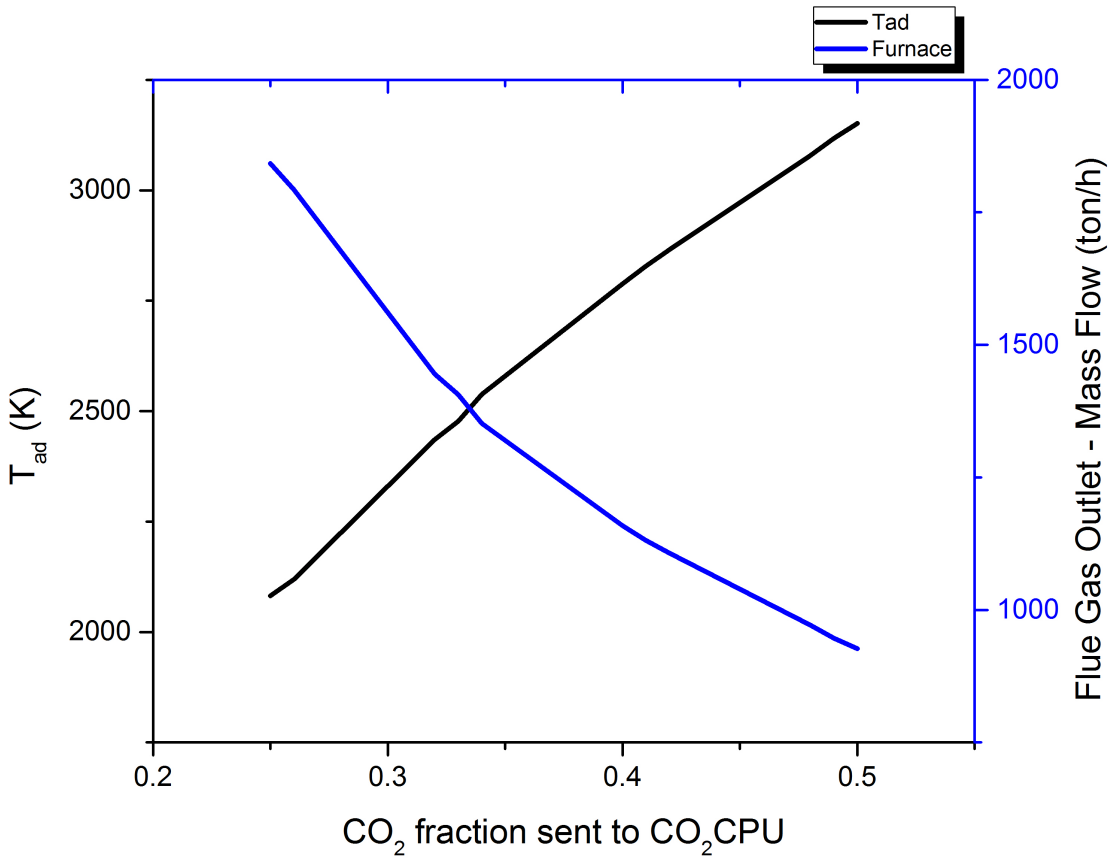


Figure D.6: Sensitivity analysis on flue gas amount sent to the GPU.

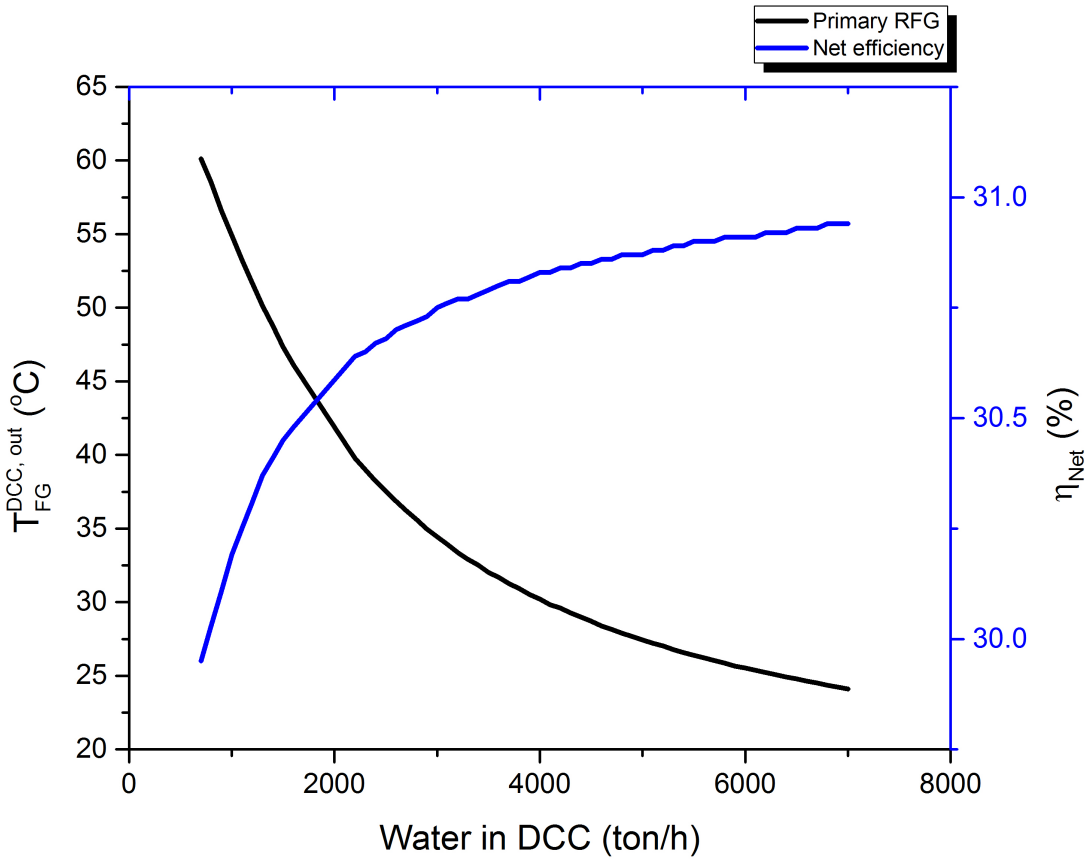


Figure D.7: Effect of cooling water sent to DCC on flue gas temperature leaving the DCC and power plant net efficiency.

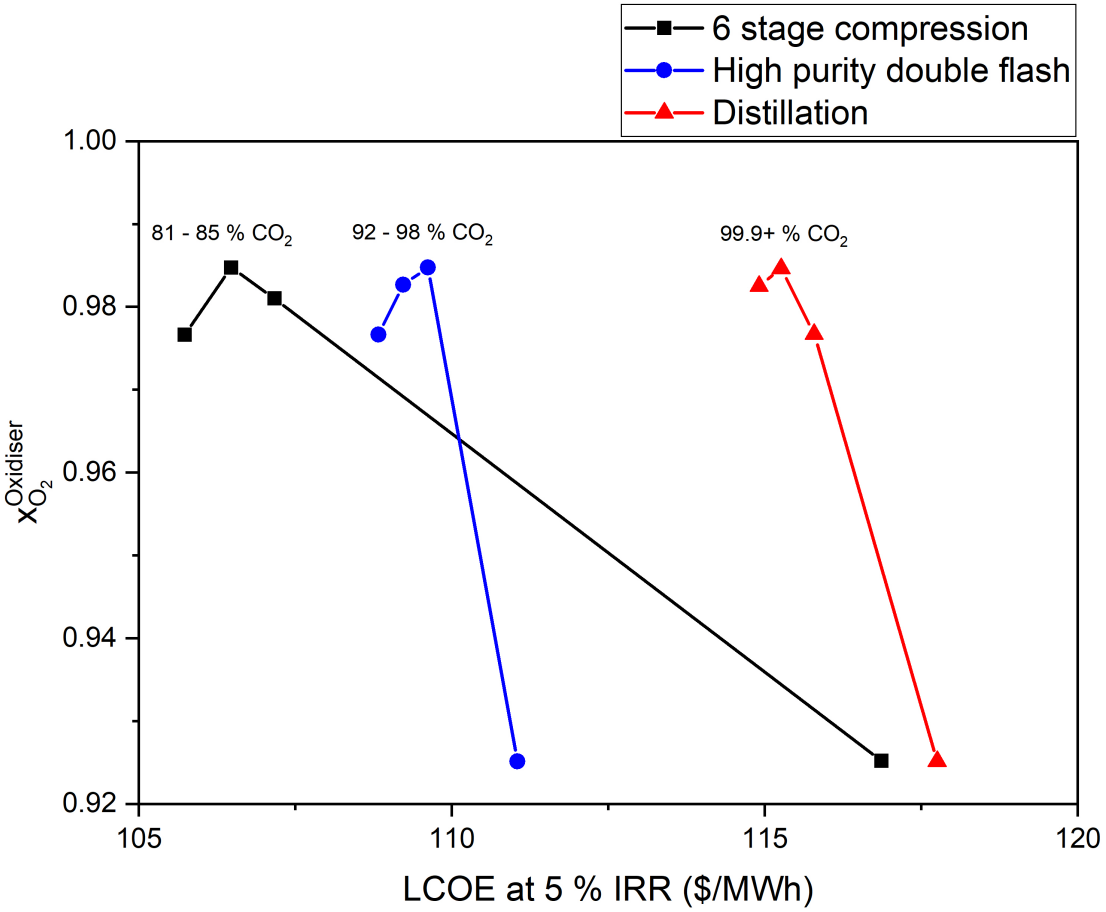


Figure D.8: Effect of O_2 purity on oxidizer and GPU process on LCOE.

Appendix E

Techno-economic analysis

E.1 CEPCI

Table E.1: CEPCI values

Year	CEPCI	Year	CEPCI
1990	357.6	2003	402
1991	361.3	2004	444.2
1992	358.2	2005	468.2
1993	359.2	2006	499.6
1994	368.1	2007	525.4
1995	381.1	2008	575.4
1996	381.7	2009	521.9
1997	386.5	2010	550.8
1998	389.5	2011	585.7
1999	390.6	2012	584.6
2000	394.1	2013	567.3
2001	394.3	2014	576.1
2002	395.6	2015	556.8

E.2 ASU

Using the procedure detailed by Ward [258], Katell and Wellman [259] it was found that the ASU produces oxygen at the cost of 107.07 $/t$_{O_2}$. Should we decide on selling just N_2 (this strategy was chosen because O_2 will be used for the oxy-fuel combustion), it would be at 46.96 $/t for an IRR of 5 %. Due to the confidentiality nature of this type of information, it is hard to find actual data on the price of these industrial gases, so we must rely on comparisons with other simulations[114]. The results obtained in this study go in accordance with Schmidt and Clayton [376], having both oxygen and nitrogen sold at 30.20 $/t, assuming a conversion of 0.76 £/$. Ebrahimi also shows similar results, showing that prices can vary between 10 and 100 $/t[377].

E.3 GPU

By performing a techno-economic analysis, in the same manner as done for the ASU, we can conclude that this technology will have an LCOE between 105 and 120 $/MWh

depending on the technology used for the CO_2 CPU and O_2 purity on oxidiser. Figure D.8 shows that LCOE increases at very-low O_2 purity in the oxidizer LCOE will increase because more volume would have to be compressed on the CO_2 CPU as the amounts of N_2 will start to be considerable. The turning point observed between the 6 stage compression and flash distillation is because the flash process can significantly reduce the amounts of N_2 from the stream, reducing the costs of compressing the gas to high pressure.

Appendix F

Flexibility

F.0.1 Coal-fired

Day off-peak electricity price

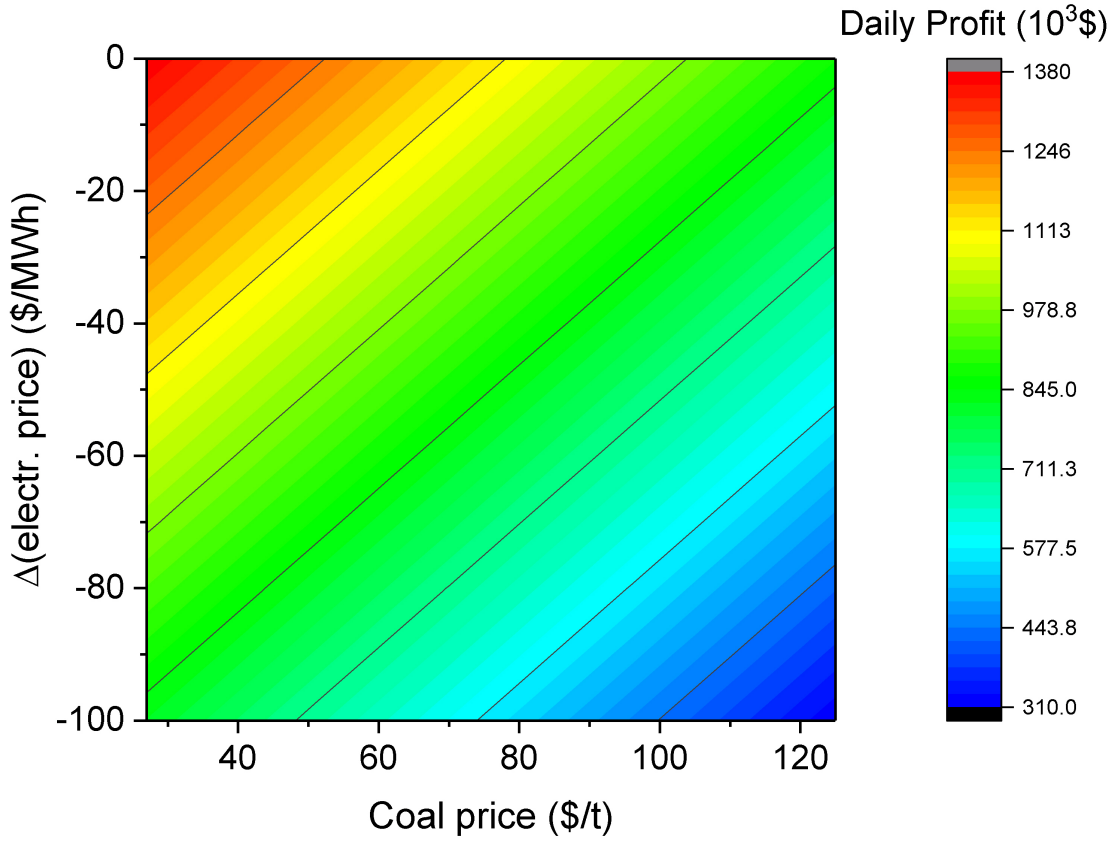


Figure F.1: Sensitivity analysis of the effect of coal price and difference of day off-peak electricity price relative to peak electricity price on daily profits for the schedule detailed in Figure 7.4 b. Lower deviations from peak electricity price and lower fuel price lead to higher daily profits.

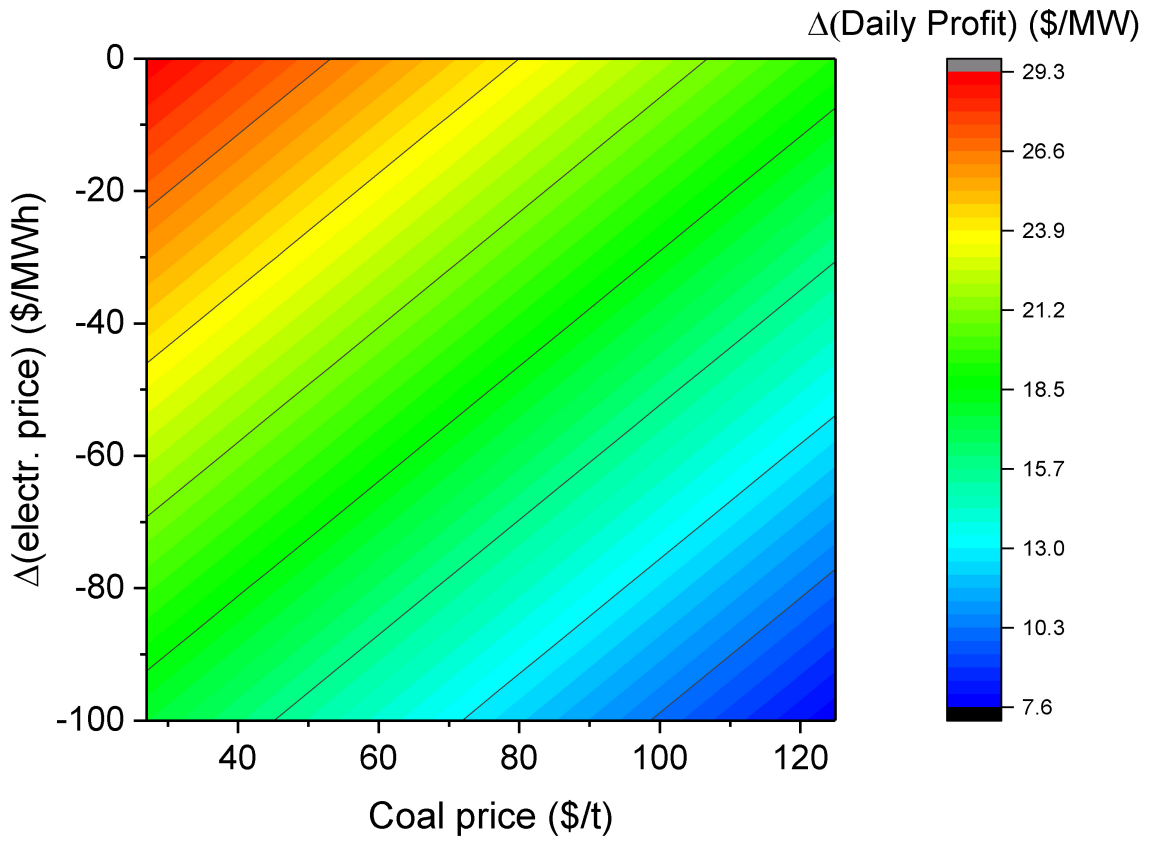


Figure F.2: Sensitivity analysis of the effect of coal price and difference of day off-peak electricity price relative to peak electricity price on the variation of daily profit between the schedule represented in Figure 7.4 b using LOX storage and without LOX storage. It can be observed that regardless of the situation, LOX storage has higher daily profits.

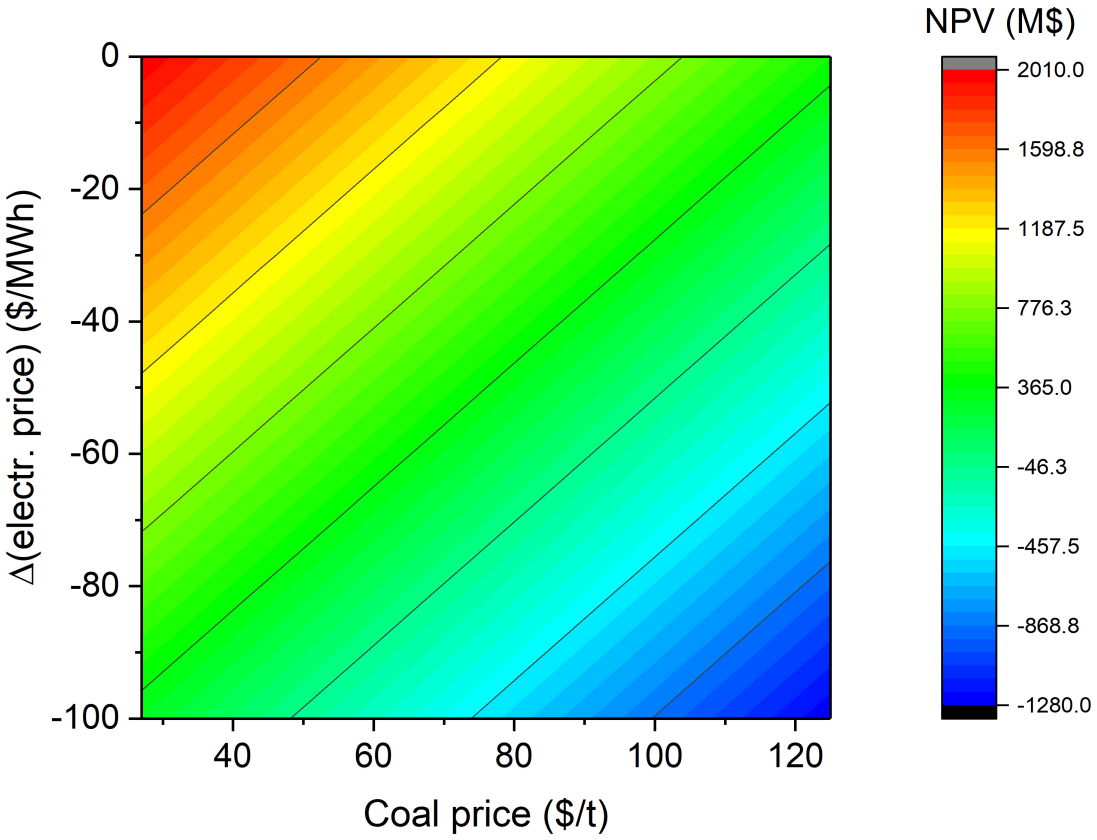


Figure F.3: Sensitivity analysis on coal price and difference between day off-peak electricity price and peak electricity price, analysing their effect on NPV for the schedule represented in Figure 7.4 b. Lower electricity price difference and lower coal cost increase NPV. Negative NPV occurs on the lower-right half of the figure, indicating that if coal prices are high, then this process should only be considered if there is low difference between night off-peak and peak electricity price.

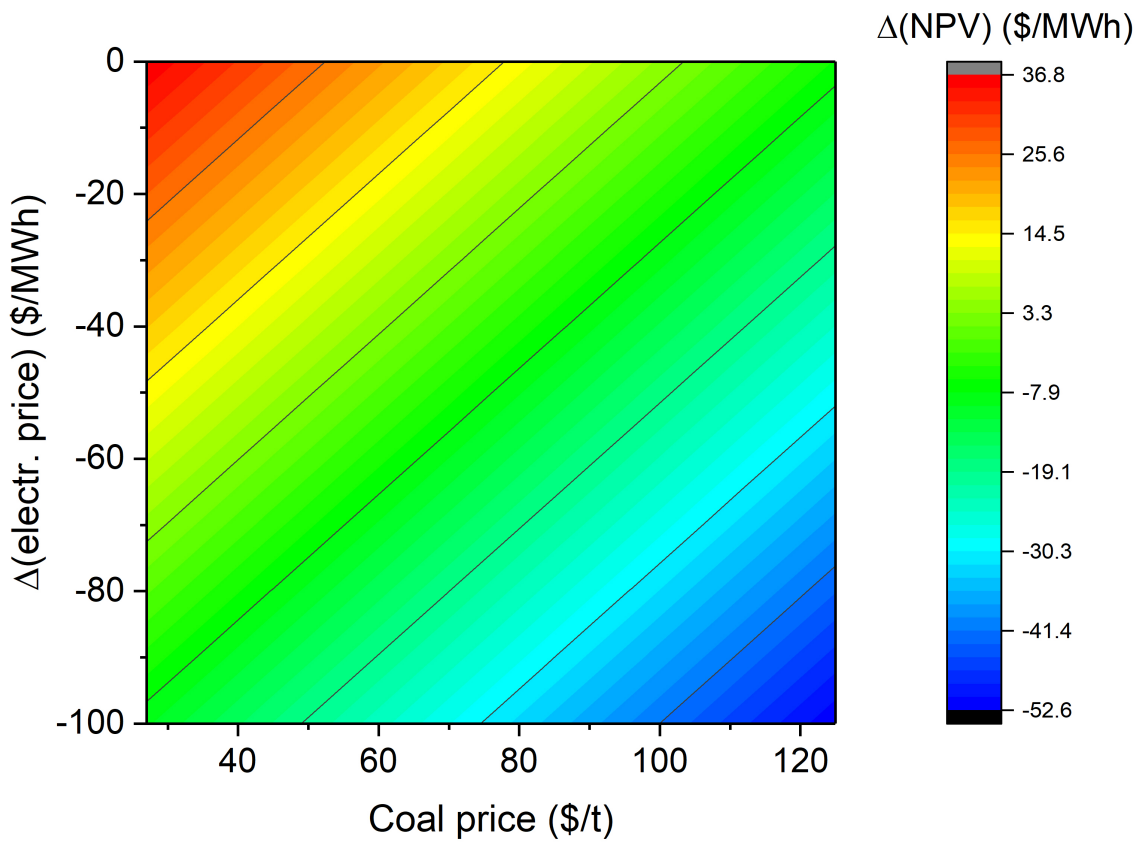


Figure F.4: Sensitivity analysis on coal price and difference between day off-peak electricity price and peak electricity price, analysing their effect on the NPV difference between the case with LOX storage and without LOX storage for the schedule represented in Figure 7.4 b. Storing oxygen becomes more economical at lower price difference and lower coal price, since the plant is discharging LOX during this time period. Interestingly, LOX storage is more economical when positive NPV occur, as seen in Figure F.3.

Night off-peak electricity price

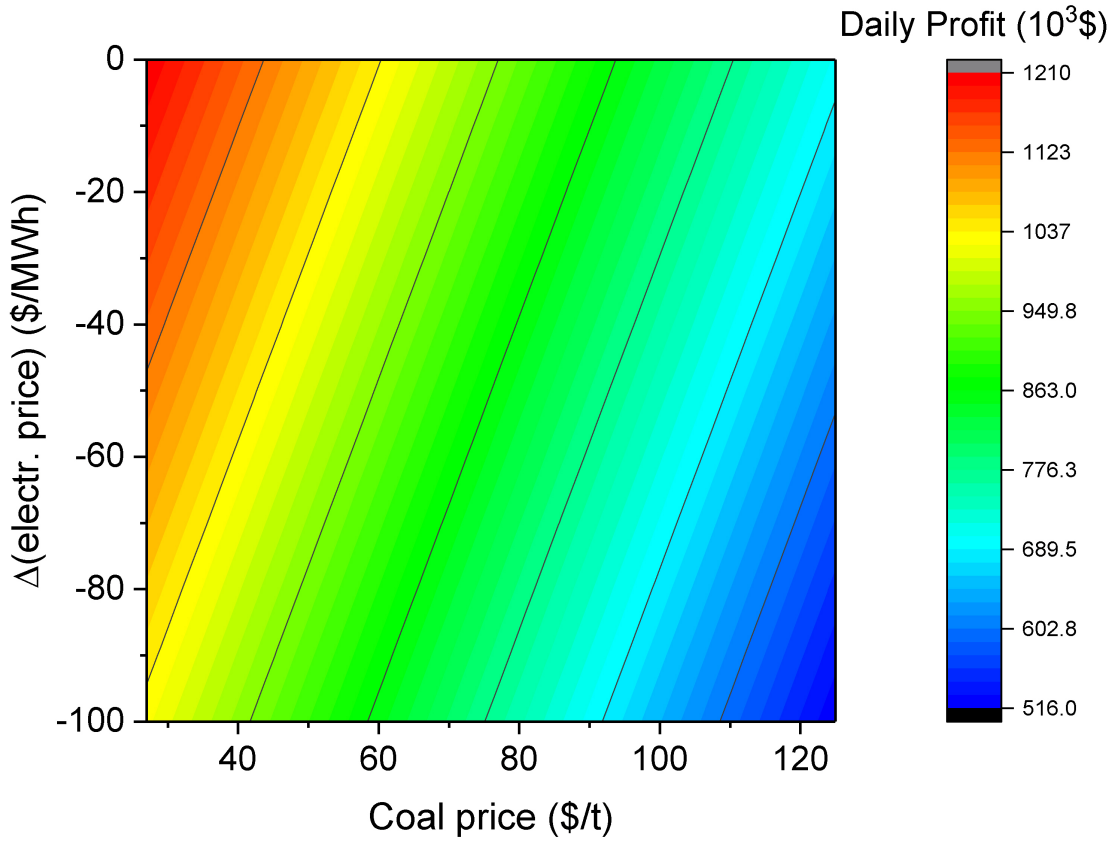


Figure F.5: Sensitivity analysis on varying coal cost and night off-peak electricity price with respect to daily peak electricity price on daily profits for the schedule represented in Figure 7.4 b. It can be observed that a similar effect to Figure F.1 is obtained, although the night off-peak price variation has less impact on daily profits.

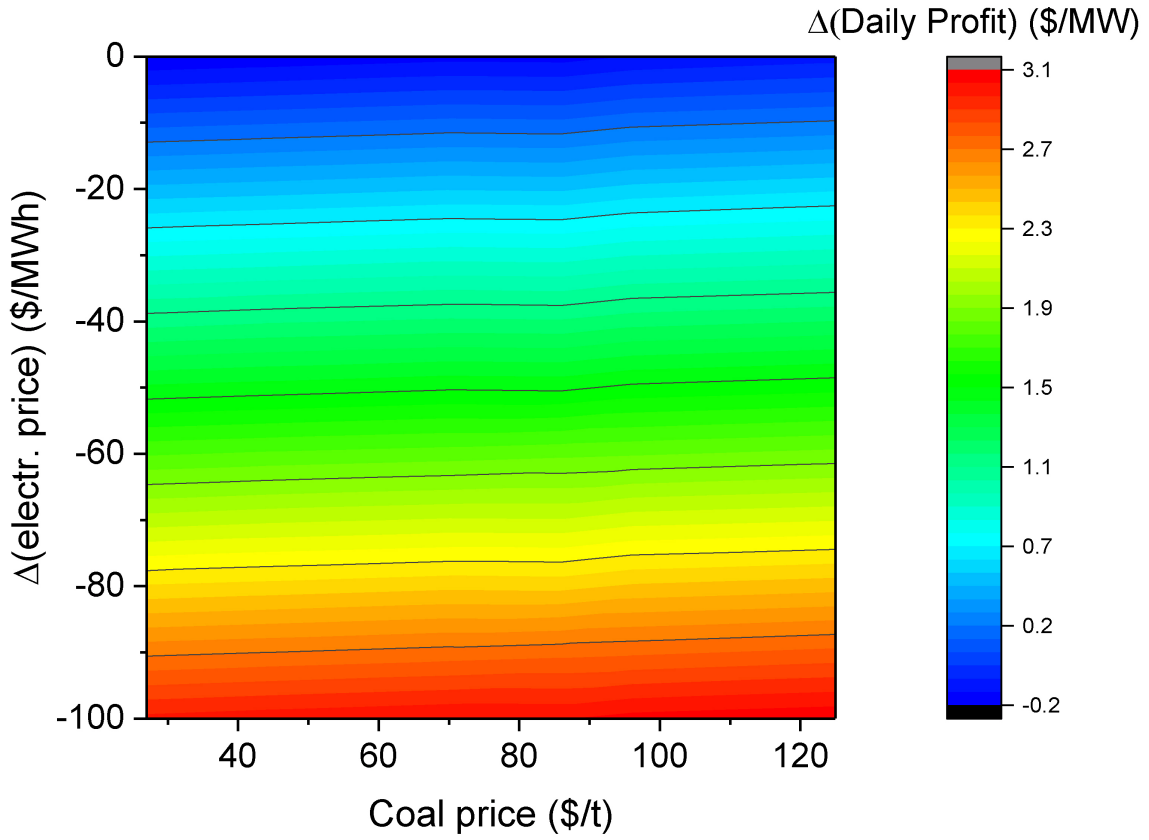


Figure F.6: Sensitivity analysis on varying coal cost and night off-peak electricity price with respect to daily peak electricity price on the difference between daily profits for the case with LOX storage and without LOX storage for the schedule represented in Figure 7.4 b. It can be clearly seen that night off-peak electricity price has a large impact on determining whether to use LOX storage or not. Indeed, if electricity if being sold at night at $30/MWh lower than during peak electricity prices, it then becomes advantageous to store LOX and discharge it during the day.

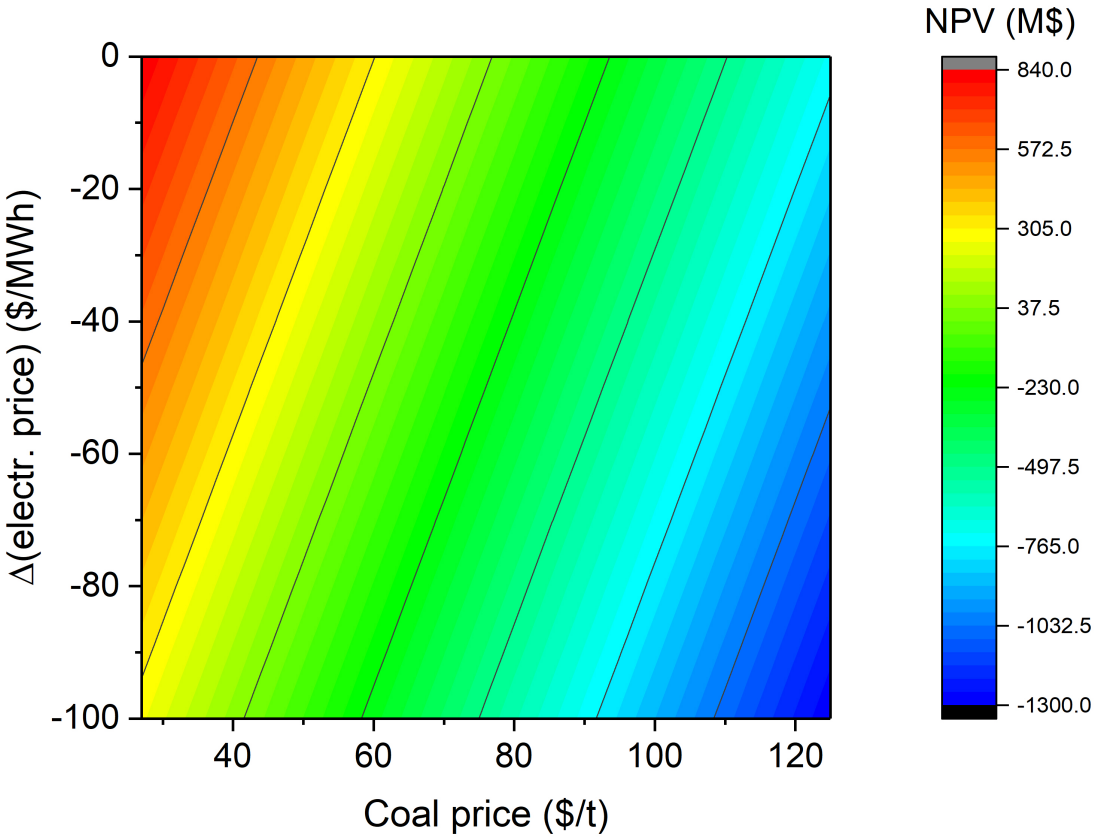


Figure F.7: Sensitivity analysis on coal price and the difference between night off-peak electricity price with peak electricity price, analysing the effect on NPV for the schedule represented in Figure 7.4 b. Coal price appears to be the main factor affecting NPV, where increased coal prices incurr lower NPV. Indeed, coal price above $80/t yields negative NPV at electricity price difference larger than $20/MWh.

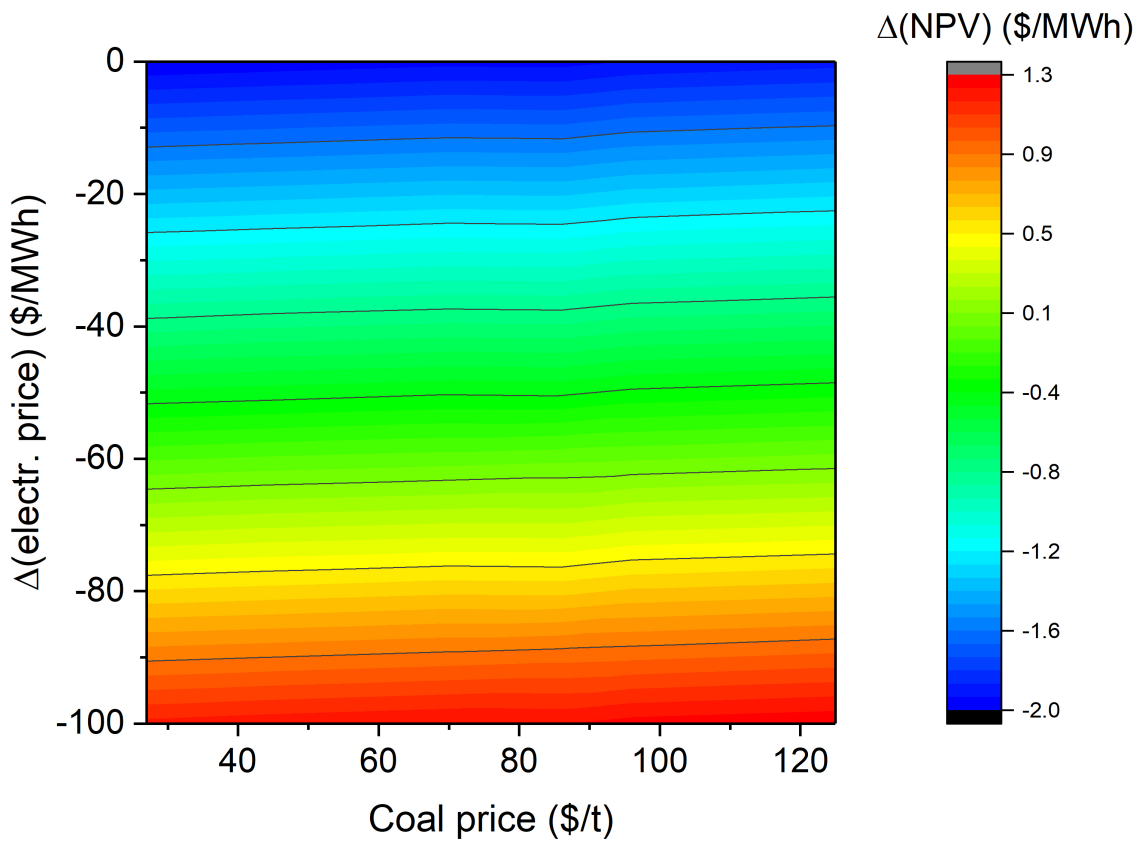


Figure F.8: Sensitivity analysis on coal price and the difference between night off-peak electricity price with peak electricity price, analysing the effect on NPV difference between the case of LOX storage with the case without LOX storage for the schedule represented in Figure 7.4 b. Contrary to NPV, the difference of electricity price at night with respect to peak price is the main factor affecting whether LOX storage is more economical than having no storage. Indeed, LOX storage becomes more economical at a price difference within $65/MWh.

Day and night off-peak electricity price

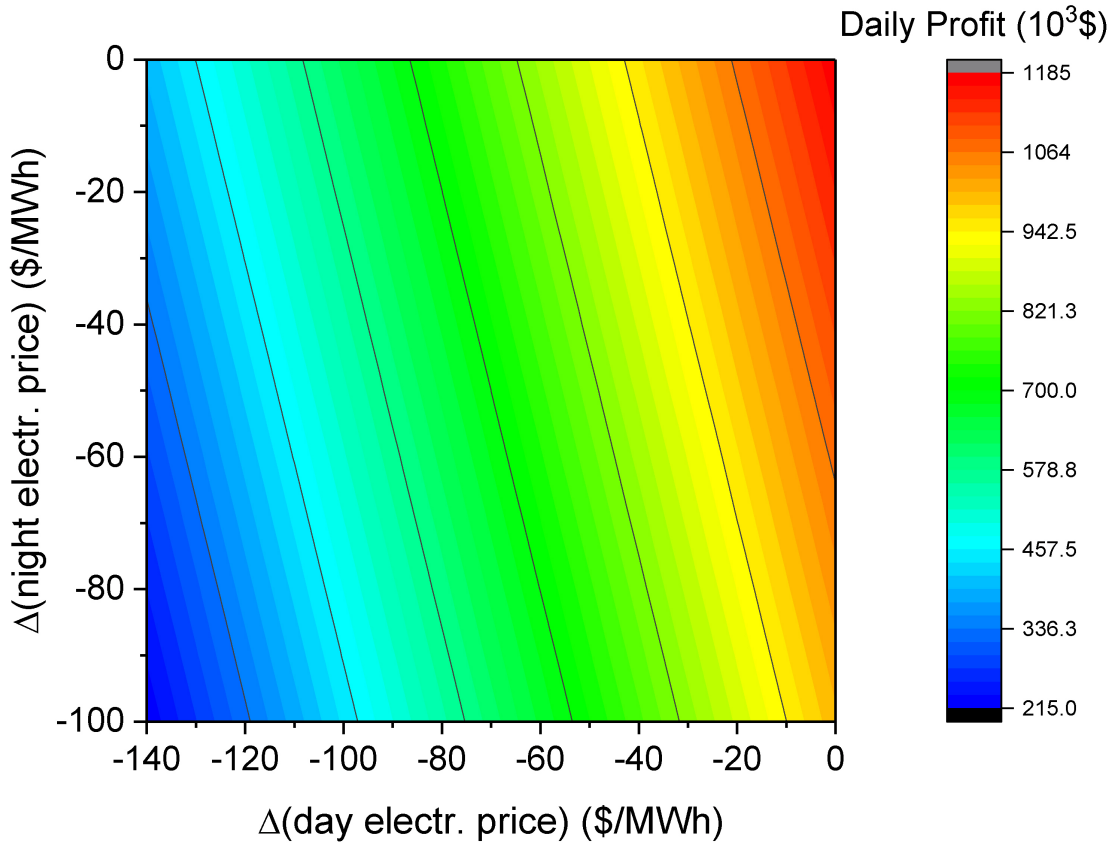


Figure F.9: Sensitivity analysis of night and day off-peak electricity prices relative to peak electricity price and their effect on daily profit for an oxy-combustion process firing coal with cost $86/t for the schedule represented in Figure 7.4 b. The higher the electricity prices, the greater the profit. It must be noted that day off-peak electricity price variation has a greater impact on profit.

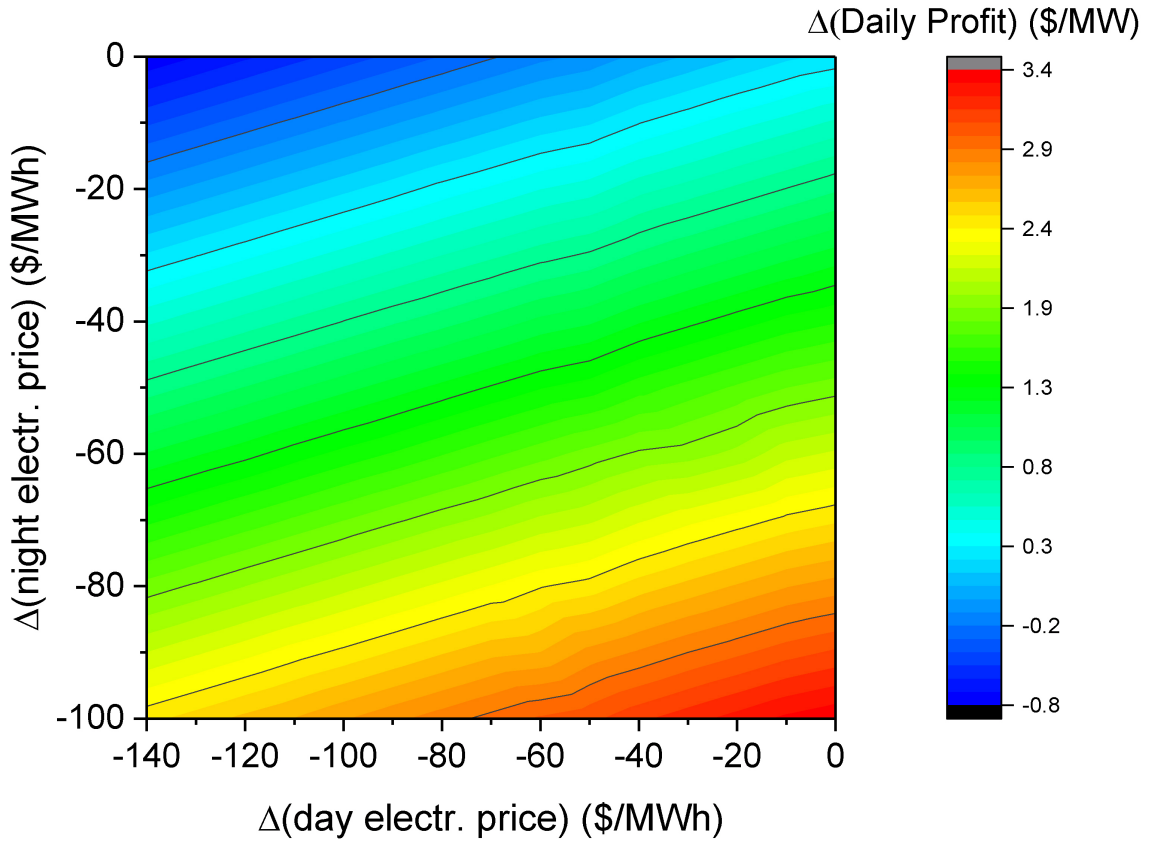


Figure F.10: Sensitivity analysis of night and day off-peak electricity prices relative to peak electricity price and their effect on the difference of daily profit between the case of LOX storage and without storage for an oxy-combustion process firing coal with cost $86/t for the schedule represented in Figure 7.4 b. Here, the night off-peak electricity price has a greater impact on whether LOX storage should be considered or not. Indeed, LOX storage should be considered if night off-peak electricity price is within $20/MWh lower than peak electricity price, especially if day off-peak electricity prices are low. However, this is unlikely to occur, since it would require day off-peak prices be lower than night off-peak prices.

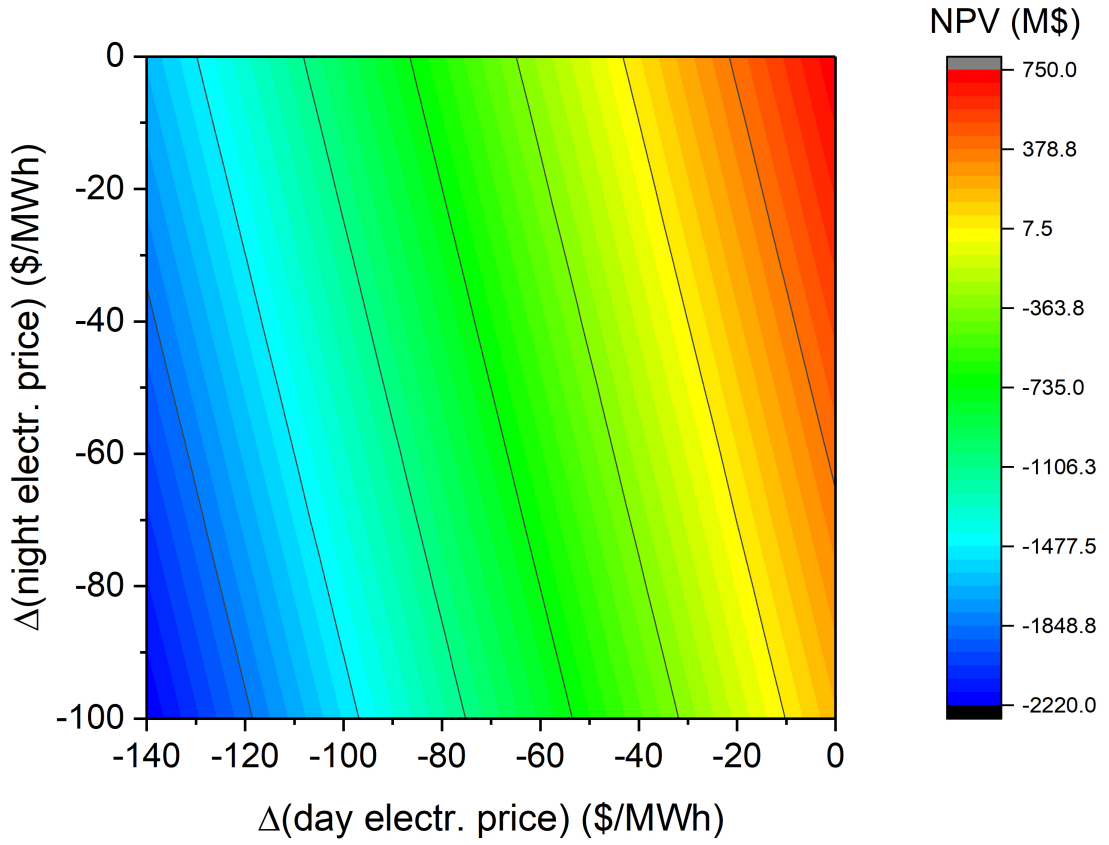


Figure F.11: Sensitivity analysis on the difference between both night and day off-peak electricity prices with respect to peak electricity price and their effect on NPV for an oxy-combustion process firing coal with cost $86/t for the schedule represented in Figure 7.4 b. It can be seen that the day off-peak price has a higher impact on NPV, since during this period the plant is operating at full capacity. Positive NPV can be achieved if the difference between day off-peak electricity price and peak electricity price is smaller than $50/MWh.

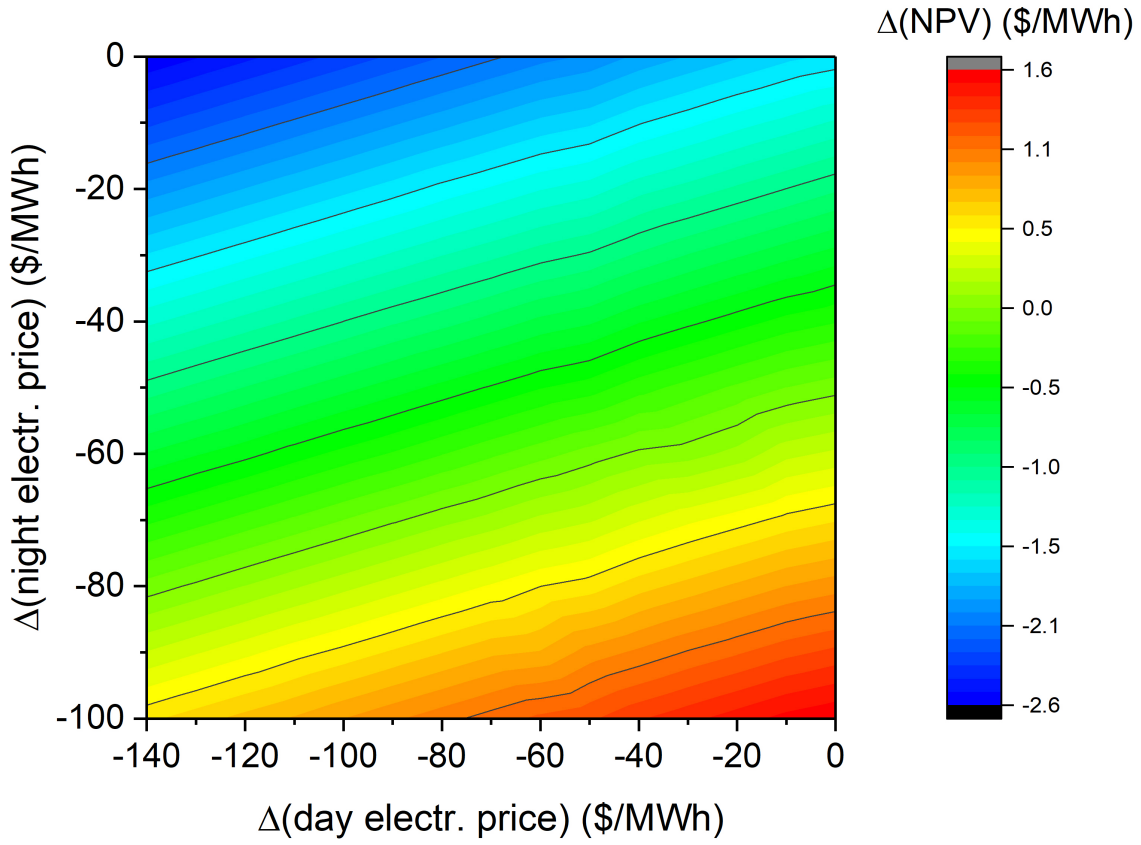


Figure F.12: Sensitivity analysis on the difference between both night and day off-peak electricity prices with respect to peak electricity price and their effect on NPV difference between the case of LOX storage with the case without LOX storage for an oxy-combustion process firing coal with cost $86/t for the schedule represented in Figure 7.4 b. Here, night off-peak electricity price has a greater impact on the outcome. LOX storage becomes a more economical option if night off-peak electricity price is more than $50/MWh below peak electricity price.

F.0.2 Biomass-fired

Day off-peak electricity price

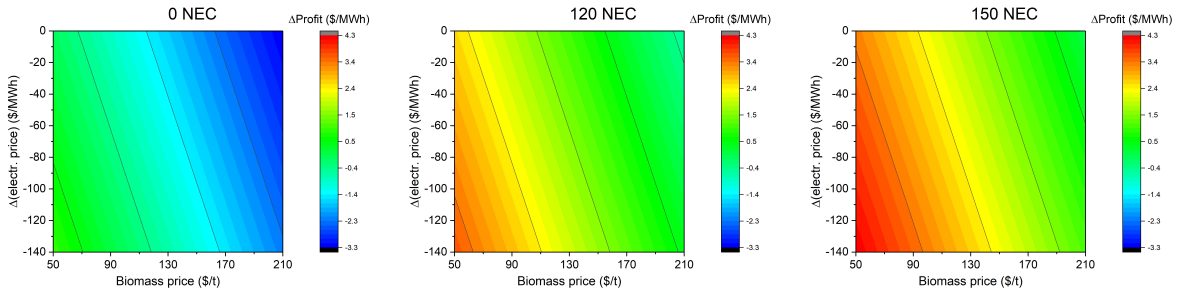


Figure F.13: Sensitivity analysis of the effect of biomass price with NEC auctioned at different prices, and difference of day off-peak electricity price relative to peak electricity price on the variation of daily profit between the schedule represented in Figure 7.4 a using LOX storage and without LOX storage. LOX storage yields increased daily profits however,the increased benefit from LOX storage becomes less pronounced as NEC are auctioned at higher prices.

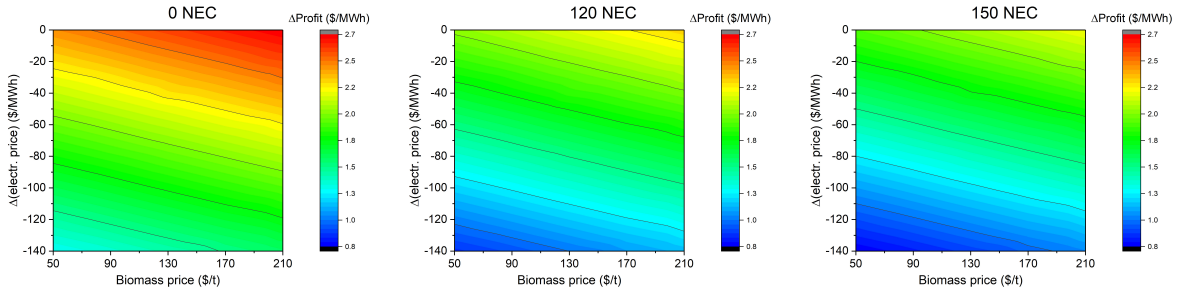


Figure F.14: Sensitivity analysis of the effect of biomass price with NEC auctioned at different prices, and difference of day off-peak electricity price relative to peak electricity price on the variation of daily profit between the schedule represented in Figure 7.4 b using LOX storage and without LOX storage. LOX storage yields increased daily profits however,the increased benefit from LOX storage becomes less pronounced as NEC are auctioned at higher prices.

Night off-peak electricity price

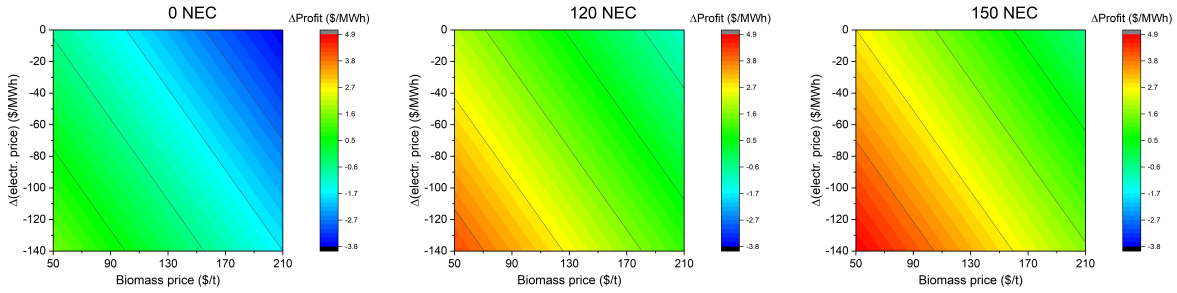


Figure F.15: Sensitivity analysis on varying biomass cost and auctioning NEC at different prices, and night off-peak electricity price with respect to daily peak electricity price on the difference between daily profits for the case with LOX storage and without LOX storage for the schedule represented in Figure 7.4 a. It can also be observed that night electricity price has higher impact on whether to store LOX or not, with this effect less pronounced the higher the price of NEC. Indeed, above \$110/t_{CO_2} storing LOX becomes inadvisable if electricity prices deviate less than \$10/MWh from peak electricity prices.

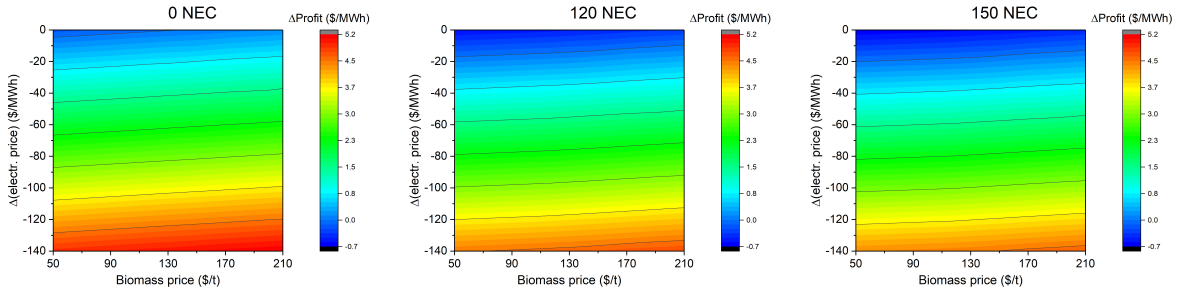


Figure F.16: Sensitivity analysis on varying biomass cost and auctioning NEC at different prices, and night off-peak electricity price with respect to daily peak electricity price on the difference between daily profits for the case with LOX storage and without LOX storage for the schedule represented in Figure 7.4 b. It can also be observed that night electricity price has higher impact on whether to store LOX or not, with this effect less pronounced the higher the price of NEC. Indeed, above \$110/t_{CO_2} storing LOX becomes inadvisable if electricity prices deviate less than \$10/MWh from peak electricity prices.

Day and night off-peak electricity price

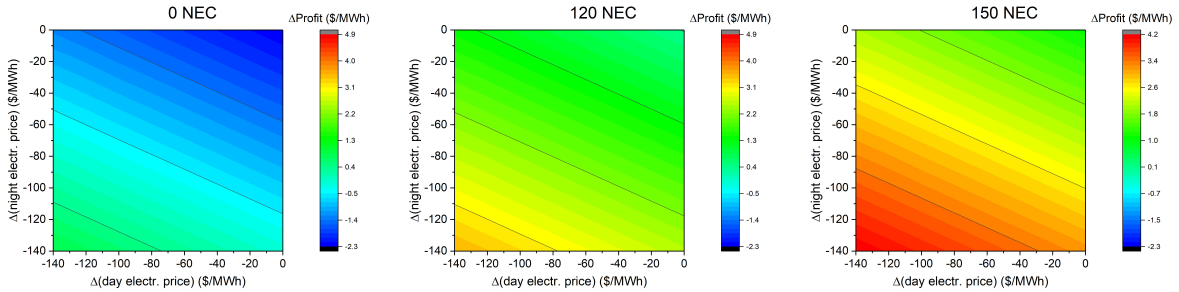


Figure F.17: Sensitivity analysis of night and day off-peak electricity prices relative to peak electricity price and their effect on the difference of daily profit between the case of LOX storage and without storage for an oxy-combustion process firing biomass with cost $117/t and auctioning NEC at different prices for the schedule represented in Figure 7.4 a. LOX storage is preferable when no NEC are being auctioned. However, LOX storage becomes less attractive as NEC start being auctioned. The higher the electricity prices, the greater the profit. It must be noted that day off-peak electricity price variation has a greater impact on profit.

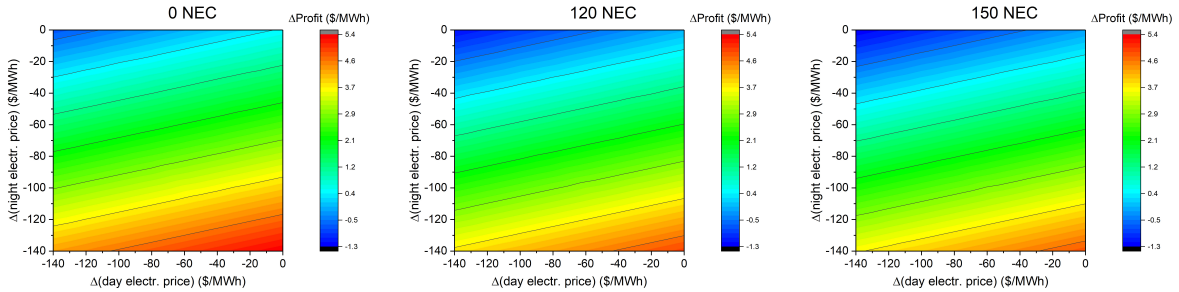


Figure F.18: Sensitivity analysis of night and day off-peak electricity prices relative to peak electricity price and their effect on the difference of daily profit between the case of LOX storage and without storage for an oxy-combustion process firing biomass with cost $117/t and auctioning NEC at different prices for the schedule represented in Figure 7.4 b. LOX storage is preferable when no NEC are being auctioned. However, LOX storage becomes less attractive as NEC start being auctioned. Here, the night off-peak electricity price has a greater impact on whether LOX storage should be considered or not. Indeed, LOX storage should be considered if night off-peak electricity price is within $20/MWh lower than peak electricity price, especially if day off-peak electricity prices are low. However, this is unlikely to occur, since it would require day off-peak prices be lower than night off-peak prices.